IAEA TECDOC SERIES

Benchmark Analyses on the Control Rod Withdrawal Tests Performed during the PHÉNIX End-of-Life Experiments

IAEA

International Atomic Energy Agency

BENCHMARK ANALYSES ON THE CONTROL ROD WITHDRAWAL TESTS PERFORMED DURING THE PHÉNIX END-OF-LIFE EXPERIMENTS

The following States are Members of the International Atomic Energy Agency:

AFGHANISTAN	GHANA	PAKISTAN
ALBANIA	GREECE	PALAU
ALGERIA	GUATEMALA	PANAMA
ANGOLA	HAITI	PAPUA NEW GUINEA
ARGENTINA	HOLY SEE	PARAGUAY
ARMENIA	HONDURAS	PERU
AUSTRALIA	HUNGARY	PHILIPPINES
AUSTRIA	ICELAND	POLAND
AZERBAIJAN	INDIA	PORTUGAL
BAHAMAS	INDONESIA	QATAR
BAHRAIN	IRAN, ISLAMIC REPUBLIC OF	REPUBLIC OF MOLDOVA
BANGLADESH	IRAQ	ROMANIA
BELARUS	IRELAND	RUSSIAN FEDERATION
BELGIUM	ISRAEL	RWANDA
BELIZE	ITALY	SAN MARINO
BENIN	JAMAICA	SAUDI ARABIA
BOLIVIA	JAPAN	SENEGAL
BOSNIA AND HERZEGOVINA	JORDAN	SERBIA
BOTSWANA	KAZAKHSTAN	SEYCHELLES
BRAZIL	KENYA	SIERRA LEONE
BRUNEI DARUSSALAM	KOREA, REPUBLIC OF	SINGAPORE
BULGARIA	KUWAIT	SLOVAKIA
BURKINA FASO	KYRGYZSTAN	SLOVENIA
BURUNDI	LAO PEOPLE'S DEMOCRATIC REPUBLIC	SOUTH AFRICA
CAMBODIA		SPAIN
CAMEROON	LATVIA	SRI LANKA
CANADA	LEBANON	SUDAN
CENTRAL AFRICAN REPUBLIC	LESOTHO	SWAZILAND
	LIBERIA	SWEDEN
CHAD	LIBYA	SWITZERLAND
CHILE	LIECHTENSTEIN	SYRIAN ARAB REPUBLIC
CHINA	LITHUANIA	TAJIKISTAN
COLOMBIA	LUXEMBOURG	THAILAND
CONGO	MADAGASCAR	THE FORMER YUGOSLAV REPUBLIC OF MACEDONIA
COSTA RICA	MALAWI	
CÔTE D'IVOIRE	MALAYSIA	TOGO
CROATIA	MALI	TRINIDAD AND TOBAGO
CUBA	MALTA	TUNISIA
CYPRUS	MARSHALL ISLANDS	TURKEY
CZECH REPUBLIC	MAURITANIA	UGANDA
DEMOCRATIC REPUBLIC OF THE CONGO	MAURITIUS	UKRAINE
	MEXICO	UNITED ARAB EMIRATES
DENMARK	MONACO	UNITED KINGDOM OF GREAT BRITAIN AND NORTHERN IRELAND
DOMINICA	MONGOLIA	
DOMINICAN REPUBLIC	MONTENEGRO	
ECUADOR	MOROCCO	UNITED REPUBLIC OF TANZANIA
EGYPT	MOZAMBIQUE	
EL SALVADOR	MYANMAR	UNITED STATES OF AMERICA
ERITREA	NAMIBIA	URUGUAY
ESTONIA	NEPAL	UZBEKISTAN
ETHIOPIA	NETHERLANDS	VENEZUELA
FIJI	NEW ZEALAND	VIET NAM
FINLAND	NICARAGUA	YEMEN
FRANCE	NIGER	ZAMBIA
GABON	NIGERIA	ZIMBABWE
GEORGIA	NORWAY	
GERMANY	OMAN	

The Agency's Statute was approved on 23 October 1956 by the Conference on the Statute of the IAEA held at United Nations Headquarters, New York; it entered into force on 29 July 1957. The Headquarters of the Agency are situated in Vienna. Its principal objective is "to accelerate and enlarge the contribution of atomic energy to peace, health and prosperity throughout the world".

IAEA-TECDOC-1742

BENCHMARK ANALYSES ON THE CONTROL ROD WITHDRAWAL TESTS PERFORMED DURING THE PHÉNIX END-OF-LIFE EXPERIMENTS

REPORT OF A COORDINATED RESEARCH PROJECT 2008–2011

INTERNATIONAL ATOMIC ENERGY AGENCY
VIENNA, 2014

COPYRIGHT NOTICE

All IAEA scientific and technical publications are protected by the terms of the Universal Copyright Convention as adopted in 1952 (Berne) and as revised in 1972 (Paris). The copyright has since been extended by the World Intellectual Property Organization (Geneva) to include electronic and virtual intellectual property. Permission to use whole or parts of texts contained in IAEA publications in printed or electronic form must be obtained and is usually subject to royalty agreements. Proposals for non-commercial reproductions and translations are welcomed and considered on a case-by-case basis. Enquiries should be addressed to the IAEA Publishing Section at:

Marketing and Sales Unit, Publishing Section
International Atomic Energy Agency
Vienna International Centre
PO Box 100
1400 Vienna, Austria
fax: +43 1 2600 29302
tel.: +43 1 2600 22417
email: sales.publications@iaea.org
http://www.iaea.org/books

FOREWORD

The IAEA supports Member State activities in advanced fast reactor technology development by providing a major fulcrum for information exchange and collaborative research programmes. The IAEA's activities in this field are mainly carried out within the framework of the Technical Working Group on Fast Reactors (TWG-FR), which assists in the implementation of corresponding IAEA activities and ensures that all technical activities are in line with the expressed needs of Member States. In the broad range of activities, the IAEA proposes and establishes coordinated research projects (CRPs) aimed at improving Member States' capabilities in fast reactor design and analysis.

An important opportunity to conduct collaborative research activities was provided by the experimental campaign run by the French Alternative Energies and Atomic Energy Commission (CEA, Commissariat à l'énergie atomique et aux énergies alternatives) at the PHÉNIX, a prototype sodium cooled fast reactor. Before the definitive shutdown in 2009, end-of-life tests were conducted to gather additional experience on the operation of sodium cooled reactors. Thanks to the CEA opening the experiments to international cooperation, the IAEA decided in 2007 to launch the CRP entitled Control Rod Withdrawal and Sodium Natural Circulation Tests Performed during the PHÉNIX End-of-Life Experiments.

The CRP, together with institutes from seven States, contributed to improving capabilities in sodium cooled fast reactor simulation through code verification and validation, with particular emphasis on temperature and power distribution calculations and the analysis of sodium natural circulation phenomena. The objective of this publication is to document the results and main achievements of the benchmark analyses on the control rod withdrawal test performed within the framework of the PHÉNIX end-of-life experimental campaign.

The IAEA expresses its appreciation to all participants in the CRP for their dedicated efforts in preparing this publication. The IAEA officer responsible for this publication was S. Monti of the Division of Nuclear Power.

CONTENTS

1. INTRODUCTION

1.1. OBJECTIVE OF THE CRP

Before the definitive shutdown of the prototype sodium cooled fast reactor Phénix, occurred in the year 2009, the French Commissariat à l'Energie Atomique et aux Energies Alternatives (CEA), together with Electricité de France (EdF) and AREVA, decided to carry out a final set of experimental tests, in order to gather data and additional knowledge on relevant aspects of the operation of pool type sodium cooled fast reactors (SFR). The Phénix end-of-life tests programme allowed the systematic and comprehensive collection of the expertise gained in the field of fast reactor technology from 35 years of reactor operation.

Recognizing the unique opportunity offered by this programme, and thanks to the CEA readiness to open it for international collaboration, in 2007 the IAEA, within the framework of the Technical Working Group on Fast Reactors (TWG-FR) activities, decided to establish a coordinated research project (CRP) devoted to 'Control rod withdrawal and sodium natural circulation tests performed during the Phénix end-of-life experiments'.

The overall objective of the CRP was to improve the participants' analytical capabilities in various fields of research and design of sodium cooled fast reactors. A necessary condition towards achieving this objective is a wide international verification and validation effort of the analysis methodology and codes currently employed in the fields of fast reactor neutronics, thermal hydraulics and plant dynamics.

More specifically, the CRP aimed at improving SFR modeling and simulation methods and design capabilities in the field of temperature and power distribution evaluation, as well as of the analysis of sodium natural circulation phenomena.

Apart from the general outcome of enhanced international team building and technical cooperation, the CRP was expected to have the following outcomes:

— Improved understanding of fast reactors neutronics and thermal hydraulics;

— Improved understanding of the methodology employed to simulate fast reactors (data and computer codes);

— Improved verification and validation status of this methodology.

Two Phénix end-of-life tests were analysed, the 'control rod withdrawal test' and the 'sodium natural circulation test'.

The results of the part of the CRP devoted to benchmark analyses on the 'sodium natural circulation test' were already published by the IAEA in 2013 [1]. This report is intended to document the results of the second part of the CRP, devoted to the benchmark analyses on the 'control rod withdrawal test'.

The safety application of the Generation IV (GEN IV) reactors, with respect to severe accidents potentially leading to generalized core melting, is founded on two complementary directions: an axis of prevention and an axis of mitigation. Among the accidental initiator sequences, inadvertent withdrawal of control rods must be considered. In a fast reactor, control rods are normally inserted in the core at the beginning of cycle to compensate for reactivity swing due to the irradiation cycle. A control rod withdrawal induces two main effects on the core: a general power increase mitigated by thermal feedback effects; power shape deformations around the faulted control rod (the more the core is uncoupled, the stronger the deformation is). The control rod withdrawal test conducted in Phénix was especially designed to study power shape deformations induced by control rod insertion/withdrawal.

1.2. INTEREST OF PHÉNIX CONTROL ROD WITHDRAWAL TEST FOR CODE VERIFICATION AND VALIDATION

For those Member States with relevant fast reactors programmes, it is essential to develop high performance and multipurpose modelling and simulation tools to be employed in the different areas of reactor physics, thermal hydraulics, structural mechanics, and safety analyses among others.

To this end, broad R&D efforts are focused on the reduction of the calculation uncertainties, on the development of more powerful and reliable codes and methods and on the possibilities of coupling of codes in complete multi-physics and multi-scale simulation tools.

In this process, the activities of verification, validation and qualification of calculation codes are fundamental. From this point of view, the experimental data gathered during the Phénix end-of-life experimental campaign represented a unique resource to carry out code-to-code comparisons and validation analyses. In particular, the benchmark on the 'control rod withdrawal' allowed CRP participants to investigate and verify several neutronics calculation codes currently used in the analyses of liquid metal cooled fast reactors, as far as their capability to correctly evaluate the control rod efficiency, the reactivity S-curve and the core power deformation due to insertion and withdrawal of control rods.

The benchmark analyses were carried out comparing the results of the calculation with the large amount of experimental data obtained in Phénix. Moreover, the evaluation of a large set of plant parameters allowed performing accurate code-to-code comparisons, with the overall purpose to understand the critical open issues and recognize gaps which will require further investigations.

1.3. RESEARCH COORDINATION MEETINGS AND CRP PARTICIPANTS

After the definition of the CRP specifications and input data provided by CEA in the course of 2007, three research coordination meetings (RCM) and a conclusive consultants' meeting were held between 2008 and 2012, i.e.:

— First (kick-off) RCM, Vienna, 24–26 September 2008. At this meeting the participants defined the different work packages and responsible persons, and provided indications on the codes and data they plan to use, as well as their intended contributions;
— Second RCM, Marcoule (France), 14–16 October 2009. At this meeting the participants presented and discussed the results of the pre-test calculations and reviewed the status of the agreed upon CRP tasks;
— Third RCM, Argonne (USA), 17–19 November 2010. At this meeting the participants presented and discussed the results of the post-test calculations and defined the structure of the CRP final report.
— Consultants' Meeting, Vienna, 25–27 September 2012. The meeting was devoted to summarizing and comparing the final CRP results, discussing the source of the main discrepancies and the need of future R&D activities, as well as allocating tasks for the preparation of the final CRP TECDOC and the joint paper to be presented at the ICAPP2013 Conference.

The organizations participating in the CRP were: ANL from the USA, CEA and IRSN from France, IGCAR from India, IPPE from the Russian Federation, JAEA from Japan, KIT from Germany and PSI from Switzerland.

2. GLOBAL OVERVIEW OF THE FAST REACTOR PHÉNIX AND THE END OF LIFE PROJECT

Phénix reactor core consists of an array of hexagonal assemblies, with a width across flats of 127 mm, for an overall length of 4.3 m. Each assembly contains 217 pins. The fuel is mixed uranium–plutonium oxide. Within the core, a central fissile zone, comprising two regions, involving different enrichment values, is surrounded by annular fertile zones, and further out by steel reflectors, and lateral neutron shielding rods.

Reactor control was ensured, initially, by means of 6 control rods, involving two distinct drive mechanisms. A further rod, positioned at the core centerline, was added in 1996.

Six intermediate heat exchangers, connected in pairs to the three secondary loops, remove the heat generated by the core. These are straight tube heat exchangers, and primary sodium is circulated along the outside of the tubes.

Auxiliary systems, located outside the vessel, ensure primary sodium storage, filling, draining, and purification functions.

Three secondary loops serve to transfer heat from the intermediate heat exchangers to the steam generators (see Fig. 1).
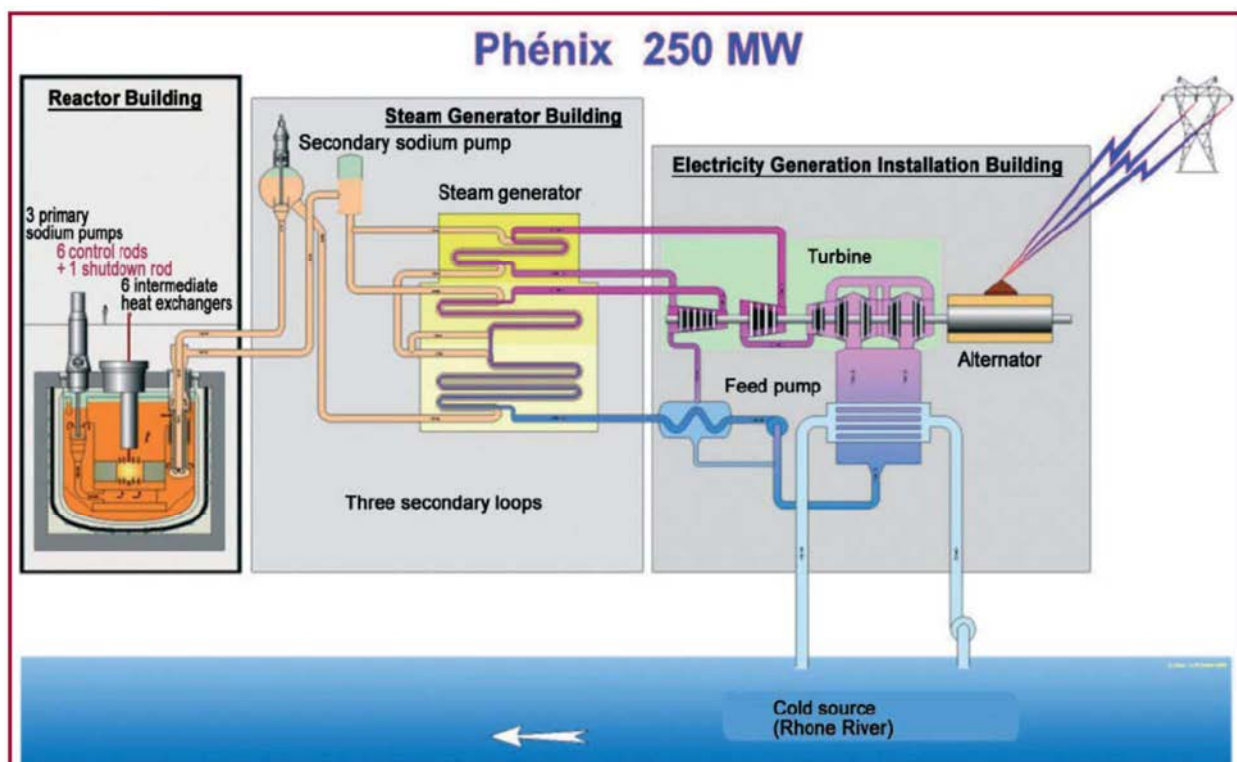
FIG. 1. Principle schematic of the power plant.

Each loop holds some 140 t sodium, and comprises one mechanical sodium circulation pump, located inside the expansion tank, main pipes, 500 mm in diameter, a buffer tank, and auxiliary systems ensuring sodium storage, filling, and purification.

Each secondary loop feeds a steam generator, comprising three stages: evaporator, superheater, and reheater, each of these in turn comprising 12 S-shaped modules (double-S-shaped modules, for the evaporators). Each module comprises 7 tubes, held inside a shell, water circulating inside the tubes, and sodium outside them, countercurrently.

The steam generators are each held inside an enclosure, or casing, strong enough to withstand a sodium leak incident, involving a sodium–water reaction. Stacks, in the upper region, and hatches, in the lower region, make it possible to ensure air circulation inside the casings, providing the means normally used for reactor decay heat removal, during outage periods, when the feedwater plant is not operating.

Refuelling is carried out with the reactor shut down, and with primary sodium temperature standing at 250 °C (see Fig. 2).
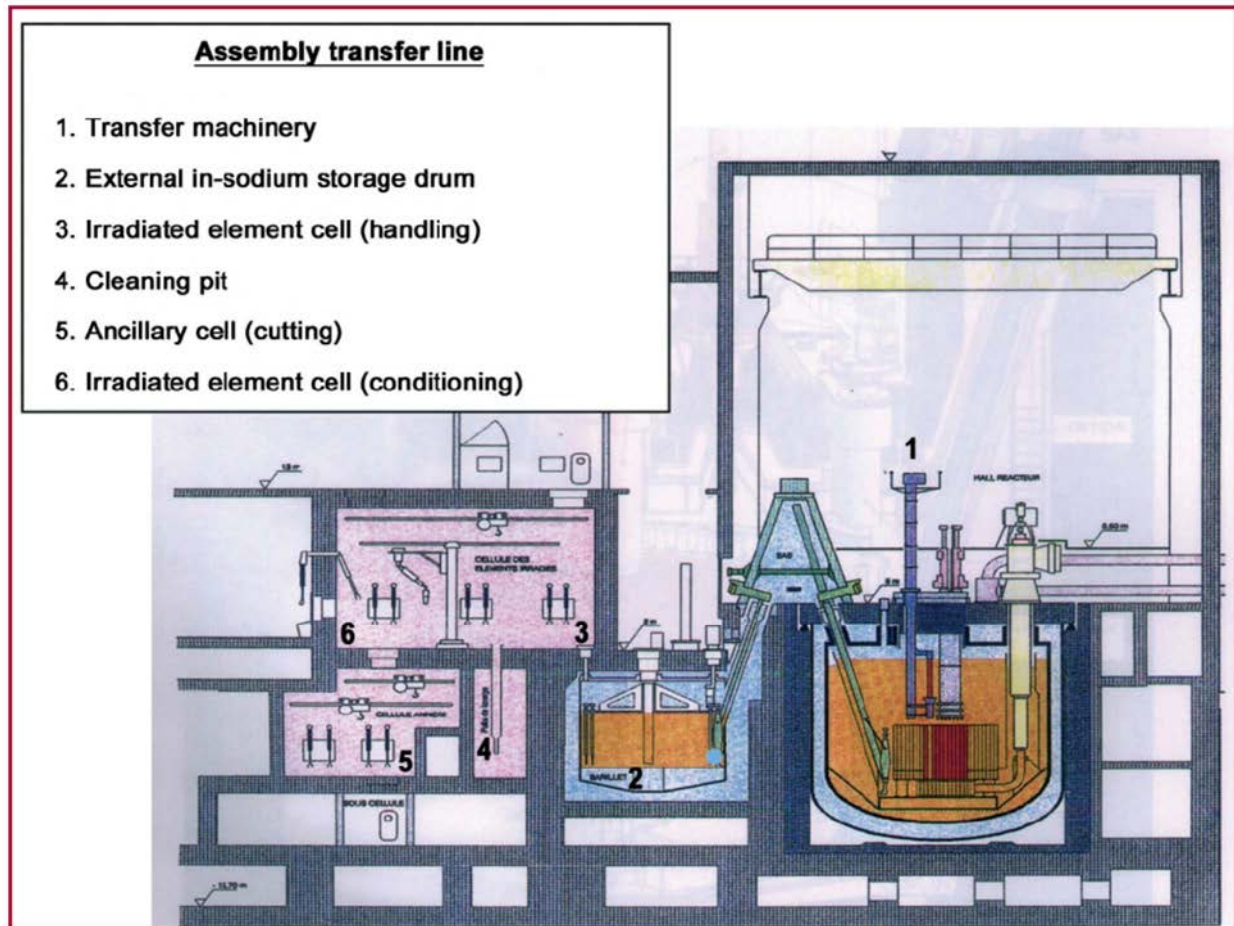
FIG. 2. Schematic of the fuel handling.

Elements in the core are transferred to internal storage positions, to allow for initial decay, and subsequently removed inside a sodium filled pot, using a transfer ramp, to the external storage drum. Internal handling of core elements is effectuated through combined rotations of the rotating plug, and transfer arm.

Once assembly decay heat has fallen off sufficiently, assemblies are transferred to the irradiated element (hot) cell, for the purposes of washing off residual sodium, cutting away assembly structural components, and placing the pins in containers.

These hot cells are also used to carry out post irradiation examinations, and operations to assemble experimental irradiation devices. These cells are fitted with a neutronography reactor.

Fresh assemblies are stored on site, in air, in a storage facility. After inspection, they are loaded into the external storage drum, and subsequently into the reactor, taking the reverse route to irradiated assemblies.

Some technical characteristics are set out in Table 1.

TABLE 1. TECHNICAL CHARACTERISTICS

Parameter	563-MW regime 1974–1993	350-MW regime 1993–2009
Thermal power (MW)	563	345
Gross electrical power (MW)	250	142
Net electrical power (MW)	233	129
Neutron flux at core centerline (n/cm2·s)	$7 \cdot 10^{15}$	$4.5 \cdot 10^{15}$
Primary sodium core outlet temperature (°C)	560	530
Primary sodium core inlet temperature (°C)	400	385
Secondary sodium SG inlet temperature (°C)	550	525
Superheated steam temperature (°C)	512	490
Turbine HP cylinder steam pressure (bar)	163	140

2.1. OVERVIEW OF THE 'END OF LIFE TESTS' PROJECT

After 35 years of operation, a campaign of end-of-life tests was performed at Phénix before the final shutdown [1– 4]. The final list of tests was established after collecting several proposals from 2007. Then, the phase of studies in support of the individual safety reports and the development of the specific devices was started. In agreement with the French Nuclear Safety Authority, a training programme for the operating teams was set up. It consisted of presenting the operators with the test aims, their sequencing and related risks. To ensure successful testing, this programme also saw the operators take part in drawing up the operational documents, called Trial Instruction Programs, as well as in running sessions on the reactor simulator, when this was possible.

The very first test was carried out in May 2008 but most of them were performed after the end of the last electricity production cycle between May 2009 and January 2010.

These tests aimed at broadening the experimental base for validating neutronics (ERANOS and DARWIN), thermal-hydraulics (TRIO_U and CATHARE) and fuel (GERMINAL) computer codes on the one hand, and on the other hand to provide a better understanding of the automatic shutdowns caused by a sudden drop in reactivity that had occurred in 1989 and 1990.

Ten different tests of four types were performed [3].

Thermal hydraulic tests		Fuel test	
1.	Asymmetrical transient	8.	Partial fuel melting
2.	Natural convection		
Core physics tests		**Negative reactivity transient investigations tests**	
3.	Decay heat	9.	Experimental carrier/Blankets interactions
4.	Control rod offsetting	10.	Core flowering
5.	Subassembly reactivity worth		
6.	Control rod worth		
7.	Sodium void		

2.2. THERMAL-HYDRAULICS

Two tests were performed in the thermal-hydraulics area: asymmetrical regimes and natural convection. Two specific instrumented devices equipped with several tenths of thermocouples were added to the reactor for these two thermal-hydraulic tests, one in the hot plenum and the other one in the cold plenum to measure the axial sodium temperature profile.

For the first test, the trip of one of the two secondary pumps produced *azimuthal and axial dissymetries* in the cold plenum. The lack of cooling created a hot shock in the cold plenum of the primary vessel at the outlet of the two intermediate heat exchangers connected to the corresponding secondary circuit. The axial temperature distributions were recorded showing the buoyancy influence on the flow pattern. The azimuthal distribution was also recorded by the standard reactor instrumentation giving a large data base for the qualification of thermal-hydraulics codes.

For the *natural convection* test, the primary pumps were tripped from a 30% nominal power regime. Decay heat was first removed by thermal losses on secondary piping and then by the air natural circulation in the steam generators casing. In the final phase of the test, one secondary pump was also tripped, the other one remaining in operation for safety reasons. Specific sensors were added on the steam generators casing to measure air temperatures and velocities at different positions [5].

2.3. CORE PHYSICS

In the core physics area, five tests were performed [4]:

Measurement of individual subassembly reactivity worth. By placing successively in the core central position fresh and used fuel and fresh and used blankets, the effect of burnup on the reactivity was measured by reaching the control rod critical position for each case. The separate effect of fissile and fission products inventories in each case were discriminated by measuring similar fresh fuel subassemblies having different plutonium contents. One additional measurement was done by placing a sodium filled subassembly.

Six different configurations were studied:

— 1 high burn up standard fuel sub-assembly;
— 1 fresh standard fuel sub-assembly;
— 1 experimental fuel sub-assembly (with reduced Pu mass);
— 1 sub-assembly without fissile material (only sodium and steel);
— 1 fresh blanket sub-assembly;
— 1 high burn up blanket sub-assembly.

Decay heat measurements. The measurements were performed for a wide range of time from one hour to twelve days after the scram by doing thermal balances with the reactor on isothermal conditions. The system behavior is represented by the equation below:

$$I \, d\Theta/dt = D + P - L \tag{1}$$

I: Thermal inertia of the whole system,

Θ: Mean sodium temperature,

D: Decay heat,

P: Supplied power by other sources (pumps, etc),

L: Thermal losses.

By measuring the sodium mean temperature as a function of time, the core decay heat was calculated with this equation.

Control rod withdrawal. Several control rod position configurations were explored to create distorted radial power distributions at nominal power. Individual subassemblies powers on these configurations were deduced from the sub-assembly (S/A) outlet temperatures measurements. The aim of the 'Operating with offset rods' test was to study the influence of control rod position on the spatial distribution of power within the core. During the test the control rods were progressively offset in relation to each other while maintaining constant the total power. The report is dedicated to the analysis of this test.

Several *control rod worth measurement* methods were implemented in order to improve the knowledge of control rod worth in the upper part of the core:

— Static methods when the reactor is subcritical;
— Rod balancing when the reactor is critical;
— Rod drop measurements (partial rod drop).

The assessment of the *reactivity effect produced by a gas bubble into the core* is a key issue in the safety studies of future sodium cooled fast neutron reactors. The final tests of the Phénix reactor represented a unique opportunity to experimentally check and to validate calculations made by the neutronic codes for such safety studies. The principle of the test was to simulate the displacement of a gas bubble in the core by replacing the B_4C absorber contained in a control rod by a helium filled tank.

Several measurement methods were used to determine the reactivity effect of this helium tank, the reactor being critical:

— Measurements by balancing the helium rod against the control rod;
— Dynamic parameter measurements, monitoring the change in reactivity according to the continuous displacement of the helium 'rod';
— Measurements by helium 'rod' drop.

2.4. FUEL TEST

In the fuel behaviour area, a 'power to melt test' was done using three specially designed capsules containing MOX fuel pins (Fig. 3), at different burnups (0, 4 and 8at/%) and with different geometries on a six minutes duration power transient from 86 % to 106 % nominal power.

Subsequent post irradiation examinations are needed to obtain the whole results.

A fuel melted fraction of approx 10% in mass is expected locally at the maximum neutron flux axial level for some pins.
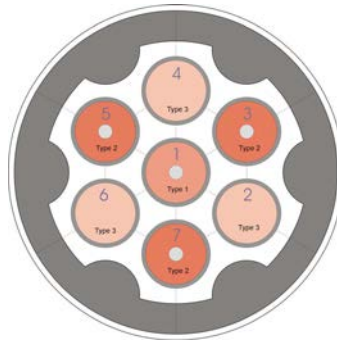
FIG. 3. Rig for partial fusion of the fuel.

These results will be used to complete the validation database of the fuel thermo-mechanical behavior code GERMINAL.

2.5. NEGATIVE REACTIVITY TRANSIENT (AURN) INVESTIGATIONS TESTS

The analysis of the AURN transients performed in the early 1990s had concluded that the most likely mechanism for a fast decrease of the core reactivity was a radial core deformation named core 'flowering'. The investigated scenario producing such flowering is based on the neutronic and thermal-hydraulic interaction between a moderated experimental carrier ('DAC' subassembly) and the surrounding blanket subassemblies is considered like most plausible (Fig. 4).
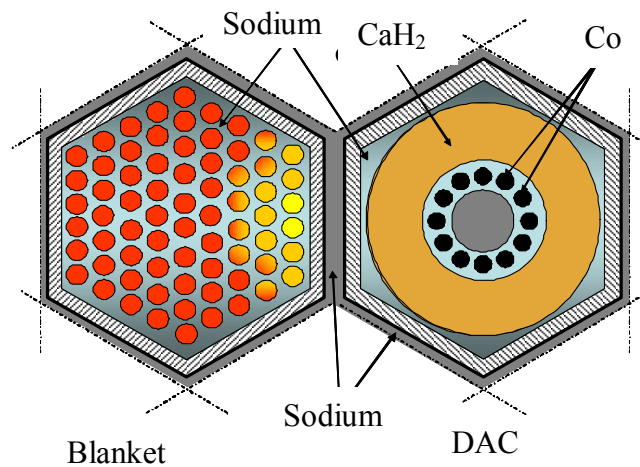
FIG. 4. 'Blanket – DAC' configuration.

The conjunction of the increased power in the blankets due to neutron moderation and the low sodium flow in the 'DAC' was supposed to lead to sodium boiling. The collapse of sodium vapor bubbles induces the core flowering and the correspondent negative reactivity. The scenario was explored by reproducing a similar configuration at 2/3 power over flow conditions. Special measurements of the sodium flowrate inside the *experimental DAC S/A* were carried out with an Eddy current flowmeter.
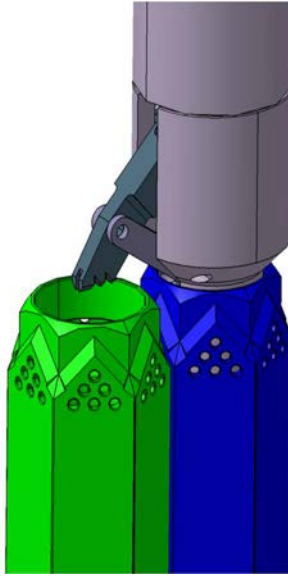
FIG. 5. Special device for measurements of flowrate inside DAC S/A and of outlet sodium temperatures on blanket and DAC S/As.

3. DESCRIPTION OF THE PHÉNIX CONTROL ROD SHIFT TEST

The control rod shift test was one of the various Phénix end-of-life tests performed in 2009. The main goal was to determine the impact of a control rod insertion and extraction on the radial power distribution in the fissile core at nominal power. Several configurations were explored during the test. Individual subassembly powers for these configurations were deduced from the sub-assemblies outlet temperatures measurements [6].

3.1. DESCRIPTION OF THE INSTRUMENTATIONS USED FOR THE TEST

No specific instrumentation was developed for this test. Only classic instrumentations such as the in/out vessel neutronic chambers and the S/A outlet thermocouples were used. Fig. 6 shows the different locations of these instrumentations.
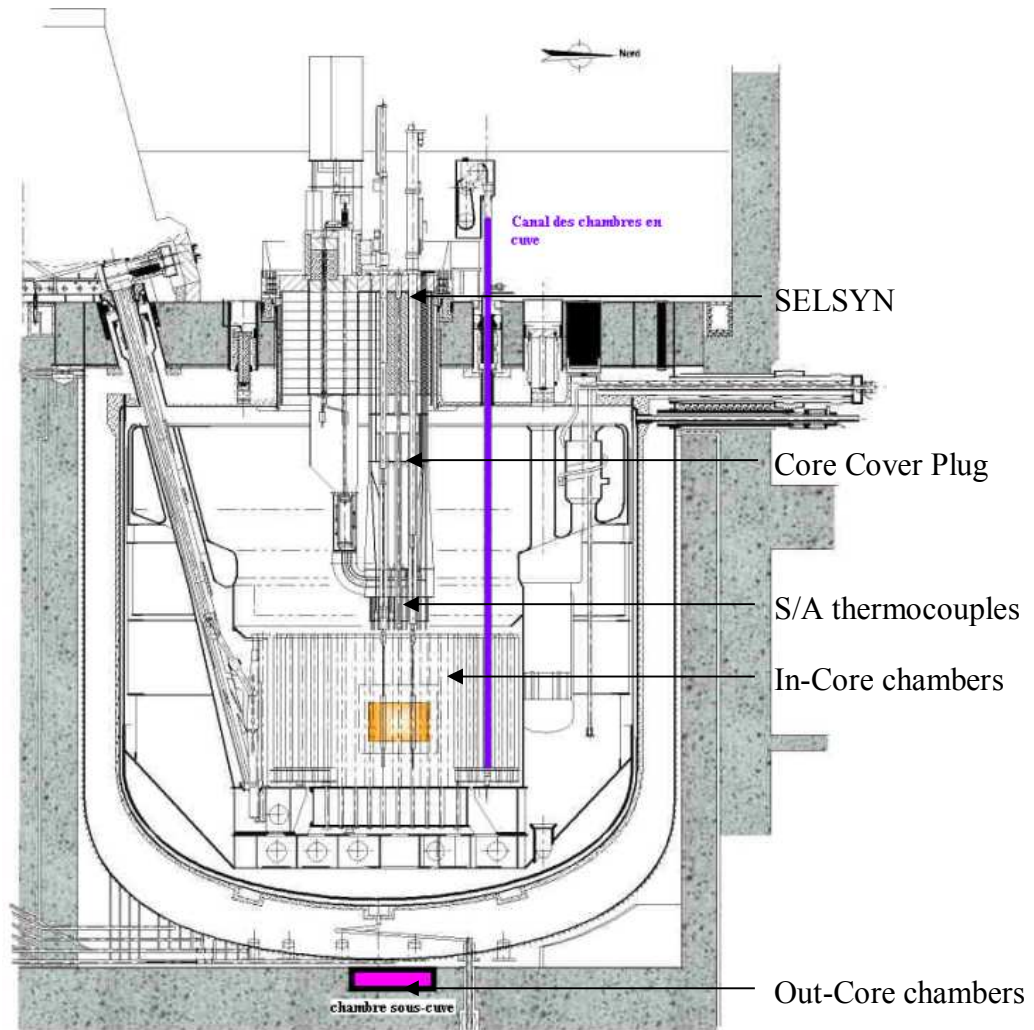
FIG. 6. Location of the instrumentations.

3.1.1. Temperature measurements

In order to detect an abnormal temperature elevation in the core, S/As are equipped with thermocouples (type K – Chromel/Alumel) located at the top of their head. The monitored S/As are shown on Fig. 7 (120 S/As in yellow). Thermocouples are attached to a grid of the core cover plug (Fig. 7), so there is no mechanical link with S/A. They are located at 75 mm (at 560 °C) of the S/A's outlet (Fig. 8).
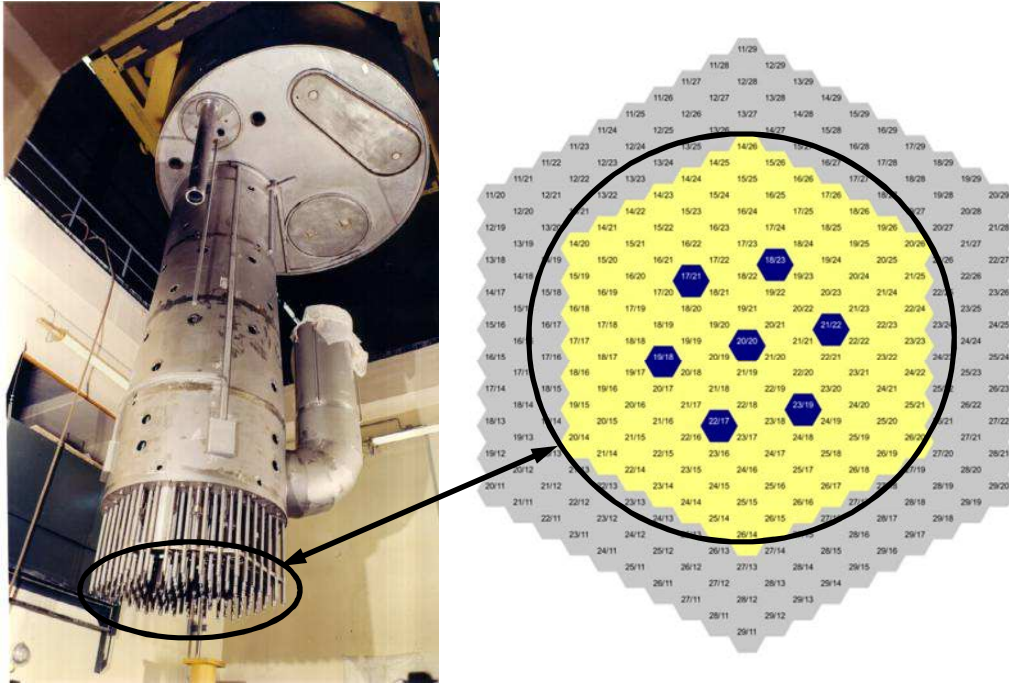
FIG. 7. Location of the S/A thermocouples on the core cover plug.
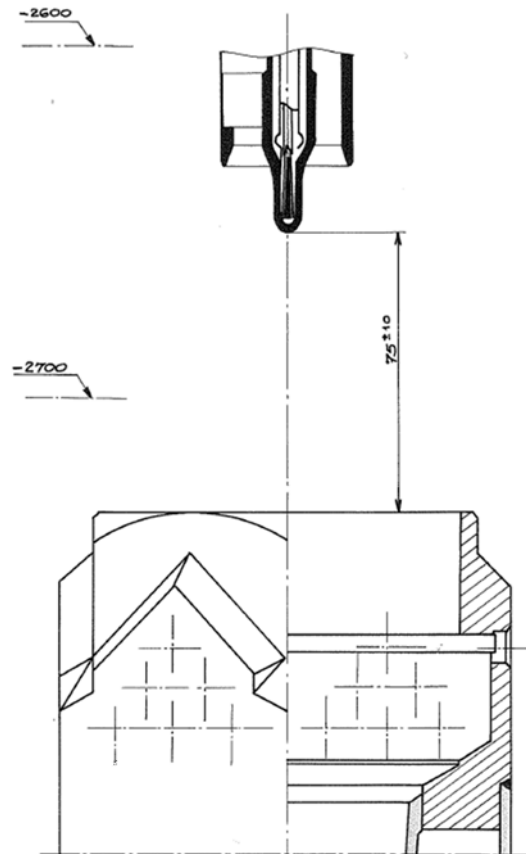
FIG. 8. Location of the thermocouples on the S/As.

3.1.2. Neutronic instrumentation

In-vessel chambers are used to monitor chain reaction during off-power operation state and reactor divergence. These fission chambers are not usable during power operation.

Out-vessel chambers are also used to monitor flux and power of the reactor. There are different kinds of chambers: starting chambers (boron proportional counter) and power chambers (boron ionization chamber with gamma correction). Starting chambers are used during low power operation state such as 'control rod measurement tests'. Power chambers are used during full power operation state.

Only starting chambers were used in the first part of the test, in order to calibrate the efficiency of the control rods, and power chambers were used during the second part, in order to maintain the power constant.

3.1.3. SELSYN instrumentation

Self-synchronizing devices (SELSYN) were used in Phénix to measure the fine position of the control rod mechanism which drives the lower part of the absorbing media. It does not take into account the Core/Vessel/Control rods differential dilatation. Fig. 9 presents a schematic view of this important phenomenon.

The vessel of the reactor and the control rods are linked to the ground by their upper parts. When the reactor is heating, there is an axial thermal expansion of these elements toward the bottom of the reactor. Fuel rods are linked to the diagrid of the reactor, so the fuel axial dilatation is directed toward the top of the reactor. Finally, all these different dilatations create an insertion of the absorbing part of the control rod in the core when reactor is heating.

The SELSYN give the position of the lower part of the absorbent, but the calibration was done in an isotherm state (at 250 °C). So, the value given by the SELSYN at full power state was corrected by -27.6 mm, in order to have the real position of the lower part of the absorbent from the bottom of the fissile core.
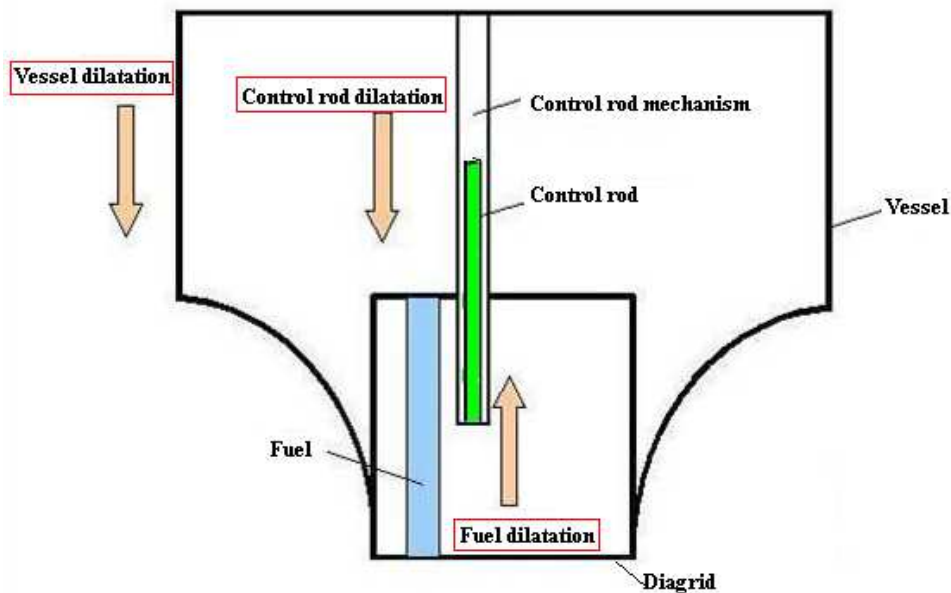
FIG. 9. Overview of the core/vessel/control rods differential dilatation.

3.2. TEST DESCRIPTION

The test was divided in two phases. During the first phase, the efficiency of the two involved control rods was measured. This phase was done when the reactor was at low power state. Some days after the second phase was dedicated to the deformation of radial power map during a full power state. Several control rod position configurations were explored to create distorted radial

power distributions at nominal power. Individual subassemblies powers on these configurations were deduced from the S/A outlet temperature measurements. During the test the control rods n°1 and n°4 were progressively offset in relation to each other while maintaining constant the total power. Sodium flow rate remains constant during the entire test.

Four control rod configurations were studied:

1. six control rods in a bank, within ±2 mm;
2. five rods in a bank and one rod offset to –266 mm in relation to the bank;
3. four rods in a bank, one rod offset to –229 mm and another to +278 mm;
4. five rods in a bank and one rod offset to +324 mm in relation to the bank.

3.2.1. Control rod worth measurements (off-power test)

In order to measure the efficiency of the two involved control rods, the balancing method was used during a low power state of the reactor on 18 May 2009. Fig. 10 shows a schematic overview of this method.

During the initial state, with the reactor in a critical stable state with a low power (~50 kW), the control rod n°1 (CR #1) is totally inserted in the core and the CR #4 is totally extracted. The first step corresponds to an insertion of the CR #4. The amount of the insertion of anti-reactivity could be retrieved based on the application of the inverse kinetic method. Using a succession of steps, it was possible to compute the S-curves for the two control rods and their total worth.
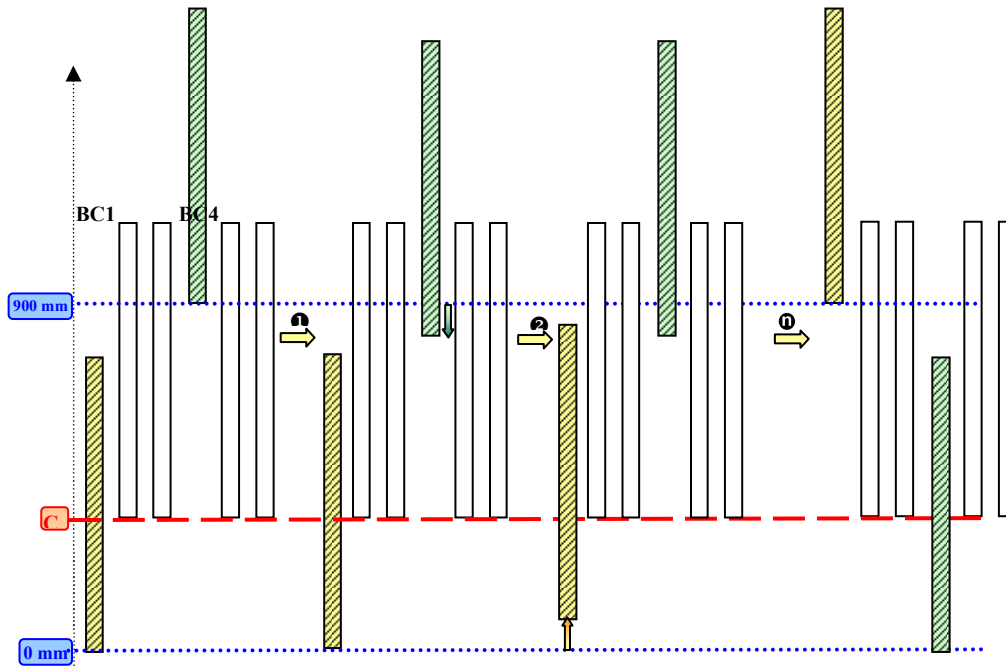
FIG. 10. Schematic view of the balancing method.

3.2.2. Control rod shift (on-power test)

This second part of the test was performed on two days (June 15th 2009 to June 16th 2009).

3.2.2.1. Initial state

In order to gain safety margins on the temperatures of the core intern structures, the speed of the secondary pumps was increased to improve the core cooling. Moreover, the reactor power was decreased to 340 MW(th). The global parameters of the core during the test are given in Table 2.

TABLE 2. INITIAL STATE OF THE REACTOR

	Nominal state	Initial state
Reactor power	350 MW(th)	335.4 MW(th)
Primary pumps speed	540 rpm	540 rpm
Secondary pumps speed	705 rpm	780 rpm
Inlet sodium temperature	380°C	373.5 °C
Outlet sodium temperature	530°C	522.7 °C
Average temperature at the entrance of the IHX (Intermediate Heat Exchanger)	508°C	495°C

All the six control rods are on 'rod bank', that it means that they have the same spatial elevation. The control rods positions are given in Table 3 at full power state corrected by the core/vessel/control rod differential dilatations.

Fig. 11 presents the loading plan of the core during the test. The core is constituted by different S/As:

54 S/A - Inner core (yellow)

56 S/A - Outer core (orange)

86 S/A - Blanket (blue-green)

6 control rods + 1 emergency rod (dark blue)

Shielding & reflector S/A (gray)

Finally, Fig. 12 presents the sodium heating per S/As for the initial state. These values are used in order to compute the power deviation per S/As.
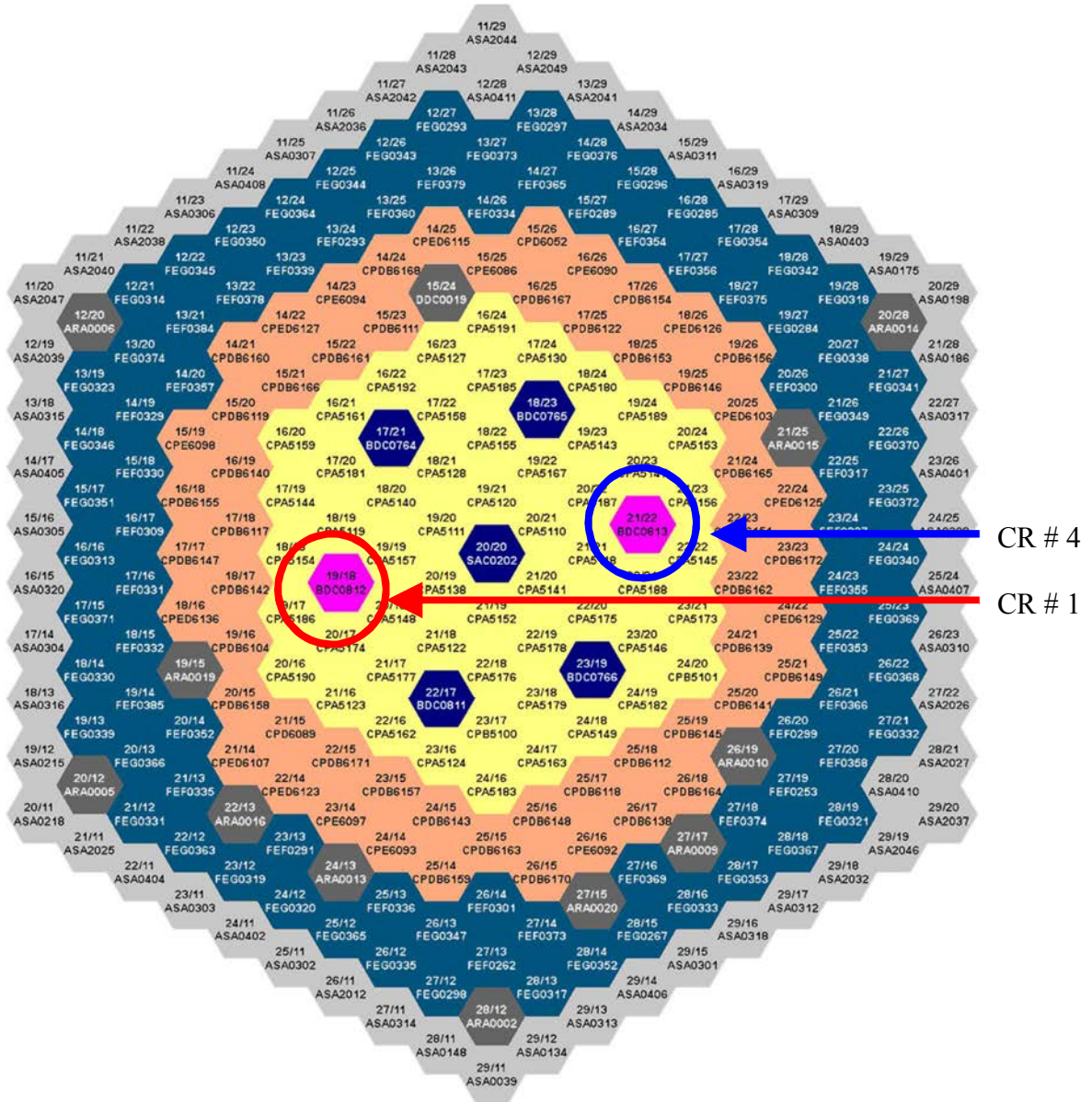
FIG. 11. Loading plan of the core.
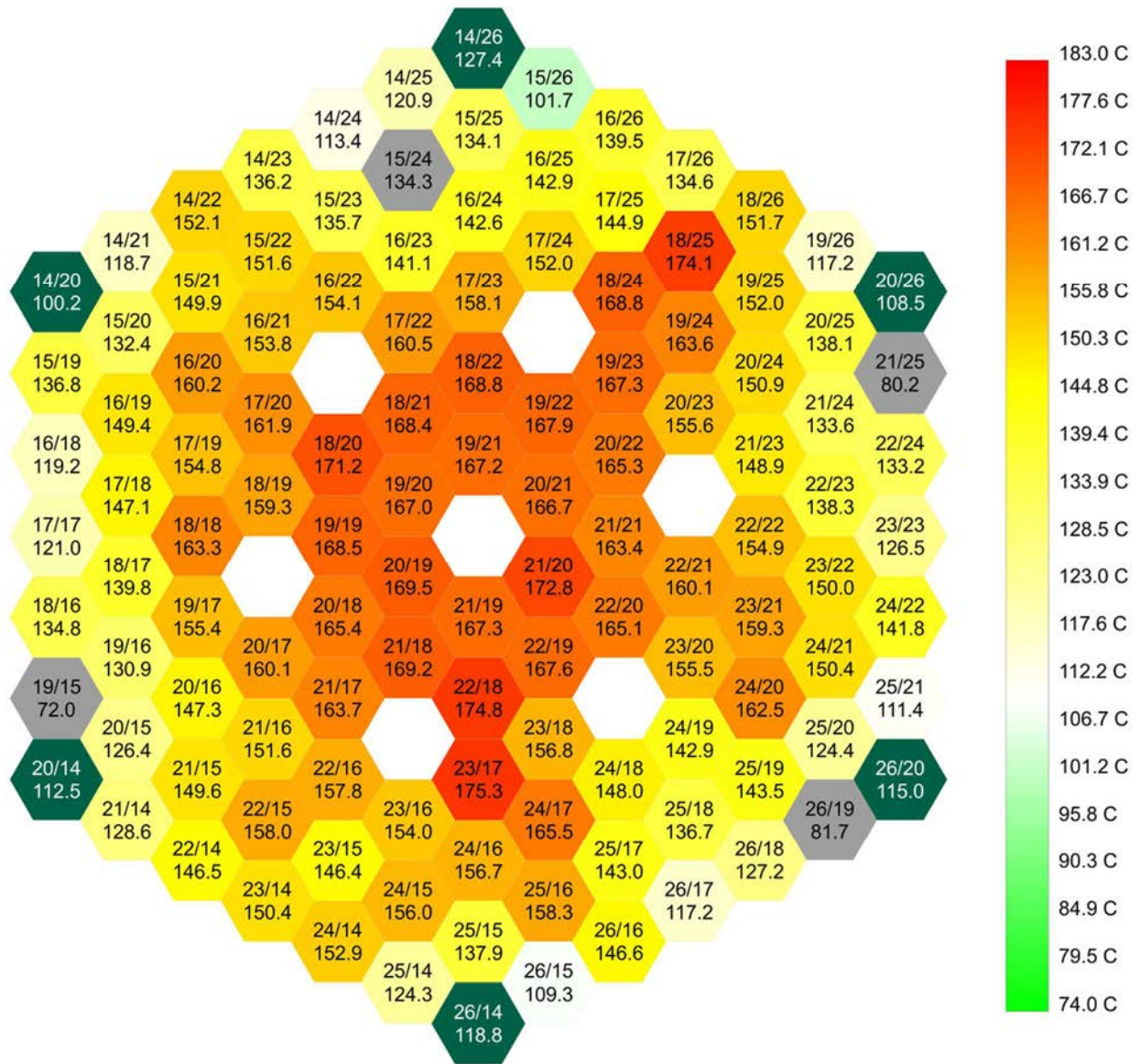
FIG. 12. Sodium heating per S/As - initial state.

3.2.2.2. Tested configurations

During this test, three configurations were tested. Fig. 13 summarizes these configurations.
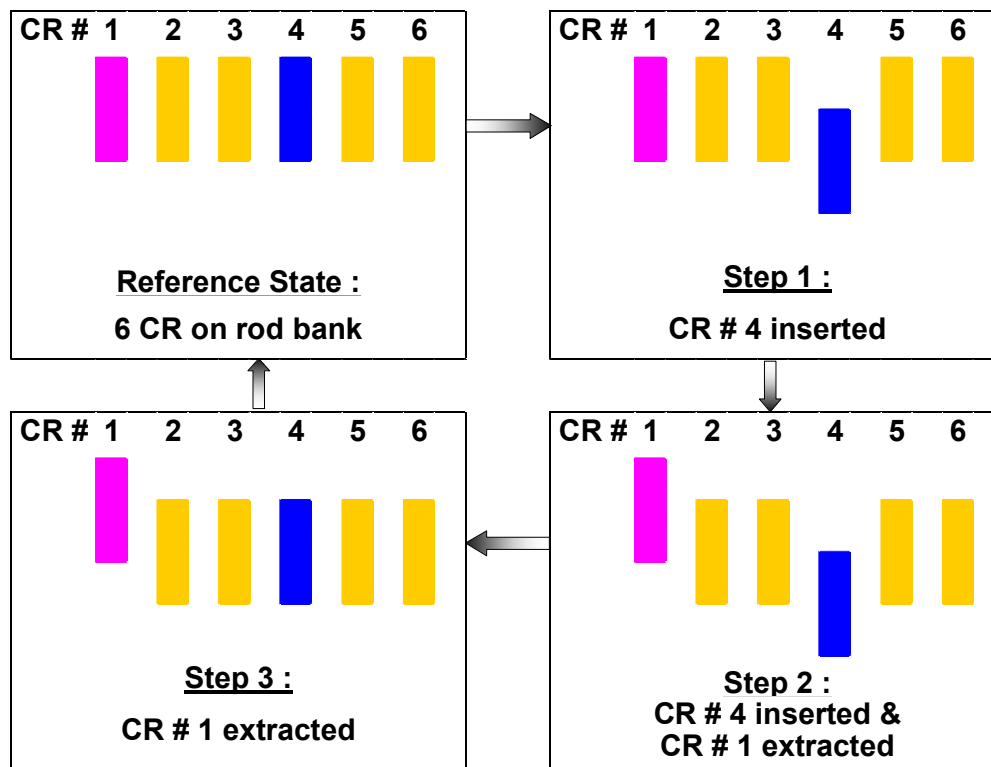
FIG. 13. Schematic overview of the control rods shift.

Table 3 presents reactor's conditions measured during the different steps of the test.

TABLE 3. GLOBAL PARAMETERS OF THE REACTOR DURING THE 5 STEPS

| | Power (MW) | Mean core temperature (°C) | | Control Rod position (mm) | | | | | |
| | | | | 19/18 | 22/17 | 23/19 | 21/22 | 17/21 | 18/23 |
		Inlet	Outlet	CR n°1	CR n°2	CR n°3	CR n°4	CR n°5	CR n°6
Reference State	335.4	373.5	522.7	558,3	557,4	558,0	557,4	557,4	557,6
Step 1	337.0	373.8	523.8	608,5	608,6	606,6	340,8	608,5	607,8
Step 2	338.7	373.8	524.3	848,4	567,7	571,0	340,6	566,3	573,5
Step 3	336.3	373.5	523.2	848,4	523,6	523,4	523,4	523,5	523,5
Final State	335.2	373.3	522.2	559,6	558,7	558,7	559,4	559,5	559,4

Control rod positions are given in Table 3 at full power state and take into account core/vessel/control rod differential dilatations. Note that the origin of Z-axis is 5mm below the fissile core. The uncertainty (at 2σ) on the total power of the reactor is around 5 MW(th).

3.3. TEST RESULTS

3.3.1. Control rods efficiency

Efficiencies of the control rods were estimated with the balancing method which is a compensation method. CR #4 was withdrawn from the bottom to the top of the core whereas CR #1 was alternatively inserted in an opposite movement. The inserted reactivities (positive and negative alternatively) could be retrieved after each elementary rod displacement by inverting the neutron kinetic equations that describe the variations of the neutronic population and the delayed neutron precursor concentrations. The global S-curves were then computed by aggregation of elementary steps for both control rods.

The measured integral worth of CR #1 and CR #4 are 3.9 $ and 3.8 $ respectively, with an effective delayed neutron fraction k_{eff} equal to 325±16 pcm (1pcm = 10^{-5} $\Delta k/k$ with k the neutron multiplication coefficient). Fig. 14 shows the two control rod S-curves. As the two control rods underwent nearly the same ageing, the fact that CR #1 and CR #4 have similar worth illustrates the naturally good symmetry of the flux distribution in the core.
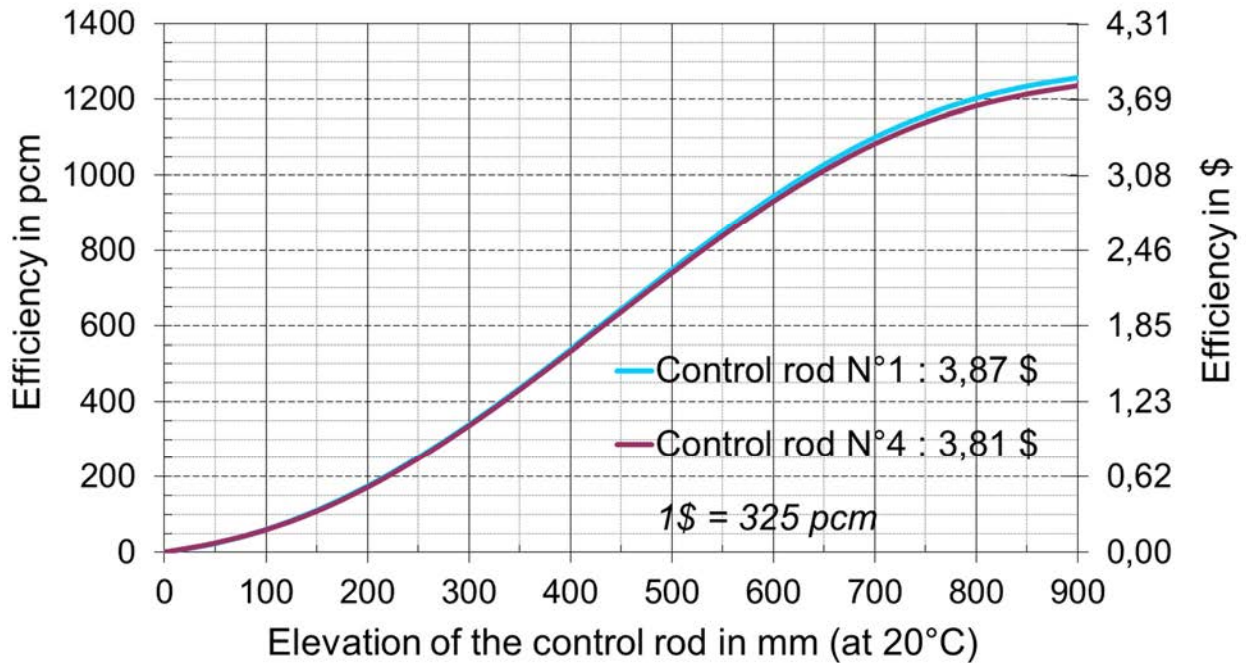
FIG. 14. S-curves of the opposite control rods No 1 and 4[1].

3.3.2. Power shape perturbations (on-power test)

3.3.2.1. Power deviation calculations

Individual powers can be computed with the following equation:

$$P_i = Q_i * C_P(Na) * (T_i - T_e) \tag{2}$$

where:

---

[1] The unit $ corresponds to the value of the Phénix's β_{eff} in pcm.

T_i is the outlet temperatures (°C),
T_e is the inlet temperature of the core (°C),
Q_i is the sodium mass flowrate in S/A (kg/s),
$C_P (Na)$ is the sodium specific heat capacity (J/kg/K),
P_i is the total power per S/As (W).

Note that, heat transfers between sub-assemblies are assumed negligible and are not taken into account in the power balance.

The sodium flow rate remained constant throughout the whole test (there was no action on primary pumps). Moreover, we assumed that flowrate redistribution in the fissile zone due to the change in sodium heating was insignificant. So, relative power deviations $\delta_{rel}(P_i)$ between the reference configuration and the initial one could be computed as follow (in %):

$$\delta_{rel}P_i = \frac{\delta P_i}{P_i^{Initial}} = \frac{Q*Cp*(\Delta T_i - \Delta T_i^{Initial})}{Q*Cp*\Delta T_i^{Initial}} = \delta_{rel}(\Delta T_i)$$

(3)

The power deviation was fully determined by the variation of sodium heating between two configurations. Uncertainties in temperature measurements were made of statistical and systematic uncertainties. The first ones were linked to random disturbance and could be reduced to 0.1 °C thanks to temporal average over a long period (>30 min). The second ones were biases linked to the thermocouples' history (ageing, calibration, thermal-hydraulic neighborhood). These biases could be assumed time-independent and thus cancelled for the power deviation calculations.

3.3.2.2. Results

During the first step of the test, CR #4 was positioned 266 mm under the control rod bank level. According to its S-curve (see Fig. 14), it corresponds to a 'virtual' insertion of nearly -540 pcm. This insertion had the following consequences on the power shape (see Fig. 15):

— in the vicinity of the inserted control rod, a power reduction was observed with a maximal negative deviation of -9.5 ± 1.3 %, corresponding to a variation of sodium heating of (-14.1 ± 1.0) °C. Nearly a third of the core was affected by this cooled area.
— compensation effects, due to constant power, induced a general temperature increase in the opposite part of the core.
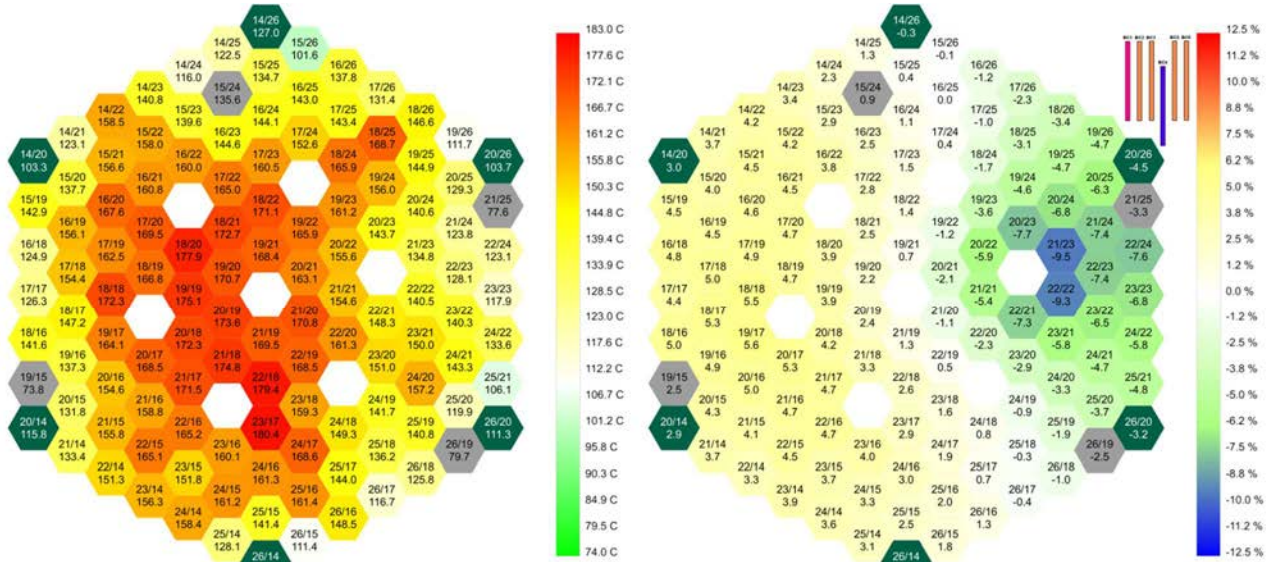
FIG. 15. Sodium heating (a) and power deviation (b) per S/As – step 1: CR No 4 inserted.

For the second step of the test, CR #4 and CR #1 were inserted and withdrawn 229 mm and 278 mm respectively from the control rod bank level, which corresponded to reactivity insertions of -470 pcm and +345 pcm respectively. The impacts on the core were as follows (Fig. 16):

— Close to the inserted control rod, there was a power reduction with a maximal negative deviation of -10.9 ± 1.3 % corresponding to a variation of sodium heating of -16.3 ± 1.0 °C.
— Around the withdrawn control rod, there was a power increase with a maximal positive deviation of +12.1 ± 1.4 % corresponding to a variation of sodium heating of +18.7 ± 1.0 °C.
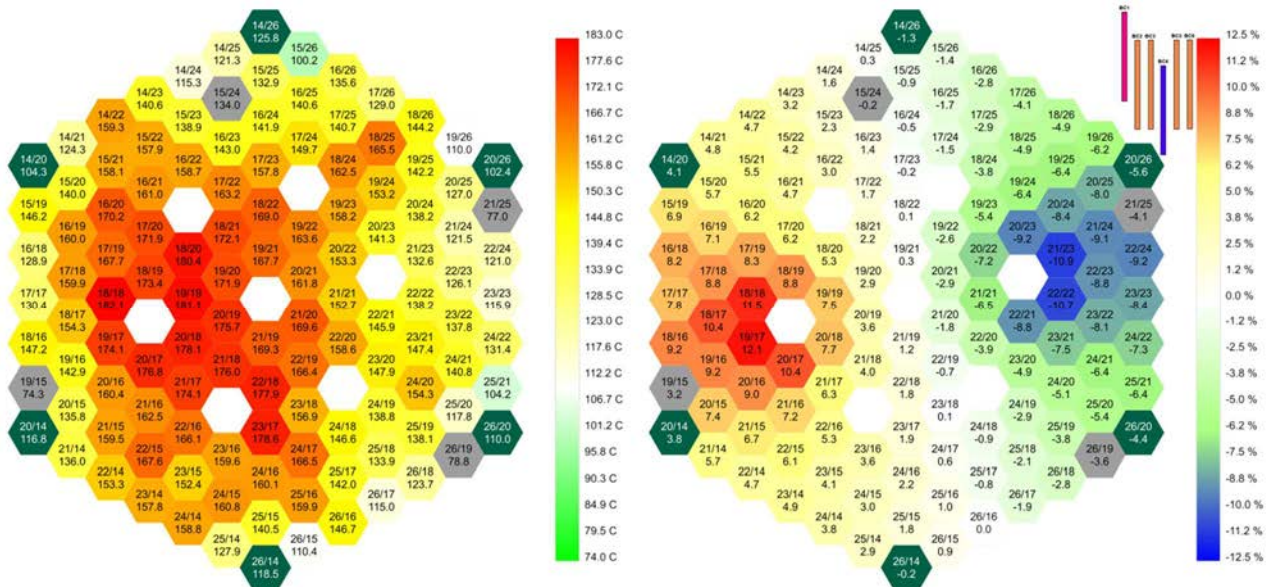
FIG. 16. Sodium heating (a) and power deviation (b) per S/As – step 2: CR No 4 inserted & CR No 1 extracted.

For the third step, CR #1 was positioned 324 mm over the control rod bank level, which corresponded to nearly + 437 pcm. The measured impact is (Fig. 17):

20

— In the vicinity of the withdrawn control rod, there was a power rise with a maximal positive deviation of +9.1 ± 1.4 % corresponding to +14.1 ± 1.0 °C.

— Compensation effects, due to constant power, induced a general temperature decrease in the opposite part of the core.
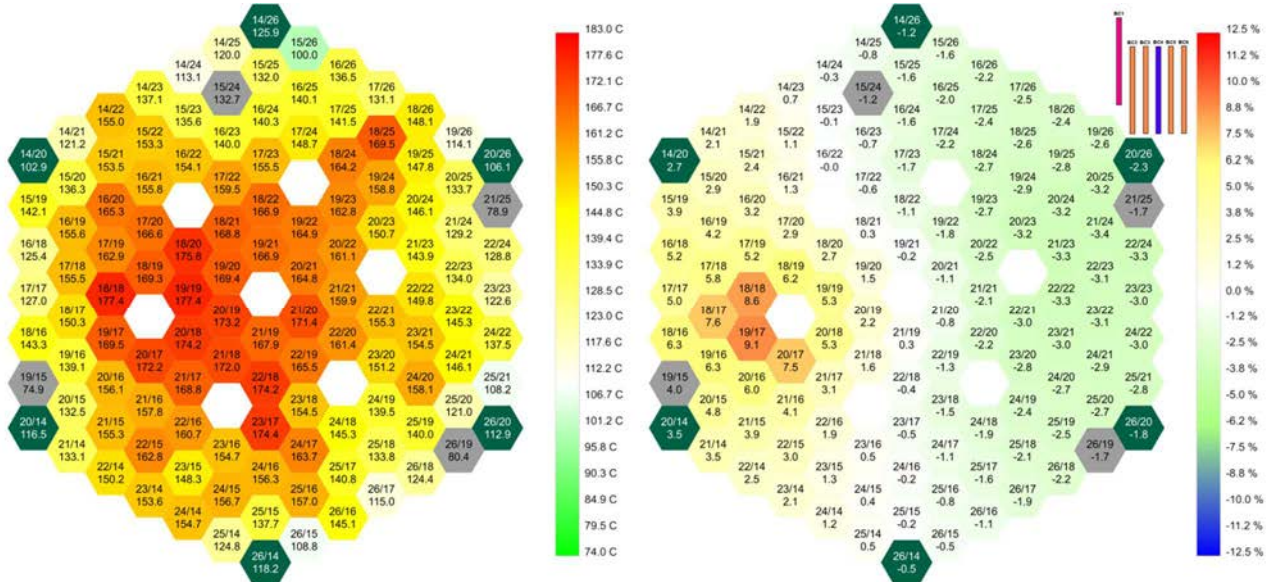
FIG. 17. Sodium heating (a) and power deviation (b) per assemblies – step 3: CR n°1 extracted.

As expected, the maximum deviation of the power shape was reached when both control rods were shifted in opposite directions. This measured deflection of ±12% confirms that the Phénix core cannot be considered as a point reactor (spatial effects cannot be disregarded) despite its relatively small size compared with commercial size reactors in which the neutron diffusion length in the fissile zone is small in comparison with the core diameter (Superphénix, European Fast Reactor, etc.).

4. DESCRIPTION OF THE BENCHMARK SPECIFICATIONS

This section presents the benchmark specifications and the core data needed for neutronic calculations.

4.1. CORE DATA

4.1.1. Geometrical description

Geometrical descriptions given in Section 4.1 are at 20 °C.

4.1.1.1. Fuel and blanket S/A

Fig. 18–19 present an overview of the fissile and blanket sub-assemblies (S/A) in the Phénix reactor. Fig. 20 presents two radial sections of the fuel S/A. The active zone of the fuel S/A is composed by three zones: the upper axial blanket (UAB) which is a fertile zone, the fissile zone,

and the lower axial blanket (LAB) which is a fertile zone. Table 4 presents the fine description of these two kinds of S/As.
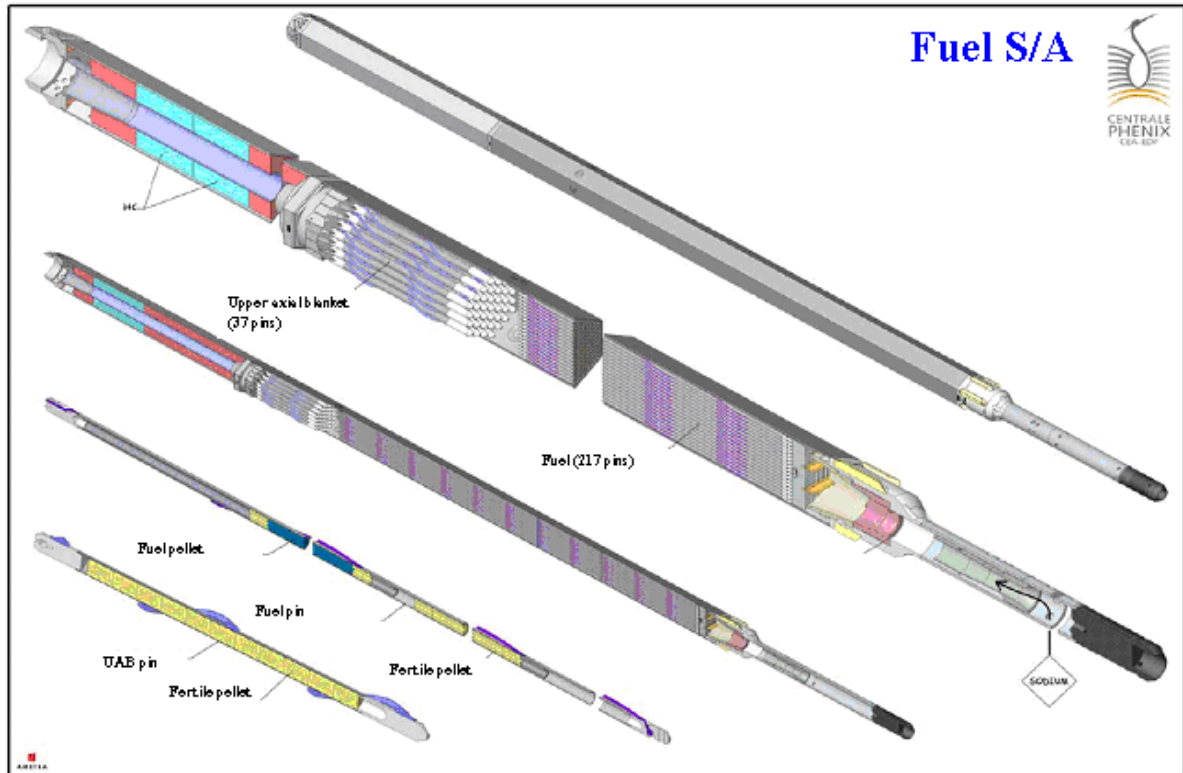
FIG. 18. Fuel S/A.
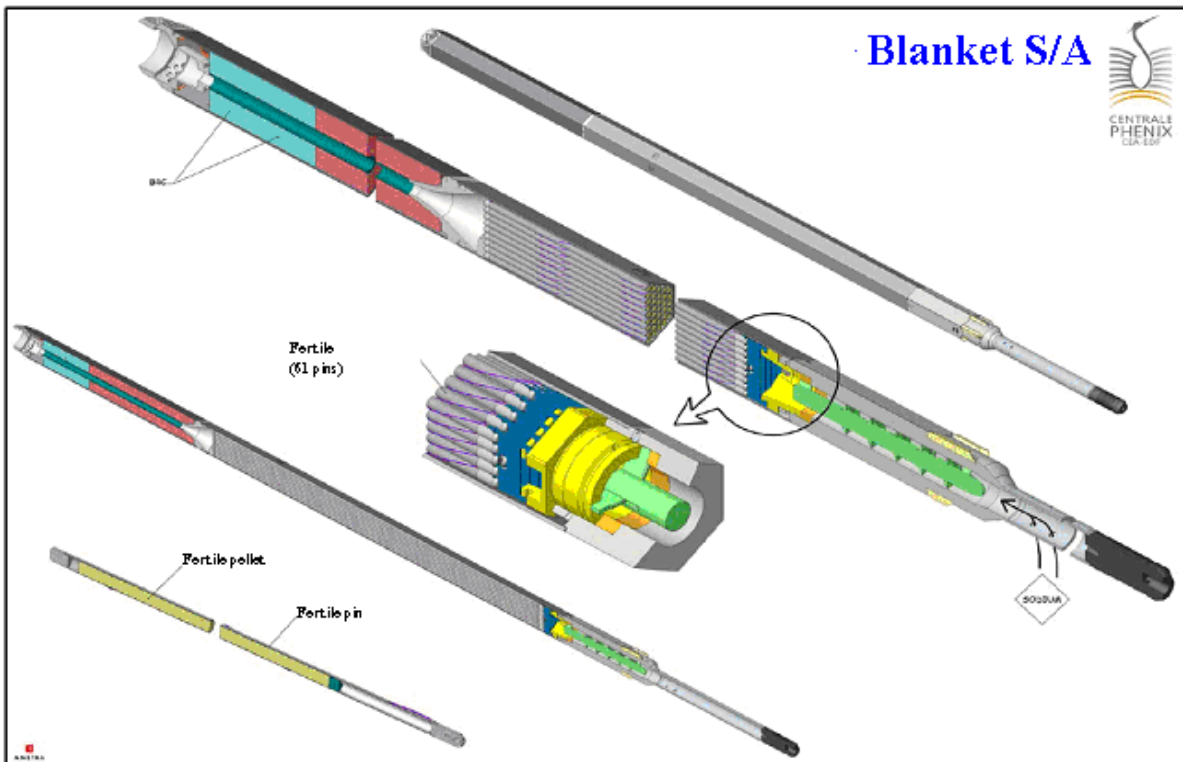
FIG. 19. Blanket S/A.
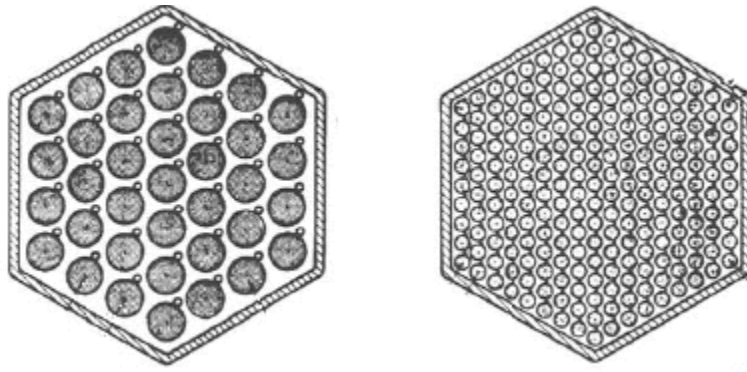
FIG. 20. Fuel S/A (left=upper axial blanket, right=fissile and lower axial blanket).

TABLE 4. FINE DESCRIPTION OF FUEL AND FERTILE S/AS

		Fuel	Axial blanket (upper)	Axial blanket (lower)	Radial blanket
# pins		217	37	217	61
S/A pitch	cm	12.72	12.72	12.72	12.72
External pitch wrapper tube	cm	12.37	12.37	12.37	12.37
Internal pitch wrapper tube	cm	11.69	11.69	11.69	11.69
Central hole diameter	cm	-	-	0.15	-
Pellet external diameter	cm	0.542	1.295	0.55	1.215
Clad internal diameter	cm	0.565	1.325	0.565	1.245
Clad external diameter	cm	0.655	1.425	0.655	1.34
Space wire diameter	cm	0.115	0.386	0.115	0.108
Spacer wire pitch	cm	15	14.5	15	20
Pins pitch	cm	0.7773	1.8197	0.7773	1.4572
Height	cm	85	26.20	33.651	164.851
Total height	cm	264.853			

4.1.1.2. Control rods

Fig. 21–22 present the overview of the main control rod and his wrapper tube. Table 5 gives a fine description of the control rod.
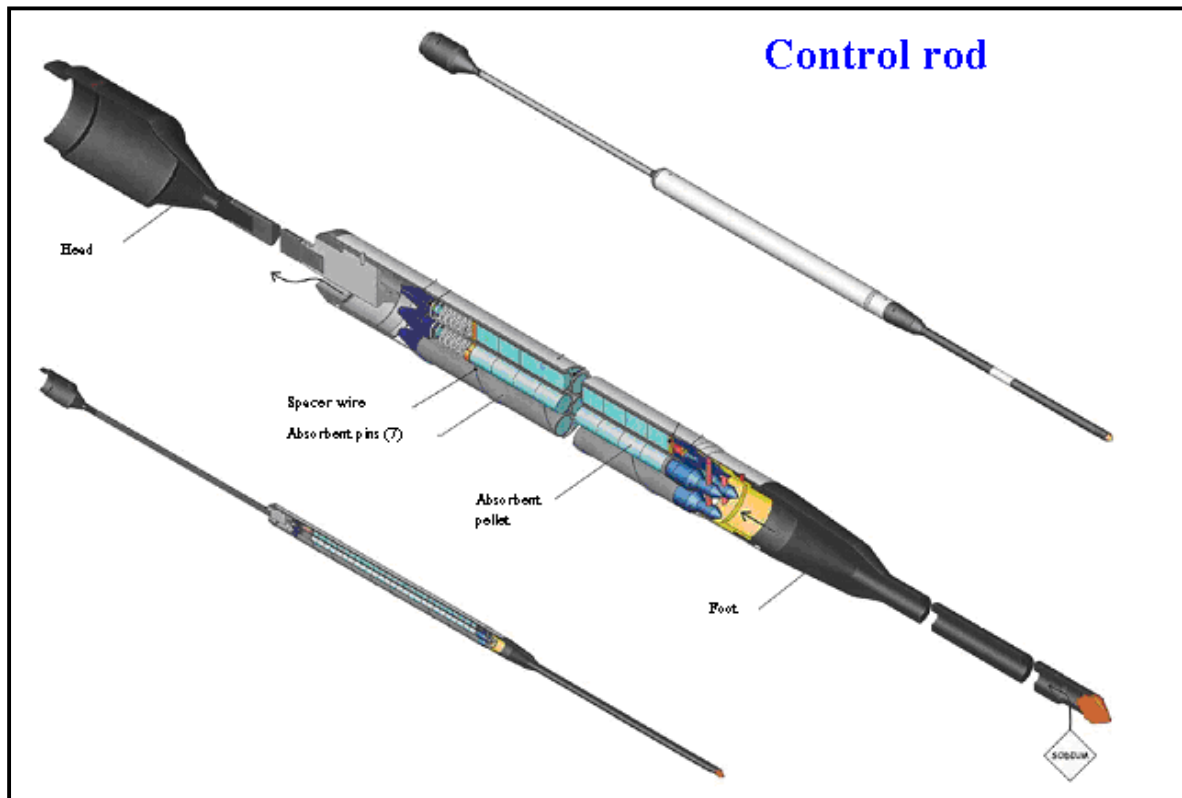
FIG. 21. Control rod.
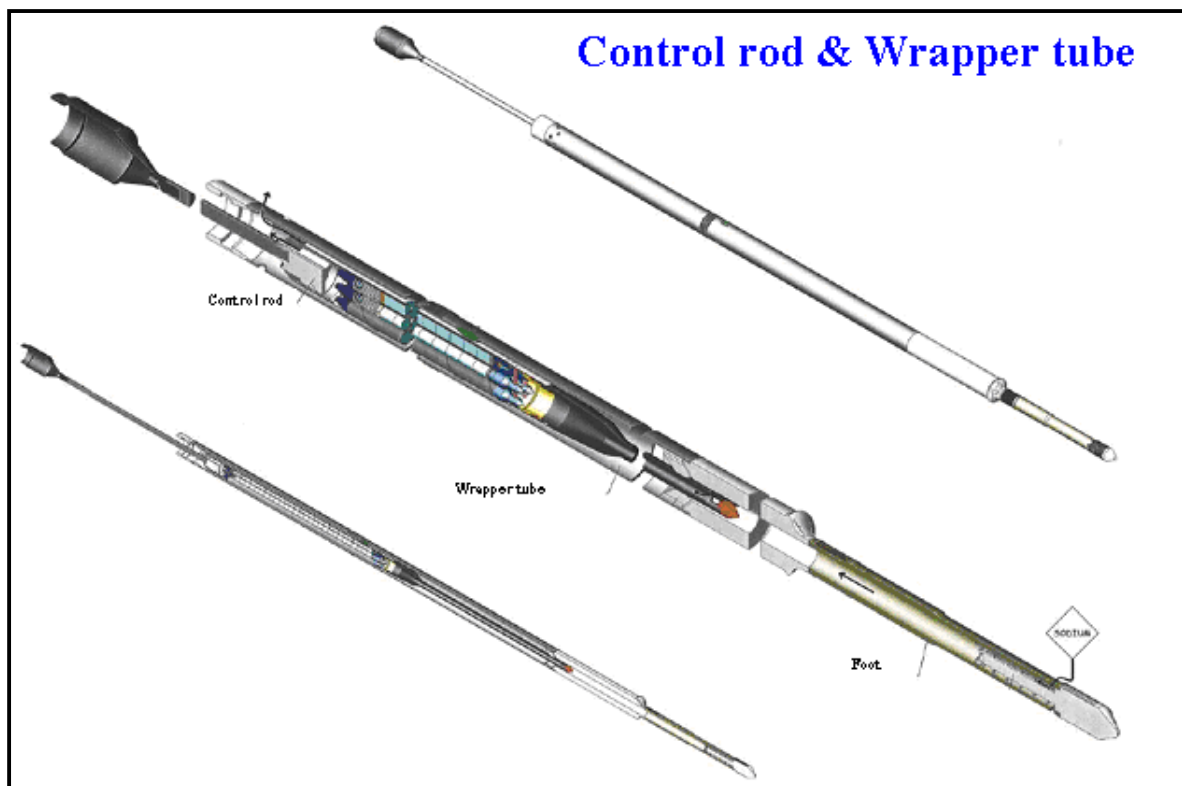
FIG. 22. Control rod and CR wrapper tube.

TABLE 5. FINE DESCRIPTION OF MAIN CONTROL ROD S/*AS*

	CR part	unit	Control rods data
	# Fuel pins		7
	Pitch (cm)	cm	12.72
A	Tube external diameter	cm	12.37
	Tube internal diameter	cm	11.22
B	CR external diameter	cm	9.50
	CR internal diameter	cm	9.20
C	Pellet external diameter	cm	2.35
D	Clad internal diameter	cm	2.6
	Clad external diameter	cm	2.8
E	Spacer wire diameter	cm	0.17
	Spacer wire pitch	cm	11.1
F	Flow equalizer triangle	cm²	1.1759
	Absorber height	cm	94.5
	Total height	cm	264.853
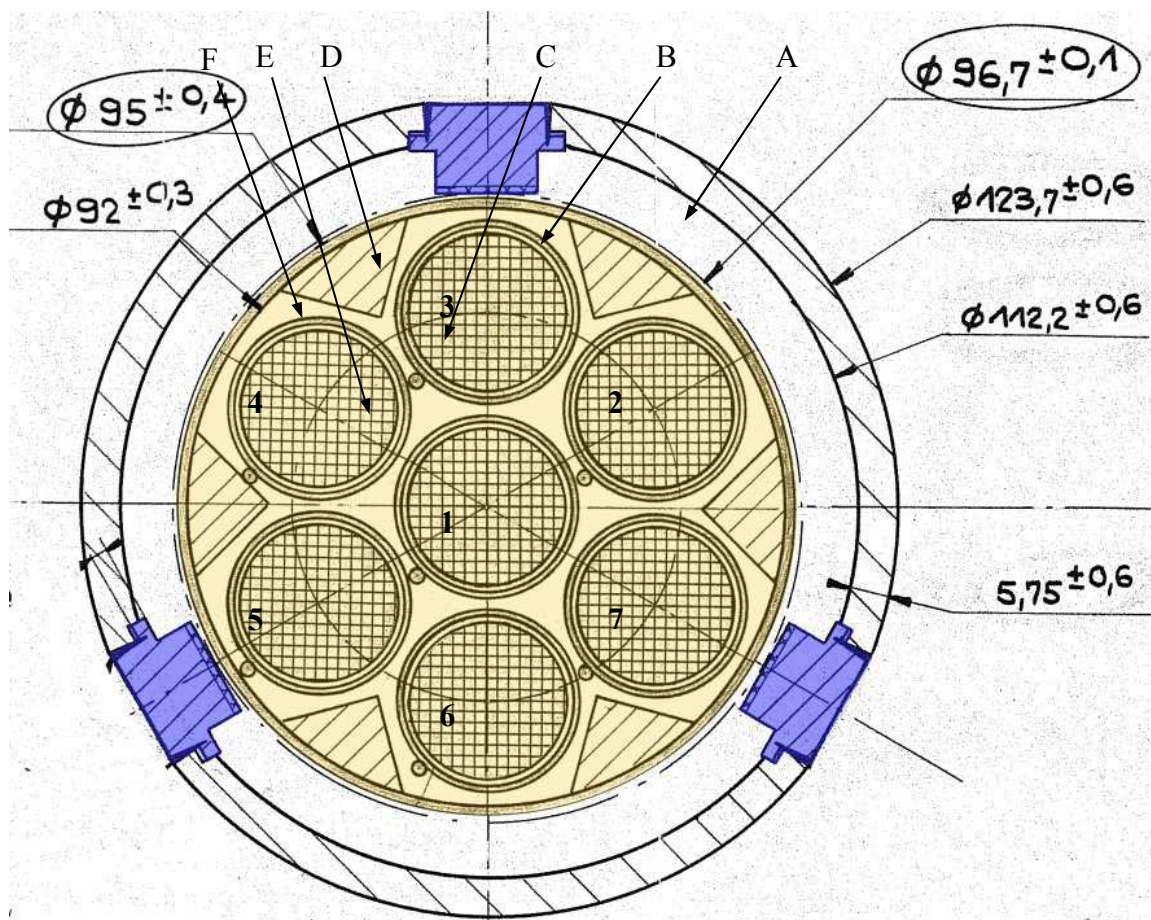
FIG. 23. Main control rod's scheme (units are mm).

Fig. 23 gives the global shape of main control rods (SCP). In this figure, the yellow part indicates the axially moveable part of the control rod. The blue part indicates the supports which are used to guide the control rod. There is no need to describe this blue part because these supports are only 58 mm height in comparison with the absorber height of 945 mm. Furthermore, they are located outside the fissile zone of 85 cm height. Consequently, the external part of the control rod can be described as a simple tube.

Table 6 gives the position of each absorber rod center, relative to the control rod center.

TABLE 6. POSITIONS OF THE ABSORBENT RODS IN THE MAIN CONTROL RODS

	1	2	3	4	5	6	7
X (cm)	0	+2.572	0	-2.572	-2.572	0	+2.572
Y (cm)	0	+1.485	+2.970	+1.485	-1.485	-2.970	-1.485
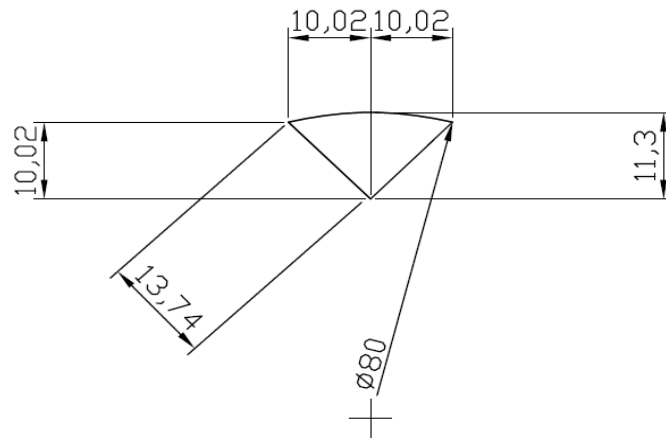
FIG. 24. Detail of the 'F' part of CR: 'flow equalizer triangle' (units are mm).

Fig. 24 shows details of a part of the CR: the flow equalizer triangle. These triangles are used to reduce the sodium flow, in order to improve the cooling of the absorber rods. They are in steel material, and are on all the height of the moveable part of the CR.

Note that control rods are considered to be at their beginning of life. There is no need to consider the burnup history effect of the control rods.

Concerning the emergency control rod (SAC), it is not necessary for this benchmark to know its heterogeneous description. Consequently, the homogeneous volume fractions of SAC are given in Table 8 in Section 4.1.1.4.

4.1.1.3. Shielding S/A

Table 7 presents the fine description of the different kinds of reflectors S/As.

TABLE 7. FINE DESCRIPTION OF SHIELDING S/AS

	unit	ARA	Diluent	ASA (Schielding)
# Pins		7	6	1
Hexagonal pitch	cm	12.72	12.72	12.72
External pitch wrapper tube	cm	12.37	12.37	12.37
Internal pitch wrapper tube	cm	11.69	11.69	11.69
Pellet external diameter	cm	3.80	3.80	11.69
Spacer wire diameter	cm	0.32	0.32	-[2]

4.1.1.4. Homogeneous modelling of the core

Volume fractions for each S/A type are given in Table 8.

TABLE 8. VOLUME FRACTIONS FOR EACH S/A TYPE AT 20°C

No.	Zone name	Volume fraction (%)				
		Fuel	Steel	Sodium	B$_4$C	Vacuum
1	Core 1	38.83 %	25.09 %	36.08 %	/	/
2	Core 2	38.83 %	25.09 %	36.08 %	/	/
3	Lower blanket 1	38.83 %	25.09 %	36.08 %	/	/
4	Upper blanket 1	36.41 %	19.05 %	44.54 %	/	/
5	Lower blanket 2	38.83 %	25.09 %	36.08 %	/	/
6	Upper blanket 2	36.41 %	19.05 %	44.54 %	/	/
7	Radial blanket	53.00 %	18.91 %	28.09 %	/	/
8	Transition zone between fuel and upper blanket	/	38.31 %	47.33 %	/	14,36%
9	Axial shielding	/	50.00 %	50.00 %	/	/
10	Diluent	/	63.92 %	36.08 %	/	/
11	Shielding ARA	/	66.20 %	33.80 %	/	/
12	Shielding ASA	/	78.70 %	18.10 %	/	3,20%
13	Control rod (SCP)	/	27.77 %	50.56 %	21.67 %	/
14	CR follower (SCP & SAC)	/	21.32 %	78.68 %	/	/
15	Emergency Control Rod (SAC)	/	27.53 %	53.90 %	18.57 %	/
16	Sodium	/	/	100.00 %	/	/
17	Steel	/	100.00 %	/	/	/

Note that in homogeneous modeling described in Table 8, all the vacuum gaps between the pellets and the cladding are diluted into the 'fuel' volume fraction. The central hole of lower axial blanket pellets is also diluted into 'fuel' volume fraction.

Furthermore, it was assumed in the first step of the benchmark that upper and lower axial shielding have the same composition. Note that the axial model of S/A is simplified for the zones furthest away from the fissile zone (the top and the bottom of S/As are not modelled).

---

[2] There is no spacer wire for ASA Shielding S/A.

4.1.1.5.   Axial description at 20 °C

Details of the axial modeling are reported in Fig. 25.
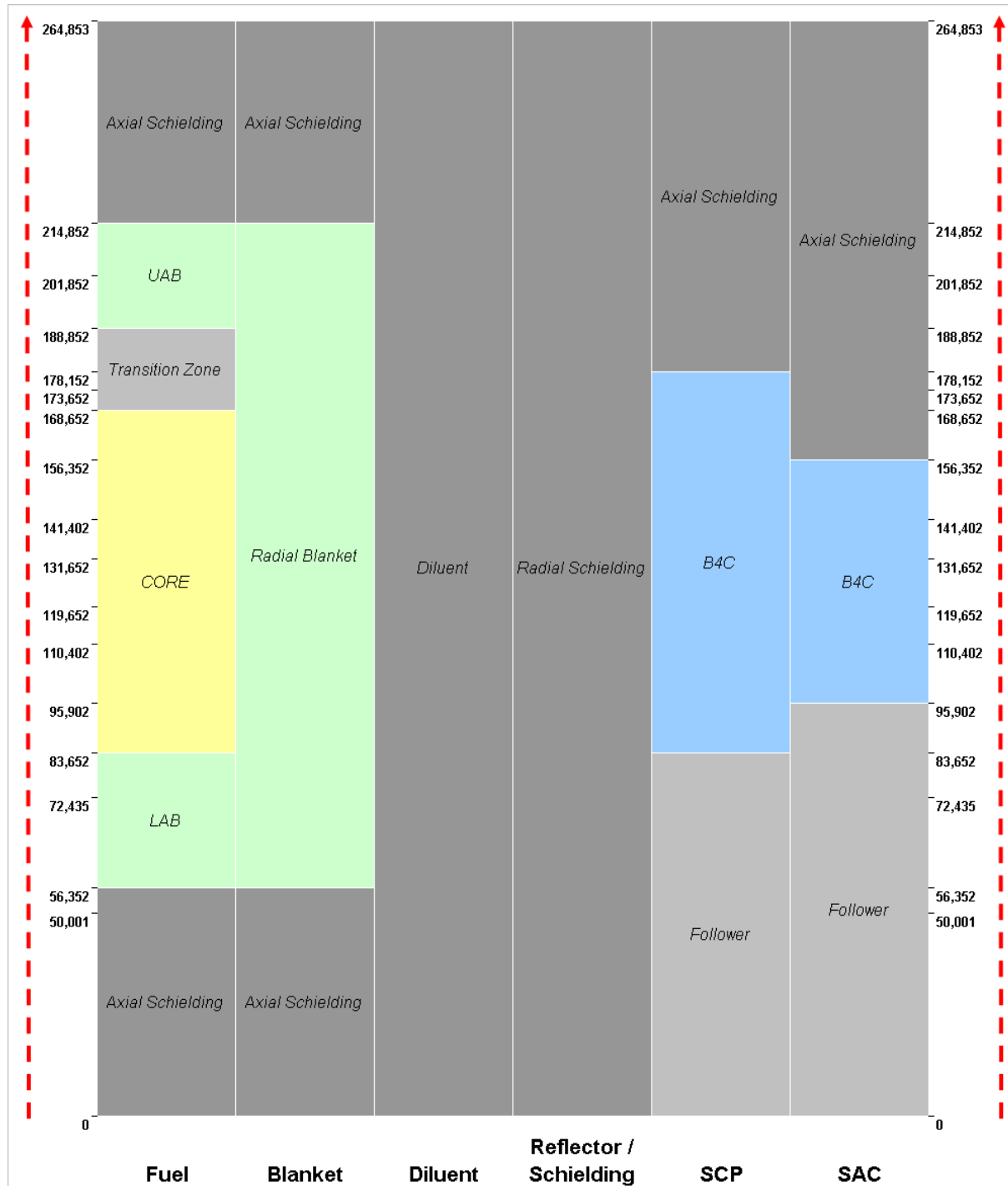
FIG. 25. Axial modeling.

Control rods (SCP & SAC) can move between '0 mm' level and '900 mm' level. The CR elevation reference level '0 mm' is 5 mm below the fissile zone. In the axial modeling (see Fig. 25), these levels correspond respectively to '83.152 cm level' and '173.152 cm level'.

4.1.2. Core composition

4.1.2.1. Fuel isotopic compositions and core loading map

Fig. 26 presents the core loading plan used for this test.
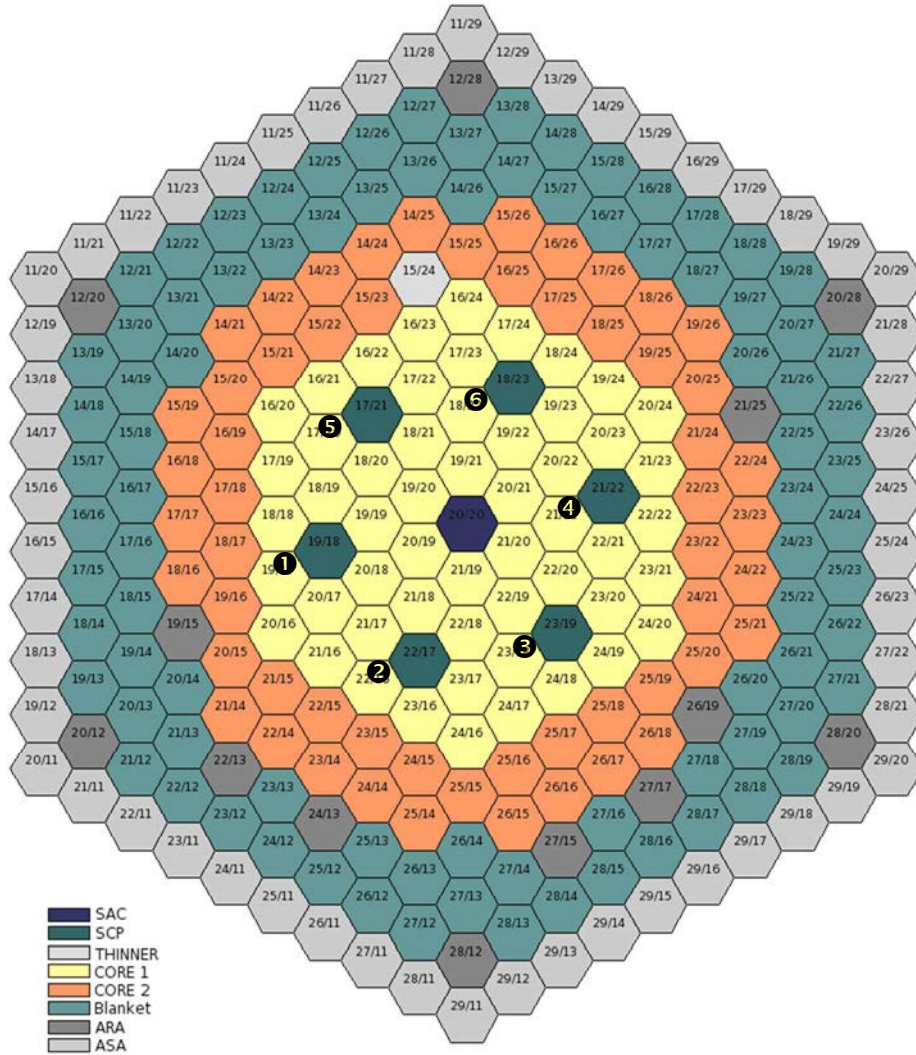
FIG. 26. Loading plan of the test.

The homogenized number densities provided for the active core and blanket zone come from average concentrations on the core. They are presented in Table 9 at 20 °C.

TABLE 9. ISOTOPIC DENSITIES FOR THE AVERAGE CORE ZONES AT 20 °C (1E^{-24} at/cm^3)

10^{-24}.at/cm3	Blanket[3]	LB1[3]	C1[3]	UB1[3]	LB2[3]	C2[3]	UB2[3]
AM241	2,008E-08	2,736E-08	9,102E-05	2,259E-09	1,379E-08	1,176E-04	3,968E-09
AM242F	*1,000E-10*	*1,000E-10*	*1,000E-10*	*1,000E-10*	*1,000E-10*	*1,000E-10*	*1,000E-10*
AM242M	1,610E-10	*1,000E-10*	2,428E-06	*1,000E-10*	*1,000E-10*	2,867E-06	*1,000E-10*
AM243	1,100E-10	*1,000E-10*	3,322E-06	*1,000E-10*	*1,000E-10*	3,737E-06	*1,000E-10*
B10	*1,000E-10*	*1,000E-10*	*1,000E-10*	*1,000E-10*	*1,000E-10*	*1,000E-10*	*1,000E-10*
B11	*1,000E-10*	*1,000E-10*	*1,000E-10*	*1,000E-10*	*1,000E-10*	*1,000E-10*	*1,000E-10*
C	*1,000E-10*	*1,000E-10*	*1,000E-10*	*1,000E-10*	*1,000E-10*	*1,000E-10*	*1,000E-10*
CM242	1,822E-10	1,552E-10	2,378E-06	*1,000E-10*	*1,000E-10*	2,742E-06	*1,000E-10*
CM243	*1,000E-10*	*1,000E-10*	*1,000E-10*	*1,000E-10*	*1,000E-10*	*1,000E-10*	*1,000E-10*
CM244	*1,000E-10*	*1,000E-10*	4,235E-07	*1,000E-10*	*1,000E-10*	4,190E-07	*1,000E-10*
CM245	*1,000E-10*	*1,000E-10*	*1,000E-10*	*1,000E-10*	*1,000E-10*	*1,000E-10*	*1,000E-10*
CM246	*1,000E-10*	*1,000E-10*	*1,000E-10*	*1,000E-10*	*1,000E-10*	*1,000E-10*	*1,000E-10*
CM247	*1,000E-10*	*1,000E-10*	*1,000E-10*	*1,000E-10*	*1,000E-10*	*1,000E-10*	*1,000E-10*
CM248	*1,000E-10*	*1,000E-10*	*1,000E-10*	*1,000E-10*	*1,000E-10*	*1,000E-10*	*1,000E-10*
NP237	*1,000E-10*	*1,000E-10*	*1,000E-10*	*1,000E-10*	*1,000E-10*	*1,000E-10*	*1,000E-10*
NP239	*1,000E-10*	*1,000E-10*	*1,000E-10*	*1,000E-10*	*1,000E-10*	*1,000E-10*	*1,000E-10*
NP239	*1,000E-10*	*1,000E-10*	*1,000E-10*	*1,000E-10*	*1,000E-10*	*1,000E-10*	*1,000E-10*
O	4,541E-02	3,712E-02	4,314E-02	3,275E-02	3,740E-02	4,263E-02	3,290E-02
PU238	5,932E-10	5,213E-10	2,272E-05	*1,000E-10*	2,722E-10	2,759E-05	*1,000E-10*
PU239	2,344E-04	3,241E-04	3,115E-03	1,214E-04	2,686E-04	3,754E-03	1,362E-04
PU240	6,869E-06	1,219E-05	1,334E-03	1,999E-06	8,214E-06	1,635E-03	2,961E-06
PU241	1,764E-07	3,312E-07	1,088E-04	2,663E-08	1,953E-07	1,321E-04	5,692E-08
PU242	3,380E-09	6,416E-09	4,843E-05	2,559E-10	3,270E-09	6,017E-05	6,148E-10
SFPPU239	1,513E-05	5,023E-05	1,559E-03	9,229E-06	3,796E-05	1,633E-03	1,069E-05
SFPPU240	6,723E-09	2,149E-07	1,301E-04	3,948E-08	1,624E-07	1,363E-04	4,572E-08
SFPPU241	6,723E-10	1,075E-07	9,004E-05	1,974E-08	8,119E-08	9,433E-05	2,286E-08
SFPPU242	6,723E-13	1,075E-10	4,002E-06	1,974E-11	8,119E-11	4,192E-06	2,286E-11
SFPU235	1,304E-05	2,620E-05	2,401E-05	4,813E-06	1,980E-05	2,515E-05	5,573E-06
SFPU238	3,905E-05	3,070E-05	1,941E-04	5,640E-06	2,320E-05	2,033E-04	6,531E-06
U234	*1,000E-10*	*1,000E-10*	*1,000E-10*	*1,000E-10*	*1,000E-10*	*1,000E-10*	*1,000E-10*
U235	6,623E-05	5,155E-05	4,149E-05	4,698E-05	6,354E-05	3,759E-05	4,741E-05
U236	1,800E-06	2,538E-06	3,178E-06	9,988E-07	2,455E-06	2,570E-06	1,215E-06
U238	2,249E-02	1,810E-02	1,592E-02	1,618E-02	1,830E-02	1,473E-02	1,624E-02

---

[3] The gap between the pellet and the cladding is diluted in the pellet.

Remarks:

In Table 9, 'Blanket' corresponds to radial blanket, 'UB1' and 'LB1' correspond respectively to upper and lower blanket for core 1 S/A, 'UB2' and 'LB2' corresponds respectively to upper and lower blanket for core 2 S/A.

The isotopes for which concentration is inferior or equal to 1.0E-10 are represented only as 'traces'. They are used by ERANOS code in burn up calculation, so they are not necessary in this benchmark.

AM242F corresponds to the Am242 ground state (Am242g) and AM242M corresponds to the Am242 metastable state.

SFP 'X' means (pseudo) solid fission product of nucleus 'X', that is to say that gaseous fission products of nucleus 'X' are totally removed. Note that each fission of a nucleus 'X' creates 2 new nucleuses SFP 'X'. Reference data of this SFP nucleus are presented in Table 10:

TABLE 10. DESCRIPTION OF THE FISSION PRODUCT USED IN ERALIB

Isotopes	Mass[4] (amu)	NGCE (MeV)	GCE (MeV)	NGFE (MeV)	GFE (MeV)	DIS (s^{-1})
sfpU235	93.868	0	8.0000	0	0	0
sfpU238	97.263	0	8.0000	0	0	0
sfpPu239	94.175	0	8.0000	0	0	0
sfpPu240	97.057	0	8.0000	0	0	0
sfpPu241	98.840	0	8.0000	0	0	0
sfpPu242	97.057	0	8.0000	0	0	0

Legend:

amu	=	atomic mass unit (1 amu = 931.494 MeV/c^2)
NGCE	=	Non-Gamma Capture Energy
GCE	=	Gamma Capture Energy
NGFE	=	Non-Gamma Fission Energy
GFE	=	Gamma Fission Energy
DIS	=	DISintegration constant (lambda=ln(2)/$T_{1/2}$)

Finally, Fig. 27 presents the averaged burnup in GWd/t of each S/A and should be compared with Fig. 28 which presents real burnups.

---

[4] Masses are only given for Solid Fission Product (SFP).
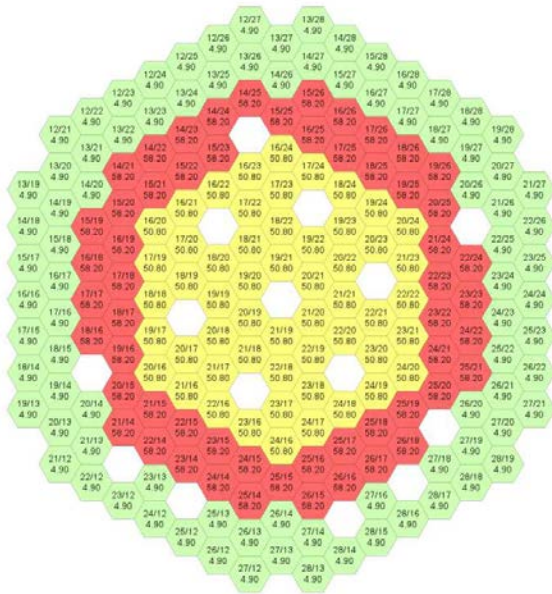
Burn-up (GWj/t) - Average Loading plan n°56-181

FIG. 27. Burnup of each S/As for the average core.
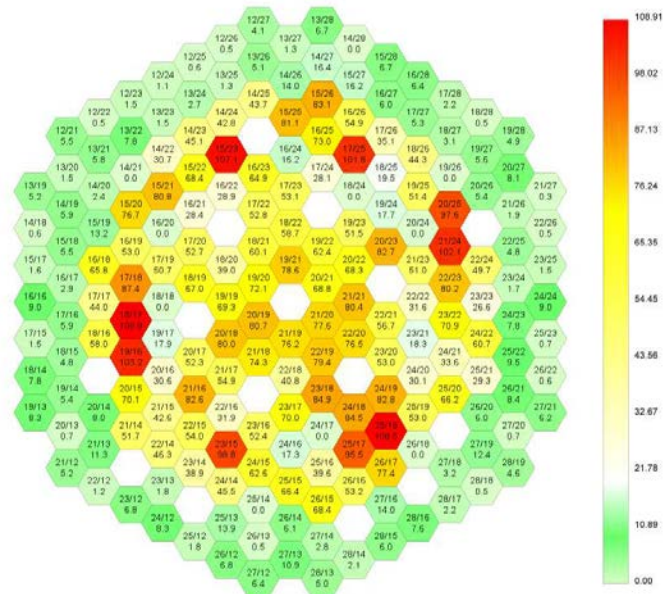
Burn-up max (GWj/t) - Loading plan n°56-181

FIG. 28. Burnup per S/As (initial state).

4.1.2.2. Isotopic densities of other materials

4.1.2.2.1.　Stainless steel 316

Density: 7.95 g/cm^3

Mass fractions (%) are reported in Table 11:

TABLE 11. MASS FRACTIONS OF THE SS316

FE54	3.56%	**NI60**	3.73%
FE56	58.38%	**NI61**	0.16%
FE57	1.43%	**NI62**	0.53%
FE58	0.18%	**NI64**	0.14%
CR50	0.71%	**MO**	2.75%
CR52	14.23%	**TI**	0.40%
CR53	1.64%	**CU**	0.10%
CR54	0.42%	**SI**	0.70%
NI58	9.44%	**MN**	1.50%

4.1.2.2.2.　Sodium

Density: 0.95 g/cm^3

Mass fractions (%) are reported in Table 12:

TABLE 12. MASS FRACTIONS OF THE SODIUM

NA23	100.00%

4.1.2.2.3. B_4C

Density: 2.30 g/cm^3

Atomic fractions for the boron (%) are reported in Table 13:

TABLE 13. ATOMIC FRACTIONS OF THE BORON

B10	48.00%
B11	52.00%

Atomic fractions for the carbon (%) are reported in Table 14:

TABLE 14. ATOMIC FRACTIONS OF THE CARBON

C	100.00%

4.1.3. Operating conditions of different media

The temperatures listed in Table 15 are the average values used to take into account the dependence of microscopic cross-sections on media's temperature (Doppler effect).

TABLE 15. OPERATING CONDITIONS OF THE REACTOR

Zone	Temperature (°C)
Fuel	1227
Blanket	627
Structure	448
Coolant	448
Absorber	448

It is assumed that temperatures are described for the whole-core. Note that modification of the S/A temperatures due to control rod withdrawal could be considered, but it is not mandatory in this benchmark.

4.1.3.1.   Thermal expansions of the core

Thermal expansions are simulated by calculating the increase of the geometrical dimensions of S/A and core, simultaneously with the decrease of the material densities.

4.1.3.2.   Thermal expansion of S/A

For this benchmark, the method presented in Fig. 29 for S/A's thermal expansion is used.
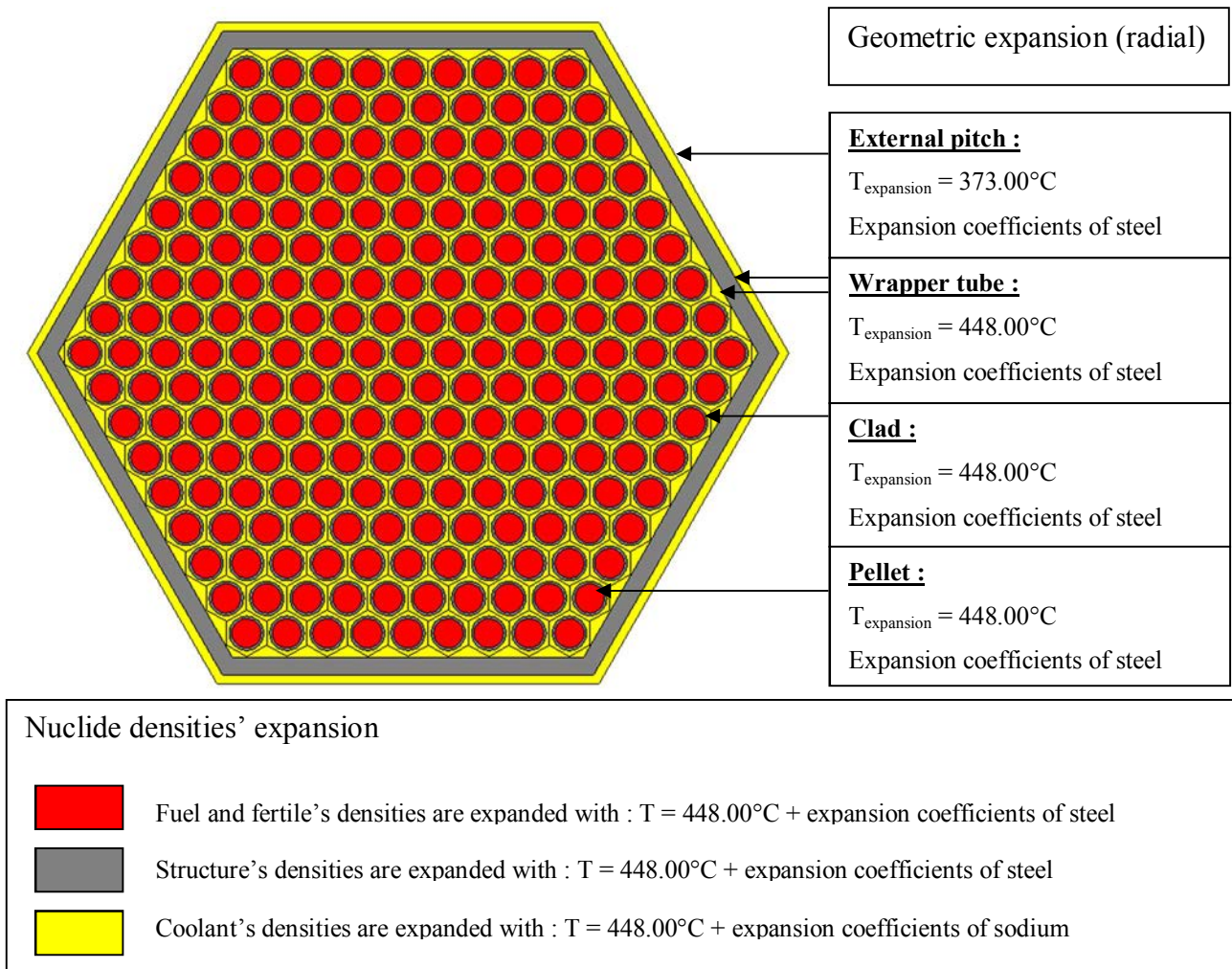
FIG. 29. Thermal expansion of S/A cells.

It is assumed that the pellets are linked to the clad, so axial expansion of S/A is only driven by steel's expansion at the reactor's average temperature (448 °C).

Note that absorber rods are expanded as structure (steels' expansion coefficients and a temperature of 448°C). For the whole control rod, the method illustrated in Fig. 29 is used.

The linear expansion coefficients listed in Table 16, combined with the temperature given above, permit to modify the density and the geometry of each material according to the operating conditions. The reference for these coefficients is the length at 20 °C.

TABLE 16. LINEAR EXPANSION COEFFICIENTS OF THE STEEL AND THE SODIUM

Temperature (°C)	Steel	Sodium
100	1.6400E-05	8.6560E-05
200	1.6900E-05	8.9030E-05
300	1.7350E-05	9.1380E-05
400	1.7800E-05	9.3910E-05
500	1.8200E-05	9.6690E-05
600	1.8500E-05	9.9540E-05
700	1.8800E-05	1.0265E-04
800	1.9000E-05	1.0588E-04
900	1.9300E-05	1.0921E-04
1000	1.9600E-05	1.1264E-04
1100	1.9900E-05	1.1617E-04
1200	2.0200E-05	1.1980E-04
1300	2.0500E-05	1.2353E-04

As it is described in the next section, linear expansion coefficients of steel are also used to modify the geometrical dimensions of the core.

4.1.3.3. Global thermal expansion of the core

The global geometry of the core is modified with two coefficients:

— A radial expansion coefficient, calculated considering the thermal expansion of the diagrid (steel), at the temperature of sodium entering the core;
— An axial expansion coefficient, calculated considering the thermal expansion of the S/A. For this benchmark, the fuel pellets are considered linked to the clad. So, the axial expansion coefficient is calculated considering the thermal expansion of steel, at the average temperature of the core.

The result of this calculation is given below:

Temperature for radial expansion: 373 °C [5]   ⇨ radial_expansion_coef = 1.00624

Temperature for axial expansion: 448 °C   ⇨ axial_expansion_coef = 1.00769

---

[5] diagrid temperature.

Note that the formula used to calculate these coefficients is:

$$\frac{l(\theta_n)}{l(\theta_0)} = 1 + \alpha(\theta_n - \theta_0) \tag{4}$$

with:

l, the length;

θ_0 and θ_n, respectively 20°C and the temperature considered for the expansion;

α, the linear expansion coefficient corresponding to the temperature.

4.1.4. S/A flows

Table 17 and Fig. 30 present the individual S/A flows (in kg/s). These flows are useful in order to calculate S/A powers from measured outlet temperatures. Indeed:

$$P_i = Q_i * C_P(Na) * (T_i^{Out} - T_{core}^{In}) \tag{5}$$

where:

Q_i	sodium flow (Kg·s^{-1});
C_P	sodium specific heat capacity (J.kg^{-1}·K^{-1});
T^{Out}_{is}	sodium outlet temperature;
T^{In}_{Core}	sodium inlet temperature.

The sodium specific heat capacity can be calculated using the following formula:

$$C_P(Na) = 1000 * (1.43674 - 5.8049.e^{-4} * \overline{T}_{ax} + 4.6229.e^{-7} * \overline{T}_{ax}^2) \tag{6}$$

where T_{ax} is the sodium axial mean temperature (°C).

TABLE 17. FLOWS PER S/A (Kg/s)

Position	Q (kg/s)	Position	Q (kg/s)	Position	Q (kg/s)	Position	Q (kg/s)
20-20	0,00	17-21	0,00	23-22	15,39	25-21	15,08
20-21	15,39	17-22	15,08	24-21	15,08	26-20	3,52
21-20	15,39	17-23	15,08	25-20	15,08	26-19	0,00
21-19	15,39	18-23	0,00	25-19	15,08	26-18	15,08
20-19	15,39	19-23	15,08	25-18	15,39	26-17	15,08
19-20	15,39	20-24	15,08	25-17	15,39	26-16	12,35
19-21	15,39	21-23	15,08	25-16	15,39	26-15	15,08
20-22	15,08	22-22	15,08	25-15	15,08	26-14	3,52
21-21	15,08	23-21	15,08	24-15	15,08	25-14	15,08
22-20	15,08	24-20	13,63	23-15	15,39	24-14	12,35
22-19	15,08	24-19	15,08	22-15	15,39	23-14	12,92
22-18	15,08	24-18	15,08	21-15	15,08	22-14	12,35
21-18	15,08	24-17	15,08	20-15	15,08	21-14	12,35
20-18	15,08	24-16	15,08	19-16	15,08	20-14	3,52
19-19	15,08	23-16	15,08	18-17	15,38	19-15	0,00
18-20	15,08	22-16	15,08	17-18	15,39	18-16	12,35
18-21	15,08	21-16	15,08	16-19	15,08	17-17	15,08
18-22	15,08	20-16	15,08	15-20	15,08	16-18	15,08
19-22	15,08	19-17	15,08	15-21	15,08	15-19	12,35
20-23	15,08	18-18	15,08	15-22	15,39	14-20	3,52
21-22	0,00	17-19	15,08	15-23	15,39	14-21	15,08
22-21	15,08	16-20	15,08	15-24	0,00	14-22	12,35
23-20	15,08	16-21	15,08	15-25	12,92	14-23	12,93
23-19	0,00	16-22	15,08	16-25	15,08	14-24	15,08
23-18	15,08	16-23	15,08	17-25	15,39	14-25	12,35
23-17	13,64	16-24	15,08	18-25	15,39	14-26	3,52
22-17	0,00	17-24	15,08	19-25	15,08	15-26	15,08
21-17	15,08	18-24	15,08	20-26	3,52	16-26	12,35
20-17	15,08	19-24	15,08	21-25	0,00	17-26	15,08
19-18	0,00	20-25	12,92	22-24	12,35	18-26	12,35
18-19	15,08	21-24	15,08	23-23	15,08	19-26	15,08
17-20	15,08	22-23	15,39	24-22	12,35		
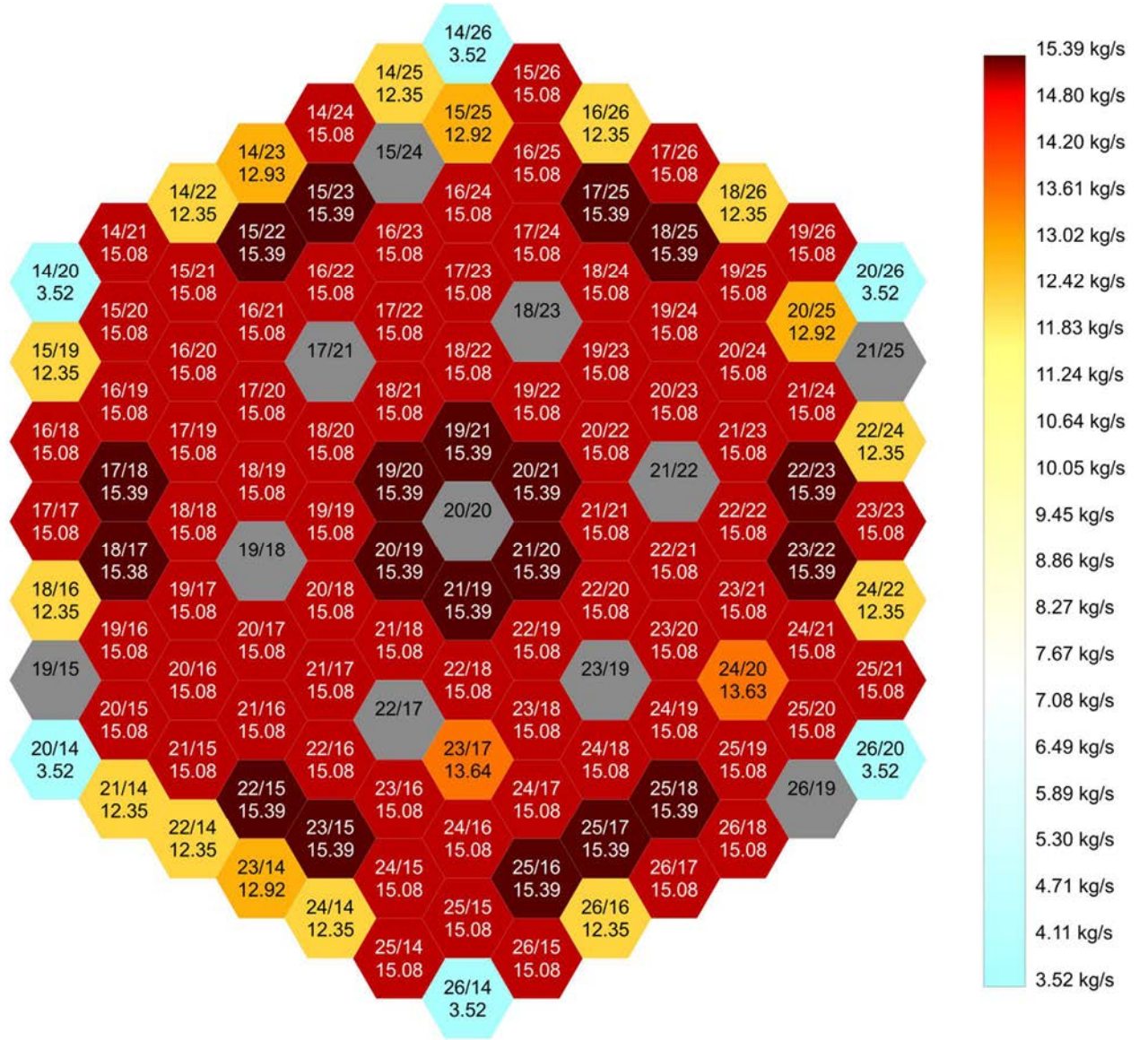
FIG. 30. Flows per S/A (initial state).

4.2. OUTPUT PARAMETERS TO BE CALCULATED.

4.2.1. K_{eff}

A comparison on k_{eff} (without unit) or reactivity (in pcm) values is done for the following cases:

— All CR at a level of 900mm;
— Reference state (see Section 3);
— Step 1: CR #4 inserted (see Section 3);
— Step 2: CR #1 extracted and CR #4 inserted (see Section 3);
— Step 3: CR #1 extracted (see Section 3).

4.2.2. Control rods worth

A comparison on control rods worth between high level (900 mm) and low level (0 mm) was carried out (in pcm). S-curve is drawn using eleven points uniformly distributed between 0 mm and 900 mm (each 100 mm).

4.2.3. Total flux and power distributions

Comparisons were done on flux and power distributions for each step of the test. In particular, the following values were computed:

— Maximum flux values (neutron/cm²·s) by S/A;
— Total power (fissile core + axial blankets) produced (MW(th)) for each S/A;
— Deviations (%) on total power for each S/A (between the first and the others steps).

4.2.4. Optional calculations

Calculations listed below were optional for the control rod withdrawal test. They are generally computed in neutronics code benchmark, and they contributed to the discussion.

4.2.4.1. Temperature effects

To study the effects of temperature modeling (thermal expansion and Doppler effect), calculations could be done for a unique temperature of 250 °C for the whole-core (inlet and outlet core temperature, material temperatures, etc.). Calculations could be done on the output data described in Sections 4.2.1 and 4.2.2.

4.2.4.2. Temperature effects: Doppler effect only

Doppler effect is evaluated by calculating the k_{eff} of two different states:

— $k_{eff\,(1)}$: geometry and cross-sections at full power state. The control rods are outside the core: control rods on 'rod bank', at a level of 900 mm. This is exactly the same calculation as the one described in Section 4.2.1.
— $k_{eff\,(2)}$: geometry does not change (thermal expansion and CR elevation), but cross-section are evaluated at 250 °C for all the materials.

The Doppler coefficient is calculated as follow:

$$K_D = \frac{k_{eff(1)} - k_{eff(2)}}{k_{eff(1)} \times k_{eff(2)}} \times \frac{1}{\ln\left(T1/T2\right)} \tag{7}$$

with

T1 = fuel temperature at full power (1227 °C)

T2 = fuel temperature at the second case (250 °C)

4.2.4.3. Delayed neutron coefficient

The delayed neutron coefficient β_{eff} is evaluated. Unit proposed is 'pcm'

4.2.5. Calculation data

In order to compare cross-sections, fluxes, etc., it was recommended (not compulsory) to use the same energy group structure, which is given in Table 18.

TABLE 18. ENERGY GROUPS

Group nb	Upper Energy (eV)	Lower Energy (eV)	Average Energy (eV)	Lethargy Increase (related to 10MeV)
1	1.964E+07	1.000E+07	1.482E+07	-0.675
2	1.000E+07	6.065E+06	8.033E+06	0.000
3	6.065E+06	3.679E+06	4.872E+06	0.500
4	3.679E+06	2.231E+06	2.955E+06	1.000
5	2.231E+06	1.353E+06	1.792E+06	1.500
6	1.353E+06	8.209E+05	1.087E+06	2.000
7	8.209E+05	4.979E+05	6.594E+05	2.500
8	4.979E+05	3.020E+05	3.999E+05	3.000
9	3.020E+05	1.832E+05	2.426E+05	3.500
10	1.832E+05	1.111E+05	1.471E+05	4.000
11	1.111E+05	6.738E+04	8.923E+04	4.500
12	6.738E+04	4.087E+04	5.412E+04	5.000
13	4.087E+04	2.479E+04	3.283E+04	5.500
14	2.479E+04	1.503E+04	1.991E+04	6.000
15	1.503E+04	9.119E+03	1.208E+04	6.500
16	9.119E+03	5.531E+03	7.325E+03	7.000
17	5.531E+03	3.355E+03	4.443E+03	7.500
18	3.355E+03	2.035E+03	2.695E+03	8.000
19	2.035E+03	1.234E+03	1.634E+03	8.500
20	1.234E+03	7.485E+02	9.913E+02	9.000
21	7.485E+02	4.540E+02	6.013E+02	9.500
22	4.540E+02	3.043E+02	3.792E+02	10.000
23	3.043E+02	1.486E+02	2.265E+02	10.400
24	1.486E+02	9.166E+01	1.201E+02	11.117
25	9.166E+01	6.790E+01	7.978E+01	11.600
26	6.790E+01	4.017E+01	5.404E+01	11.900
27	4.017E+01	2.260E+01	3.139E+01	12.425
28	2.260E+01	1.371E+01	1.816E+01	13.000
29	1.371E+01	8.315E+00	1.101E+01	13.500
30	8.315E+00	4.000E+00	6.158E+00	14.000
31	4.000E+00	5.400E-01	2.270E+00	14.732
32	5.400E-01	1.000E-01	3.200E-01	16.734
33	1.000E-01	1.100E-04	5.006E-02	18.421

5. PARTICIPANTS AND NEUTRONICS CODES

5.1. ARGONNE NATIONAL LABORATORY (ANL)

The nuclear science and engineering legacy of Argonne National Laboratory (ANL) dates to before the first critical reactor (CP-1) in 1942 under the leadership of Enrico Fermi and Walter Zinn. ANL has been involved in the design, analysis and development of nuclear reactors, including fast reactors. The Experimental Breeder Reactor-I (1951) and Experimental Breeder Reactor-II (1965) have been designed, developed and operated under ANL oversight. Over the years ANL has been involved in the design of fast reactors such as CRBR, PRISM, etc. More recently, ANL has innovated advanced concepts such as the Integral Fast Reactor (IFR), small modular fast reactors, advanced burner reactors, advanced recycling reactors, and fast reactor concepts that could be competitive for future commercial deployment.

Fast reactor core physics design is one of the major strengths of ANL, and for that purpose the national laboratory has developed tools for physics analysis of fast reactor cores, including cross-section generation and whole-core analysis tools. Such capabilities have been used for the analysis of the blind calculation benchmark performed for the control rod withdrawal tests conducted during the Phénix end-of-life experiments. Since the ANL suite of tools encompasses many options, only the specific ones used for the analysis of the blind calculation benchmark are discussed in what follows.

5.1.1. Cross-section generation tool

The cross-sections used for the blind calculation benchmark cases were produced using the MC^2-2 code [7]. In recent times, a more modern version of the MC^2 code, MC^2-3, is now being used at ANL, but that capability was unavailable at the time of the analysis [8]. The MC^2-2 code solves the neutron slowing down equations using basic neutron data derived from ENDF/B data files to determine fundamental mode spectra for use in generating multigroup neutron cross-sections. The code has the ability to treat all ENDF/B-V, -VI and -VII data representations. It accommodates high order P_N scattering representations and provides numerous capabilities such as isotope mixing, delayed neutron processing, free format input, and flexibility in output data selection.

The extended transport P_1, B_1, consistent P_1, and consistent B_1 fundamental mode ultra-fine-group equations are solved using continuous slowing down theory and multigroup methods. Fast and accurate resonance integral methods are used in the narrow resonance resolved and unresolved resonance treatments. A fundamental mode homogeneous unit cell calculation is performed using either a multigroup or a continuous slowing down treatment. Multigroup neutron homogeneous cross-sections are generated in an ISOTXS format for an arbitrary group structure. A hyper-fine-group integral transport slowing down calculation (RABANL) is available as an option for more accurate resonance treatment. RABANL performs a homogeneous or heterogeneous (pin or slab) unit cell calculation over the resolved resonance energy range and generates multigroup neutron cross-sections in an ISOTXS format.

In the current analysis work, the MC^2-2 code was used for the generation of 33-group cross-sections for distinct zones of the Phénix reactor core. The specific zones for which cross-sections are generated are discussed in Section 5.1.1.2.

5.1.1.1. Nuclear cross-section library

The ENDF/B-VII Rev. 0 data processed by the ETOE-2 [9] code has been used as input neutron cross-section data to the MC^2-2 calculations.

5.1.1.2. Cross-section models for core zones

The MC^2-2 cell code has been used to generate effective/homogenized cross-sections that are used in zones of the whole-core calculations. Specific MC^2-2 runs were done for fuel regions, non fueled regions and control rod region. A correction was made for the control rod cross-sections using MCNP Monte Carlo calculation for the heterogeneous geometry to provide correction factor for the homogeneous control rod model.

Using the benchmark specification data, 33-neutron-energy-group cross-sections were generated for 17 core zones at the prescribed operating core temperatures (see Table 19 for the zones, corresponding to those given in the benchmark). The energy-group structure specified in the benchmark was used for the boundaries of the 33-group data. The volume fractions or dimensions provided in the benchmark specification at cold conditions were modified to those consistent with the temperatures at the operating conditions. The temperatures and volume fractions, and nuclides in regions, were provided as input to the MC^2-2 calculations for the different zones. The MC^2-2 code (and models) with ENDF/B-VII Rev. 0 data was used in the analysis. Isotope-dependent lumped fission product cross-sections were also generated, but using ENDF/B-VI Rev. 5 data.

For the active fuel zones, direct homogeneous calculations were done to obtain the neutron spectra for collapsing the multigroup cross-sections (2082 groups) into the 33 energy groups. For all the other regions (non fuel ones) the inhomogeneous source calculation approach was used with leakage spectrum from the adjacent active fuel zone or blanket zone or non fuel zone. Numerical experimentation indicated that using this latter approach for generating the control rod cross-sections versus including B_4C in infinite dilute amount in the fuel assembly cross-section calculation has no significant impact on the eigenvalues for the rodded state.

It is well known that the Phénix control rod assemblies (using large B_4C rods) exhibit strong heterogeneity effects particularly when a spatially homogeneous model is used to generate the control rod cross-sections. This results in an overestimation of the control rod worth. Consequently, correction factors were required to ensure that the representative rod worths are obtained with the homogeneous model. In the current work, correction for the control rod heterogeneity was obtained using MCNP5 calculation for a 7-assembly problem (1 control rod assembly surrounded by 6 fuel assemblies). ENDF/B-VI data was used in the MCNP5 calculations.

The correction factor is based on matching the MCNP5 heterogeneous solution (in-to-out rod worth) by the equivalent MCNP5 homogeneous model. A B_4C number density reduction of 25% was found necessary for this purpose. This correction factor was used in the DIF3D-VARIANT (nodal transport) solutions for the blind calculation benchmark. It should be noted that a 2-D full core MCNP5 model was used to further investigate the value of this correction. The same value of the correction factor (0.75) was found to be sufficient to account for the rod heterogeneity in the homogeneous control rod model.

TABLE 19. ZONES FOR WHICH CROSS-SECTIONS WERE PREPARED USING MC2-2

No.	Zone Name
1	Core 1
2	Core 2
3	Lower blanket 1
4	Upper blanket 1
5	Lower blanket 2
6	Upper blanket 2
7	Radial blanket
8	Plenum between fuel and upper blanket
9	Axial shielding
10	Diluent
11	Shielding ARA
12	Shielding ASA
13	Control rod (SCP)
14	CR follower (SCP & SAC)
15	Emergency Control Rod (SAC)
16	Sodium
17	Steel

5.1.2. Whole-core calculation tool

The whole-core analysis/calculations for the blind calculation benchmark have been done using the DIF3D code system [10]. The tool has both diffusion theory and transport theory solution solvers. The DIF3D-VARIANT, Variational Nodal Methods transport theory solver, has been used in this work. The DIF3D-VARIANT option solves the multigroup steady state neutron diffusion and transport equations in two- and three-dimensional Cartesian and hexagonal geometries using variational nodal methods. The transport approximations involve complete spherical harmonic expansions up to order P_{99}. Eigenvalue, adjoint, fixed source, gamma heating, and criticality (concentration) search problems are permitted. Anisotropic scattering is treated, and although primarily designed for fast reactor problems, upscattering options are also included. Flux and power density maps by mesh cell and region-wise balance integrals are provided as output by the code.

In DIF3D-VARIANT, the neutron diffusion and transport equations are solved using a variational nodal method with one mesh cell (node) per hexagonal assembly (Cartesian geometry node sizes are specified by the user). The nodal equations are derived from a functional incorporating nodal balance, and reflective and vacuum boundary conditions through Lagrange multipliers. Expansion of the functional in orthogonal spatial and angular (spherical harmonics) polynomials leads to a set of response matrix equations relating partial current moments to flux and source moments. The equations are solved by fission source iteration in conjunction with a coarse mesh rebalance

acceleration scheme. The inner iterations are accelerated by a partitioned matrix scheme equivalent to a synthetic diffusion acceleration method.

5.1.2.1. *Whole-core model*

Whole-core calculations were performed using the DIF3D-VARIANT option. The Hexagonal-Z (Hex-Z) geometry option was selected in which each assembly position is represented by Hex-Z nodes modelling different axial zones. All the radial positions specified by the benchmark were modelled. The DIF3D-VARIANT solutions used anisotropic scattering order P_1 and the full P_3 angular flux approximations; spatially used were the quadratic source, sixth-order flux, and linear leakage approximations. At the time of the calculations, only a few of the output parameters requested for blind calculation benchmark were obtained due to the fact that the specifications were being finalized at that time (e.g., no temperature effects and delayed neutron coefficients were calculated). The DIF3D-VARIANT code was used to calculate the core eigenvalue, core power distribution and integral rod worths. The code was also used to calculate the four core states with the specified positions of the 6 main control rods (SCP) at each state for which eigenvalue calculations are requested.

5.2. COMMISSARIAT A L'ENERGIE ATOMIQUE ET AUX ENERGIES ALTERNATIVES (CEA)

The French Alternative Energies and Atomic Energy Commission, also known as the CEA, is a public company established in October 1945 by General de Gaulle in order to develop nuclear science. Today, the CEA is active in four main areas: low carbon energies, defense and security, information technologies and health technologies. The development of nuclear energy remains one of the CEA's main objectives. Concerning sodium cooled fast reactors, CEA has developed and managed some test reactors such as RAPSODIE (criticality obtained in 1968; Power ~ 40 MW(th); loop reactor; 15 years of operating; located in Cadarache), Phénix (criticality obtained in 1973; 560 MW(th); pool reactor; 35 years of operating; located in Marcoule [2]). The CEA has moreover participated in the development of the Superphénix power plant (criticality obtained in 1985; 3000 MW(th); pool reactor; ~10 years of operating; located in Creys-Maleville). CEA has also been involved in international projects such as the European Fast Reactor (EFR) project and the Generation IV International forum.

FIG. 31. French fast reactors: RAPSODIE →PHÉNIX → SUPER-PHÉNIX.

5.2.1. CEA's neutronic framework for fast reactors design

Today, neutronic studies on fast reactors are realized using the ERANOS (European Reactor ANalysis Optimized System) code system [11–13] developed by CEA in the framework of a European collaboration. ERANOS is a determinist neutronic calculation framework dedicated to fast neutron reactors. It includes some cell solvers (ECCO, HETAIRE), core solvers with various

assumptions (spherical 1D models, cylindrical 2D models, hexagonal 3D models, diffusion theory, transport theory), nuclear library, and core management modules.

ERANOS can use various nuclear data bank like JEFF-3.1.1 (European data bank for fusion and fission); JENDL-3.3, ENDF-B/VII.0, JEF-2.2 and the ERALIB-1. This latter was developed by the CEA on the basis of the European JEF-2.2 nuclear library and enriched by experimental integral adjustments on French fast reactors (MASURCA, RAPSODIE, Phénix, Superphénix) [14–15]. NJOY and CALENDF codes are used to prepare the cross-section data libraries used by ERANOS.

The basic functions of the system satisfy all the requirements of fast reactor neutronic studies: cell assembly calculations, core and shielding calculations, neutron gamma propagation calculations. Scheme of ERANOS capacities is reported in Fig. 32.
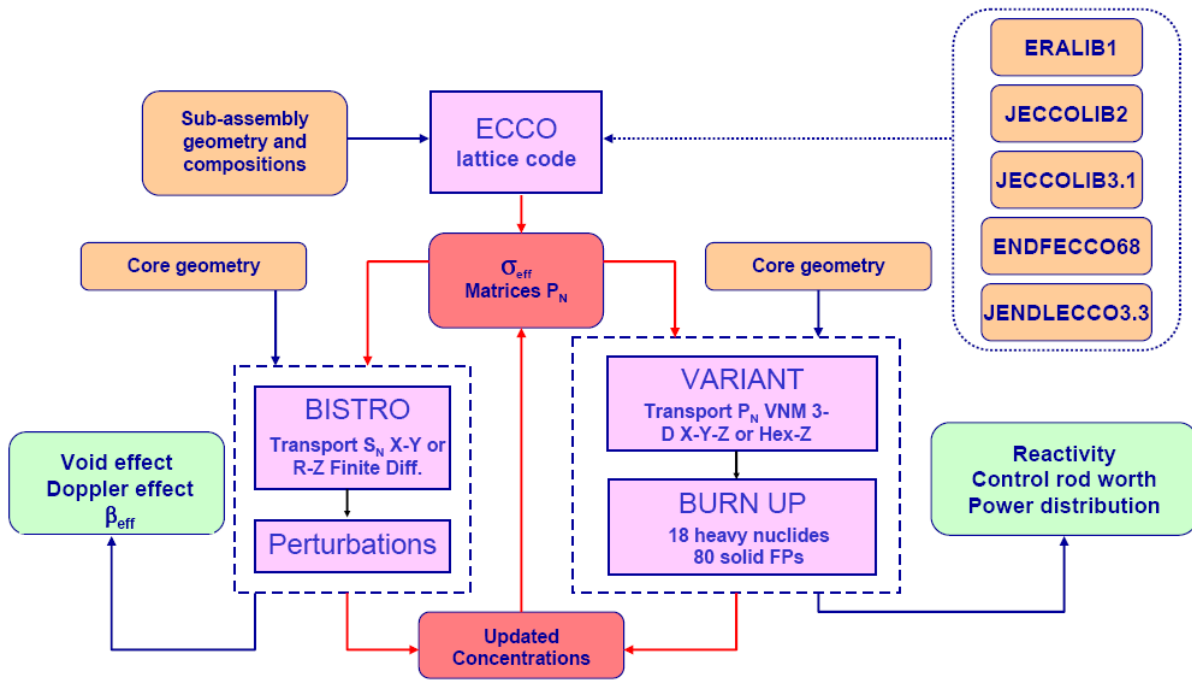

FIG. 32. Schematic diagram of ERANOS capacities.

The cell code ECCO has a resonance self-shielding solution algorithm based on the sub-group method combined with a fine group transport calculation, in plane, cylinder, rectangular and hexagonal 2D, and 3D plate geometries based on collision probabilities [16]. Various options could be used in order to treat a cell such as: the energy structure (6, 25, 33, 172, 1968 groups), the geometry (heterogeneous or homogeneous), the processing of the flux or the balance (buckling, leakage processing), the nuclides that are shelf-shielded.

For core and propagation calculations the ERANOS package includes a diffusion theory solver (1D, 2D, 3D) and transport theory solvers relying either on the S_N method (in 1D or 2D XY, RZ) or on the Variational Nodal one (in 2D Hexagonal or XY, or 3D Hexagonal-Z or XYZ). The ERANOS system provides direct and adjoint solutions for the homogeneous and inhomogeneous equations.

Specific tools have been developed in order to perform physical analysis or core management. For example:

— Burnup of a core can be simulated using evolution chains;
— Specific extraction and printout modules: reactions rates, radial and axial 1D profiles, equivalence coefficients, breeding gains, mass balances;
— Sub-critical reactivity measurement interpretation (MSM);

—Perturbation theory methods : sensitivities (k_{eff}, reaction rates, reaction indices, reactivity coefficients) ; possibility to split the reactivity effects into elementary reaction and/or isotope contributions ; uncertainty analysis on k_{eff} based on dispersion matrix data ; representativeness analysis ; equivalent x-section processing, e.g. for control rod weight calculations;

—Kinetic parameters like β_{eff} (delayed neutron fraction).

5.2.2. Calculation models

We will now present the different options used for this benchmark.

5.2.2.1. Nuclear library

Concerning the nuclear library, ERALIB-1 [14–15] was used. This data bank is an adjusted version of the international nuclear library JEF-2.2. All the adjustments were made in order to minimize variations between calculated and measured quantities for a set of experiences realized on Phénix and Super-Phénix. ERALIB-1 is today the reference library for Phénix calculations.

5.2.2.2. Cross-section generation process

The ECCO cell code [16] was used for the generation of the effective/homogenized cross-sections used later in core calculations. Thermal feedback effects (core expansions, Doppler widening effect, etc.) were taken into account in cell calculations. Thermal expansions were simulated by calculating the increase in the geometrical dimensions, simultaneously with the decrease in the material densities. Core inlet temperatures and average axial temperatures were used to estimate diagrid and fuel expansion respectively.

Temperatures for radial and axial expansion were respectively taken at 373 °C (α_{rad} = 1.00624) and 448 °C (α_{ax} = 1.00769) according to the test measurements. The expansion coefficients are calculated on Stainless Steel 316.

The temperatures listed below are the average values used to take into account the dependence of microscopic cross-sections on media's temperature (Doppler Effect).

Zone	Temperature (°C)
Fuel	1227
Blanket	627
Structure	448
Coolant	448
Absorber	448

5.2.2.2.1. Cross-section model for critical media

Concerning critical media, cell calculations were made on hexagonal realistic geometries thanks to the collision probabilities method along with the ROTH 6 approximation [16]. Self-shielding and slowing down on heavy isotopes are treated in a fine energetic mesh (1968 groups). For the other isotopes, a broad energetic mesh was used (33 groups). In a fast reactor, cross-sections depend very little on burnup, so effective cross-sections were only computed for average isotopic concentration zones (inner core; outer core; breeder core).
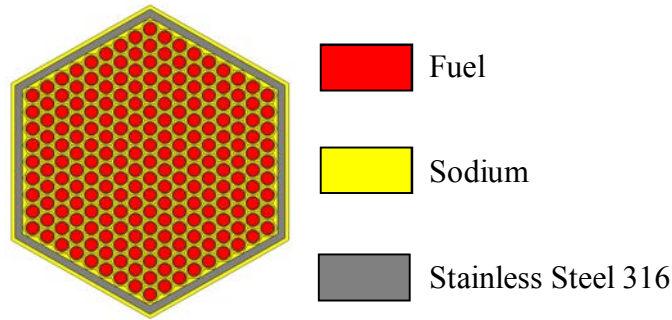
FIG. 33. Hexagonal geometry used for critical media.

5.2.2.2.2.   Cross-section model for sub-critical media

The calculations for fertile media were performed in homogeneous geometries thanks to the fundamental mode method. Self-shielding and neutron slowing down on heavy isotopes are treated in a fine energetic mesh (1968 groups). For the other isotopes, a broad energetic mesh was used (33 groups). Flux in such a cell was given by a calculation in a neighbor critical media.

5.2.2.2.3.   Cross-section model for shielding media

The calculations for shielding media were performed in homogeneous geometries thanks to the fundamental mode method self-shielding and neutron slowing down are treated in a broad energetic mesh (33 groups). Flux in such a cell was given by a calculation in a neighbor critical media.

5.2.2.2.4.   Cross-section model for absorbent media

Control rod effective cross-sections were computed using a specific scheme [17] based on the joint use of ECCO and a bi-dimensional SN-Transport solver (BISTRO [18]) on fine geometry in order to accurately process the strong local effects due to the absorber rods.The ECCO cell code was used to generate effective cross-sections of elementary media (B_4C, FILL 1, FILL 2, FUEL). A precise calculation with transport theory was then done on a fine cartesian mesh (see Fig. 34 and Fig. 35) using the SN solver BISTRO. A reactivity equivalence procedure described in Ref. [17] was finally used to generate the equivalent effective cross-sections for homogeneous control rod media.
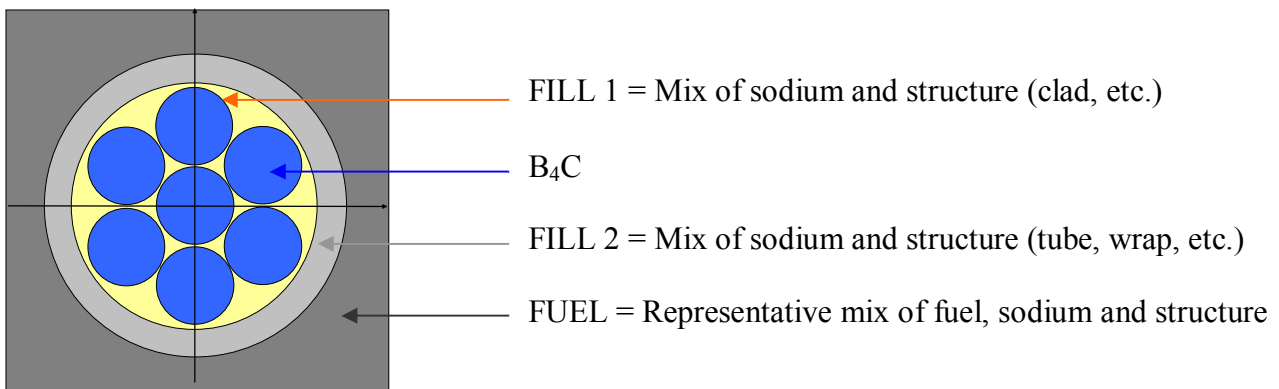

FILL 1 = Mix of sodium and structure (clad, etc.)

B_4C

FILL 2 = Mix of sodium and structure (tube, wrap, etc.)

FUEL = Representative mix of fuel, sodium and structure
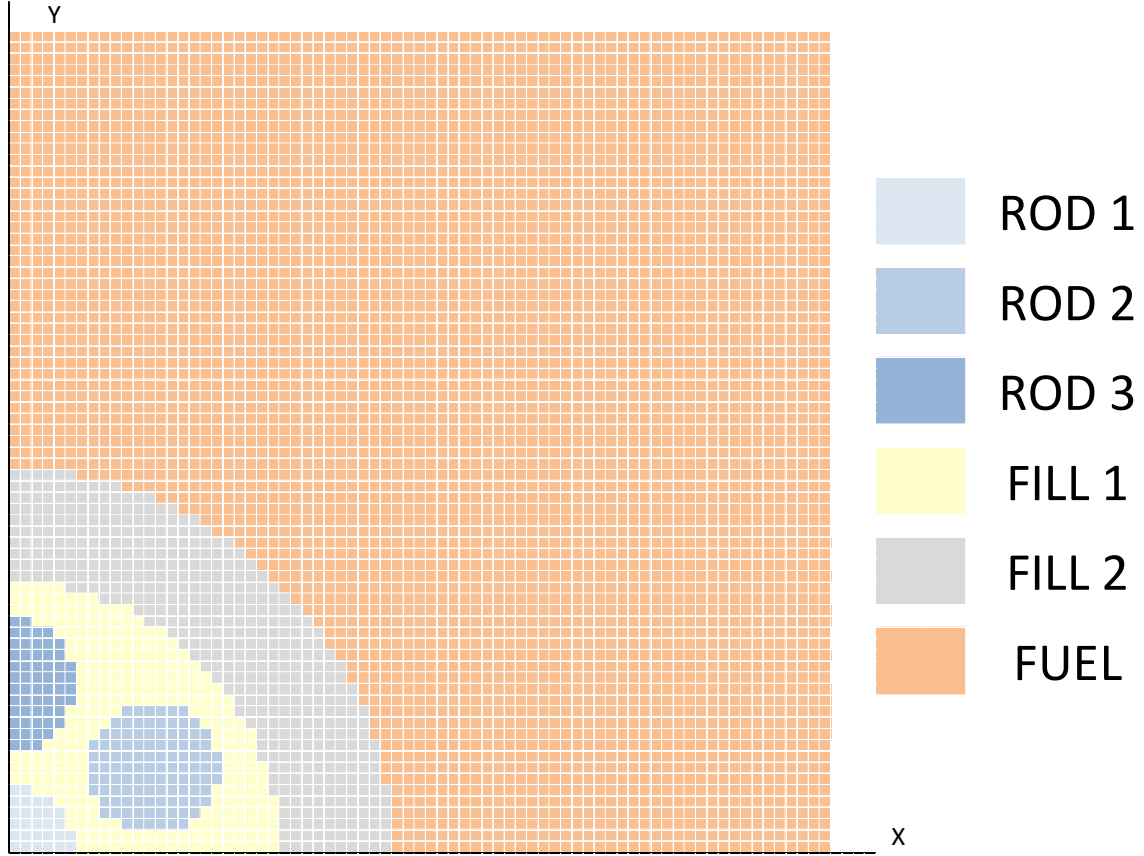
FIG. 34. Simplified geometry of SCP.

FIG. 35. Cartesian geometry used for SCP in BISTRO.

5.2.2.3. *Whole-Core calculation process*

The US (ANL) code VARIANT [10] was used in order to compute core calculations. The cross-sections used for each homogenized media comes from cell homogenization performed by ECCO.

VARIANT solves the multigroup steady-state neutron diffusion and transport equations in two- and three-dimensional Cartesian and hexagonal geometries using variational nodal methods. The transport approximations involve complete spherical harmonic expansions up to order P_{99}. Eigenvalue, adjoint, fixed source, gamma heating, and criticality (concentration) search problems are allowed. Anisotropic scattering is treated, and although primarily designed for fast reactor problems, upscattering options are also included.

Calculations were done in a hexagonal 3D geometry with an order P_3 angular expansion of the flux. Broad energy-group mesh (33 groups) was used.

Moreover, the following options were used:

— Spherical harmonic expansion order: P_3
— Flux development order in each nodes: 6
— Flux development order in surfaces: 1
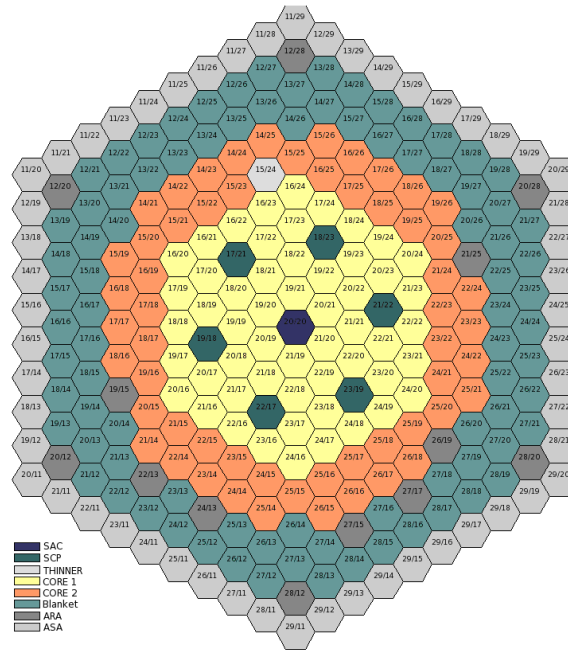— Source development order in each nodes: 2

FIG. 36. Core loading plan.

Using core calculations, it was estimated the k_{eff} and the power distribution for each state of the core during the test.

Below is shown the hexagonal mesh used by VARIANT:

Number of Inner S/A	54
Number of Outer S/A	56
Number of Breeder S/A	84
Number of Control rod	6+1

Each sub-assembly is broken up into 25 axial nodes and only 1 radial node.

Using the flux coefficients calculated by VARIANT, it was possible to recompute 7 or 19 radial points per S/A (Fig. 37).
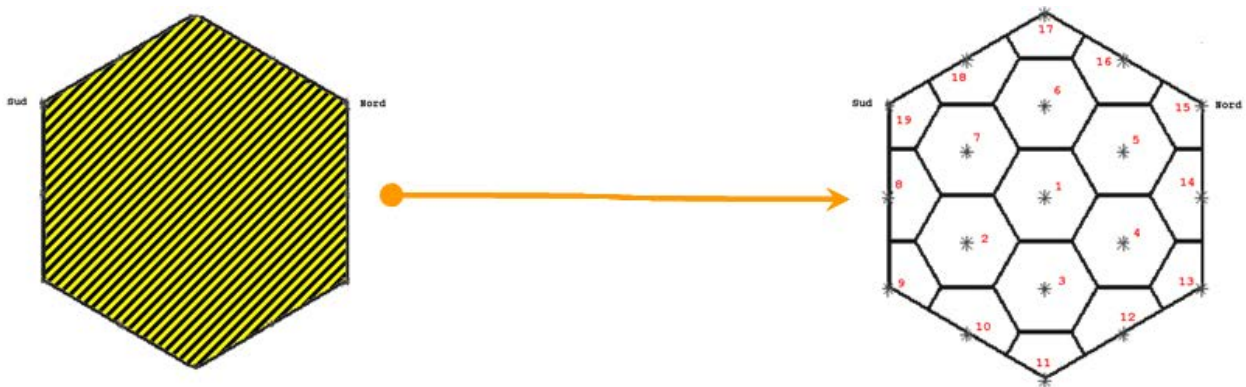
FIG. 37. Building of a fine radial mesh.

49

5.2.2.4. Power calculation

Power distributions were calculated using the calculated flux and the energy release by reactions. The assumption that gamma ray are not transported was made. However the energy linked to gamma rays is taken into account for the power balance (see Table 20).

TABLE 20. ENERGY RELEASE BY REACTIONS (CEA WITH ERALIB-1)

Nuclide	Heat / Capture [MeV]	Heat / Fission [MeV]	Nuclide	Heat/ Capture [MeV]	Heat / Fission [MeV]
U234	5,297	191,06	SFPPU241	8	0
U235	6,5452	196,29	SFPPU242	8	0
U236	5,1244	194,14	O	4,1434	0
U238	5,4789	201,03	FE54	9,299	0
NP237	5,482	198,812	FE56	7,646	0
NP239	5,1681	198,385	FE57	10,44	0
Pu238	5,647	197,2	FE58	6,581	0
PU239	6,5336	201,63	CR50	9,261	0
PU240	5,2415	204,18	CR52	7,94	0
PU241	6,3097	204,56	CR53	9,719	0
PU242	5,0342	206,41	CR54	6,246	0
AM241	5,541	206,5	NI58	9	0
AM242M	6,364	203,225	NI60	7,82	0
AM242F	6,3643	203,225	NI61	10,6	0
AM243	5,363	202,56	NI62	6,839	0
CM242	5,701	202,467	NI64	6,098	0
CM243	6,799	203,86	MO	8	0
CM244	5,52	205,55	TI	8,5137	0
CM245	6,451	206,805	CU	7,75	0
CM246	5,16	206,917	SI	8,7676	0
CM247	6,21	207,94	MN	7,2704	0
CM248	4,713	208,053	NA	6,9593	0
SFPU235	8	0	B10	0,4776	0
SFPU238	8	0	B11	3,3699	0
SFPPU239	8	0	C	4,947	0
SFPPU240	8	0			

5.3. IGCAR

The Indira Gandhi Centre for Atomic Research (IGCAR) was established in 1971, under the Department of Atomic Energy, Government of India. It is engaged in broad based multidisciplinary programme of scientific research and advanced engineering directed towards the development of fast breeder reactor technology. The Fast Breeder Test Reactor (FBTR), based on unique mixed plutonium uranium carbide fuel, first of its kind in the world and KAMINI reactor, the only operating reactor in the world using U-233 fuel, are operating in this centre. Based on the FBTR operation experience and the R&D activities of more than three decades on fast reactors, IGCAR has designed a mixed oxide, pool type 500 MW(e) Prototype Fast Breeder Reactor (PFBR) and its construction is now in the advanced stage at Kalpakkam. There are also plans to construct few more reactors of the same capacity with improved economy and safety. R&D towards the development of sodium cooled fast reactors based on metal fuels with closed fuel cycle is also on-going in this centre.

5.3.1. Codes and calculation models

IGCAR used two code systems, FARCOB and ERANOS 2.1, for this benchmark analysis [19]. Flowcharts giving various codes/modules and cross-section libraries in FARCOB [20] and ERANOS 2.1 [13] are given in Fig. 38 and Fig. 39.

Modeling of Phénix core is done based on the data provided for this benchmark analysis. By using the radial and axial expansion coefficients, the geometrical data and the atom densities of nuclides in various media at the operating temperature are estimated from the corresponding data provided at 20 °C. The neutron cross-section library used is the Russian ABBN-93 [21] set in FARCOB system whereas ERANOS 2.1 uses the JEF-2.2 based adjusted ERALIB1 library [14–15]. It has to be noted that both these cross-section libraries have been adjusted for medium-sized sodium cooled fast reactor cores with oxide fuel. In FARCOB system, the lumped fission product atom densities are reduced to half as per the convention adopted in ABBN-93 library that total yield of fission products is unity. The neutronics calculations based on multigroup 3-D diffusion theory (33 groups in ERANOS and 26 groups in FARCOB) are performed. For accurate prediction of criticality and power distribution, the heterogeneity effect has been taken into account while preparing self-shielded cross-sections for fuel, blanket and absorber rods. The complexity of these calculations depends on the model and type of medium. In FARCOB system, the NCELL code solves the neutron transport equation in 1-D cylindrical model for fuel and blanket pins by the Interface Current Method and the fluxes obtained are used for homogenizing the cross-sections, whereas in ERANOS 2.1 system, the ECCO code performs the cell calculations using the collision probability method for the 2-D hexagonal geometry descriptions of fuel and blanket S/As and the fluxes obtained are used for homogenizing the cross-sections. For SCP, a special procedure called the reactivity equivalence method is used in ERANOS 2.1 to account for the heterogeneity effect. In FARCOB system, the code COHINT [22] is used for homogenizing the absorber rod cross-sections.
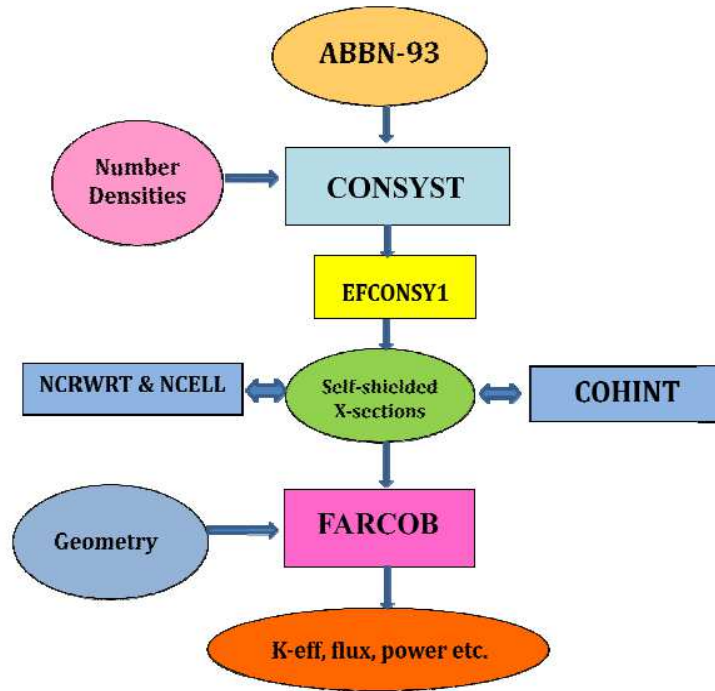
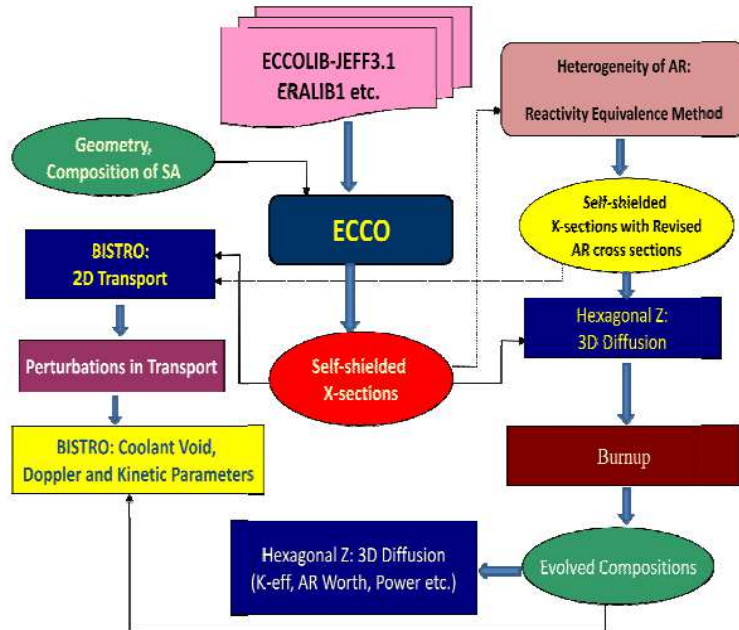*FIG. 38. Calculation scheme at IGCAR using FARCOB system.*

FIG. 39. Calculation scheme at IGCAR using ERANOS 2.1.

Fig. 40 presents the model used for homogenizing the SCP cross-sections in FARCOB system. There are seven B_4C pins surrounded by FILL-1 (region marked in yellow colour with radius r_1) and FILL-2 (region marked in green colour having radius r_2). FILL-1 corresponds to the homogeneous mixture of sodium and steel. The steel fraction is estimated based on the amount of steel present in clad, spacer wire, flow equalizer triangles and the absorber rod inner tube. Similarly, FILL-2 corresponds to the homogeneous mixture of wrapper steel and the sodium present outside

the wrapper tube. One ring of fuel S/A around SCP is considered for defining the super-cell. Thus, the outer radius (R) corresponds to the equivalent radius of seven S/A (1 SCP surrounded by 6 fuel S/A). By using COHINT code, the integral transport equation is solved by the first flight collision probability method in the super cell to get flux distribution. These fluxes are used for computing the homogenized cross-section of the cell. Table 21 gives the geometrical data and the volume fractions of materials in different mixtures of SCP which are used for homogenizing the cross-sections.
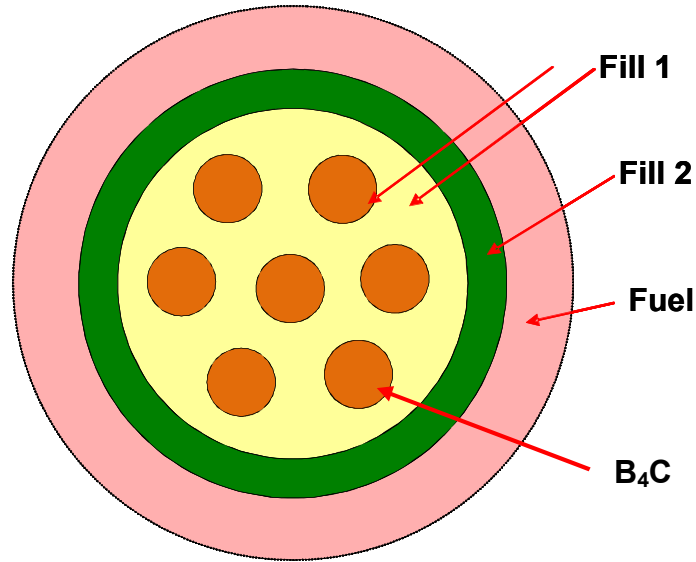
FIG. 40. Super cell for homogenization of SCP cross-sections: FARCOB.

TABLE 21. DATA USED FOR SCP HETEROGENEITY CALCULATIONS IN FARCOB AT THE OPERATING CONDITION

Medium	Volume Fraction (%)			
	Steel	Sodium	B4C	UO_2-PuO_2
Fill-1 (r_1: 4.7796 cm)	52.16	47.84	-	-
Fill-2 (r_2: 6.72 cm)	30.74	69.26	-	-
Fuel (r_3: 17.78 cm)	25.09	36.08	-	38.83
B_4C (pellet radius: 1.1823 cm)	-	-	100	-

For fuel and blanket assemblies, 1-D cylindrical geometries are used in FARCOB system, to prepare heterogeneous cross-sections (see Fig. 41). With S/A area 141.917 cm^2 at the operating condition, radius equivalent to that of fuel in a single pin (r_1) is estimated as 0.2843 cm. Similarly, equivalent radii for steel (r_2) and sodium (r_3) in these cells are 0.3648 and 0.4563 cm respectively. The values of r_1, r_2 and r_3 for upper axial blanket are 0.6667, 0.8228 and 1.10495 cm respectively. The corresponding values in radial blanket are 0.6265, 0.7298 and 0.8606 cm respectively. The cell calculation by using the interface current method is done with NCELL code. The code NCRWRT is used to convert the homogeneous cross-sections in EFFCROSS format to SMAXY format as required in NCELL code. It is also used to update the cross-section library for FARCOB calculations after preparing the heterogeneous cross-sections.
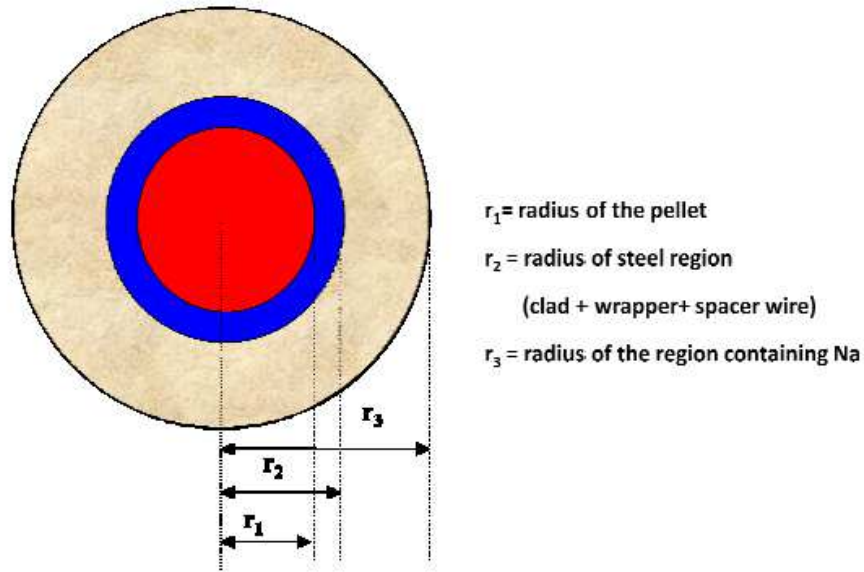
FIG. 41. 1-D cylindrical model for core and blanket assemblies: FARCOB.

In ERANOS 2.1, two dimensional ¼ models in X-Y geometry (see Fig. 42) giving the homogeneous and heterogeneous descriptions of SCP with fuel around the absorber rod, are used for treating absorber rod heterogeneity by the reactivity equivalence method [17]. Fuel is filled beyond absorber rod up to 30 cm in both X and Y direction (i.e. the value of R in Fig. 42 is 30 cm). Perturbation theory calculations are done by using 2-D S_n transport theory code BISTRO [18] to adjust the homogenized cross-section sections of SCP such that both these homogeneous and heterogeneous X-Y models have the same core reactivity. Table 22 gives the geometrical data (at 20 °C) and the volume fractions of materials in different mixtures of SCP which are used for homogenizing the cross-sections.

TABLE 22. DATA USED FOR SCP HETEROGENEITY CALCULATIONS IN ERANOS (20 ° C)

Medium	Volume Fraction (%)			
	Steel	Sodium	B4C	UO_2-PuO_2
Fill-1 (r_1: 4.75 cm)	52.16	47.84	-	-
Fill-2 (r_2: 6.6785 cm)	30.74	69.26	-	-
Fuel (R: 30 cm)	25.09	36.08	-	38.83
B_4C (pellet radius: 1.175 cm)	-	-	100	-

(a) Heterogeneous ¼ model　　　　(b) Homogeneous ¼ model
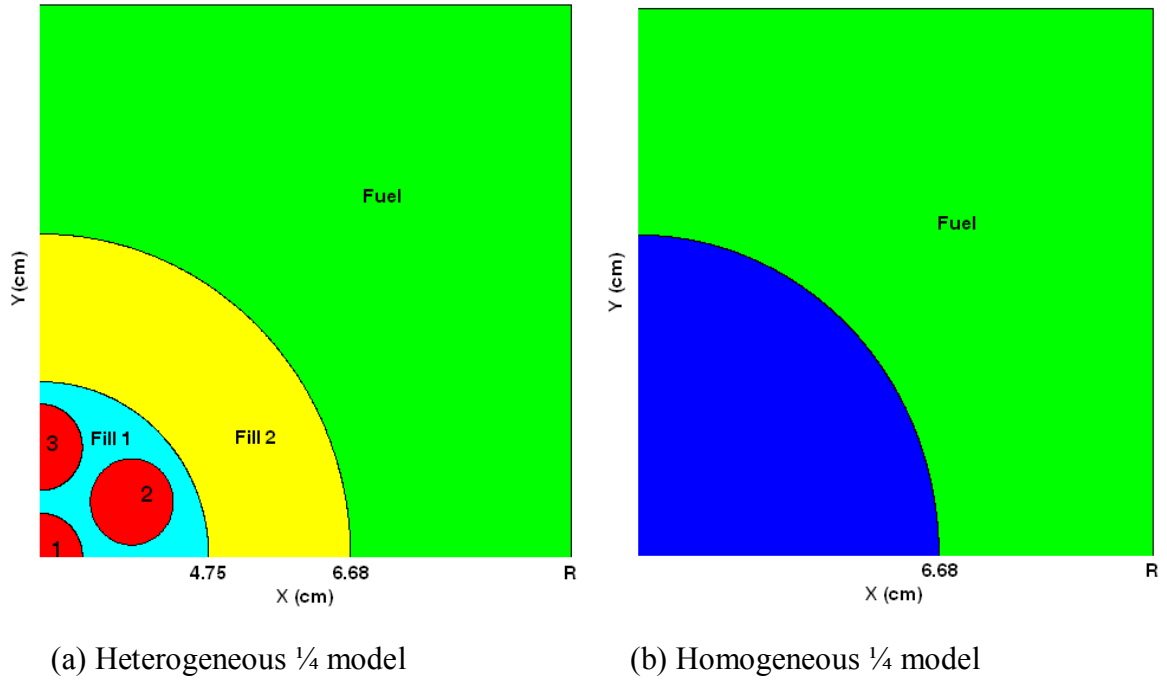
FIG. 42. X-Y models of SCP for reactivity equivalence method calculations in ERANOS 2.1.

5.4. IPPE

No data was made available by the Institute of Physics and Power Engineering (IPPE), Russian Federation.

5.5. IRSN

The IRSN is the French Institute for Radiological Protection and Nuclear Safety. Set up by law 2001-398 of 9 May 2001, under the statute of public authority of industrial and commercial nature (EPIC), it is the national public expert in nuclear and radiological risks. IRSN contributes to public policy making concerning nuclear safety and health and environmental protection against ionizing radiation. As a research and expert appraisal organization, IRSN works together with all the participants concerned by these policies while keeping an open mind.
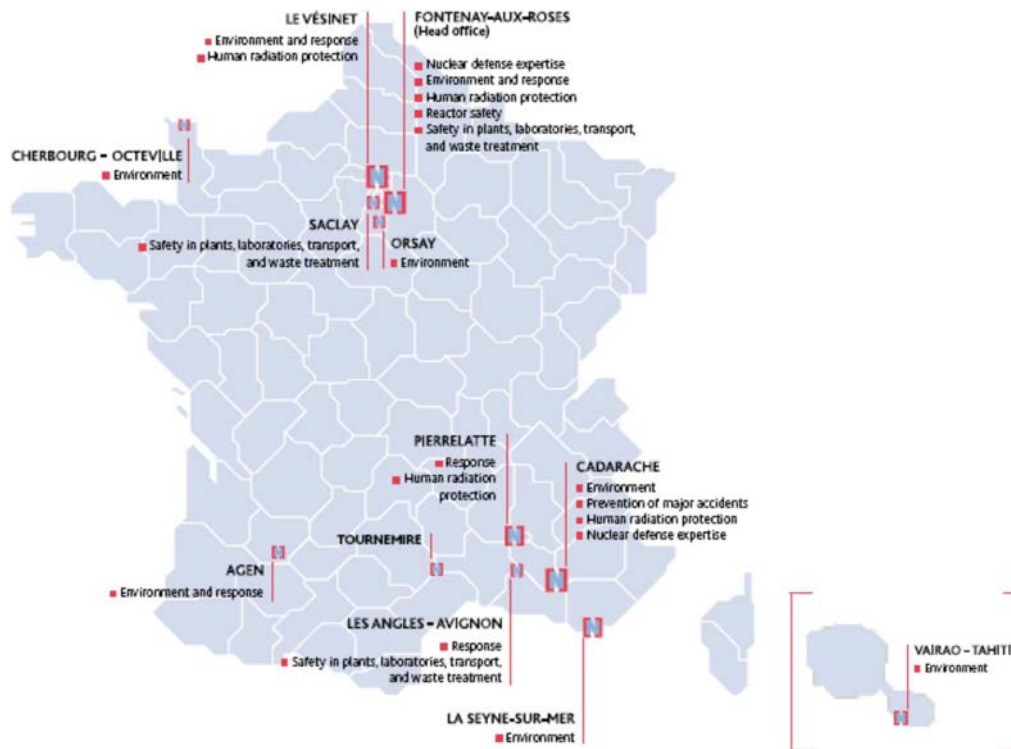
FIG. 43. IRSN main activities.

One of IRSN missions is to perform a critical assessment of safety analysis of operating and under construction reactors, as well as future projects like new sodium cooled fast reactor concepts. In this framework, one current objective of IRSN is to evaluate the ability and accuracy of numerical tools to predict consequences of accidents. Participating to the 'Control Rod Withdrawal' benchmark contributed to reaching this objective.

5.5.1. IRSN's neutronic code for fast reactors

For fast reactors deterministic core calculations, IRSN uses the ERANOS code system, developed by CEA in the framework of a European collaboration. The description of the code and all the references can be found in Section 5.2.

5.5.1.1. Nuclear library

The ERALIB-1 nuclear library has been used (cf. Section 5.2).

5.5.1.2. Cell calculations

The ECCO cell code has been used for the generation of the effective/homogenized cross-sections that are used in core calculations. Three different cell models have been tested: *Homogeneous*, *Heterogeneous_No_Eq* and *Heterogeneous_Eq* (see Fig. 44).
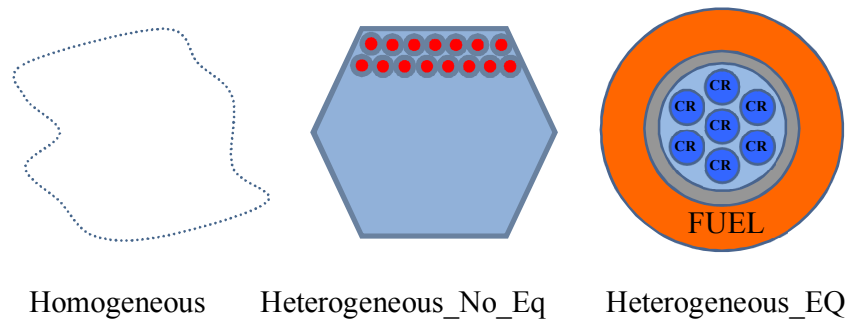
FIG. 44. Cell models for the cross-sections calculation.

— *Homogeneous*: Each subassembly region is considered as a hexagonal prism, in which concentrations of different isotopes are homogenized on the entire volume. Cross-sections shielding is performed considering uniform media with no geometry structure (e.g. infinite homogeneous media).

— *Heterogeneous_No_Eq*: For fissile media, a fine radial description is used taking into account the pin structure inside subassemblies; in this case ECCO homogenizes cross-sections by reaction rates. For media other than fissile ones the homogeneous model is used.

— *Heterogeneous_Eq*: The description of fissile media is exactly the same as the *Heterogeneous_No_Eq* model but an equivalence procedure has been used for the cross-section calculation in control rods. In fact, the strong heterogeneity of the neutron flux distribution (in space, energy and angle) inside and around this kind of subassemblies makes the prediction of their worth strongly dependent on the homogenization procedure adopted. The equivalence procedure allows the calculation of cross-sections taking into account not only the structure of CRs, but also the presence of nearby subassemblies.

All the three models have been tested for the neutronic power calculation. Other options for cell calculations are the same as those used by CEA (cf. Section 5.2).

5.5.1.3. Core calculations

The code VARIANT has been used for core calculations. The transport calculation options are the same as those used by CEA (cf. Section 5.2).

5.5.1.4. Power calculation

The total value of the power consists of power due to fission events and power released further to any neutron capture.

5.6. JAEA

The Japan Atomic Energy Agency (JAEA) has been the principal agency for the Fast Breeder Reactor (FBR) cycle development in Japan. The experimental fast reactor, Joyo, had been successfully operated for about 30 years, beginning in 1977. The prototype FBR, Monju, achieved the first criticality in 1994. Monju restarted its system start-up test (SST) in May 2010 after a 14-year interruption. Major reactor physics parameters, such as criticality, control rod worth, and isothermal temperature coefficient had been measured [23–25]. Monju is designed on the basis of research results obtained from Joyo. Monju has the role of confirming the technological data base

for design and safety evaluation tools, and of accumulating operation experiences for sodium cooled reactors, with an eye toward commercialization.

5.6.1. Neutronic codes and modeling

5.6.1.1. Overview

All of the effective cross-sections were evaluated by SLAROM-UF code with JENDL-3.3 [26–27]. JENDL-3.3 is a general purpose nuclear data library developed in Japan. It contains 337 nuclei data for 10^{-5}-2×10^6 (eV). The ABBN type group-constant set with a constant lethargy 70-energy-group structure based on JENDL-3.3 was used in the analysis. The base effective multiplication factors were calculated by the diffusion calculation code, DIF3D in 3-D Tri-Z geometry [28].

The approximations associated with the finite spatial mesh size, the diffusion theory, and the finite energy groups, were separately corrected to obtain the most accurate calculation results. The flux and power distribution were evaluated without such analytical corrections because the present study focuses on their relative change from a reference state where all the control rods are on a bank position, and the corrections contribute little according to the previous study [29]. The analysis scheme is shown in Fig. 45.

It is noted that the height of the upper blanket is modelled as 26.2 cm in the analysis according to the actual description described in Fig. 18, instead of the value 26.0 cm given in Fig. 25.

5.6.1.2. Cell calculation

5.6.1.2.1. Thermal expansion

The temperatures to consider the thermal expansion for each region are shown in Table 23. The axial averaged temperature, 448.0°C was applied to C1, C2, Breeder Blanket, SCP, SAP, ARA, and ASA. The averaged core inlet temperature, 373.6°C was applied to LB1, LB2, Lower Shield, Na follower. The averaged core outlet temperature, 523.2°C was applied to UB1, UB2 and Upper Shield.

Thermal expansion effect of the geometry was considered based on the temperature for each region. Number densities were diluted in accordance with the thermal expansions.
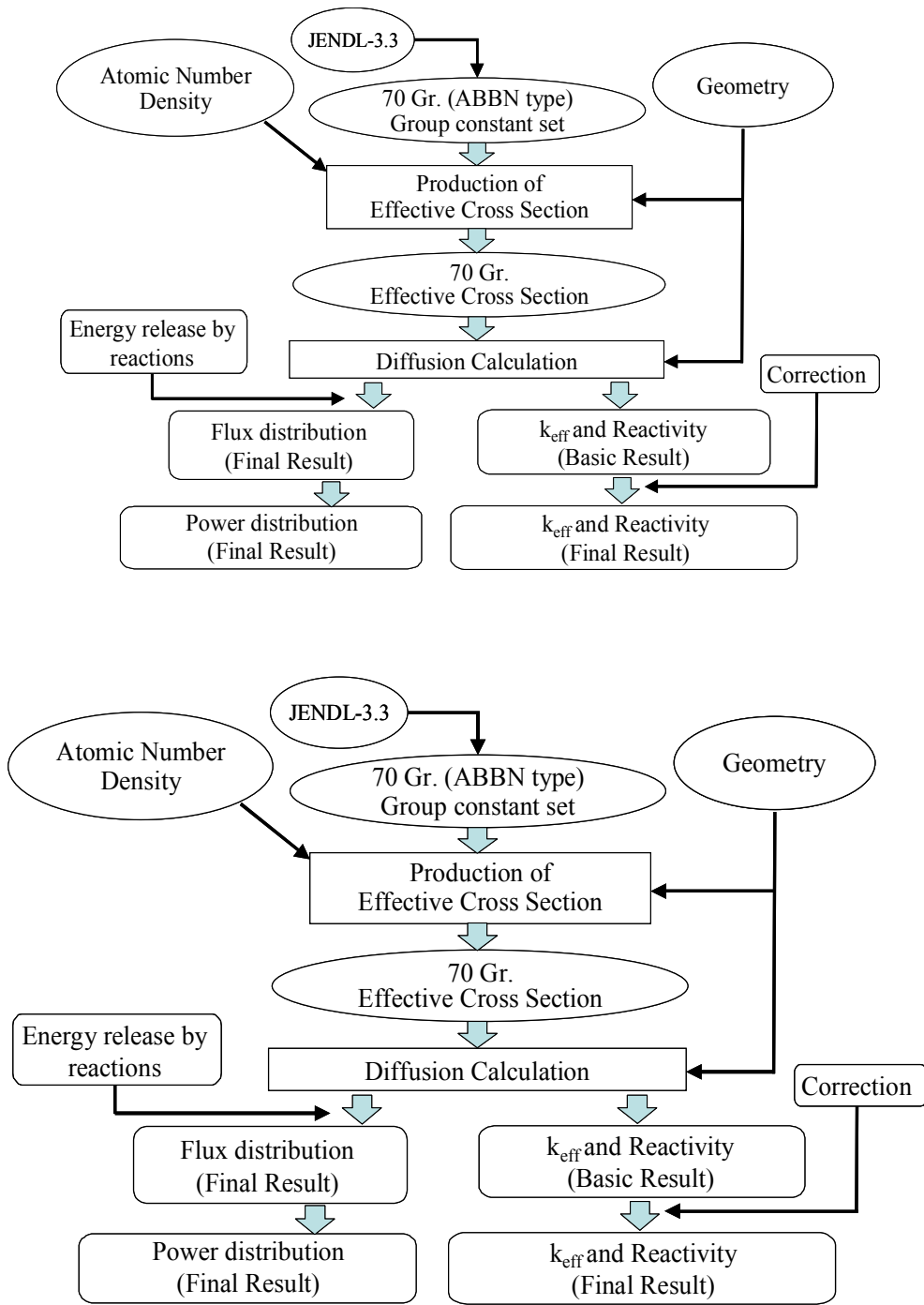
FIG. 45. Schematic diagram of analysis.

TABLE 23. TEMPERATURES AND EXPANSION COEFFICIENTS IN CORE CALCULATION

region			temperature for thermal expansion	expansion coefficient (geometry)			1/(dilution coefficient for number density) [*3)]
				axial[*1)]: α	radial[*2)]: β	volume: $\alpha\beta^2$	
Hetero	Core1, Core2	fuel, clad, spacer	448.0	1.00770	1.00626	1.02035	1.02035
		sodium					1.13306
	Breeder Blanket	fuel, clad, spacer	448.0	1.00770		1.02035	1.02035
		sodium					1.13565
	Upper Blanket	fuel, clad, spacer	523.2	1.00919		1.02186	1.02186
		sodium					1.16265
	Lower Blanket	fuel, clad, spacer	373.6	1.00626		1.01889	1.01889
		sodium					1.10221
	SCP	B$_4$C, clad	448.0	1.00770		1.02035	1.02035
		sodium					1.12960
		surrouned fuels					1.02035
Homo	Upper Shield		523.2	1.00919		1.02186	1.02186
	Lower Shield		373.6	1.00626		1.01889	1.01889
	ARA, ASA		448.0	1.00770		1.02035	1.02035
	SAP		448.0	1.00770		1.02035	1.02035
	Na follower		376.6	1.00626		1.01889	1.10221

*1) Based on the sus expansion rate at the region temperature.

*2) Based on the sus expansion rate at the averaged core inlet temperature, 373.6°C. It is assumed the radial expansion is decided by the expansion of the subassembly pitch at the core inlet temperature.

*3) The dilution of sodium was decided considering sodium thermal expansion and volume ratio.

5.6.1.2.2. Media's temperature

The estimated averaged temperatures listed below were applied in the cell calculation.

Zone type	Temperature [°C]
Fuel	1227
Blanket	627
Structure	459
Coolant	459
Absorber	459

5.6.1.2.3. Cell geometry modeling

The 1-D heterogeneous layer cell models were applied to C1, C2, lower blanket, upper blanket, breeder blanket, and SCP as shown in Fig. 46–49 [30]. Each layer radius was defined considering the thermal expansion. The super cell model was applied to SCP, where the B$_4$C region is surrounded by 6 fuel S/As in the model [30].
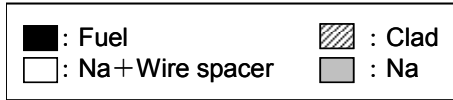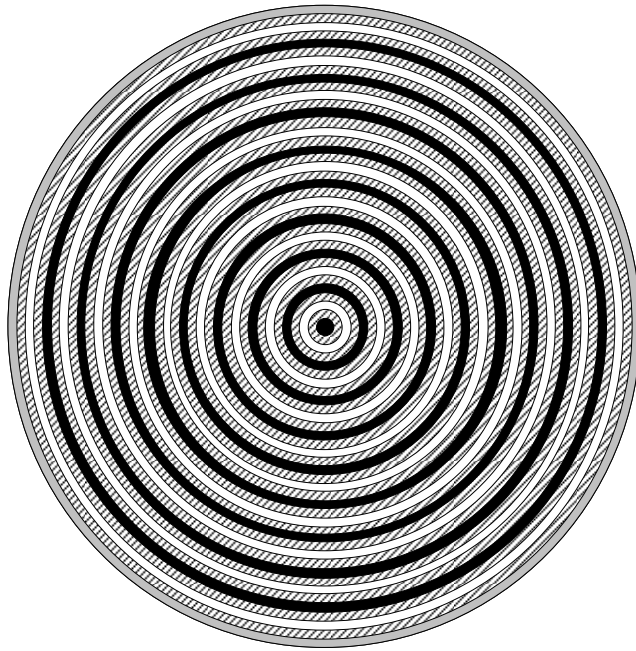
Layer No.	Material	r [cm]	
		C1, C2	LB
1	Fuel	0.285	0.284
2	Clad	0.330	0.330
3	Na + Wire spacer	0.483	0.482
4	Clad	0.542	0.541
5	Fuel	0.883	0.882
6	Clad	0.942	0.940
7	Na + Wire spacer	1.195	1.194
8	Clad	1.254	1.252
9	Fuel	1.595	1.593
10	Clad	1.654	1.652
11	Na + Wire spacer	1.908	1.905
12	Clad	1.966	1.963
13	Fuel	2.308	2.304
14	Clad	2.366	2.363
15	Na + Wire spacer	2.620	2.616
16	Clad	2.679	2.675
17	Fuel	3.020	3.016
18	Clad	3.079	3.074
19	Na + Wire spacer	3.332	3.327
20	Clad	3.391	3.386
21	Fuel	3.732	3.727
22	Clad	3.791	3.785
23	Na + Wire spacer	4.045	4.039
24	Clad	4.103	4.097
25	Fuel	4.445	4.438
26	Clad	4.503	4.497
27	Na + Wire spacer	4.757	4.750
28	Clad	4.816	4.809
29	Fuel	5.157	5.149
30	Clad	5.216	5.208
31	Na + Wire spacer	5.469	5.461
32	Clad	5.528	5.520
33	Fuel	5.869	5.861
34	Clad	5.928	5.919
35	Na + Wire spacer	6.185	6.176
36	Clad	6.545	6.535
37	Na	6.720	6.720

FIG. 46. 1-D layer cell model for C1, C2, LB.
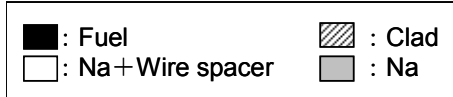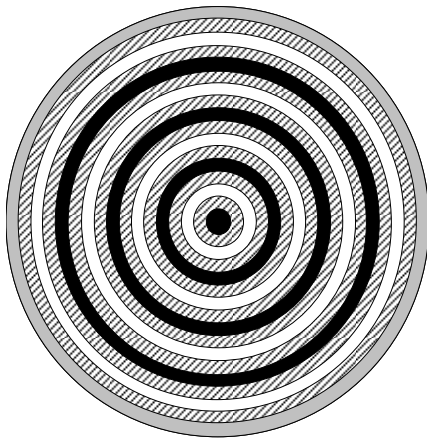
Layer No.	Material	r [cm]
		UB
1	Fuel	0.669
2	Clad	0.719
3	Na + Wire spacer	1.206
4	Clad	1.269
5	Fuel	2.072
6	Clad	2.134
7	Na + Wire spacer	2.876
8	Clad	2.939
9	Fuel	3.742
10	Clad	3.804
11	Na + Wire spacer	4.546
12	Clad	4.609
13	Fuel	5.412
14	Clad	5.474
15	Na + Wire spacer	6.194
16	Clad	6.554
17	Na	6.720

FIG. 47. 1-D layer cell model for UB.
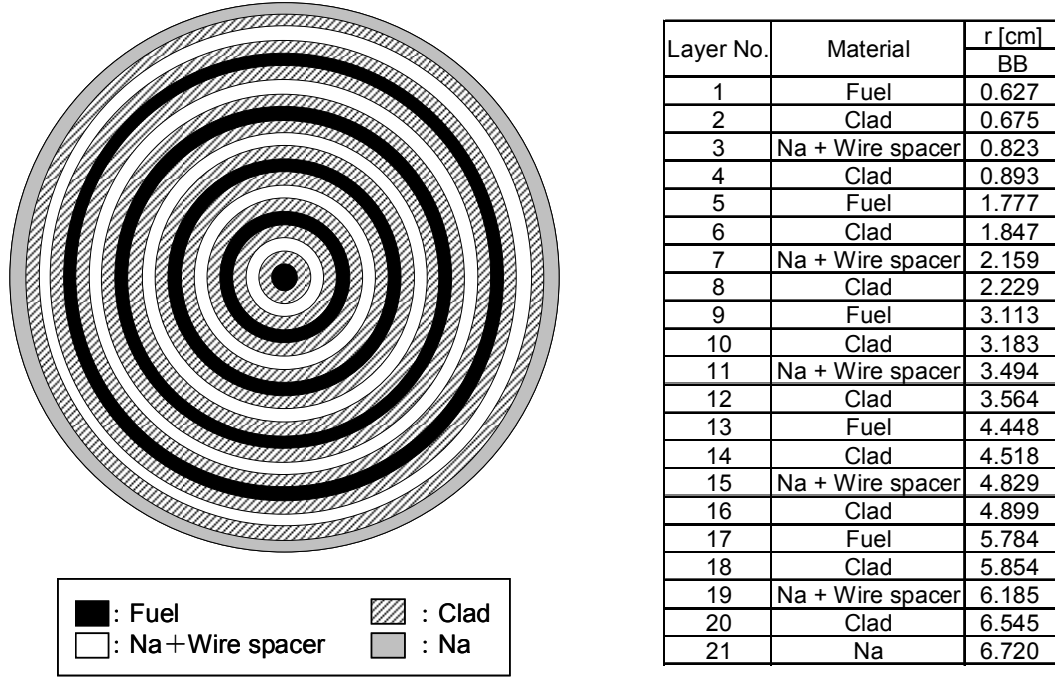
FIG. 48. 1-D layer cell model for breeder blanket.

Layer No.	Material	r [cm] BB
1	Fuel	0.627
2	Clad	0.675
3	Na + Wire spacer	0.823
4	Clad	0.893
5	Fuel	1.777
6	Clad	1.847
7	Na + Wire spacer	2.159
8	Clad	2.229
9	Fuel	3.113
10	Clad	3.183
11	Na + Wire spacer	3.494
12	Clad	3.564
13	Fuel	4.448
14	Clad	4.518
15	Na + Wire spacer	4.829
16	Clad	4.899
17	Fuel	5.784
18	Clad	5.854
19	Na + Wire spacer	6.185
20	Clad	6.545
21	Na	6.720

■ : Fuel   ▨ : Clad
□ : Na＋Wire spacer   ▥ : Na
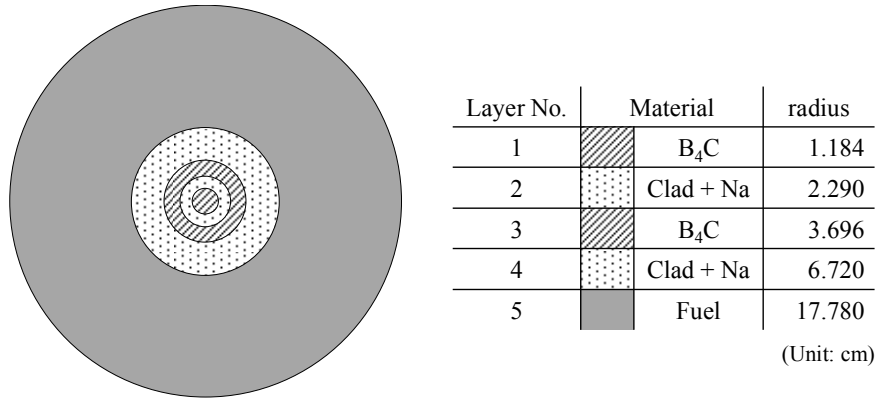
FIG. 49. 1-D layer cell model for SCP.

Layer No.	Material	radius
1	B_4C	1.184
2	Clad + Na	2.290
3	B_4C	3.696
4	Clad + Na	6.720
5	Fuel	17.780

(Unit: cm)

The Reaction Rate Ratio Preservation (RRRP) method was applied to SCP [30–31]. The RRRP method adjusts a homogenized cross-section in the B_4C region, Σ_{CR}^{hom}, to preserve the ratio of the reaction rate in the surrounding fuel region to that in the B_4C region, that is,

$$\underbrace{\frac{\int_{Fuel}\Sigma_{Fuel}(r)\Phi^{hom}(r)dr}{\int_{CR}\Sigma_{CR}^{hom}(r)\Phi^{hom}(r)dr}}_{After\ homogenization} = \underbrace{\frac{\int_{Fuel}\Sigma_{Fuel}(r)\Phi^{hetero}(r)dr}{\int_{CR}\Sigma_{CR}(r)\Phi^{hetero}(r)dr}}_{Before\ homogenization} \tag{8}$$

where the superscripts hetero and hom mean that the values are those before and after the homogenization, respectively. The homogenized cross-section, Σ_{CR}^{hom} is obtained by:

$$\Sigma_{CR}^{\text{hom}} = \frac{\int_{Fuel} \Sigma_{Fuel}(r)\Phi^{\text{hom}}(r)dr}{\int_{CR} \Phi^{\text{hom}}(r)dr} \cdot \frac{\int_{CR} \Sigma_{CR}(r)\Phi^{\text{hetero}}(r)dr}{\int_{Fuel} \Sigma_{Fuel}(r)\Phi^{\text{hetero}}(r)dr}. \tag{9}$$

5.6.1.3. Basic core calculation

Basic core calculation was carried out with a diffusion calculation code, DIF3D in Tri-Z geometry (6 meshes/S/A), in 70 energy groups, and with the effective microscopic cross-sections calculated by SLAROM-UF. The Benoist's anisotropic diffusion coefficient was applied to the basic core calculation in the criticality and control rod worth analysis.

The axial thermal expansion was considered based on the temperature shown in Table 23 and the SUS[6] expansion rate. The radial thermal expansion was considered based on the averaged core inlet temperature, 373.6 °C and SUS expansion rate.

5.6.1.3.1. Corrections

The following corrections were considered for the evaluation of criticality and control rod worth. The corrections in the control rod worth analysis were evaluated for full stroke worth.

Finite spatial mesh size

The correction factor for the finite spatial mesh size was evaluated by extrapolating the difference of the results with normal mesh division (radially: 6 meshes/S/A, axially: below 5 cm/mesh) and increased mesh division [29]. The result, corresponding to that with infinite mesh division, is described by:

$$\begin{aligned}
k_{eff}\big|_{\infty mesh} &= k_{eff}\big|_{\substack{normal \\ mesh}} + \Delta k_r + \Delta k_a \\
&= k_{eff}\big|_{\substack{normal \\ mesh}} + \frac{4}{3}\left(k_{eff}\big|_{\substack{radial \\ 24mesh/SA}} - k_{eff}\big|_{\substack{normal \\ mesh}} \right) + \frac{4}{3}\left(k_{eff}\big|_{\substack{axial \\ doubled \\ mesh}} - k_{eff}\big|_{\substack{normal \\ mesh}} \right)
\end{aligned} \tag{10}$$

where:

$k_{eff}\big|_{\infty mesh}$:   multiplication factor with infinite mesh division,

$k_{eff}\big|_{normal\ mesh}$:   multiplication factor with normal mesh division,

Δk_r: correction factor for radial mesh division,

Δk_a: correction factor for axial mesh division.

Diffusion theory

The correction for the diffusion theory was evaluated by the comparison between the diffusion calculation result by DIF3D and the transport calculation result by THREEDANT in XYZ geometry [32].

---

[6] SUS: Stainless Steel.

Finite energy groups

The correction factor for the finite energy groups was evaluated by the ultra-fine energy group calculation option of SLAROM-UF, where group constant in the 175-energty-group structure is produced using 100,000 energy group calculation below 50 keV.

5.6.1.3.2. Nuclear heating calculation

Heat rate in a material is calculated with neutron flux, number density and KERMA (Kinetic Energy Release in MAterials) as described by:

$$H = \sum_{i,g} N_i K_{i,g} \phi_g,$$ (11)

and

$$K_{i,g} = \left(Q'_{f,i} + Em_g\right)\sigma_{f,i,g} + \left(Q_{c,i} + Em_g\right)\sigma_{c,i,g} + \sum_{g'}\left(Em_g - Em_{g'}\right)\sigma_{s,i,g\to g'0},$$ (12)

$$K_{i,g} = \left(Q'_{f,i} + E_g\right)\sigma_{f,i,g} + \left(Q_{c,i} + E_g\right)\sigma_{c,i,g} + \sum_{g'}\left(E_g - E_{g'}\right)\sigma_{s,i,g\to g'}$$ (13)

$$Q'_f = Q_f - E_{NP} - E_{ND}$$ (14)

where:

H:	nuclear heat rate,
N:	number density,
K:	KERMA (Kinetic Energy Release in MAterials),
ϕ:	neutron flux,
Em:	mean neutron energy,
Q'_f:	Qf (fission Q-value) minus average energy of emitted neutrons,
Q_c:	capture Q-value,
σ_f:	microscopic fission cross-section,
σ_c:	microscopic capture cross-section,
$\sigma_{s,g\to g'}$:	microscopic scattering matrix.

The indices *i*, *g* denote the nuclide and the energy group, respectively. The Q-values are shown in Table 24. The *Em* terms represent the mechanism that the emitted neutrons are transported and contribute to heating in a place where the reactions take place.
The treatment decreases the heating in the fissile regions and increases it in the other regions area compared to the conventional treatment not considering the neutron heat transfer [33][7].

---

[7] This is the reason for the power overestimation of "Diluent" and "ARA" S/A by JAEA pointed out in the 4th meeting.

TABLE 24. ENERGY RELEASE BY REACTIONS

nuclide	heat / capture Q_c [MeV]	heat / fission Q'_f [MeV]	nuclide [1]	heat / capture Q_c [MeV]	heat / fission Q'_f [MeV]
U233	6.84	186.16	B10	2.79	0.00
U234	5.32	186.64	B11	8.63	0.00
U235	6.57	188.98	C	-6.07	0.00
U236	5.44	189.35	N	0.28	0.00
U238	5.69	192.50	O	-2.22	0.00
Np237	6.27	190.07	Na	11.65	0.00
Np239	5.14	191.03	Mg	7.34	0.00
Pu238	5.60	191.46	Al	9.73	0.00
Pu239	6.55	193.98	Cr	9.50	0.00
Pu240	5.25	192.64	Mn	9.83	0.00
Pu241	6.35	195.89	Fe	7.76	0.00
Pu242	5.22	194.46	Ni	5.55	0.00
Am241	5.67	195.44	Mo	7.84	0.00
Am241	5.67	195.44	Ta	7.49	0.00
Am243	5.79	196.22	W	0.00	0.00
Am242m	6.39	195.53	Zr	0.00	0.00
Cm242	5.68	197.53	He	0.00	0.00
Cm243	6.80	197.73	Ti	8.52	0.00
Cm244	5.50	195.40	Cu	7.94	0.00
Cm245	6.48	198.13	Si	4.10	0.00
FP from .of U238	8.00	0.00			
FP from .of U235	8.00	0.00			
FP from .of Pu239	8.00	0.00			
FP from .of Pu241	8.00	0.00			

[1] The structure materials nuclides are natural composition.

5.7. KIT

5.7.1. Family of SIMMER codes for simulation of core disruptive accidents

In safety studies of sodium cooled fast reactors, consequences of core disruptive accidents (CDAs) achieving recriticality are a major concern because of the potential mechanical energy release that can impact the integrity of the reactor vessel and/or its internal structures. The recriticality potential is related to a generic feature of sodium cooled fast reactors where the fuel is not arranged in the most reactive configuration, thus redistribution of the core materials (fuel/steel/sodium) during core disruption can lead to the positive reactivity effects and, therefore, to severe nuclear power excursions. The unprotected loss of flow accident (ULOF) is considered as a one of most probable initiation accidents. Due to a positive sodium void effect in the central core regions, sodium boiling and channel voiding may result in CDA with a primary core power excursion that initiates general core degradation: fuel melting, clad failure and/or melting, fuel ejection into coolant with possible energetic fuel-coolant interaction (FCI), molten materials motion, fuel dispersal and relocation into the channels and possible mechanical energy release. In this *initiating phase*, the subassembly can walls prevent radial fuel motion so one-dimensional material motion in the vertical direction within each subassembly determines the accident progression. In the following *transition phase*, further recompaction, formation of large molten pools with melting of the subassembly structures may occur and lead to another critical configuration (recriticality) and further to an *expansion phase* due to formation of sodium vapor bubbles with possible significant mechanical energy release to the reactor structures. In the transition phase, three-dimensional molten material motion should be treated with taking into account the feedback on neutronic involving into consideration the entire core fuel pool, formed after multiply can-wall failures. Thus, transition phase simulation requires modeling of entire core coupling the key thermodynamic and neutronic transient processes.

A SIMMER-II code was developed as the first practical tool for CDA [34], and has been used in many experimental and reactor analyses. However, experience with SIMMER-II had shown many limitations. The development of advanced computer code SIMMER-III was initiated by Japan Atomic Energy Agency (JAEA, former PNC, JNC) in the late 1980s. SIMMER-III is a two-dimensional, multi-velocity-field, multiphase, multi-component, Eulerian fluid-dynamics code coupled with a fuel-pin model and a space- and energy-dependent neutron kinetics model [35–36]. The development and assessment of SIMMER-III have been carried out in international cooperation with KIT (former FZK) and CEA. Recently, IRSN, ENEA, PSI and SCK-CEN joined the cooperation group. The development of the code has successfully reached a milestone with the completion of all the physical models originally intended for the simulation of event sequences of CDAs in fast reactors.

The development of SIMMER-IV, a three-dimensional code based on SIMMER-III technology, is being carried out. Since SIMMER-III is designed and programmed to be as generalized as possible from the beginning of the code development, SIMMER-IV [37] has been developed as a direct extension of SIMMER-III to three dimensions with retaining exactly the same framework in physical models as SIMMER-III. Since then, SIMMER-IV has been coupled with a three-dimensional neutronics code as a result of collaborative work JAEA-KIT, thereby providing integral reactor application [38].

The SIMMER-IV code consists of three basic elements [39] shown in Fig. 50:

— Fluid-dynamics model;

— Structure (fuel-pin) model;

— Neutronics model.
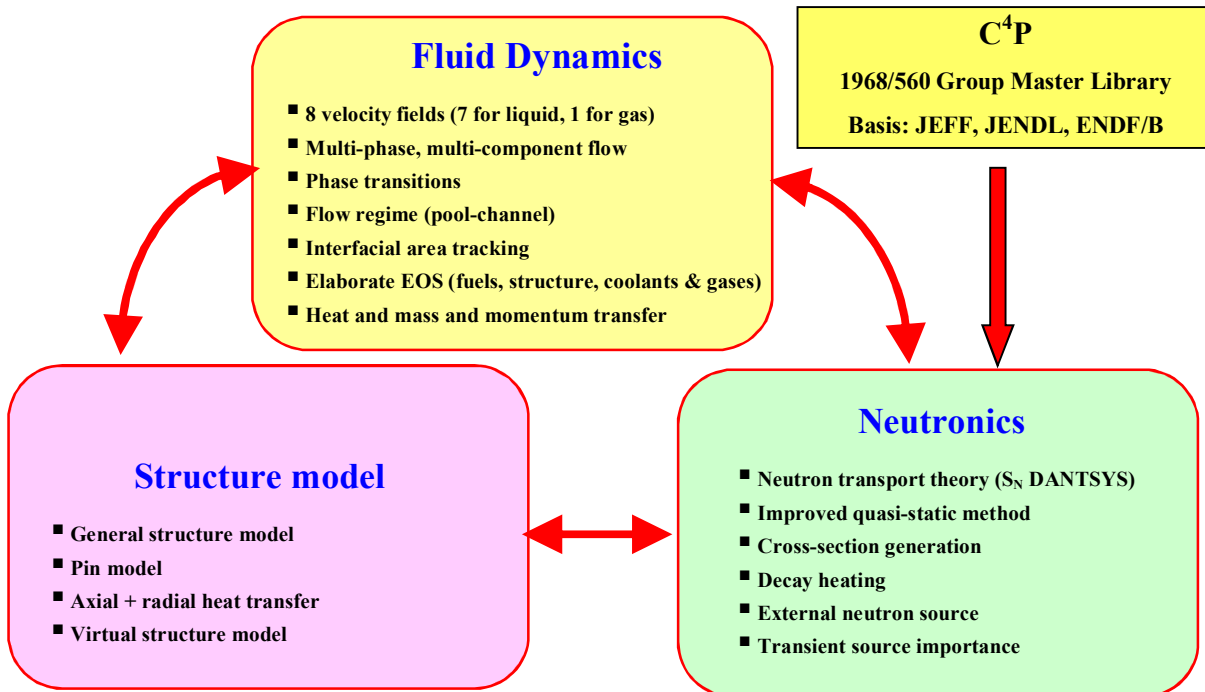
FIG. 50. Basic structure of SIMMER code.

The fluid-dynamics part (the main part of the whole code) is interfaced with the structure model through heat and mass transfer at structure surfaces. The neutronics provides nuclear heat sources

based on the time-dependent neutron flux distribution consistent with the mass and energy distributions. The SIMMER code models five basic SFR core materials; fuel, steel, sodium, control and fission gas. A material can exist in different physical states; for example, fuel can be represented as fabricated pin fuel, liquid fuel, a crust refrozen on structure, solid particles, broken fuel pellets (called chunks) and fuel vapor, whereas fission gas exists only in a single gaseous state. Fuel includes fertile and fissile components to represent different enrichment zones in the core. These two (fertile and fissile) materials are assumed to be mixed intimately; hence a single temperature is assigned as an energy component. The structure field components, which consist of fuel/control pins and can walls, are immobile until they are melted. For the mobile components the number of velocity fields in the recent version of SIMMER-III/IV (ver.E) has been extended from three to eight; thereby improving the precision and extending the applicability of the code.

Material density and energy component distributions are obtained through mass, momentum and energy conservation equations. Multi-velocity-field formulation and the fluid convection solution algorithm are based on a time-factorization approach developed for the AFDM code [40]. In this approach, intra-cell interfacial area source terms, momentum exchange functions and heat-and-mass transfer are determined separately from inter-cell fluid convection. A semi-implicit procedure is used to solve inter-cell convection on an Eulerian staggered mesh. A higher-order differencing scheme is also implemented to improve the resolution of fluid interfaces by minimizing numerical diffusion. This solution procedure of separating intra-cell transfers from fluid convection is believed to be the most practical for complex multi-component systems like SIMMER.

The structure model not only represents the stationary structure in the core, but it also traces the time-dependent disintegration of fuel pins and wrapper can walls. The canwall model can treat two separate left and right canwalls, which are assumed to be located at the mesh-cell boundaries. The presence of a canwall at the cell boundary prevents radial fluid convection, and provides an option for the surface where fuel can freeze and/or vapor can condense. The current version incorporates a multi-node treatment for the internal part of the canwall.

The neutronics part of SIMMER solves the time-dependent multi-group neutron transport equation with the improved quasi-static method. The models for the flux shape calculation are based on TWODANT (in 2D) and THREEDANT (in 3D) [41], S_n transport codes employing the diffusion synthetic acceleration scheme [42]. Effective cross-sections are calculated from a set of infinite diluted cross-sections and self-shielding factors by the cross-sections generator that is a part of the code, and updated at every reactivity step to reflect changes in material number densities and temperatures. The structure and generation routes of the SIMMER cross-section libraries are show in Fig. 51. The standard 11-group library is applied to the fast reactor systems. It is based on the KFKINR-26 group library developed in the past at FZK and tested with experiments. Recently, the latest data for minor actinides and some other nuclides (for transmutation studies) have been added to the standard library. In addition, several obsolete data have been replaced by recent values for the selected isotopes. This standard 11-group CS library has a long application history an it is routinely applied with SIMMER for fast reactor analyses at KIT (former FZK). The intensive verification and benchmarking again other neutronics codes have proven no serious drawbacks (taking into account the small number of energy groups) but very reasonable results for a number of fast reactor systems. More details on the SIMMER-III/IV developments can be found in Ref. [39].

In Phénix EOL benchmark CRP, the steady-state Control Rod Withdrawal tests were simulated with three-dimensional SIMMER-IV code. This benchmark is an important part of the validation assessment of the new SIMMER-IV code. A SIMMER set-up includes modeling of control and shut-down rods at different locations corresponding to the experimental data. Fuel and structure compositions given in the benchmark definition input data are used [43–44].

SIMMER-IV steady-state calculations at the different CR configurations provide detailed information about spatial distribution of the basic core parameters. These results are presented and discussed in the following section.
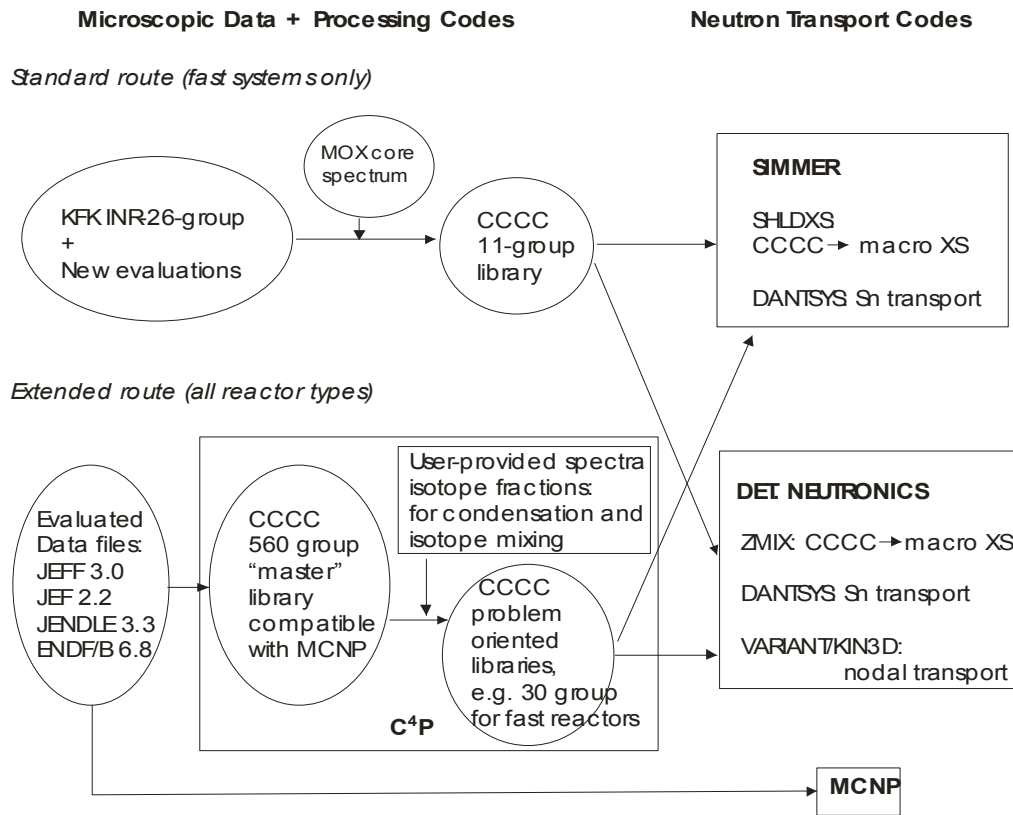
FIG. 51. SIMMER cross-section libraries.

5.7.2. Modeling of Phénix core with SIMMER-IV code

According to the Phénix core layout provided by CEA [44], the core cross-section model has been established for the SIMMER-IV meshing system as shown in Fig. 52. Since a standard rectangular Cartesian system is used in SIMMER-IV, every hexagonal subassembly is modelled by two rectangular cells with the same cross area as shown in right-hand-side part in Fig. 52.

FIG. 52. SIMMER-IV meshing in cartesian 3D: hexagonal subassemblies are transformed in two rectangular cells.

One cross-section of the axial meshing system is shown in Fig. 53. The control rods can be rearranged in a way that reflects the real CRs movement in Phénix EOL CRW tests making five mesh configurations in total:

— Reference state;
— Step 1;
— Step 2;
— Step 3;
— Final State.

69
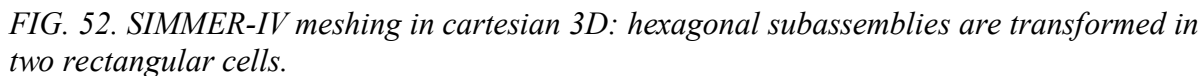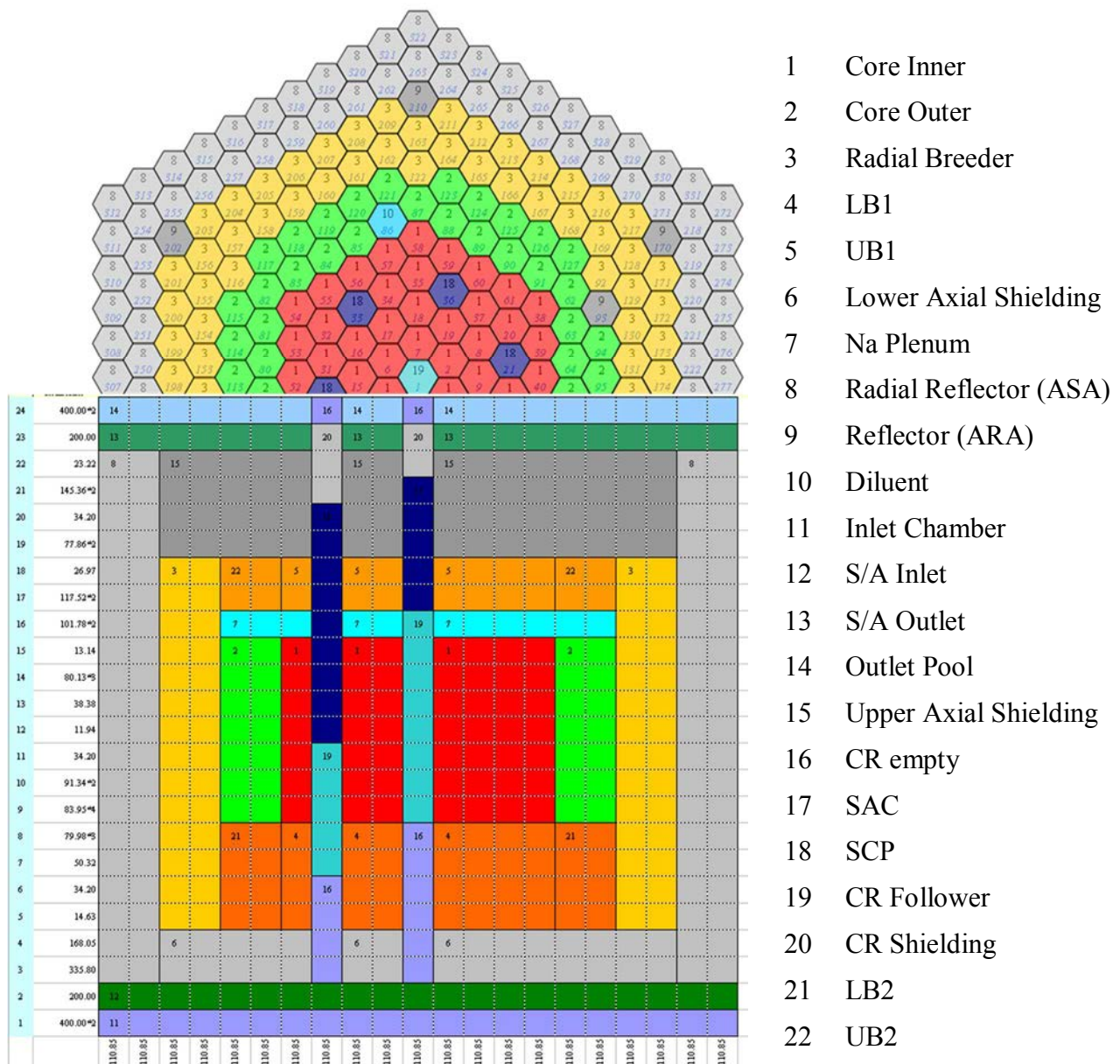
FIG. 53. Axial core meshing.

1	Core Inner
2	Core Outer
3	Radial Breeder
4	LB1
5	UB1
6	Lower Axial Shielding
7	Na Plenum
8	Radial Reflector (ASA)
9	Reflector (ARA)
10	Diluent
11	Inlet Chamber
12	S/A Inlet
13	S/A Outlet
14	Outlet Pool
15	Upper Axial Shielding
16	CR empty
17	SAC
18	SCP
19	CR Follower
20	CR Shielding
21	LB2
22	UB2

Modelling of the control rod insertion in the SIMMER-IV meshing system is shown in Fig. 54 for the different insertion stages.
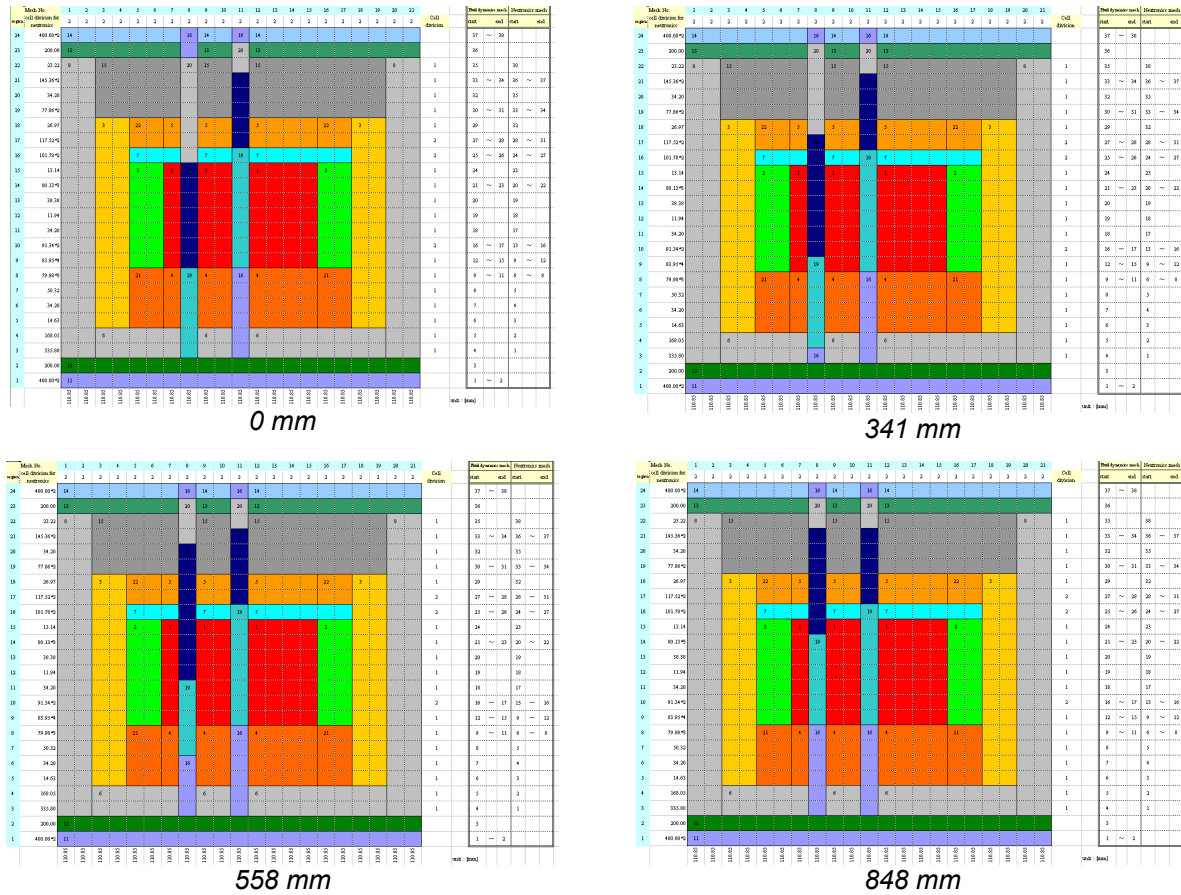
FIG. 54. Modeling of control rods insertion in SIMMER-IV meshing system.

5.7.3. Isotopic compositions and fuel mass adjustment

In SIMMER, an isotopic composition is assigned using fissile/fertile material model. Two isotopic vectors should be defined as an input. For MOX fuel, the 'fertile' material usually includes uranium isotopes while 'fissile' is composed of Pu isotopes, minor actinides and fission products. Then, the isotopic composition in a particular core region is calculated as a combination of the fissile and fertile materials with the given enrichment. In SIMMER, the 'fissile' and 'fertile' vector can be assigned, in principle, for the several 'isotopic' regions, and even cell-wise, but materials from such isotopic regions cannot be mixed together. However, since the fuel movement and mixing is a key phenomenon in a severe accident simulation that is a main SIMMER application, the single isotopic region is usually assigned. In this case, the isotopic composition deviation through the core regions cannot be modelled precisely but should be approximated with a proper selection of two isotopic vectors and zone enrichments. This is usually an optimization problem when the goal is to minimize an error in the mass of the most important isotopes in the most important core regions (fissile core) as well as to conserve the total fuel mass in the system. Such optimization has been performed for the SIMMER input. The total distribution of the fuel isotopes is given in Table 25 while the mass error is shown in Table 26. The most significant error is in the mass of Pu isotopes. In the inner fissile core C1 plutonium mass is ~1% overestimated while in the outer core C2, Pu mass is underestimated on the same value about 1%.

TABLE 25. SIMMER ISOTOPIC COMPOSITION

Mass [kg]	Region[*1]							total
	Core 1[*2]	Lower axial blanket for core 1[*2]	Upper axial blanket for core 1[*2]	Core 2[*3]	Lower axial blanket for core 2[*3]	Upper axial blanket for core 2[*3]	Blanket[*4]	
AM241	9.51	0.40	0.10	11.68	0.34	0.12	2.99	25.13
AM242M	0.24	0.01	0.00	0.30	0.01	0.00	0.08	0.64
AM243	0.33	0.01	0.00	0.40	0.01	0.00	0.10	0.86
CM242	0.24	0.01	0.00	0.29	0.01	0.00	0.07	0.62
CM244	0.04	0.00	0.00	0.05	0.00	0.00	0.01	0.10
FIPRO	77.38	3.24	0.81	95.07	2.74	0.94	24.35	204.54
O	292.99	97.16	61.99	303.48	101.45	64.59	1271.04	2192.70
PU238	2.27	0.10	0.02	2.79	0.08	0.03	0.71	6.00
PU239	311.37	13.04	3.24	382.55	11.01	3.80	97.99	823.00
PU240	135.05	5.66	1.41	165.92	4.78	1.65	42.50	356.96
PU241	11.01	0.46	0.11	13.53	0.39	0.13	3.47	29.10
PU242	4.98	0.21	0.05	6.12	0.18	0.06	1.57	13.16
U235	4.54	2.03	1.33	4.36	2.14	1.38	27.03	42.81
U236	0.12	0.06	0.04	0.12	0.06	0.04	0.74	1.17
U238	1562.84	699.39	456.46	1498.20	735.54	474.72	9295.70	14722.84

TABLE 26. SIMMER ESTIMATION ERROR IN ISOTOPIC MASS COMPOSITION

Mass Error [kg]	Region[1]							total
	Core 1[2]	Lower axial blanket for core 1[2]	Upper axial blanket for core 1[2]	Core 2[3]	Lower axial blanket for core 2[3]	Upper axial blanket for core 2[3]	Blanket[4]	
AM241	0.41	0.40	0.10	-0.51	0.34	0.12	2.98	3.83
AM242M	0.00	0.01	0.00	0.00	0.01	0.00	0.08	0.10
AM243	-0.01	0.01	0.00	0.01	0.01	0.00	0.10	0.14
CM242	0.00	0.01	0.00	0.00	0.01	0.00	0.07	0.10
CM243	0.00	0.00	0.00	0.00	0.00	0.00	0.00	0.00
CM244	0.00	0.00	0.00	0.00	0.00	0.00	0.01	0.02
O	6.85	-0.34	-0.33	10.20	-0.40	-0.33	1.24	16.90
PU238	0.03	0.10	0.02	-0.04	0.08	0.03	0.71	0.93
PU239	2.61	0.33	-0.21	-3.32	0.08	-0.22	0.03	-0.70
PU240	2.26	5.18	1.35	-2.82	4.44	1.56	39.62	51.58
PU241	0.13	0.45	0.11	-0.17	0.38	0.13	3.39	4.43
PU242	0.12	0.21	0.05	-0.15	0.18	0.06	1.57	2.03
U235	0.50	0.04	0.01	0.56	-0.40	0.01	-0.18	0.54
U236	-0.19	-0.04	0.01	-0.14	-0.04	0.00	0.00	-0.41
U238	-8.30	-7.79	-1.70	-9.38	-6.01	-2.03	-62.10	-97.29

5.7.4. Modelling of steady-state via transient simulation

To reach the steady-state at the nominal power level, SIMMER simulation is started with input data described in the previous sections. To simplify the input of the SIMMER code a region-wise (not cell-wise) input parameters, such as coolant, cladding and fuel temperatures are usually provided as an initial guess, from which the code automatically generates internally cell-wise field data and distributions of all quantities. This steady-state iteration would be very short if detailed fields were already provided a priori. Otherwise, the iteration from initial conditions to a balanced steady state may take longer time, both real and CPU. Actual time depends on the consistency of the initial guess.

Simplified pressure and density distributions and only rough approximate temperature distributions are given as the initial conditions, as well as zero values for the initial reactivity and the nominal value for the reactor power. As a result, at start of the calculation, there exists a strong inconsistency between the different field values. The code has to iterate now itself to approach a consistent steady-state in which all parameters are in equilibrium. All material temperatures and material densities are changing and have their impact on the neutron cross-sections, and therefore, on reactivity and power. The monitoring of the power and also the speed up the iteration procedure is performed via insertion of an external effective reactivity. The final steady state SIMMER calculation data set thus represents a state where all thermal-hydraulic parameters as density, temperature, pressure and velocity profiles are in a consistent balance with the neutronic data,

especially the overall reactivity, the overall nuclear power but also the local power distribution. The reactivity history for all test stages is shown in Fig. 55. All feedback effects are 'on' and finally in balance for a steady state. The steady-state conditions are reached after 30-40 seconds of the transient calculation. The entire SIMMER simulation has been performed for fifty seconds to make sure that all possible transient effects, such as flow development inside low-velocity regions, have died out and the steady-state conditions are fully reached.

Thus a full consistency is finally achieved within the neutronic-thermalhydraulic SIMMER modelling (and correspondingly checked by the independent ERANOS model). On the other hand, due to the chosen approximations and the modelling method, some final parameters do not exactly correspond to the nominal conditions provided by CEA [44]. Table 27 compares the reactor power and fissile core outlet temperature for the five CR position tests.

TABLE 27. REACTOR POWER AND OUTLET TEMPERATURE

	Power (MW)		Bulk Fissile Core Outlet Temperature (°C)	
	Experiment	SIMMER	Experiment	SIMMER
Reference State	335.4	334.8	522.7	526.7
Step 1	337.0	336.3	523.8	527.6
Step 2	338.7	338.2	524.3	528.5
Step 3	336.3	335.5	523.2	527.0
Final State	335.2	334.6	522.2	526.4
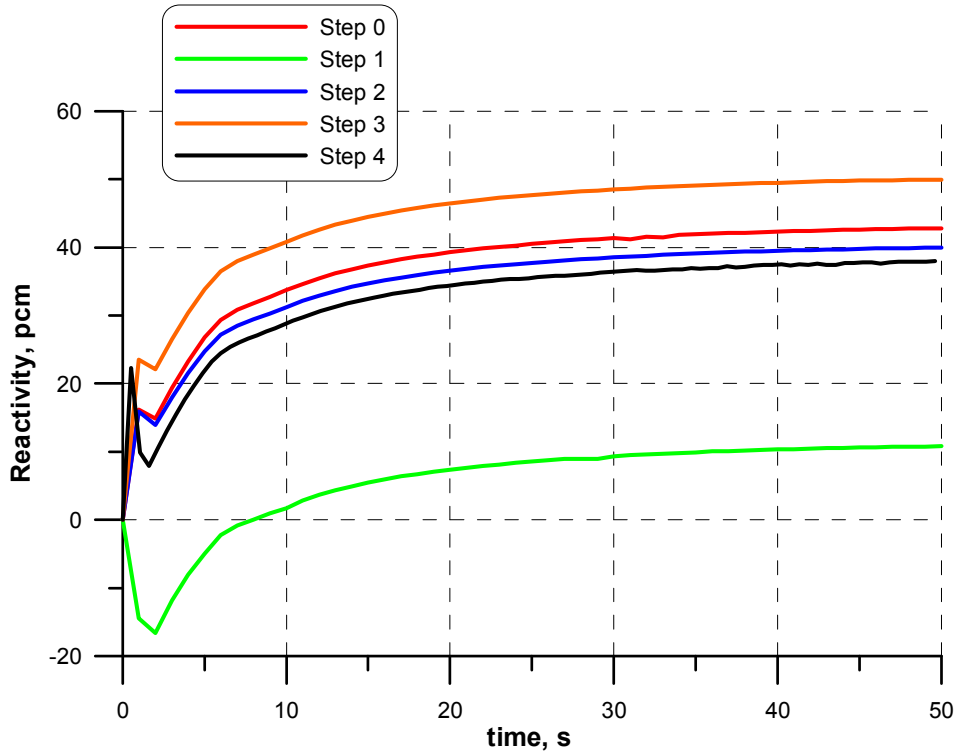
FIG. 55. Reactivity change from initial conditions to equilibrium steady-state.

5.7.5. Core flowrate distribution

In SIMMER, subassembly flowrates are not assigned directly, but calculated according to the pressure boundary conditions and the internal hydraulic resistance of subassemblies. Thus, proper orifice coefficients have to be assigned to reach the desired flowrate distribution given by the CEA input data (Section 3.3, S/A flows [44]). In addition, pressure boundary conditions should be adjusted to ensure the total flowrate through the core and other parts. The inlet orifice coefficients have been adjusted for the every S/A group. The group is defined by the subassemblies with exactly same flowrate value. The comparison between test input data (Section 3.3, S/A flows [44]) and SIMMER-calculated flowrates is give in Table 28. Since the mass flow rates for the control and shutdown rods are not defined in Ref. [44] (defined as zero) the average flow rate in CR and SR subassemblies is accepted as 1.86 kg/s that corresponds to the total flow rate in control rods 13 kg/s given in Ref. [43]. Note that CEA input data assume constant flow rate through the several main S/A groups, however in SIMMER calculations, the flow rate distribution fluctuates slightly due to the flow non-uniformity resulting from flow re-distribution in the core inlet and outlet plena, radial reactor power and temperature heating distribution, etc. The average flow rate in the every S/A group is in a very good agreement with CEA input data (Section 3.3, S/A flows [44]).

The SIMMER-IV model described in this section was used as a basis to perform required simulations.

TABLE 28. REACTOR POWER AND OUTLET TEMPERATURE

Position	CEA Input Flowrate kg/s	SIMMER Flowrate kg/s	Group Average kg/s	S/A type
20-20	0.00	1.86	1.86	SAC
21-22	0.00	1.86	1.86	SCP
23-19	0.00	1.86		
22-17	0.00	1.86		
19-18	0.00	1.86		
17-21	0.00	1.86		
18-23	0.00	1.86		
15-24	0.00	0.34	0.33	THINNER
21-25	0.00	0.33	0.33	ARA
26-19	0.00	0.33		
19-15	0.00	0.33		
20-26	3.45	4.29	4.29	Blanket
26-20	3.45	4.29		
26-14	3.45	4.29		
20-14	3.45	4.29		
14-20	3.45	4.29		
14-26	3.45	4.29		
22-24	12.09	12.08	12.08	Blanket
24-22	12.09	12.08		
26-16	12.09	12.07		
24-14	12.09	12.07		
22-14	12.09	12.08		
21-14	12.09	12.07		
18-16	12.09	12.07		
15-19	12.09	12.08		
14-25	12.09	12.08		
18-26	12.09	12.08		
14-22	12.10	12.09	12.09	Core 2
16-26	12.10	12.09		
15-25	12.65	12.64	12.63	Core 2
23-14	12.65	12.63		
20-25	12.66	12.65	12.65	Core 2
14-23	12.66	12.65		
23-17	13.35	13.34	13.34	Core 1
24-20	13.35	13.34		
16-23	14.76	15.75	14.74	Core 1
26-18	14.76	14.23		
25-14	14.76	14.24		
20-22	14.77	15.31	14.76	Core 1
21-21	14.77	15.32		
22-20	14.77	15.31		
22-19	14.77	15.31		
22-18	14.77	15.31		
21-18	14.77	15.30		
20-18	14.77	15.31		
19-19	14.77	15.31		
18-20	14.77	15.31		
18-21	14.77	15.31		
18-22	14.77	15.32		
19-22	14.77	15.30		
20-23	14.77	15.32		
22-21	14.77	15.32		
23-20	14.77	15.32		
23-18	14.77	15.32		
21-17	14.77	15.32		
20-17	14.77	15.33		
18-19	14.77	15.32		
17-20	14.77	15.32		
17-22	14.77	15.33		
17-23	14.77	15.33		
19-23	14.77	15.32		
20-24	14.77	15.32		
21-23	14.77	15.33		
22-22	14.77	15.32		
23-21	14.77	15.32	14.76	Core 1

Position	CEA Input Flowrate kg/s	SIMMER Flowrate kg/s	Group Average kg/s	S/A type
24-19	14.77	15.32		
24-18	14.77	15.32		
24-17	14.77	15.32		
24-16	14.77	15.33		
23-16	14.77	15.32		
22-16	14.77	15.32		
21-16	14.77	15.32		
20-16	14.77	15.32		
19-17	14.77	15.33		
18-18	14.77	15.32		
17-19	14.77	15.32		
16-20	14.77	15.32		
16-21	14.77	15.32		
16-22	14.77	15.32		
16-24	14.77	15.32		
17-24	14.77	15.32		
18-24	14.77	15.32		
19-24	14.77	15.32		
21-24	14.77	13.75		
24-21	14.77	13.77		
25-20	14.77	13.74		
25-19	14.77	13.76		
25-15	14.77	13.75		
24-15	14.77	13.77		
21-15	14.77	13.77		
20-15	14.77	13.75		
19-16	14.77	13.75		
16-19	14.77	13.76		
15-20	14.77	13.76		
15-21	14.77	13.76		
16-25	14.77	13.77		
19-25	14.77	13.76		
23-23	14.77	13.74		
25-21	14.77	13.74		
26-17	14.77	13.74		
26-15	14.77	13.74		
17-17	14.77	13.75		
16-18	14.77	13.75		
14-21	14.77	13.74		
14-24	14.77	13.75		
15-26	14.77	13.75		
17-26	14.77	13.74		
19-26	14.77	13.74		
18-17	15.06	15.05	15.05	Core 2
20-21	15.07	16.06	15.06	Core 1
21-20	15.07	16.06		
21-19	15.07	16.05		
20-19	15.07	16.06		
19-20	15.07	16.05		
19-21	15.07	16.05		
22-23	15.07	14.57		
23-22	15.07	14.56		
25-18	15.07	14.57		
25-17	15.07	14.57		
25-16	15.07	14.57		
23-15	15.07	14.57		
22-15	15.07	14.57		
17-18	15.07	14.56		
15-22	15.07	14.56		
15-23	15.07	14.57		
17-25	15.07	14.57		
18-25	15.07	14.57		

5.8. PSI

A static model of the Phénix core was first developed with the ERANOS code. This allowed preparing the macroscopic cross-sections and derivatives used in the PARCS code to enable a 3D neutronics coupling to the thermal–hydraulics in TRACE. This section presents the development and verification of the models.

5.8.1. ERANOS model

ERANOS-2.1 [11] is a deterministic neutronics code developed by the CEA with an emphasis on fast reactor analysis, particularly liquid metal fast reactors. Two ERANOS modules have been used in this study, viz. ECCO [16] and VARIANT [45]. ECCO was used to generate cell-averaged, self-shielded macroscopic cross-sections according to the reactor region. These calculations were based on the JEF-2.2 nuclear data library. For the first phase of the blind calculations all regions were treated by ECCO homogeneously, while for the final solution fuel and CR regions were treated by ECCO heterogeneously, and the other zones were treated homogeneously. According to the CRP benchmark description, the fuel has been assumed to be at 1227 ºC, the blanket at 627 ºC, and everything else (i.e. structure, coolant and absorber) at 448 ºC. Fine (1968) group cross-sections were collapsed to a coarse (33) group structure for use in full-core, transport-theory calculations with VARIANT. The hexagonal 3D full-core calculations yielded the effective multiplication factor k_{eff} and the distributions of flux and power throughout the core. In the hexagonal plane, each S/A represented a homogeneous node, implying that the hexagonal node sizing corresponded to the S/A pitch (12.7 cm). In the vertical plane, node boundaries were chosen to correspond to borders between reactor zones (reflector to blanket, blanket to fuel, etc.), with additional node boundaries added in order to ensure that all nodes were less than 12 cm in length. Node boundaries were also added at the borders between CR absorber and follower regions, according to their positions for a given CR configuration. The core presented in Fig. 56 has been fully described with 110 fuel S/As, 86 blanket S/As, six CR S/As, one safety rod, and three additional rings of reflector S/As.
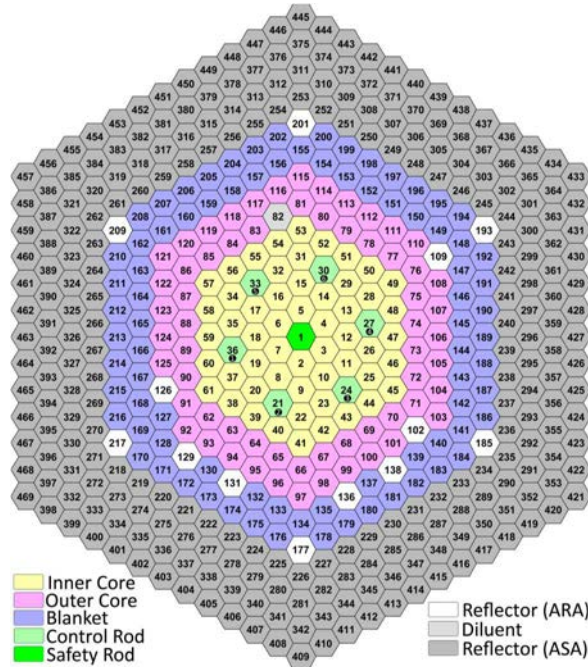
FIG. 56. Horizontal cross-section of the Phénix core as configured during the CRS test (reduced power state of 350MW(th)) with sub-assembly numbering.

5.8.2. PARCS model

The Phénix core was modeled in PARCS with homogeneous computational nodes in hexagonal-z geometry. The nodalization scheme was the same as that used in ERANOS, except that node boundaries were not added explicitly at the border between control absorber and follower regions. Unlike ERANOS, PARCS uses macroscopic cross-sections for a reference state and accounts for the reactivity feedbacks, corresponding to specific conditions, by using derivatives of the macroscopic cross-section with respect to state variables. As the code was originally developed for light water reactor applications, the cross-section parameterization was modified at PSI to enable fast-spectrum system analysis. The equation below represents the current procedure for recalculating a macroscopic cross-section during transients:

$$
\Sigma(T_f, \rho_c, R, H, Z) = \Sigma_0 + \left[\frac{\partial \Sigma}{\partial \ln T_f}\right]_{T_{f_0}} (\ln T_f - \ln T_{f_0})
$$
$$
+ \left[\frac{\partial \Sigma}{\partial \rho_c}\right]_{\rho_{c_0}} (\rho_c - \rho_{c_0}) + \left[\frac{\partial \Sigma}{\partial R}\right]_{R_0} (R - R_0) \tag{15}
$$
$$
+ \left[\frac{\partial \Sigma}{\partial H}\right]_{H_0} (H - H_0) + \left[\frac{\partial \Sigma}{\partial Z}\right]_{Z_0} (Z - Z_0)
$$

where Σ is the macroscopic cross-section, T_f the fuel temperature, ρ_c the coolant density, R the average core radius, H the average core height, and Z the control rod position. The subscript 0 refers to the values at the reference state (usually chosen at room temperature).

The dependence considered is linear in each case, except for the Doppler effect where a logarithmic dependency on fuel temperature is assumed. Also, the modified version of PARCS allows one to compute the core geometry (taking into account the axial and radial expansions) accordingly to the evolution of the structural material temperatures.

The reference macroscopic cross-sections (R_0) and the different derivatives for use in PARCS (time-dependent, 3D nodal, diffusion theory) were produced using ERANOS (ECCO and VARIANT with the diffusion approximation).

Different core states were simulated to compute each of the cross-section derivatives. The reference state 'REF', defined for calculation of the macroscopic cross-sections R_0, was chosen to be room temperature (293 K). To account for the Doppler effect (i.e. to calculate the derivatives with respect to the fuel temperature), the core simulation was repeated with the fuel temperature changed to a higher temperature (arbitrarily chosen at 1000 K), with all other input values being kept the same (this core calculation will be referred to as 'DOP' from here on). Due to the very small coolant density variations in the considered test and to the low value of the coolant temperature reactivity coefficient in the Phénix core the coolant density effect is not presented in the analysis. The axial expansion effect was obtained from a core calculation for room temperature, but with axially expanded fuel regions (core state 'AXI'), corresponding to a temperature of 1000 K. Finally, the radial expansion effect was obtained from a computation at room temperature but with a dilated fuel assembly interassembly gap (core state 'RAD'), again corresponding to 1000 K. The total core fuel mass was preserved in all the considered states, and expansion coefficients were implemented according to the benchmark specification.

Table 29 summarizes the different core states for which macroscopic cross-sections were obtained in order to compute the derivatives with respect to each state variable. The reference macroscopic cross-sections and the corresponding derivatives were then processed from ERANOS outputs into PARCS format using a FORTRAN procedure, ERANOSTOPARCS. The six control rods and the safety rod (see Fig. 56) have been simulated explicitly in order to allow individual positioning of

each CR. Each control assembly (CA) is described with the corresponding follower region, the change of cross-sections due to the presence of the absorber being effectively simulated through derivatives. These have been validated against 'static' modeling, in which the CA lower region was explicitly defined with the follower cross-sections and the upper region with the absorber cross-sections.

TABLE 29. DESCRIPTION OF THE CORE STATES CONSIDERED FOR COMPUTING THE DERIVATIVES OF THE MACROSCOPIC CROSS-SECTIONS WITH RESPECT TO THE DIFFERENT STATE VARIABLES.

Case	REF	DOP	AXI	RAD
T_F (K)	293	1000	293	293
ρ_c (kg/m^3)	950	950	950	950
Δh (cm)	0	0	2.197	0
Δp (cm)	0	0	0	0.170

5.8.3. TRACE model

For a detailed 3D thermal–hydraulic analysis of the Phénix core behavior, a full core model has been developed with TRACE [46]. Every single fuel S/A has been represented by a dedicated 'pipe' component and its associated 'htstr' (heat structure) component. Consequently, the model consists of 110 parallel pipe and htstr components for the representation of the 54 inner core S/As and 56 outer core S/As. This has allowed simulation of assembly-wise power and temperature distributions. The S/As in the blanket and reflector region have been grouped in one channel each, since less detail is needed in these regions. This can be seen schematically in Fig. 57.
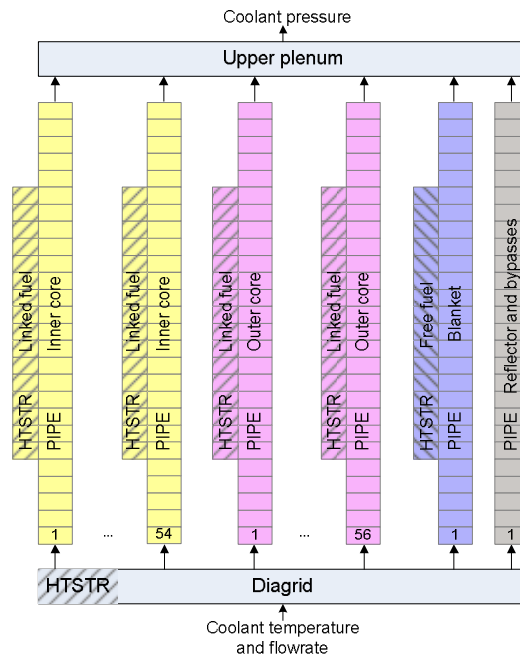
FIG. 57. Schematic of the TRACE full core model.

Due to the code's limitations, all fuel pins were modeled as linked fuel with a closed fuel-clad gas gap, using a gas-gap conductance of 5000 W/m^{2}K (as recommended in the benchmark specifications of the NC test [5]). A gap conductance of 2500 W/m^{2}K was used in the blanket pins.

The flowrate was assumed to be equal in every S/A from the same region so that the gagging was identical for every pipe within one region. The boundary conditions imposed include inlet temperature, inlet flowrate and outlet pressure, according to the CRP description.

5.8.4. TRACE/PARCS mapping scheme

PARCS has been coupled directly to TRACE, with the latter providing the temperature and coolant-density field information to PARCS during the steady-state and transient calculations. At the same time, PARCS provides TRACE with the power distribution. This is achieved using an appropriate mapping scheme, linking both the pipe component nodes and the heat-structure nodes to the corresponding neutronics nodes. This was made easier by the fact that the nodalization schemes in the PARCS and TRACE models were chosen to be identical.

5.8.5. Verification of the coupled TRACE/PARCS model using ERANOS

The coupled TRACE/PARCS model was checked by comparing the computational results with ERANOS calculations. Effectively, the core states listed in Table 29 were calculated with both models to systematically check the derivatives used in PARCS. All temperatures were fixed at 1000 K. First, the reference macroscopic cross-sections were tested by removing all the derivatives. With the geometry having been kept constant (by setting the thermal expansion coefficients equal to zero), the k_{eff} obtained essentially corresponded to the 'REF' core state. Each of the derivatives was checked individually, one at a time, by removing all derivatives from the PARCS input except the one being tested. The results of these code-to-code comparisons are given in Table 30, along with a comparison of the different reactivity feedbacks.

TABLE 30. COMPARISONS OF THE EFFECTIVE MULTIPLICATION FACTORS, OBTAINED WITH ERANOS AND WITH TRACE/PARCS, FOR THE DIFFERENT CORE STATES.

	ERANOS		TRACE/PARCS	
	k_{eff}	$\Delta\rho$ (pcm)	k_{eff}	$\Delta\rho$ (pcm)
REF	1.01674		1.01081	
DOP	1.00821	−853	1.00229	−852
AXI	1.01151	−523	1.00644	−437
RAD	1.00871	−803	1.00268	−813

There is some discrepancy in the axial expansion feedback because the two codes treat the effect in slightly different ways, viz. the feedback effect due to changes in the CR position is computed separately in PARCS whereas, in ERANOS, it is included in axial expansion feedback. Large discrepancies were found in the code-to-code comparison for the coolant density effect (not shown in the table). Its small magnitude in the Phénix core makes difficult the accurate assessment, and also it is unimportant for this study. Otherwise, the reactivity feedbacks are in good agreement between ERANOS and TRACE/PARCS. It is also noteworthy that calculating the four feedbacks separately in PARCS, and then summing them (−2184 pcm), yields nearly identical results compared to a single calculation with all feedbacks present simultaneously (−2206 pcm). This indicates that the employed parametrization of the cross-sections, which assumes independence of the different derivatives, is a good approximation. It can be noticed from Table 30 that the k_{eff} values obtained with TRACE/PARCS are systematically about 600 pcm lower than the corresponding values from ERANOS, even though both sets of neutronics calculations are based on

diffusion theory. The differences can be attributed mainly to the different nodal schemes. VARIANT uses a variational nodal method based on the even-parity form of the transport equation [45], whereas PARCS uses the Triangle-based Polynomial Expansion Nodal (TPEN) method [47]. For an accurate solution, the latter method requires discontinuity factors to adequately treat flux discontinuities at the node boundaries [48]. Thus, for example, the radial heterogeneity of the Phénix core (between the fissile and the fertile regions) would need to be modeled using assembly discontinuity factors (ADFs), which would improve treatment of the discontinuity of the homogeneous flux at the borders between zones (typically, between the outer core and the blanket region) [49]. A brief study using ADFs in PARCS has shown a significant dependence of k_{eff} on the latter, and further work would need to be done for improvement of the code-to-code results in this context.

The comparison of the computed power distributions shows that PARCS is in very good agreement with ERANOS (<2% discrepancy) in the fissile core (S/A number lower than 125), but that it under-predicts the power in the blanket S/As by almost 15% (see Fig. 58).

a) Absolute assembly-wise power calculated by ERANOS and TRACE/PARCS

b) Relative discrepancy (%) on the power calculations by ERANOS and TRACE/PARCS
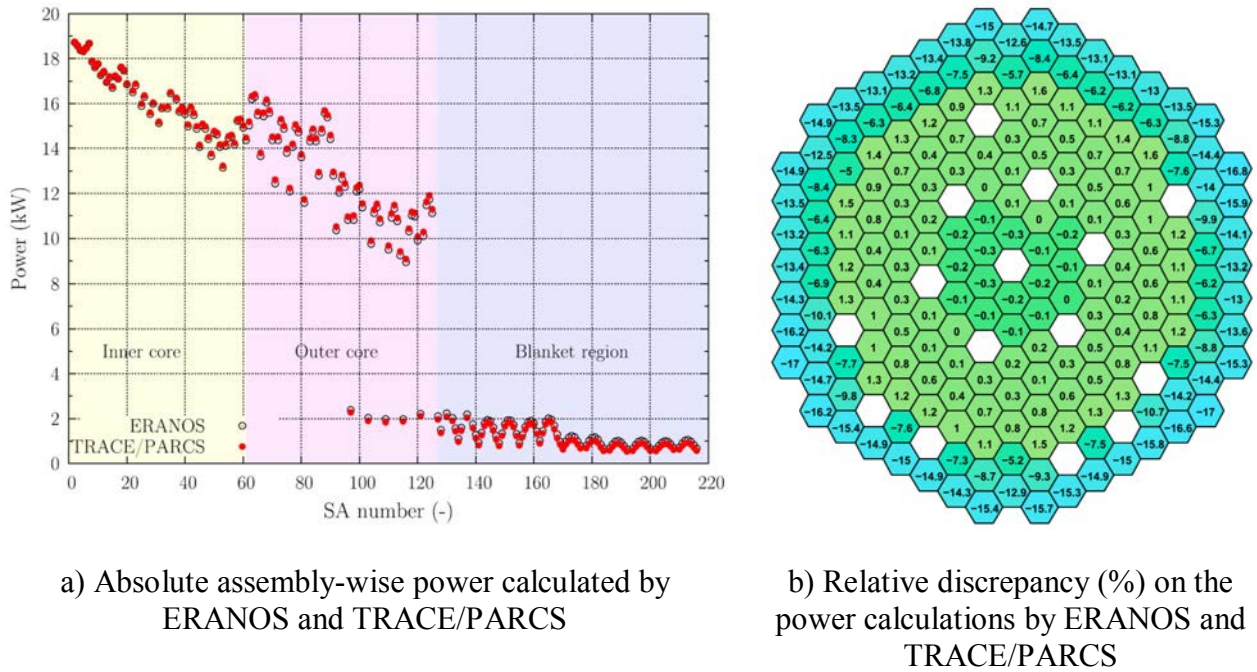
FIG. 58. Comparison of ERANOS and TRACE/PARCS computed power distribution at 335 MW(th) with all temperatures fixed at 1000 K. CR positions correspond to step 1.

Nevertheless, considering that the power generated in the blanket region corresponds to less than 7% of the total power, and that the power distribution in the fissile core is in very good agreement, the present PARCS model has been considered accurate enough for application to the transient analysis. A complete model describing the flux discontinuity in the different radial zones (inner core, outer core and blanket region) would be needed for a more precise modeling of the Phénix core with PARCS.

6. BLIND CALCULATIONS

6.1. INTRODUCTION

The first part of the IAEA CRP on Phénix EOL tests was dedicated to blind calculations and gave rise to the 2nd RCM. The purpose of these blind calculations was to compare the calculation methods of each participant, without any reference in terms of experimental results. Before this RCM, a document [43] was sent to all of the participants defining the core data needed for the neutronic calculations. The results obtained by each participant were presented during the 2nd RCM.

6.2. CALCULATIONS CONDITIONS

6.2.1. Core data given for the neutronic blind calculations

All the blind calculations were realized before the test, so provided core data was obviously different from the real test data. Differences are the following:

— The core loading (cf. Fig. 59);
— The control rods elevation for each step of the test (cf. Table 31);
— The isotopic densities (cf. Table 32);
— The temperatures:
  - For thermal expansion of the core, the sodium inlet temperature was considered to be equal to 380 °C, so the radial linear expansion coefficient was equal to 1.00638; the sodium averaged temperature was fixed to 459 °C (sodium outlet is 538 °C), so the axial linear expansion coefficient was 1.00792;
  - For neutronic aspects (self-shielded cross-section calculation), the temperatures considered are noted in Table 33 below;
— The global power of the core: 350 MW(th).

ERANOS MODELISATION OF THE CORE
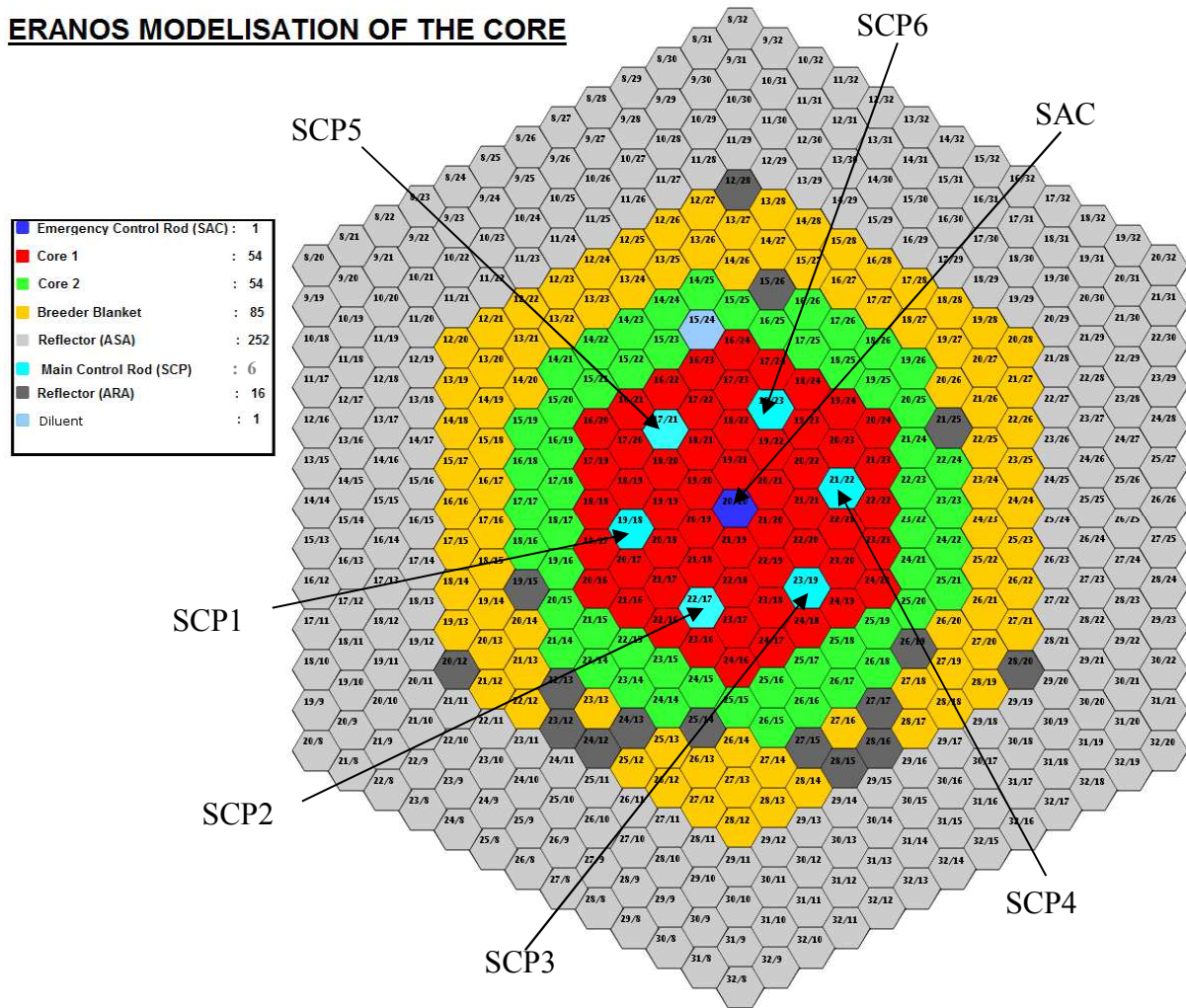
FIG. 59. Core loading defined for blind calculations.

TABLE 31. CONTROL ROD EXTRACTION (FROM THE INTERFACE BETWEEN LOWER AXIAL BLANKET AND FISSILE, AT 20°C) FOR EACH STEP OF THE BLIND CALCULATIONS

	SAC	SCP1	SCP2	SCP3	SCP4	SCP5	SCP6
Core Position	20/20	19/18	22/17	23/19	21/22	17/21	18/23
Step 1	900 mm	581 mm	581 mm	581 mm	581 mm	581 mm	581 mm
Step 2	900 mm	660 mm	660 mm	660 mm	**300 mm**	660 mm	660 mm
Step 3	900 mm	**900 mm**	621 mm	621 mm	**300 mm**	621 mm	621 mm
Step 4	900 mm	**900 mm**	551 mm	551 mm	551 mm	551 mm	551 mm

TABLE 32. ISOTOPIC DENSITIES INSIDE THE CLADS OF EACH CORE ZONE

10^{-24}. at/cm3	Core 1	Core 2	Radial Blanket	Upper Blanket Core 1	Upper Blanket Core 2	Lower Blanket Core 1	Lower Blanket Core 2
U235	4.062092E-05	4.024228E-05	6.117305E-05	5.121843E-05	4.765216E-05	5.601220E-05	6.430420E-05
U236	3.259701E-06	2.264818E-06	1.605481E-06	1.113137E-06	1.035745E-06	3.068900E-06	3.437790E-04
PU238	2.329286E-05	2.506499E-05	5.209661E-10	2.596206E-11	3.017176E-04	7.148510E-10	1.910780E-10
U238	1.575958E-02	1.482554E-02	2.243398E-02	1.743691E-02	1.569373E-02	1.829043E-02	1.807500E-02
NP239	3.204185E-22	2.372511E-22	1.099884E-22	6.735873E-23	6.668951E-23	1.937480E-22	1.380840E-22
PU239	3.055230E-03	3.833204E-03	2.320255E-04	1.368598E-04	1.236078E-04	3.495560E-04	2.250390E-04
PU240	1.301461E-03	1.624323E-03	6.802871E-06	2.295137E-06	2.275627E-06	1.362420E-05	5.959280E-06
PU241	1.128366E-04	1.307455E-04	1.692802E-07	3.154559E-08	3.713804E-08	3.958430E-07	1.249340E-07
PU242	4.806778E-05	6.040999E-05	2.880320E-09	2.852196E-10	3.669186E-10	8.042730E-09	1.790200E-09
AM241	8.893773E-05	1.188079E-04	1.547535E-08	2.243314E-09	2.383922E-09	2.700410E-08	8.130470E-09
SFPU235	1.280697E-05	1.088404E-05	1.275021E-05	5.608931E-06	8.828931E-06	2.943450E-05	1.587650E-05
SFPU238	1.035230E-04	8.797943E-05	3.817833E-05	6.572892E-06	1.034627E-05	3.449320E-05	1.860510E-05
SFPPU239	8.313843E-04	7.065558E-04	1.478761E-05	1.075539E-05	1.693000E-05	5.644230E-05	3.044420E-05
SFPPU240	6.937105E-05	5.895522E-05	6.572273E-09	4.601255E-08	7.242765E-08	2.414640E-07	1.302420E-07
SFPPU241	4.802610E-05	4.081514E-05	6.572273E-10	2.300627E-08	3.621382E-08	1.207320E-07	6.512120E-08
SFPPU242	2.134495E-06	1.814007E-06	6.572273E-13	2.300627E-11	3.621382E-11	1.207320E-10	6.512120E-11
O	4.287690E-02	4.280570E-02	4.508460E-02	3.531343E-02	3.245235E-02	3.889080E-02	3.751460E-02
AM243	3.484359E-06	3.212285E-06	4.815981E-11	2.319373E-12	3.177804E-12	1.489610E-10	2.425120E-11
CM242	2.743013E-06	2.739608E-06	1.365987E-10	7.871902E-12	1.103157E-11	2.160420E-10	6.046180E-11
CM244	4.621753E-07	3.179191E-07	1.911208E-12	4.317471E-14	6.405343E-14	6.462190E-12	7.698450E-13
AM242M	2.602521E-06	2.473720E-06	1.087245E-10	5.803088E-12	7.603676E-12	1.534360E-10	4.204980E-11
AM242F	1.000000E-10	1.000000E-10	1.000000E-10	9.803922E-11	9.803922E-11	1.000000E-10	1.000000E-10
B10	1.000000E-10	1.000000E-10	1.000000E-10	9.803922E-11	9.803922E-11	1.000000E-10	1.000000E-10
B11	1.000000E-10	1.000000E-10	1.000000E-10	9.803922E-11	9.803922E-11	1.000000E-10	1.000000E-10
C	1.000000E-10	1.000000E-10	1.000000E-10	9.803922E-11	9.803922E-11	1.000000E-10	1.000000E-10
U234	1.000000E-10	1.000000E-10	1.000000E-10	1.000000E-10	1.000000E-10	1.000000E-10	1.000000E-10
NP237	1.000000E-10	1.000000E-10	1.000000E-10	1.000000E-10	1.000000E-10	1.000000E-10	1.000000E-10
NP239	1.000000E-10	1.000000E-10	1.000000E-10	1.000000E-10	1.000000E-10	1.000000E-10	1.000000E-10
CM243	1.000000E-10	1.000000E-10	1.000000E-10	1.000000E-10	1.000000E-10	1.000000E-10	1.000000E-10
CM245	1.000000E-10	1.000000E-10	1.000000E-10	1.000000E-10	1.000000E-10	1.000000E-10	1.000000E-10
CM246	1.000000E-10	1.000000E-10	1.000000E-10	1.000000E-10	1.000000E-10	1.000000E-10	1.000000E-10
CM247	1.000000E-10	1.000000E-10	1.000000E-10	1.000000E-10	1.000000E-10	1.000000E-10	1.000000E-10
CM248	1.000000E-10	1.000000E-10	1.000000E-10	1.000000E-10	1.000000E-10	1.000000E-10	1.000000E-10

TABLE 33. AVERAGED TEMPERATURES CONSIDERED FOR MICROSCOPIC CROSS-SECTION CALCULATION

Zone	Temperature (°C)
Fuel	1227
Blanket	627
Structure	459
Coolant	459
Absorber	459

The complete description of the core was given to the participants, and the choice was let to realize homogeneous or heterogeneous description of the assemblies.

6.2.2. Output data calculated

The output values calculated by each participant were:

— Control rods worth between '0 mm' and '900 mm' levels: the integral worth value and the shape of the S-curve;
— K_{eff} values for each step of the test;
— Average and maximum flux per sub-assembly, and power distributions for each of the 4 steps.

6.2.3. Calculation methods used by each participant

Table 34 and Table 35 summarize the calculation methods used by each participant. The first table describes the deterministic calculations made with diffusion theory; the second table refers to the deterministic calculations realized with transport theory (orange columns) and calculations made with Monte Carlo method (yellow column).

TABLE 34. CALCULATION METHODS USING DIFFUSION THEORY

	ANL	IGCAR	IGCAR	IPPE	JAEA
Calculation method	deterministic: DIF3D-nodal	deterministic: ERANOS 2.1	deterministic: FARCOB	deterministic: TRIGEX	deterministic: DIF3D
Nuclear data library	ENDF/BVII	ERALIB-1 (sodium adjusted JEF-2.2 data)	ABBN93.01A	ABBN93.01A	ABBN based on JENDL3.3
Energetic structure	33 groups	33 groups	26 groups	26 groups	70 groups
Cell calculation	MC2-2: **homogeneous** description	ECCO: **heterogeneous 2D** description	FARCOB: **heterogeneous 1D** description	TRIGEX: **homogeneous** description	SLAROM-UF : **heterogeneous 1D** description
Control Rod calculation	**reduction in B4C** number density by 25% (comparison between deterministic and MCNP code)	ECCO: heterogeneous 2D description + **reactivity equivalence method**	COHINT: **homogenization using fluxes** from 2D collision probability transport calculation	TRIGEX: **homogeneous** description	SLAROM-UF : **heterogeneous 1D** description +**reaction rate ratio preservation** method
Core calculation	3D geometry with **nodal diffusion** theory	H3D: 3D geometry with **finite difference diffusion** theory	3D geometry with **diffusion** theory	TRIGEX: XYZ 3D geometry with **diffusion** method	DIF3D: XYZ 3D geometry with **diffusion** method
Other					**thermic axial model** refined compared to CEA proposal model
					transport correction + mesh correction + energetic mesh correction applied to reactivity calculation

TABLE 35. CALCULATION METHODS USING DETERMINISTIC TRANSPORT THEORY (ORANGE COLUMNS) AND MONTE CARLO METHOD (YELLOW COLUMN)

	ANL	CEA	IPPE	PSI
Calculation method	deterministic: DIF3D-VARIANT	deterministic: ERANOS 2.1	Monte Carlo: MMKKENO	deterministic: ERANOS 2.1
Nuclear data library	ENDF/BVII	ERALIB-1 (sodium adjusted JEF-2.2 data)	ABBN93.01A	ERALIB-1 (sodium adjusted JEF-2.2 data)
Energetic structure	33 groups	33 groups	299 groups	33 groups
Cell calculation	MC2-2: **homogeneous** description	ECCO: **heterogeneous 2D** description		ECCO: **homogeneous** description
Control Rod calculation	**reduction in B4C** number density by 25% (comparison between deterministic and MCNP code)	ECCO + BISTRO: heterogeneous 2D description + **reactivity equivalence method**	MMKKENO: **Monte Carlo** Calculation with **heterogeneous** description	ECCO: **homogeneous** description
Core calculation	3D geometry with **nodal transport** theory (VARIANT T612)	HEX 3D geometry with **nodal transport** theory (VARIANT T612)		HEX 3D geometry with **nodal transport** method (VARIANT)

6.3. COMPARISON OF RESULTS OBTAINED BY EACH PARTICIPANTS

6.3.1. Rod bank reactivity worth calculations

The reactivity worth of the control rods moving on a bank between 0 mm and 900 mm was evaluated by each participant. The integral values are described in Fig. 60.

☐ PSI	9344
■ IGCAR (ERANOS)	9146
☐ IGCAR (FARCOB)	9135
■ IPPE(TRIGEX)	9000
☐ ANL (DIF-3D)	7873
■ ANL (VARIANT)	7753
☐ JAEA with corrections	7680
☐ CEA	7640
■ JAEA	7585
☐ IPPE (MMKKENO)	7480
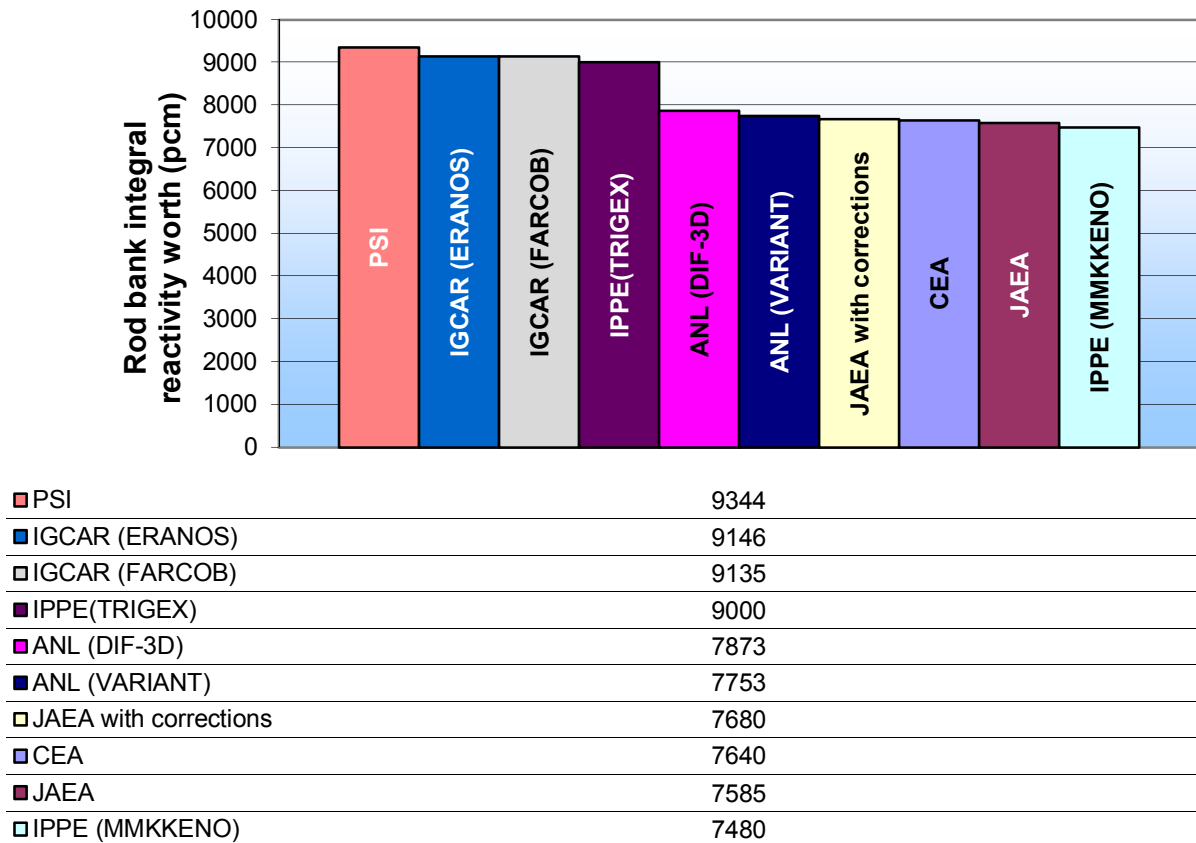
FIG. 60. Rod bank integral reactivity worth (in pcm) calculated by each participant.

It is possible to see in Fig. 60 that there are two groups of results: the first one (around 9150 pcm) compound by PSI, IGCAR and IPPE/TRIGEX results, and the second one (near 7670 pcm) composed by ANL, JAEA, CEA and IPPE/MMKKENO results. There is approximately 1500 pcm of difference between these two groups of results.

The main difference between calculation methods is the model used for control rod cross-sections generation. In control rods, spatial self-shielding has a very important effect, which is not obviously well represented in homogeneous and 1D- models. Thus, in a deterministic code, the generation of control rods cross-sections needs a special treatment to take into account the spatial homogenization over the cells. Several methods of homogenization were applied in this benchmark:

— JAEA chose to modify the homogeneous cross-sections by a method which preserve the reaction rate ratio of a heterogeneous model of control rod;
— CEA and IGCAR/ERANOS used a reactivity equivalence method between homogeneous and heterogeneous description of control rods;
— ANL reduced by 25% the B4C density by comparison between deterministic and MCNP code.

These special treatments do not have to be used in a Monte Carlo code because the real geometry of the control rods can be represented without any homogenization: that is why IPPE/MMKKENO results are situated in the second group, and ANL used the Monte Carlo MCNP code as a reference. IGCAR results are situated in the first group of values, whereas particular treatments have been applied on control rods cross-sections. After verifying the input data, IGCAR found that the control rod geometry considered for blind calculations was not correct. The rectification of this point was made on the IGCAR model for the post test calculations.

The shape of the rod bank S-curve was calculated by each participant as it can be seen in Fig. 61.
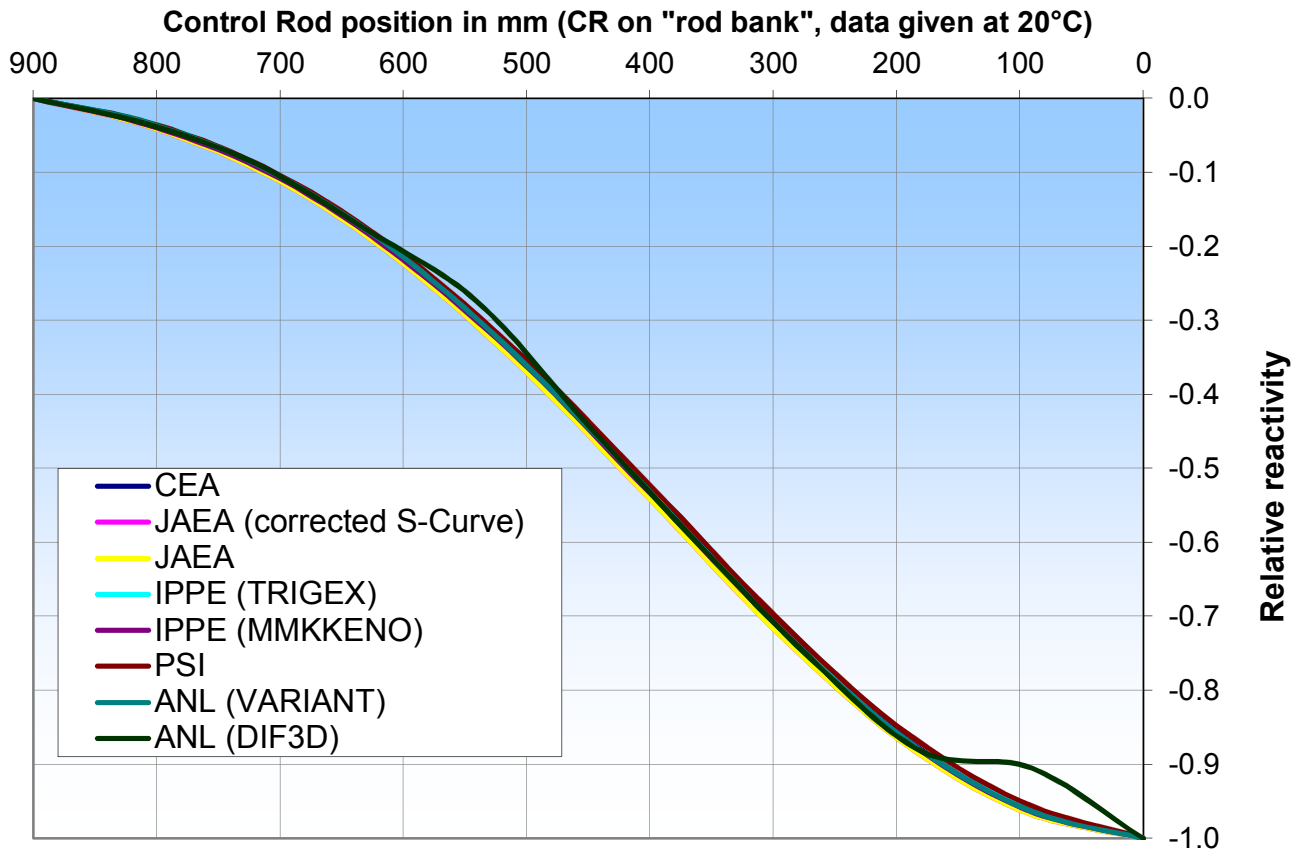
FIG. 61. Rod bank reactivity worth shape evaluated by each participant between 0 and 900 mm.

The antireactivity introduced by the insertion of all the control rods at the same time was evaluated by each participant, and these antireactivity values were normalized to the integral worth (between 0 and 900 mm). That is why results shown in Fig. 61 are expressed in 'relative reactivity', on a scale between 0 and -1.

There is a good coherence between all participants' results, except for ANL with DIF-3D code: at 90 mm level, an 'accident' in the shape is noted. One other difference, but less important, appears at 540 mm level. The cause invoked for these discrepancies can be some problems on calculation mesh description when control rods were moved. Concerning the other participants, the average discrepancy between the maximal and the minimal relative values is 1.1%. The greatest discrepancy observed is 1.9% (at 400 mm level, between JAEA and PSI values), which is a weak discrepancy.

6.3.2. Reactivity calculated for each step of the test

Each of the four steps of the blind calculations has a different reactivity value due to the movements of the control rods reported in Table 31. These reactivities have been evaluated by each participant and are reported in Fig. 62.

For each step, the reactivity values evaluated by each participant are very different: there is around 3200 pcm of discrepancy between the maximal (CEA) and the minimal (IPPE/TRIGEX) values. From a step to another step, the variations of reactivity are weak, so the discrepancies between each participant along the steps remain quite constant. The differences come from several items such as calculation methods, nuclear data libraries (including the treatment of pseudo fission products, noted 'SFP' in Table 32), energetic structure, cell calculation methods, control rod calculation

methods, core calculation methods, treatment of thermal effects between 20 °C and nominal power, etc. All these items have an impact on the calculated reactivity, either positive or negative.

	Step 1	Step 2	Step 3	Step 4
CEA	1553	1620	1597	1597
ANL (VARIANT)	837	904	879	880
IGCAR (ERANOS)	475	539	509	515
ANL (DIF-3D)	337	394	372	382
PSI	308	392	368	357
JAEA	172	249	229	222
IPPE (MMKKENO)	94	201	174	160
IGCAR (FARCOB)	-397	-348	-351	-358
IPPE(TRIGEX)	-1639	-1569	-1596	-1600
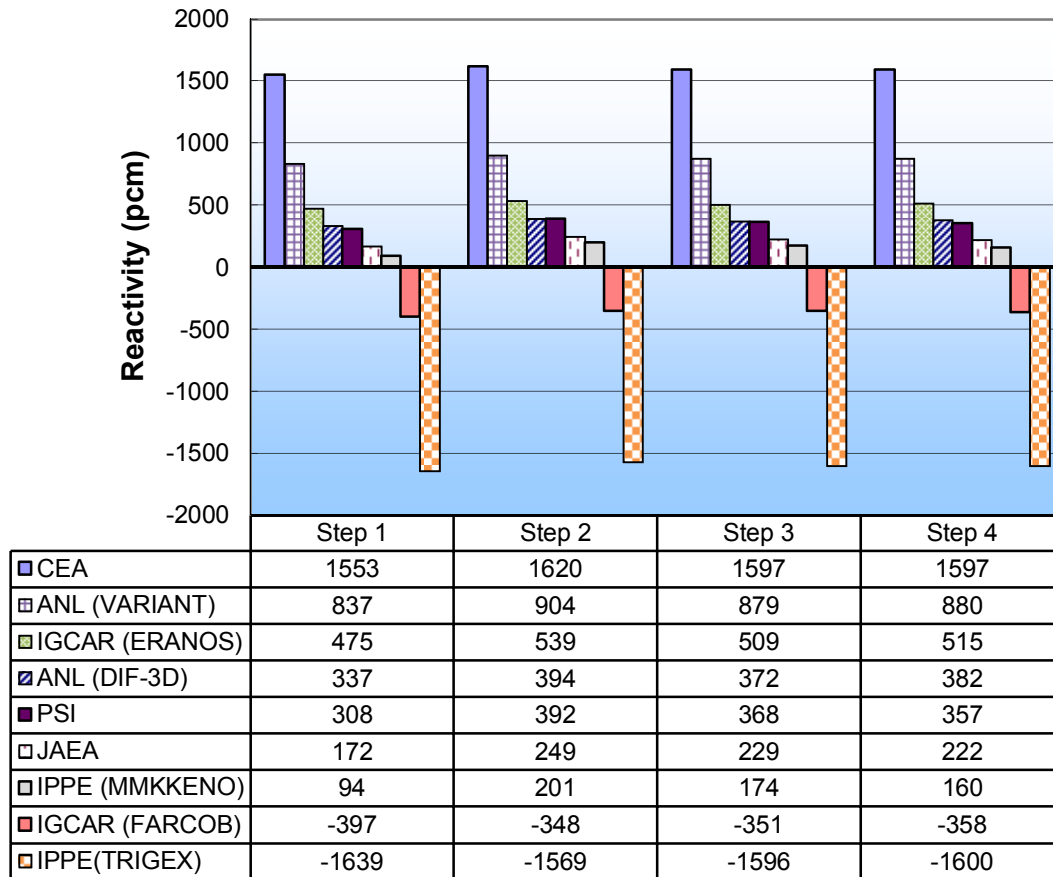
FIG. 62. Reactivity calculated for each step of the blind calculations.

At this stage, it is not possible to conclude more precisely as the blind calculation steps were defined for arbitrary control rods positions (no reference values are available).

6.3.3. Comparison of flux and power calculated for each assembly

All participants have calculated for the four steps the following parameters:

— Total power per sub-assembly;
— Power deviation per sub-assembly (with reference to the first step);
— Maximum flux per sub-assembly;
— Average flux per sub-assembly (Fissile + Fertile zone),

In the following sections, the results obtained by the participants are compared only for the first and the third steps, that are the reference and the most perturbed states. In order to represent the discrepancies between values, one radial profile will be plotted, between the position 20/14 and the position 20/26 (Fig. 59).

6.3.3.1. Comparison of power calculated

Fig. 63–64 plot the power calculated by each participant for the assemblies along the profile, for the first (reference) and the third step (most shifted state).

90
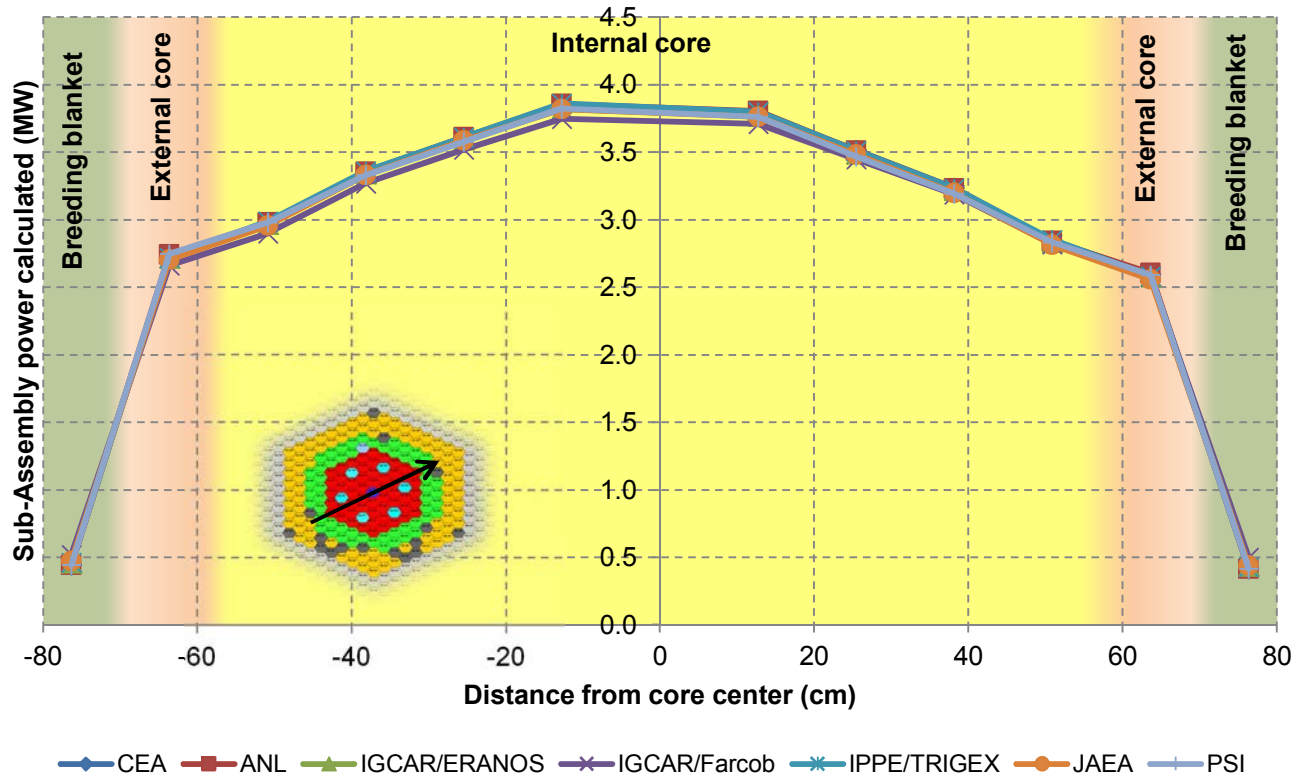
FIG. 63. Sub-assembly power calculated for the first step (reference state).
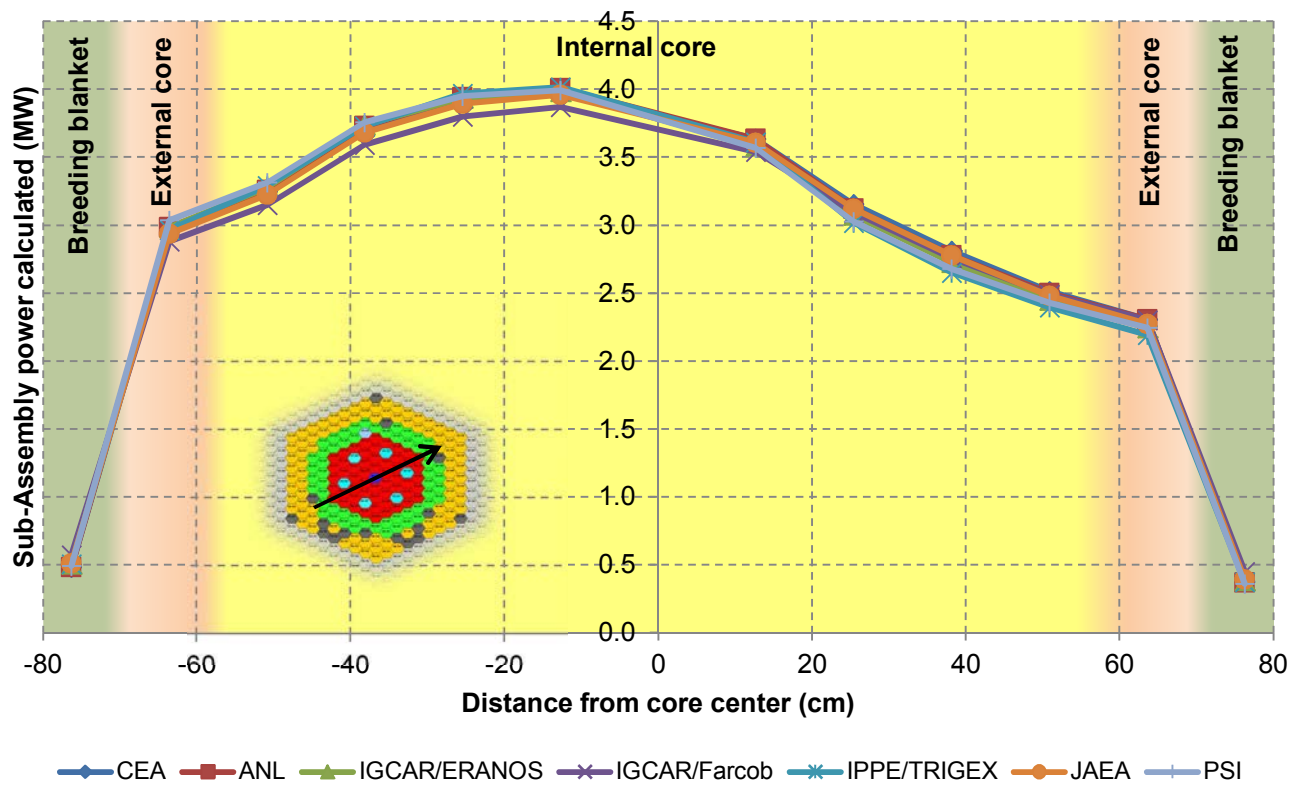
FIG. 64. Sub-assembly power calculated for the third step (most shifted state).

Concerning the power calculated for each sub-assembly, the two previous figures show a very good coherence between all the participants. The greatest difference observed between the maximal and the minimal value for each sub-assembly plotted on Fig. 63 (reference state) is 0.11 MW, which corresponds to 3% of relative difference. Regarding the step 3, the largest difference observed between the maximal and the minimal value for each sub-assembly plotted on Fig. 64 is 0.17 MW, which is around 5% of relative discrepancy. These differences on power calculations are very weak.

Fig. 65 represents the power deviations between the step 3 and the step 1 calculated with the following formula:

$$deviation\ (\%) = \frac{(Power\ step3 - Power\ step1)}{Power\ step1} * 100. \tag{16}$$
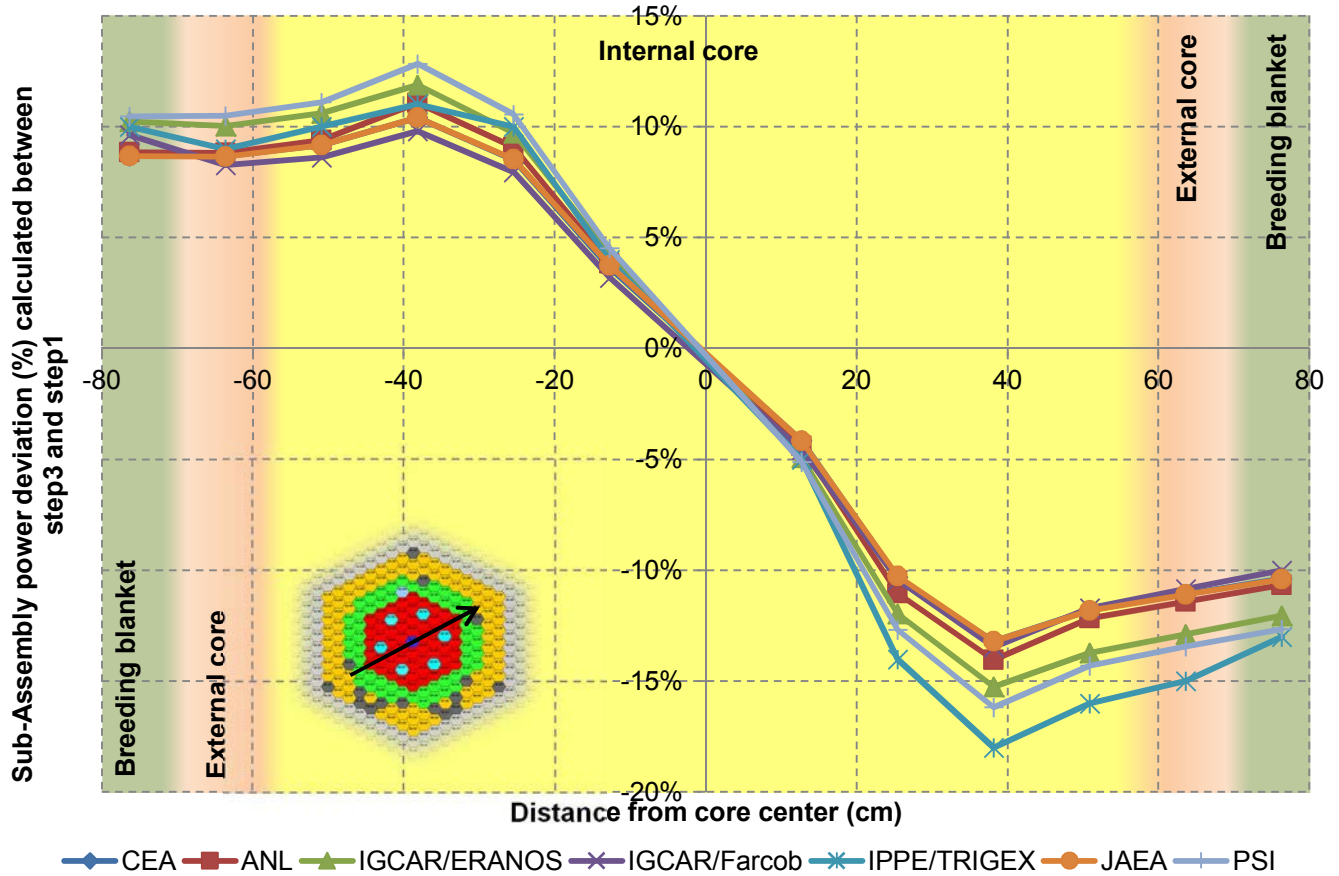
FIG. 65. Power deviations calculated between step 3 and step 1.

The greatest difference between two participants' results in the positive part of the internal core reaches 3.0% (PSI-IGCAR/Farcob), while in the negative part of the internal core it reaches 4.8% (JAEA-IPPE/TRIGEX). These kinds of differences on power deviation calculated can be considered as significant but reasonable, and are due for the main part to the individual control rod worth calculation. Thus, the amplitude of the power deviation is coherent with the integral control rods worth seen in Fig. 61. Participants who have the greatest power deviation amplitude (IPPE/TRIGEX, PSI) are the same as those who have the greatest integral control rods worth.

All the results were not presented in this report, and some dispersion had been seen in radial fertile zones or near the reflectors, but these dispersions were not very important.

6.3.3.2. Comparison of calculated flux

Two parameters were calculated for each sub-assembly: average flux (fissile + fertile zone) and maximum flux. The three following figures present the results obtained by the participants for maximal flux calculations.
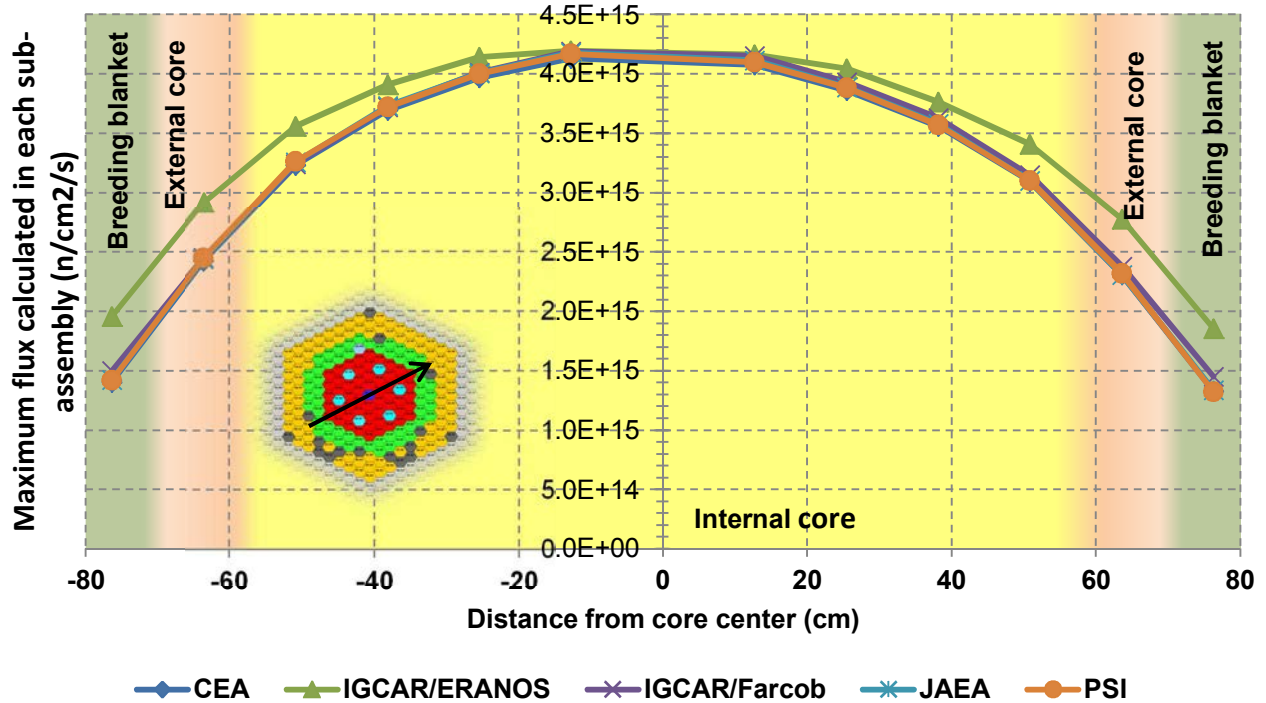
FIG. 66. Maximum flux calculated for the first step (reference state).
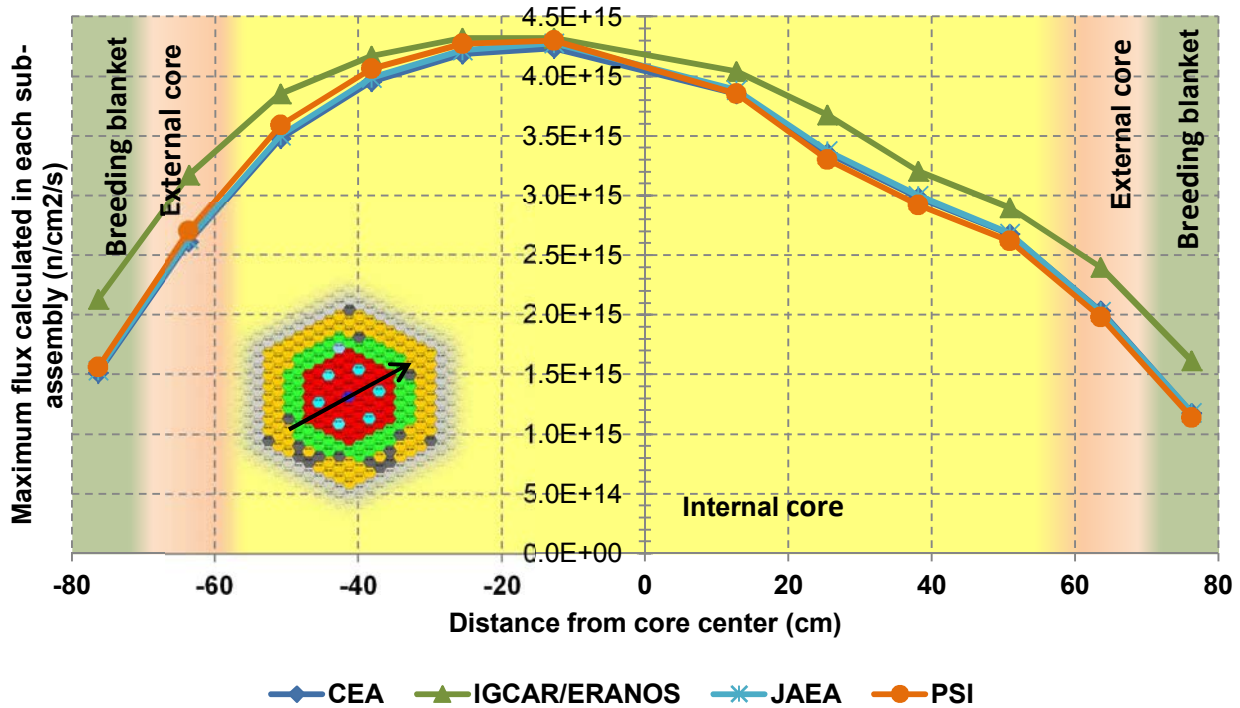
FIG. 67. Maximal flux calculated for the third step (most shifted state).

A misunderstanding problem happened for several participants, concerning the volumes to be considered for the average flux. The description of this volume was not well understood by all the participants, which implied huge differences between participants' results. So, for this report, it was chosen to present only the results of maximum flux calculations.

It can be noted that PSI maximum flux values were around $1.0E+9$ n/cm^2/s whereas the other participants presented values in $1.0E+15$ n/cm^2/s, so a factor of $1.0E+6$ was systematically applied to the PSI maximum flux values.

Taking into account this correction factor for PSI, the discrepancies between CEA, IGCAR/FARCOB (step 1 only) and PSI are very weak: 3% of discrepancy maximum are observed in internal and external core zones, for steps 1 and 3. In the breeding blanket zone, this discrepancy is a little more important and reaches at maximum 10%.

The IGCAR/ERANOS values deviate from these latter values by 10% maximum in the inner core, around 20% in the outer core, and approximately 40% in the first ring of breeding blanket, for step 1 and step 3 calculations.
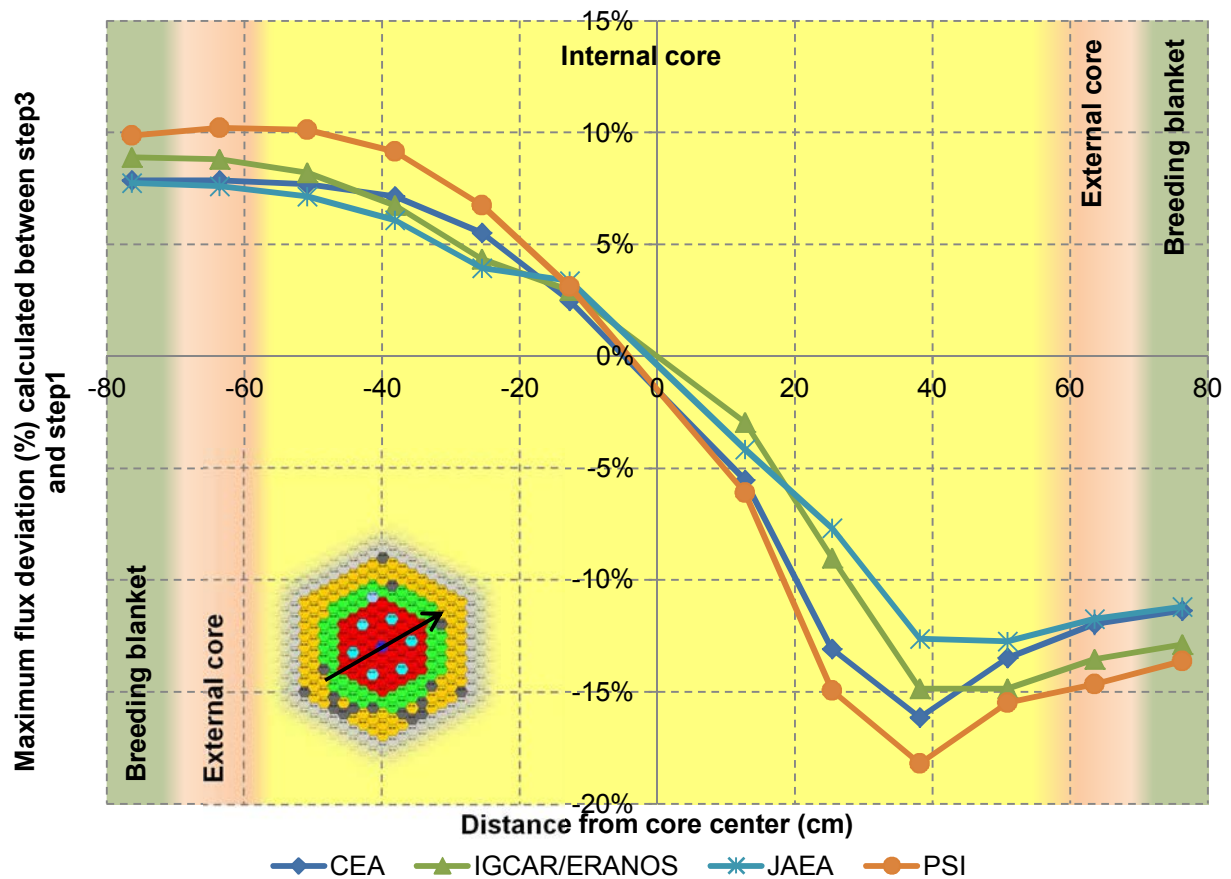
FIG. 68. Maximum flux deviations calculated between step 3 and step 1.

Like for power deviations, the results of maximum flux deviations are nearly equivalent for all the participants. The largest differences observed on this radial profile between two participants are 3.1% on the positive part of the deviation, and 7.3% on the negative part. These differences are close to those concerning the power deviation and can be considered as weak. As it was already remarked, the amplitudes of the flux deviations are linked to the integral control rods worth seen in Fig. 61 i.e. PSI gave the greatest control rods worth and the largest flux deviation amplitude, and it is the opposite conclusion for JAEA results.

6.4. CONCLUSION

This benchmark was a great occasion to discuss about calculation methods and exchange some methods of work. The comparison of results obtained by each participant brought the following conclusions:

— Concerning the control rod worth, there is a good coherence on S-curves shape (except some problems of mesh), but two groups of integral control rod worth values (near 9 000 pcm and near 7 600 pcm) were observed. This difference can be attributed to the utilization (or not) of a special treatment applied to the homogenized control rods cross-sections generated during the calculation scheme;
— A great dispersion (between -1 600 pcm and +1 600 pcm) was observed on absolute reactivity calculated for each step of the test. This can be explained by the various calculation methods and nuclear data libraries;
— A very good consistency was noted on power calculations, and power deviations (3% to 5% of relative discrepancies);
— The flux calculations presented a quite good coherence between participants (3% to 10% in the inner core, 3% to 20% in the outer core and 10% to 40% in the first ring of breeding blanket). Regarding the maximum flux deviations profile, all participants gave results close one to each other (3% to 7% of relative discrepancy).

The purpose of next phase of the CRP was to improve calculation methods, update reactor model with experimental data and compare calculations to measurements obtained during the test. This permitted to share between participants experimental validating elements for their calculation methods.

7.   FINAL CRP RESULTS

This section presents the results of the benchmark calculations conducted by each participant.

7.1. CEA

7.1.1.   Core reactivity margin

The reactivity margin of the core corresponds to the reactivity when all the control rods are completely withdrawn in their parked position (ie. position '900 mm'). By convention, in Phénix the origin of the Z-axis is located 5 mm below the bottom of the fissile column.

This reactivity margin was computed for two different states of the reactor in order to estimate the temperature effects impacts (Doppler effect, core thermal expansion):

— The off-power state which corresponds to an isothermal state (250 °C);
— The nominal state which corresponds to a reactor power of 350 MW(th).

Results are presented in Table 36. Temperature effects are not negligible. By convention, reactivity is given in pcm and is computed using the following formula :

$$\rho = \frac{k_{eff} - 1}{k_{eff}} * 10^5$$

(17)

TABLE 36. CORE REACTIVITY MARGIN (CEA RESULTS)

	Off-power state	Nominal State	Temperature effects
Reactivity (pcm)	3914.5	3081.0	-833.5

7.1.2. Control rods worth

The characterization of the control rods efficiencies is one of the main safety issues in a fast reactor. Calculation tools should be able to reproduce such parameters.

A S-curve corresponds to the efficiency of a control rod between its parked position (ie. position '900 mm') and its inserted position (ie. position '0 mm'). The control rods S-curve was computed by a succession of '100 mm' steps.

It was also computed for two different reactor states in order to estimate the impacts of effects (Off-power state, Nominal state).

Results are provided in Table 37 and Fig. 69. Temperature effects on the control rods worth are very weak (less than 0.6%). The control rod worth is defined as the deviation between the '900mm' reactivity and the '0mm' reactivity. This parameter is worth 7531 pcm for the nominal state.

TABLE 37. CONTROL RODS S-CURVE (CEA RESULTS)

Control rods positions at 20°C (mm)	Normalized Reactivity (pcm)		Deviation (%)
	Off-power state	Nominal state	
900	7578,4	7530,7	-0,6%
800	7302,9	7259,7	-0,6%
700	6778,1	6739,3	-0,6%
600	5951,7	5916,9	-0,6%
500	4848,0	4817,5	-0,6%
400	3553,0	3528,2	-0,7%
300	2227,5	2210,1	-0,8%
200	1088,3	1078,7	-0,9%
100	327,1	323,6	-1,1%
0	0,0	0,0	/
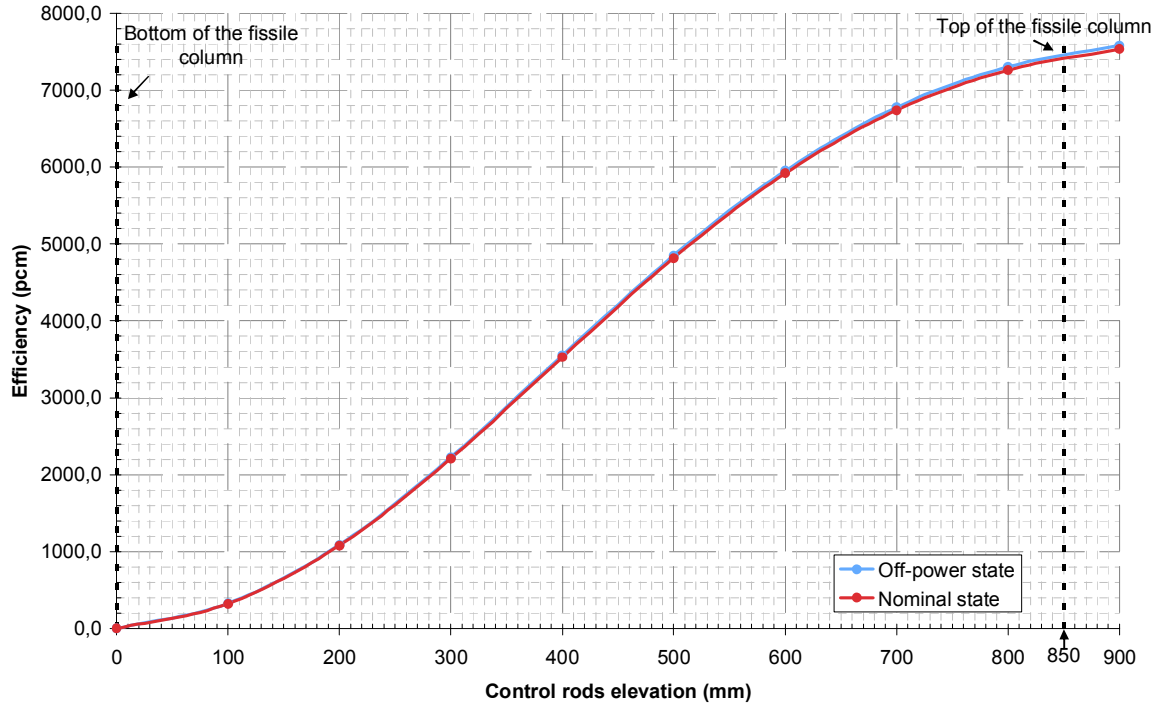
FIG. 69. Control rods S-curve (CEA results).

7.1.3. Core reactivity during the different test states

Table 38 presents the core reactivity calculated by the ERANOS code system for the various state of the test. The control rods elevations are given at nominal state and take into account the core/vessel/control rods differential expansions (this effect is explained in Section 3.1.3).

The reactivities for each step should be equal to zero. However the calculated reactivities are nearly equal to 1000 pcm. This important difference is linked to the choice to use a core averaged description. Another study performed with a detailed description of each S/As in terms of composition and geometry shows a deviation of around 260 pcm between experimental and computed reactivities with the ERALIB1 nuclear database. The uncertainty concerning the k_{eff} estimation for ERANOS coupled to the ERALIB 1 database is around 140 pcm.

Table 38 shows furthermore the reactivity balance which is defined as the reactivity deviation between a step and the initial step. During the test this balance was necessarily equal to zero. The calculated balance is less than 10 pcm, which is satisfying. This show on one hand a good estimation of the reactivity insertion due to control rods movements and on the other hand a good estimation of the control rods efficiencies.

TABLE 38. CORE REACTIVITY DURING THE VARIOUS STATE OF THE TEST

CR #	Control rods elevation (mm)						Reactivity (pcm)[8]	Δρ (pcm)
	1	2	3	4	5	6		
CR Position	19/18	22/17	23/19	21/22	17/21	18/23		
Initial state	558,3	557,4	558,0	557,4	557,4	557,6	985,7	/
State 1 (07H later)	608,5	608,6	606,6	**340,8**	608,5	607,8	995,1	9,4
State 2 (13H later)	**848,4**	567,7	571,0	**340,6**	566,3	573,5	991,0	5,3
State 3 (20H later)	**848,4**	523,6	523,4	523,4	523,5	523,5	989,2	3,5

7.1.4. Flux and power distributions

7.1.4.1. Computed values

Results concerning total power and maximum flux per S/A are presented in Fig. 70–71. The integral reactor power was fixed according to the measured power during the test. These power values are provided in Table 39. No S/A exceed the power value of 3.9 MW and the flux value of 4.07×10^{15} n·cm^{-2}·s^{-1}. These maximal values are reached for the state 2 which corresponds to the maximal deformation of the flux distribution.

TABLE 39. INTEGRAL POWER OF THE REACTOR

	Reference State	State 1	State 2	State 3
Integral power (MW(th))	335.4	337.0	338.7	336.3

---

[8] Given reactivities take into account reactivity loss due to Burnup effect.
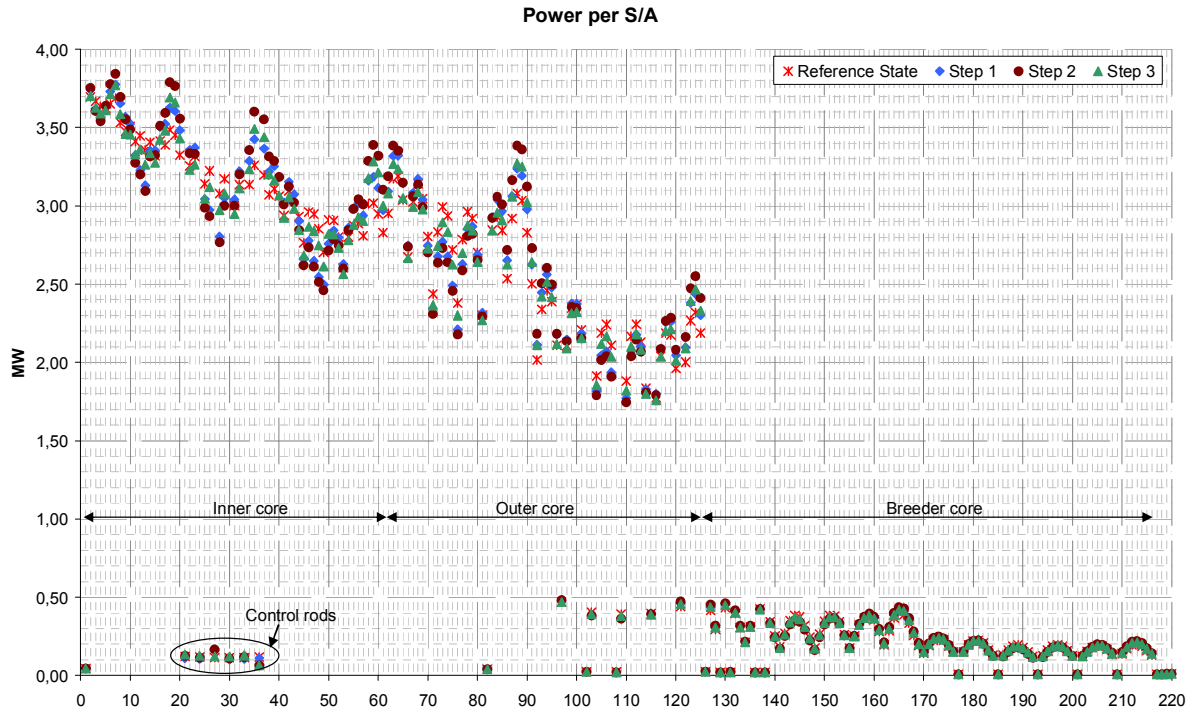
FIG. 70. Power distributions (CEA results).
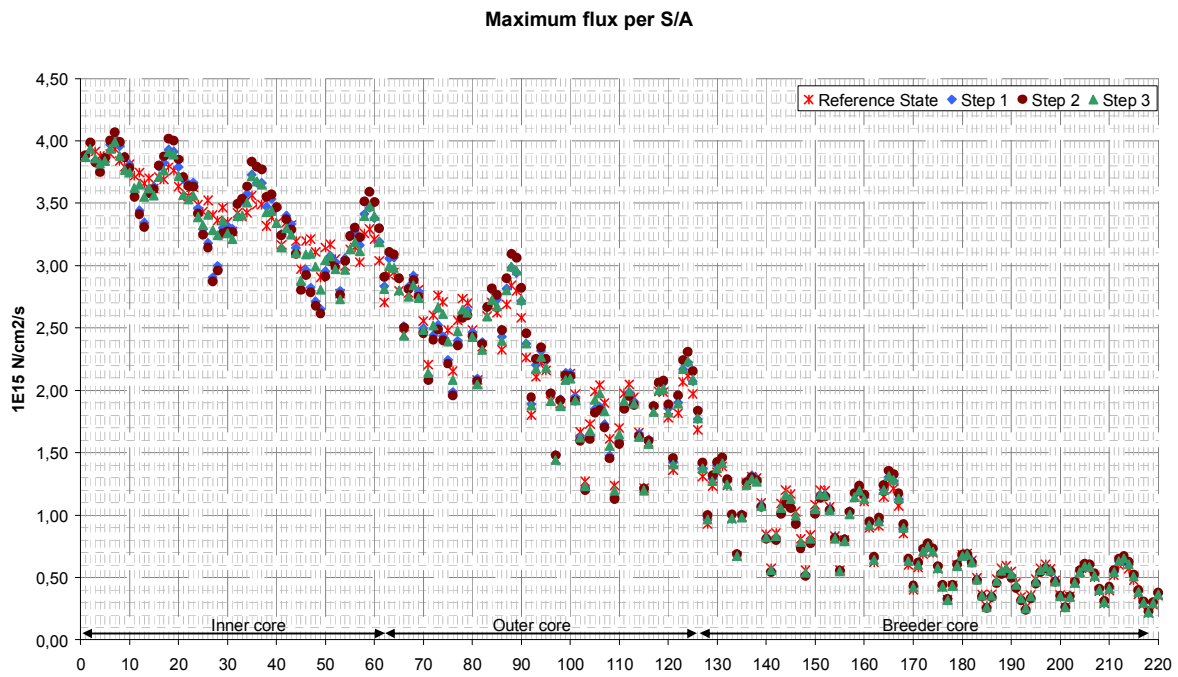
FIG. 71. Maximum flux distributions (CEA results).

Fig. 72–75 present the same results in a map form. These charts highlight the impact of the control rods movements on the power and flux spatial distribution. As expected, the flux and power increase near the extracted control rod and decrease near the inserted control rod.
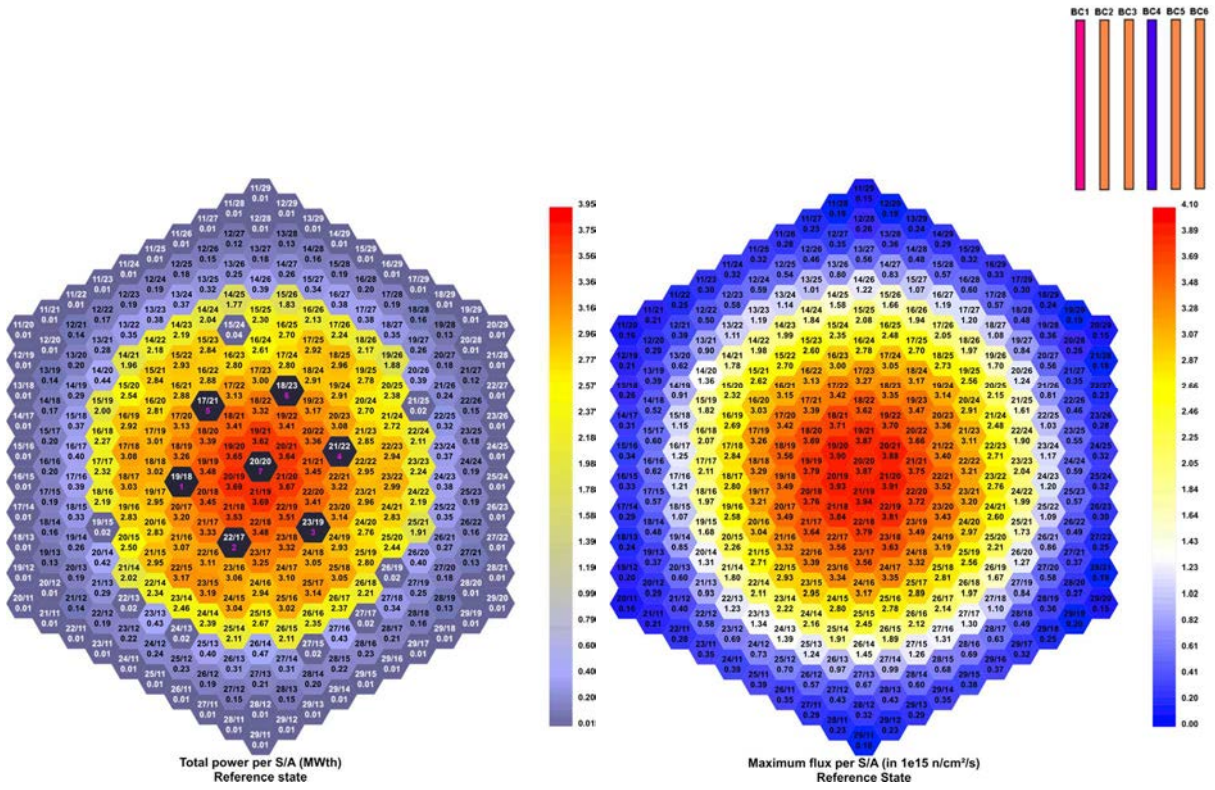
FIG. 72. Flux and power distributions for the reference state (CEA results).
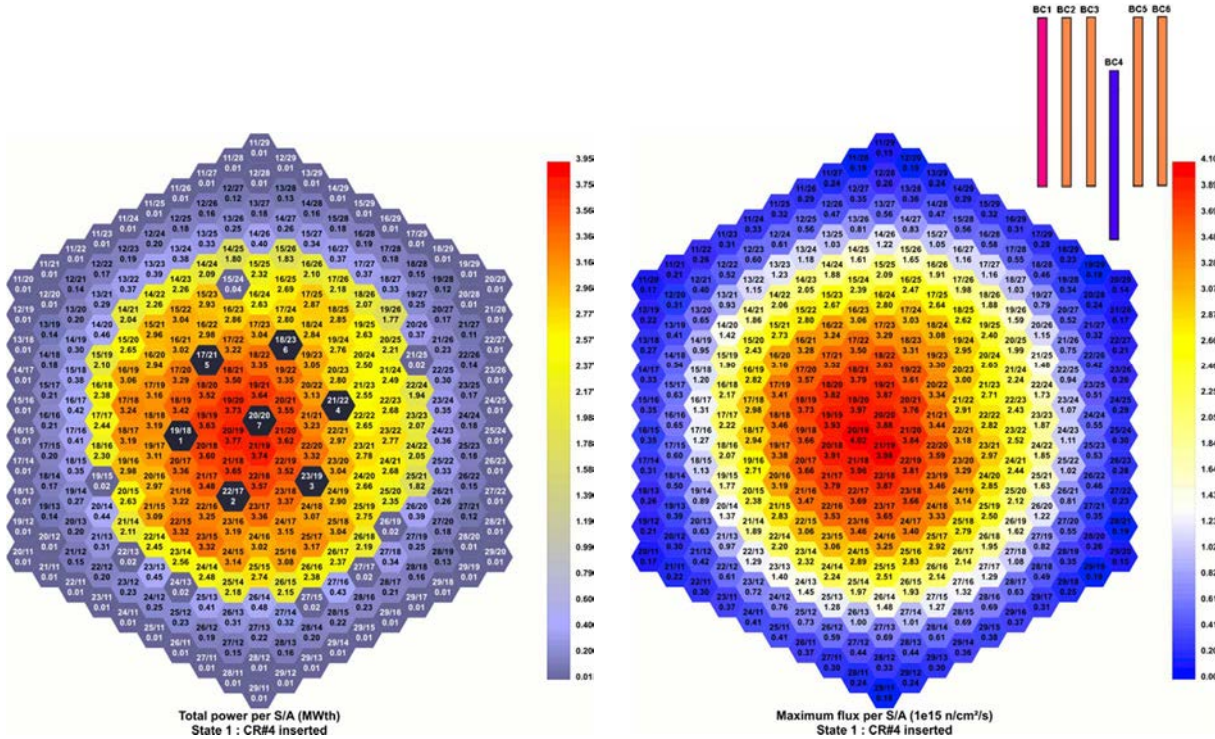
FIG. 73. Flux and power distributions for the state 1 (CEA results).

Total power per S/A (MWth)
State 2 : CR#1 extracted & CR#4 inserted

Maximum flux per S/A (in 1e15 n/cm²/s)
State 2 : CR1# extracted & CR#4 inserted
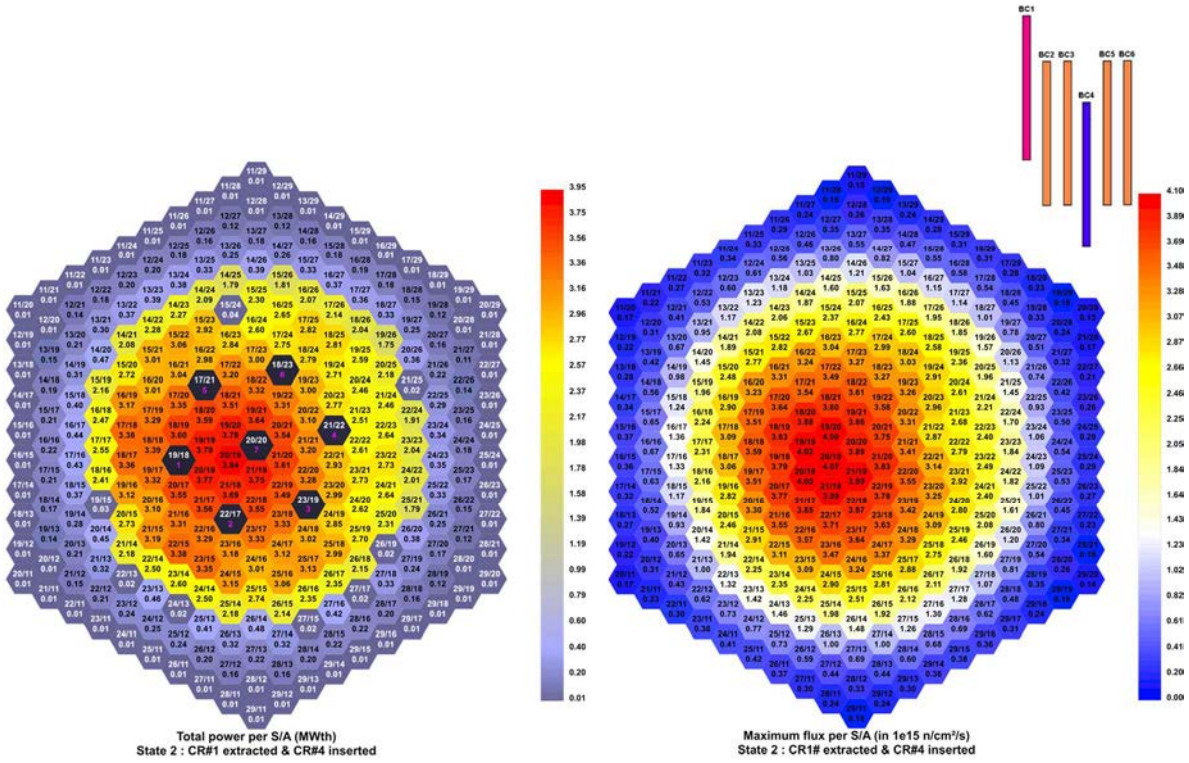
FIG. 74. Flux and power distributions for the state 2 (CEA results).

Total power per S/A (MWth)
State 3 : CR#1 extracted

Maximum flux per S/A (1e15 n/cm²/s)
State 3 : CR#1 extracted
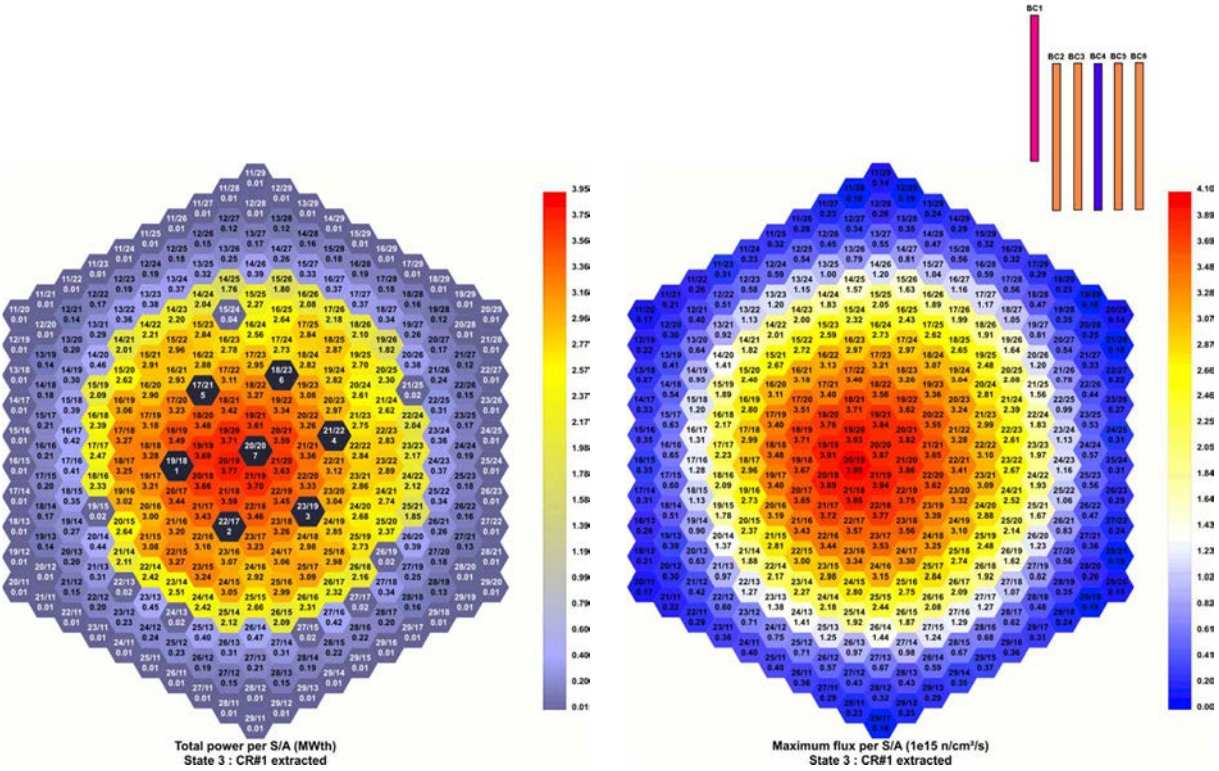
FIG. 75. Flux and power distributions for the state 3 (CEA results).

101

7.1.4.2. Comparison with measured values

Fig. 76 presents the ratio between calculated power and measured power per S/A. This figure presents also the ratio between the real burnup and the average burnup of S/A used in the calculations. Most of the discrepancies between measured and calculated values could be explain by the average core description.
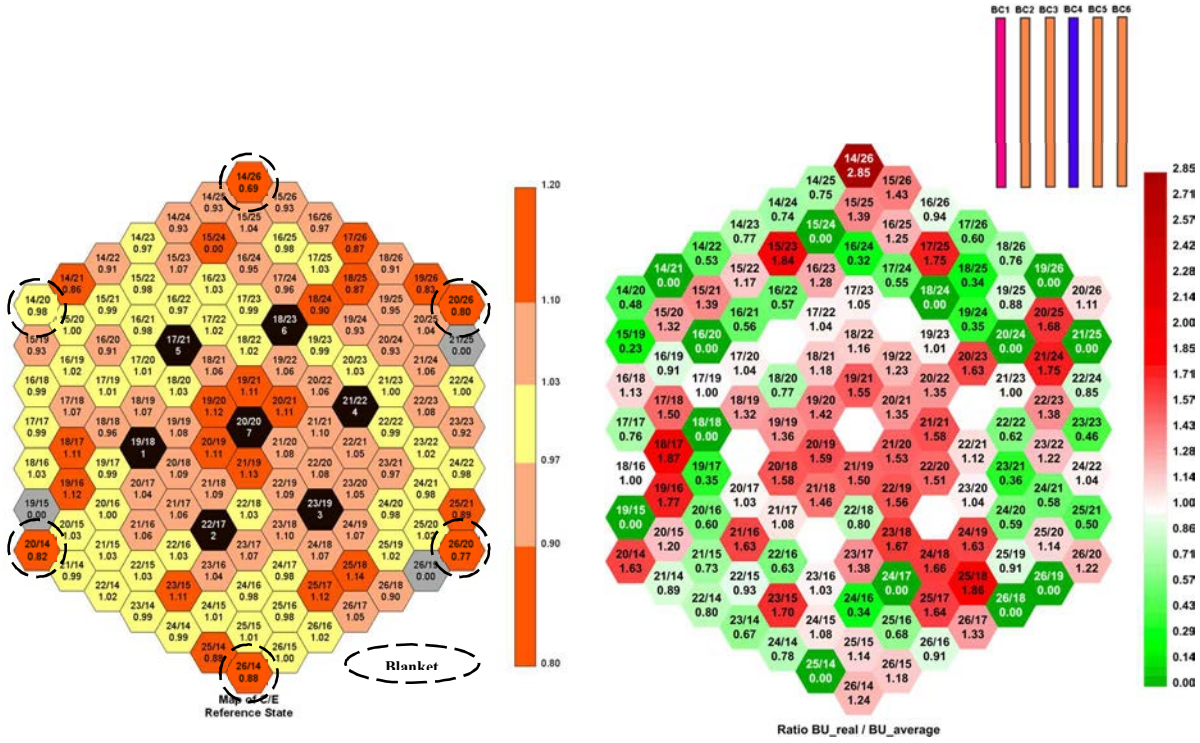
FIG. 76. Ratio P_calculated/P_measured - reference state.

Another study performed with a detailed description of each S/As in terms of composition and geometry shows weaker discrepancies on power results (<3%).

Results concerning the other steps of the test are nearly the same, so they are not presented here.

7.1.5. Power deviation distributions

7.1.5.1. Calculated values

The results of power deviation are given for each state in Fig. 77. The maximal deformation was reached during the state 2 with a value of ± 12%.
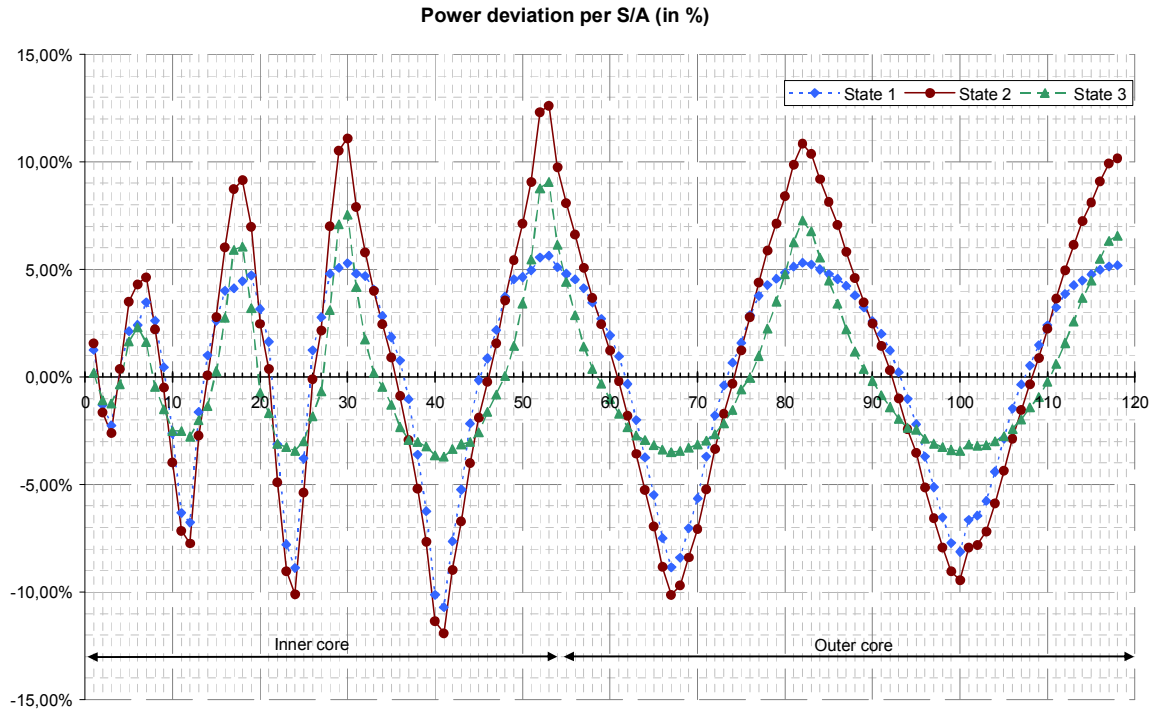
FIG. 77. Power deviation distributions (CEA results).

Fig. 78–80 present the power deviation map for the different states. The core is divided in two sectors separated by a neutral line. In the case of the state 2, the deformation is nearly symmetric because the insertions of (anti)-reactivity due to the control rods shifting are nearly equal.
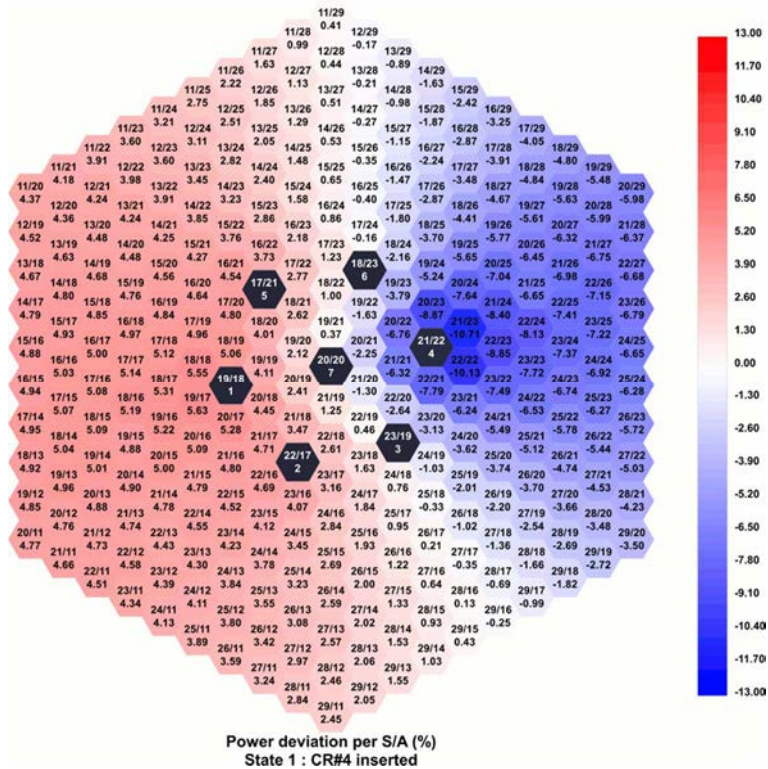
FIG. 78. Power deviation distribution for the state 1 (CEA results).

Power deviation map (in %)
State 2 : CR#1 extracted & CR#4 inserted
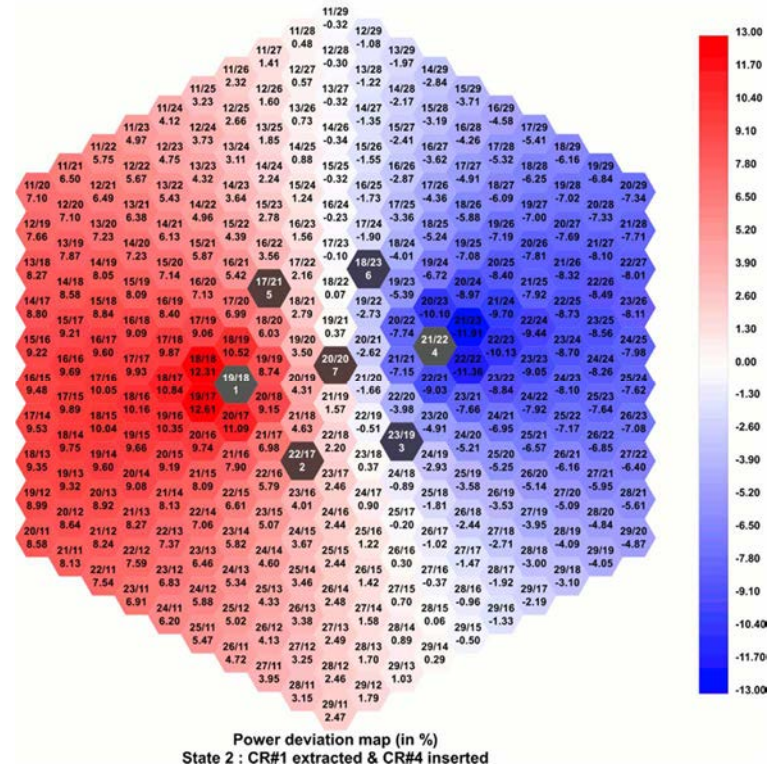
FIG. 79. Power deviation distribution for the state 2 (CEA results).

Power deviation per S/A (%)
State 3 : CR#1 extracted
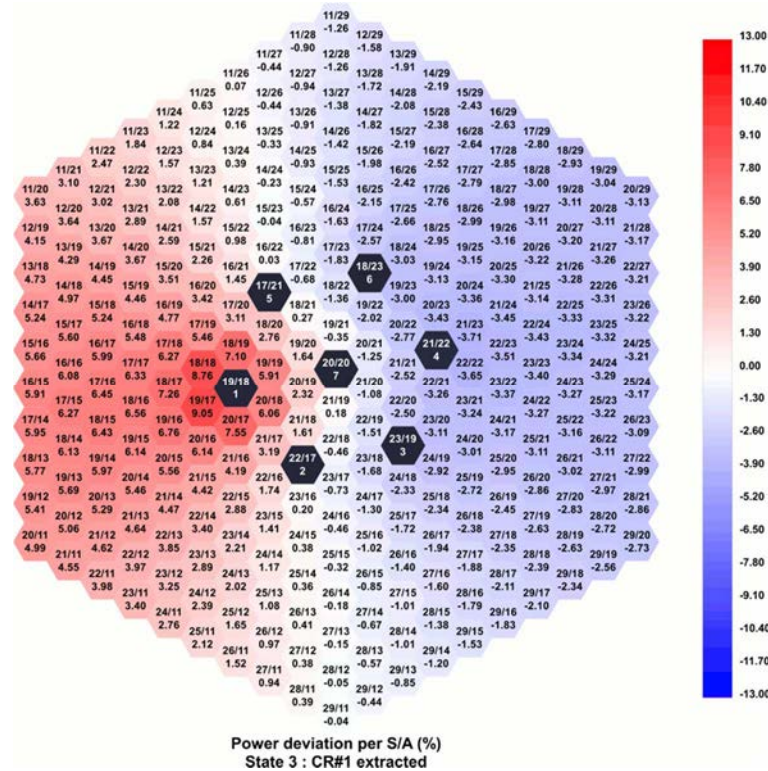
FIG. 80. Power deviation distribution for the state 3 (CEA results).

104

7.1.5.2. Comparison with the measured values

The results of the comparison between measured and calculated power deviations maps are presented in Fig. 81. This comparison is satisfying for the fissile S/As, even if the calculations seem to weakly overestimate the deformations. The calculation scheme does not take into account Doppler feed-back effects linked to the deformations of fuel temperature maps.
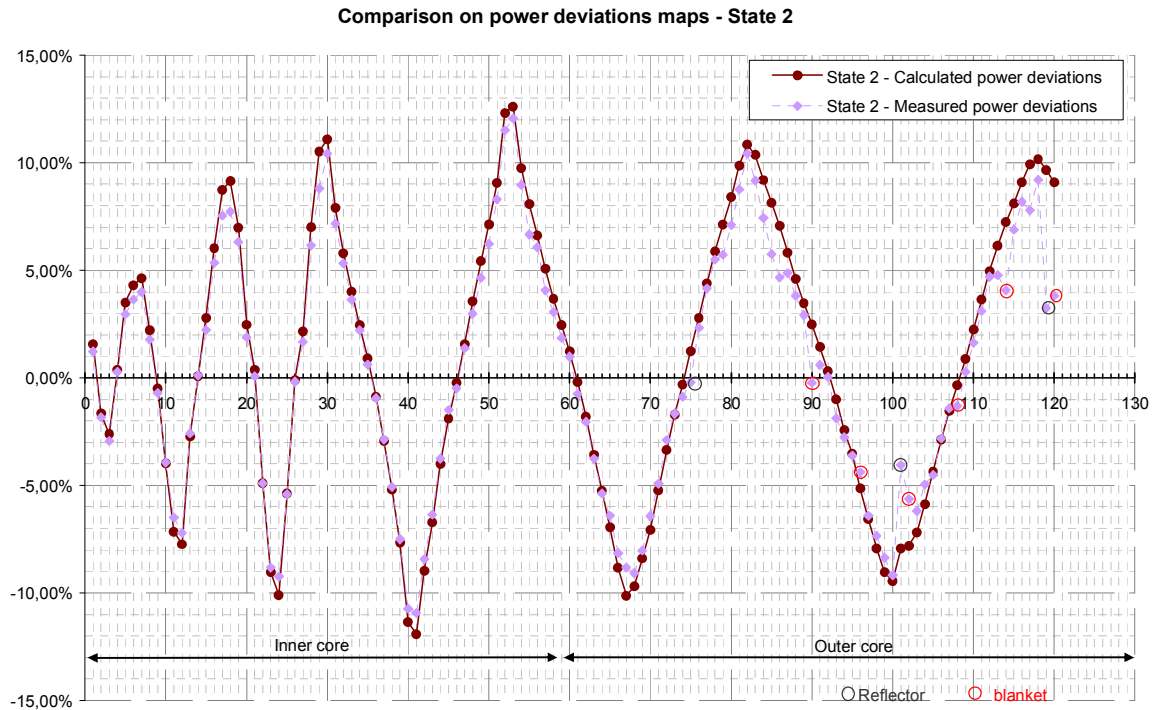
FIG. 81. Comparison between calculated and measured power deviations maps - State 2 (CEA Results).

The biggest discrepancies are located on fertile and reflector S/As. Fig. 82 proposes a comparison between calculated and measured power deviations along a radial profile. This profile includes two blankets S/As. It shows clearly discrepancies in the fertile zone and a good agreement in the fissile core.
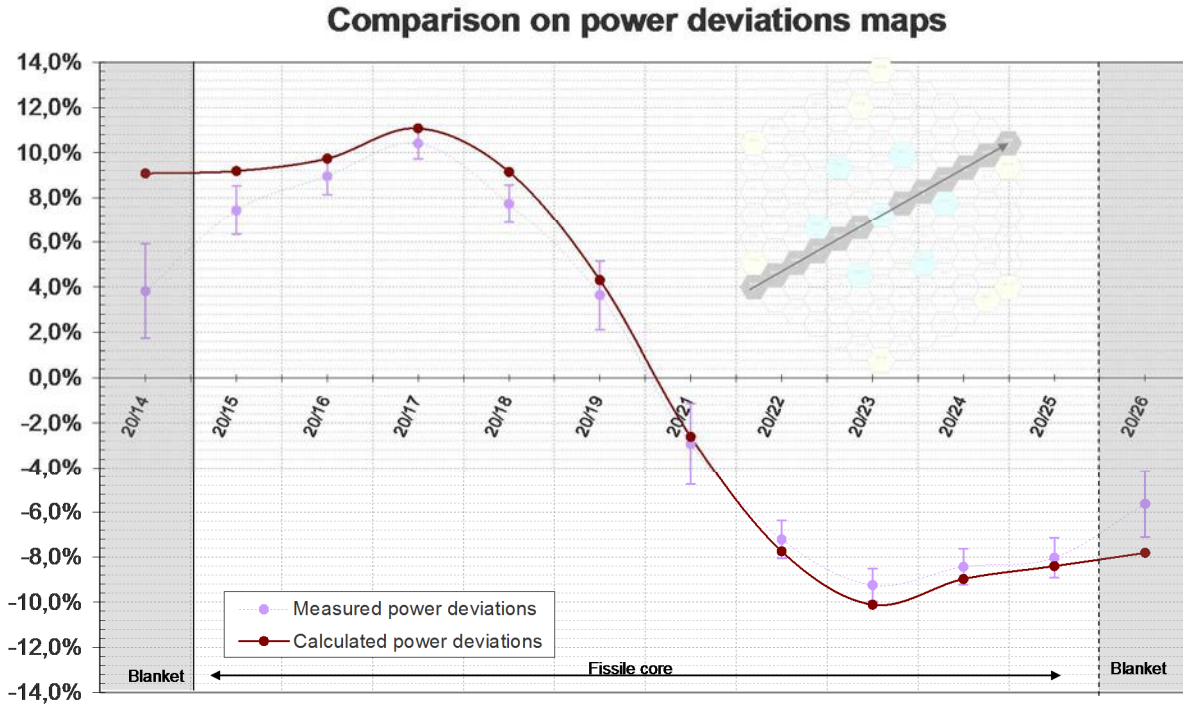
FIG. 82. Calculated and measured radial power deviations profiles (CEA Results).

7.1.6. Conclusions

The use of an average core description has an important impact on the reactivity estimation and power map estimations but it has finally a weak impact on power deviations maps.

Calculations seem to weakly overestimate the impact of the control rod shifting. However, discrepancies are weak for the fissile part of the core. Concerning the fertile part, several explanations could be given in order to understand the discrepancies:

— Problem in mass balance for blanket S/A, whose evolution was computed with flux calculated using the diffusion theory;
— Heat transfers between fertile and nearby fissile which could influence the measured power balance of S/A;
— Sodium mixing between fertile and fissile flows ($Q_{fertile} \sim 3$ kg.s^{-1} vs. $Q_{fissile} \sim 15$kg.s^{-1}).

Finally, ERANOS is able to produce good predictions concerning control rods impacts on the core power map.

7.2. IGCAR

7.2.1. Control rods worth

The results of the analysis on control rod worth are shown in Table 40 and Fig. 83.

TABLE 40. CONTROL RODS WORTH (BANK)

CR position (bank) (mm)	Integral Worth (pcm)	
	FARCOB	ERANOS
0	0	0
100	327	262
200	930	772
300	1843	1605
400	3044	2739
500	4435	4078
600	5840	5451
700	7029	6608
800	7823	7377
900	8154	7698
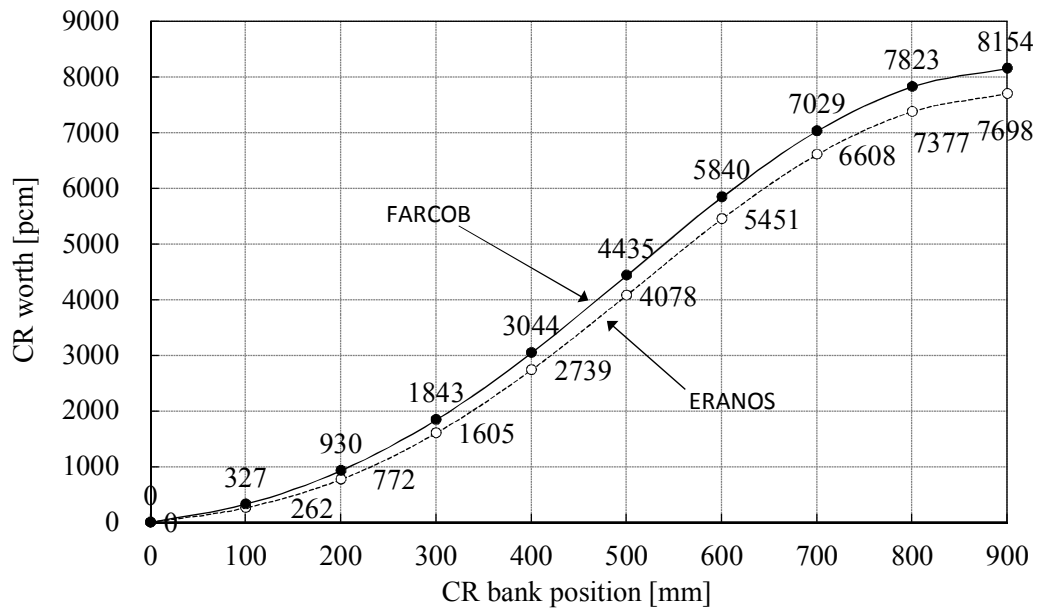
FIG. 83. Control rods S-curve (bank).

7.2.2. Core reactivity during the different test states

The results of the analysis on K_{eff} (reactivity) are shown in Table 41.

TABLE 41. CORE REACTIVITY

		Reference State	Step.1	Step.2	Step.3	Final State
FARCOB	Keff	1.00580	1.00588	1.00598	1.00587	1.00592
	Reactivity (pcm)	577	585	594	584	589
ERANOS	Keff	1.00856	1.01002	1.00948	1.00949	-
	Reactivity (pcm)	849	992	939	940	-

7.2.3. Flux and power distribution

7.2.3.1. Maximum Flux distribution

The maximum flux distributions for each S/A are shown in Fig. 84–88 (FARCOB) and Fig. 89–93 (ERANOS).
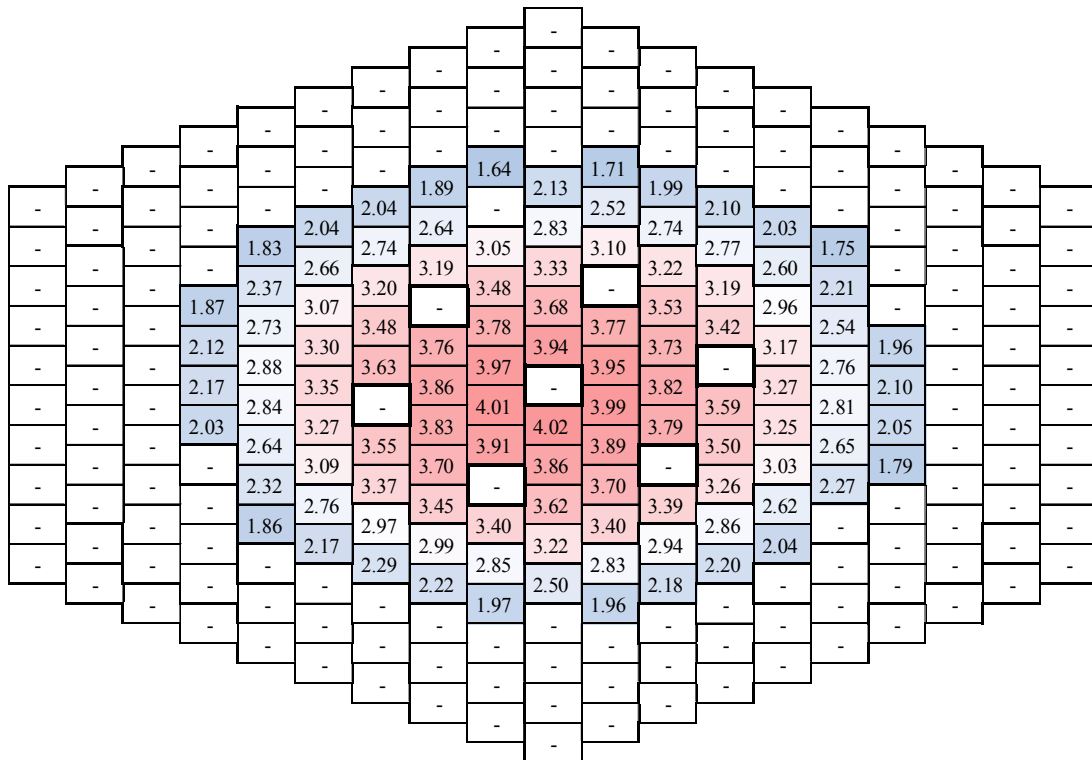
FIG. 84. Maximum flux distribution by FARCOB (reference state, $\times 10^{15}$ (n/cm^2 ·s)).
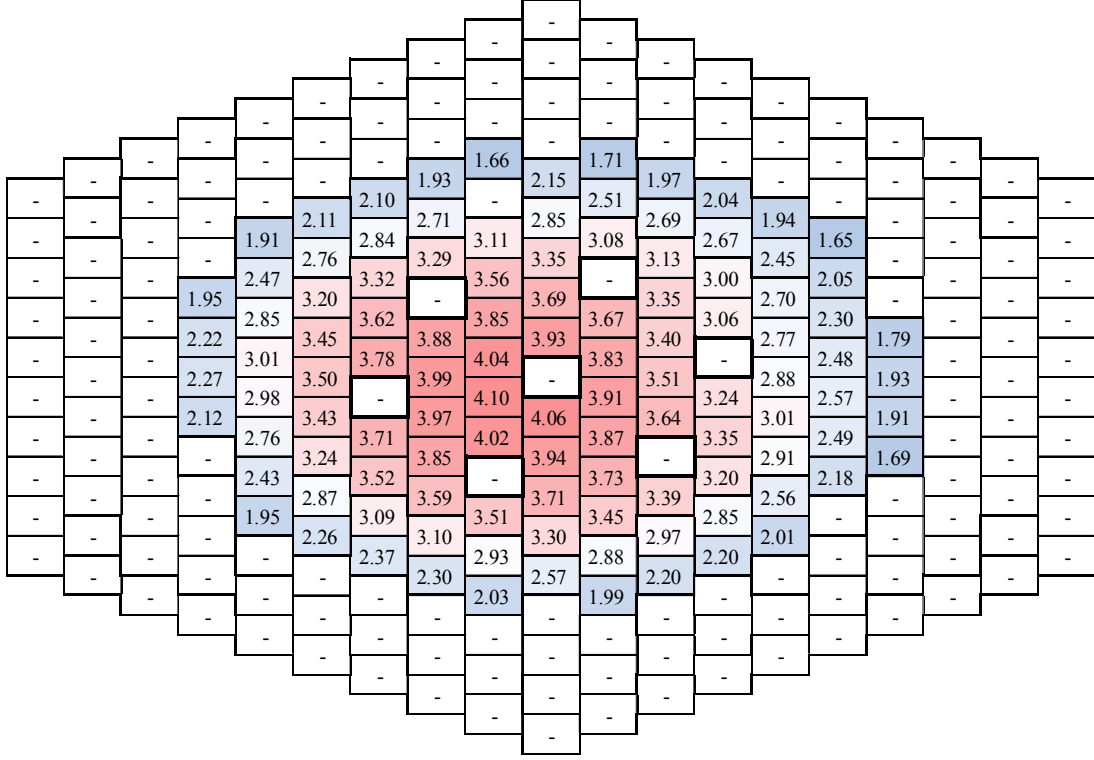
FIG. 85. Maximum flux distribution by FARCOB (step 1, $\times 10^{15}$ n/cm^2 ·s)).
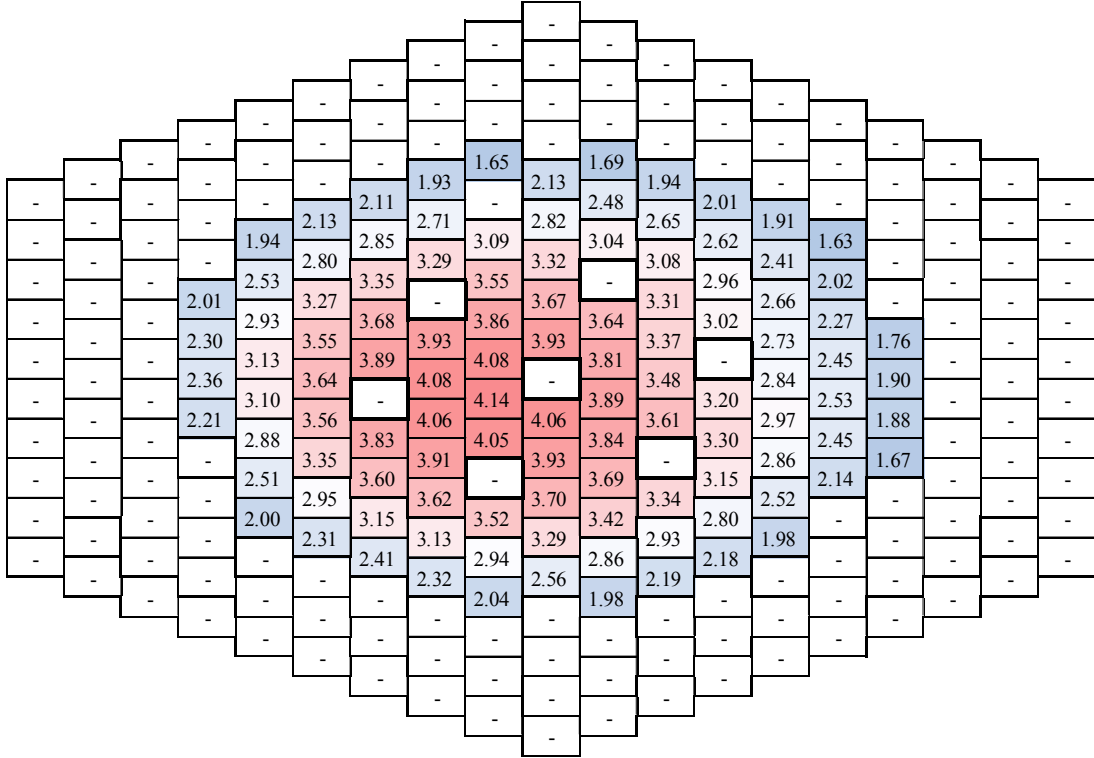
FIG. 86. Maximum flux distribution by FARCOB (step 2, $\times 10^{15}$ (n/cm^2 ·s)).

109
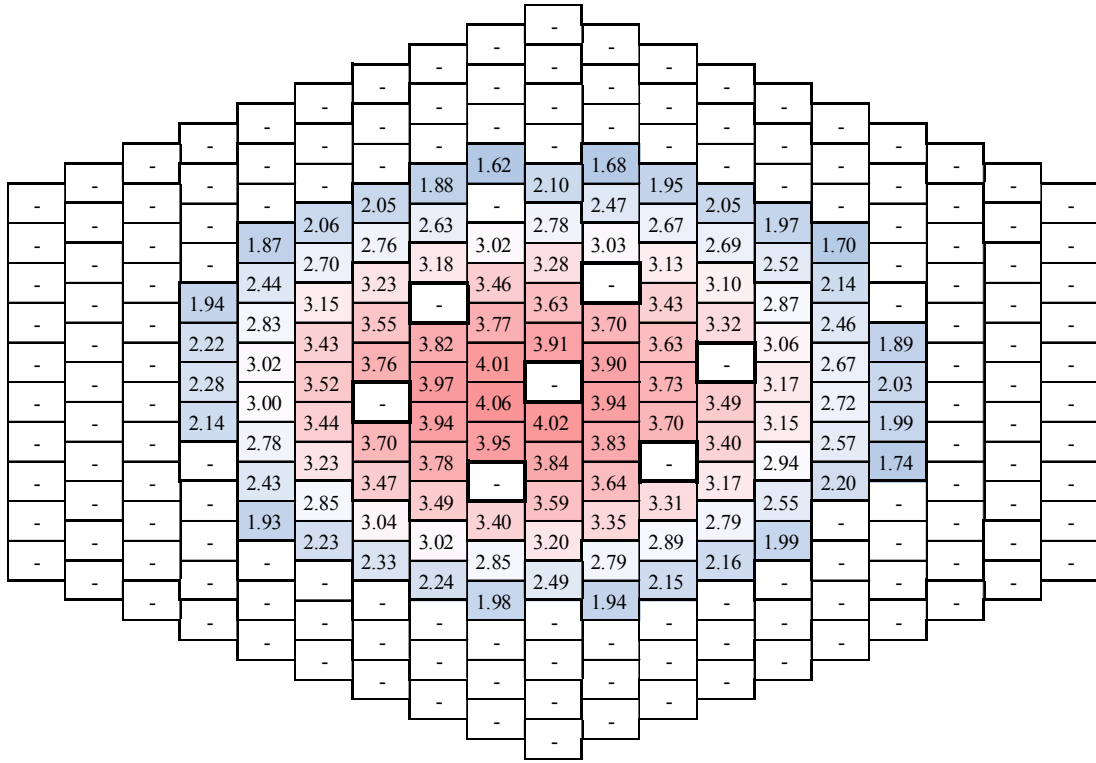
FIG. 87. Maximum flux distribution FARCOB (step 3, $\times 10^{15}$ (n/cm^2 ·s)).
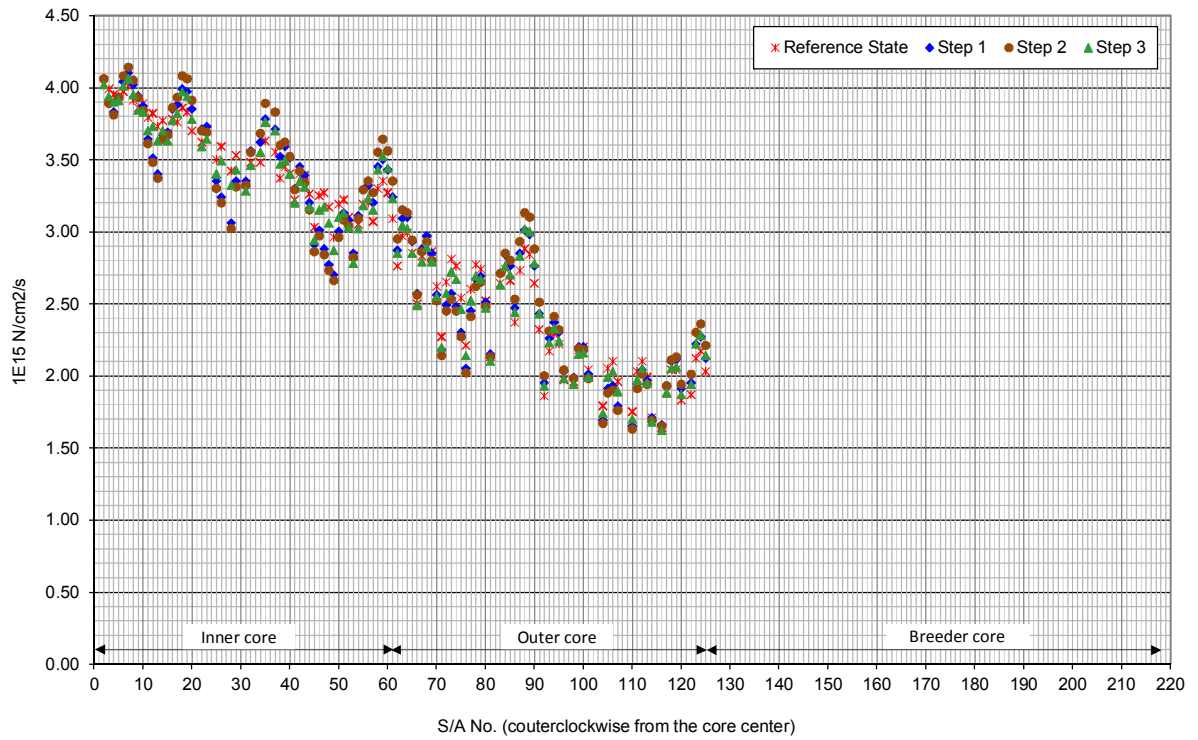
FIG. 88. Maximum flux distributions by FARCOB (all steps).

110
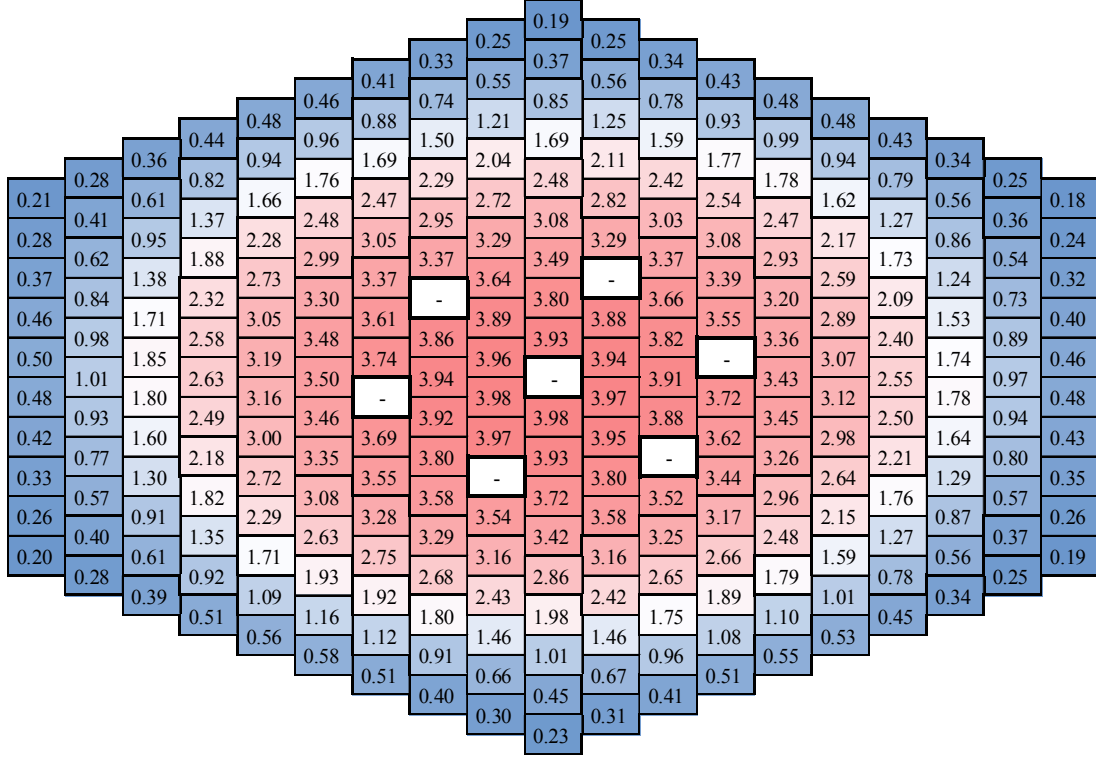
FIG. 89. Maximum flux distribution by ERANOS (reference state, ×1015 (n/cm2 ·s)).
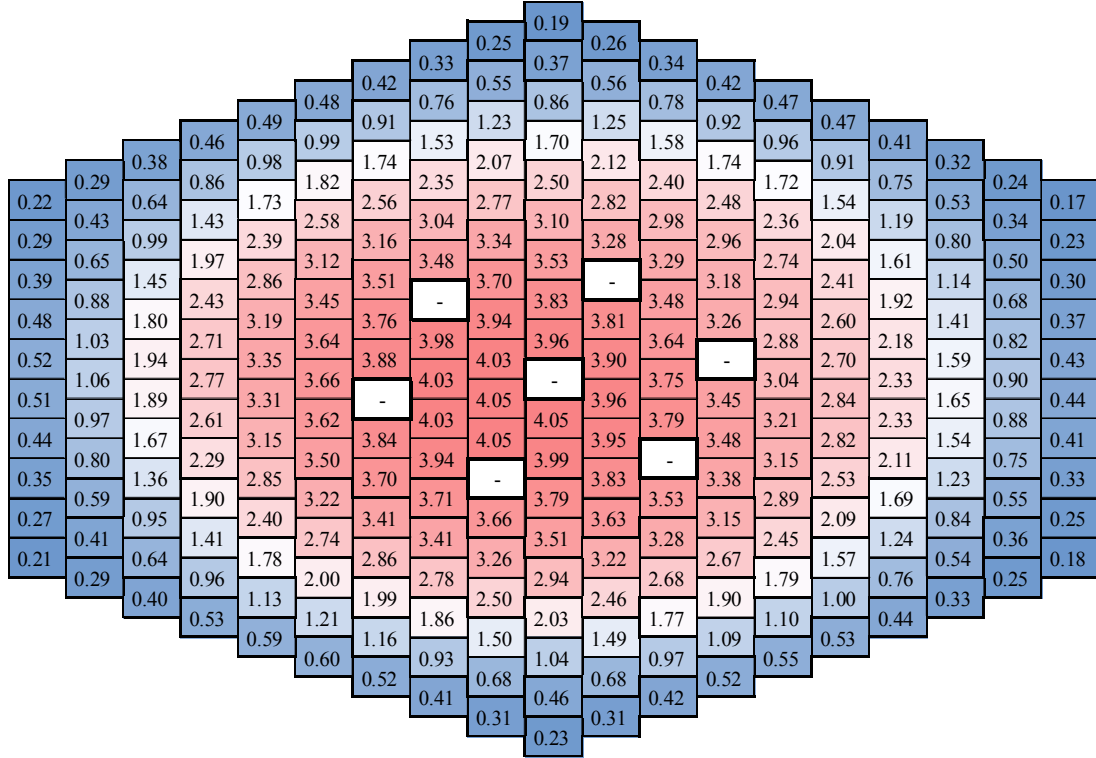
FIG. 90. Maximum flux distribution by ERANOS (step 1, ×10^{15} (n/cm^2 ·s)).
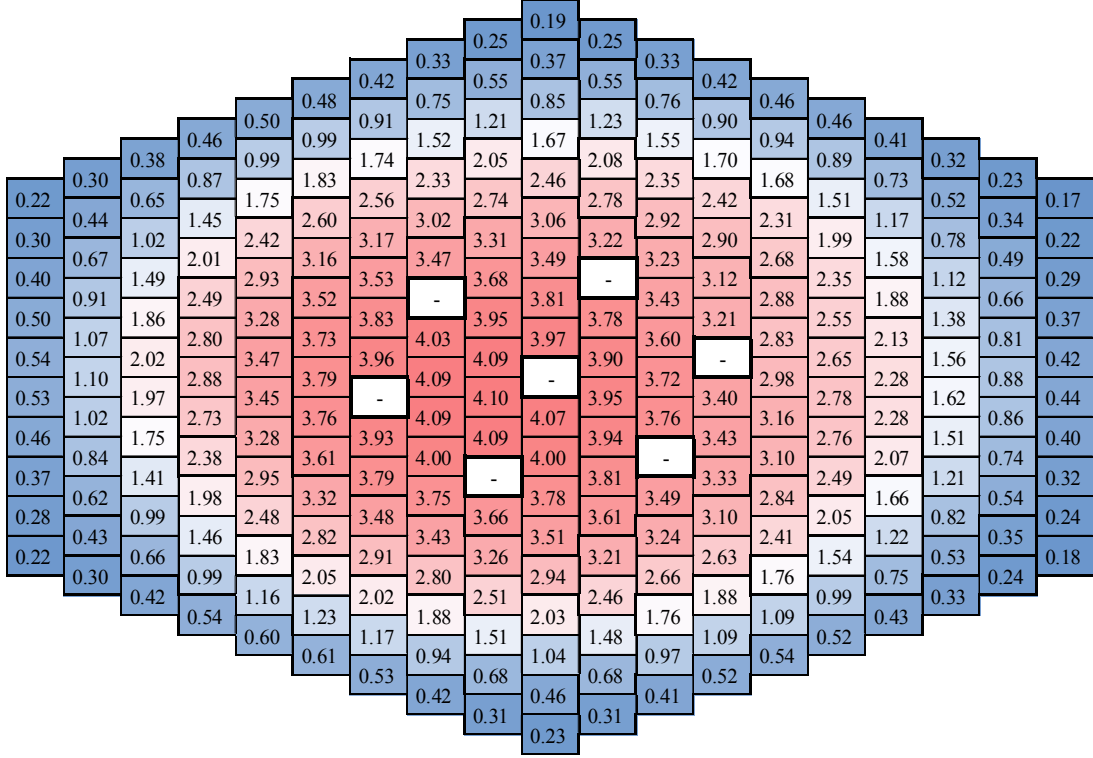
FIG. 91. Maximum flux distribution by ERANOS (step 2, ×10¹⁵ (n/cm² ·s)).

FIG. 91. Maximum flux distribution by ERANOS (step 2, $\times 10^{15}$ (n/cm² ·s)).

FIG. 92. Maximum flux distribution by ERANOS (step 3, ×10¹⁵ (n/cm² ·s)).
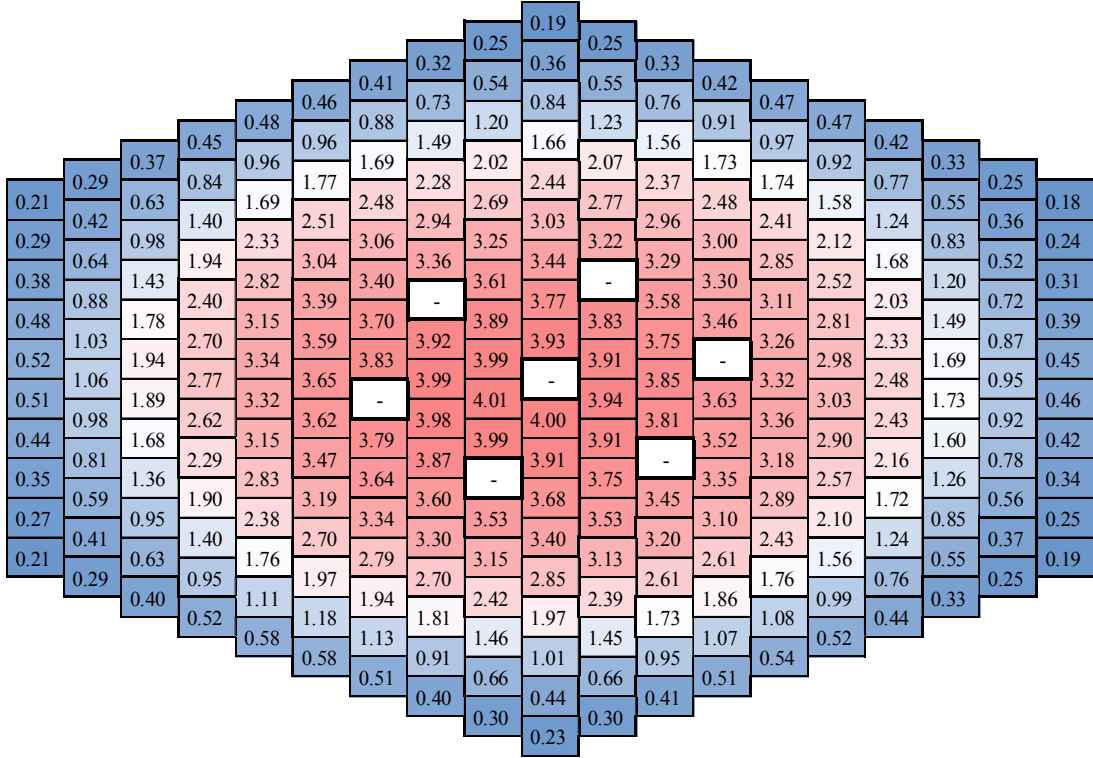
FIG. 92. Maximum flux distribution by ERANOS (step 3, $\times 10^{15}$ (n/cm² ·s)).
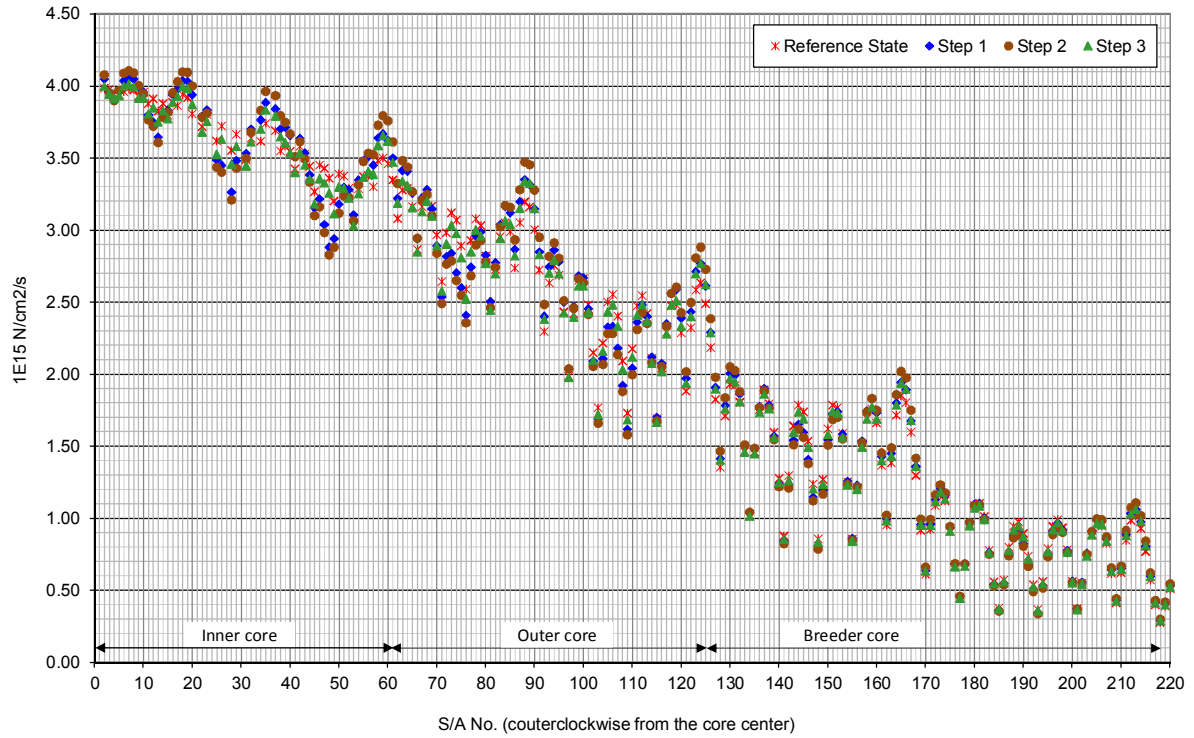
FIG. 93. Maximum flux distributions by ERANOS (all steps).

7.2.3.2. Total power distribution

The total power distributions of each S/A are shown in Fig. 94–98 (FARCOB) and in Fig. 100–104 (ERANOS). The C/E values of the total power in Reference state and step 2 are shown in Fig. 99 (FARCOB) and Fig. 105 (ERANOS).

FIG. 94. Total power distribution by FARCOB (reference state, (MW(th))).

FIG. 95. Total power distribution by FARCOB (step 1, (MW(th))).
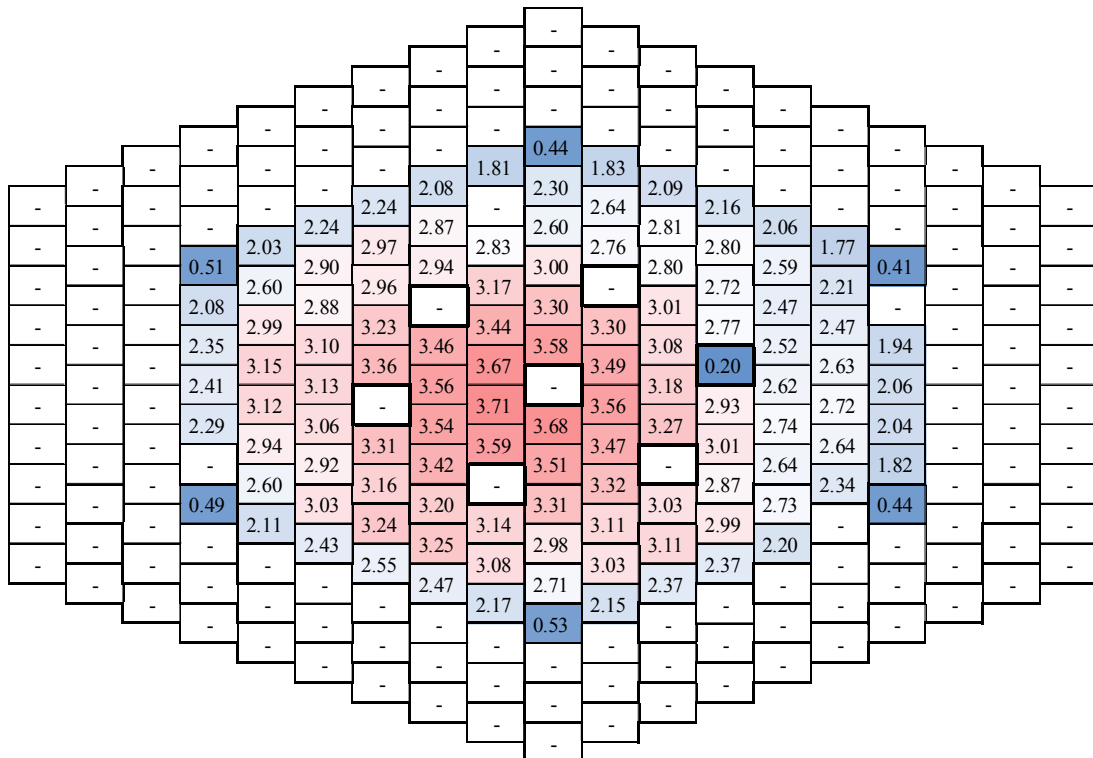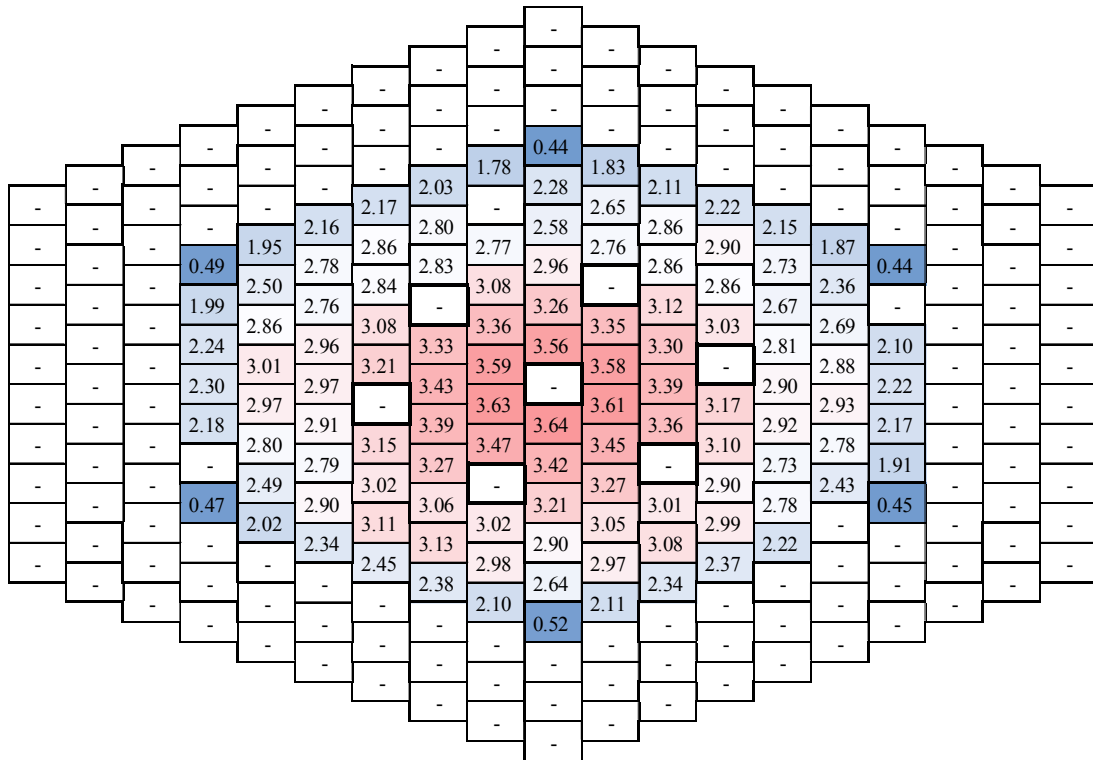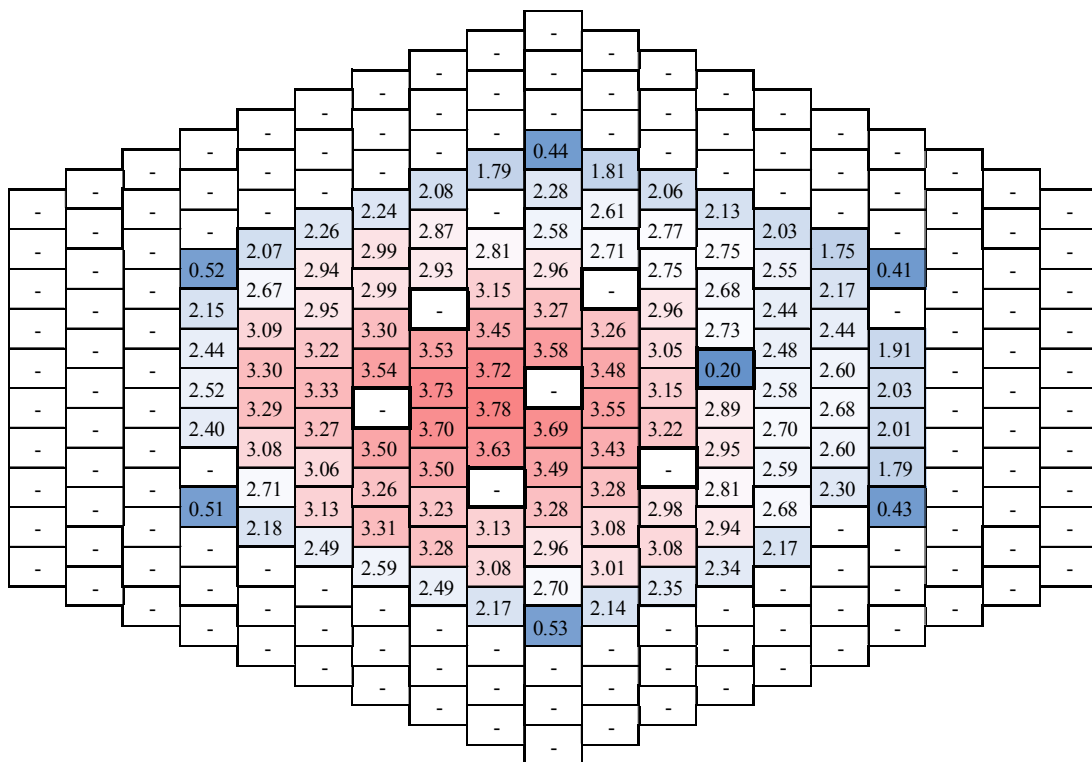
FIG. 96. Total power distribution by FARCOB (step 2, (MW(th))).
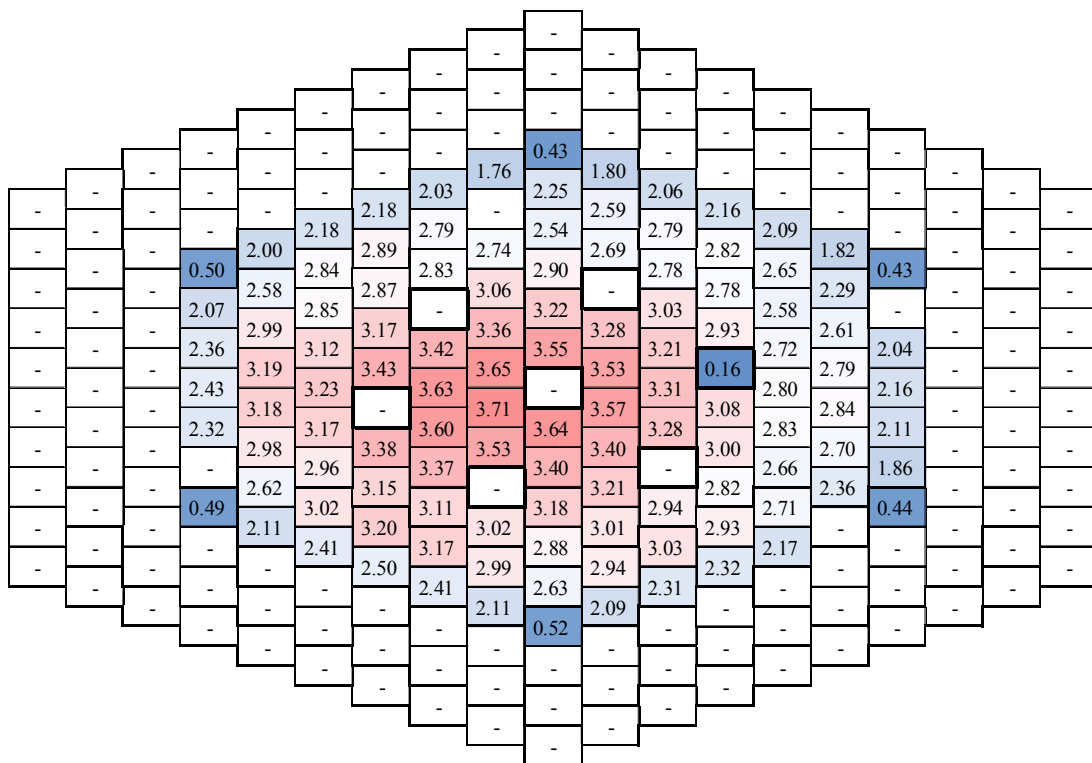
FIG. 97. Total power distribution by FARCOB (step 3, (MW(th))).
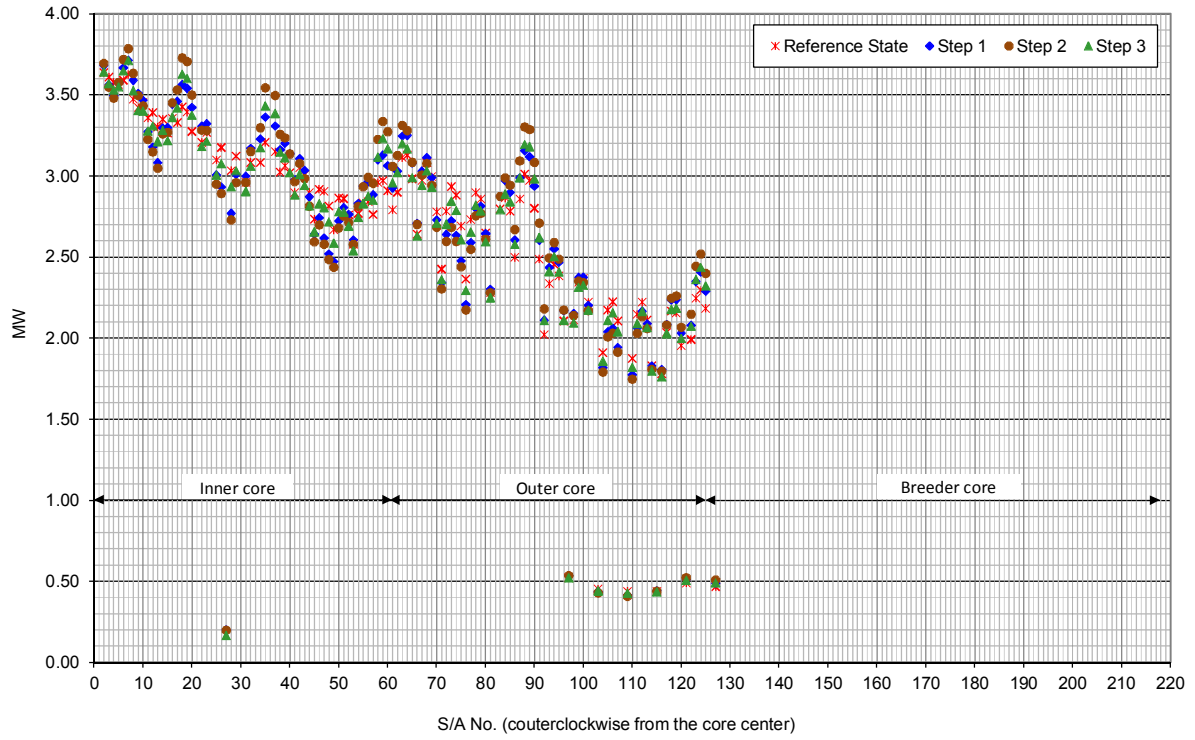
FIG. 98. Total power distributions by FARCOB (all steps).
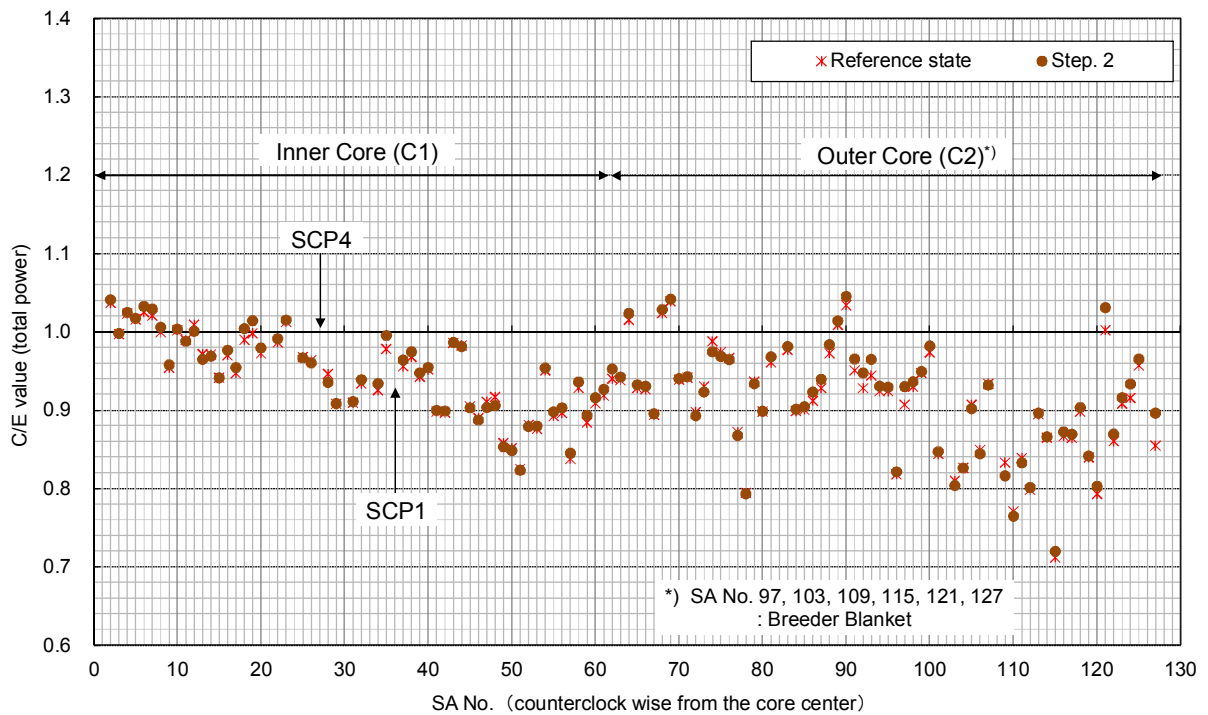
FIG. 99. C/E values for total power distributions by FARCOB (inner and outer core, reference state and step 2).
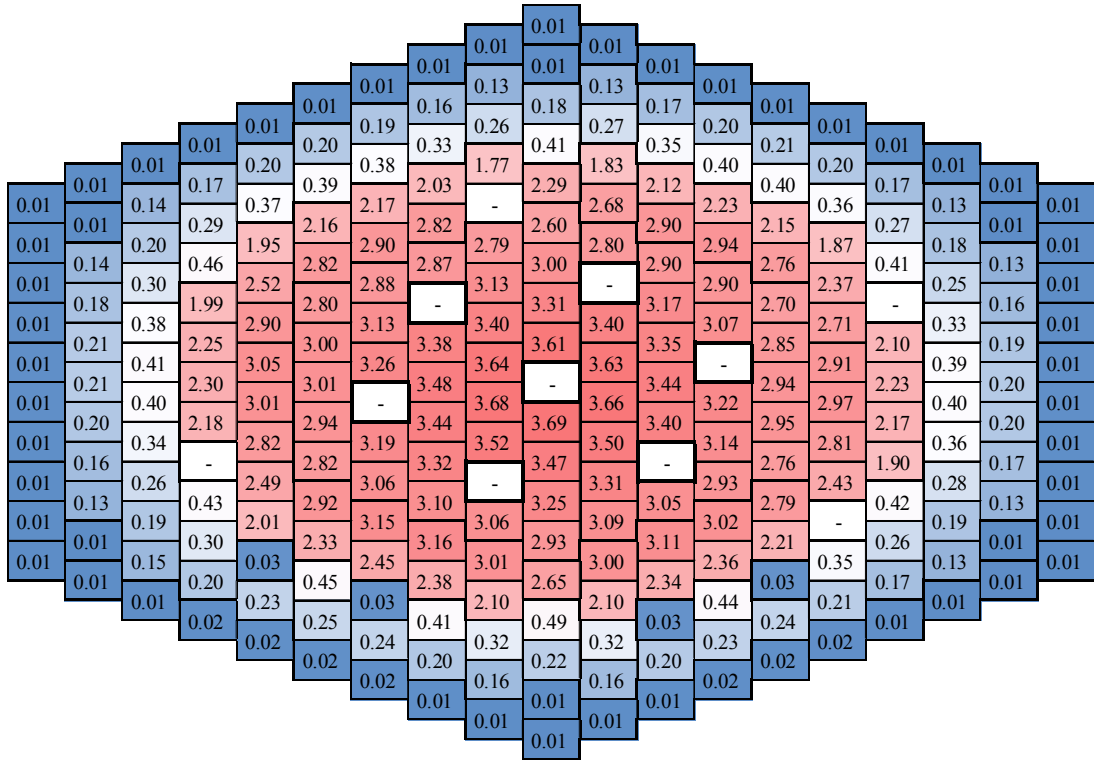
FIG. 100. Total power distribution by ERANOS (reference state, (MW(th))).
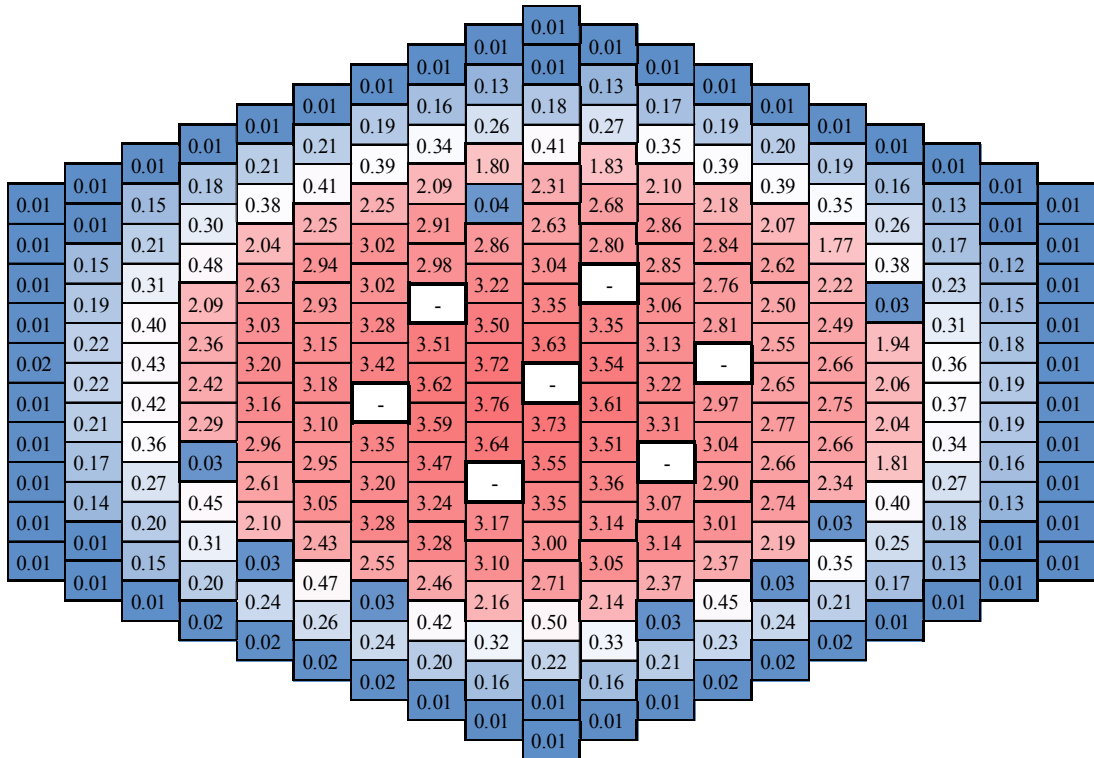
FIG. 101. Total power distribution by ERANOS (step 1, (MW(th)))
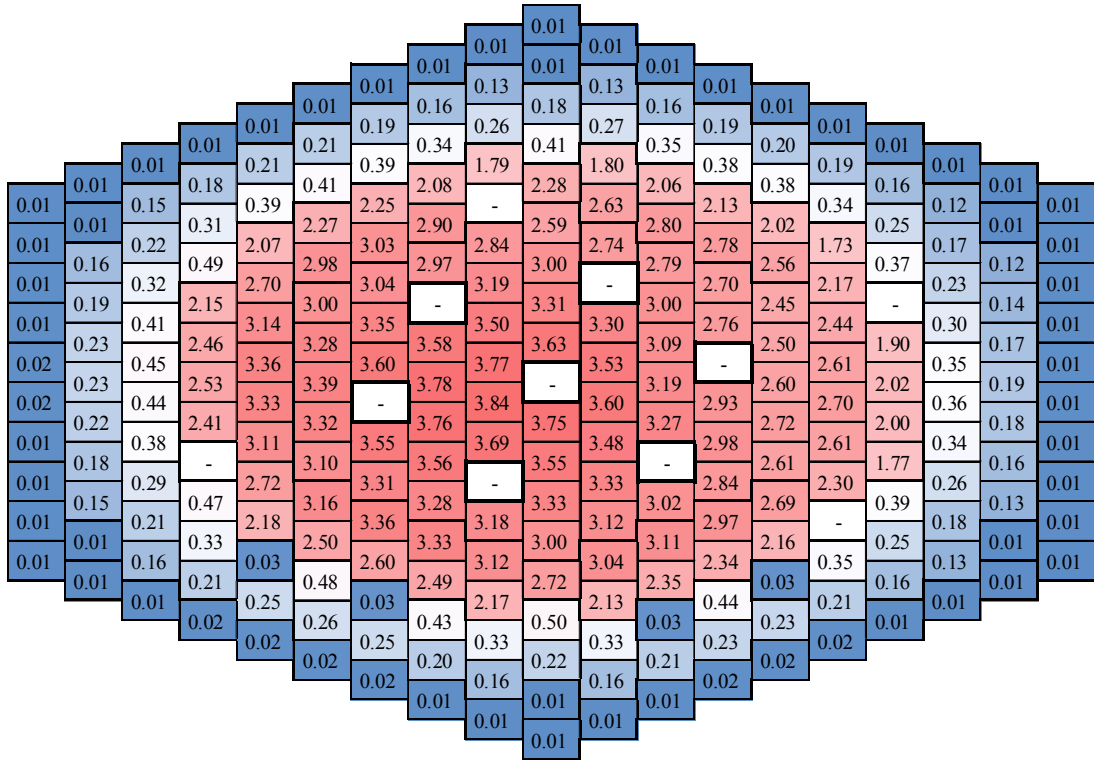
FIG. 102. Total power distribution by ERANOS (step 2, (MW(th))).
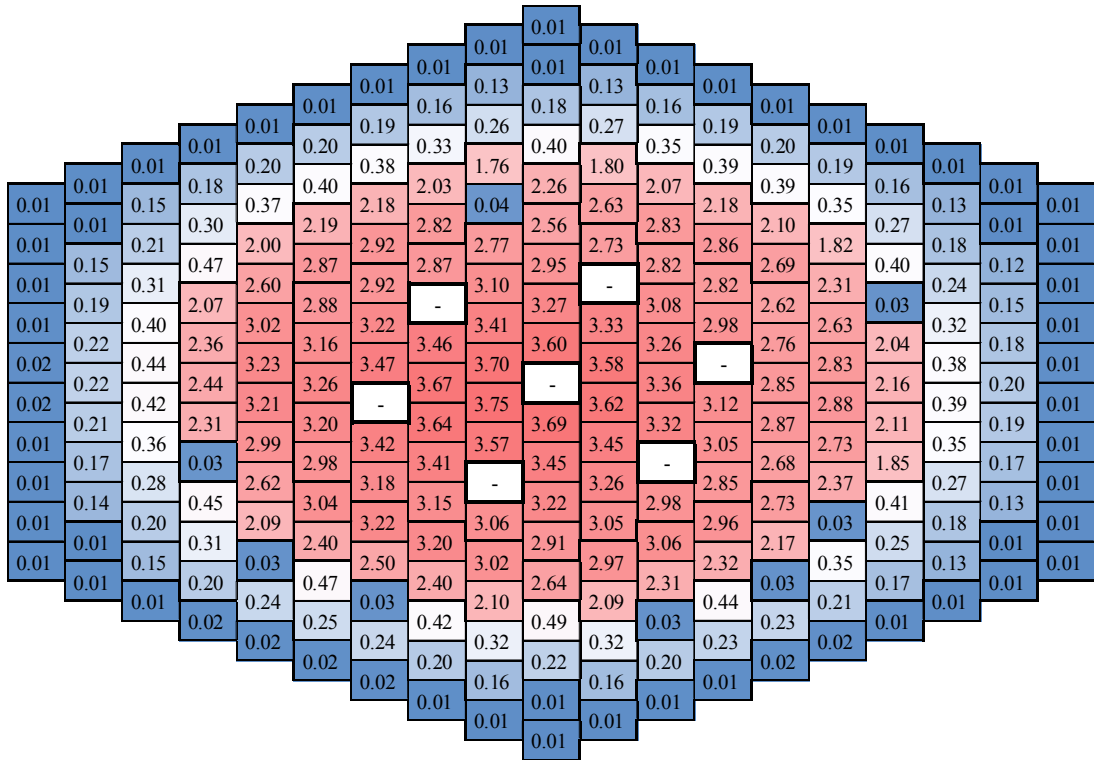
FIG. 103. Total power distribution by ERANOS (step 3, (MW(th))).

118
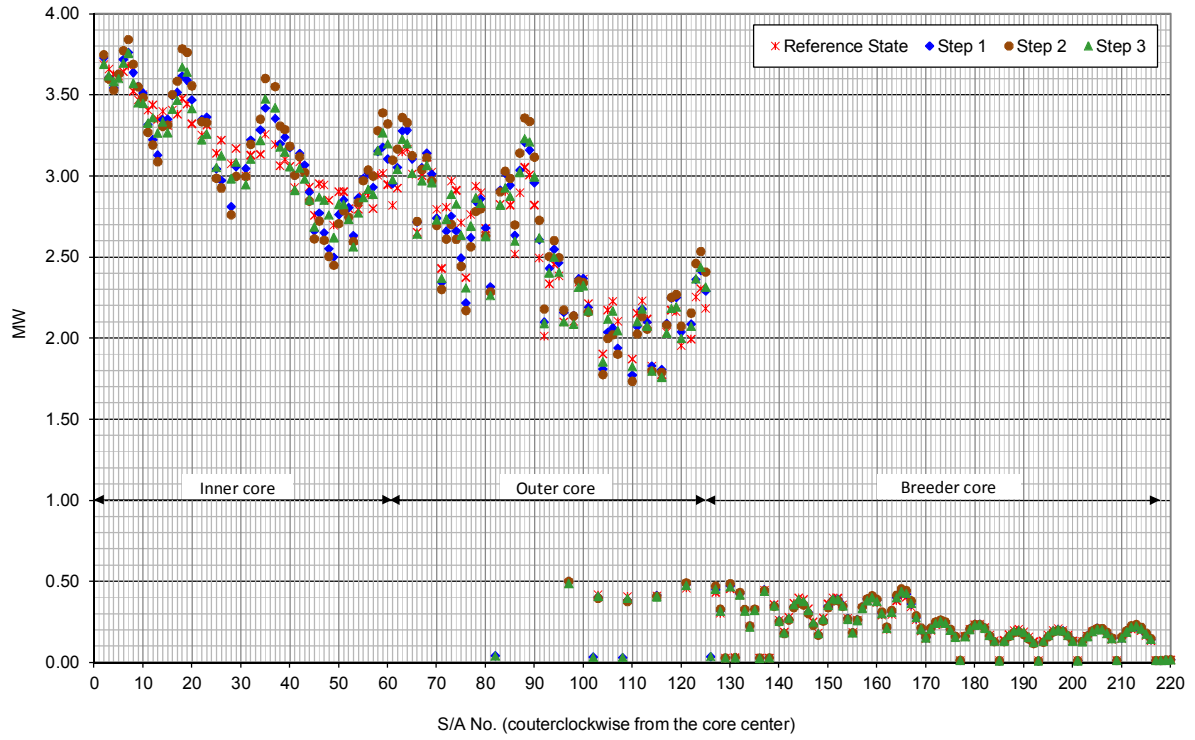
FIG. 104. Total power distributions by ERANOS (all steps).
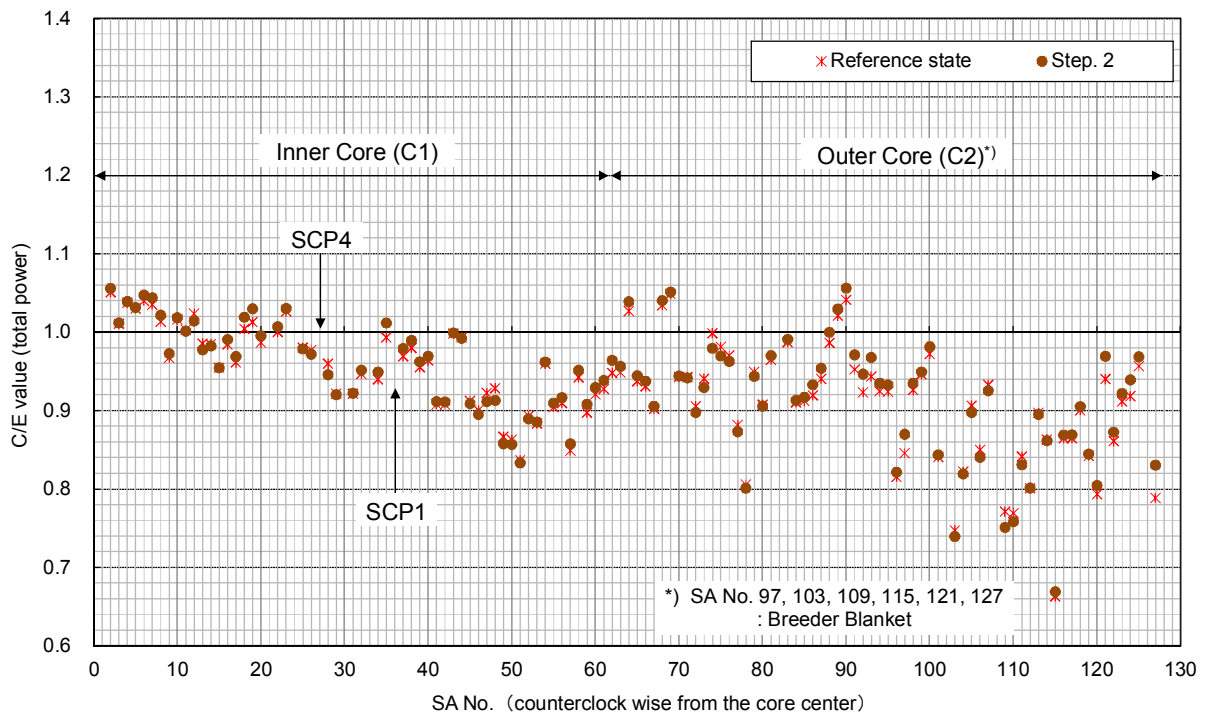
FIG. 105. C/E values for total power distributions by ERANOS (inner and outer core, reference state and step 2).

7.2.4. Power deviation distributions

The deviations (%) of the S/A total power from reference state are shown in Fig. 106‑108 (FARCOB) and Fig. 110‑112 (ERANOS). Fig. 109 (FARCOB) and Fig. 113 (ERANOS) summarize the C-E value of the deviations in step 1–3 for inner and outer core.
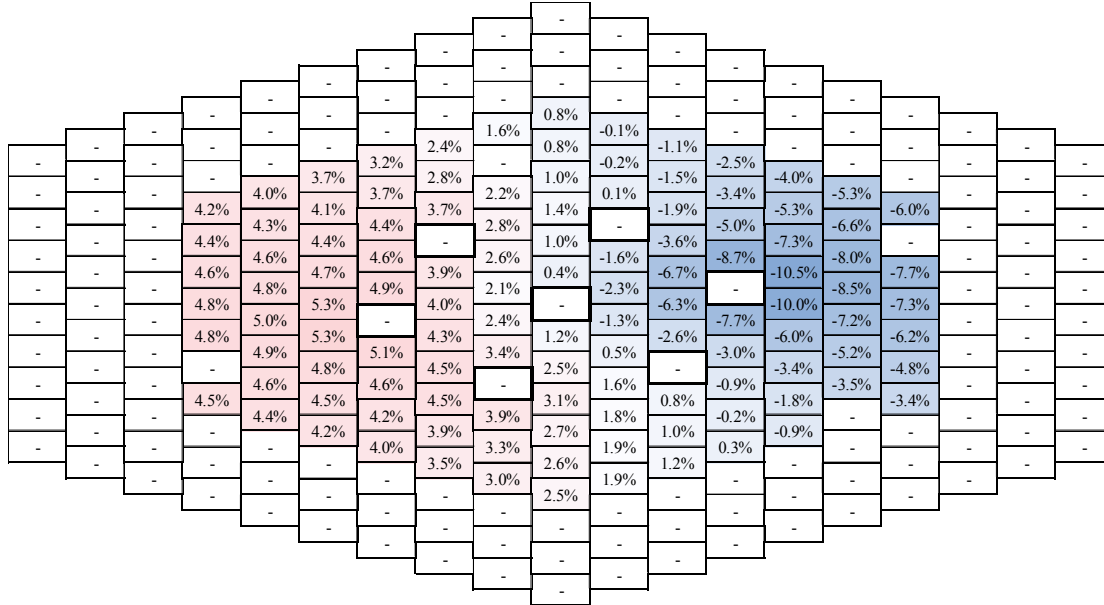
FIG. 106. Deviation of the total power from reference state by FARCOB (step 1, (%)).
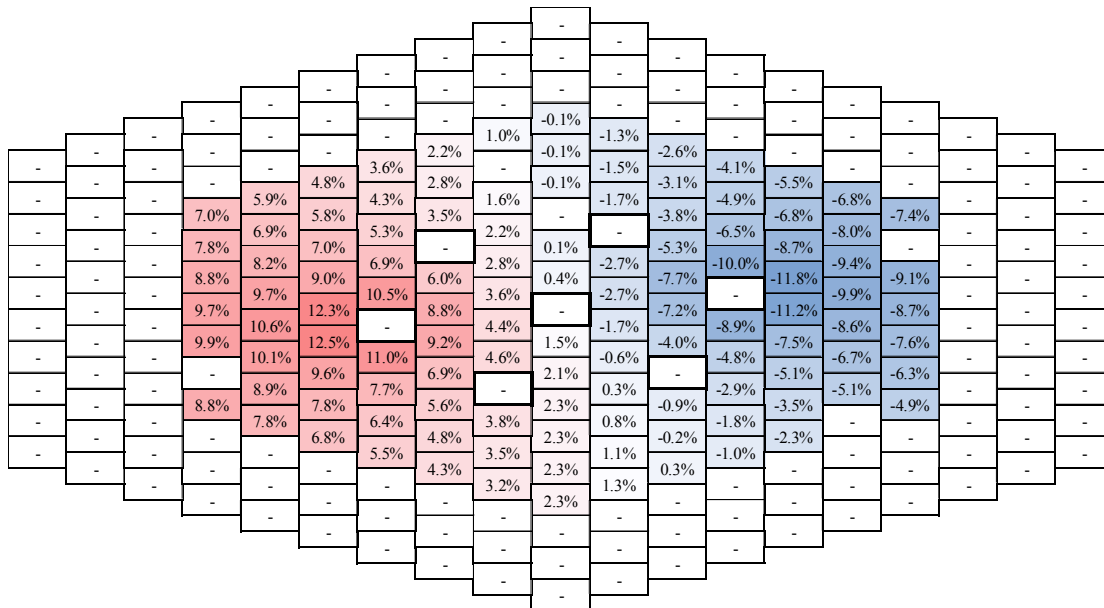
FIG. 107. Deviation of the total power from reference state by FARCOB (step 2, (%)).
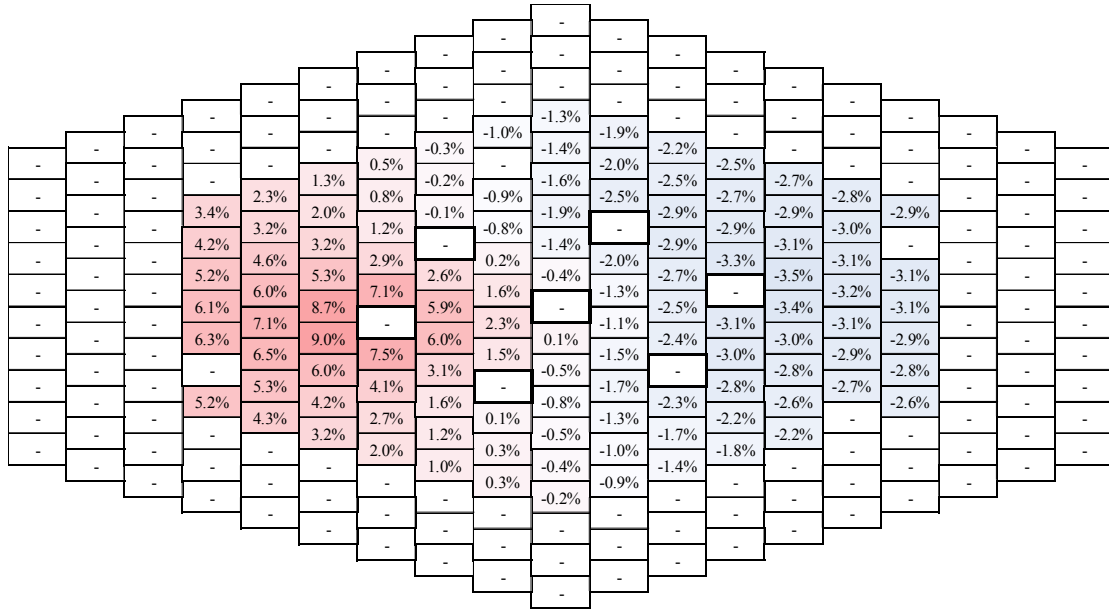
FIG. 108. Deviation of the total power from reference state by FARCOB (step 3, (%)).
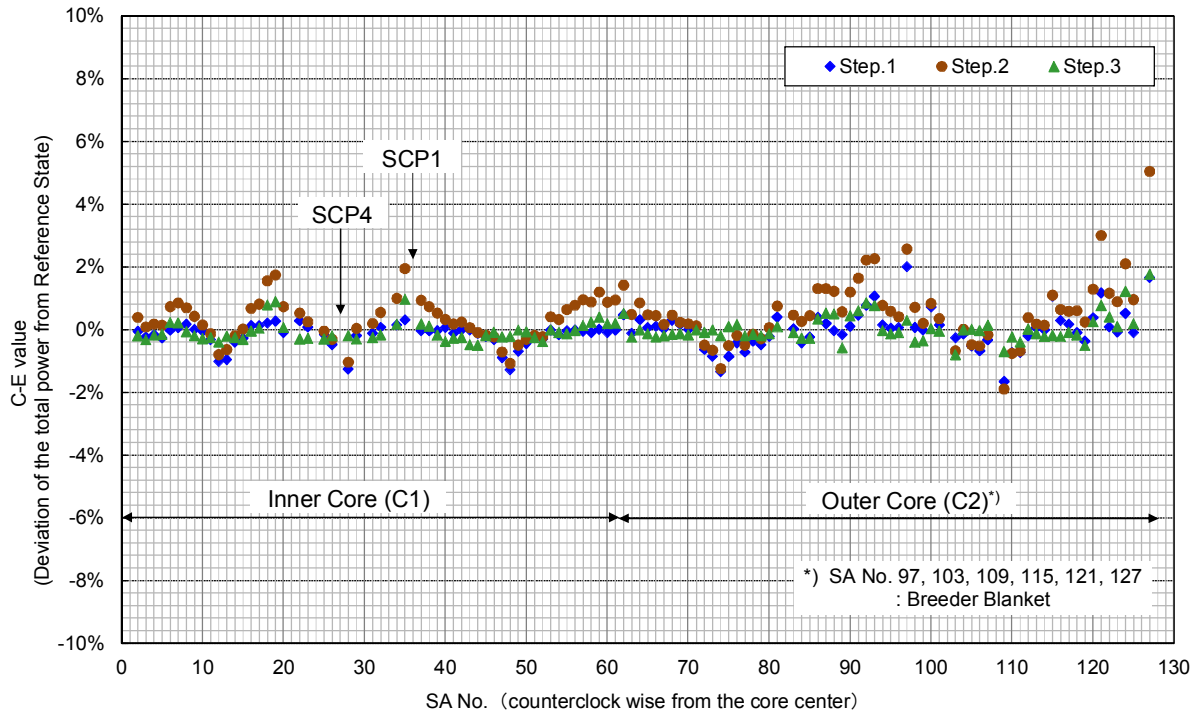
FIG. 109. C-E value for deviation of the total power from reference state by FARCOB (%) (all steps).

FIG. 110. Deviation of the total power from reference state by ERANOS (step 1, (%)).

FIG. 111. Deviation of the total power from reference state by ERANOS (step 2, (%)).

122

FIG. 112. Deviation of the total power from reference state by ERANOS (step 3, (%)).

FIG. 113. C-E value for deviation of the total power from reference state by ERANOS (%) (all steps).
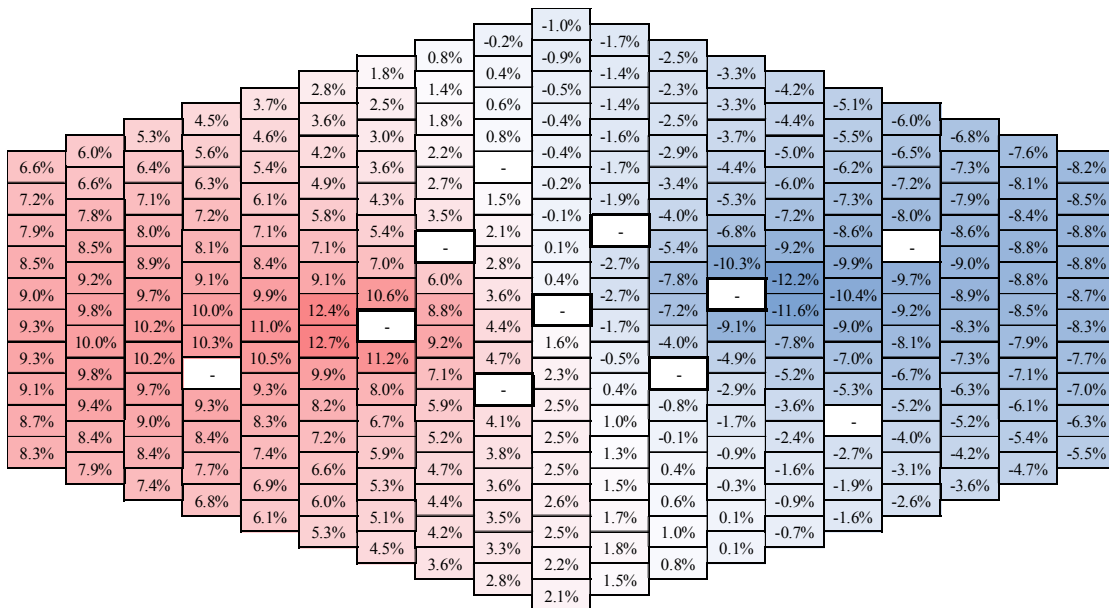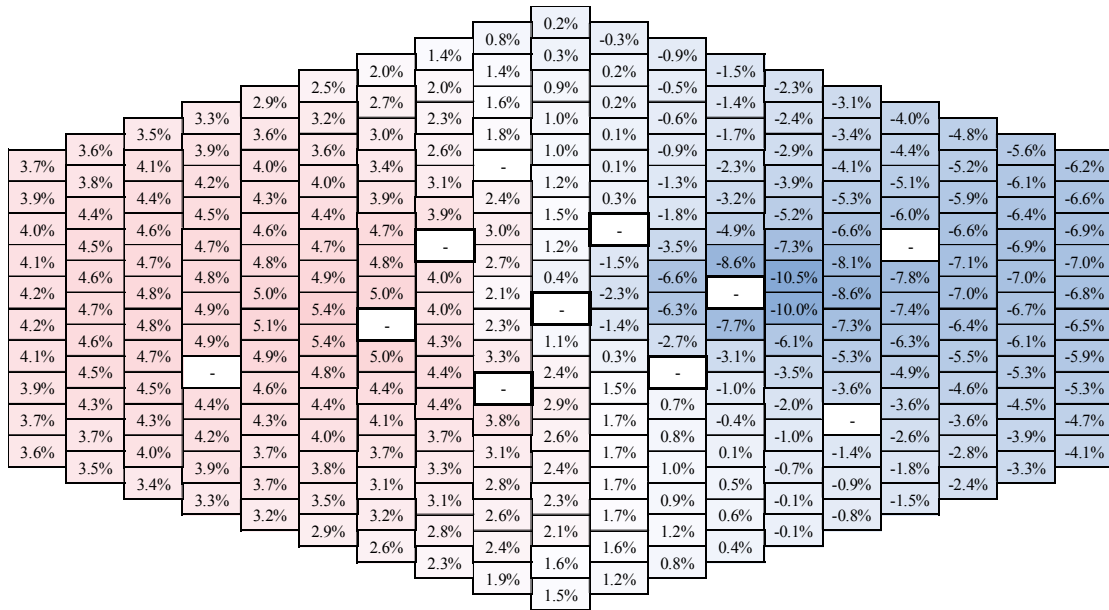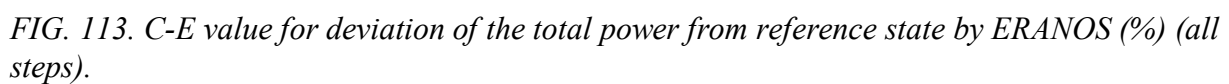
7.3. IPPE

7.3.1. Control rods worth

The results of the analysis on control rod worth are shown in Table 42 and Fig. 114.

TABLE 42. CONTROL RODS WORTH (BANK)

CR position (bank) (mm)	Integral Worth (pcm)
0	0
100	295
200	1008
300	2110
400	3399
500	4673
600	5776
700	6631
800	7168
900	7461
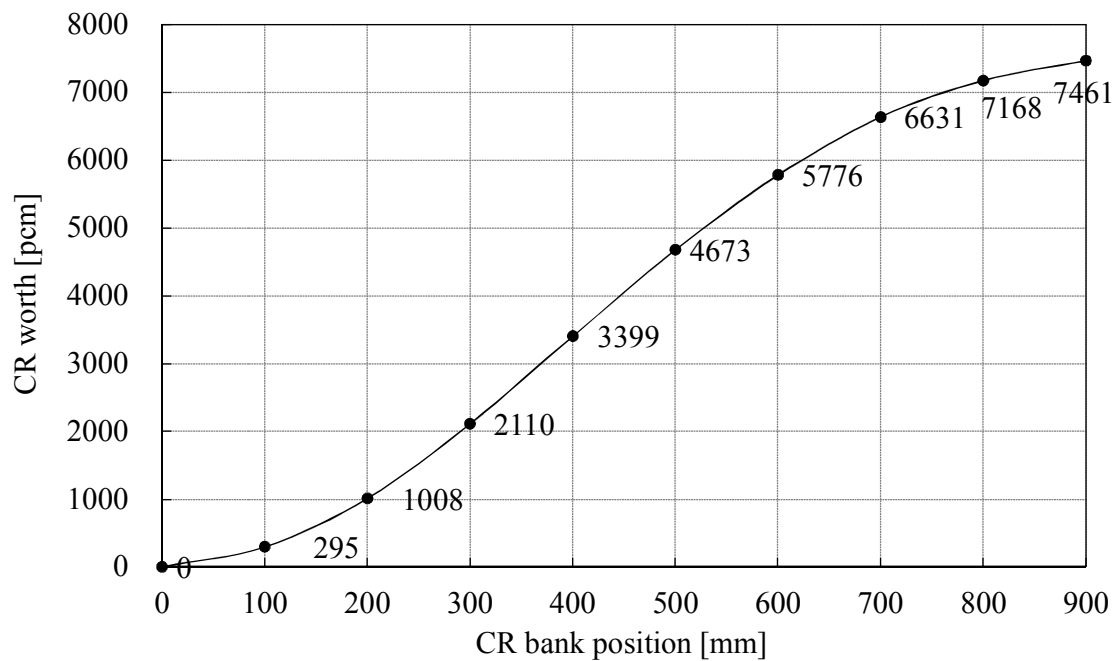
FIG. 114. Control Rods S-curve (bank).

7.3.2. Core reactivity during the different test states

The results of the analysis on K_{eff} (reactivity) are shown in Table 43.

TABLE 43. CORE REACTIVITY

	Reference State	Step.1	Step.2	Step.3	Final State
Keff	1.00211	1.00234	1.00228	1.00266	1.00243
Reactivity (pcm)	211	233	227	265	242

7.3.3. Flux and power distribution

7.3.3.1. Maximum Flux distribution

The maximum flux distributions for each S/A are shown in Fig. 115–119.
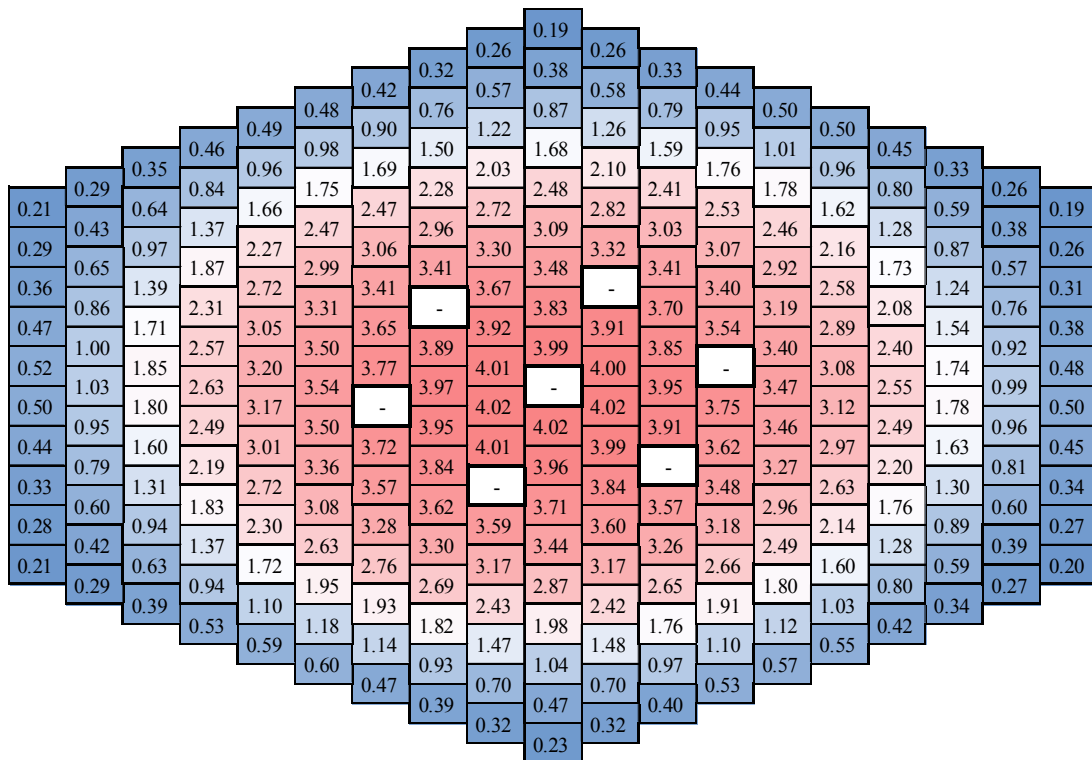
FIG. 115. Maximum flux distribution (reference state, $\times 10^{15}$ (n/cm^2·s)).
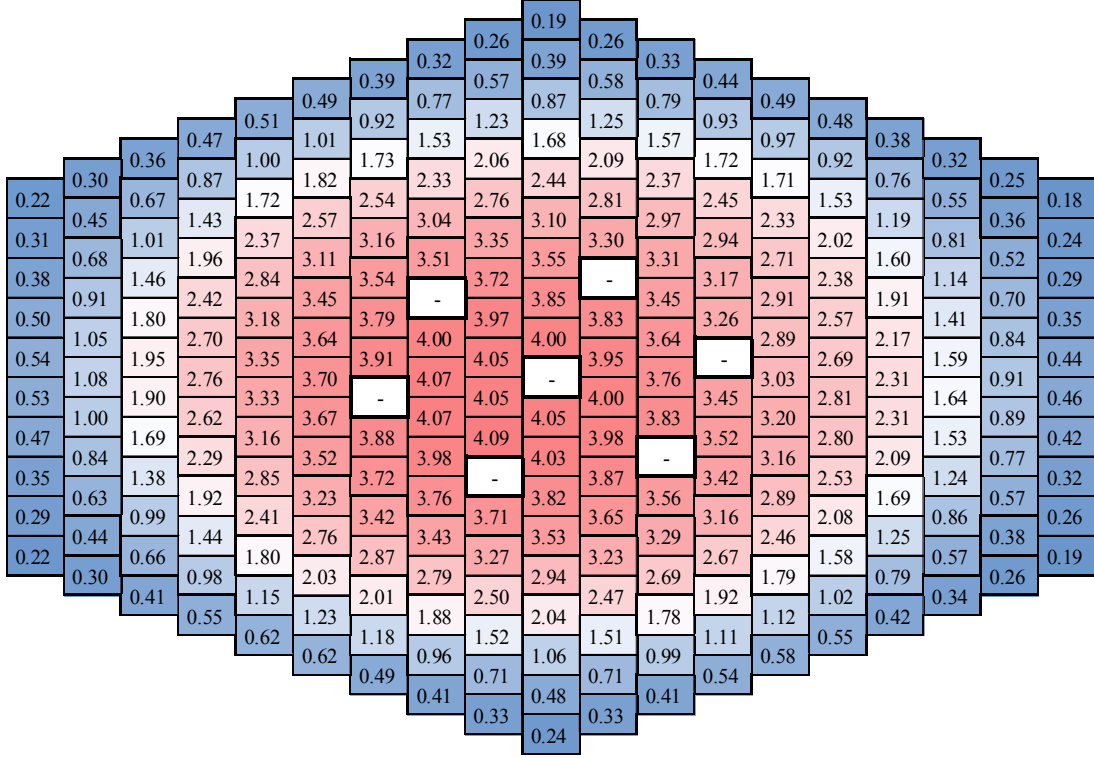
FIG. 116. Maximum flux distribution (step 1, $\times 10^{15}$ n/cm^2 ·s)).
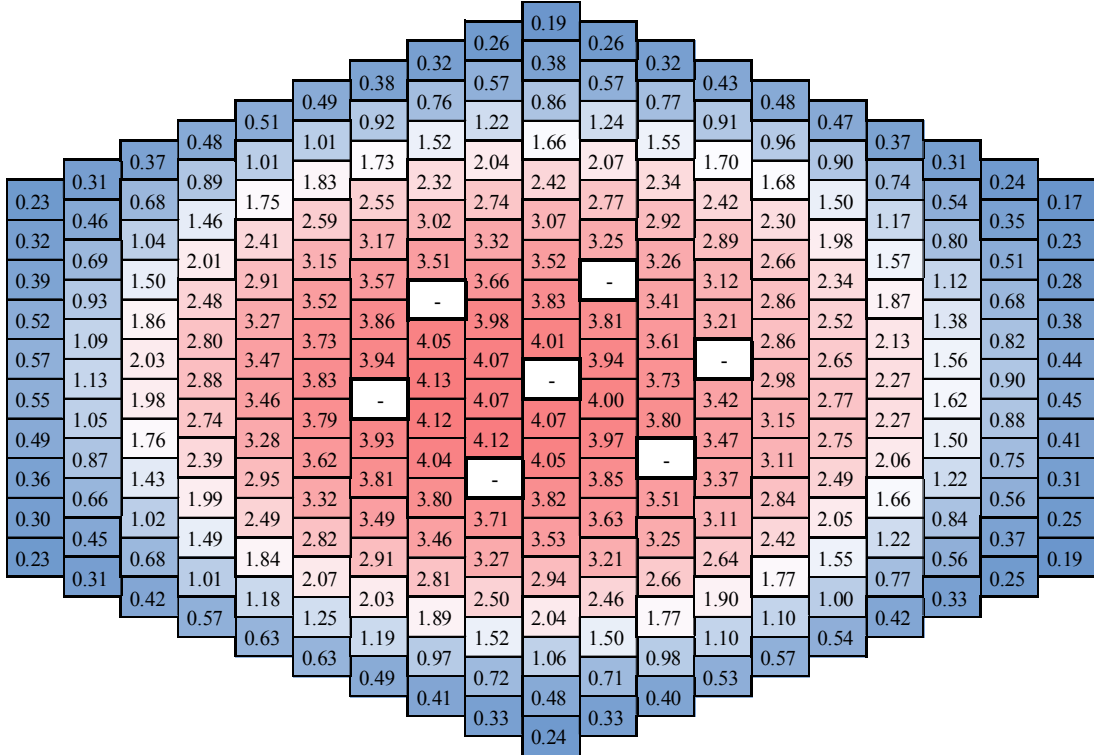
FIG. 117. Maximum flux distribution (step 2, $\times 10^{15}$ (n/cm^2 ·s)).
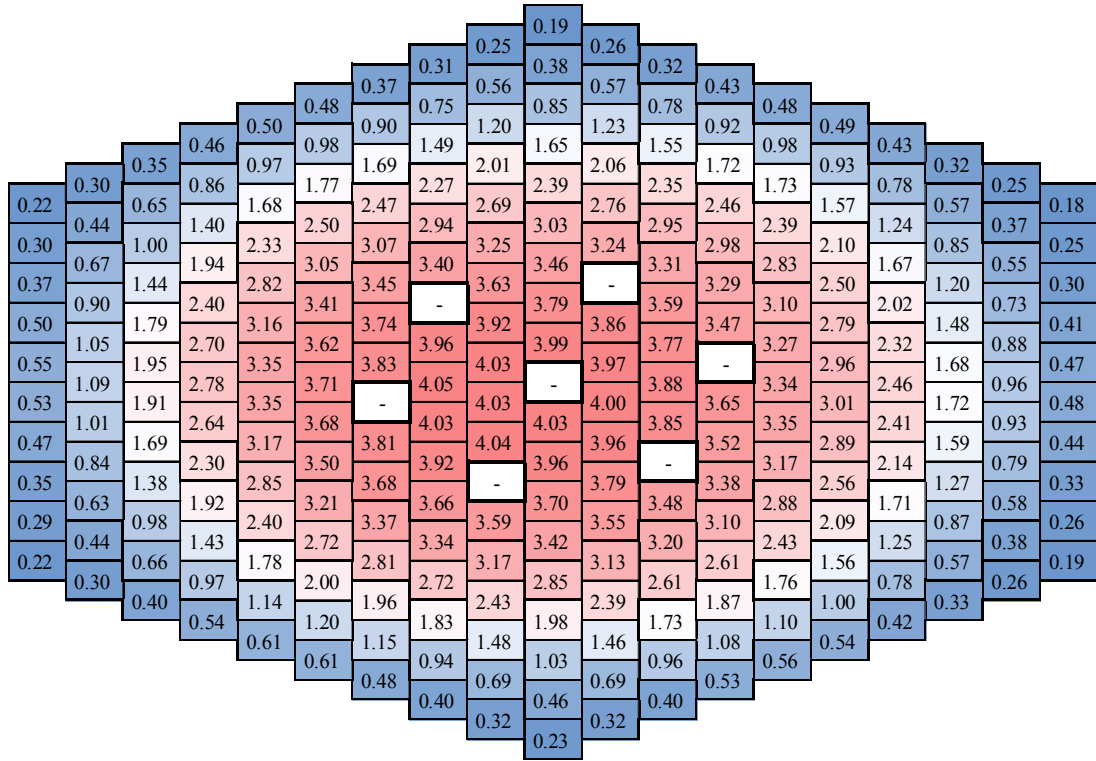
FIG. 118. Maximum flux distribution (step 3, $\times 10^{15}$ (n/cm^2 ·s)).
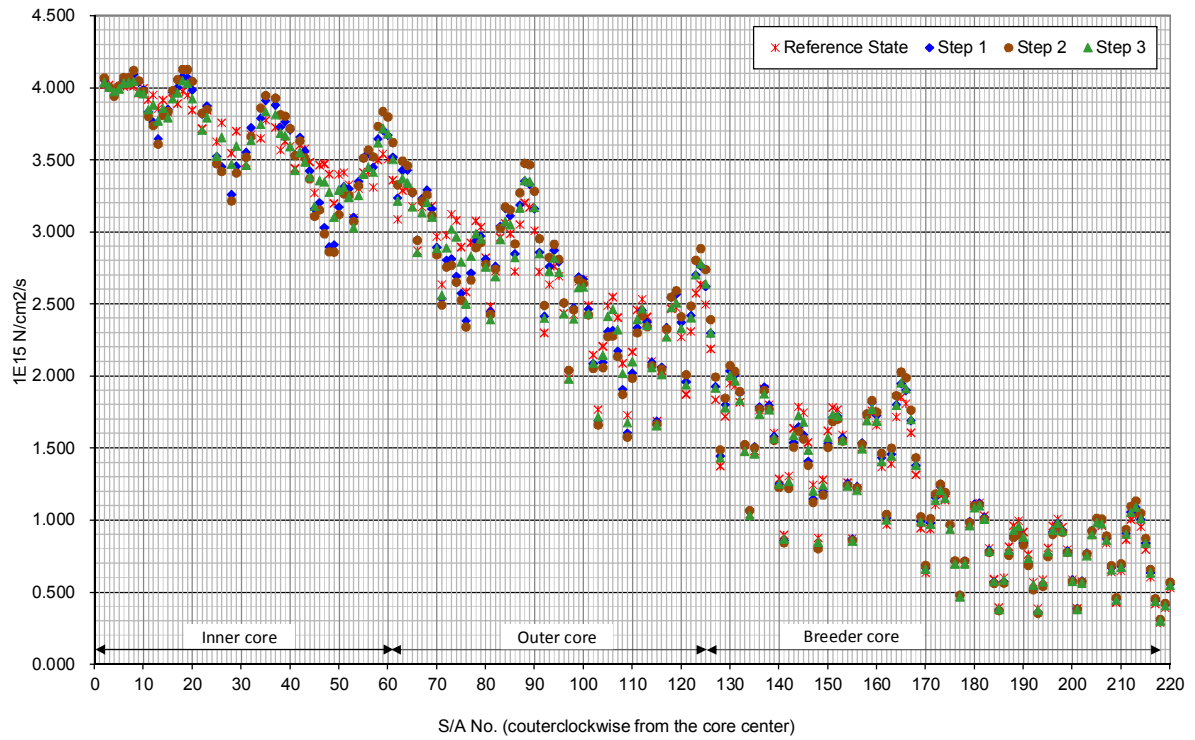
FIG. 119. Maximum flux distributions (all steps).

7.3.3.2. Total power distribution

The total power distributions of each S/A are shown in Fig. 120–124. The C/E values of the total power in reference state and step 2 are shown in Fig. 125.
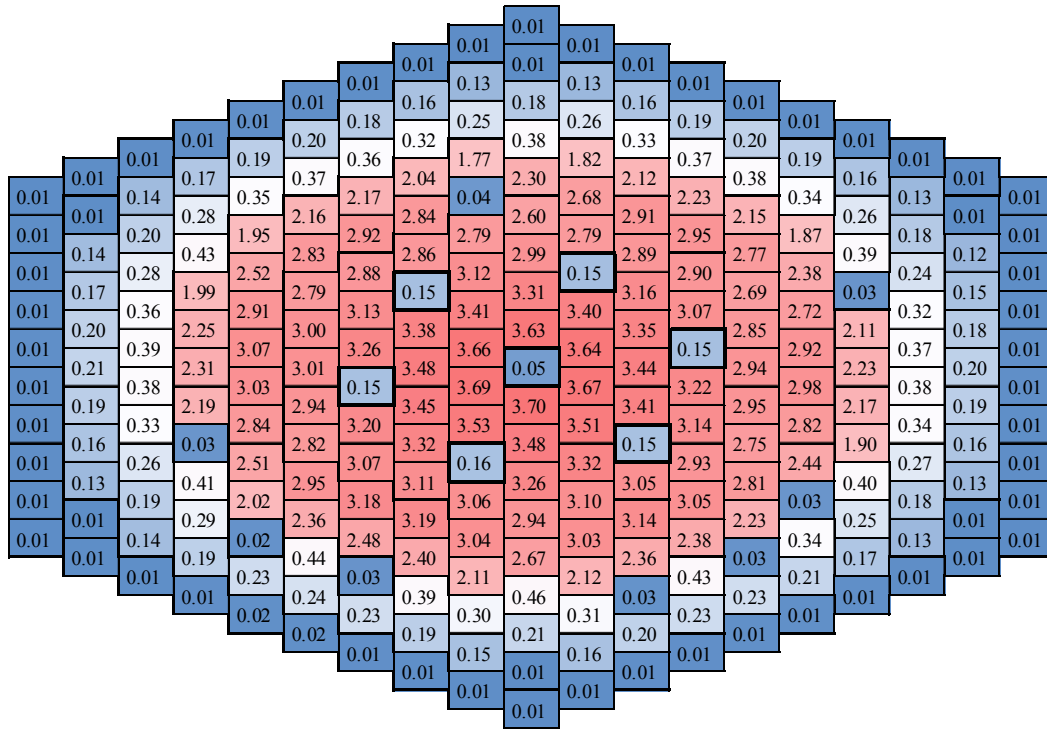
FIG. 120. Total power distribution (reference state, (MW(th))).
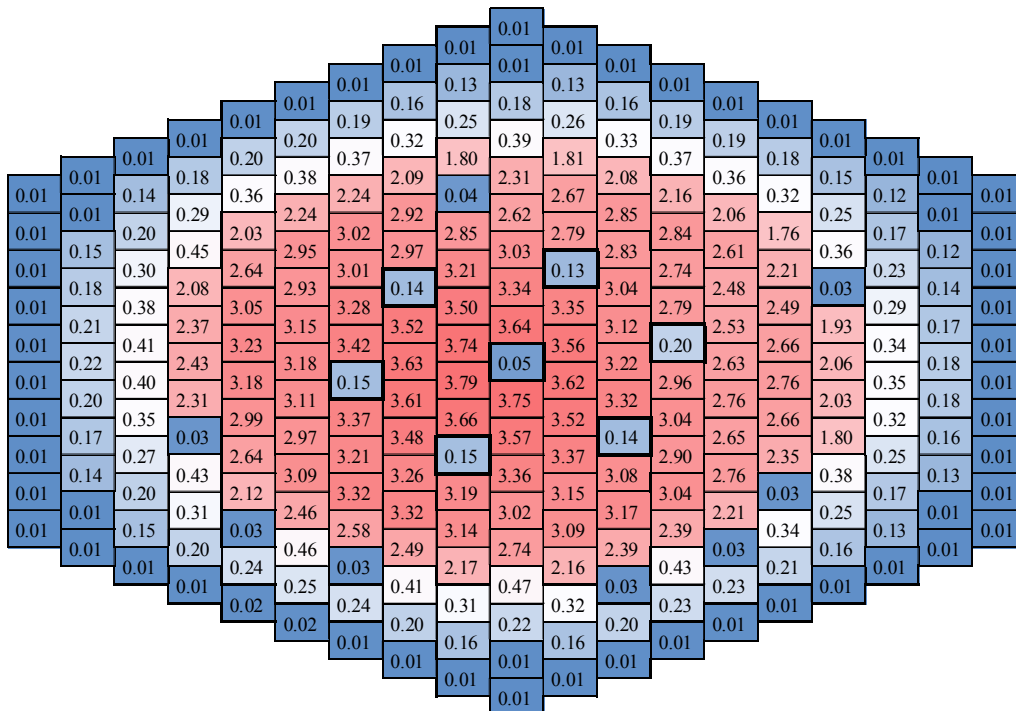
FIG. 121. Total power distribution (step 1, (MW(th))).
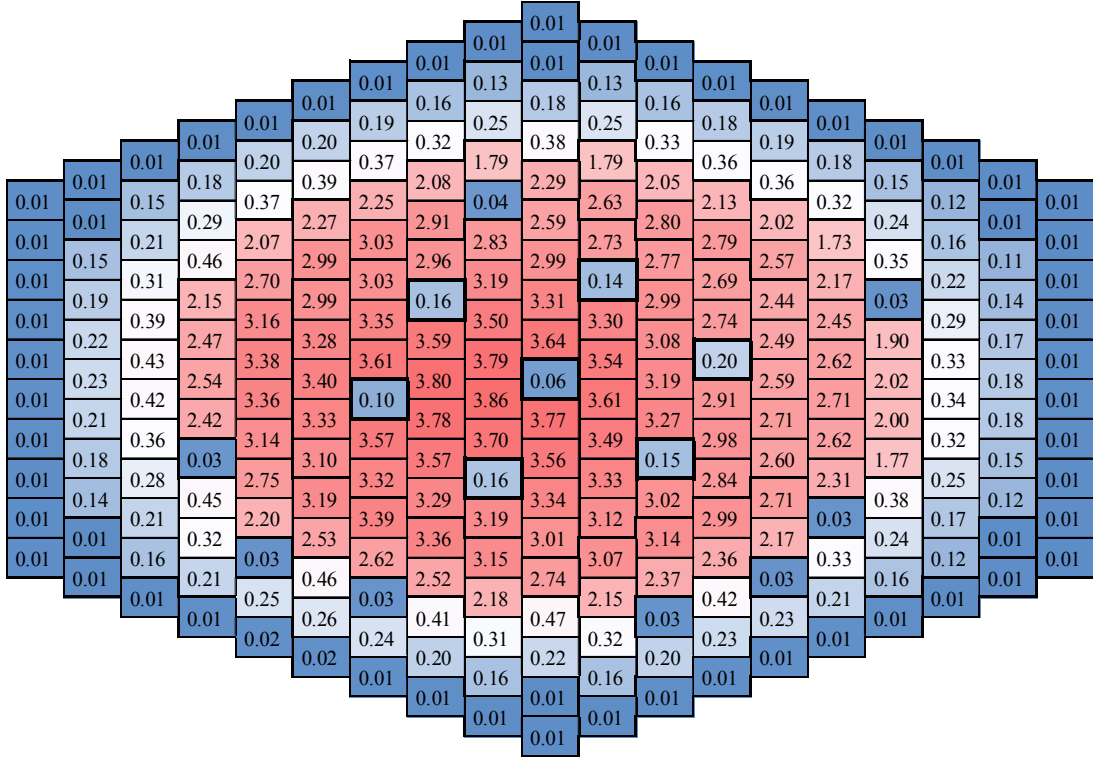
FIG. 122. Total power distribution (step 2, (MW(th))).
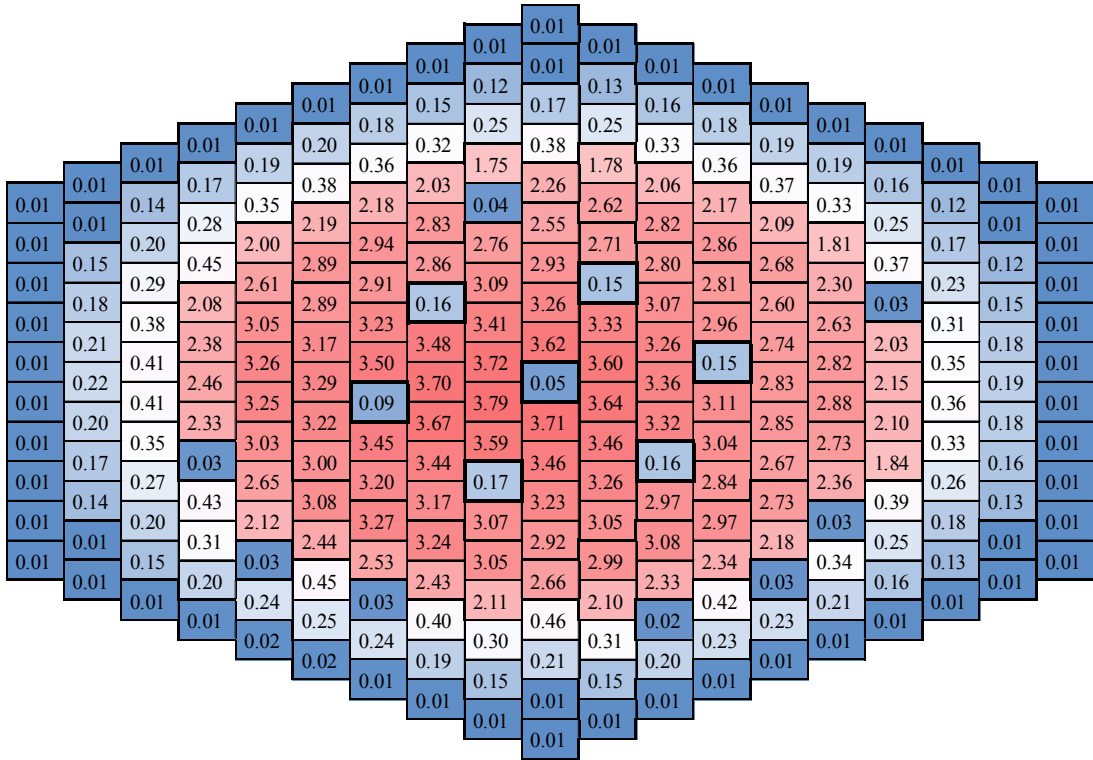
FIG. 123. Total power distribution (step 3, (MW(th))).
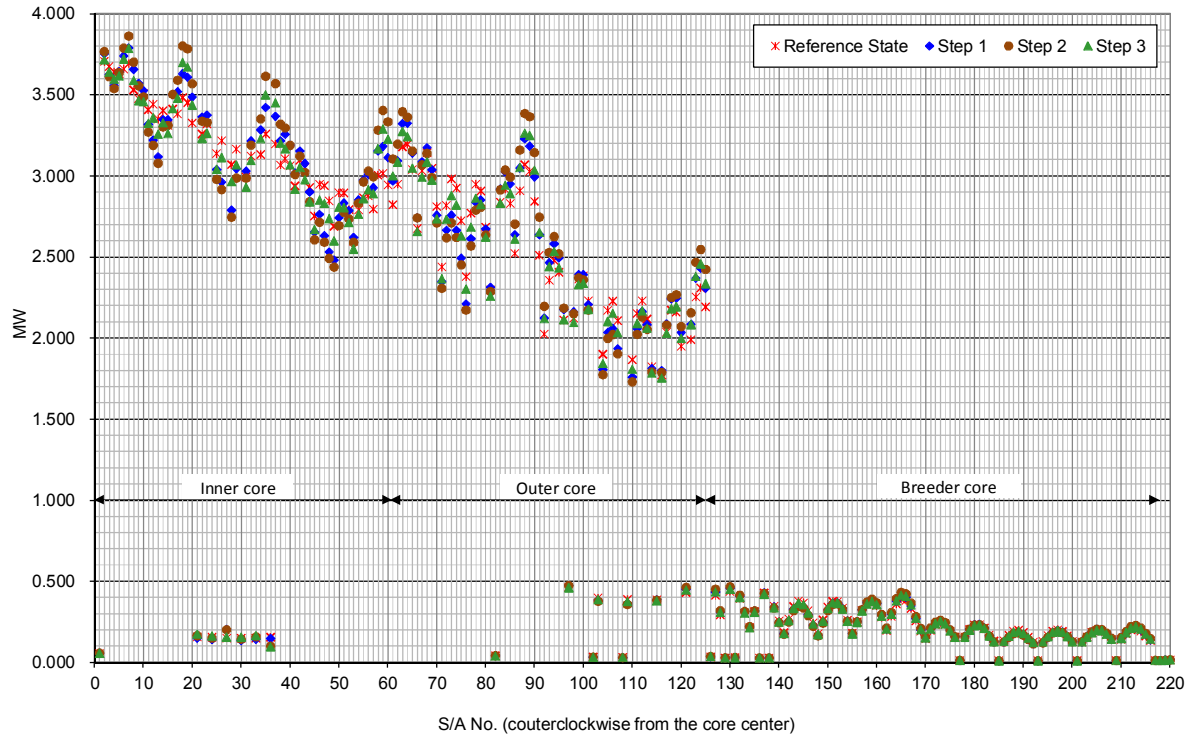
FIG. 124. Total power distributions (all steps).
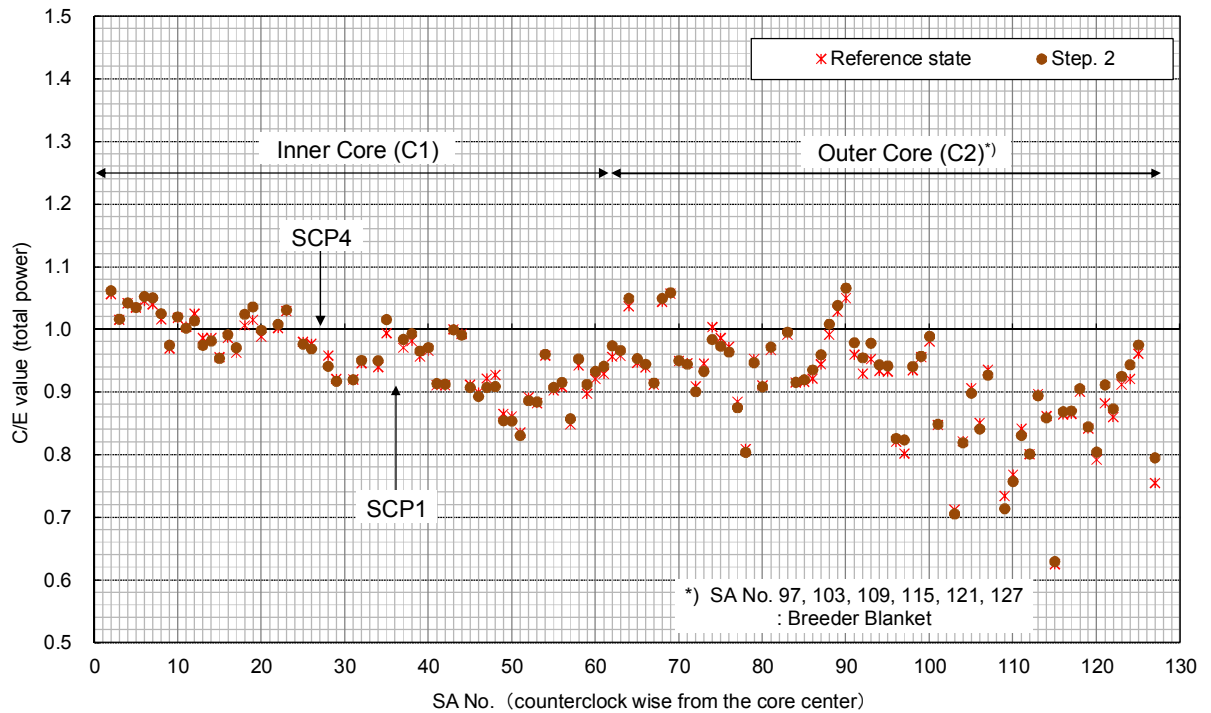
FIG. 125. C/E values for total power distributions (Inner and outer core, reference state and step 2).

7.3.4. Power deviation distributions

The deviations (%) of the S/A total power from reference state are shown in Fig. 126–128. Fig. 129 summarizes the C-E value of the deviations in step 1-3 for inner and outer core.
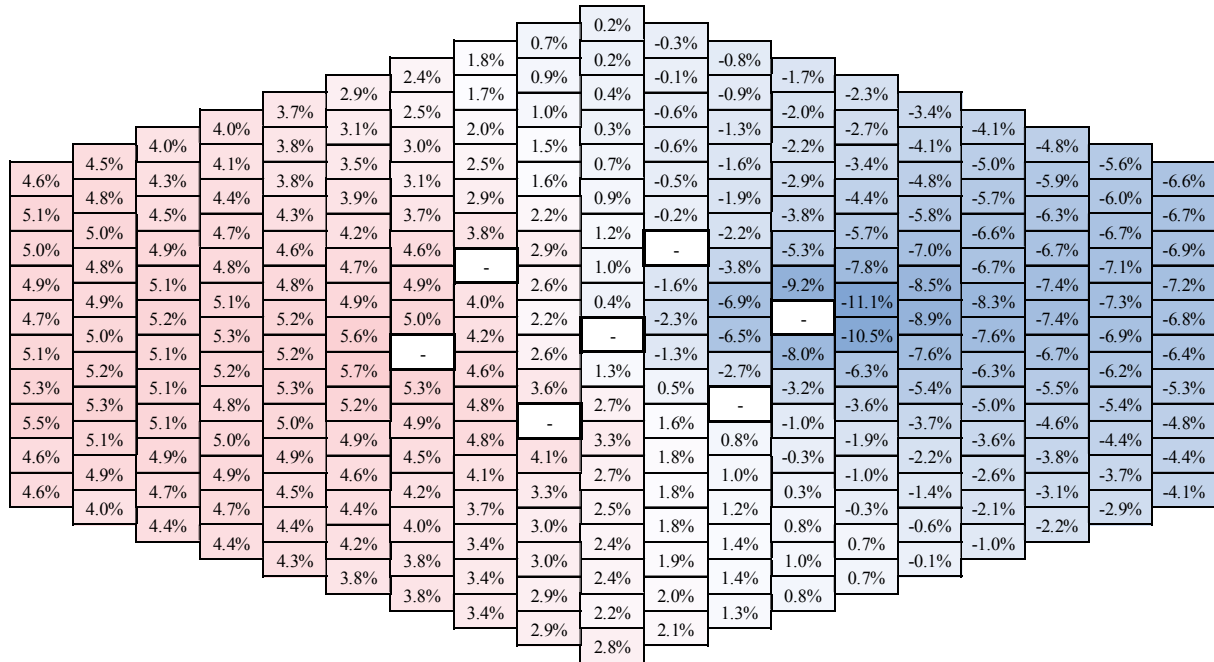
FIG. 126. Deviation of the total power from reference state (step 1, (%)).

FIG. 127. Deviation of the total power from reference state (step 2, (%)).

FIG. 128. Deviation of the total power from reference state (step 3, (%)).
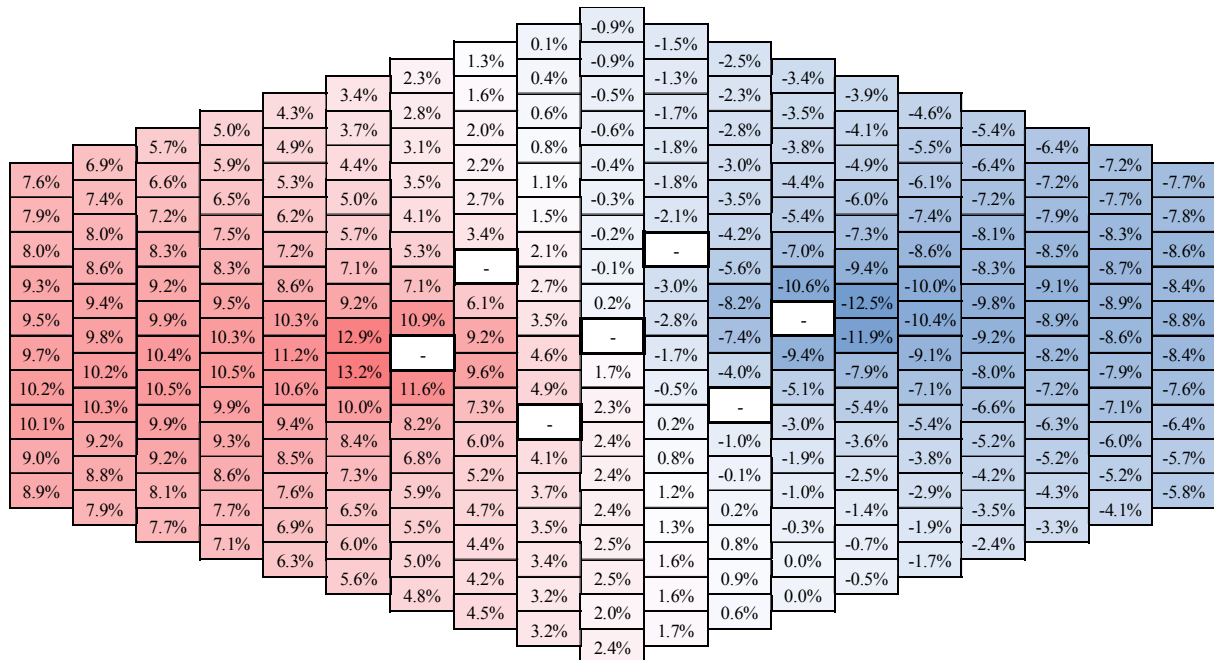
FIG. 129. C-E value for deviation of the total power from reference state (%) (all steps).
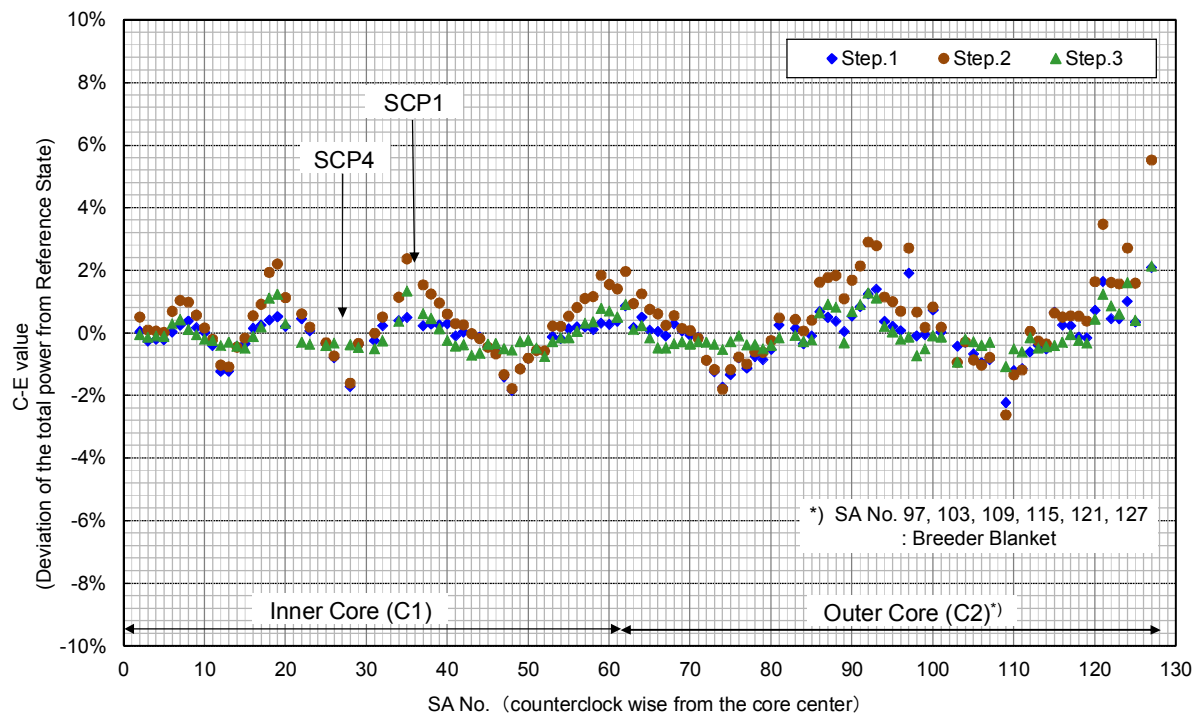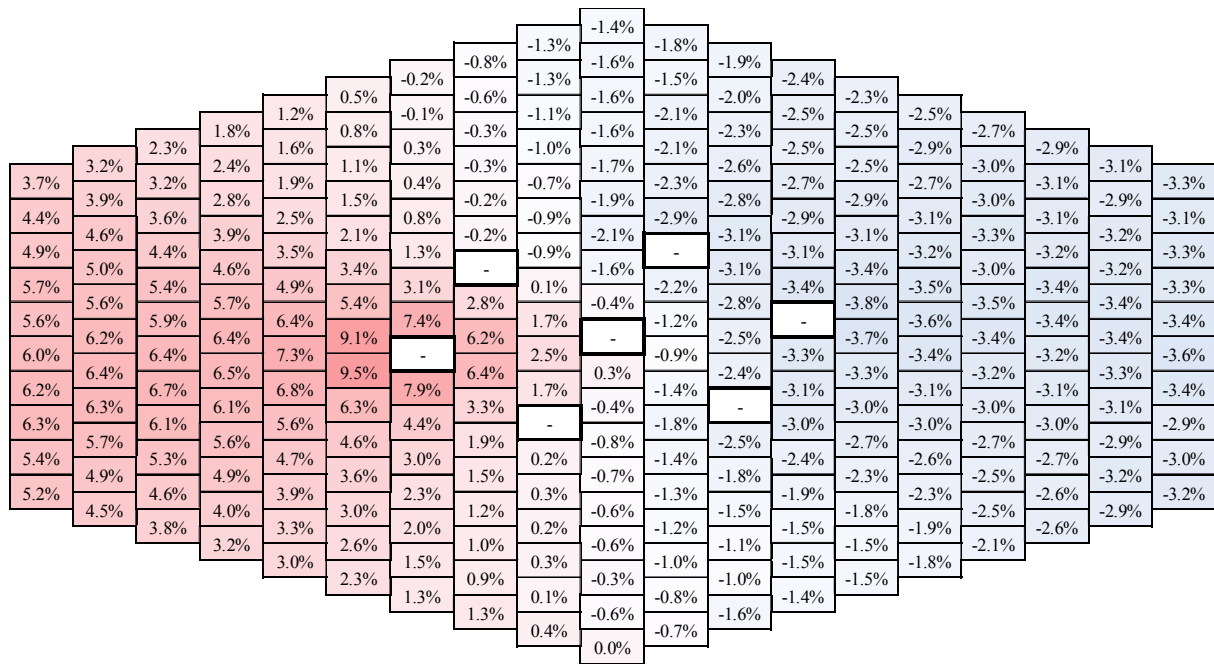
7.4. IRSN

7.4.1. Core reactivity margin

The reactivity margin of the core corresponds to the core reactivity when all the control rods are on 'rod bank', that is to say completely extracted (at a level of 900 mm).

The reactivity is given in pcm and it is evaluated using the following formula :

$$\rho = \frac{k_{eff} - 1}{k_{eff}} * 10^5 \qquad (18)$$

The reactivity margin has been calculated for two different reactor states: the nominal power state (100% NP - 350 MW(th)) and the off-power state (0% NP with a uniform core temperature of 250 °C). The aim was to evaluate the temperature effects[9].

Obtained results are given in Table 44. They have been obtained using the *Heterogeneous_EQ* cell model described in Section 5.5.

TABLE 44. CORE REACTIVITY MARGIN (IRSN RESULTS)

	Off-Power	Nominal Power	Temperature effects
Reactivity (pcm)	3790	3162	-628

7.4.2. Control rods worth

As already defined, the control rods worth is the difference between the core reactivity when all CRs are completely withdrawn (900 mm) and the core reactivity when CRs are completely inserted (0 mm).

The control rods insertion has been simulated by steps of 100 mm. This allows obtaining 11 coordinates reactivity/CRs_position which have been used to draw the S-curve. It represents the control rods efficiency between their two extreme positions (900 mm and 0 mm).

As for the reactivity margin, the S-curve has been calculated for both the nominal power state and the off-power state. Results obtained with the *Heterogeneous_EQ* cell model are shown in Table 45 and Fig. 130. They are considered as the reference results.

---

[9] Temperature effects= ReactivityMargin (Nominal Power state) - ReactivityMargin (Off-Power state)

TABLE 45. CONTROL RODS S-CURVE (IRSN RESULTS)

Control rods positions at 20°C (mm)	Normalized Reactivity[10] (pcm)		Deviation[11] (%)
	Off-Power state	Nominal Power state	
900	7644	7565	-1.03%
800	7364	7290	-1.00%
700	6833	6766	-0.98%
600	6000	5940	-1.00%
500	4892	4841	-1.04%
400	3593	3552	-1.14%
300	2261	2232	-1.28%
200	1114	1098	-1.44%
100	341	335	-1.75%
0	0	0	/
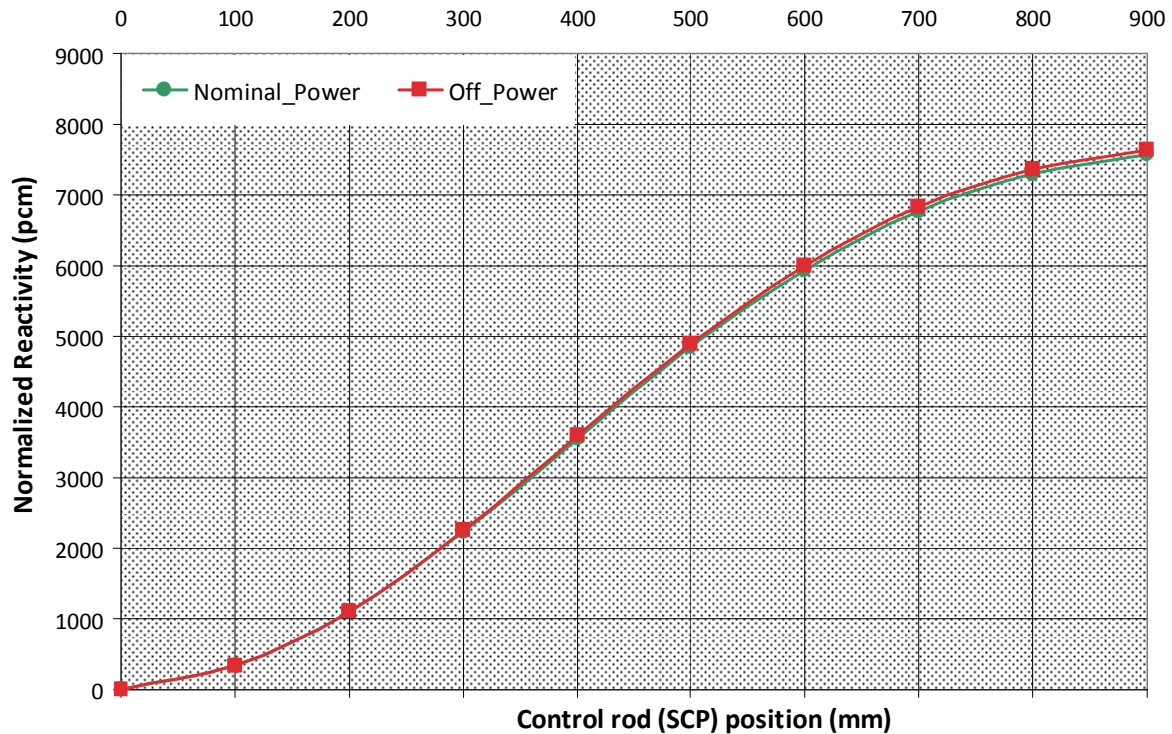
FIG. 130. Control rods S-curve (IRSN results).

The control rods worth for the nominal power state is of 7565 pcm. Temperature effects (difference between 100% NP and 0% NP) on it are negligible (~1%).

---

[10] *Normalized Reactivity = ρ(x00 mm) - ρ(0 mm)*, with x from 0 to 9

[11] $Deviation = (\dfrac{\rho(NomPower) - \rho(OffPower)}{\rho(OffPower)}) * 100$

It is worth noting that the used cell model (cf. Section 5.5) has a strong influence on control rods worth. Results obtained with the 3 tested models for the nominal power state are compared in Fig. 131.
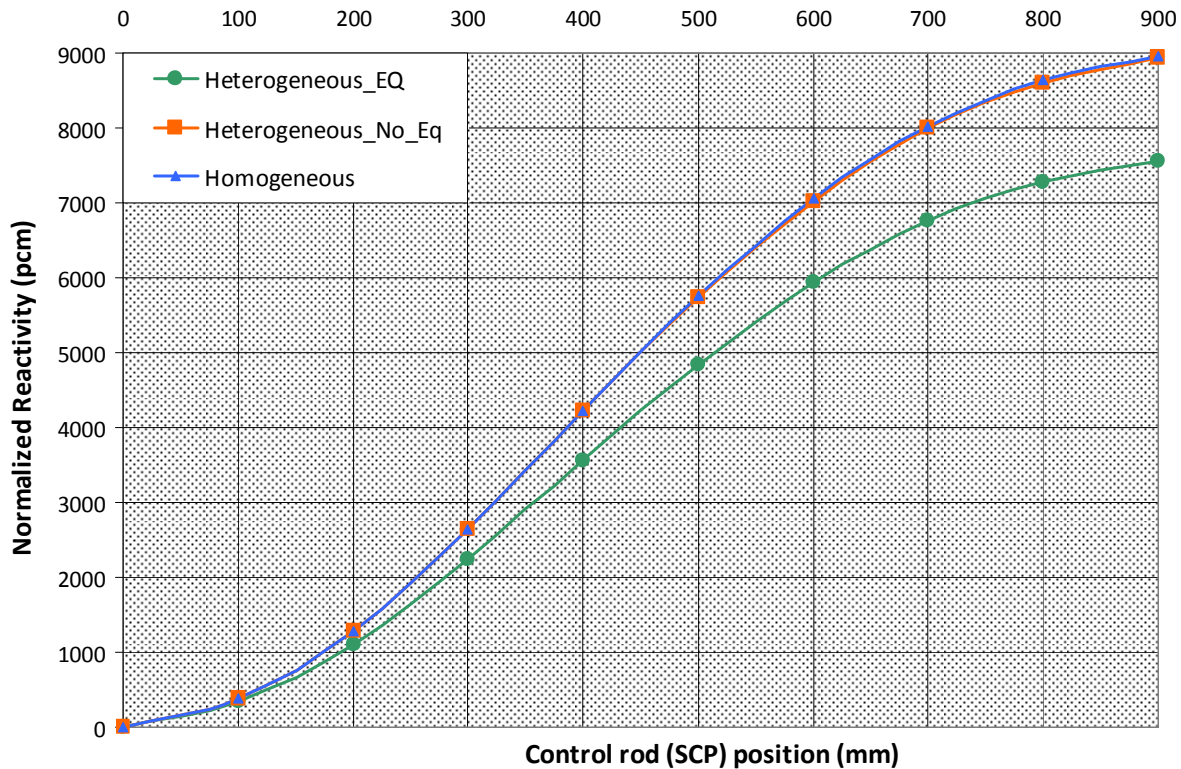
FIG. 131. Control rods worth using the 3 tested cell models.

Results are almost identical for the *Homogeneous* and the *Heterogeneous_No_Eq* models, while the *Heterogeneous_EQ* model (considered as the reference model) gives quite different values for the S-curve. The difference on the total curtain worth is of about 1500 pcm.

These results stress the need of a special control rods treatment when using a deterministic code.

7.4.3. Core reactivity during the different test states

The k_{eff} has been calculated for the 4 steps of the test using the 3 tested cell models (cf. Section 5.5). Results are shown in Fig. 132.

	Reference State	Step1	Step2	Step3
■ Homogeneous	73	93	98	91
■ Heterogeneous_No_Eq	718	737	744	738
■ Heterogeneous_EQ	1002	1016	1019	1018
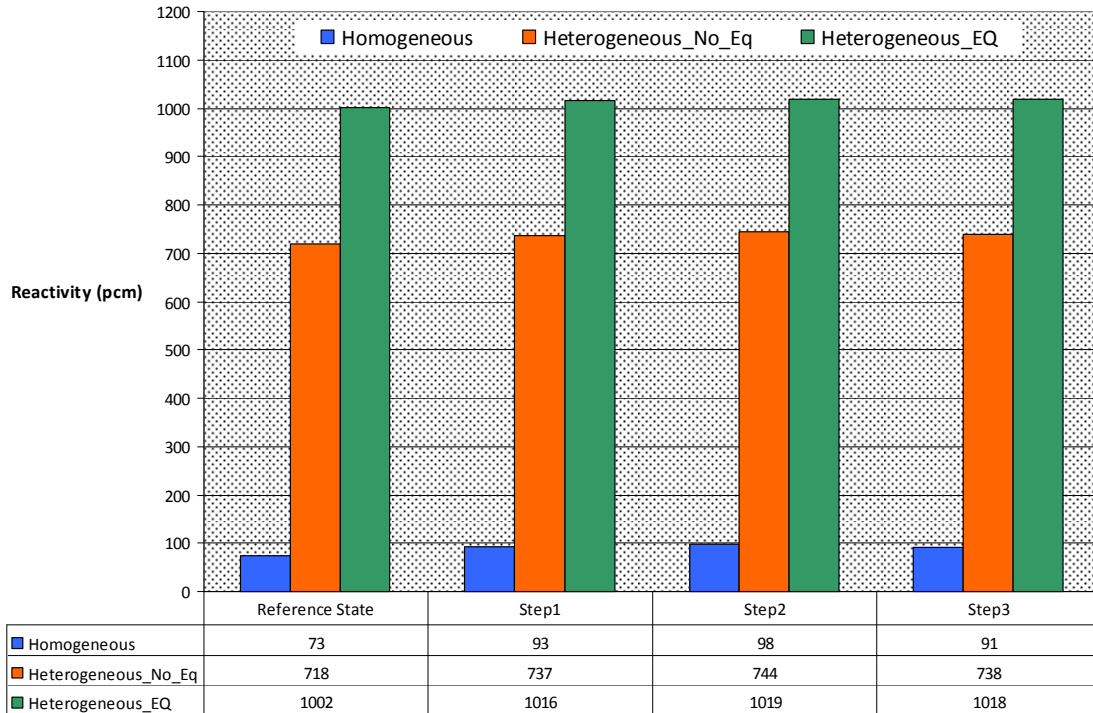
FIG. 132. Results of criticality calculations for the core using the 3 tested cell models.

The reactivity value should be 0 pcm since the reactor was in a critical state for all the different steps of the test. However, the used benchmark model presents different approximations: among them, one of the most important is the simplified burnup core map proposed (the real burn–up of the different subassemblies is not taken into account). Consequently, the calculated reactivity value can be different.

Two important considerations can be done:

1. Results obtained for the 4 states with the same models are consistent, i.e. the reactivity value is almost constant as expected;
2. The adopted cell model has a strong influence on reactivity values.

7.4.4. Flux and power distributions

7.4.4.1. Calculated values

The neutronic power distribution per subassembly and the value of the axial maximum flux per subassembly have been calculated for the 4 steps of the experiment. The results obtained with the *Heterogeneous_EQ* model are shown in Fig. 133–134.
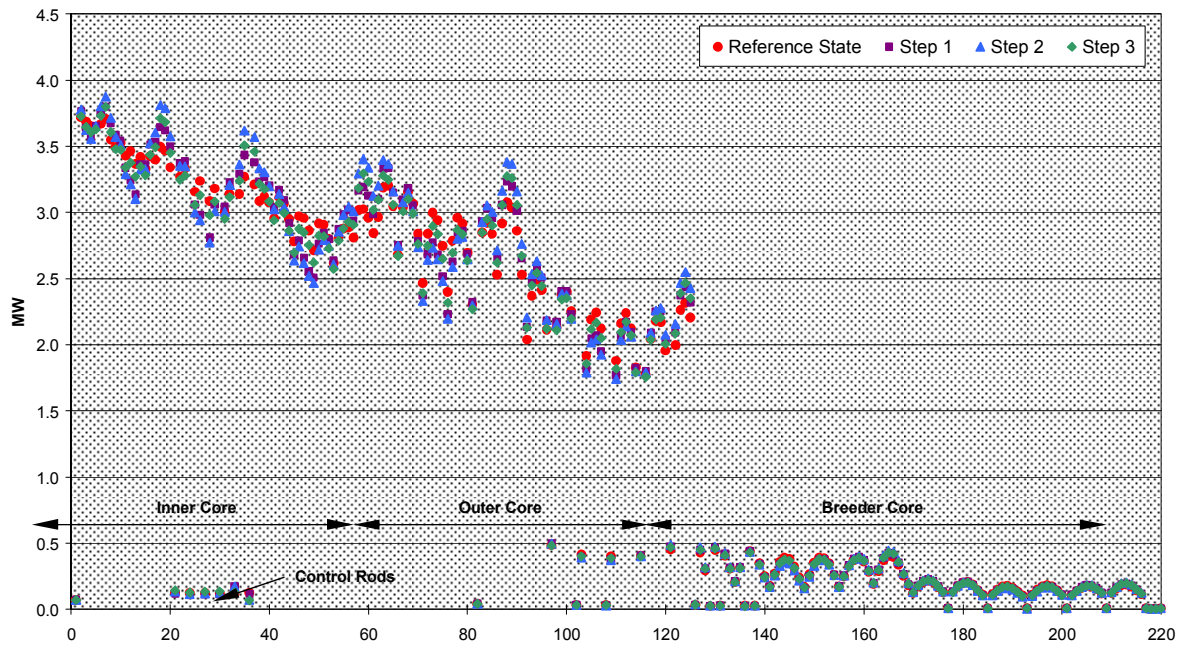
FIG. 133. Calculated power distribution by subassembly (IRSN results).
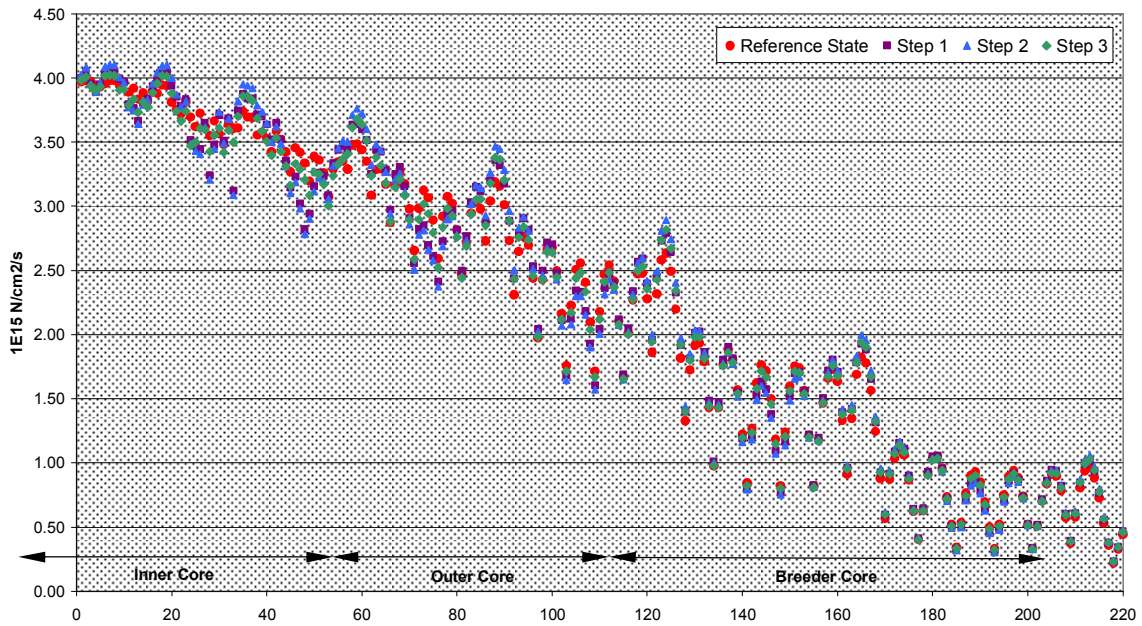
FIG. 134. Calculated axial maximum flux per subassembly (IRSN results).

The maximum power value per subassembly is 3.873 MW(th). The maximum flux value is $4.1E+15$ n·cm^{-2}·s^{-1}. Both values are reached in the second step of the test.

The same values are shown in Fig. 135–138, which give a better idea of the power and flux spatial distributions on the whole core.
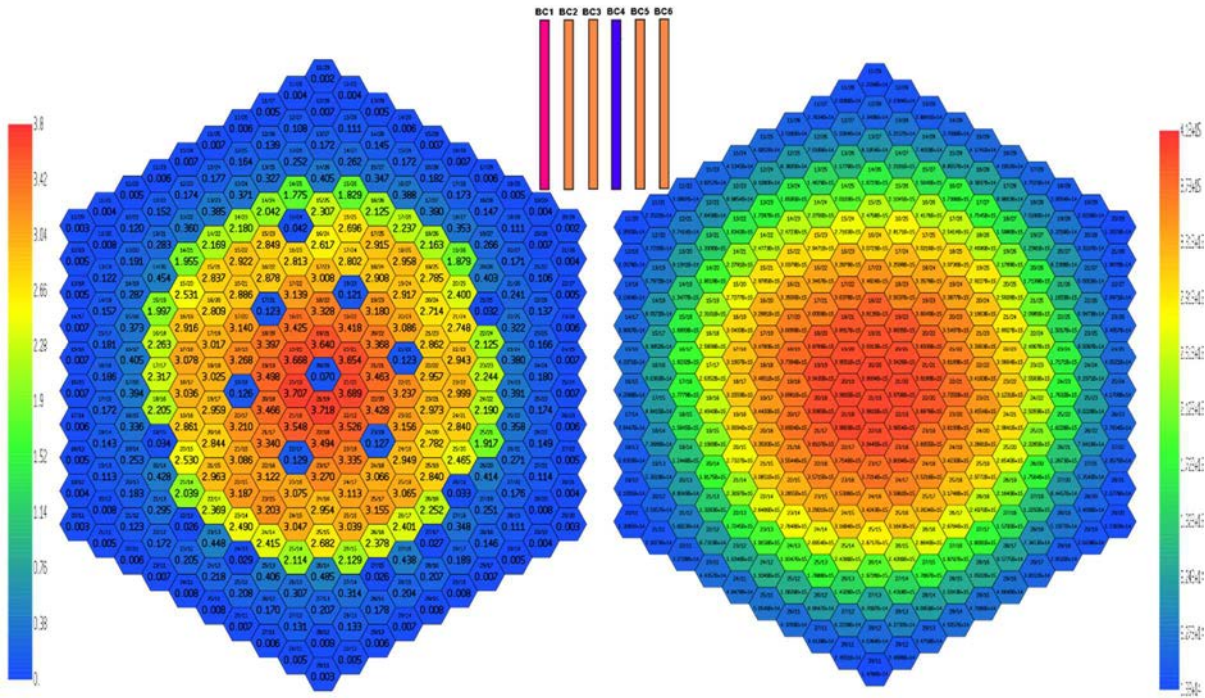
FIG. 135. Power and maximum flux distributions for the reference state (IRSN results).
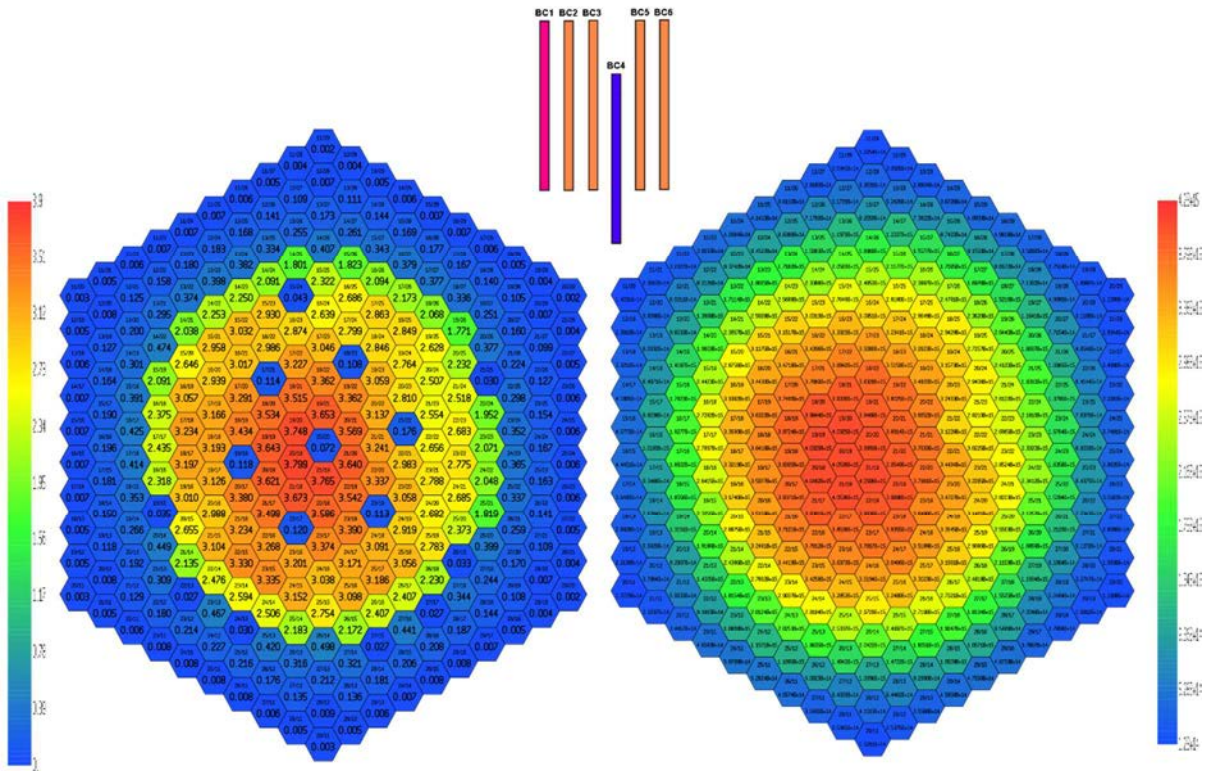
FIG. 136. Power and maximum flux distributions for step 1 (IRSN results).

138
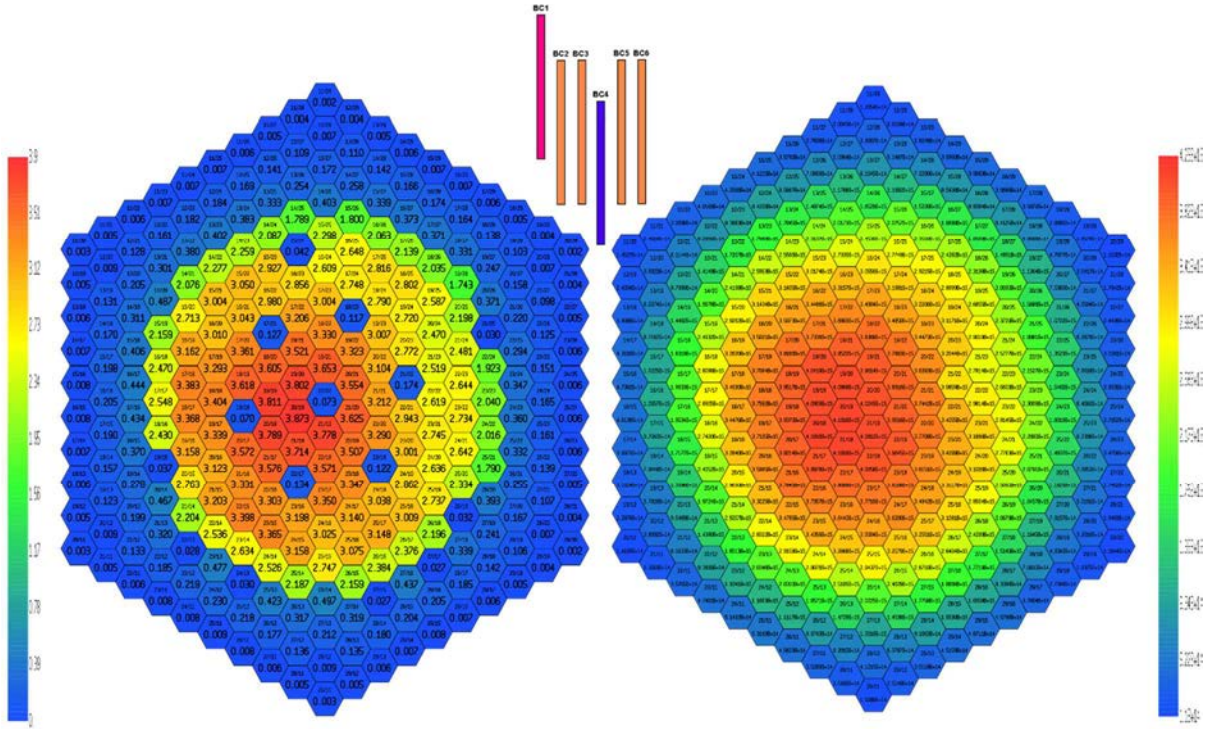
FIG. 137. Power and maximum flux distributions for step 2 (IRSN results).
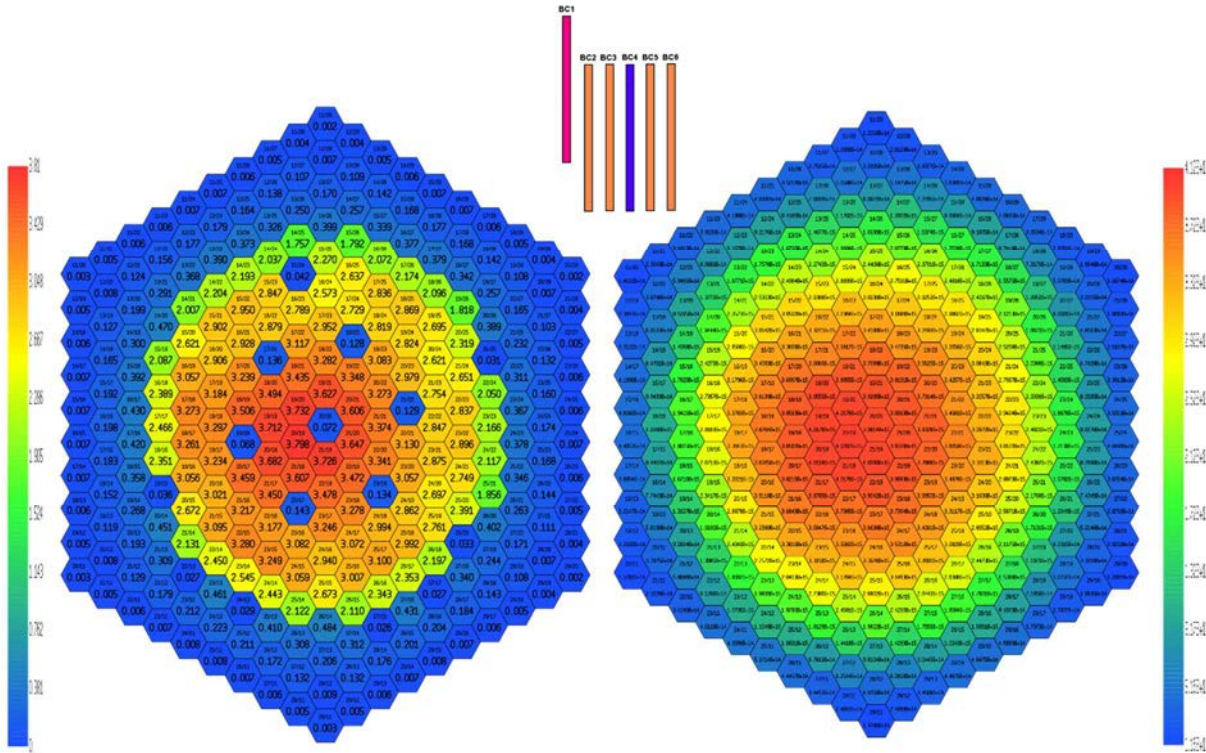
FIG. 138. Power and maximum flux distributions for step 3 (IRSN results).

7.4.4.2. *Comparison with measured values*

Fig. 139 shows the differences in % ((C-E)/E*100) between the calculated power distribution and the experimental one for the reference state. The cell model used for the calculation is the Heterogeneous_EQ.
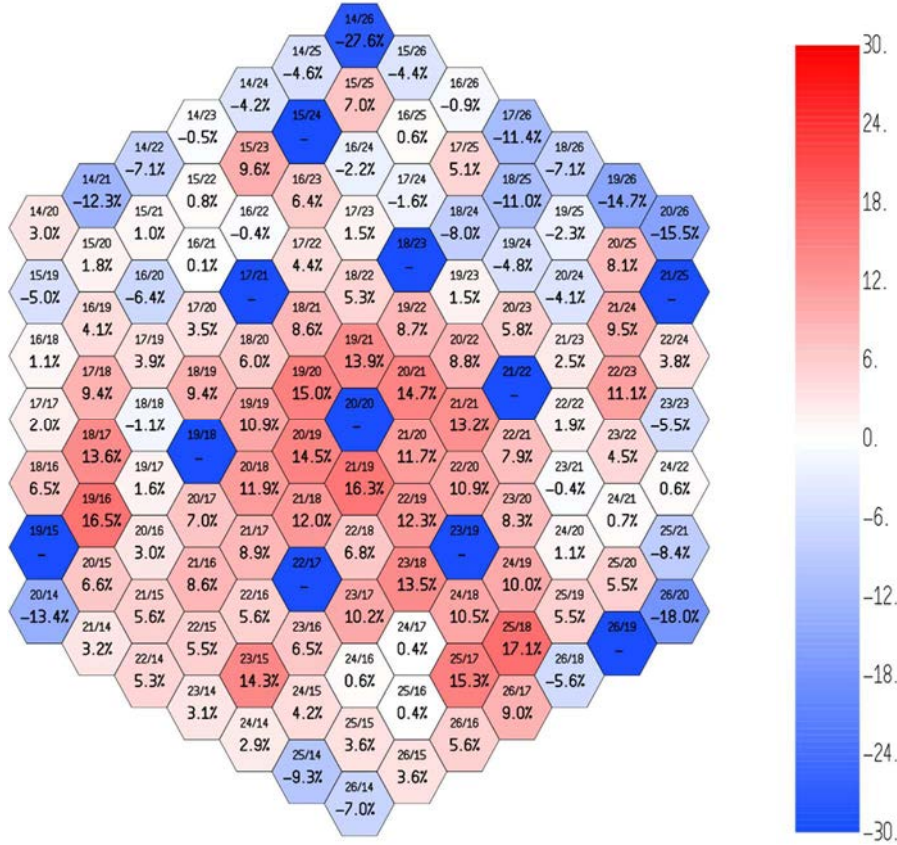
FIG. 139. Difference on integral power (%) between calculated and measured values, reference state – Heterogeneous_EQ.

The average discrepancy is around 7% with peaks of ~ 28% (subassembly 14/26). The same order of discrepancies, as well as their distribution, between calculated and experimental values has been found for the other 3 steps of the test.

These differences can be linked to the code approximations and to benchmark data. The latter include input data (geometries, isotopic compositions and temperatures) and sodium temperature measurements. Concerning code approximations, ERANOS has been employed to its full potential for this specific case, i.e. using all the options which entail as less approximations as possible: the transport solver, the ERALIB1 nuclear data library and the heterogeneous 2D model with the equivalence procedure for control rods for which concerns the cross-sections calculation.

Regarding input data, a main approximation has been done when considering broad core concentrations meshes, i.e. neglecting the burnup of different subassemblies. The investigation of a hypothetic link between this approximation and the discrepancies distribution in the core has been carried out through the analysis of the sodium flow rates (Fig. 140).
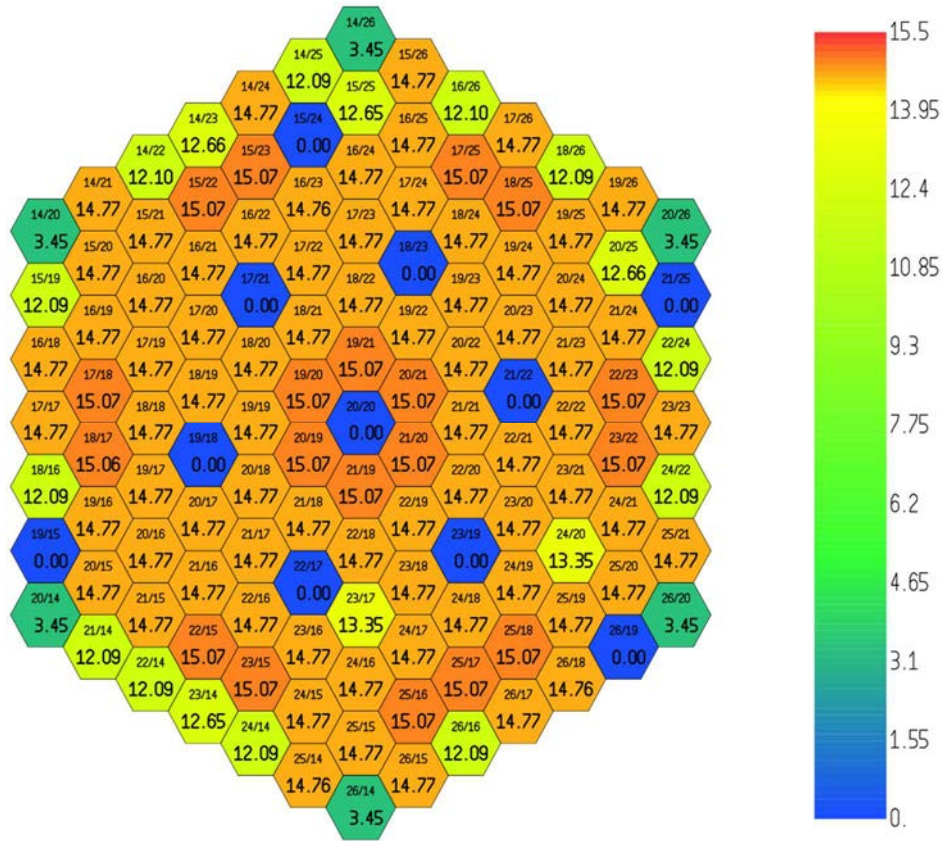
FIG. 140. Sodium flow rates (Kg/s) in the Phénix core.

A comparison of the values provided in Fig. 139 with the values given in Fig. 140 demonstrates that the discrepancies between calculated and measured thermal powers are, generally, more notable for the S/As with higher sodium flow rates.

The different flow rates could be linked to the different levels of burnup. In fact, the less the fuel is burned, the more is the thermal power produced and consequently the more is the flow rate needed for the heat removal. Finally, this analysis puts in evidence that the simplified burnup map could be one of the main reasons of important discrepancies in certain zones of the core. CEA, using a more precise burnup distribution, confirmed this assumption.

Concerning the cell model used, obtained results show that it has a negligible influence on the power distribution calculation.

7.4.5. Power deviation distributions

7.4.5.1. Calculated values

The power deviation per subassembly with respect to the reference state is shown in Fig. 141 for all the steps of the test. The cell model used for the calculation is the Heterogeneous_EQ.
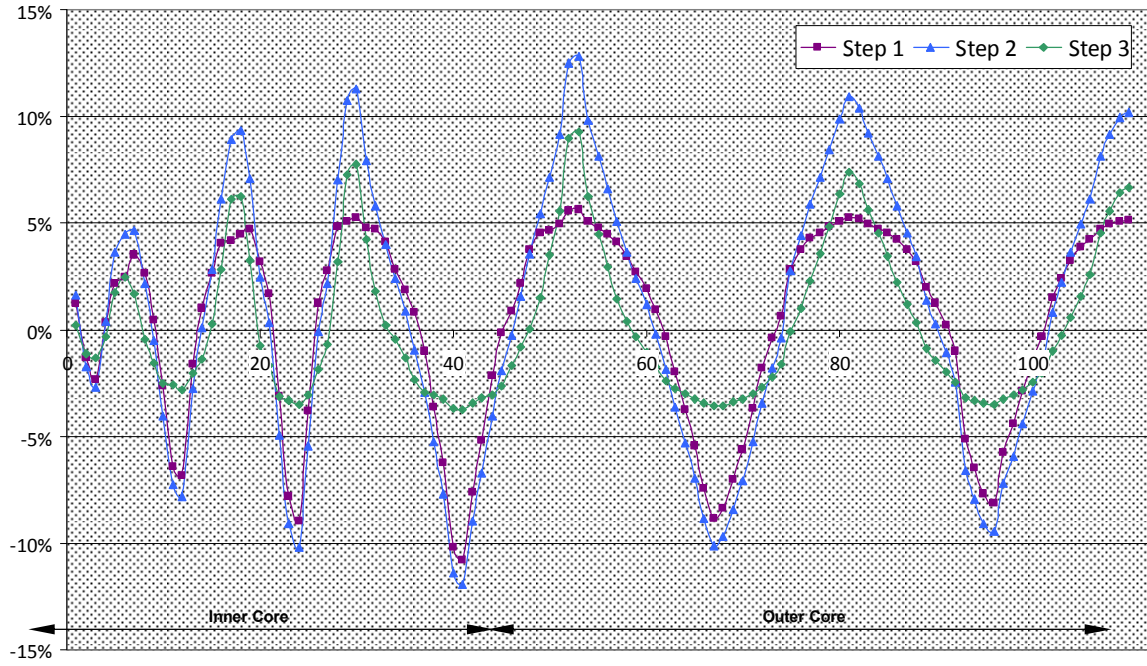
FIG. 141. Calculated power deviation (%) with respect to the reference state.

The maximum power deviation is of about 12% and it is obtained in the second step. The same values are shown in Fig. 142–144.
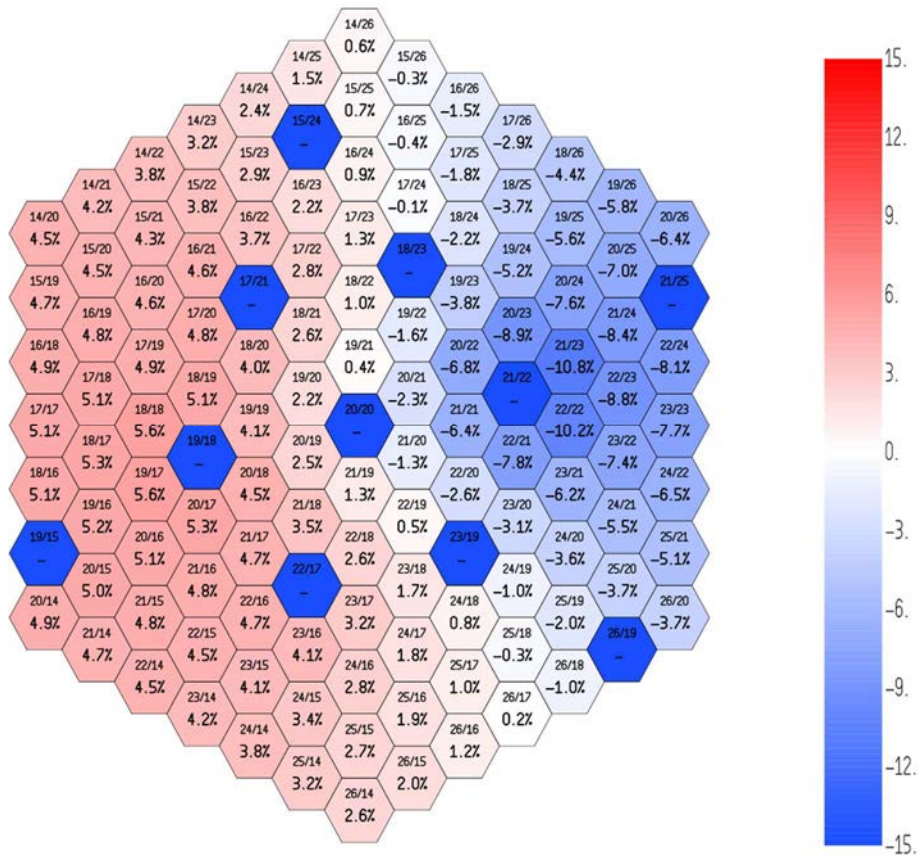
FIG. 142. Calculated power deviation with respect to the reference state – step 1.
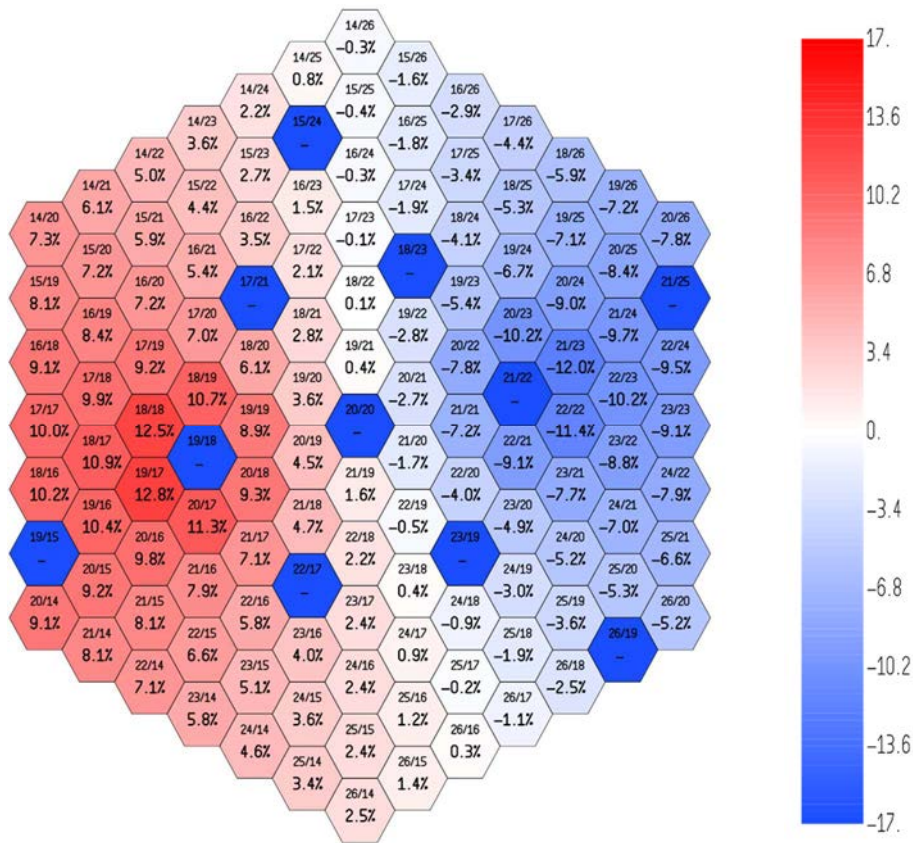
FIG. 143. Calculated power deviation with respect to the reference state – step 2.
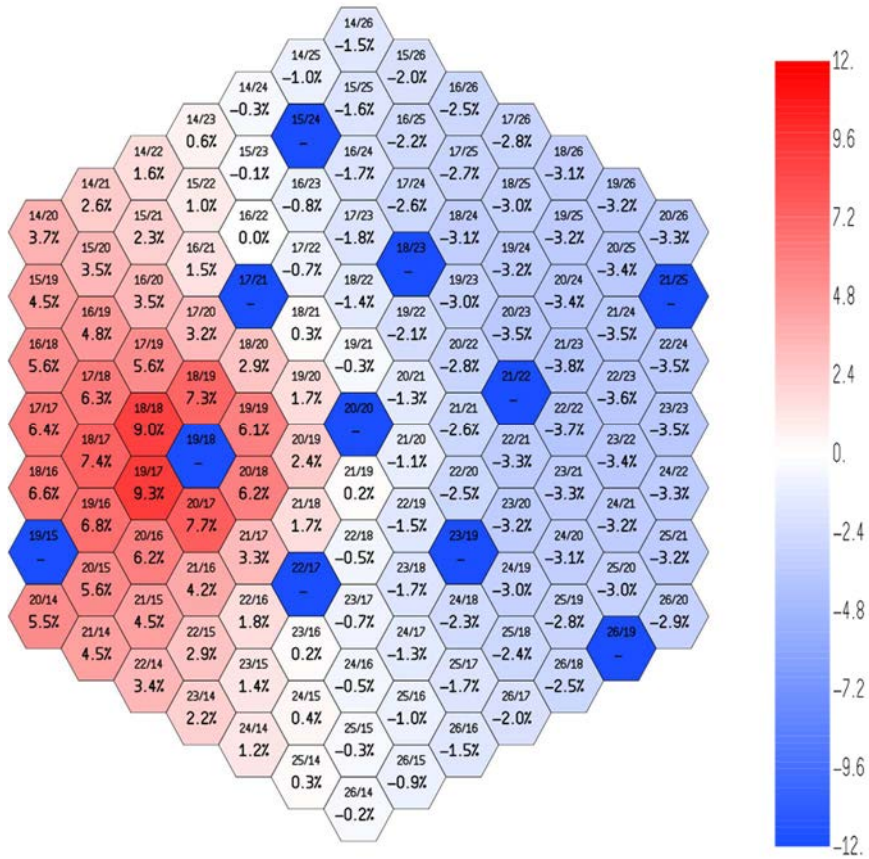
FIG. 144. Calculated power deviation with respect to the reference state – step 3.

7.4.5.2. Comparison with measured values

The comparison between calculated and measured power deviations is shown in Fig. 145 for the second step of the test (the second step is the one with maximum deviations).
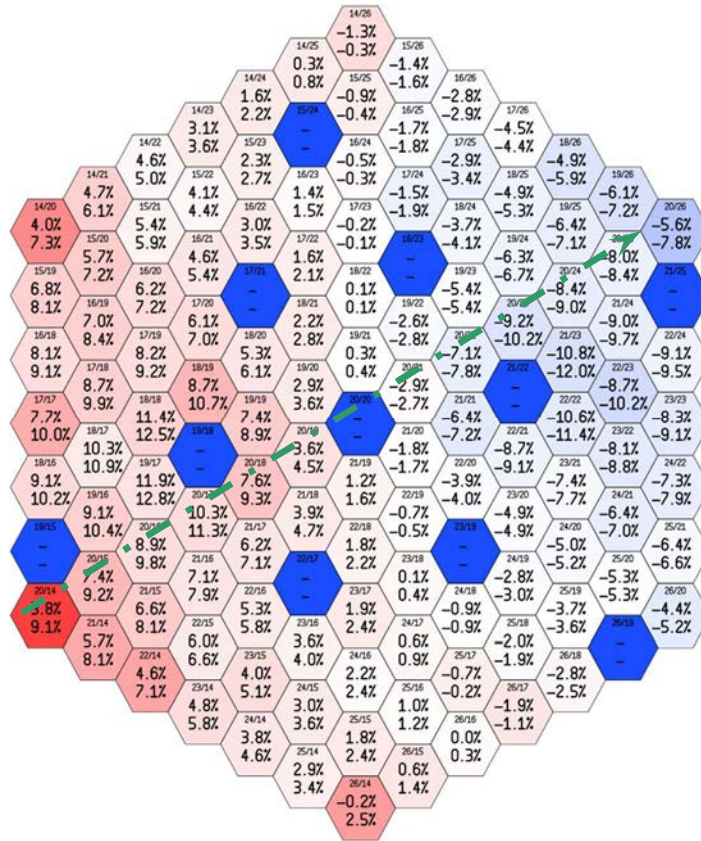
FIG. 145. Measured and calculated power deformations (step 2 - reference state) – Heterogeneous_EQ.

The above value in each hexagon is the measured power deformation between the second step and the reference state. In the figure, which shows the calculated power deformation, the colour scale is proportional to the difference between the two values.

Fig. 145 shows that the code slightly overestimates the effect of control rods withdrawal both when the rod is extracted (increasing of power, red in the picture) and when the rod is inserted (decreasing of power, blue in the picture). The burnup effect seems to have a weak effect on the evaluation of power deformations (hypothesis confirmed by CEA).

The effect of the different cell models is represented in Fig. 146 where measured and calculated power deformations are shown for the 13 subassemblies placed on the green dashed line in Fig. 145.
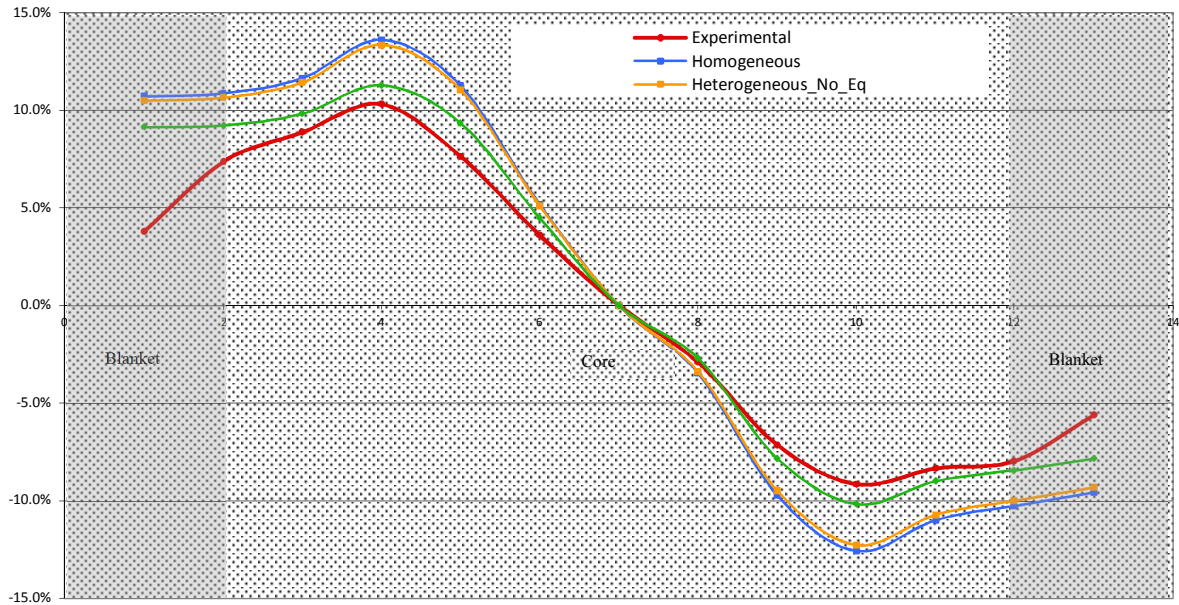
FIG. 146. Power deviation using the 3 tested cell models: step 2 – reference state.

In the core zone, discrepancies are always lower than 4% for the *Homogeneous* and the *Heterogeneous_No_Eq* cell models, while for the blanket zone they can reach 7%. When the *Heterogeneous_EQ* model is used, discrepancies are lower than 2% in the core zone and they can reach 5.3% in the blanket zone.

The influence of the cell model on power deformations is weak and the results obtained with the 3 tested models are globally satisfactory.

Concerning discrepancies in the core zone, they can be due to temperature effects (Doppler and expansion effects). CEA confirmed that the main problem is in the core/vessel/control rod expansion estimation.

For the discrepancies near the blanket zones, two explanations can be pointed out. First of all, there is a heat transfer between fertile and nearby fissile S/As which is not taken into account in the power computation. Moreover, the important difference of sodium flow rates between the two kinds of S/A can cause a mixing effect which alters the measurements.

CEA confirmed these hypotheses.

7.4.6. Conclusions

The adopted cell model has a strong effect on the core reactivity and on the control rods worth evaluation. On the contrary, it has a very weak impact on the power distribution and on the power deformation calculation.

Concerning the comparison with experimental data:

— Discrepancies between calculated and measured data on power distribution in a specific state are important: the average value is of about 7% with peaks of about 28%;
— Discrepancies between calculated and measured data on power distribution deformations between two states are small: less than 2% in the core zone, less than 6% in the blanket zone.

Discrepancies on power distribution are mainly due to the simplified burnup core map proposed. So, the calculation of power distributions (for steady states in this specific case) in the core needs more precise burnup data, consistent with the spatial discretization adopted for power calculations.

The small discrepancies on power deformations are mainly due to expansion effects in the core zone and to the lack of consistency between measurements and modelling in the blanket zone.

In conclusion, in the framework of the Control Rod Withdrawal end-of-life test, ERANOS gives satisfactory results concerning the impact of control rods insertion/extraction on the Phénix core power distribution.

7.5. JAEA

7.5.1. Core reactivity margin

The reactivity margin has been calculated for two different reactor states. Results are shown in Table 46. The diffusion theory effect is dominant in the corrections.

— The off-power state which corresponds to an isothermal state (250 °C);
— The nominal state which corresponds to a reactor power of 350 MW(th).

TABLE 46. CORE REACTIVITY MARGIN

		Off-power state [1]	Nominal State [2]	Temperature effects [3]
	Basic (keff)	1.02946	1.01967	-
Correction (keff)	Finite Spatial Mesh Size	-0.00138	-0.00159	-
	Diffutionss Theory	0.00723	0.00676	-
	Finite Energy Groups	0.00184	0.00170	-
	total	0.00768	0.00687	-
	Final (keff)	1.03714	1.02654	-
	Reactivity (pcm)	3581	2585	-996.1

[1] "Off-power state" corresponds to an isothermal state (250 °C).
[2] "Nominal state" corresponds to a reactor power of 350 MWth.
[3] Temperature effects= Reactivity Margin (Nominal Power state) - Reactivity Margin (Off-Power state).

7.5.2. Control rods worth

The results of the analysis on control rod worth are shown in Table 47 and Fig. 147. The finite mesh size effect and the diffusion theory effect are mostly cancelled out. Thus, the total of the bias is small. The total control rod worth is 7536 pcm.

TABLE 47. CONTROL RODS WORTH (BANK)

CR position (bank) (mm)	Basic (pcm)	Bias				Final (pcm)
		Finite Spatial Mesh Size	Diffusion Theory	Finite Energy Group	total	
0	0					0
100	309					309
200	1046					1046
300	2160					2160
400	3476					3476
500	4768	1.03983	0.96201	0.99971	1.00003	4768
600	5880					5880
700	6717					6717
800	7248					7249
900	7536					7536
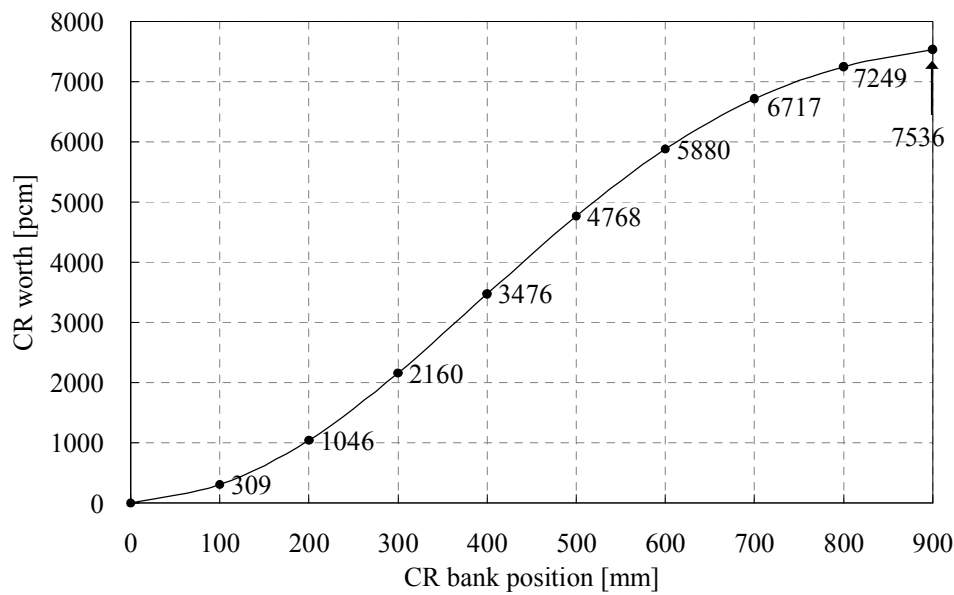
FIG. 147. Control rods S-curve (bank).

7.5.3. Core reactivity at critical states

The results of the analysis on K_{eff} are shown in Table 48. The results show a systematic overestimation of approx. 500 pcm (measurement: 0 pcm). Their dispersion is small, approx. ±10 pcm. The systematic overestimation could be attributed to the use of averaged number densities based on averaged burnup and averaged material's temperature for each region.

TABLE 48. CORE REACTIVITY

		Reference State	Step.1	Step.2	Step.3	Final State
	Basic (keff)	0.99829	0.99847	0.99838	0.99842	0.99846
Correction (keff)	Finite Spacial Mesh Size	-0.00208	-0.00221	-0.00219	-0.00214	-0.00209
	Diffusion Theory	0.00712	0.00717	0.00723	0.00716	0.00712
	Finite Energy Groups	0.00159	0.00159	0.00160	0.00160	0.00159
	total	0.00662	0.00656	0.00663	0.00662	0.00661
	Final (keff)	1.00491	1.00503	1.00501	1.00504	1.00507
	Reactivity (pcm)	488	500	499	501	504

7.5.4. Flux and power distribution

7.5.4.1. Flux distribution

The results of the analysis on flux distribution are shown in Fig. 148–152. The values in the figures denote the maximum flux in each sub-assembly. The maximum flux among the sub-assemblies appears near the core center in step 2 and the value is 4.15×10^{15} n/cm^2·s.
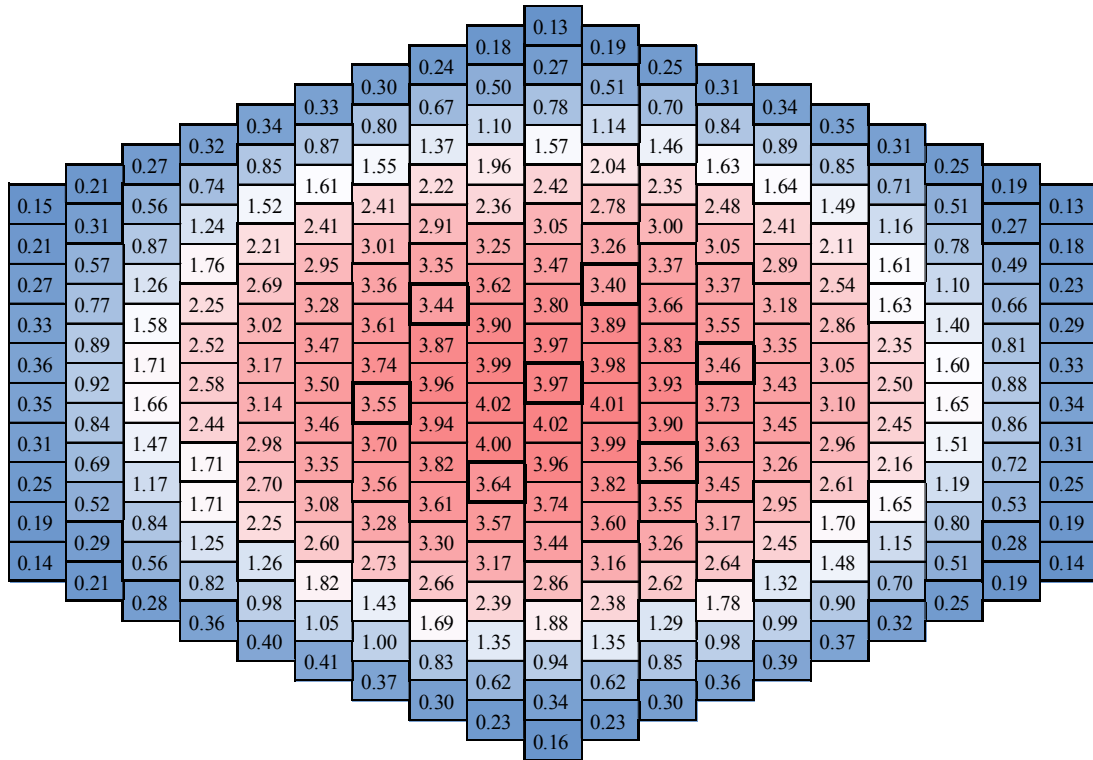
FIG. 148. Flux distribution (reference state, $\times 10^{15}$ (n/cm^2 ·s)).
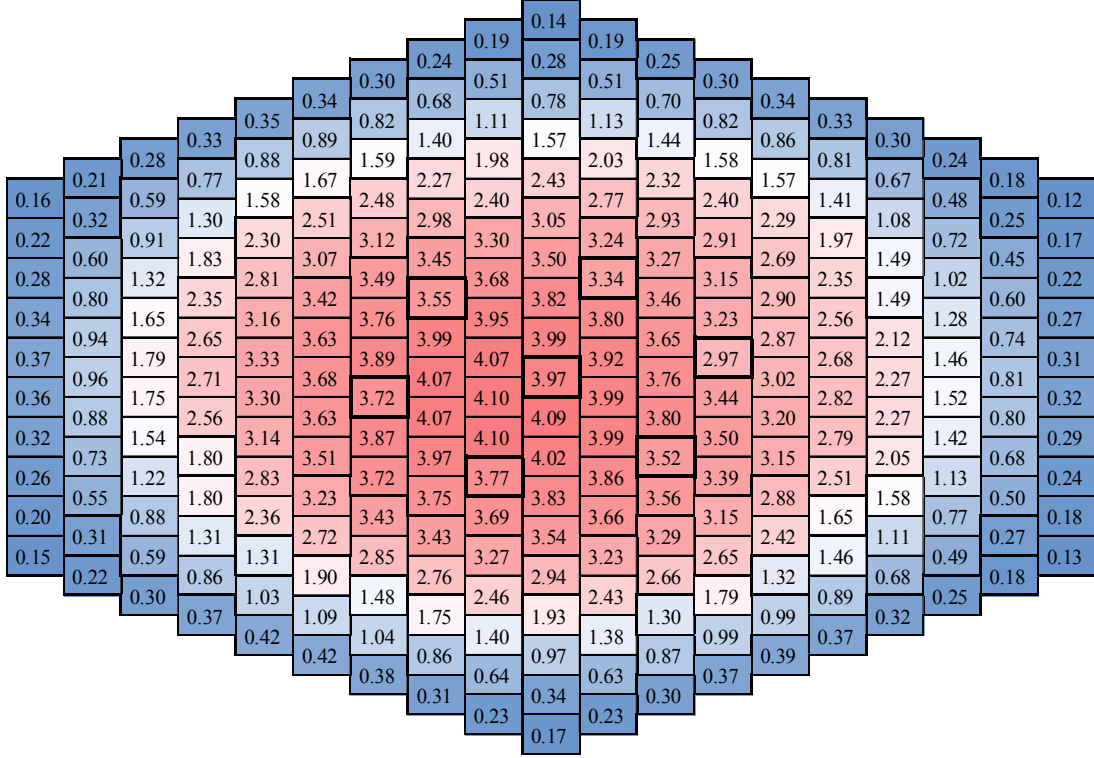
FIG. 149. Flux distribution (step 1, $\times 10^{15}$ n/cm$^2 \cdot$s)).
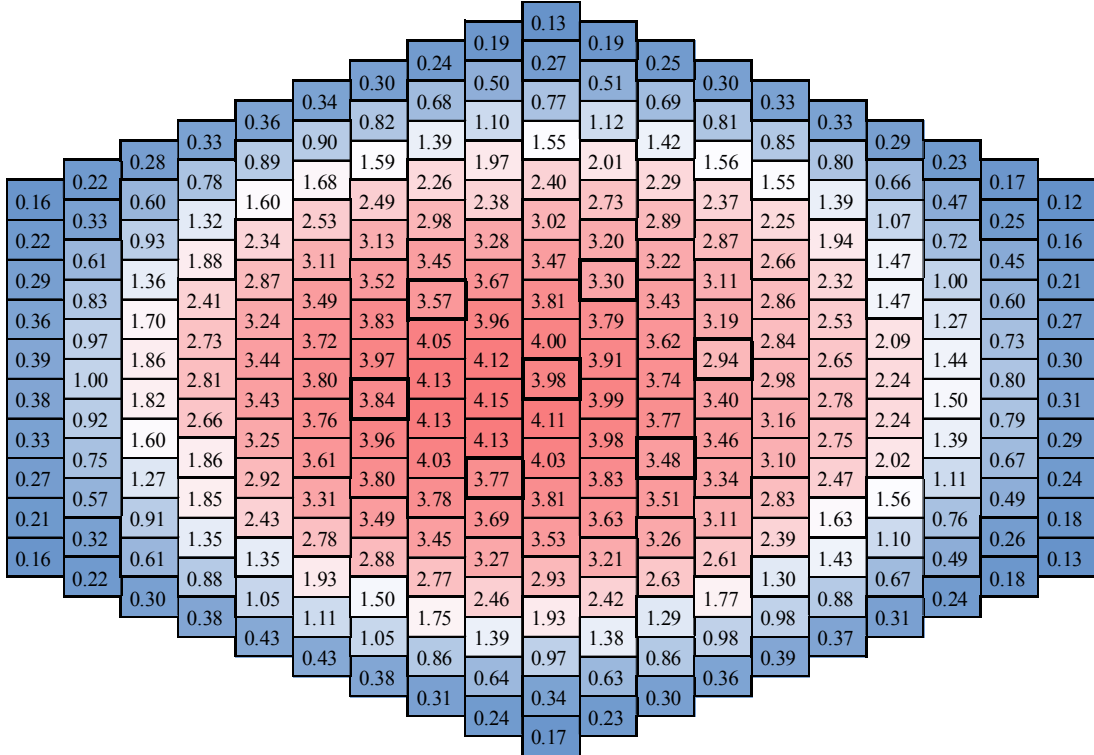
FIG. 150. Flux distribution (step 2, $\times 10^{15}$ (n/cm$^2 \cdot$s)).
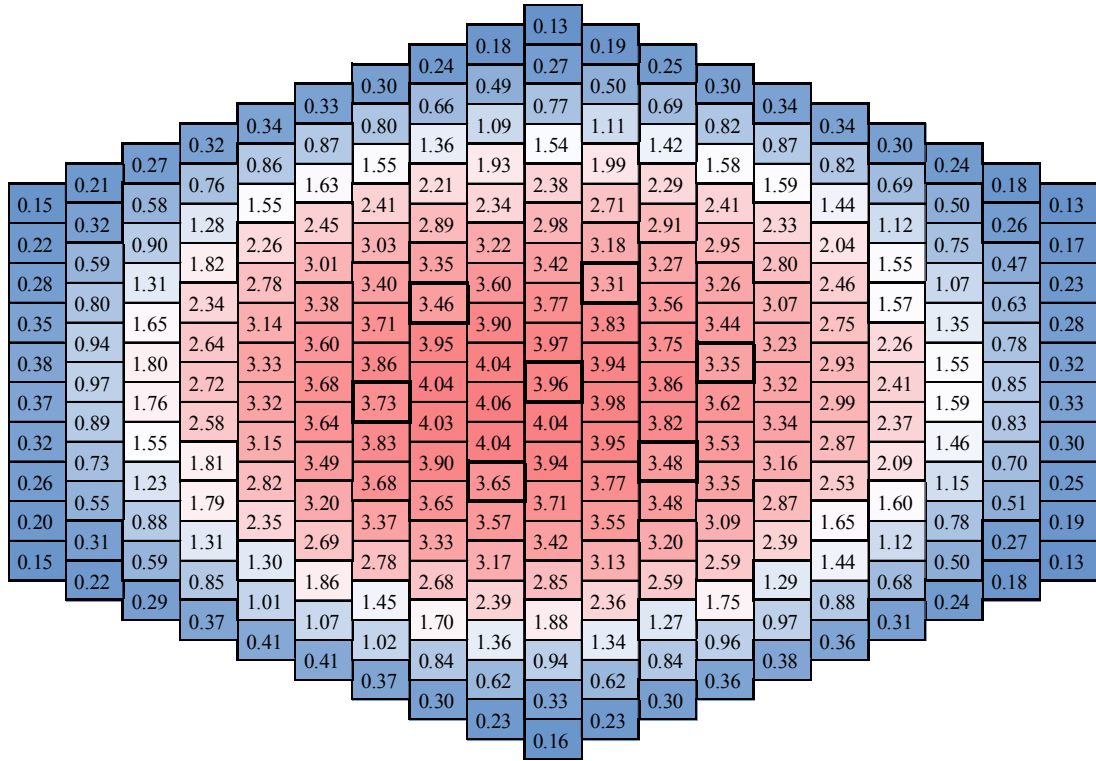
FIG. 151. Flux distribution (step 3, $\times 10^{15}$ (n/cm² ·s)).
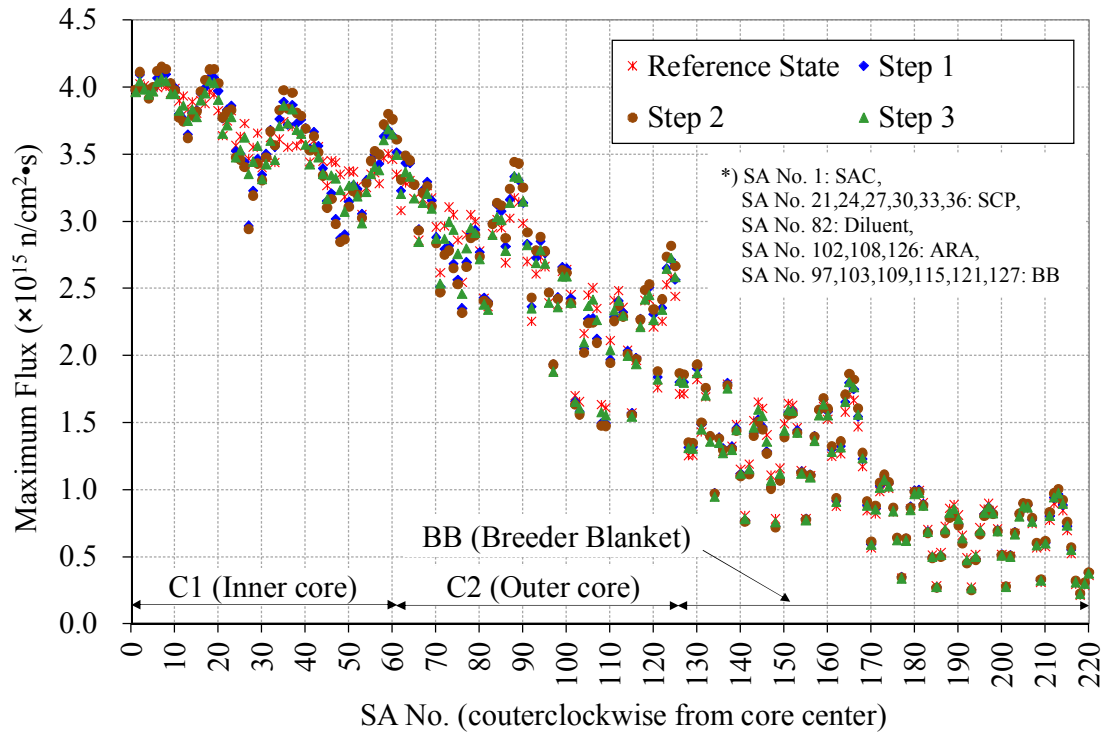
FIG. 152. Flux distributions (all steps).

7.5.4.2. Power distribution

The results of the analysis on S/A power distribution are shown in Fig. 153–157. The C/E values for reference state are shown in Fig. 158. The average C/E values for the reference state are 1.03±0.06, 0.98±0.07 and 0.87±0.11 for inner core (C1), outer core (C2) and breeder blanket (BB), respectively[12]. Good agreement is observed for inner and outer cores, whereas a systematic discrepancy between the calculation and the measurement is observed for breeder blanket. The discrepancy in the breeder blanket region could be attributed to the following factors:

— *Heat transferring through wrapper tube*

  Heat transferring between fertile and nearby fissile sub-assemblies through wrapper tube is not negligible considering their respective mean temperatures (respectively 470 °C and 420 °C). This effect is not considered in the presented analysis.

— *Sodium mixing at outlet flows*

  Sodium mixing between fissile and fertile outlet flows is not negligible considering their respective flow rates (respectively 15 kg/s and 3 kg/s). This effect is not considered in the presented analysis.

— *Averaged number density*

  Averaged number densities based on averaged burnup were used in the analysis. this can cause the dispersion in the C/E values. Detailed study for the above factors is necessary in the case of discussing the analytical accuracy for the absolute power distribution.
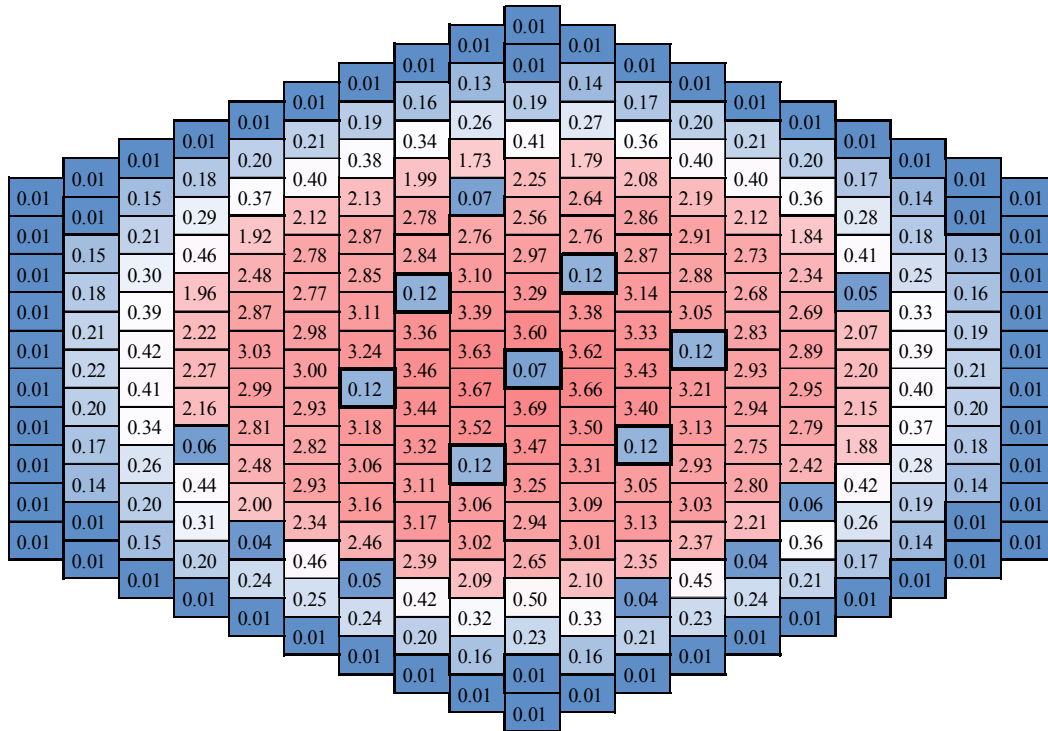
FIG. 153. S/A power distribution (reference state, (MW(th))).

---

[12] The averaged value and its standard deviation. Breeder blanket: 6 assemblies in 7th layer.
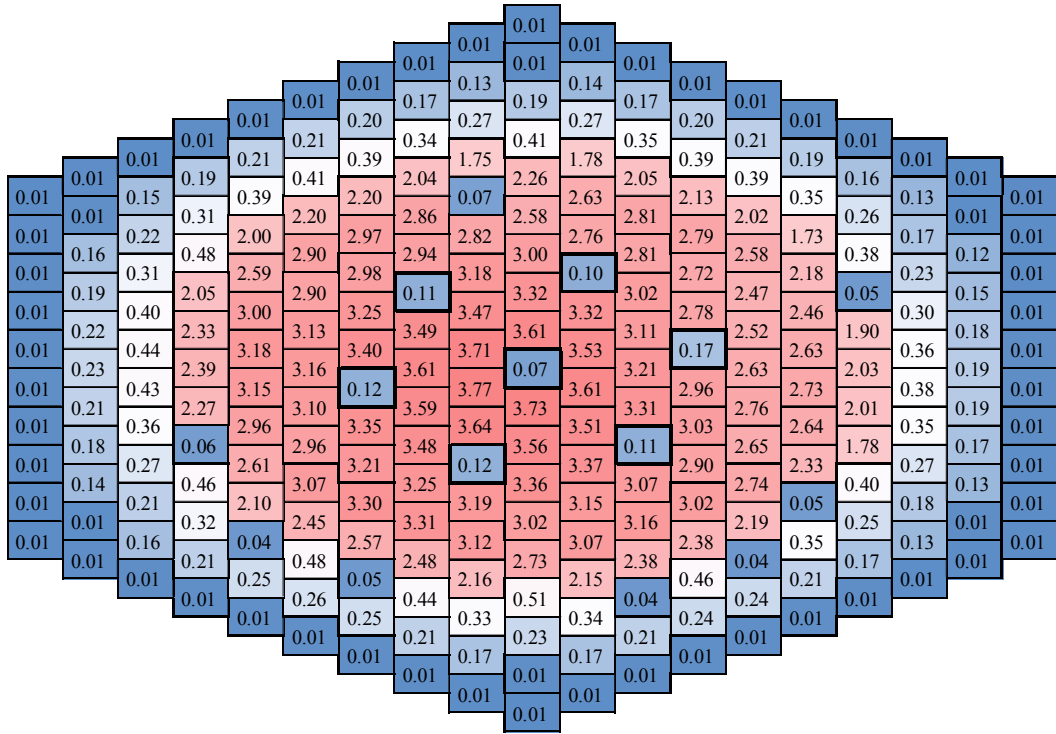
FIG. 154. S/A power distribution (step 1, (MW(th))).
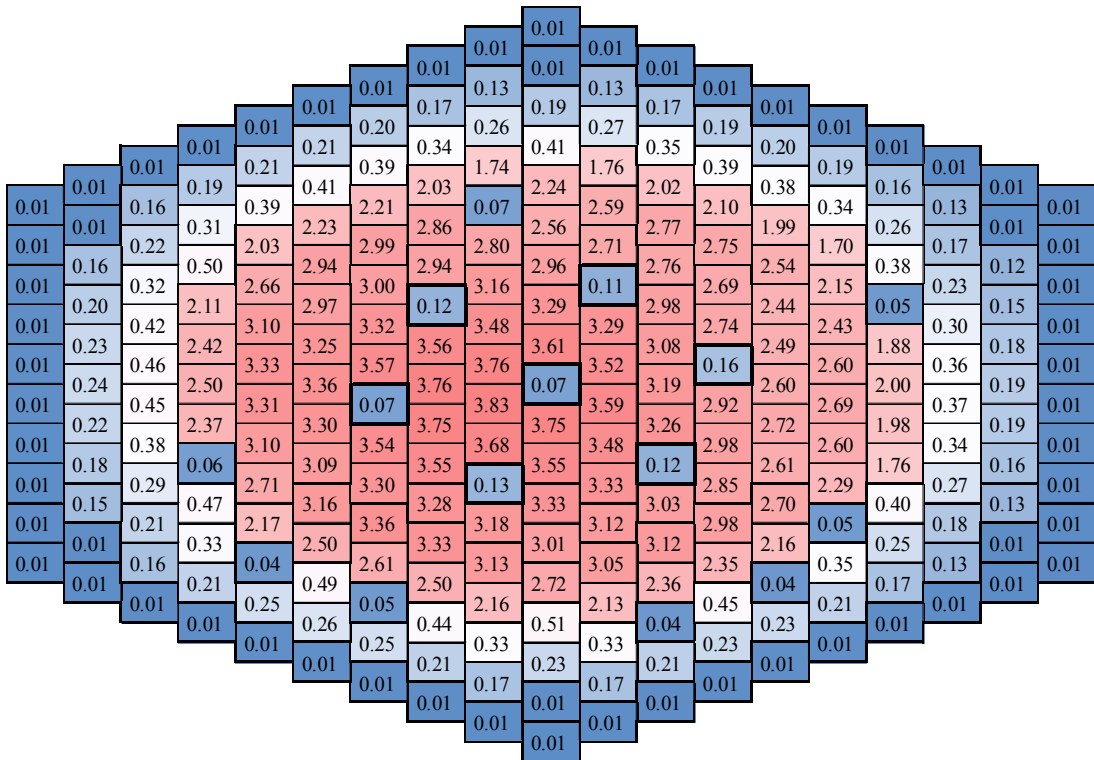
FIG. 155. S/A power distribution (step 2, (MW(th))).
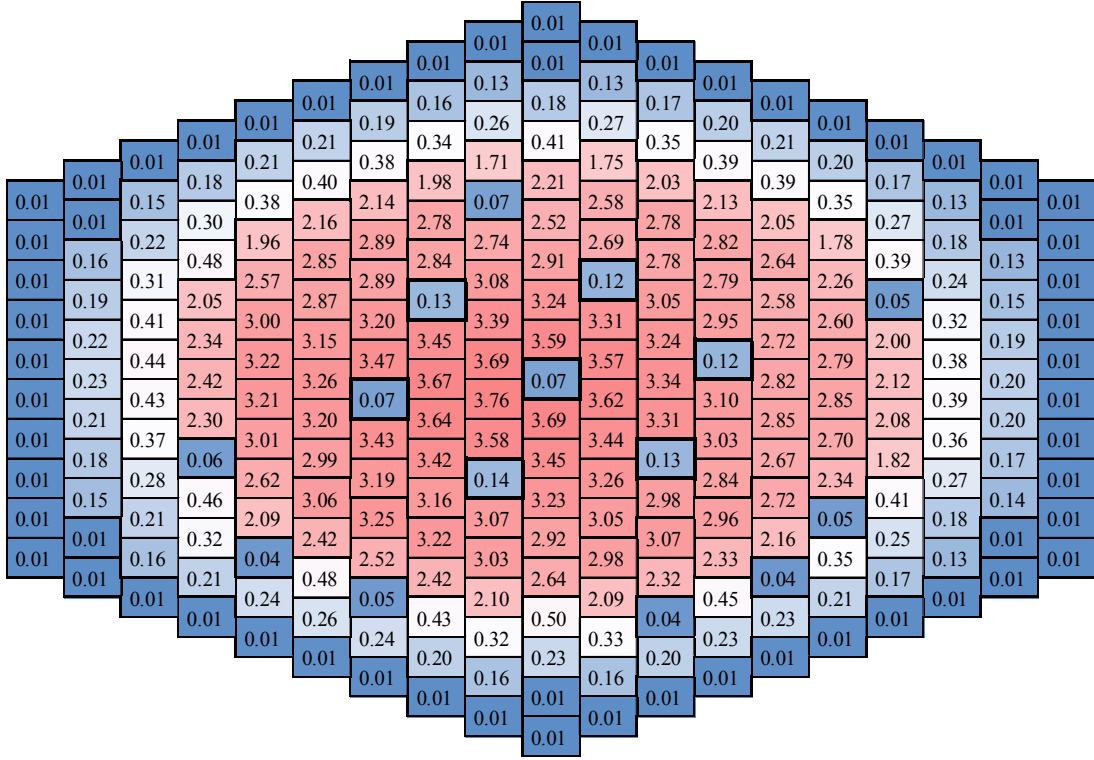
FIG. 156. S/A power distribution (step 3, (MW(th))).
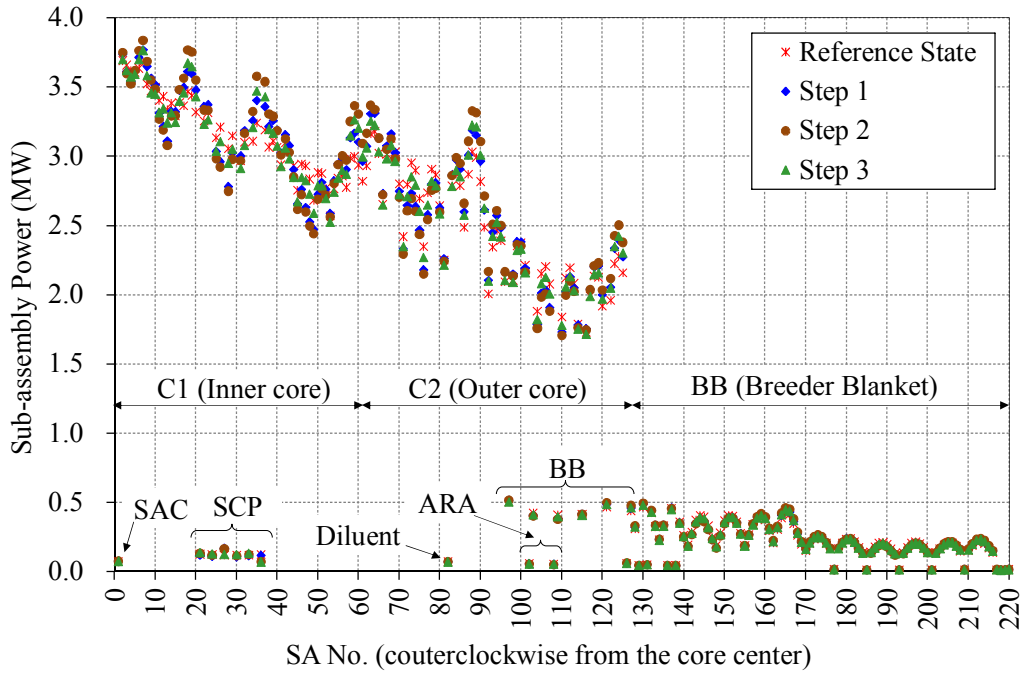
FIG. 157. S/A power distributions (all steps).
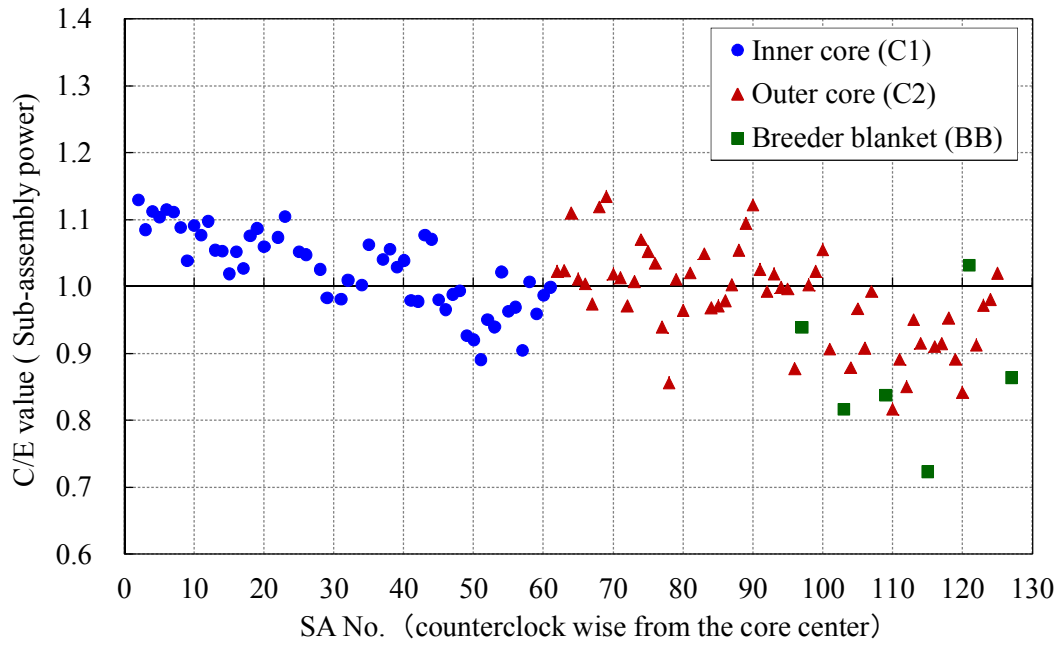
FIG. 158. C/E values for S/A power distributions (inner and outer cores, reference state).

7.5.5. Power distribution deviation

The deviations (%) of the S/A power from reference state are shown in Fig. 159–161. The maximum deviation is +12.5/-12.0 % in step 2 and occurs in the same positions as those of the measurement. The discrepancy from the measurement (C/E) is +0.6/-1.1 % for the measurement maximum deviation, +11.9/-10.9 %.

Fig. 162 summarizes the C/E value of the deviations in step 1–3 for inner and outer cores. The C/E values are approx. ±2 % in inner and outer cores.
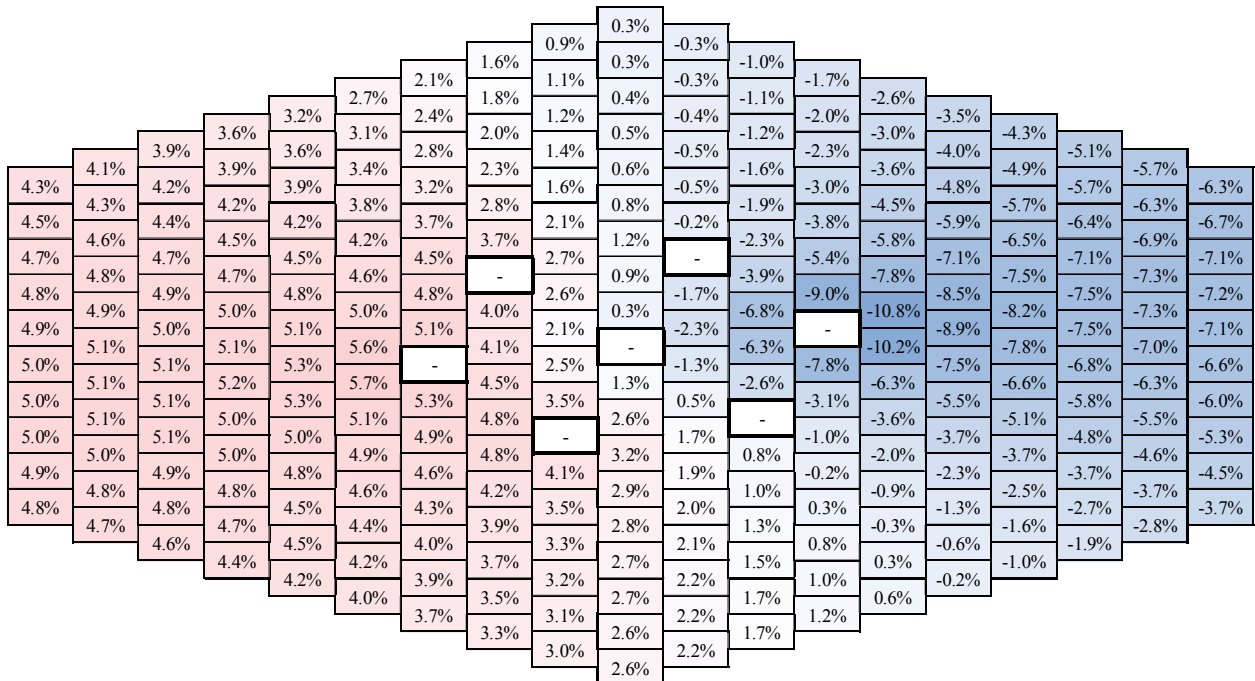
FIG. 159. Deviation of the S/A power from reference state (step 1, (%)).
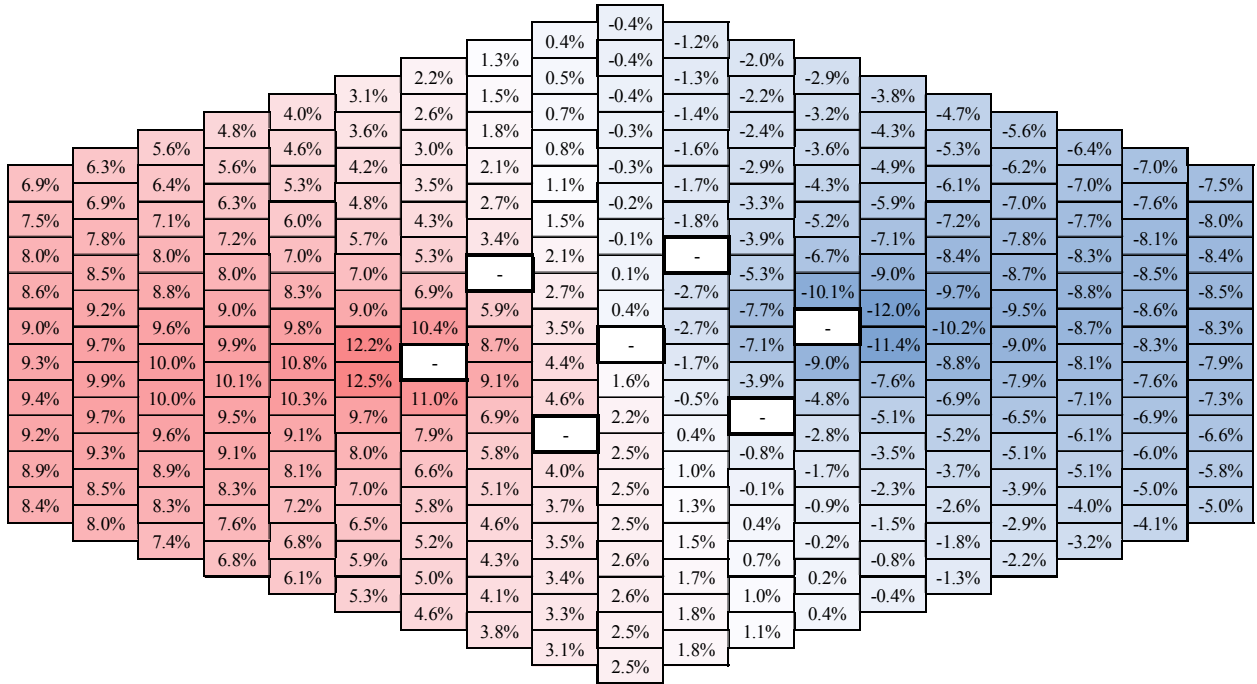
FIG. 160. Deviation of the S/A power from reference state (step 2, (%)).
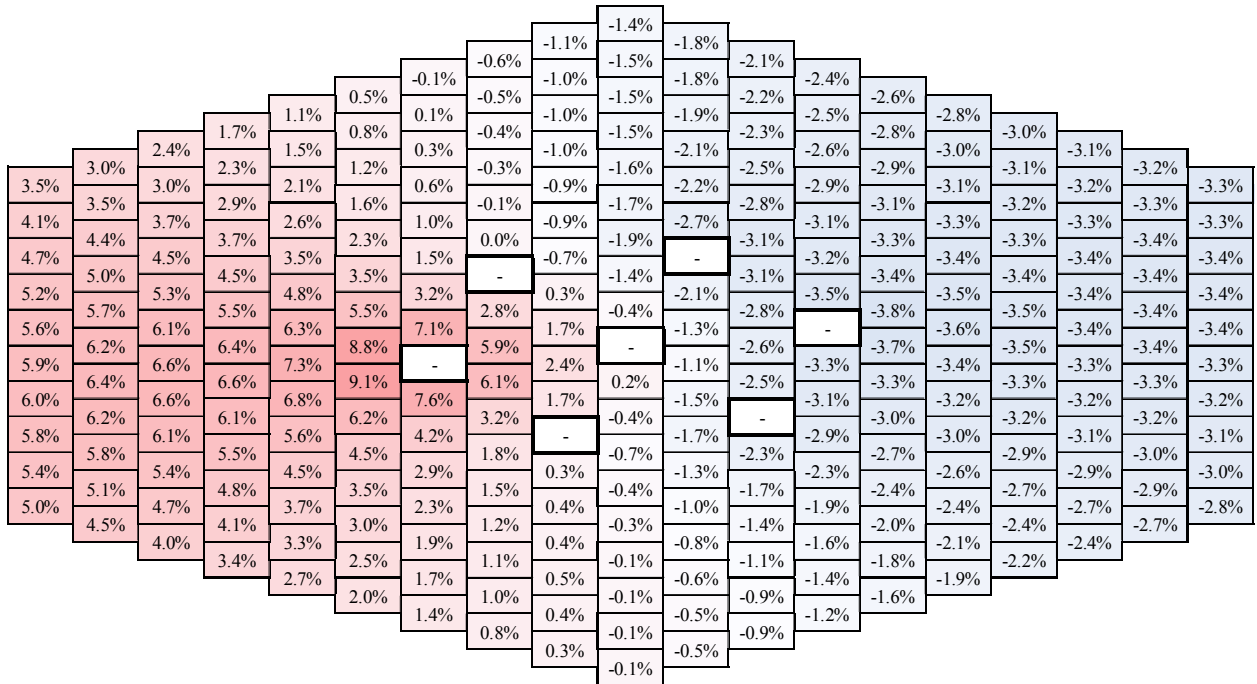
FIG. 161. Deviation of the S/A power from reference state (step 3, (%)).

155
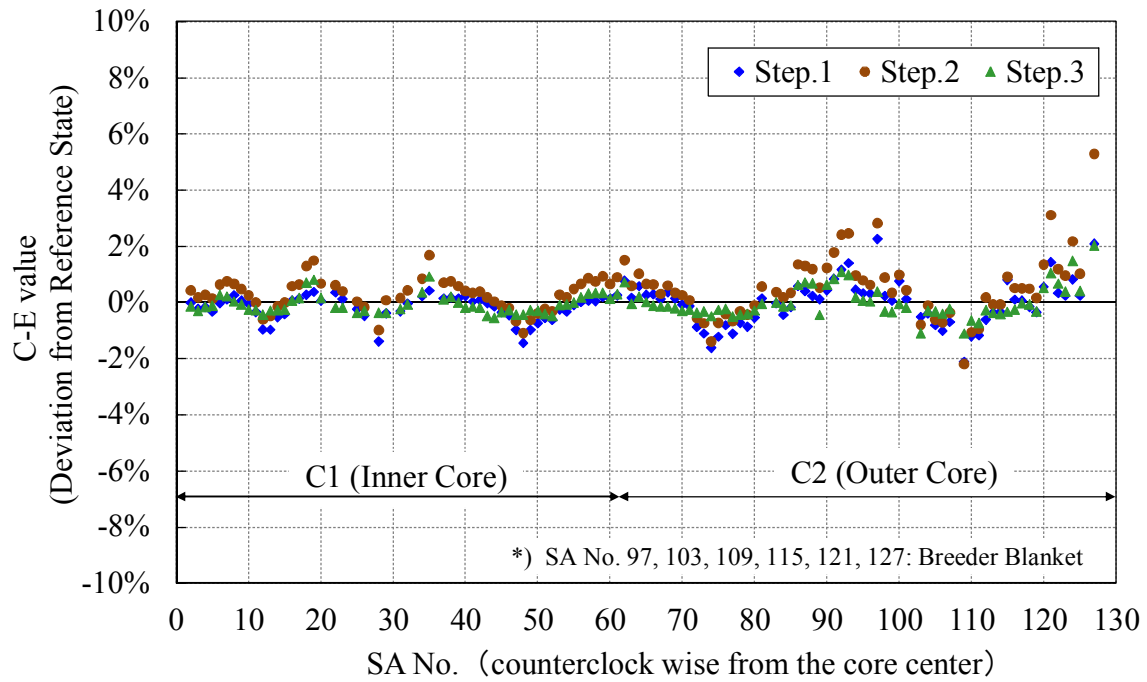
FIG. 162. C-E value for deviation of the S/A power from reference state (%).

7.6. KIT

7.6.1. Control rods worths

Calculation results of the control rod worths are given in Table 49 and Fig. 163. The total control rod worth is 8947 pcm.

TABLE 49. CONTROL RODS WORTH

Rod Position (mm)*	K_{eff} (at 20 °C)	Reactivity (pcm)	Integral Worth (pcm)
0	0.936485	-6782	-8947
343.1611	0.966023	-3517	-5682
524.447	0.993154	-689	-2854
558.34	0.997722	-228	-2393
608.322	1.003921	391	-1774
846.89	1.021672	2121	-44
859.89	1.022059	2158	-7
859.89	1.022059	2158	-7
859.89	1.022059	2158	-7
1061.83	1.022127	2165	0
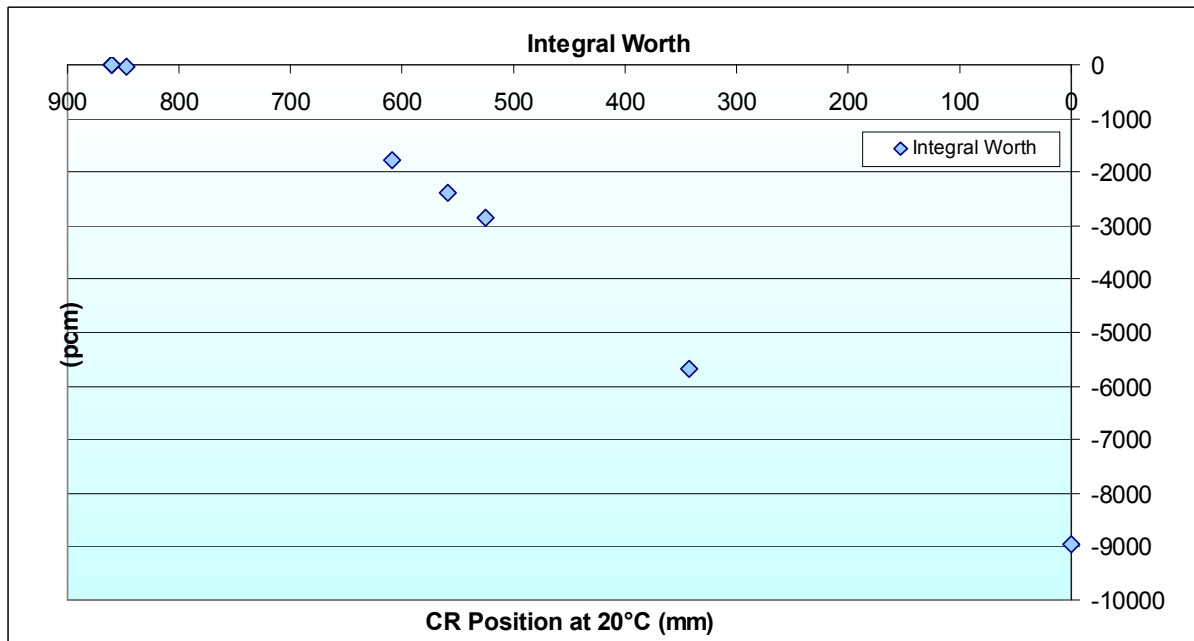
FIG. 163. Control rods S-curve.

As it will be shown in Section 8.3, the standard SIMMER model overestimates the total CR bank worth at about 15 % (see Table 58). To improve our understanding and the SIMMER computation model, an additional study has been performed. It has been found that the origin of the mentioned discrepancy mainly arises from the treatment of the neutron cross-sections (XSs). In fact, each reactor region is approximated by default in SIMMER by a homogeneous mixture of reactor materials, thus the heterogeneity effects are not taken into account in the XS processing. The adjustment of the Boron concentration is one of the methods developed in the past [50] to improve the accuracy in predicting control rod reactivity effects. Having this in mind, neutronics investigations of the Phénix reactor have been performed at KIT [51] by means of the ECCO [16] and ERANOS [12] codes to evaluate the factor to be applied to the $_{10}B$ enrichment of the B_4C absorber in the SIMMER code in order to take into account the reactivity effect associated with the heterogeneity of the control rod absorber region. With this aim, the reactivity worths for two 1D models describing the CR S/A and the six surrounding fuel S/As have been compared. The first model (labeled as 'heterogeneous'), shown in Fig. 164(a), is employed with the ECCO code. In this heterogeneous model, the effect of heterogeneity is taken into account. The second model is shown in Fig. 164(b), and it is employed in the ERANOS BISTRO module [52]. For this 'homogeneous' model the neutron XSs of fuel and absorber S/As are processed assuming that each region (CR, fuel) is an infinite homogeneous medium, similarly to the XS processing in SIMMER. By computing the reactivity effects of the CR withdrawal with the two models, one can evaluate the 'effective' 10B content in the homogeneous model which gives the same CR worth as the real content in the heterogeneous model.

Layer No.	Radius (cm)
CR – 1	1.30
CR – 2	1.56
CR – 3	2.74
CR – 4	3.46
CR – 5	4.13
CR – 6	4.75
CR – 7	6.19
CR – 8	6.68
Fuel – 1	7.33
Fuel – 2	7.97
Fuel – 3	9.90
Fuel – 4	11.64
Fuel – 5	14.00
Fuel – 6	16.17
Fuel – 7	17.25
Fuel – 8	17.67

Legend (heterogeneous): Fuel (red); Absorber (blue); Sodium (yellow); Na/Steel (64.5% / 35.5%); Na/Steel (62.6% / 37.4%); Na/Steel (56.8% / 43.2%); Na/Steel (34.2% / 65.8%); Na/Steel (25.3% / 74.7%)

Legend (homogeneous): Fuel/Na/Steel (38.83% / 36.08% / 25.09%); B4C/Na/Steel (21.67% / 50.56% / 27.77%)

FIG. 164. Heterogeneous (a) and homogeneous (b) models of the CR and surrounding fuel S/As. Volume fractions of the different components are provided.

Calculations have been performed by using the JEFF3.1 nuclear data library [53] and by using an 11 energy discretization, similar to that employed in SIMMER. Results concerning k_∞ and CR reactivity worth are shown in Table 50. Results show that the reference CR reactivity worth (-20177 pcm) is obtained in the homogeneous model if the 10B content in the B4C is reduced from 48 to 34.6 wt.% in the homogeneous model. The model based on this approach, i.e. on reduction of the 10B enrichment, has been implemented in SIMMER-IV to take into account the heterogeneity effect. The updated SIMMER result for the CR bank reactivity worth is -7472 pcm (see also Fig. 185). One can see that taking into account the absorber heterogeneity effect allows getting a SIMMER estimation that is very close to the ERANOS one, while the homogeneous CR model overestimates the total bank worth in the Phénix reactor by about 1250 pcm that is in line with the heterogeneity effect value (~1500 pcm) obtained earlier by IRSN and discussed in Section 7.4.2

TABLE 50. REACTIVITY LEVELS AND CONTROL ROD REACTIVITY WORTH COMPUTED FOR THE HETEROGENEOUS AND HOMOGENEOUS MODELS.

	Heterogeneous model	Homogeneous model	Homogeneous model (34.6 wt.% B4C depleted)
CR inserted	1.03918	0.98534	1.02301
CR withdrawal	1.31488	1.28916	1.28916
CR reactivity worth (pcm)	**-20177**	**-23918**	**-20180**

7.6.2. Core reactivity during the difference test states

The results of the analysis on K_{eff} and reactivity are shown in Table 51. Initial K_{eff} is calculated for the uniform temperature distribution given by CEA input data set (see Table 52). These values should correspond to the results of the temperature-uniform neutronics codes, like ERANOS. In SIMMER-IV calculations, the final steady state is calculated with a real temperature distribution that changes slightly the reactivity as shown in the last column of Table 51.

TABLE 51. K-EFF AND REACTIVITY CHANGE

	K_{eff}(Initial)	K_{eff}(Steady-State)	Reactivity Change, (Initial-to-Steady) pcm
Reference State	1.00032	1.00075	43
Step 1	1.00046	1.00057	11
Step 2	1.00054	1.00094	40
Step 3	1.00019	1.00069	50
Final State	1.00051	1.00089	38

TABLE 52. INITIAL TEMPERATURE DISTRIBUTION

Zone	Temperature (°C)
Fuel	1227
Blanket	627
Structure	448
Coolant	448
Absorber	448

7.6.3. Flux and power distribution

7.6.3.1. Maximum neutron flux distribution

The distribution of the maximal neutron flux (core midplane) is shown in Fig. 165. In non disturbed reference state, the maximum flux value $\sim 3.90 \times 10^{15}$ (n/cm^2·s) is reached in the second row fuel S/A (21/19 and 20/19). Among experimental steps, the maximal flux $\sim 4.06 \times 10^{15}$ (n/cm^2·s) is observed on step 2 in the same S/A (20/19). Fig. 166 shows the deviation of the maximal neutron flux from the reference state. The maximal deviation about -25% is observed on step 1 and step 2.
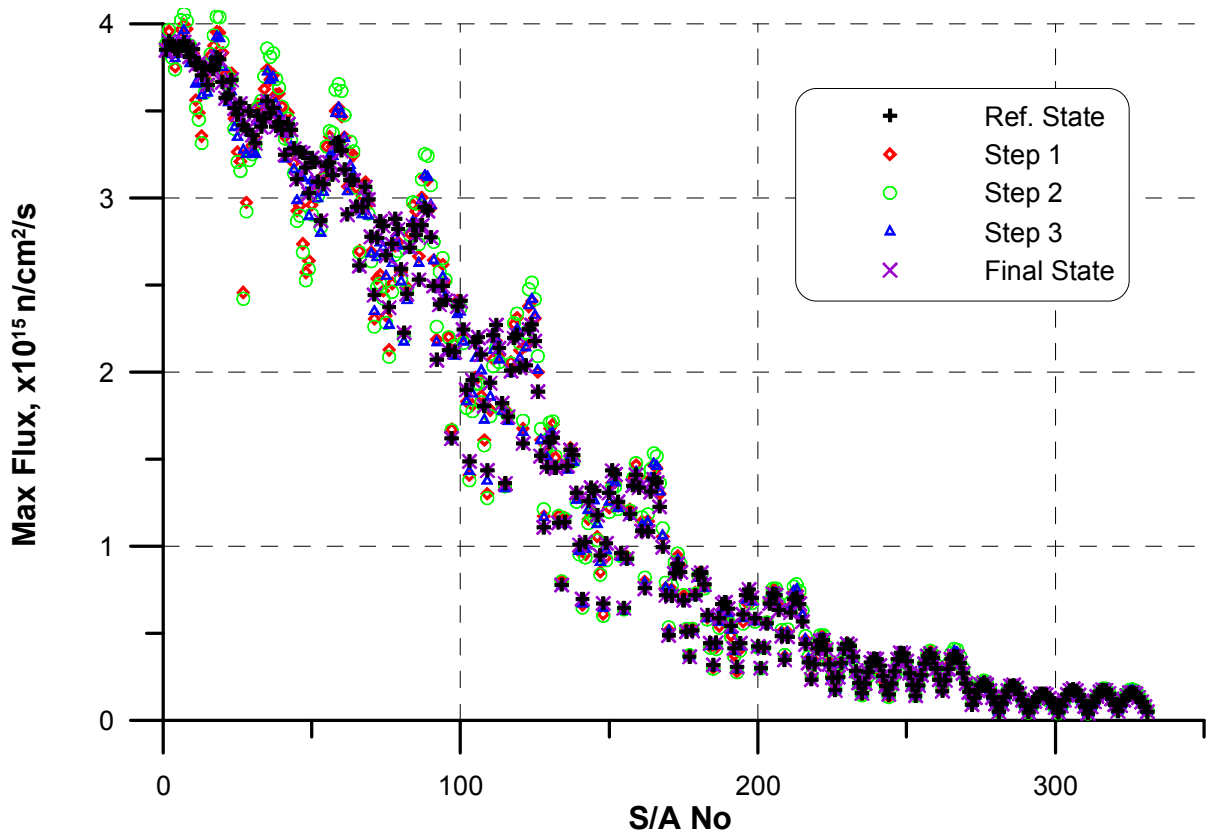
FIG. 165. Maximal neutron flux distribution vs. S/A number.
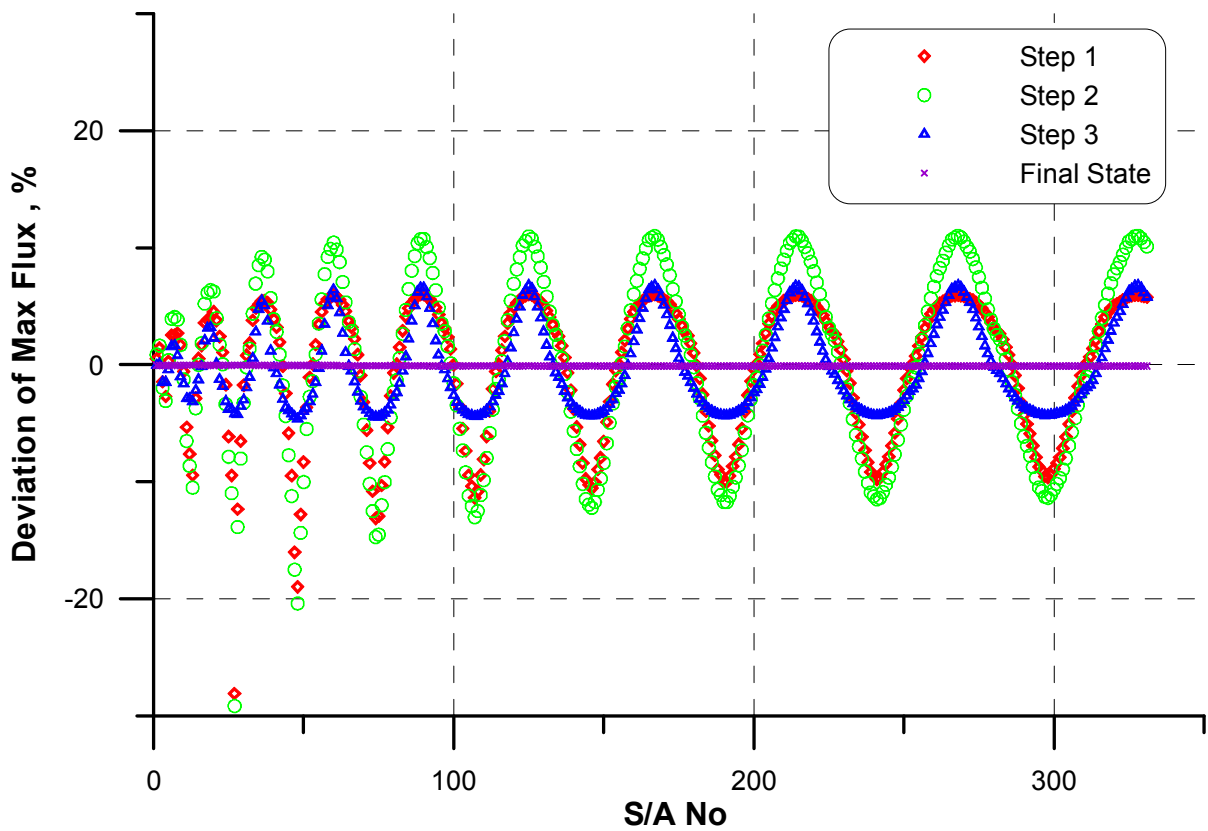
FIG. 166. Deviation of maximal neutron flux for CR withdrawal steps.

7.6.3.2. Total power distribution

The S/A power distributions for the reference case and three sequential CR withdrawal tests are shown in Fig. 167–170. Maximal and minimal power subassemblies are marked with white border. These power distributions are also plotted in Fig. 171–172 for comparison. S/As are numbered counter-clock-wise, staring from the core center according to the CEA input data sheet. The maximal power reaches 3.91 MW (S/A 20/19) on step 2. Obviously, the maximal power deviations about +/- 40% are observed for the inserted/withdrawn control rods SCP1 and SCP4. Among fuel S/As, the maximal positive deviation is about 16% on step 2 at the outmost ring of the inner core near withdrawn control rod position (S/A 19/17). The maximal negative deviation -14% is observed in the inner core S/A (22/22) near inserted control rod.
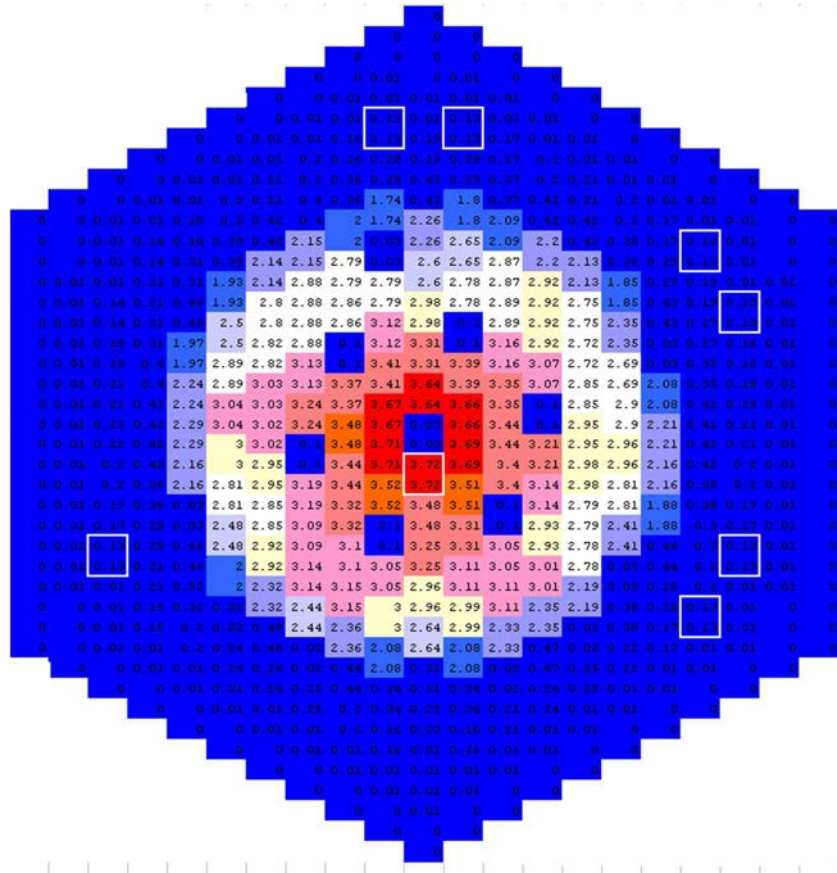
FIG. 167. Reference state: power distribution per S/A, MW.
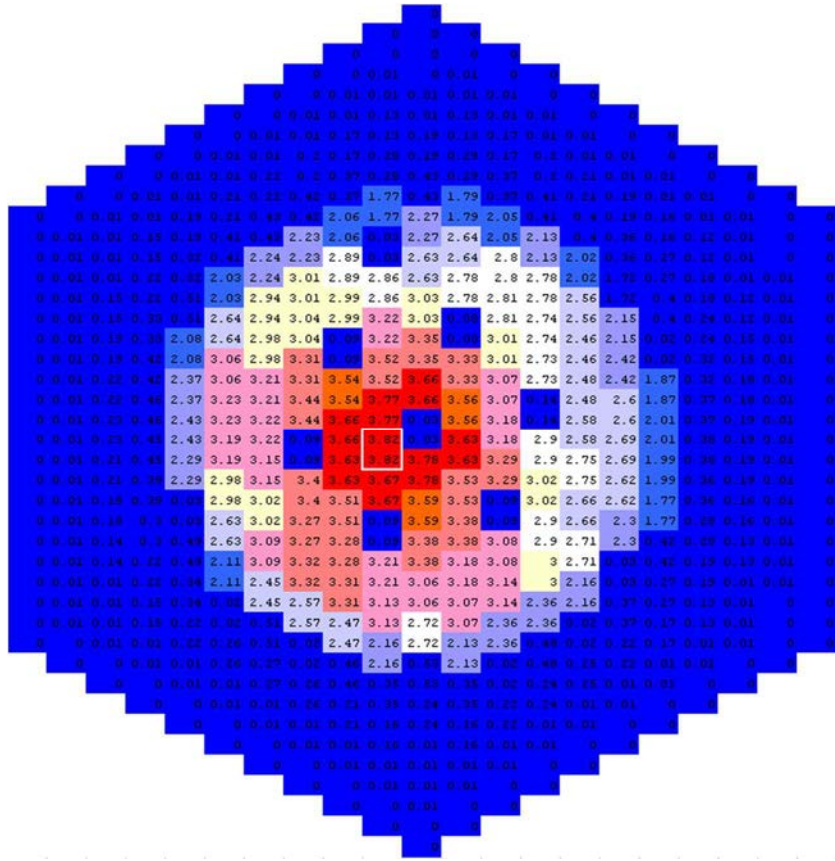
FIG. 168. Step 1: power distribution per S/A, MW.
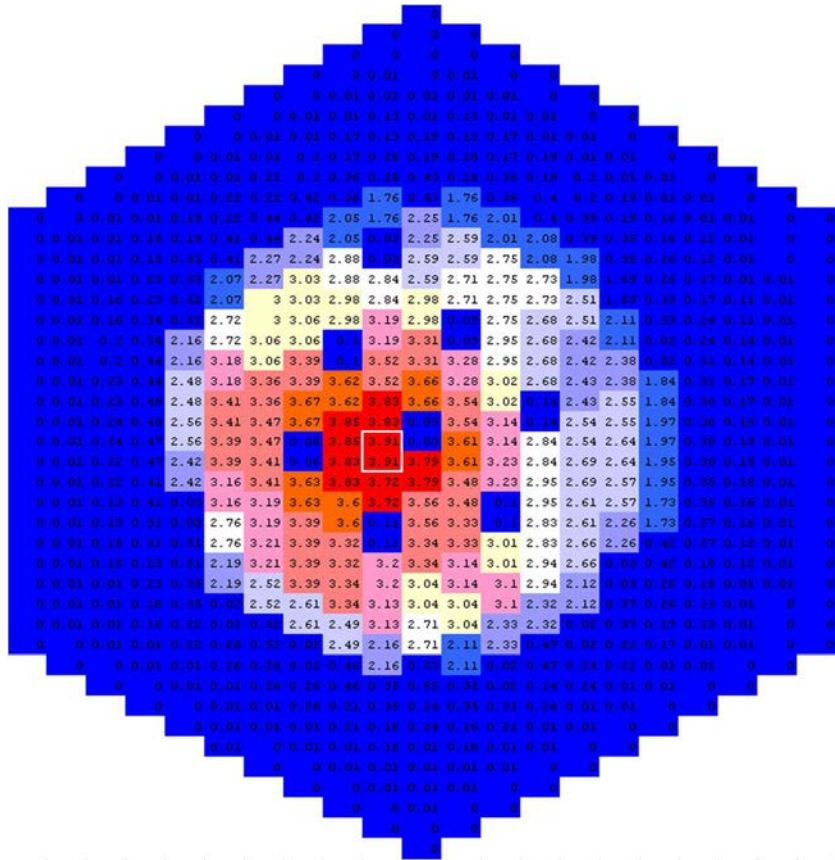
FIG. 169. Step 2: power distribution per S/A, MW.

162
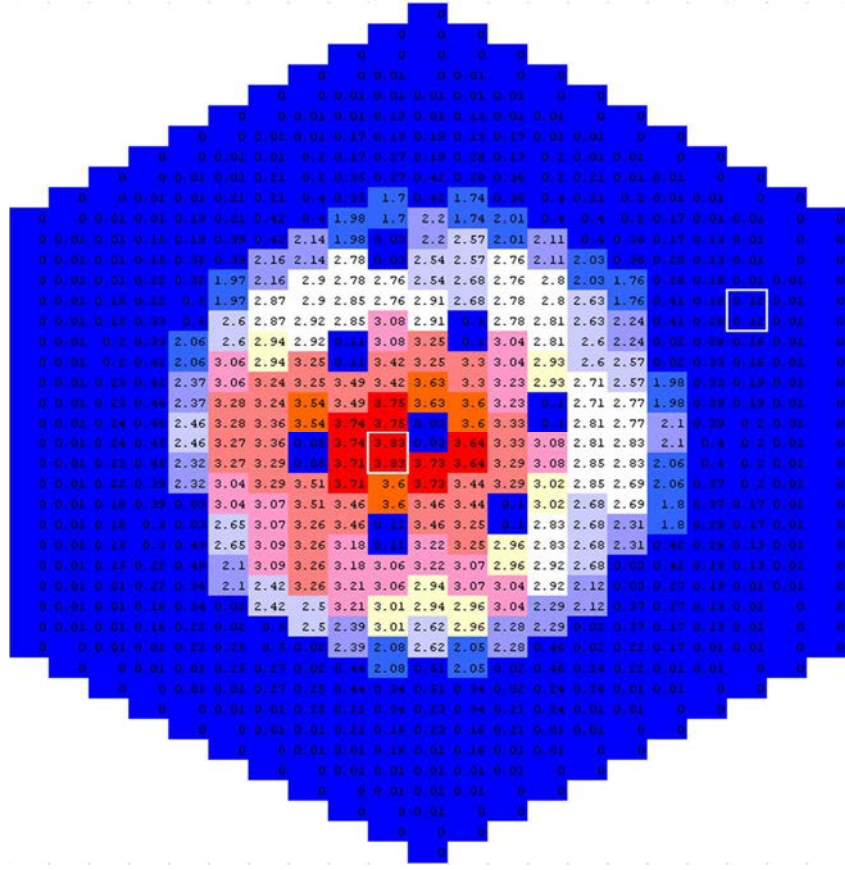
FIG. 170. Step 3: power distribution per S/A, MW.
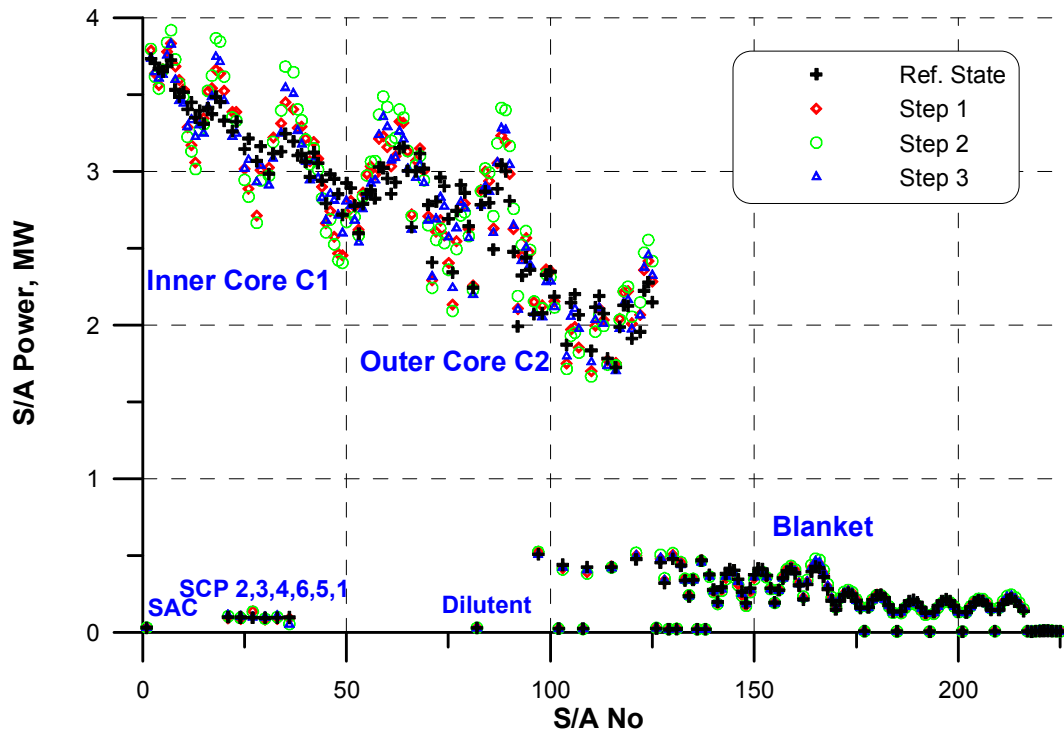
FIG. 171. Power distribution per S/As.
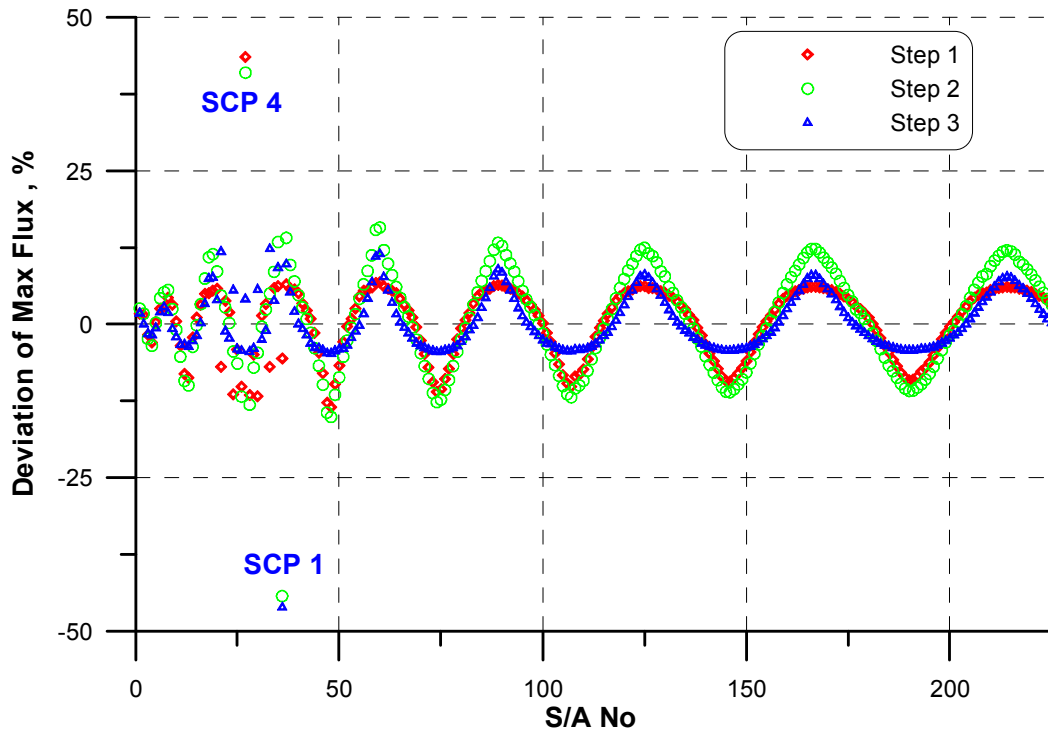
FIG. 172. Relative deviation of S/A power for CR withdrawal steps.

7.6.4. Outlet coolant temperature

Fig. 173 shows the distribution of the sodium outlet temperature for all experiment steps. The maximal temperature ~572 °C is reached in several S/As on step 1 and step 2. The biggest relative change in the outlet temperature values is observed in inserted/withdrawn control rods channels SCP 4 and SCP 1.
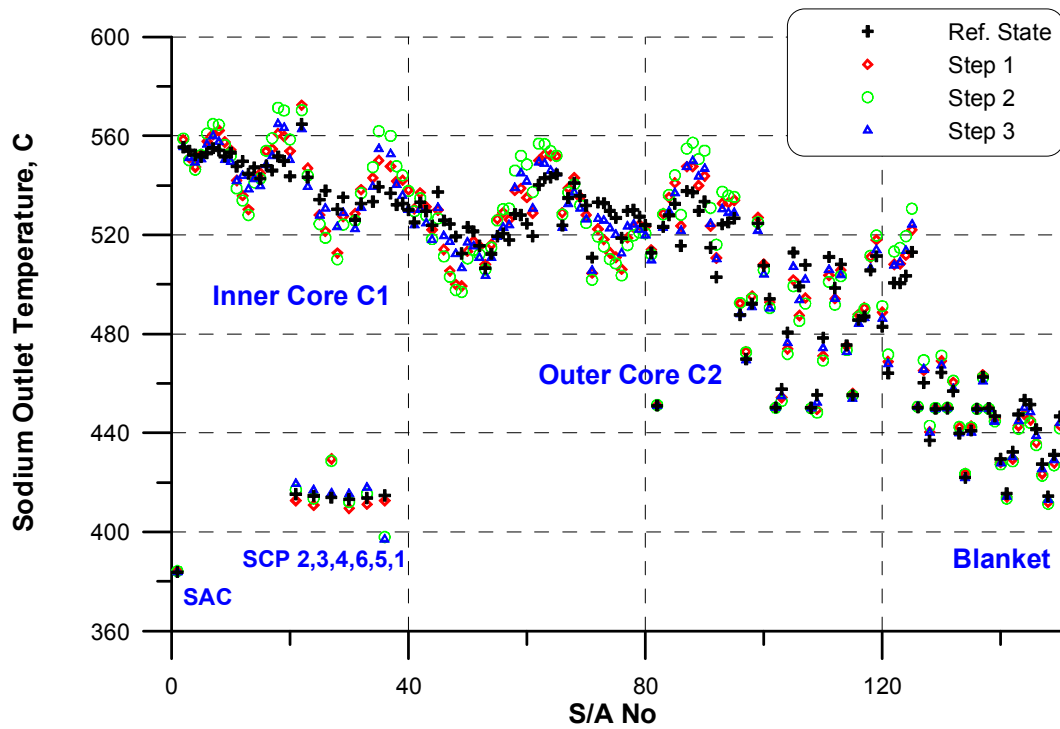
FIG. 173. Outlet sodium temperature distribution.

7.7. PSI

The Control Rod Shift test has been used for supplementary validation of the FAST code system [54–55], through the effective testing of Phénix core models set up using its constituent codes – ERANOS and PARCS for the neutronics, and TRACE for the thermal–hydraulics. The current section is based on Ref [56]. As already mentioned above, at the second phase of the exercise the homogeneous treatment of the fuel regions and control rod regions was replaced by the heterogeneous representation.

7.7.1. Control rods worth

Result of the control rod bank worth calculated with the ERANOS code is shown in Table 53 and Fig. 174. The total control rod bank worth is found to be 8070 pcm.

TABLE 53. CONTROL RODS WORTH (BANK)

CR position (mm)	Rod bank worth (pcm)
0	0.0
100	292.1
200	847.8
300	1719.3
400	2880.3
500	4240.5
600	5635.0
700	6833.9
800	7653.6
900	8070.0
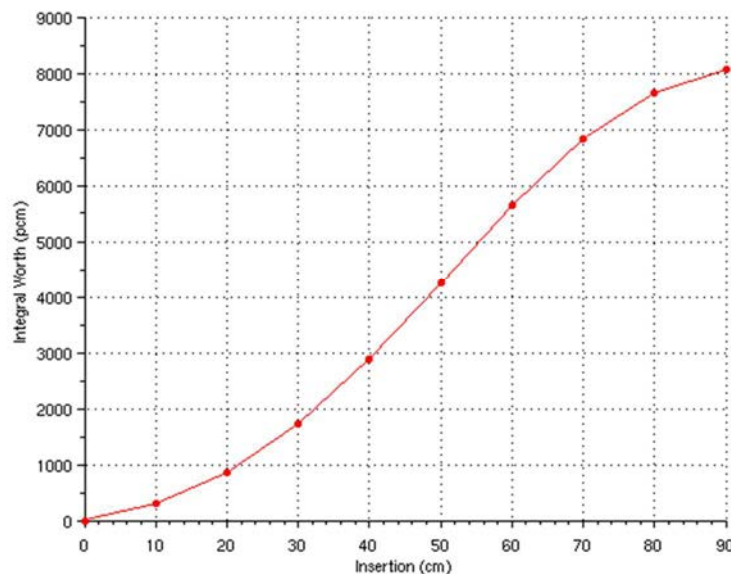
FIG. 174. Control rod bank S-curve.

7.7.2. Core reactivity during the difference test states

The results of the analysis for k_{eff} (reactivity) calculated by ERANOS code for the hot states are shown in Table 54. The table shows little change in reactivity from one step to another, only ~10 pcm spread.

TABLE 54. CORE REACTIVITY

	k-eff	reactivity (pcm)
Reference	1.00593	589.5
Step 1	1.00604	600.4
Step 2	1.00602	598.4
Step 3	1.00602	598.4

7.7.3. Flux and power distribution

The maximum flux distributions for each S/A are shown in Fig. 175. The total power distributions of each S/A calculated by ERANOS are shown in Fig. 176. The C/E values of the total power in reference state and step 2 are shown in Fig. 177.
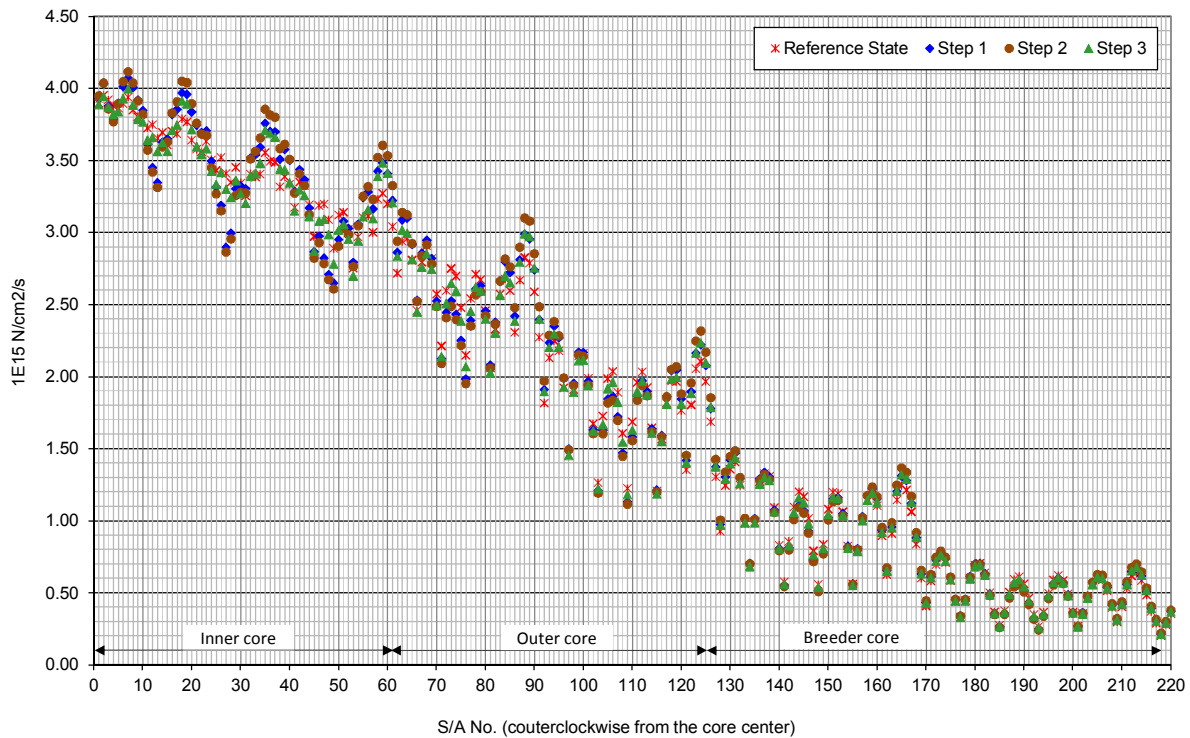
FIG. 175. Maximum flux distributions calculated by ERANOS (all steps).
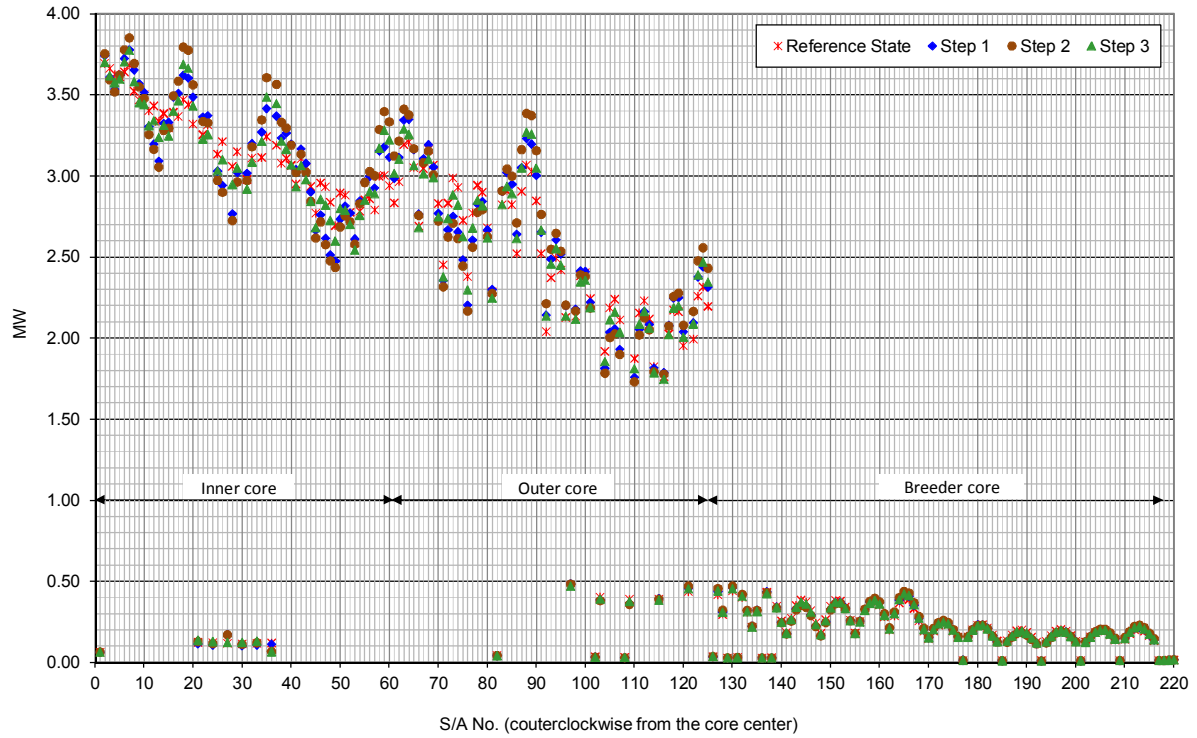
FIG. 176. Total power distributions calculated by ERANOS (all steps).
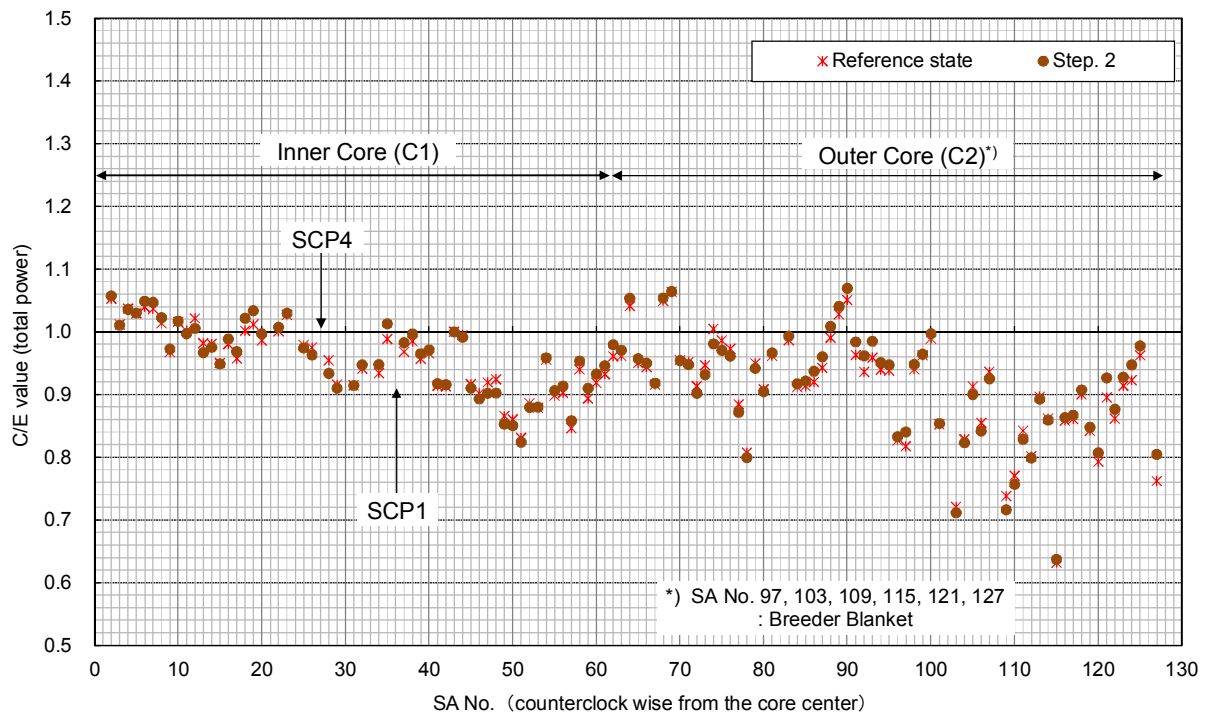
FIG. 177. C/E values for total power distributions (inner and outer core, reference state and step 2).

167

7.7.4. Power deformation due to the different control-rod configurations

The different steps of the CRS test have been simulated with both the ERANOS and the coupled TRACE/PARCS models. Fig. 178 shows the absolute power distribution corresponding to step 3, as calculated with ERANOS and TRACE/PARCS. The difference in the absolute power between ERANOS and TRACE/PARCS is similar to that calculated at 1000 K, with a very good agreement in the fuel S/As and around 15% discrepancy in the blanket S/As, due to the reasons explained before. The integral worth of all six control rods was estimated to be about 8000 pcm by both ERANOS and PARCS.
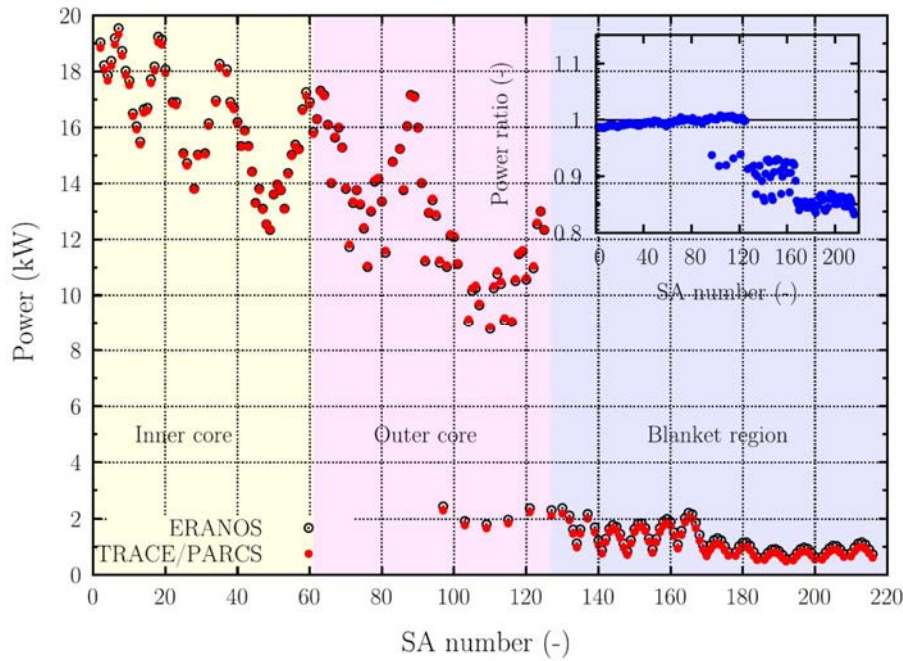
FIG. 178. Comparison of TRACE/PARCS and ERANOS computed power distributions at 335MW(th) for the CR configuration of step 3.

Fig. 179 presents a map of the power deformation calculated with TRACE/PARCS for step 3, relative to Step 1. Step 3 shows the largest deformation of the power, as expected based on the control assembly positions. With this CR configuration, the core is divided into 4 symmetrical azimuthal sectors, and the maximal experimental relative deformations are +12.6% in S/A 60 (next to the extracted CR) and −12.0% in S/A 48 (next to the inserted CR). These deformations are well predicted by TRACE/PARCS.
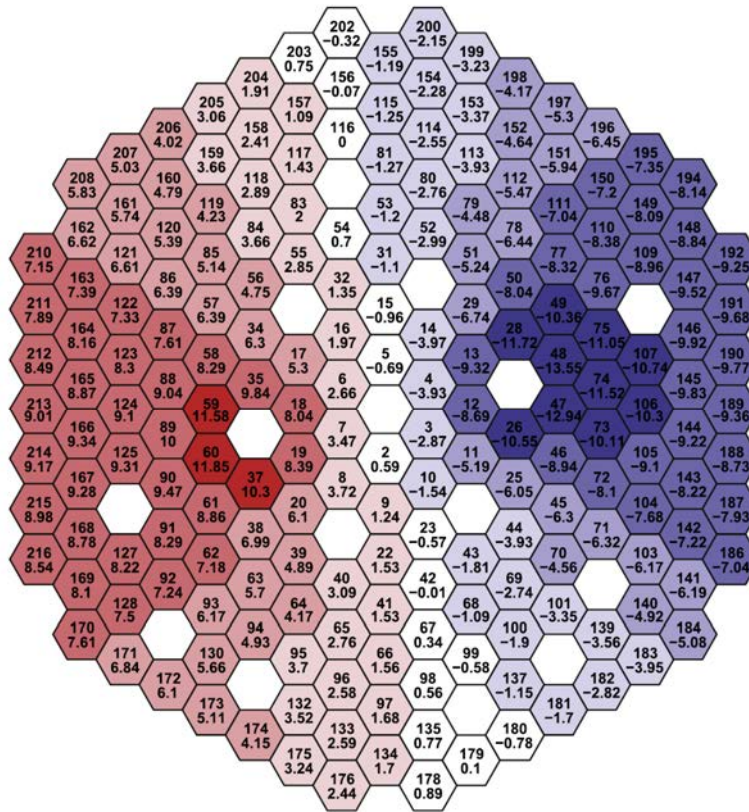
FIG. 179. Map of the power deformation between step 1 and 3 calculated by TRACE/PARCS. (top: S/A number, bottom: deformation in %).

The measured power deformations resulting from the shifts of the CRs between the reference state (step 1) and the other three steps of the CRS test are presented in Fig. 180, along with the corresponding TRACE/PARCS predictions and, in Fig. 181, along with the corresponding ERANOS predictions. One can clearly say that there is generally very good agreement between ERANOS calculations, TRACE/PARCS calculations and experimental results.

Fig. 182 presents a 2D map of the assembly-wise relative differences in the power deformation between test data and the computed results for step 3 relative to step 1, using the TRACE/PARCS and ERANOS models. It can be seen that TRACE/PARCS predictions are in very good agreement with the experimental data, with less than 4.5% error when comparing the power deformation between the different steps. This maximal error corresponds to a blanket assembly (S/As 97, 103, 109, 115, 131, 127 are in the blanket). The maximum deviation in the fissile S/As is located around the inserted CR, with a value less than to 2.8%. ERANOS predictions have a maximum error of 5.6% in the blanket S/As, and of 3.1% in the fuel S/As. The discrepancy for the S/As around the extracted CR is of the same order as that around the inserted CR, but with opposite sign. In general, the deformation of power is slightly over-predicted by both models.
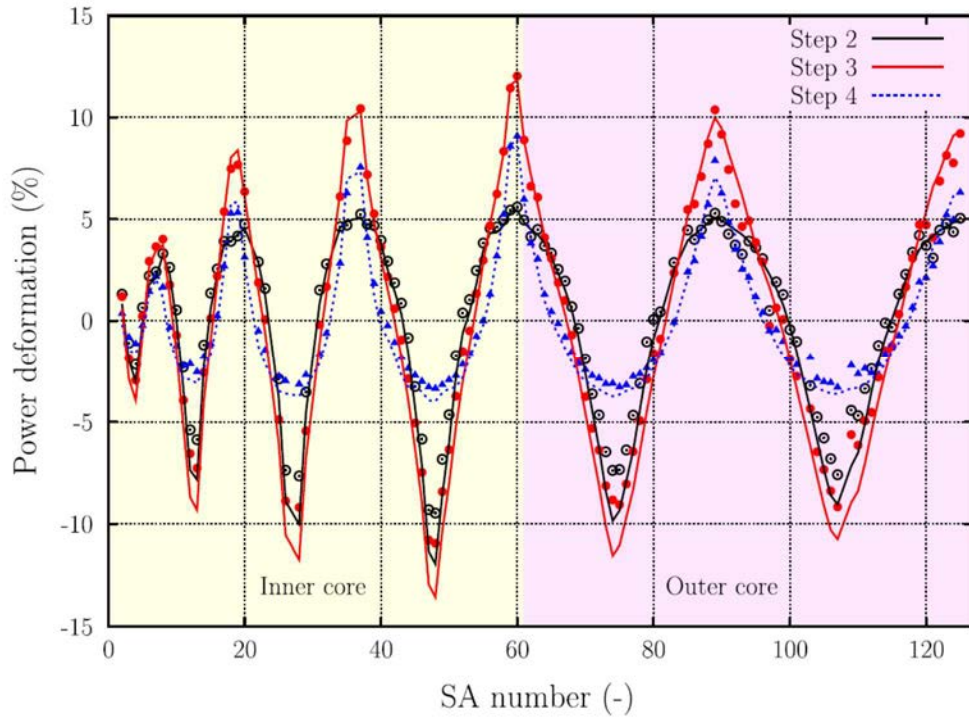
FIG. 180. Comparison of the power deformations for the different steps of the CRS test, measured (points) and calculated with TRACE/PARCS (lines).
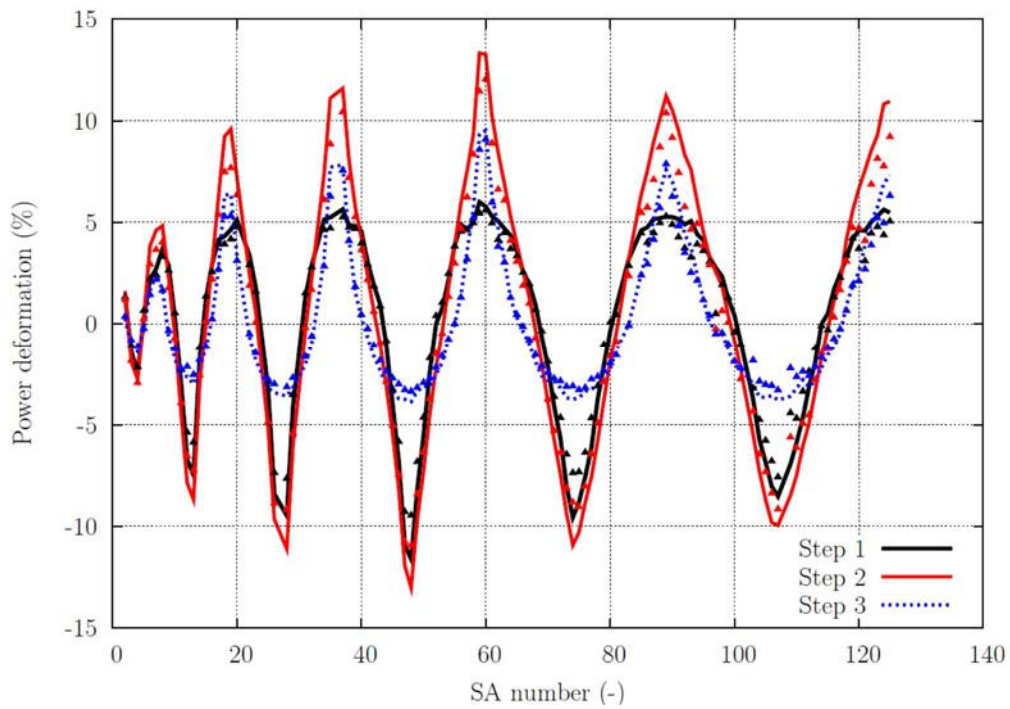
FIG. 181. Comparison of the power deformations for the different steps of the CRS test, measured (points) and calculated with ERANOS (lines).
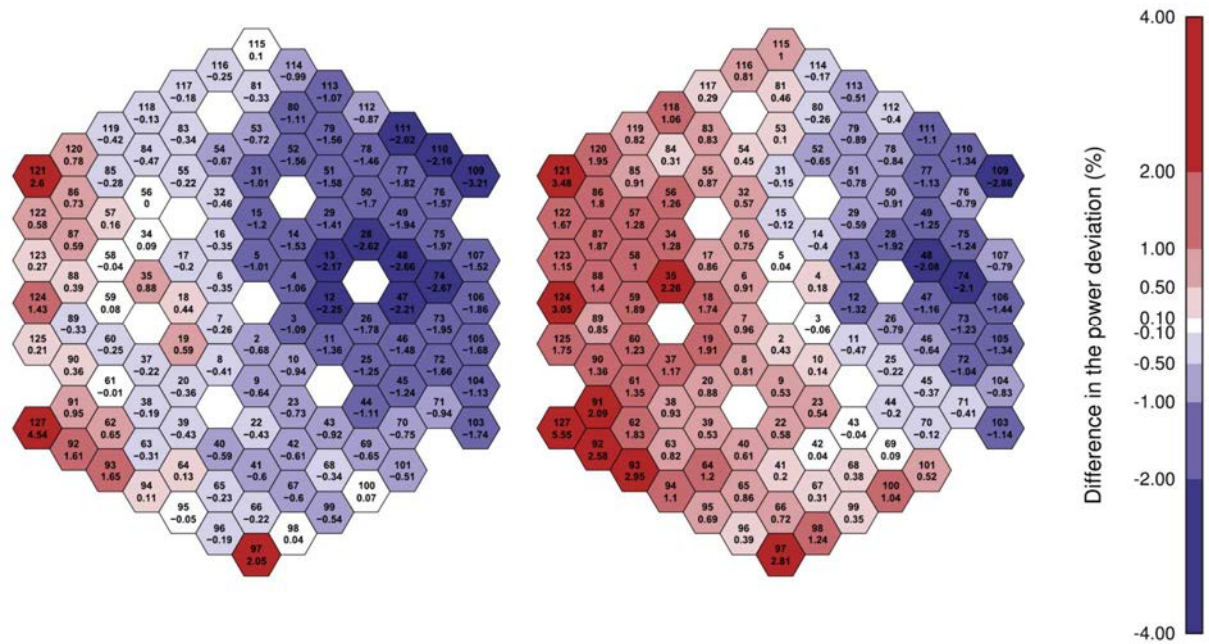
FIG. 182. Relative differences between the calculated and measured power deviation for step 3 relative to step 1 (top: S/A numbers, bottom: relative differences in %).

The maps corresponding to steps 2 and 4 are not presented here, but it can be seen from Fig. 180 that the biggest discrepancies with respect to the experimental data are found for step 3, which also corresponds to the largest power deformation.

7.7.5. Comparison of calculational and experimental results for the outlet coolant temperature

Table 55 shows that the specified flowrate distributions at 350 MW(th) (1988 kg/s) and at 120 MW(th) (1284 kg/s) were well reproduced by the gagging scheme implemented in the TRACE/PARCS model. Based on the data available, only a region-by-region check could be performed (the experimental assembly-wise flowrate was not available).

TABLE 55. COMPARISON OF TRACE CALCULATED RESULTS (CALC.) FOR THE FLOWRATE (KG/S) WITH THE BENCHMARK SPECIFICATIONS (SPEC.) FOR 350 MW(TH) AND 120MW(TH) POWER.

	350MW(th)		120MW(th)	
	Spec.	Calc.	Spec.	Calc.
Inner core	861	849	1055	552
Outer core	779	780		503
Blanket	226	236	149	148
Reflector	122	123	80	81

Fig. 183a) compares the experimental outlet temperature in the fissile core with the TRACE/PARCS prediction for the reference state (335 MW(th)). The assembly-wise absolute differences (prediction minus measurement) are displayed in Fig. 183b). The highest discrepancies are seen in the outer core S/As (last two rows in the figure), with up to 53 °C over- and 18 °C under-estimation of the measurements. High discrepancies are also seen in the central row of the inner core, where the temperatures are, on average, over-predicted by 25 °C. Considering the good

agreement of the radial power distribution between TRACE/PARCS and ERANOS in the fissile core (Fig. 183), it is clear that the discrepancies on the outlet temperature distribution are mainly due to an inaccurate modeling of the S/A-wise flow distribution. It is noteworthy to recall that the experimental gagging of the Phénix core has not been specified in the benchmark definition and that, in the TRACE model, the flowrate has been assumed to be equal in S/As from the same core region. Thus, although the region-wise flowrate has been shown to be in good agreement with the test data, no experimental values were available for comparison of the assembly-wise flowrate distribution.
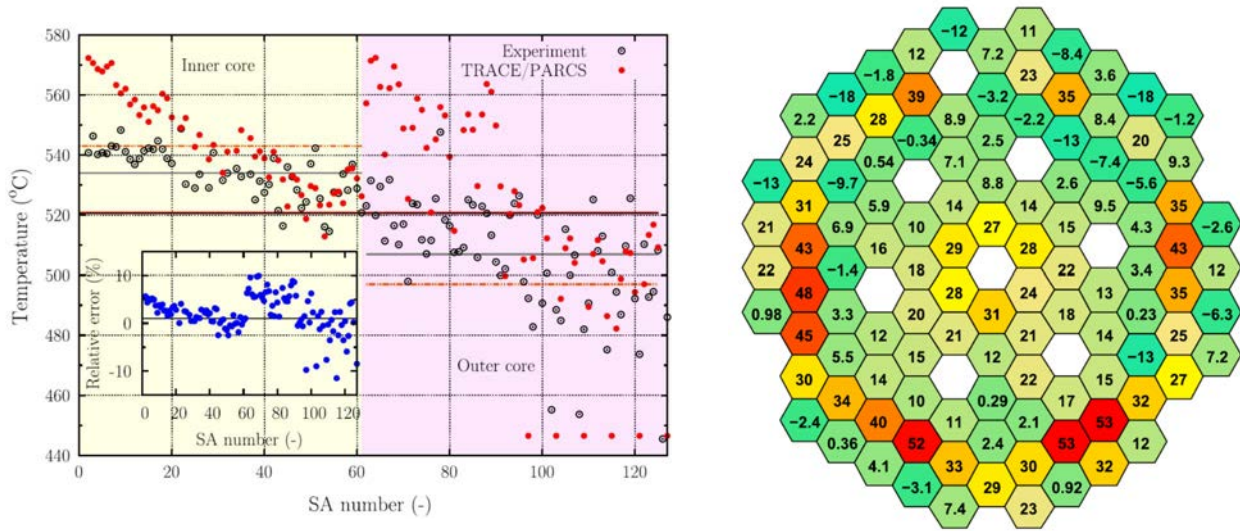
a) Sodium outlet temperature. Region-wise and core averaged temperatures are represented by dashed and solid lines, respectively.

b) Absolute difference (ºC)

FIG. 183. Sodium outlet temperature in the inner core calculated with TRACE/PARCS and compared to the measured data for the reference state of the CRS test (335 MW(th)).

Comparing the calculated and measured temperatures averaged over the different zones, one can see that the predicted average temperature is 10 ºC higher in the inner core and 10 ºC lower in the outer core. This indicates that the flowrate distribution is slightly under-estimated in the inner core. When averaging over the entire fissile core, the heat balance is very well reproduced with both the experimental and calculated temperatures being 521 ºC. Clearly, in conjunction with the detailed radial power distribution obtained from the 3D model, the specification of the detailed core gagging is necessary for an accurate modeling and prediction of the S/A temperatures.

It is clearly useful to assess the sensitivity of the results to the temperature distribution. Apart from the nodal scheme, the major difference between ERANOS and TRACE/PARCS predictions resides in the temperatures used to calculate the reactivity feedbacks. As mentioned in Section 5.8, the temperatures used in ERANOS for the fuel, structure and coolant are constant, whereas in the coupled calculation, TRACE provides PARCS with the 3D temperature distributions for the different materials. In order to study the importance of the 3D effects, a calculation has been carried out with TRACE/PARCS using the same temperatures as those used in the ERANOS model. This was done by using TRACE to fix the temperature of the fuel at 1227 ºC, that of the blanket at 627 ºC, and all other temperatures at 448 ºC. Results for the power deformation for step 3 relative to step 1 are presented in Fig. 184, as calculated with TRACE/PARCS, PARCS with fixed temperatures and ERANOS. The TRACE/PARCS and PARCS calculations are very similar, showing very small effects of the temperature distribution on the power deformation, and thus on

the calculated changes in the neutronics feedbacks. This confirms that the ERANOS model can be used without modification to calculate the power deformation between the different CR positions.
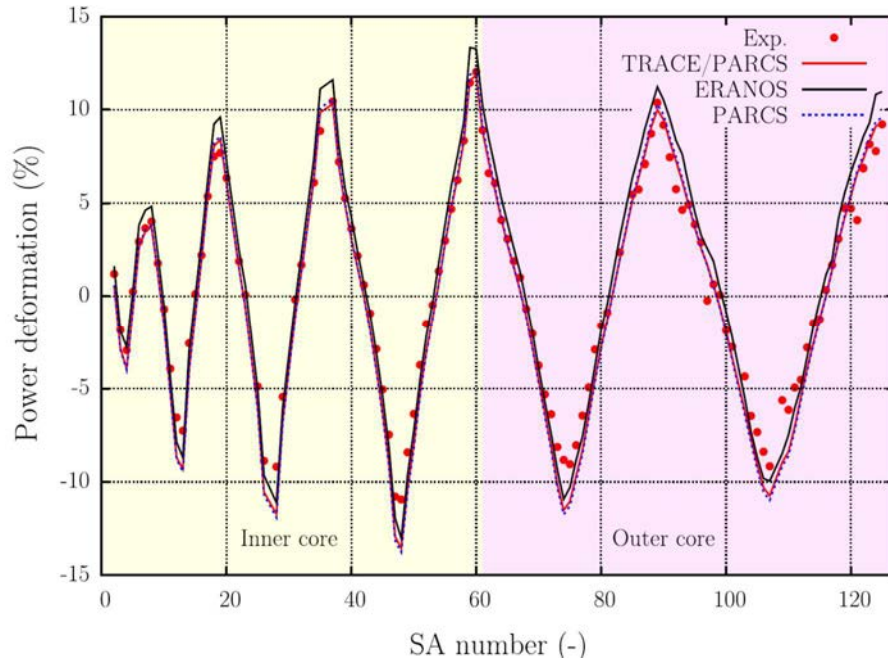
FIG. 184. Comparison of the calculated (lines) and measured (points) power deformation between step 1 and step 3, using the different models.

7.7.6. Conclusions

Data from the Phénix EOL control-rod-shift (CRS) test have permitted an assessment of the FAST code system's capability to model SFR control assemblies. First, an ERANOS model of the Phénix core was developed. This, in turn, led to the development and verification of a coupled TRACE/PARCS model. The comparison of the predictions with the CRS test data for different control rod configurations has shown the capabilities of both models to accurately predict the resulting power deformation, with a maximal relative error of 5.6% in the blanket S/As and 3.1% in the fissile S/As. The explicit accounting of the temperature distribution for the reactivity feedback calculation has been found to have very little impact on the predicted power deformation. In conclusion, the presented analysis has demonstrated the capability of ERANOS and TRACE/PARCS to satisfactorily model the control assemblies of the Phénix core. As such, use of the CRS test data has enabled an important step further to be made in validation of the FAST code system for SFR core analysis. Testing of the code system's capability to adequately model scenarios with significant reactivity feedback effects is reported in another part of the current study, which concerned the analysis of the unprotected phase of the Phénix EOL Natural Convection (NC) Test [57].

8. RESULTS OF THE COMPARISONS

8.1. SHORT COMPARISON OF THE CALCULATION SCHEMES

The calculation models and codes used by the participants are summarized in Table 56.

TABLE 56. COMPARISON OF CALCULATION METHODS

	Participant	Cell code	Core composition	Code	Method	Cell Treatment	Control Rod Treatment	Nuclear library	No. of Groups
	IPPE	CONSYST	Averaged	MMKKENO	Monte-Carlo	Het 2D	Heterogeneous (3D) calculation	ABBN-93	299
	JAEA	SLAROM-UF	Averaged	DIF3D	Diffusion	Het 1D	Heterogeneous (1D) calculation + Reaction Rate Ratio Preservation method	JENDL-3.3	70
	CEA	ECCO	Averaged	ERANOS VARIANT	Transport	Het 2D	Heterogeneous (2D) calculation + corrected cross-sections with SN transport method	ERALIB-1	33
	CEA	ECCO	Detailed	ERANOS VARIANT	Transport	Het 2D	Heterogeneous (2D) calculation + corrected cross-sections with SN transport method	ERALIB-1	33
	IRSN	ECCO	Averaged	ERANOS VARIANT	Transport	Het 2D	Heterogeneous (2D) calculation + corrected cross-sections with SN transport method	ERALIB-1	33
	IGCAR(1)	ECCO	Averaged	ERANOS H3D	Diffusion	Het 2D	Heterogeneous (2D) calculation + corrected cross-sections with SN transport method	ERALIB-1	33
	IGCAR(2)	CONSYST	Averaged	FARCOB	Diffusion	Het 1D	2D calculation without corrections	ABBN-93	26
	PSI	ECCO	Averaged	ERANOS	Transport	Het 2D	2D calculation without corrections	ERALIB-1	33
	KIT	SIMMER-IV	Averaged	SIMMER-IV	Transport	Hom	Homogeneous (0D) calculation without corrections	KFKINR-26	11
	ANL	MC^2-2	Averaged	DIF3D/VARIANT	Transport	Hom	Heterogeneous (2D) calculation + corrected cross-sections with Monte-Carlo method	ENDF/B-VII	33

8.1.1. Nuclear library

The CEA, IGCAR, IRSN and PSI have used ERALIB-1, which is the CEA adjusted version of the European JEF-2.1 library [14–15]. IGCAR and IPPE have used the Russian library ABBN-93 [21]. JAEA and KIT have used their own evaluation files known as JENDL-3.3 [26] and KFKI-NR respectively. ANL used ENDF/B-VII Rev.0 data.

8.1.2. Cell codes and cell calculation schemes

Self-shielded cross-sections of structure media have been computed with homogeneous models. Various cell models have been used for fuel media. KIT has used a homogeneous cell model with an 11-group energetic scheme. JAEA (SLAROM-UF [27]) and IGCAR (CONSYST) have used 1D cell model for fuel assemblies with 70-group and 26-group energetic scheme respectively. Self-shielding and slowing down are treated in JAEA calculations with an ultra-fine energetic scheme (100,000 groups) in order to refine the resonance shielding treatment for the core reactivity and control rod worth estimations. CEA, PSI, IRSN and IGCAR (ECCO [11], [16]) have used 2D models for fuel cells with a 33-group energetic scheme. Self-shielding and slowing down are treated with a fine energetic scheme (1968 groups) in order to produce 33-group effective cross-sections. IPPE (CONSYST) has used 2D model for fuel cells with a 299-group energetic scheme. ANL has

used homogeneous cell calculations, starting with a 2082 cross-section data library in MC^2-2, to generate 33-group cross-sections for the whole-core analysis.

8.1.3. Core solvers

The transport theory has been used by most of the participants except IGCAR and JAEA. IGCAR and JAEA have used the diffusion theory with transport theory corrections for the core reactivity estimations. IPPE has used Monte Carlo estimations using the MMKENO code.

8.1.4. Control rod cross-section processing schemes

The processing of control rod self-shielded cross-sections needs specific schemes in order to accurately treat the local effects in absorber rods. CEA, IRSN and IGCAR have used a 2D SN transport calculation (BISTRO [18]) on the refined control rod geometry in order to correct ECCO cross-sections with a reactivity equivalence method [17]. IGCAR has used a 2D Pij transport calculation in order to correct CONSYST cross-sections with a flux preservation method [22]. JAEA has used a reaction-rate ratio preservation method on a 1D cell model in SLAROM-UF cross-sections [30–31]. KIT, PSI and IPPE have not used refined schemes for control rod cross-section processing. A 7-sub-assembly heterogeneous Monte Carlo model was used to obtain correction factors for the equivalent homogeneous control rod cells (hex-Z) in the ANL analysis approach.

8.2. REACTIVITY FOR EACH STEP

Table 57 summarizes the reactivities computed for all the test states. The use of the 'average compositions' assumption leads to significant reactivity bias (~+ 730 pcm) compared with a critical state ('0 pcm'). Uncertainties on axial control rod position and discrepancies on control rod efficiencies are obviously responsible for these reactivity biases even if they cannot totally explain them. A thorough analysis of core geometry and mass by JAEA has shown a few deviations in heavy nuclide mass which cannot explain current discrepancies. Focus on ERANOS reactivity results shows a reactivity impact of less than 200 pcm due to core solvers (diffusion, transport), which contributes to the current discrepancies, but cannot totally explain the differences. Remaining discrepancies come from nuclear data and cell calculation methods. It is also important to focus on fission products. Virtual fission products given in the benchmark specifications were coherent with the model used in the ERALIB-1 nuclear library: '1 fission produces 2 virtual fission products'. On the contrary, models used in ABBN-93, for example, make the following assumption: '1 fission produces 1 virtual fission product'. This inconsistency, if not corrected, can lead to the overestimation of the fission product reactivity worth. IGCAR/FARCOB has corrected this in their core model to be consistent with input data, while KIT and IPPE have not.

TABLE 57. REACTIVITY FOR THE 4 STATES OF THE WITHDRAWAL TEST

Participant	Reference State	CR No 4 inserted	CR No 1 extracted & CR No 4 inserted	CR No 1 extracted
IPPE	211 pcm	233 pcm	227 pcm	265 pcm
JAEA	488 pcm	500 pcm	499 pcm	501 pcm
CEA *(ave. / det.)*	986 / 261 pcm	998 / 268 pcm	996 / 268 pcm	997 / 272 pcm
IRSN	1002 pcm	1016 pcm	1019 pcm	1018 pcm
IGCAR/ERANOS	849 pcm	992 pcm	939 pcm	940 pcm
IGCAR/FARCOB	577 pcm	585 pcm	594 pcm	583 pcm
PSI	590 pcm	600 pcm	598 pcm	598 pcm
KIT	32 pcm	46 pcm	54 pcm	19 pcm

Note that the reactivity swings between one state and the reference state are lower than 20 pcm for all the calculations except IGCAR/FARCOB and IPPE (due to Monte-Carlo uncertainties). These physical parameters depend only on control rod efficiencies, interaction effects between control rods (ex. Shadowing effect, etc.) and control rod shifts.

8.3. CURTAIN TOTAL WORTH AND S-CURVE

8.3.1. Total curtain worth

The total curtain worth is the difference between the core reactivity when the 6 SCPs are completely withdrawn (at 900 mm) and the core reactivity when they are completely inserted (at 0 mm). The SAC rod is supposed to be always withdrawn. Fig. 185 shows the value of the total curtain worth calculated by each participant. KIT and ANL results refer to the pre-test core loading plan while all the others refer to the post-test core loading plan. Nevertheless, since the difference in control rod worth for the two plans is small (cf. Section 6), it seemed reasonable to include these results in the comparison.
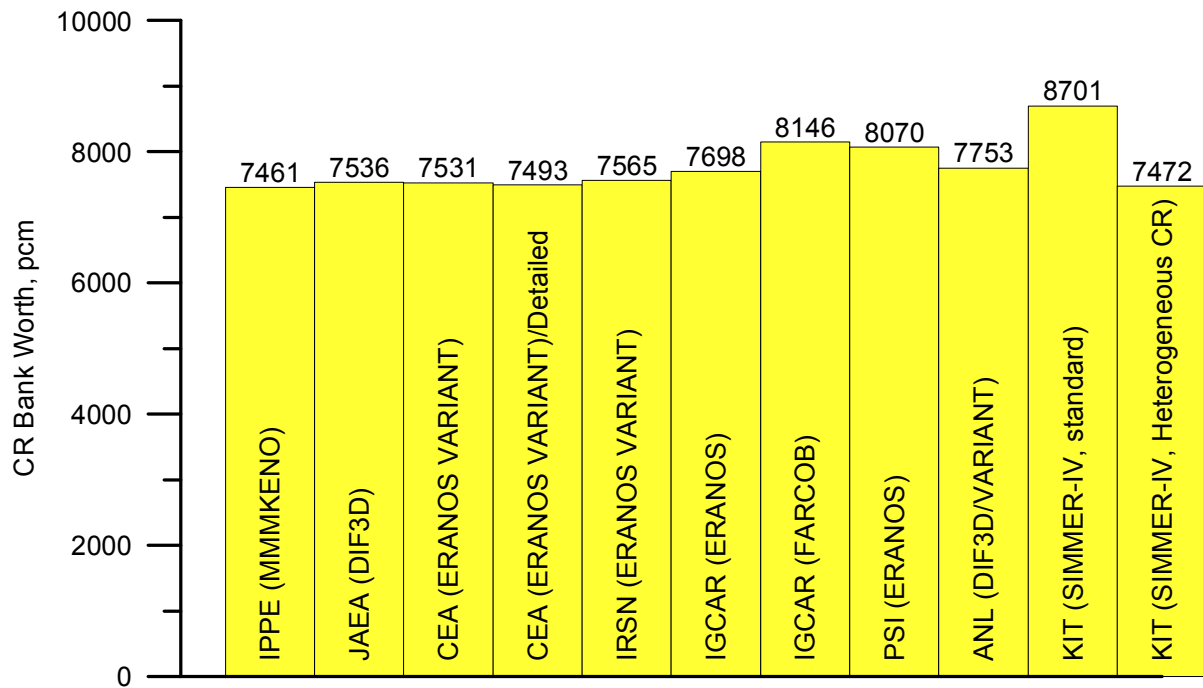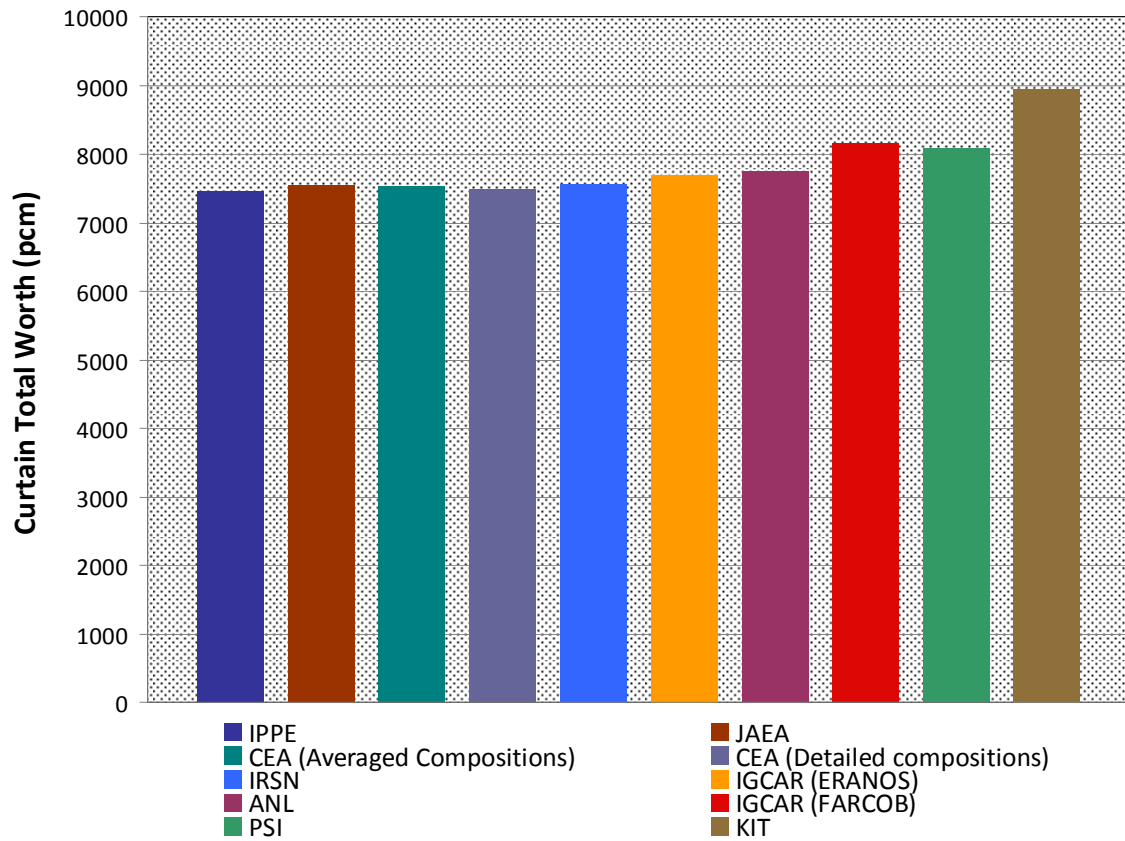
FIG. 185. Total worth of 6 SCP's calculated by the participants.

TABLE 58. TOTAL WORTH OF ABSORBER RODS (6 SCPS)

	Participant	Total Curtain Worth (pcm)
	IPPE	7461
	JAEA	7536
	CEA (Averaged Comp.)	7531
	CEA (Detailed Comp.)	7493
	IRSN[13]	7565
	IGCAR: ERANOS	7698
	IGCAR: FARCOB	8146
	PSI	8070
	KIT (Homogeneous Absorber)	8947
	KIT (Heterogeneous Absorber)	7472
	ANL	7753

Results in Fig. 185 and Table 58 can be divided in two groups. This difference can be explained on the basis of the control rod treatment. First group participants use either a Monte-Carlo code (IPPE) or a refined scheme for control rod cross-section processing (JAEA, CEA, IRSN, IGCAR/ERANOS, ANL). Second group participants use deterministic codes without refined scheme for control rod cross-section processing (IGCAR/FARCOB, PSI, KIT), which can lead to an overestimation of the total reactivity worth up to ten percent.

Note that IGCAR/ERANOS and ANL values are slightly higher than the others members of the first group. This is due to the use of the diffusion solver for IGCAR and to the use of homogeneous fuel cell models for ANL.

KIT specifies that a standard SIMMER-IV homogeneous absorber model overestimates the total CR bank worth at about 15%. A simple heterogeneous absorber model can be employed in SIMMER as described in Section 7.6.1. However one should take into account the fact that it makes little sense to include fine control rod effects in severe accident analysis codes like SIMMER, because in typical core disruptive accident simulation, the control rods are usually neglected for the sake of 'conservative' approach. In addition, a special absorber treatment is necessary when CR rods fail and B4C becomes homogeneous forming an eutectic allow with molten steel under high-temperature conditions.

Finally, note that the CEA demonstrated that the discrepancy between an average core model and a detailed one, in terms of sub-assembly compositions, is lower than 0.5% which is negligible.

8.3.2. Control rod efficiencies

S-curves, or control rod efficiency curves, are simulated by extracting all control rods by steps of 100 mm and computing the core reactivity for each state. They are presented in Fig. 186. Note that KIT results are represented by only 7 points since the axial mesh in SIMMER-IV was not designed for S-curve calculations but for the control rod withdrawal test only. Also note that KIT results are given for the standard homogeneous absorber model. Differential efficiency curves, represented in Fig. 187, can be defined as the derivative of the S-curves and represents the reactivity inserted by a control rod insertion of 1 mm.

There is a good agreement among all participants. S-curves shapes differ only on the absolute values of the differential efficiency which is due to the control rod treatment (cf. Section 8.3.1).

---

[13] The IRSN performed also some tests using different calculation options. They are discussed in chapter 7.4.
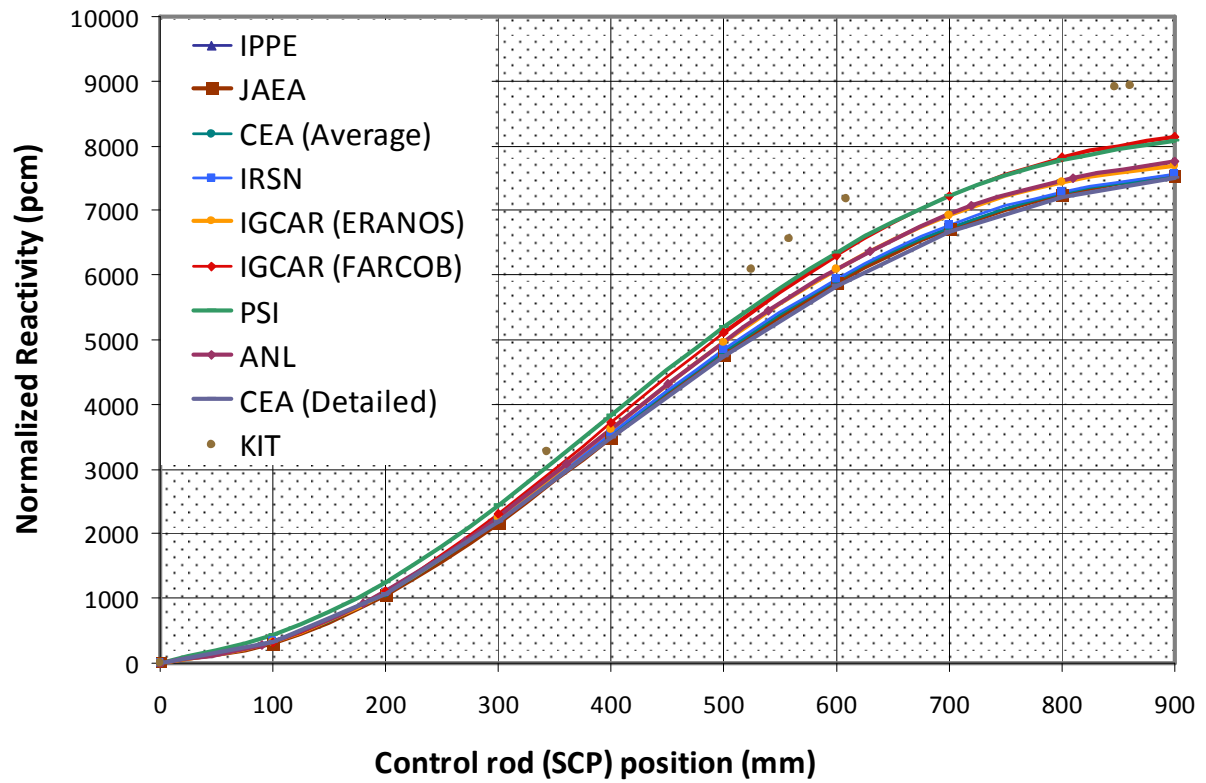
FIG. 186. Control rod efficiencies calculated by the participants.
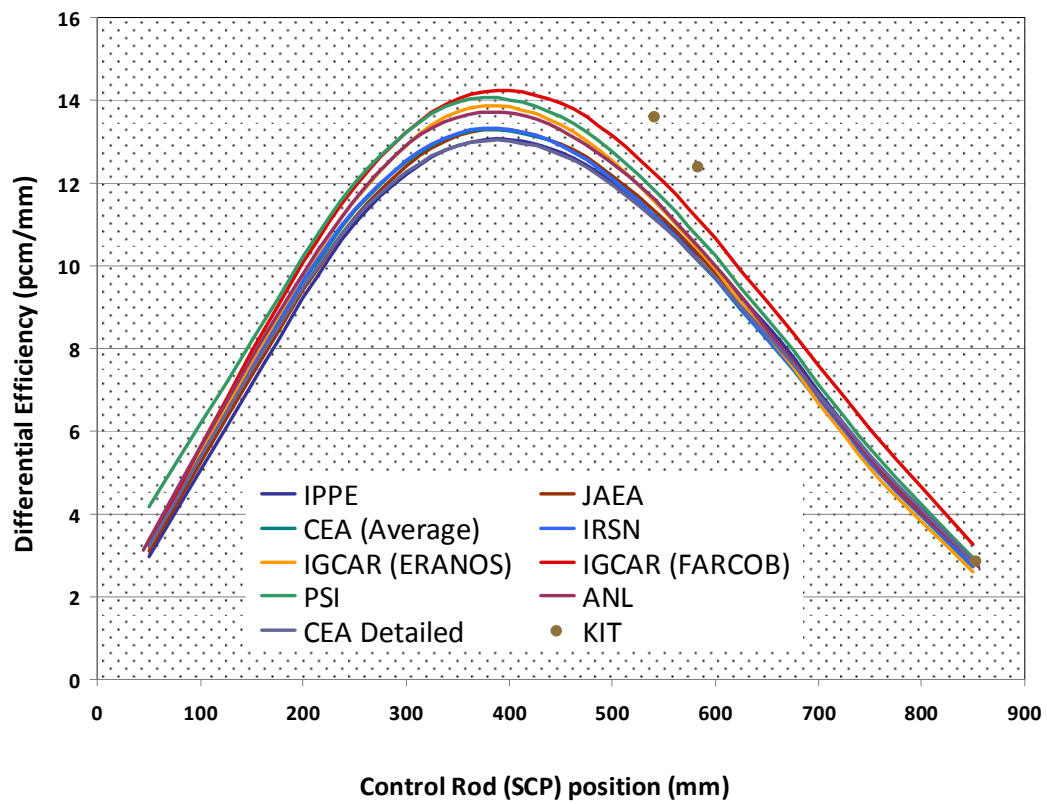
FIG. 187. Differential efficiencies calculated by the participants.

These comparisons finally stressed the need of using refined schemes for control rod cross-section processing in order to estimate control rod efficiencies. The results from KIT on S-curve are not enough to allow a complete comparison with the other participants. SIMMER-IV results on S-curve are given for the standard homogeneous absorber model. Preliminary calculations (see Section 7.6.1) show that introduction of the heterogeneous SIMMER model allows more accurate prediction of the S-curve, similar to the ones from other participants.

8.4. COMPARISON OF POWER ESTIMATIONS

Comparisons between calculated and measured power and power deviation values were only done on the first six S/A rings, which corresponds to the monitored part of the core.

8.4.1. Powers by sub-assembly

The powers per subassembly for the reference state and the maximal deformation state are shown in Fig. 188–189 in a S/A line from 20/8 to 20/32. The standard deviation among the participants hardly reached 5% on the fissile core, which is a good point. Discrepancies between measured and calculated values are significant and can be explained by the average core description (see the CEA results for the averaged core and the detailed one). Studies performed with a detailed description of S/As show lower discrepancies (<3%).

All the S/A powers for all steps estimated by each participant are detailed in Fig. 190–197. For the reference case, a comparison is also provided among the participants in Fig. 198–199.

CEA (averaged)	Fig. 190 (page 182)
IGCAR (ERANOS)	Fig. 191 (page 182)
IGCAR (FARCOB)	Fig. 192 (page 183)
IPPE (MMKKENO)	Fig. 193 (page 183)
IRSN	Fig. 194 (page 184)
JAEA	Fig. 195 (page 184)
KIT	Fig. 196 (page 185)
PSI	Fig. 197 (page 185)

Core maps showing ratio between calculated and measured powers (C/M) per S/A are given in Fig. 200–239 for all states. All results are presented with the same color scale in order to simplify comparisons.

CEA (averaged)	Fig. 200–203 (page 187)
CEA (detailed)	Fig. 204–207 (page 189)
IGCAR (ERANOS)	Fig. 208–211 (page 191)
IGCAR (FARCOB)	Fig. 212–215 (page 193)
IPPE (MMKKENO)	Fig. 216–219 (page 195)
IPPE (TRIGEX)	Fig. 220–223 (page 197)
IRSN	Fig. 224–227 (page 199)
JAEA	Fig. 228–231 (page 201)
KIT	Fig. 232–235 (page 203)
PSI	Fig. 236–239 (page 205)
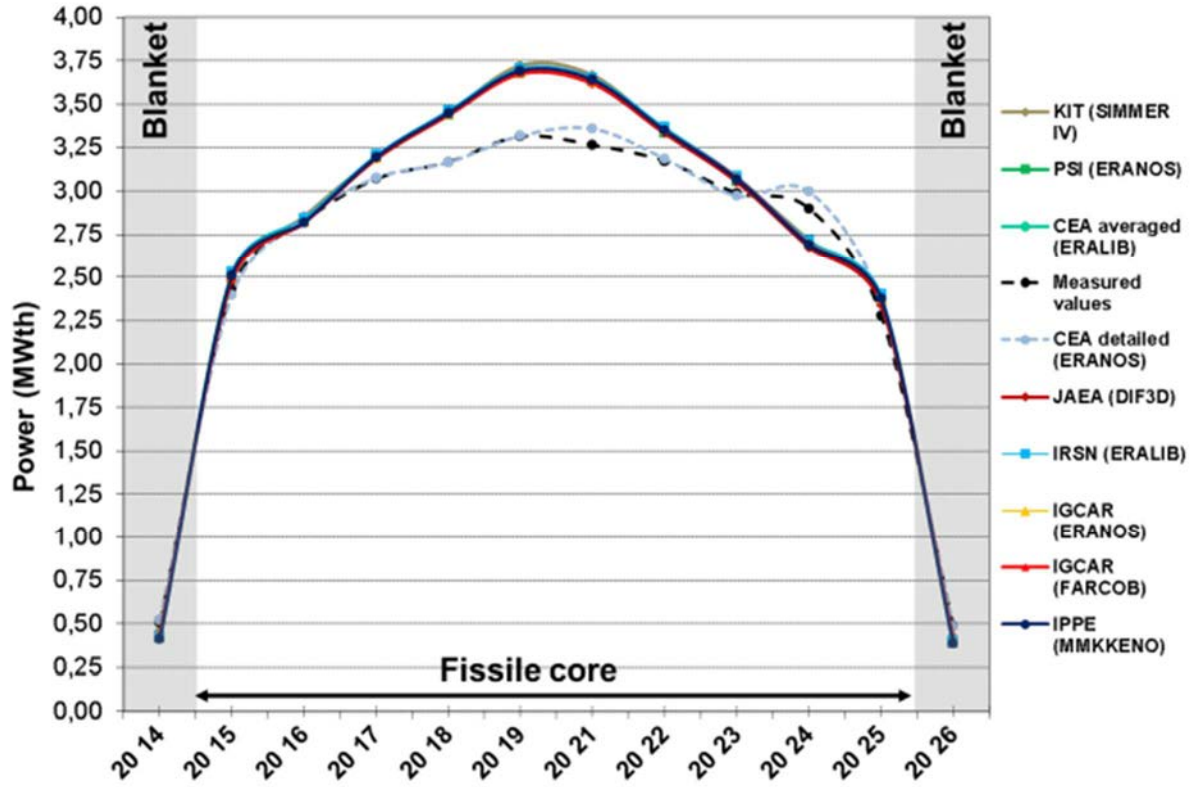
FIG. 188. Comparison between calculated and measured values (reference state).
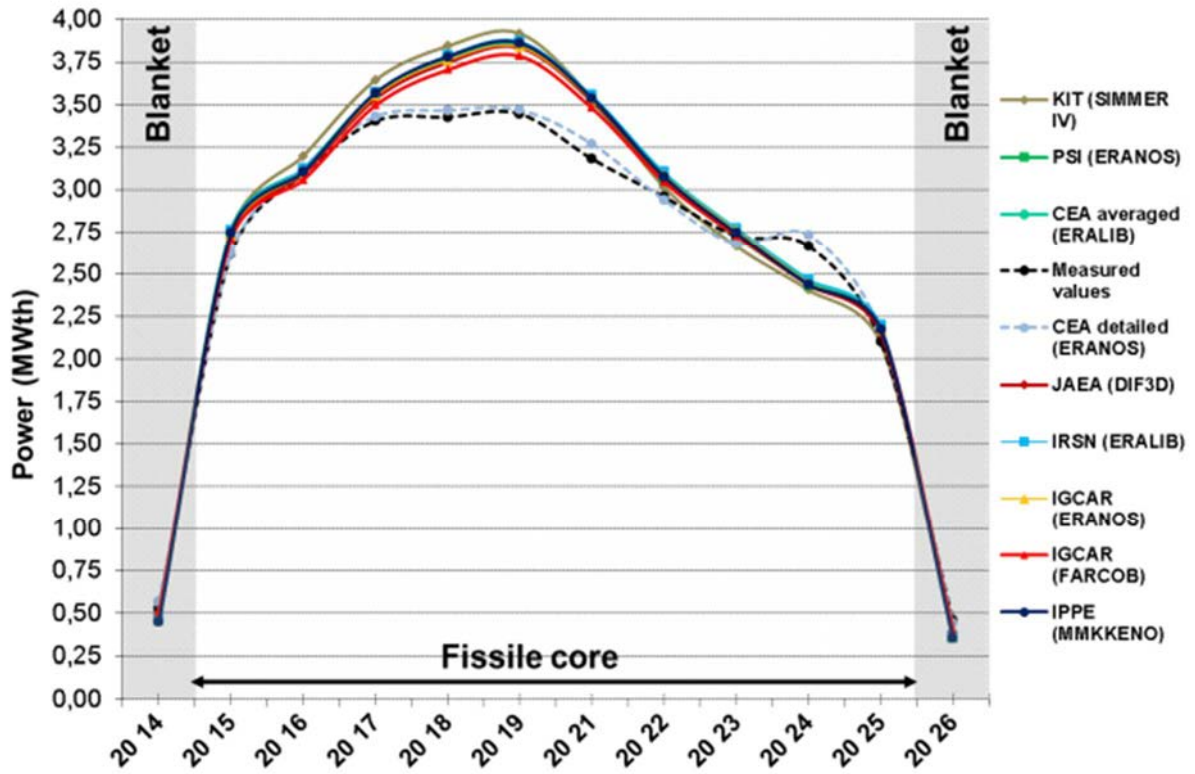
FIG. 189. Comparison between calculated and measured values (CR No 4 inserted & CR No 1 extracted).

181
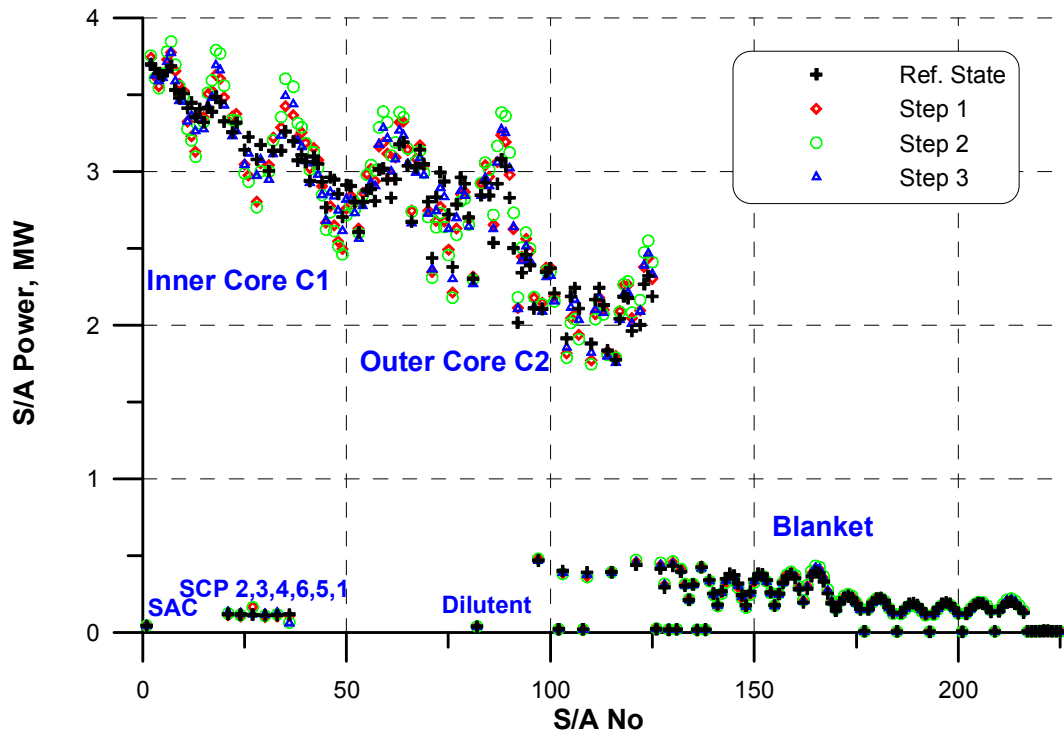
FIG. 190. S/A power for all core configurations: CEA.
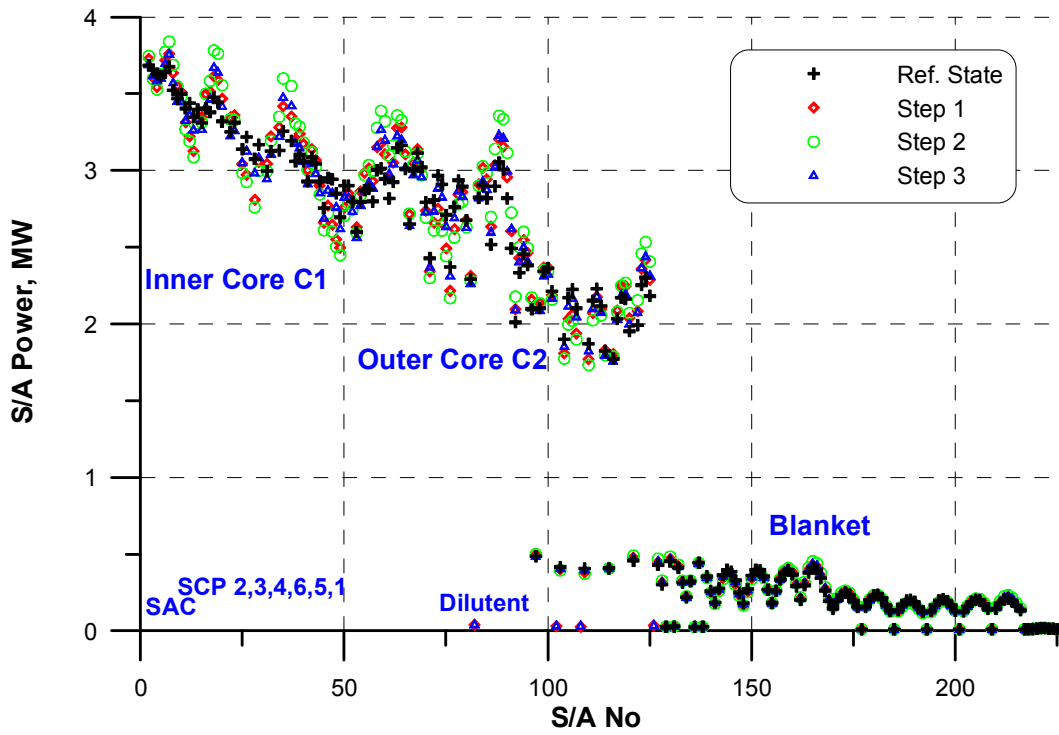
FIG. 191. S/A power for all core configurations: IGCAR-ERANOS.
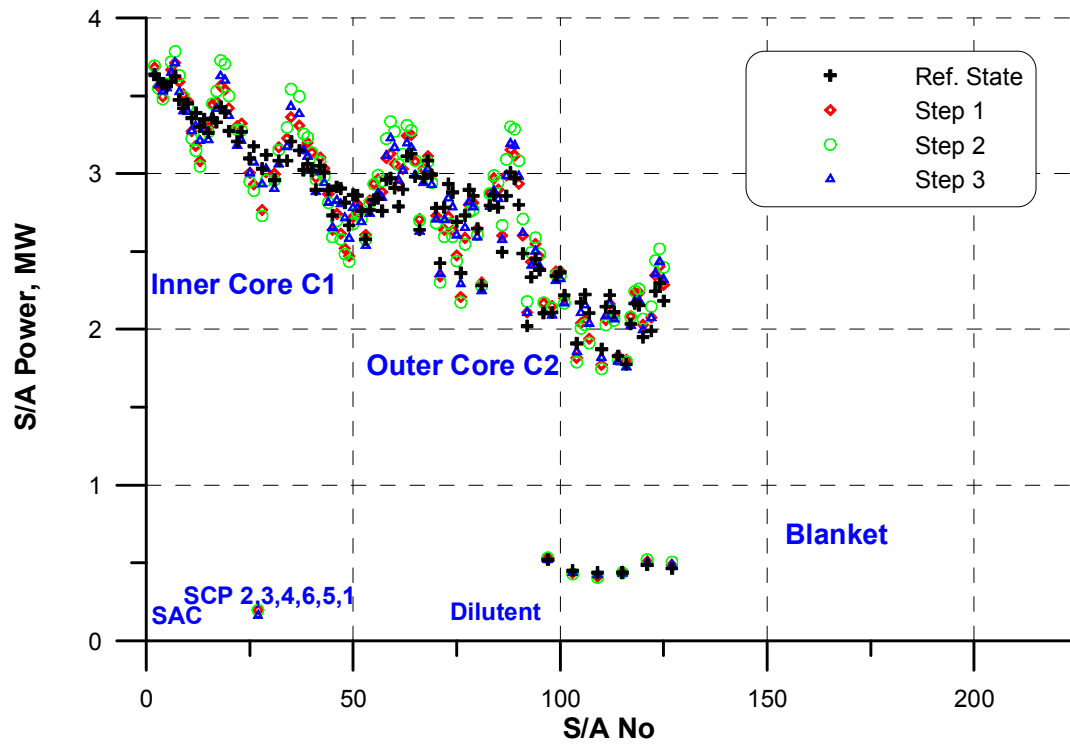
FIG. 192. S/A power for all core configurations: IGCAR-FARCOB.
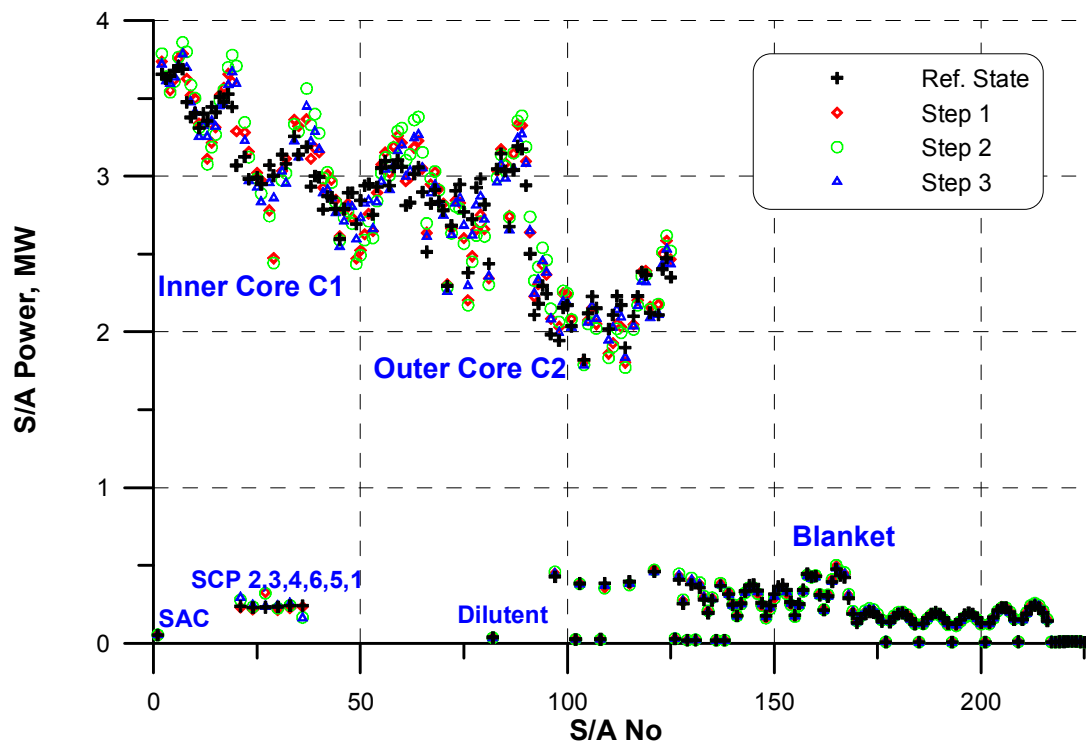
FIG. 193. S/A power for all core configurations: IPPE-MC.
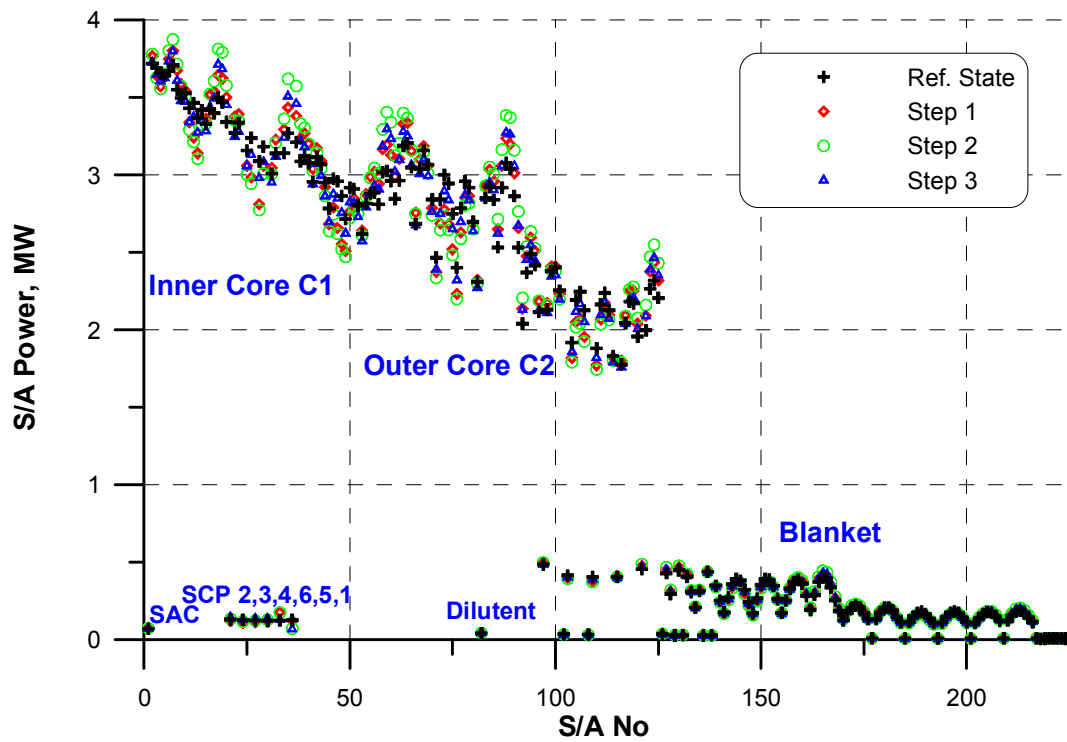
FIG. 194. S/A power for all core configurations: IRSN.
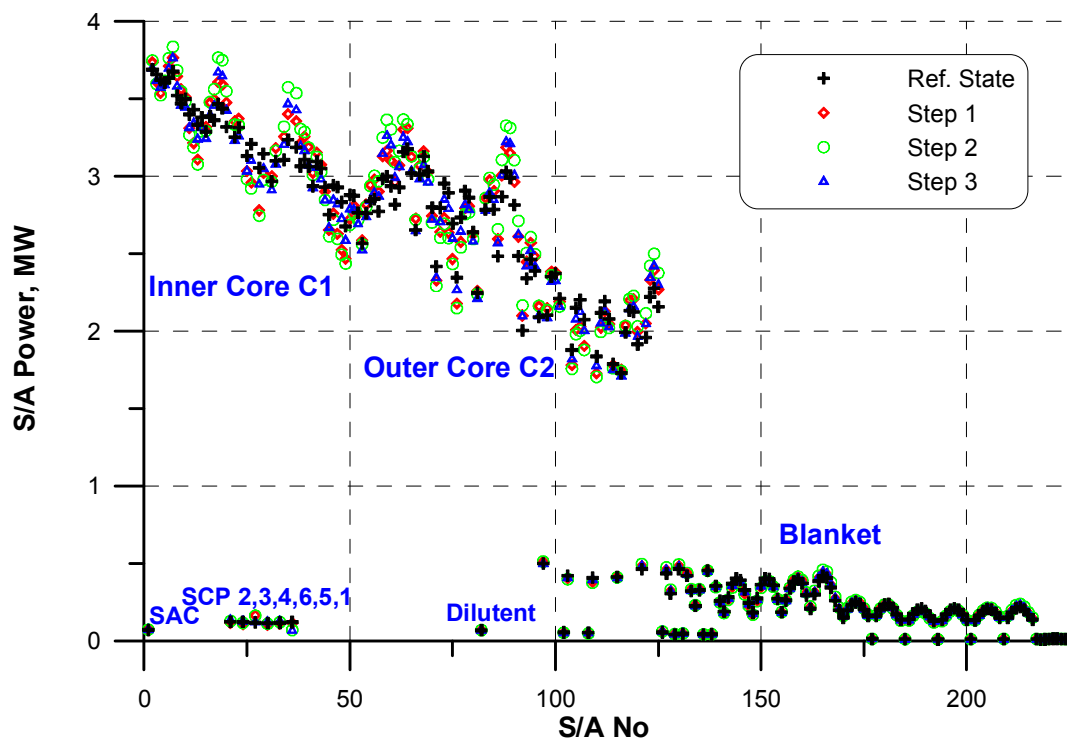
FIG. 195. S/A power for all core configurations: JAEA.
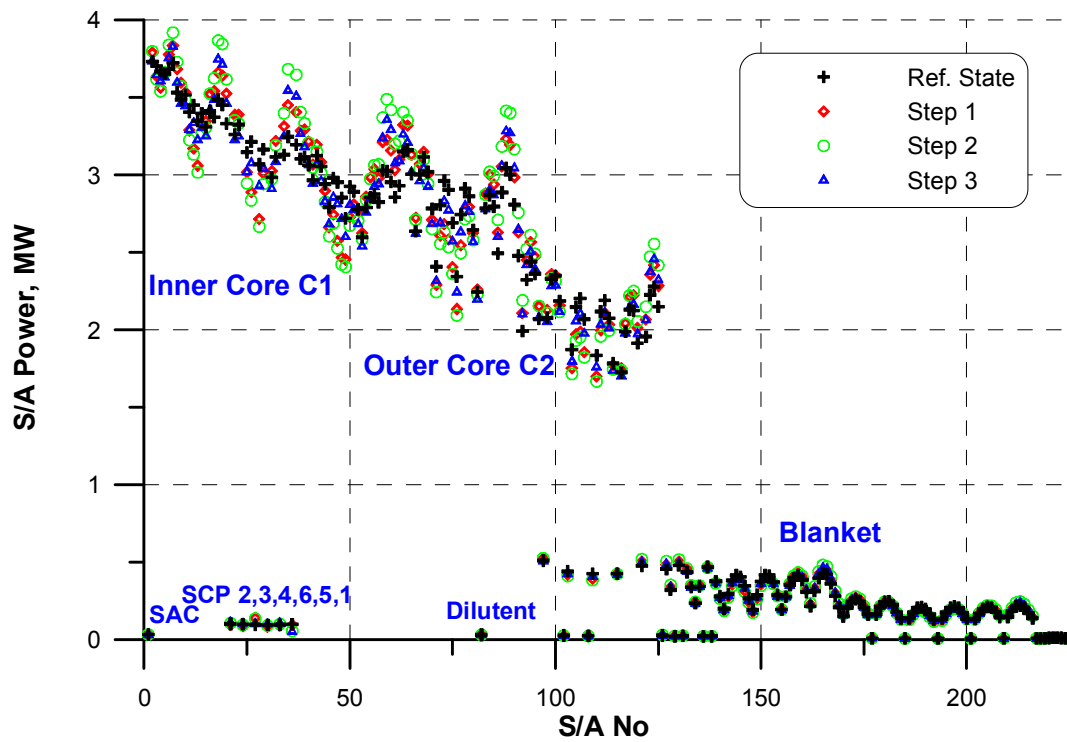
FIG. 196. S/A power for all core configurations: KIT.
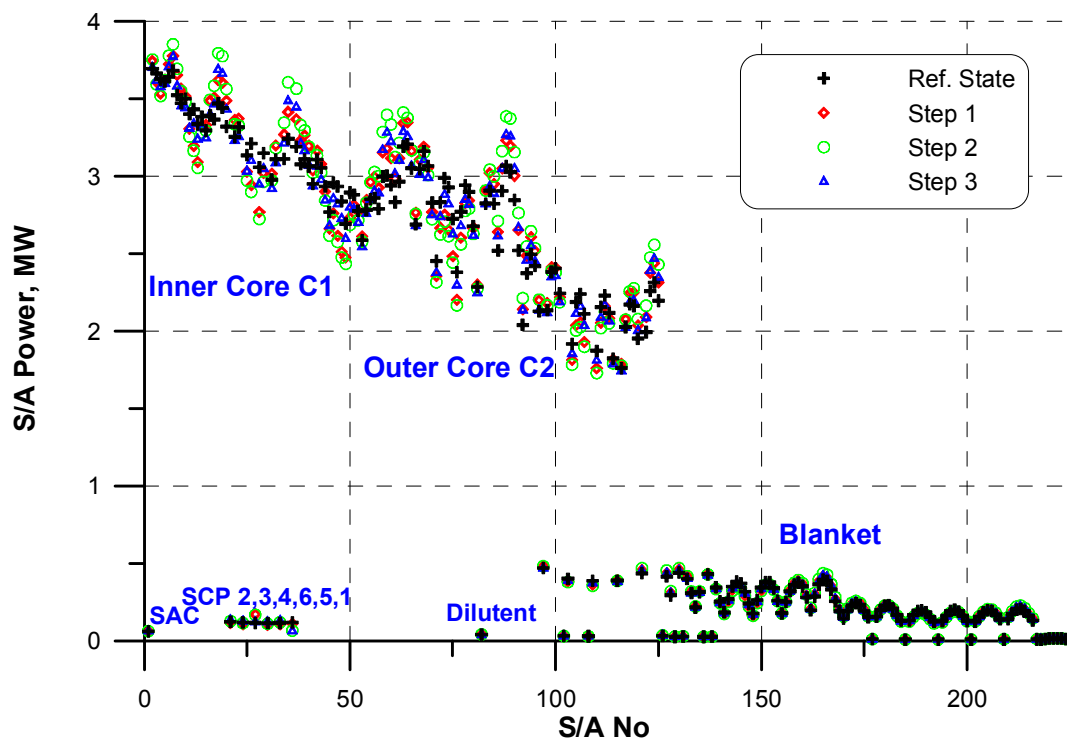
FIG. 197. S/A power for all core configurations: PSI.
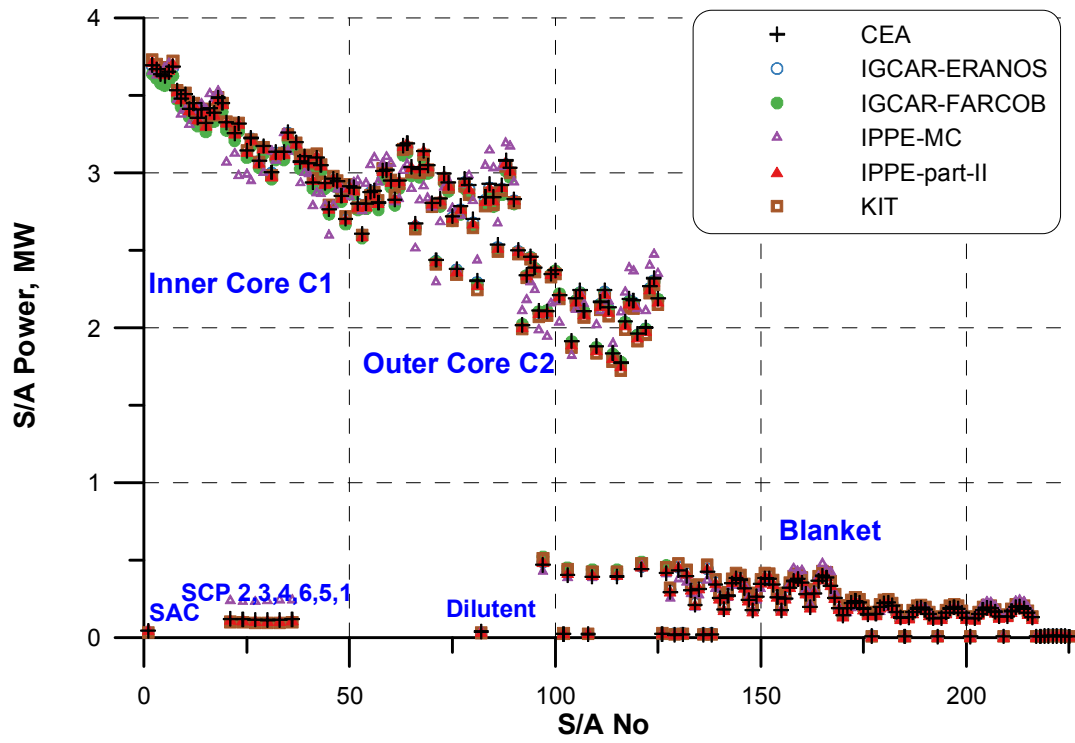
FIG. 198. Comparison of S/A power for the reference state (Part-1).
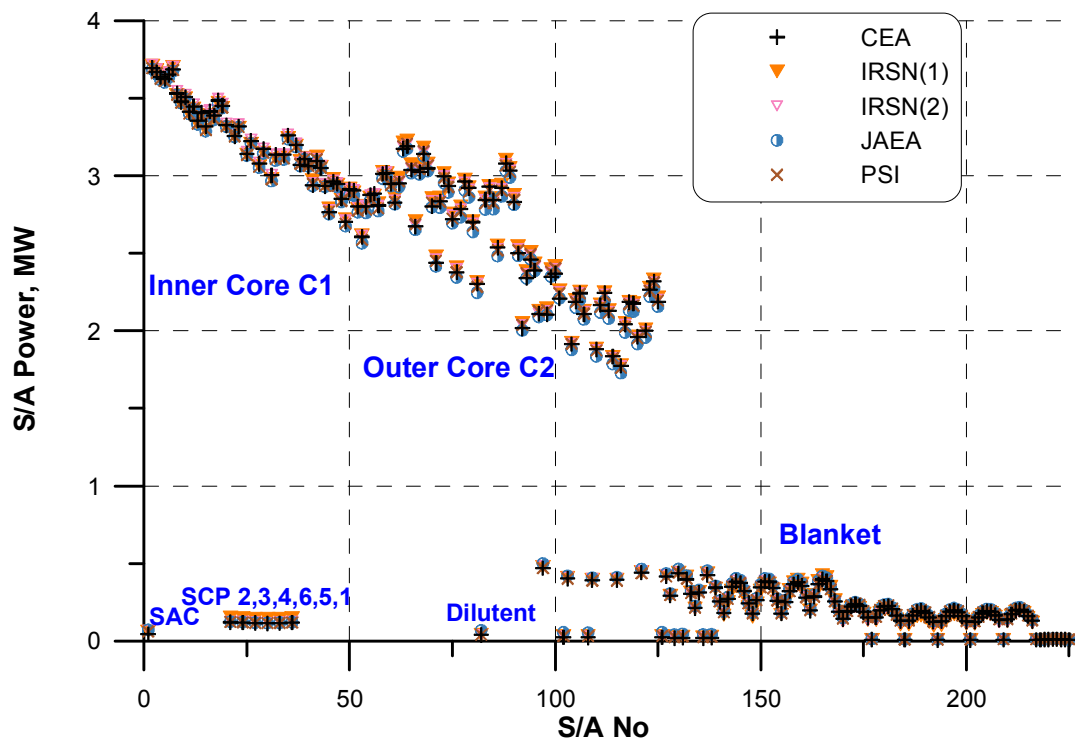
FIG. 199. Comparison of S/A power for the reference state (Part-2).
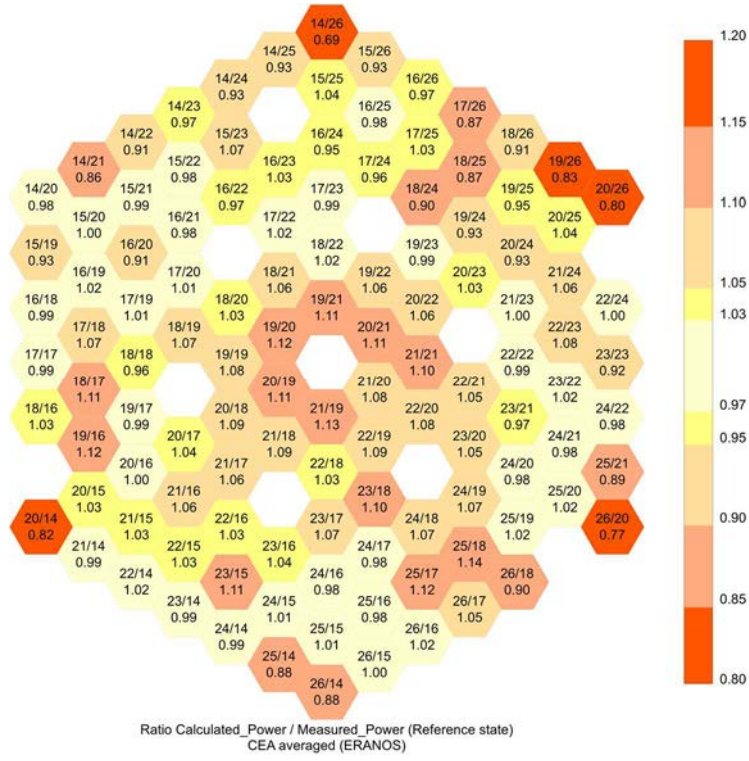
FIG. 200. C/E of S/A power for the reference state: CEA-ERANOS (averaged).
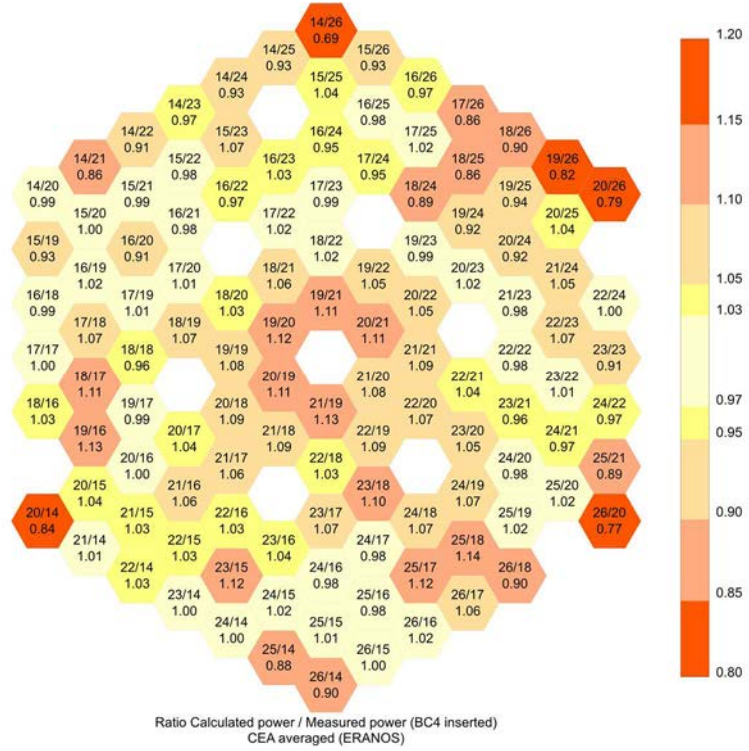
FIG. 201. C/E of S/A power for the step 1: CEA-ERANOS (averaged).

187
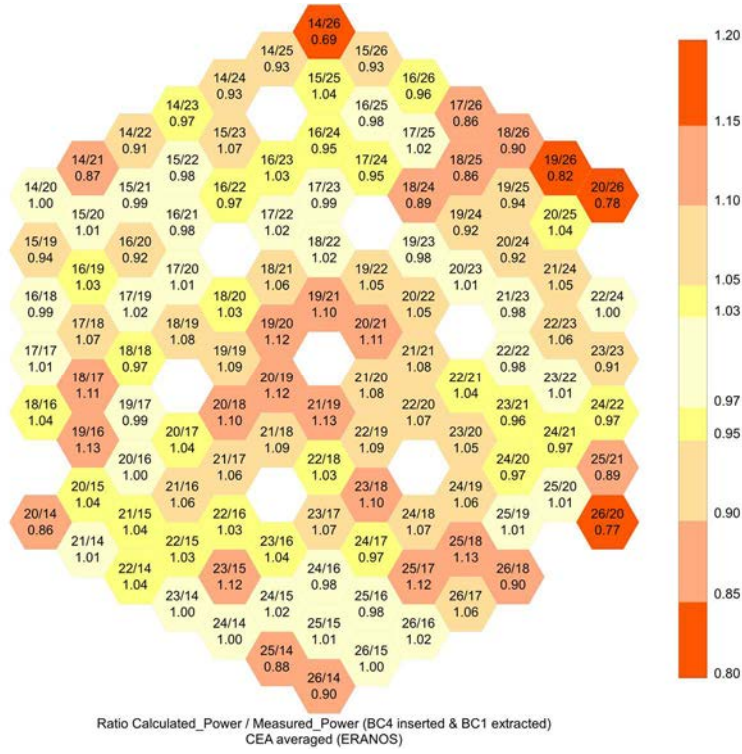
FIG. 202. C/E of S/A power for the step 2: CEA-ERANOS (averaged).
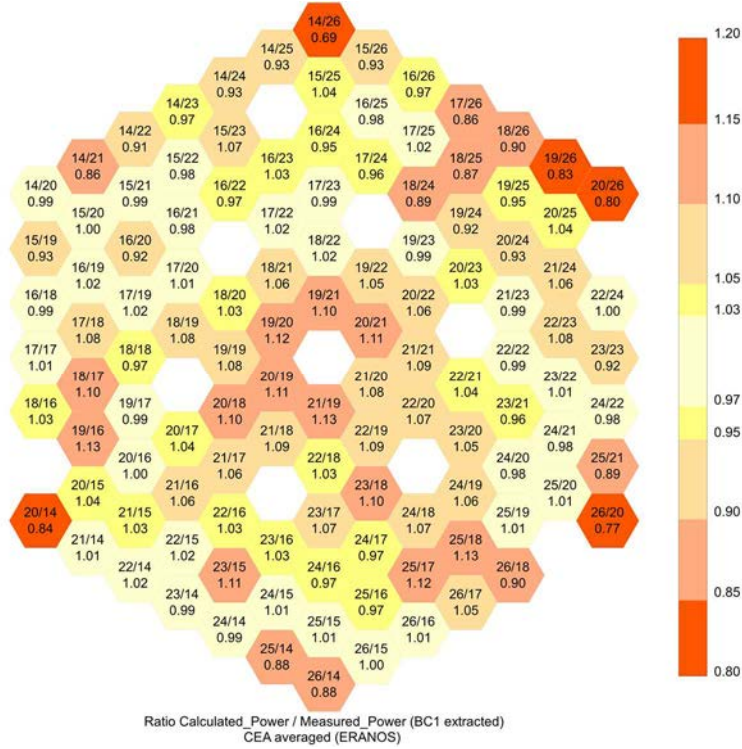
FIG. 203. C/E of S/A power for the step 3: CEA-ERANOS (averaged).
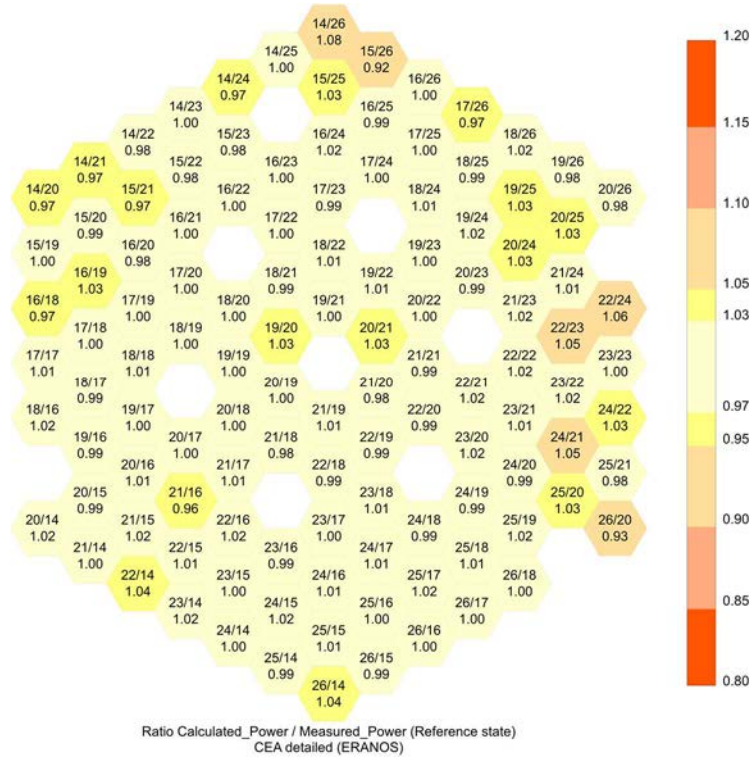
FIG. 204. C/E of S/A power for the reference state: CEA-ERANOS (detailed).
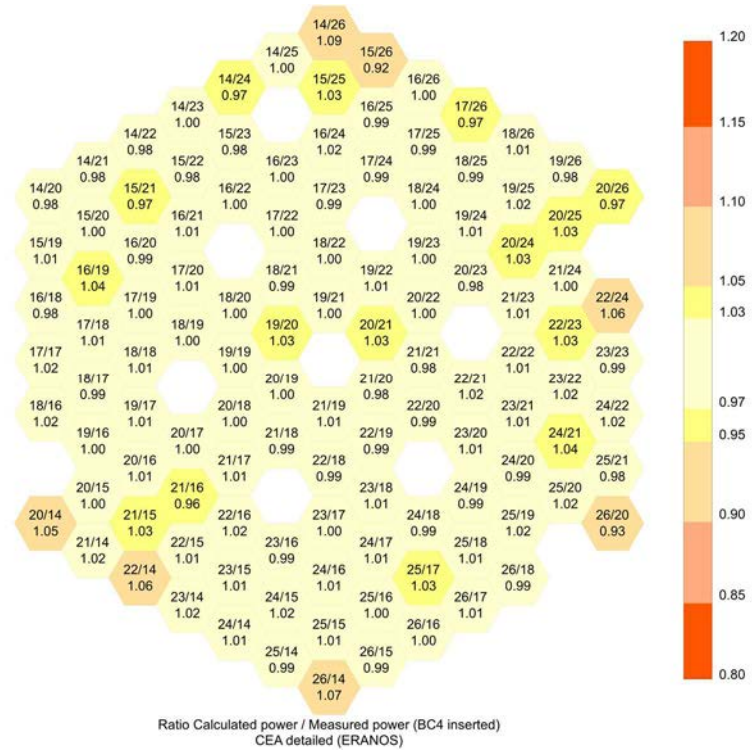
FIG. 205. C/E of S/A power for the step 1: CEA-ERANOS (detailed).
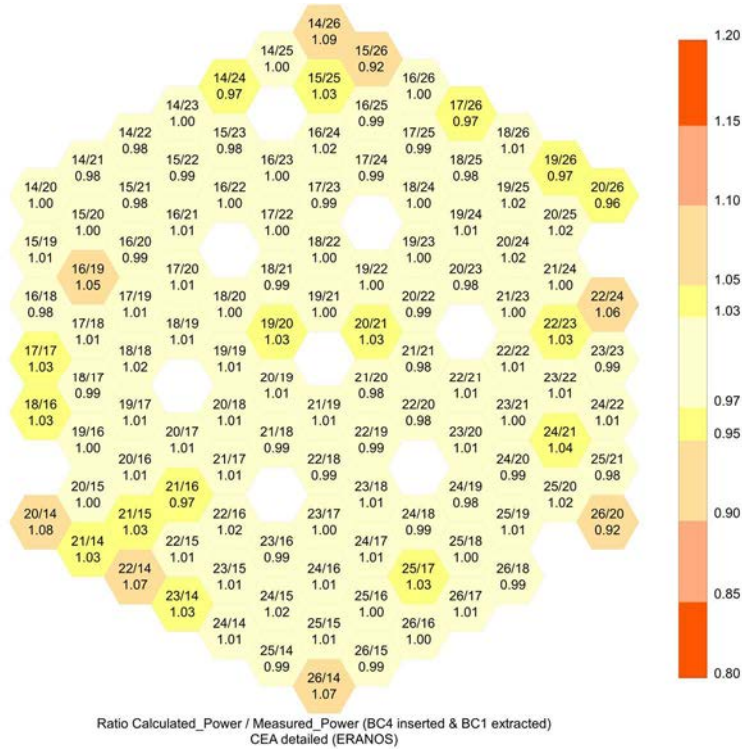
FIG. 206. C/E of S/A power for the step 2: CEA-ERANOS (detailed).
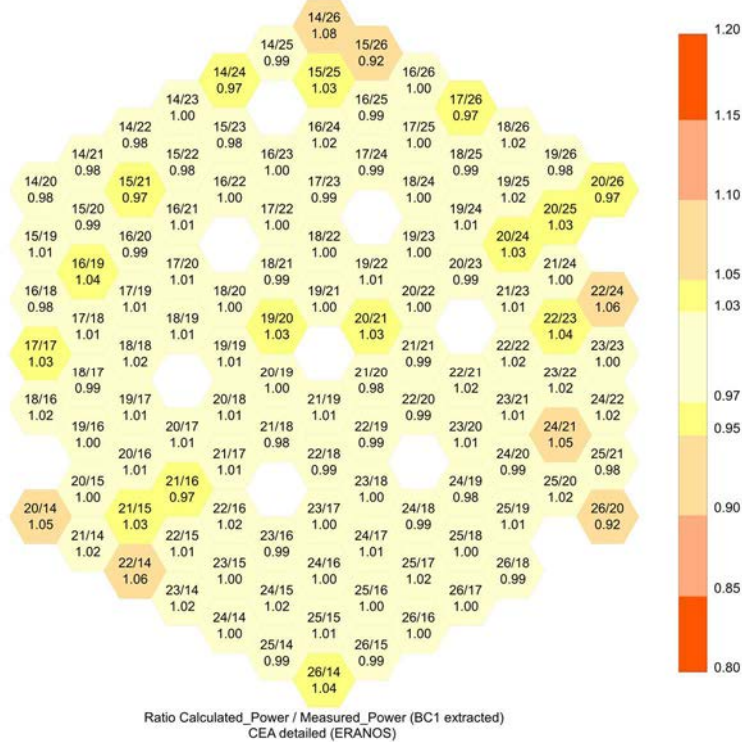
FIG. 207. C/E of S/A power for the step 3: CEA-ERANOS (detailed).
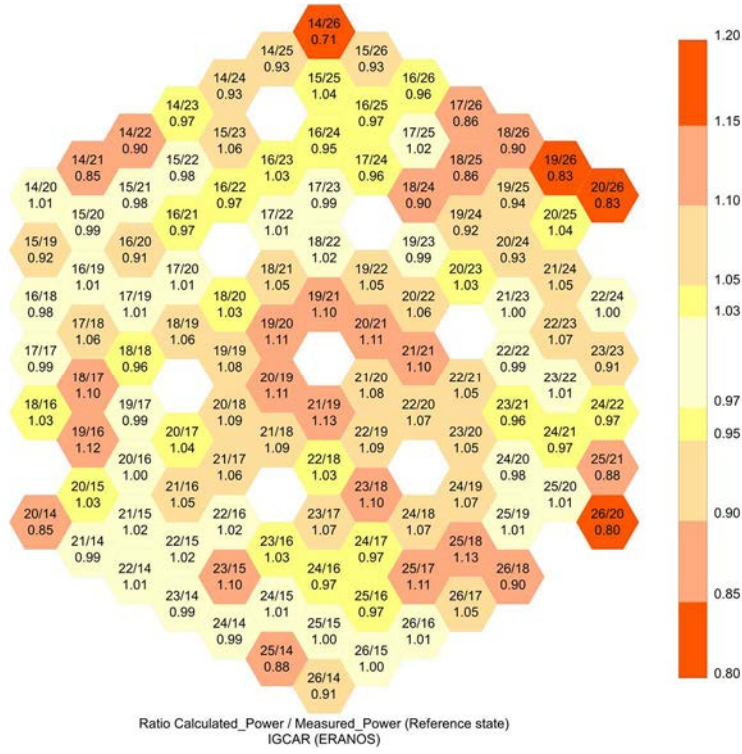
FIG. 208. C/E of S/A power for the reference state: IGCAR-ERANOS.
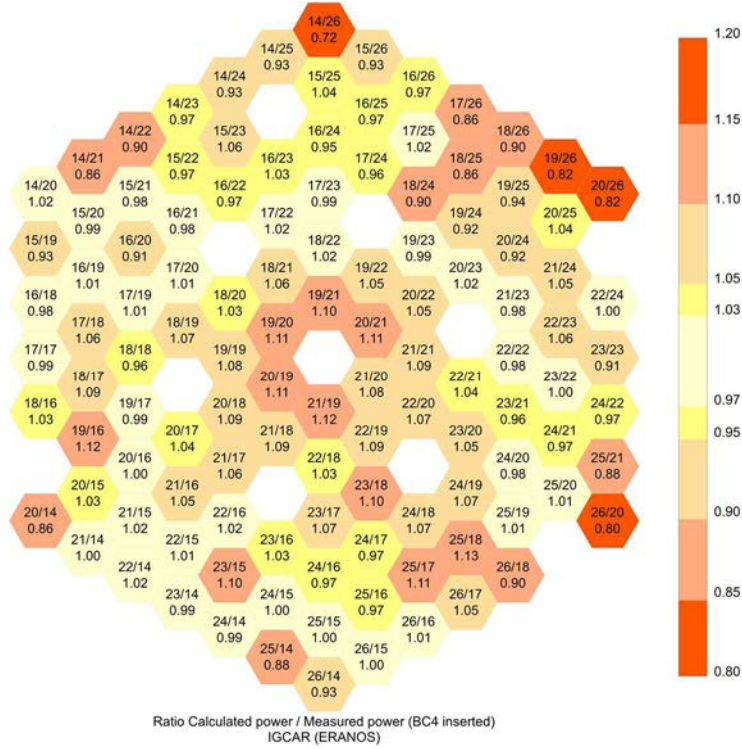
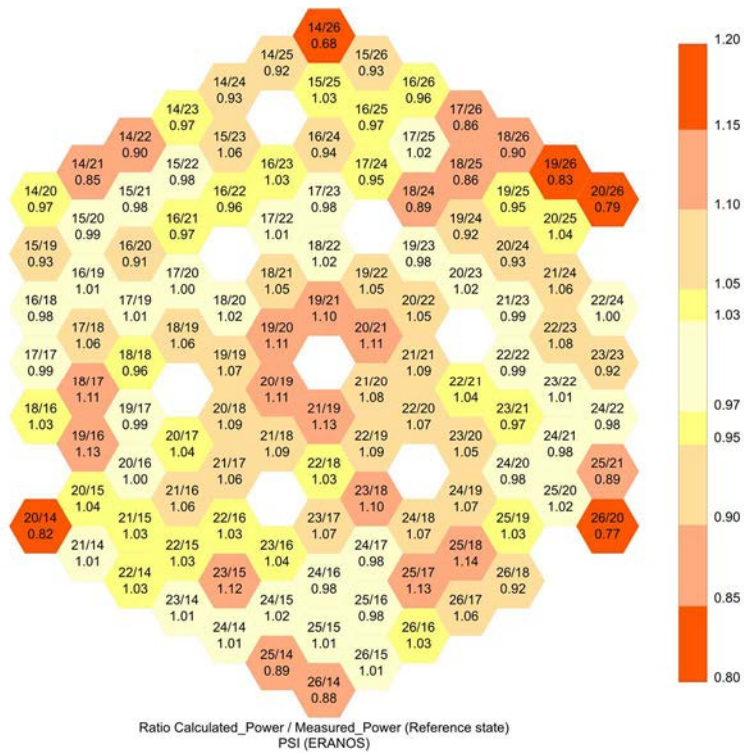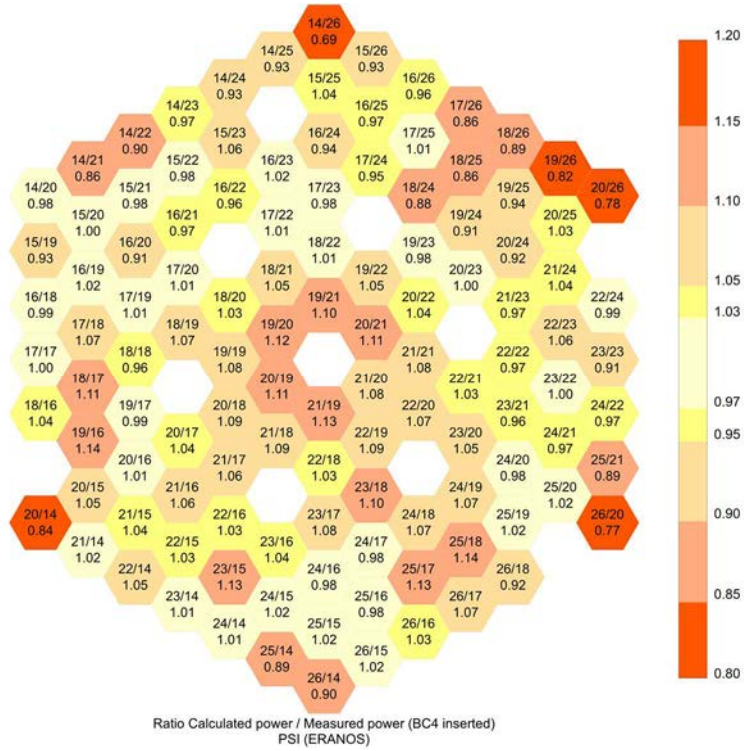*FIG. 209. C/E of S/A power for the step 1: IGCAR-ERANOS.*
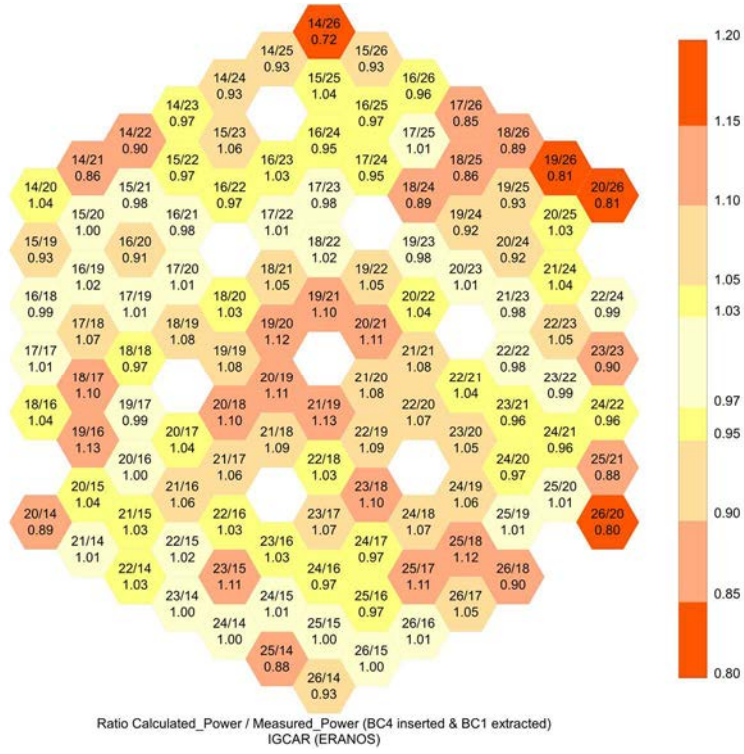
FIG. 210. C/E of S/A power for the step 2: IGCAR-ERANOS.
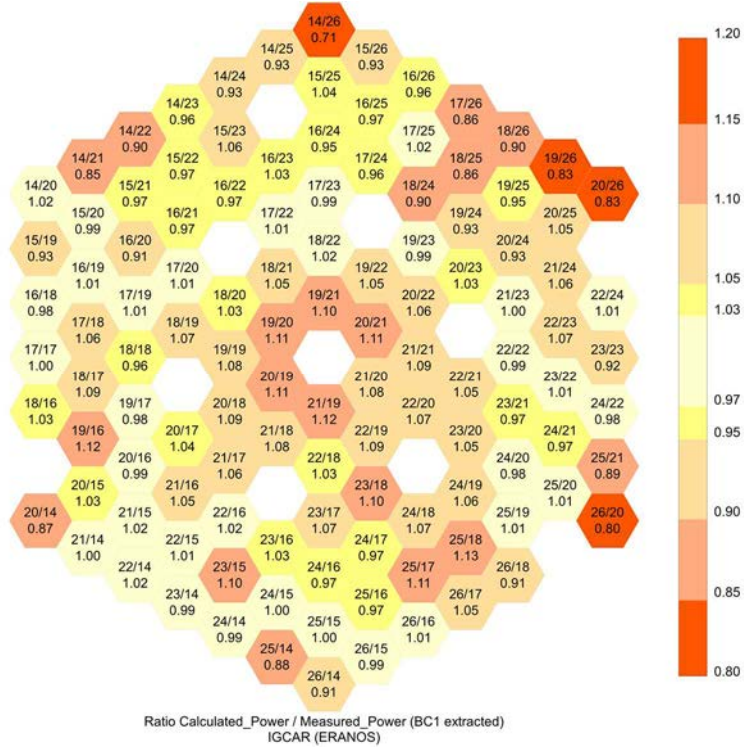
FIG. 211. C/E of S/A power for the step 3: IGCAR-ERANOS.
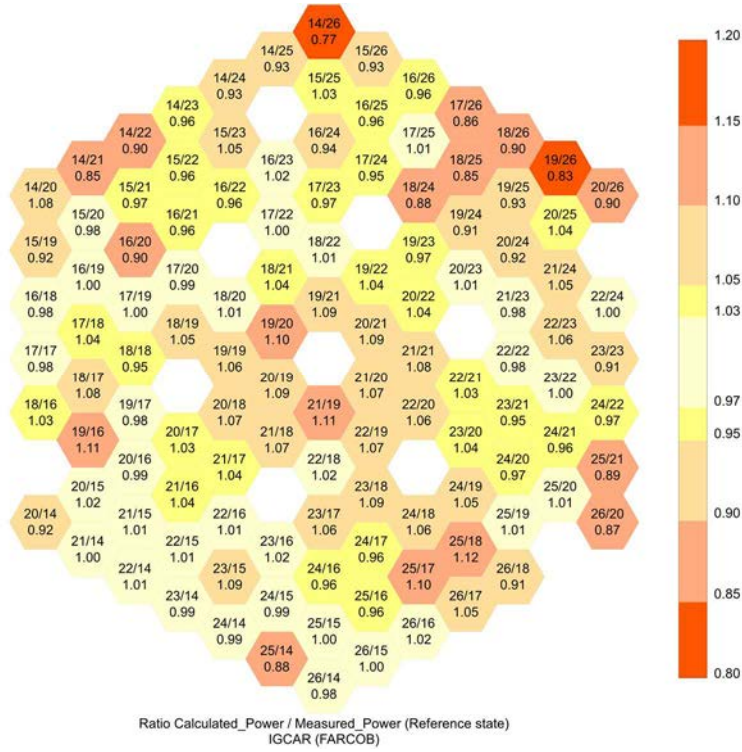
FIG. 212. C/E of S/A power for the reference state: IGCAR-FARCOB.
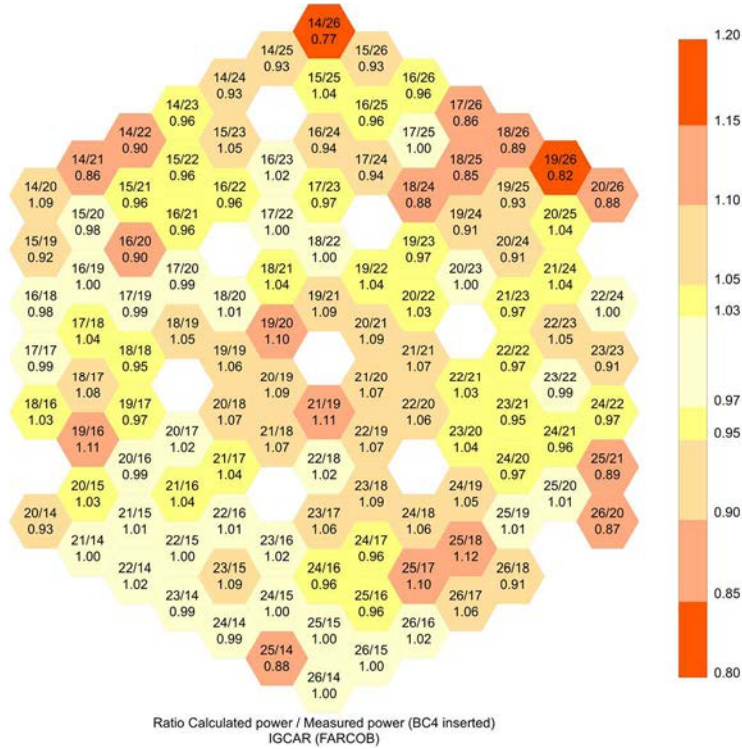
FIG. 213. C/E of S/A power for the step 1: IGCAR-FARCOB.
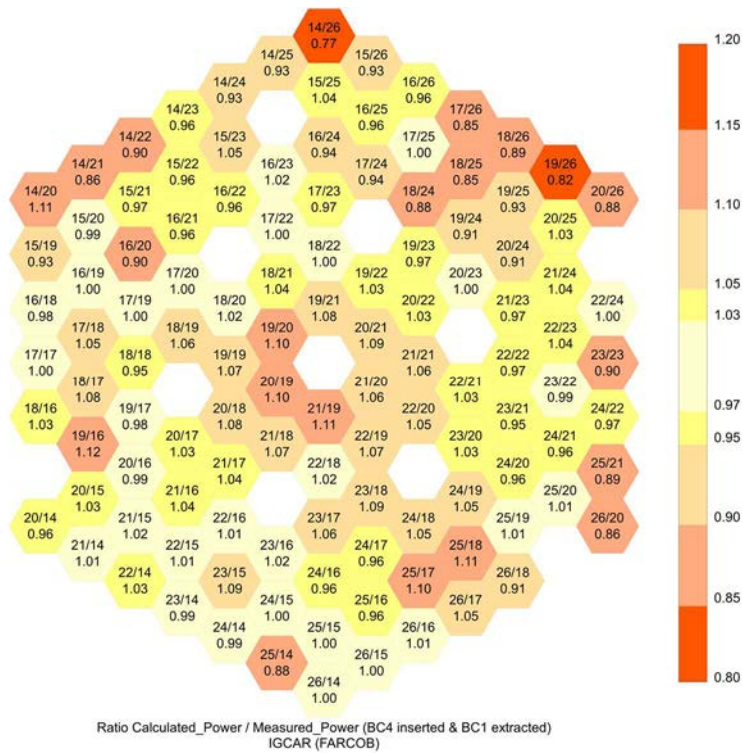
FIG. 214. C/E of S/A power for the step 2: IGCAR-FARCOB.
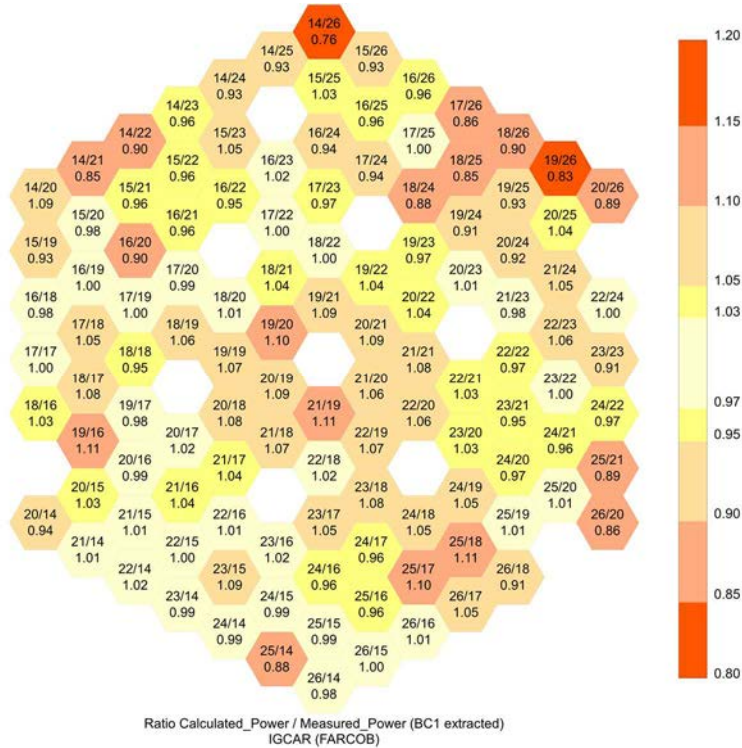
FIG. 215. C/E of S/A power for the step 3: IGCAR-FARCOB.
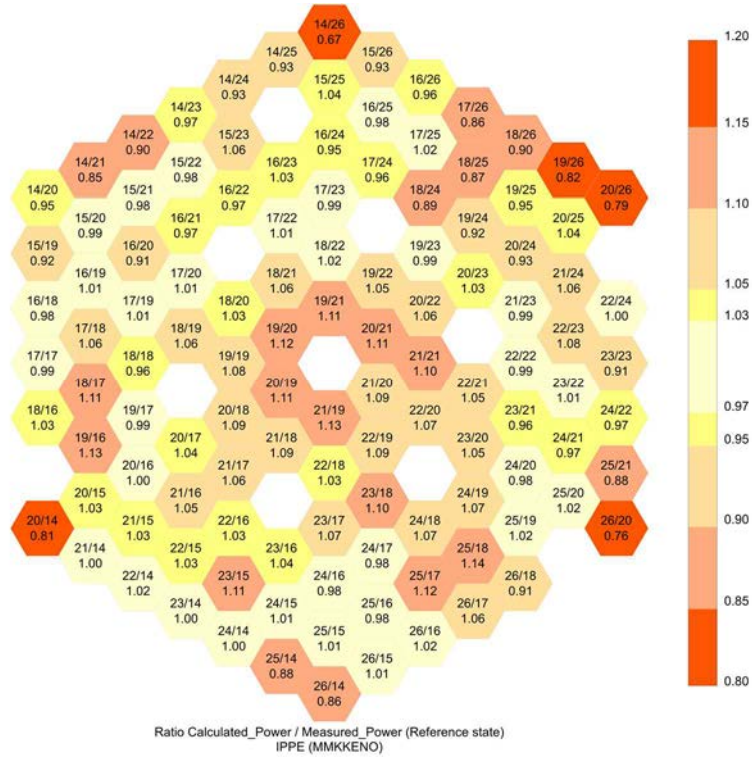
FIG. 216. C/E of S/A power for the reference state: IPPE-MMKKENO.
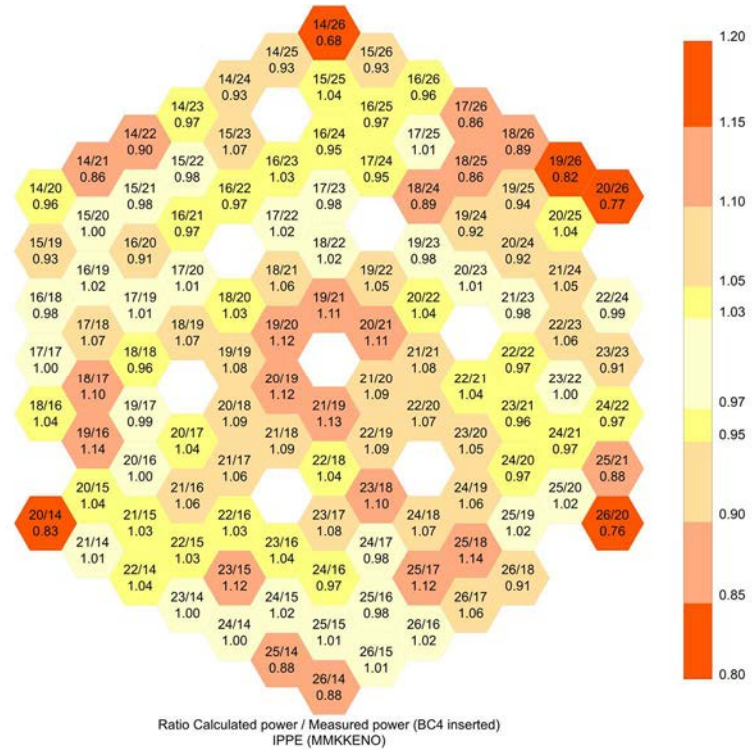
FIG. 217. C/E of S/A power for the step 1: IPPE-MMKKENO.
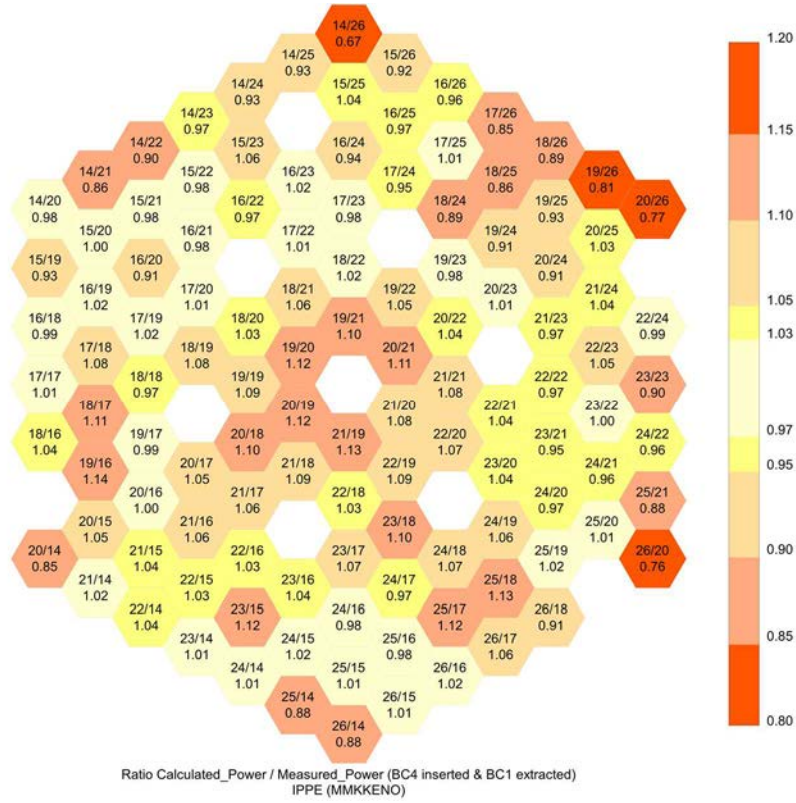
FIG. 218. C/E of S/A power for the step 2: IPPE-MMKKENO.
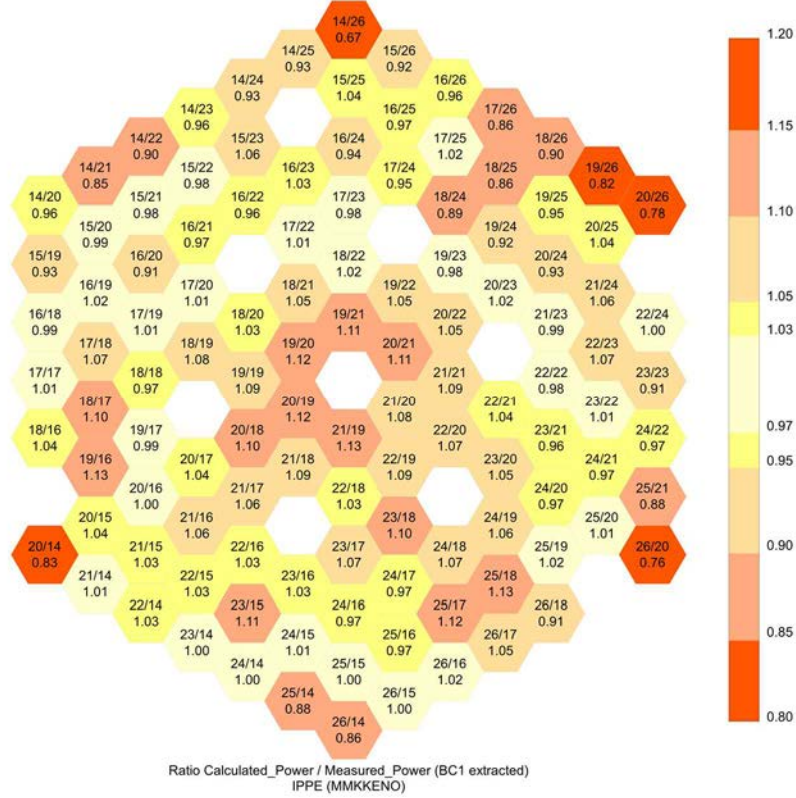

FIG. 219. C/E of S/A power for the step 3: IPPE-MMKKENO.
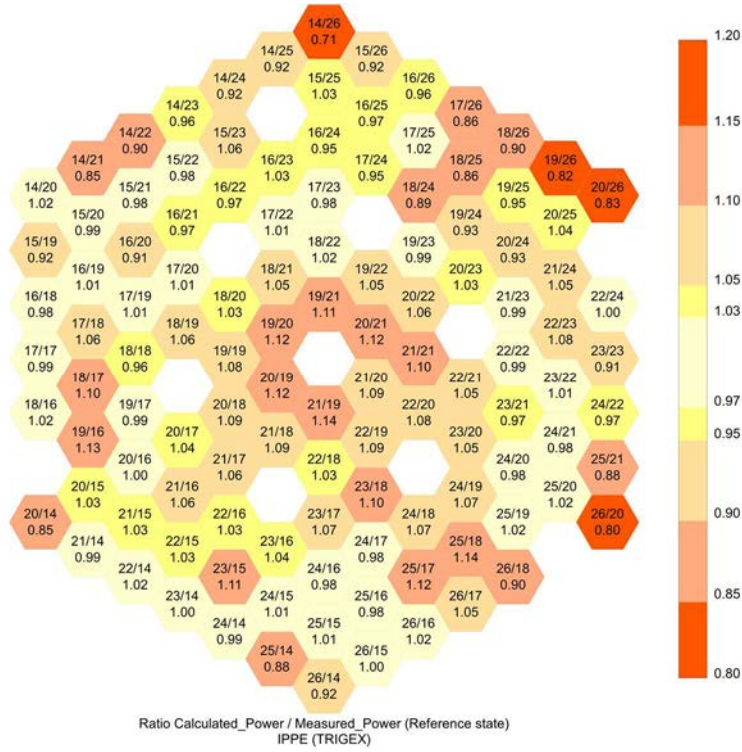
FIG. 220. C/E of S/A power for the reference state: IPPE-TRIGEX.
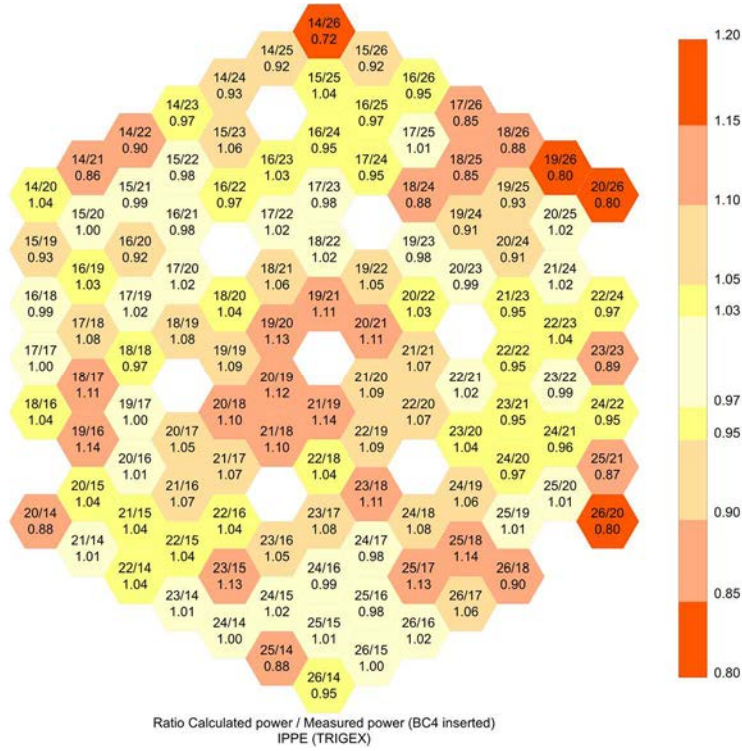
FIG. 221. C/E of S/A power for the step 1: IPPE-TRIGEX.

197

Ratio Calculated_Power / Measured_Power (BC4 inserted & BC1 extracted)
IPPE (TRIGEX)
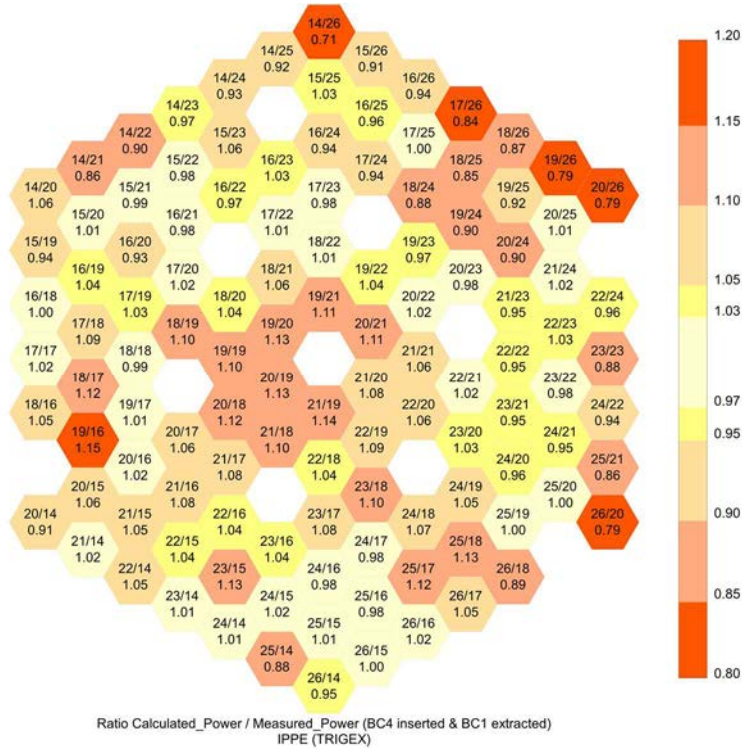
FIG. 222. C/E of S/A power for the step 2: IPPE-TRIGEX.

Ratio Calculated_Power / Measured_Power (BC1 extracted)
IPPE (TRIGEX)
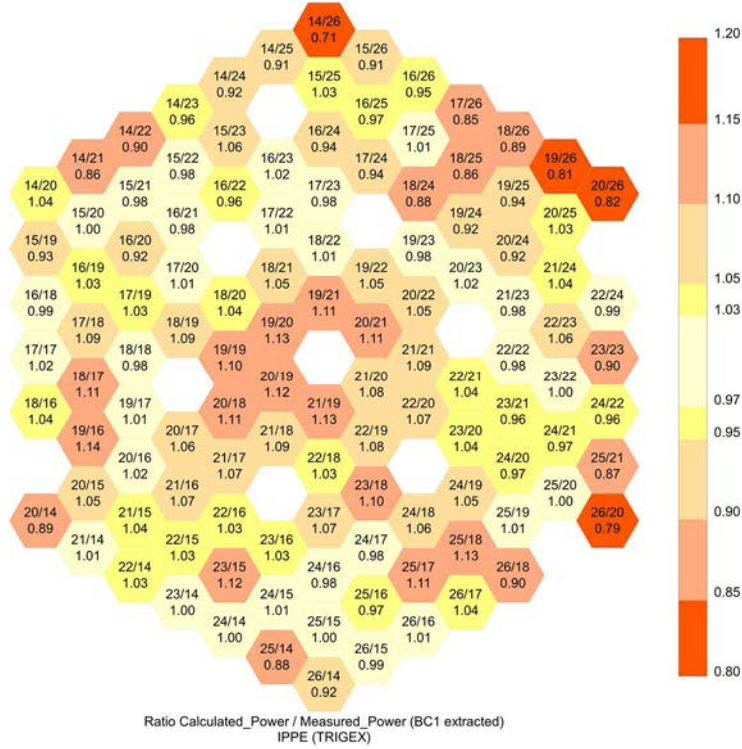
FIG. 223. C/E of S/A power for the step 3: IPPE-TRIGEX.

198
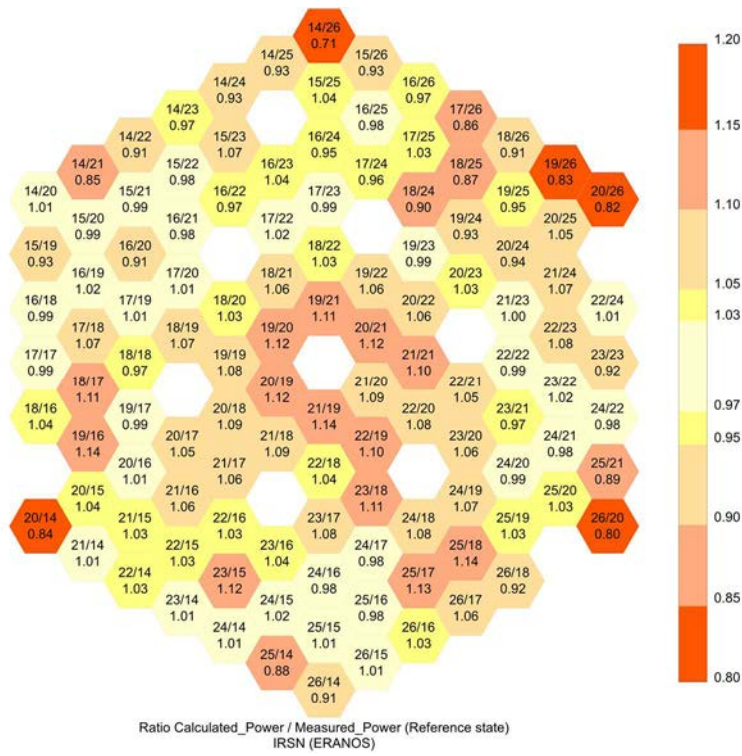
FIG. 224. C/E of S/A power for the reference state: IRSN-ERANOS.
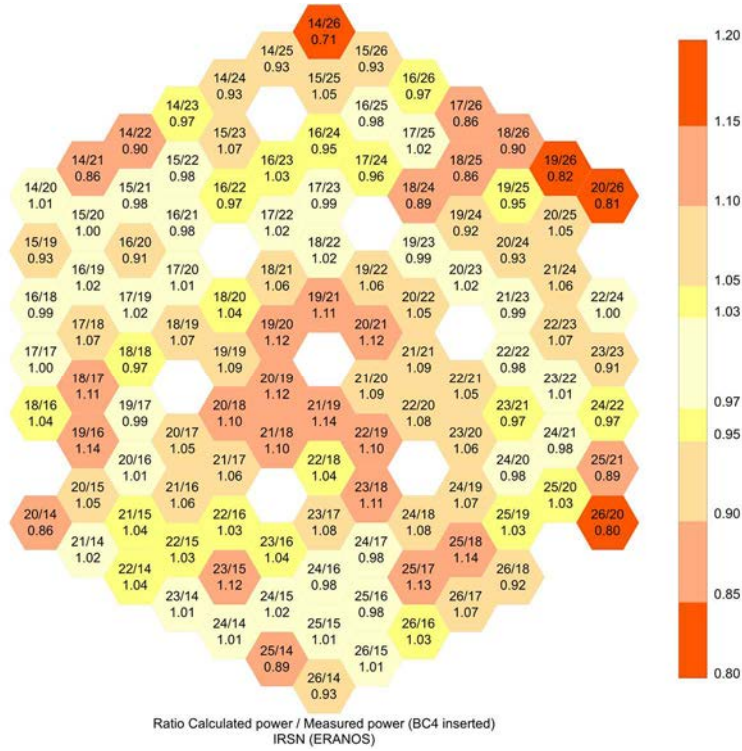
FIG. 225. C/E of S/A power for the step 1: IRSN-ERANOS.

Ratio Calculated_Power / Measured_Power (BC4 inserted & BC1 extracted)
IRSN (ERANOS)
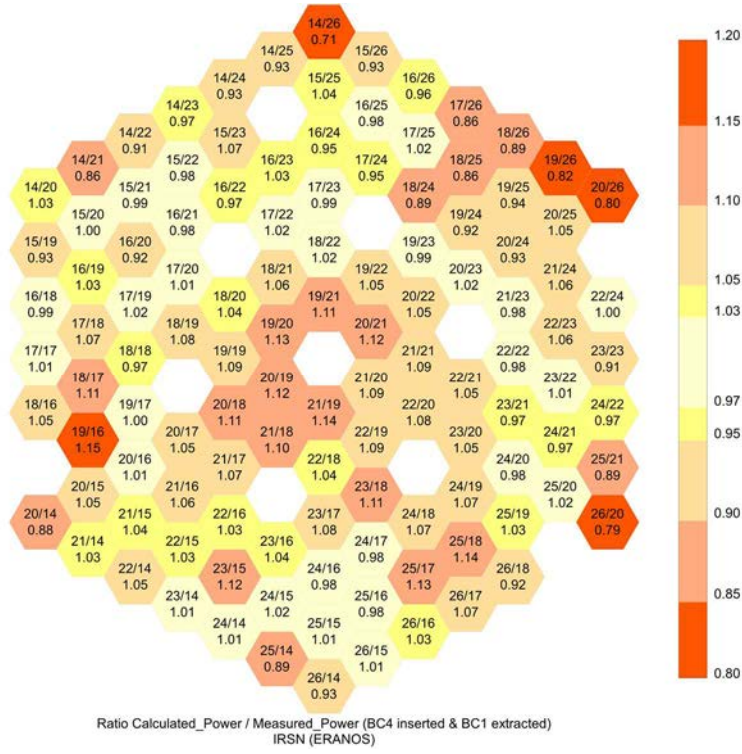
FIG. 226. C/E of S/A power for the step 2: IRSN-ERANOS.

Ratio Calculated_Power / Measured_Power (BC1 extracted)
IRSN (ERANOS)
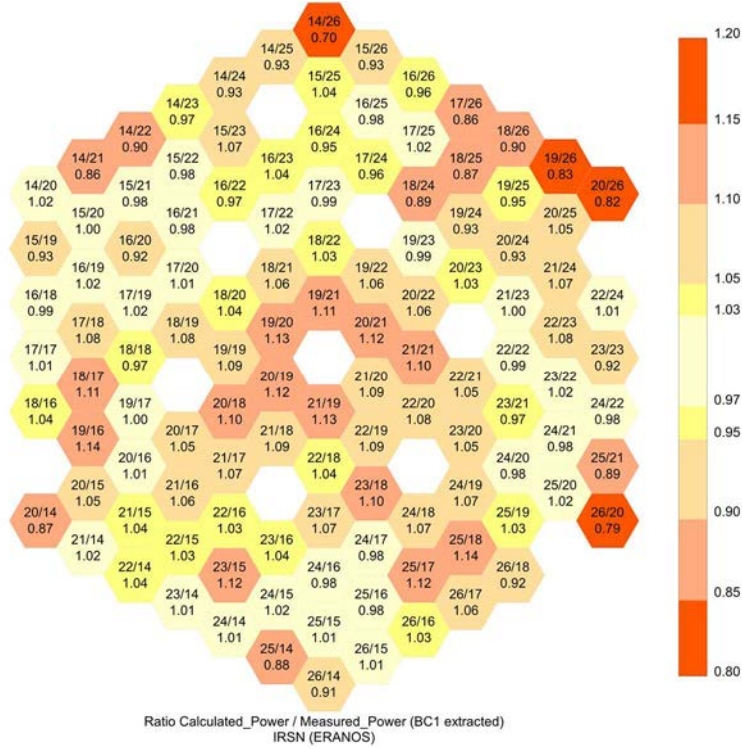
FIG. 227. C/E of S/A power for the step 3: IRSN-ERANOS.
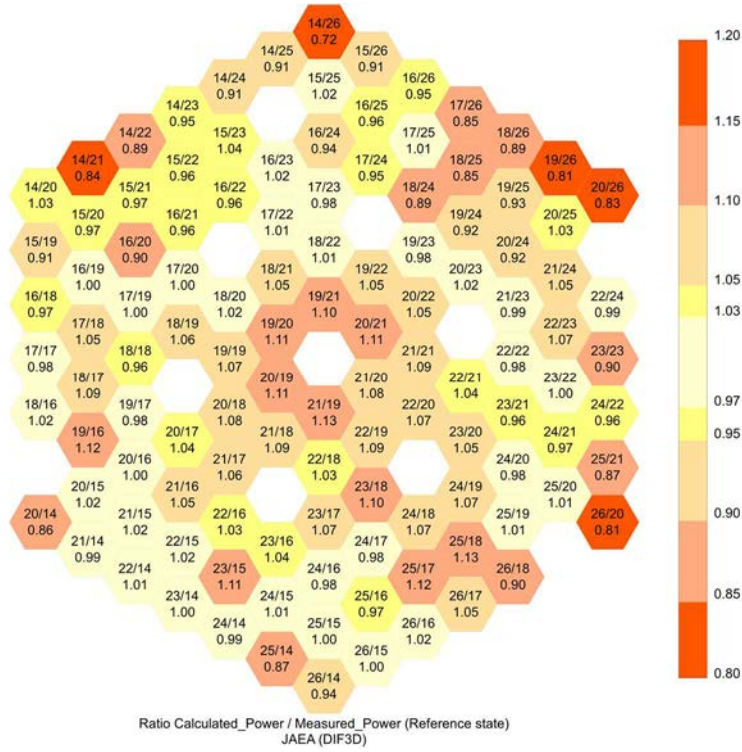
FIG. 228. C/E of S/A power for the reference state: JAEA-DIF3D.
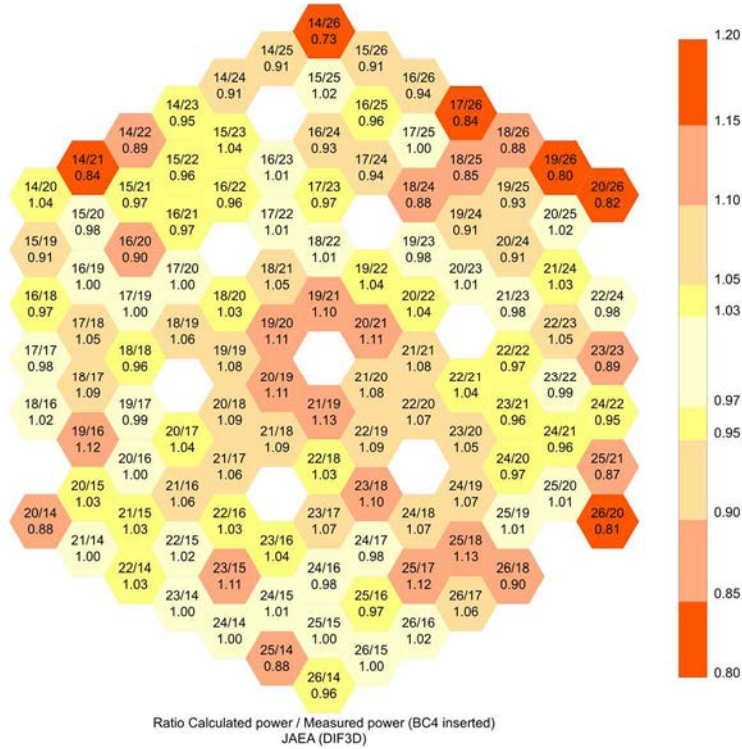
FIG. 229. C/E of S/A power for the step 1: JAEA-DIF3D.

201
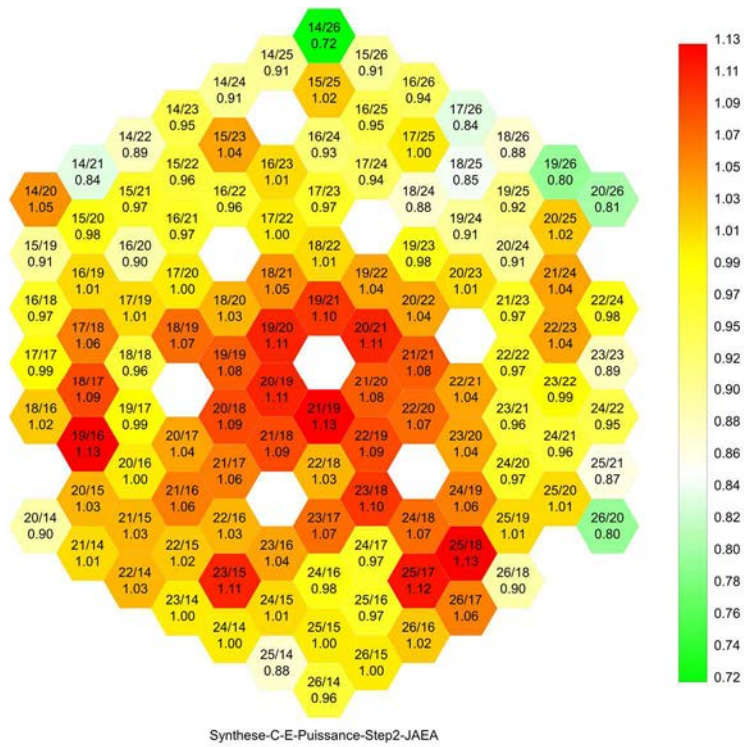
FIG. 230. C/E of S/A power for the step 2: JAEA-DIF3D.
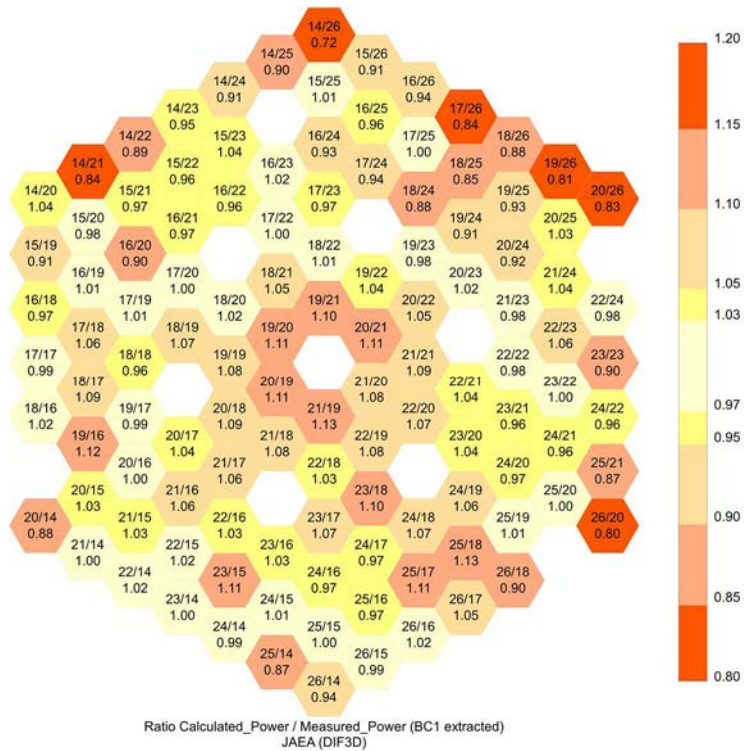
FIG. 231. C/E of S/A power for the step 3: JAEA-DIF3D.
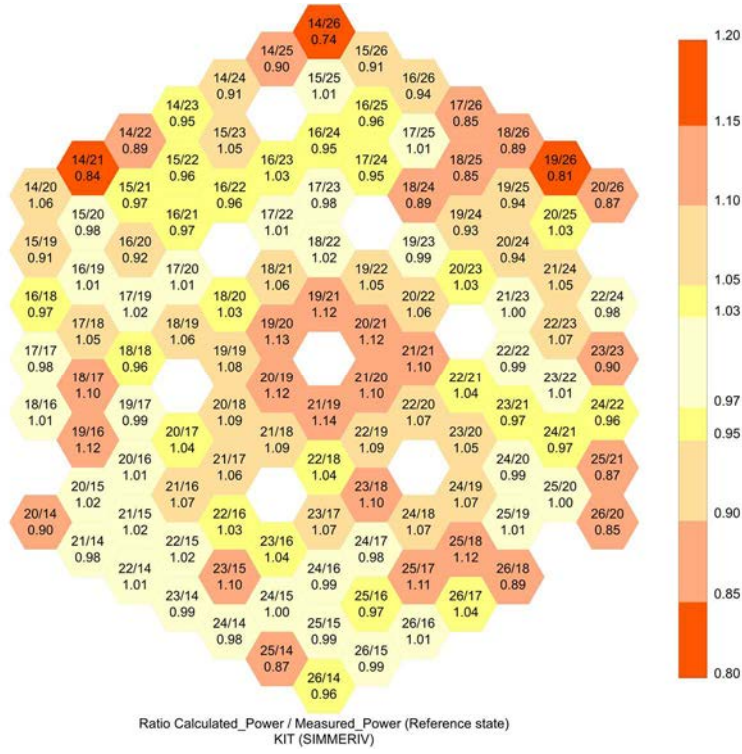
FIG. 232. C/E of S/A power for the reference state: KIT-SIMMERIV.
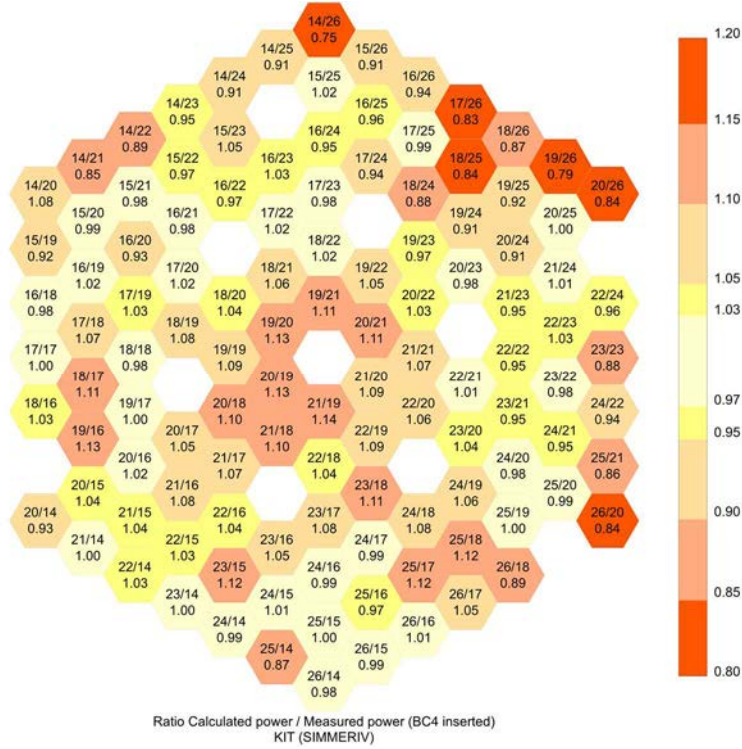
FIG. 233. C/E of S/A power for the step 1: KIT-SIMMER-IV.

203
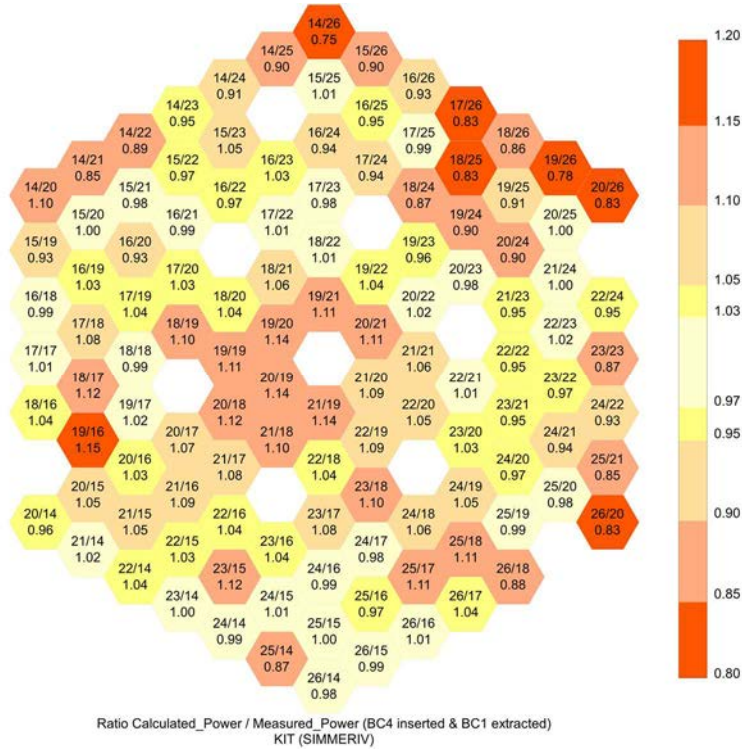
FIG. 234. C/E of S/A power for the step 2: KIT-SIMMER-IV.
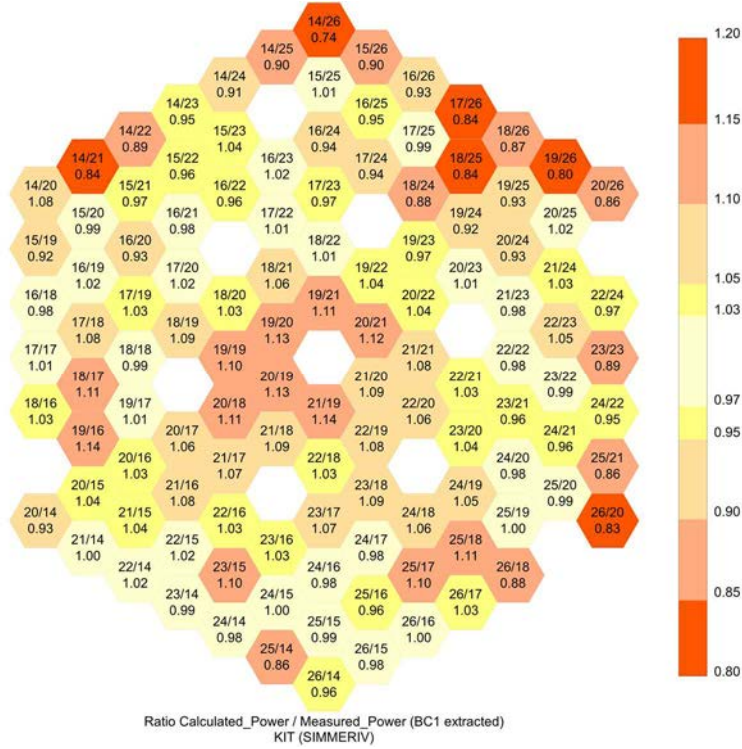
FIG. 235. C/E of S/A power for the step 3: KIT-SIMMER-IV.

FIG. 236. C/E of S/A power for the reference state: PSI-ERANOS.

FIG. 237. C/E of S/A power for the step 1: PSI-ERANOS.
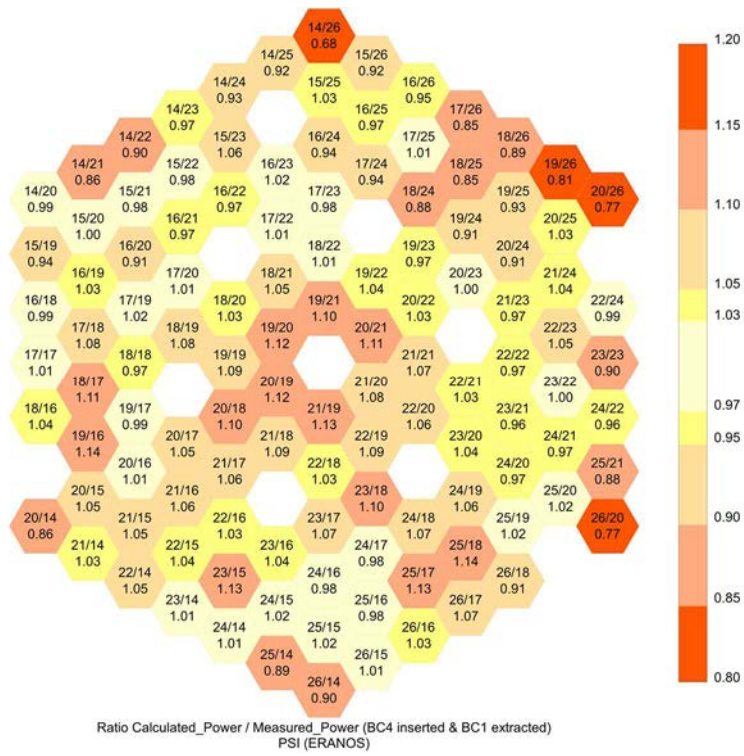
FIG. 238. C/E of S/A power for the step 2: PSI-ERANOS.
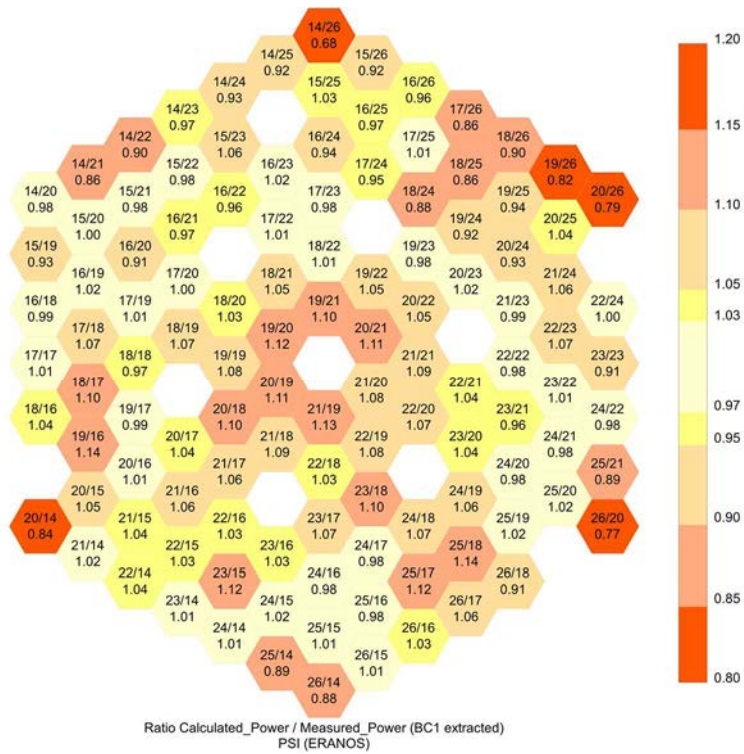
FIG. 239. C/E of S/A power for the step 3: PSI-ERANOS.

8.4.2. Power deviations by sub-assembly

Fig. 242–244 present radial profiles of power deviation results and Fig. 245–247 present power deviation results for the whole core. Measured results are presented with their experimental uncertainties. Fig. 240 illustrates the radial profile used for the comparisons in the first set of figures. This profile includes 10 fuel and 2 blanket subassemblies. In the second of set of figures, sub-assemblies are numbered starting from the central S/A as N°1 (20/20), below is S/A N°2 in the second hex ring (20/19) and then counter-clockwise from inner to outer rings (Fig. 241).
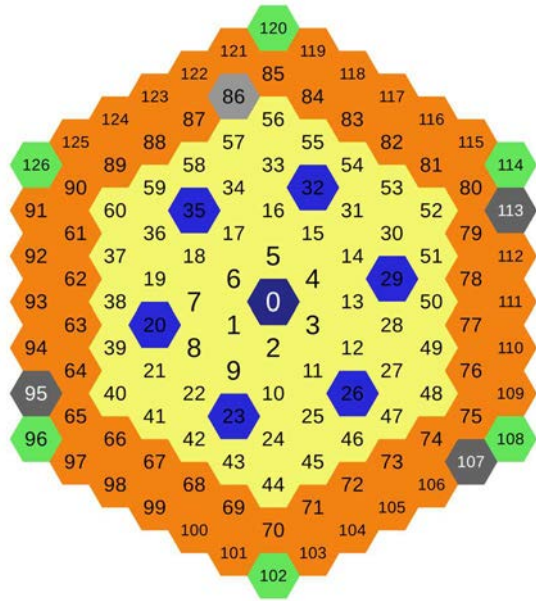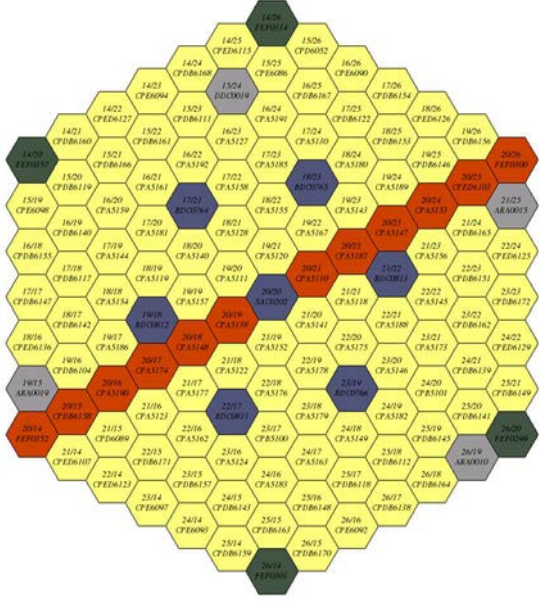
FIG. 240. Power deformation radial profile.   FIG. 241. Sub-assembly numbering order.

Power deviation results were computed by using the following formula:

$$\delta_{ass} \ (in \ \%) = \frac{\Delta P_{ass}^{Calculated}}{P_{ass}^{Calculated}(Ref)} - \frac{\Delta P_{ass}^{Measured}}{P_{ass}^{Measured}(Ref)} \tag{19}$$

The different results can be split in two distinct groups according to the use of a refined calculation scheme for self-shielding processing in absorbing rods. The first group is composed of CEA, IGCAR, IRSN and JAEA results. Differences between measured and calculated power deviations are limited to ±2% on the first five rings of the fissile core. The second group is composed of IPPE, KIT and PSI results with deviations limited to ±5%. In any case calculations overestimate the impact of the control rod shifting. This problem is mainly linked to uncertainties on control rod axial positions due to the empirical models used to estimate differential expansions of core components [6]. Some studies have shown that this overestimation cannot be linked to local Doppler feedback effects or local expansion phenomena. As for the SIMMER-IV results, the discrepancy is once again due to the homogeneous CR model.

An increase in discrepancies between calculations and measurements in the outer core and especially in the last ring of fissile sub-assemblies is observed. This is due to the hot plenum influence on the sodium flow of outer-core sub-assemblies (turbulent flow at the border of the core cover plug), which is not taken into account in our model [6].

Large deviations on the few fertile sub-assemblies located on the last outer core ring are observed. The following phenomena, which are not taken into account in our models, can explain these deviations:

— heat transfers between fertile and nearby fissile sub-assemblies through wrapper tube cannot be assumed negligible given their respective mean temperatures (470 °C and 420 °C respectively). This point has an influence on the experimental power balance of fertile sub-assemblies;

— sodium mix between fissile and fertile outlet flows cannot be assumed negligible, given their respective flow rates (15 kg.s^{-1} and 3 kg.s^{-1} respectively). The influence of the hot plenum exacerbates this problem.

Last but not least, neither the use of averaged compositions for the inner and outer core instead of detailed ones nor the various core solvers lead to main discrepancies on power deviation estimations (see differences between 'CEA/detailed' and 'CEA' results).

Finally, most of discrepancies between calculation and experience can be explained by measurement problems and by the control rod cross-sections processing model. In conclusion, a special attention has to be paid to the method used to generate control rod self-shielded cross-sections in order to reproduce not only power deviations but also control rod worth. Benchmarked codes are globally able to reproduce the local impact of a control rod withdrawal on a little-sized core compared with commercial-size reactor.

More detailed results are presented in the next sections. Figs. 248–274 present power deviations for each participant and each states of the test in the form of color maps. All these results are presented with the same color scale in order to simplify comparisons.
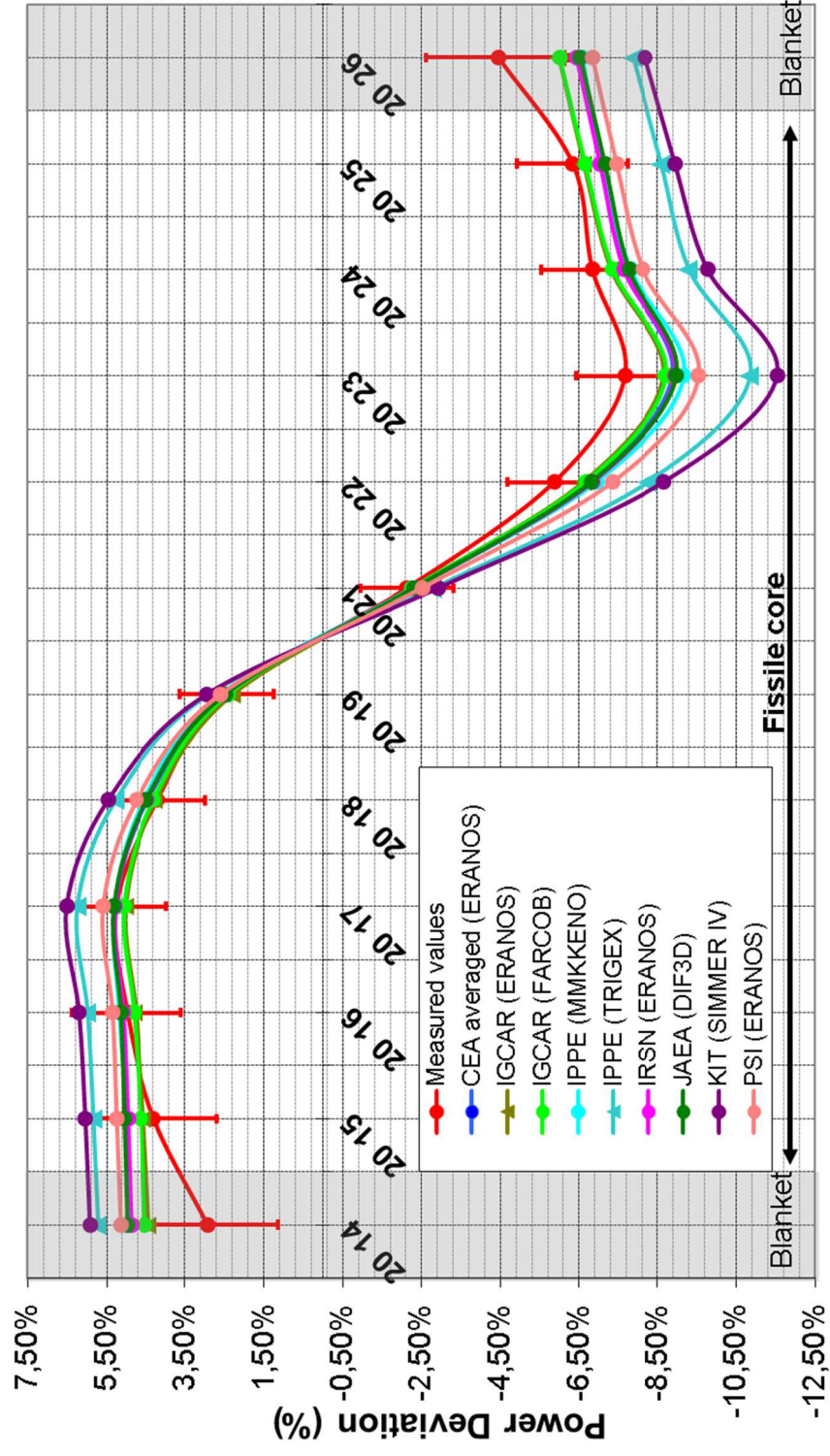
FIG. 242. Power deviation profiles (step 1 – Control rod # 4 inserted).
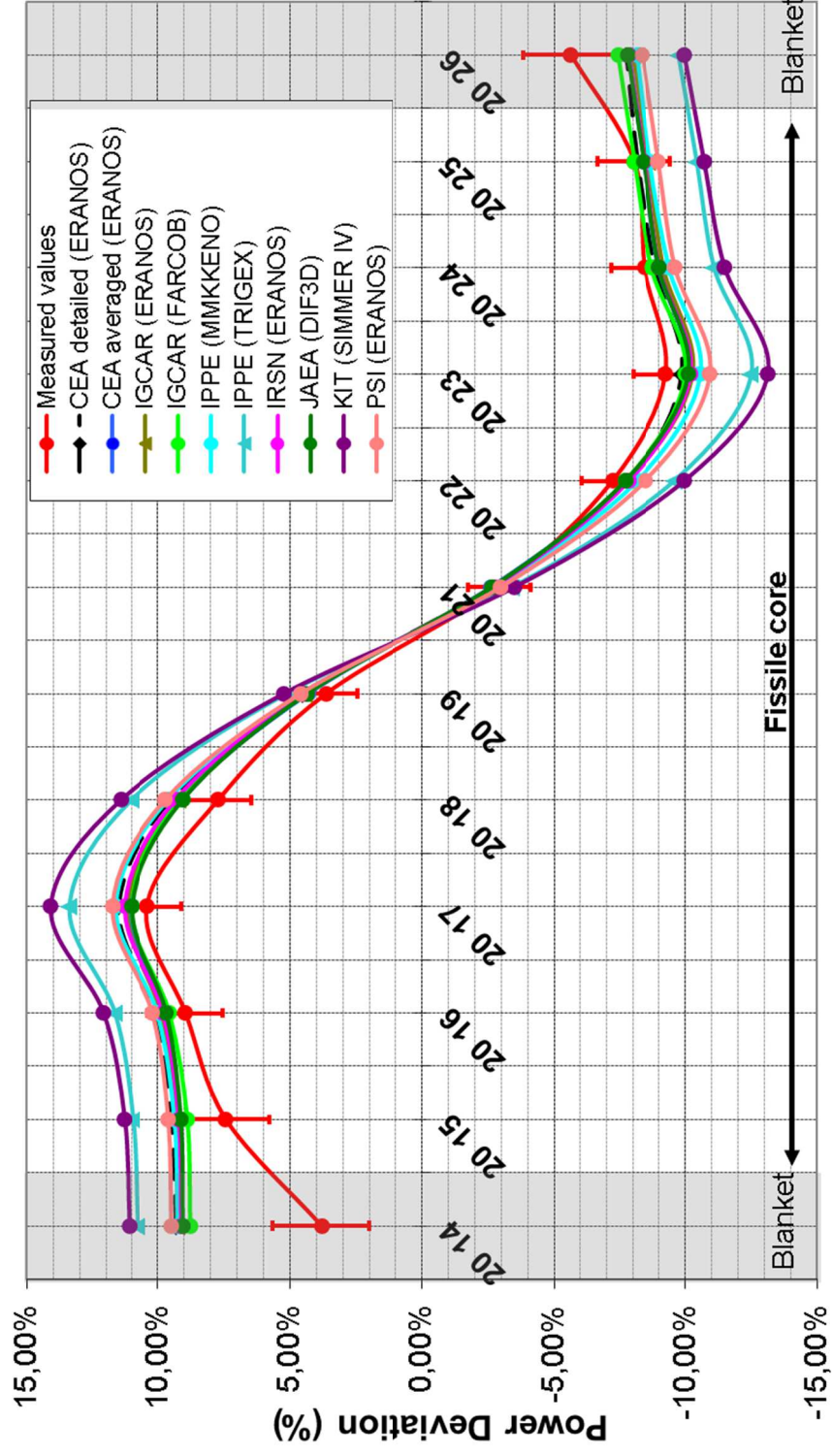
FIG. 243. Power deviation profiles (step 1 – Control rod # 4 inserted).
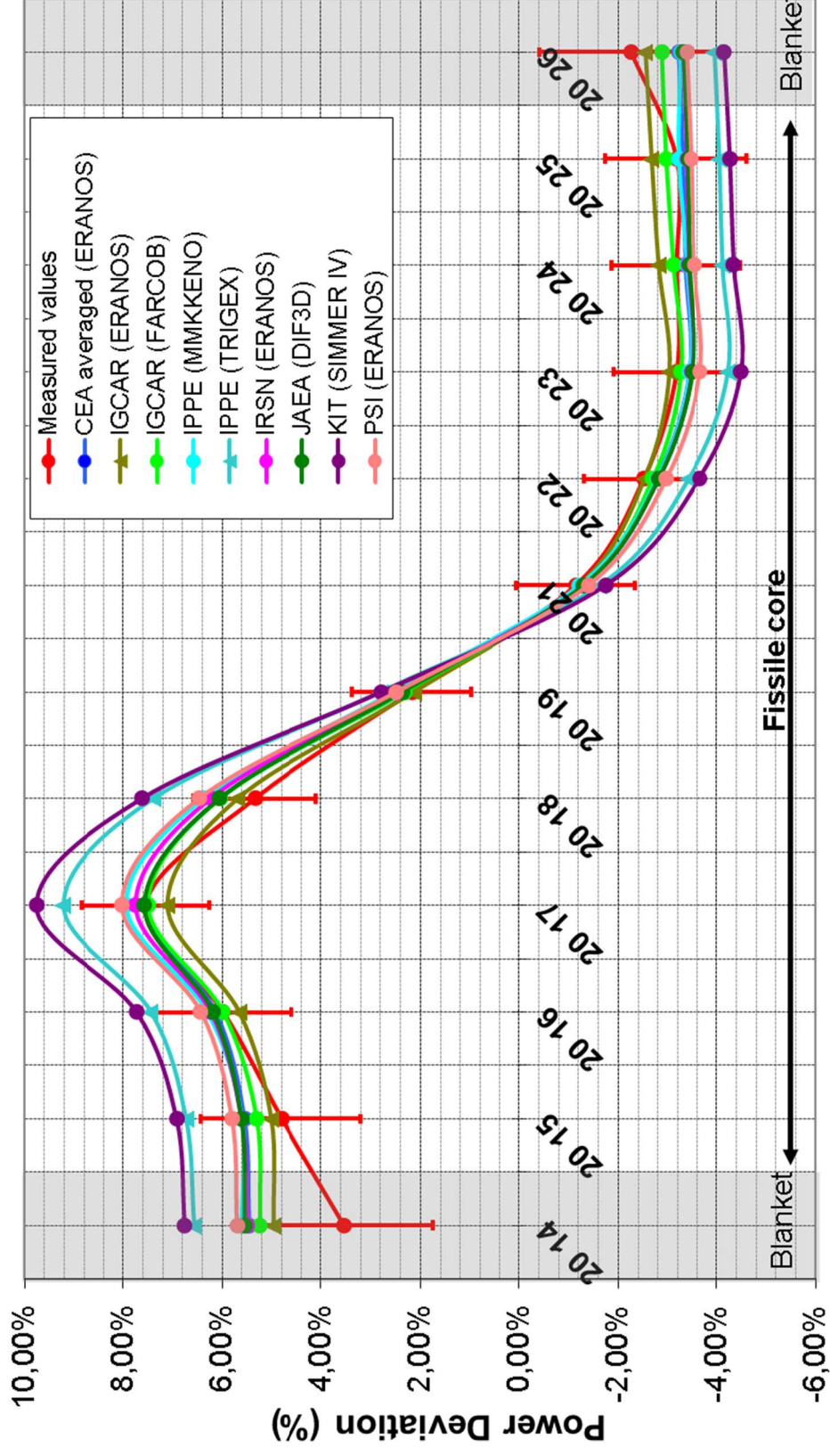
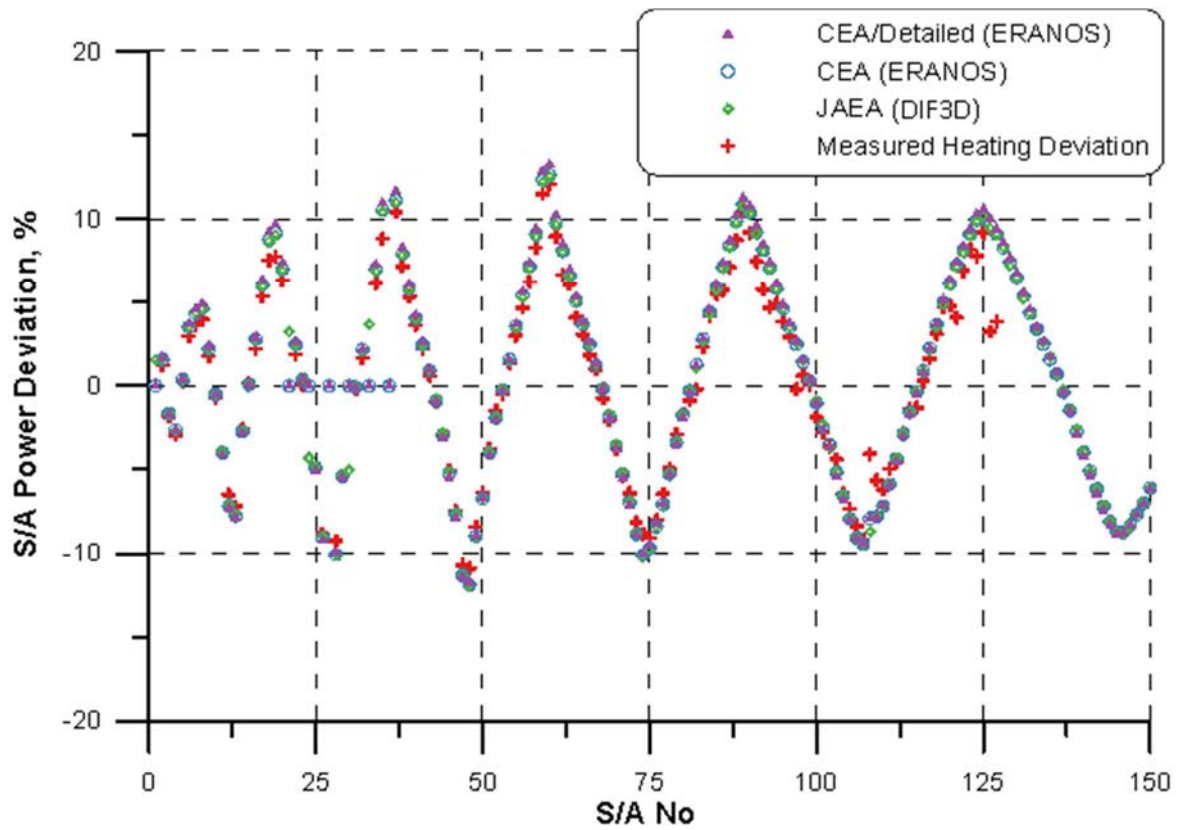FIG. 244. Power deviation profiles (step 3 – Control rod # 1 extracted).

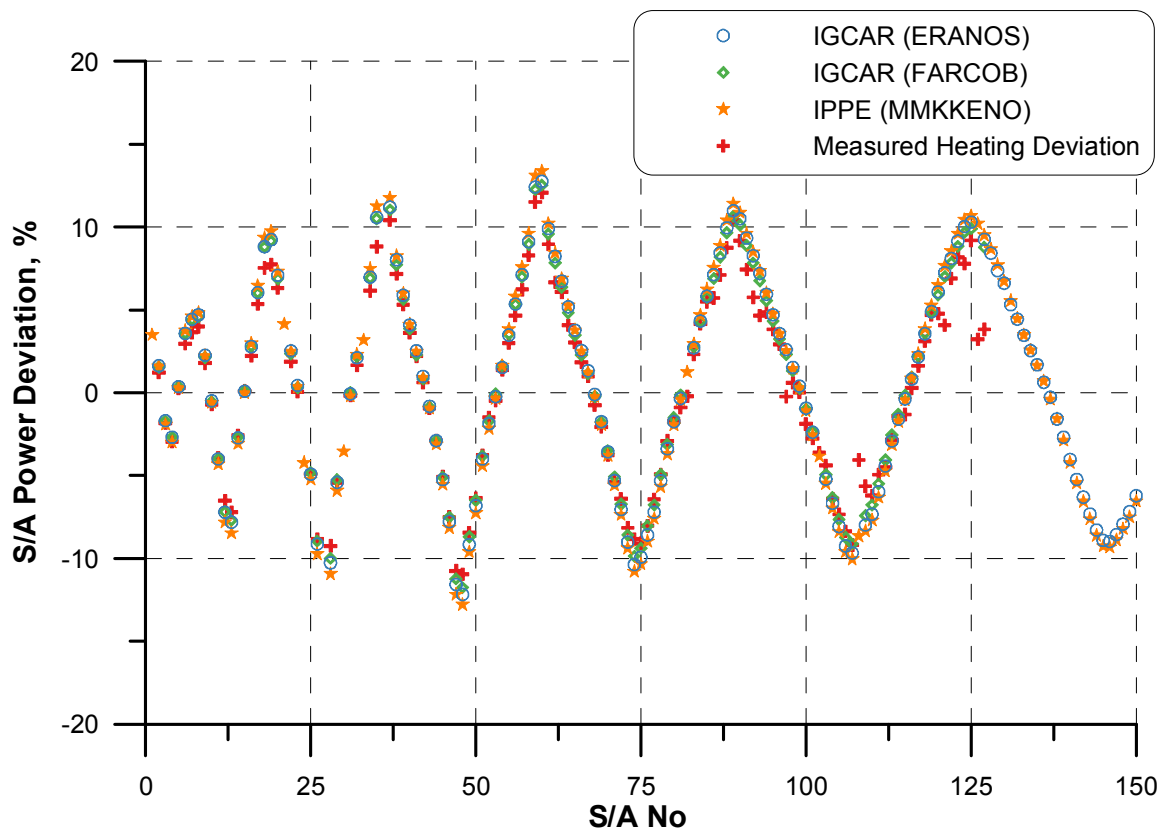*FIG. 245. Power deviations for the maximum shifted state for CEA, JAEA.*

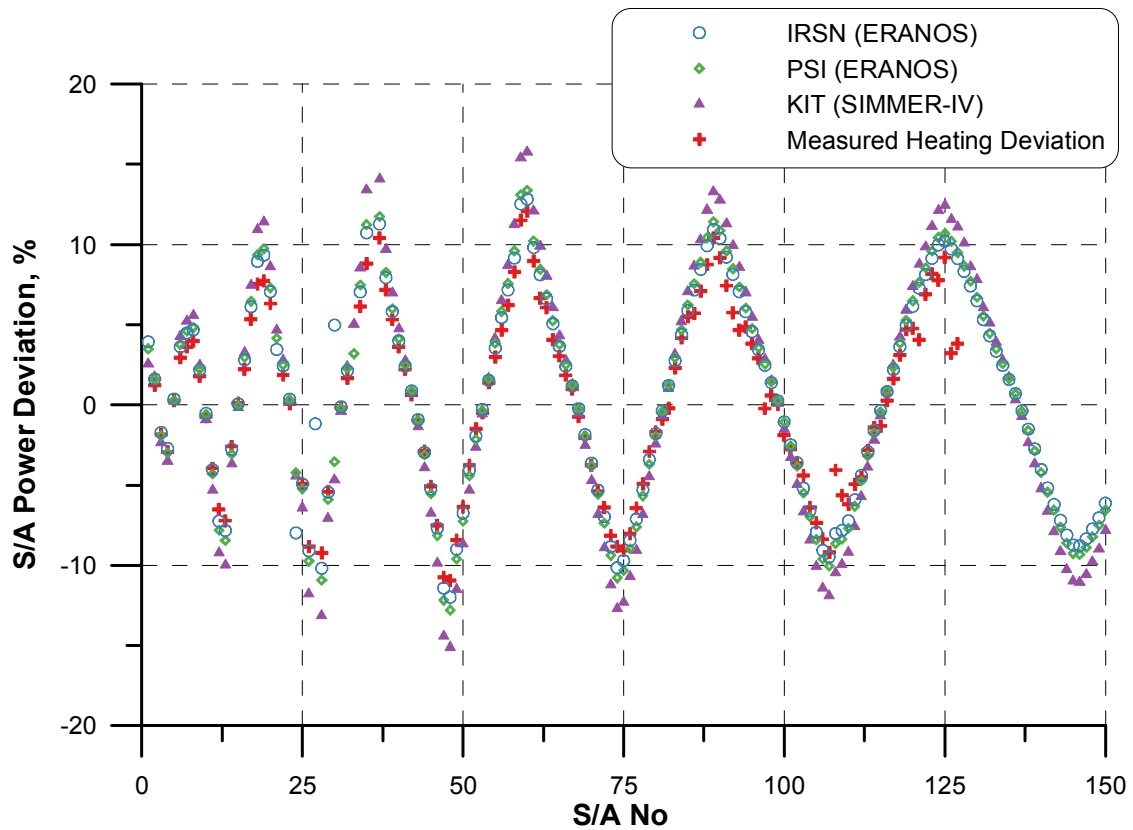*FIG. 246. Power deviations for the maximum shifted state for IGCAR and IPPE.*

212

FIG. 247. Power deviations for the maximum shifted state for IRSN, KIT and PSI.

8.4.2.1. CEA (ERANOS)

Table 59 summarizes the calculation options used by CEA to compute power deviation maps. Fig. 248–250 illustrate raw differences between calculated and measured power deviation. Calculated deviations are coherent with test values with raw differences mainly lower than 1%. However, an overestimation of the impact of the control rod shifting is notable for all steps of the test. Raw differences increase slightly near the core boundary due to the thermal hydraulic influence of hot sodium plenum. Strongest differences are located on blanket (14/20; 14/26; 20/26; 26/20; 26/14; 20/14) and internal shielding (21/25; 26/19; 19/15; 15/24).

TABLE 59. CEA CALCULATION OPTIONS

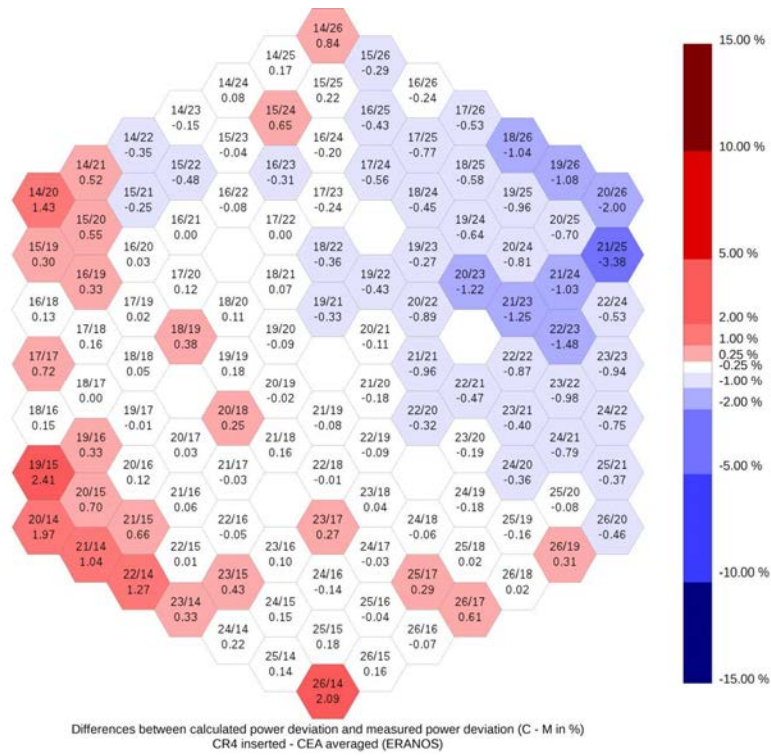|	Participant	Nuclear library	Energetic structure	Cell code	Cell Treatment	Control Rod Treatment	Code	Method
	CEA	ERALIB-1	33	ECCO	Het 2D	**Het 2D + 2D SN transport calculation**	ERANOS/VARIANT	Transport

FIG. 248. Differences between calculated and measured power deviation (C-M in %) – CR#4 inserted – CEA averaged calculation (ERANOS).
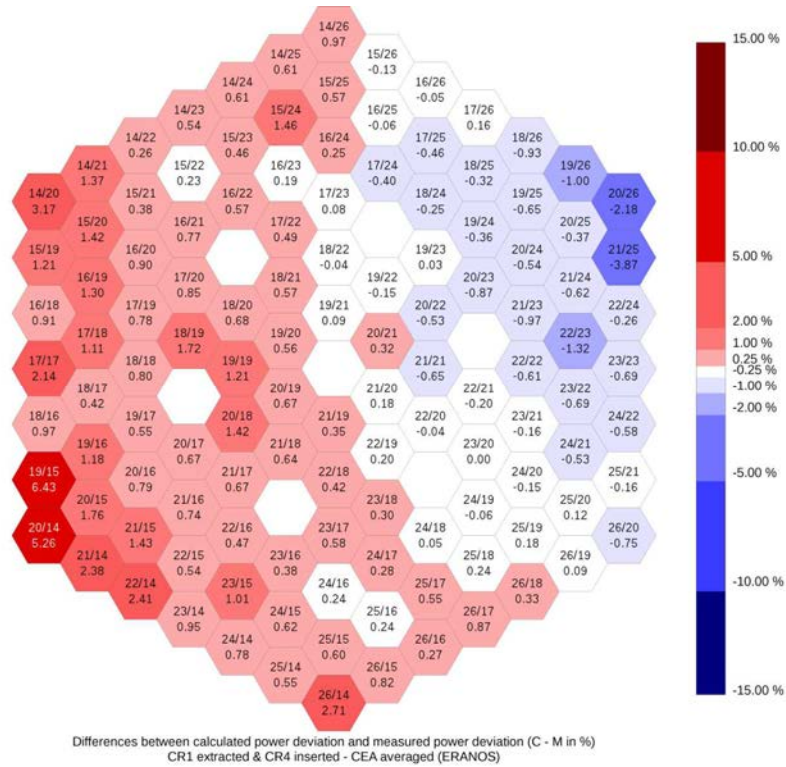

FIG. 249. Differences between calculated and measured power deviation (C-M in %) – CR#4 inserted & CR#1 extracted – CEA averaged (ERANOS).
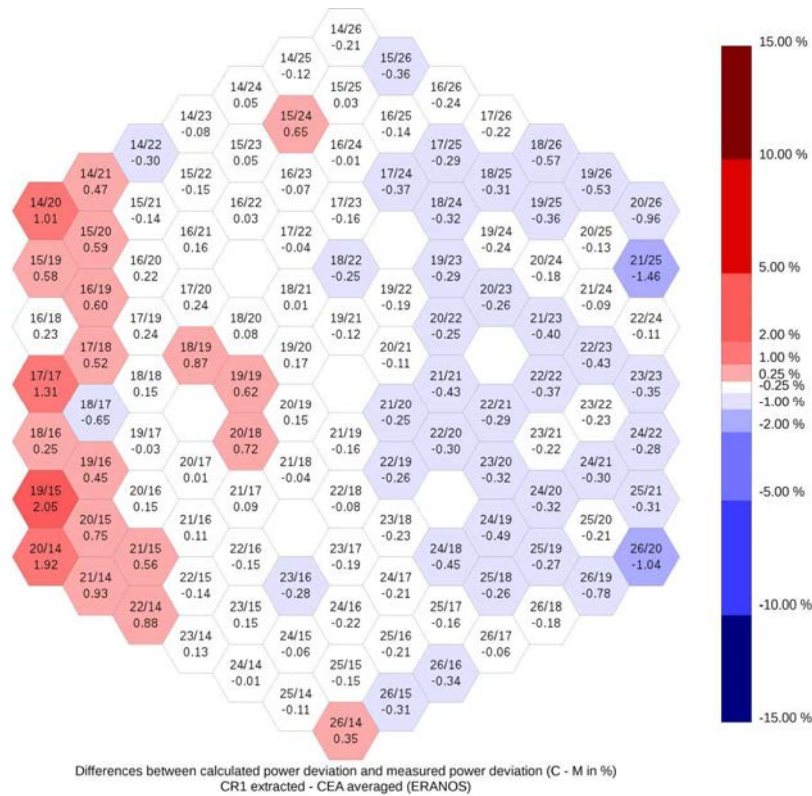
Differences between calculated power deviation and measured power deviation (C - M in %)
CR1 extracted - CEA averaged (ERANOS)

FIG. 250. Differences between calculated and measured power deviation (C-M in %) – CR#1 extracted – CEA averaged (ERANOS).

8.4.2.2. IGCAR (ERANOS)

Table 60 summarizes the calculation options used by IGCAR to compute power deviation maps with the code ERANOS. Fig. 251–253 illustrate raw differences between calculated and measured power deviation. Calculated deviations are quite coherent with test values with raw differences mainly lower than 1.5%. An overestimation of the impact of the control rod shifting is notable for all steps of the test. The use of a diffusion solver does not lead to notable modifications of the impact of control rod insertion/withdrawal on the whole core. Raw differences increase near the core boundary due to the thermal hydraulic influence of hot sodium plenum. Strongest differences are located on blanket (14/20; 14/26; 20/26; 26/20; 26/14; 20/14) and internal shielding (21/25; 26/19; 19/15; 15/24).

TABLE 60. IGCAR (1) CALCULATION OPTIONS

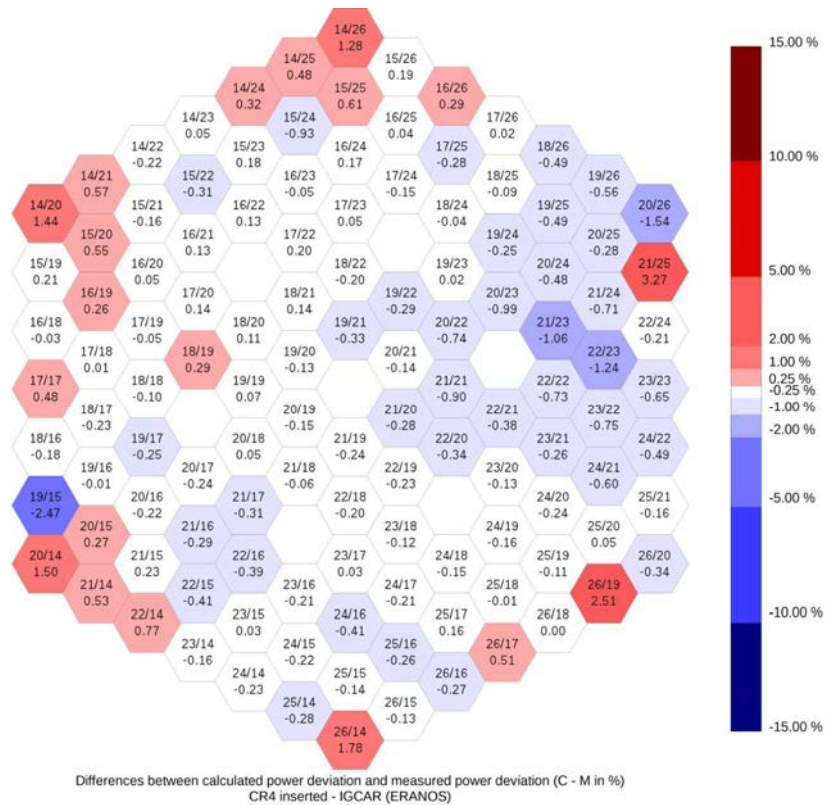|	Participant	Nuclear library	Energetic structure	Cell code	Cell Treatment	Control Rod Treatment	Code	Method
	IGCAR(1)	ERALIB-1	33	ECCO	Het 2D	Het 2D + 2D SN transport calculation	ERANOS/H3D	Diffusion

FIG. 251. Differences between calculated and measured power deviation (C-M in %) – CR#4 inserted – IGCAR (ERANOS).
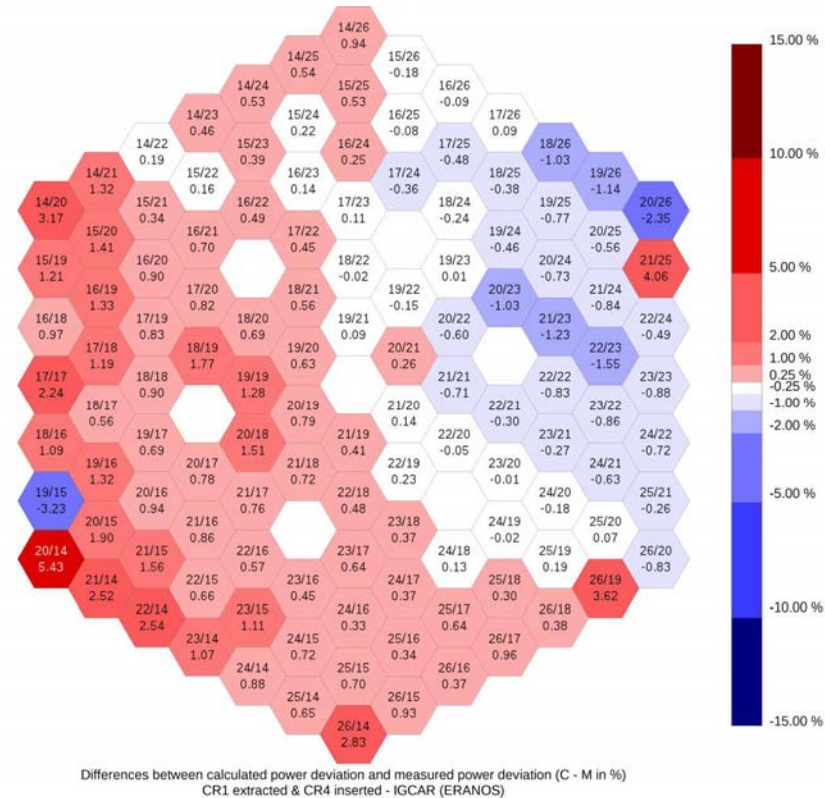

FIG. 252. Differences between calculated and measured power deviation (C-M in %) – CR#4 inserted & CR#1 extracted - IGCAR (ERANOS).
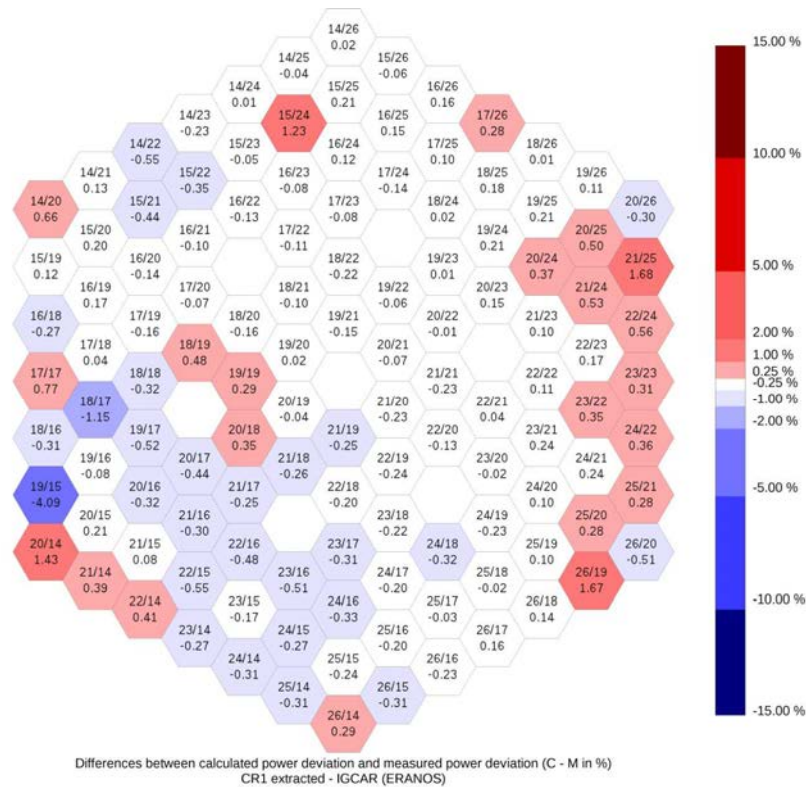
216

Differences between calculated power deviation and measured power deviation (C - M in %)
CR1 extracted - IGCAR (ERANOS)

FIG. 253. Differences between calculated and measured power deviation (C-M in %) – CR#1 extracted – IGCAR (ERANOS).

8.4.2.3. IGCAR (FARCOB)

Table 61 summarizes the calculation options used by IGCAR to compute power deviation maps with the code FARCOB. Fig. 254–256 illustrate raw differences between calculated and measured power deviation. Calculated deviations are coherent with test values with raw differences mainly lower than 1%. An overestimation of the impact of the control rod shifting is notable for all steps of the test. The use of a diffusion solver does not lead to notable modifications of the impact of control rod insertion/withdrawal on the whole core. Raw differences increase near the core boundary due to the thermal hydraulic influence of hot sodium plenum. Strongest differences are located on blanket (14/20; 14/26; 20/26; 26/20; 26/14; 20/14) and internal shielding (21/25; 26/19; 19/15; 15/24).

TABLE 61. IGCAR (2) CALCULATION OPTIONS

Participant	Nuclear library	Energetic structure	Cell code	Cell Treatment	Control Rod Treatment	Code	Method
IGCAR(2)	ABBN-93	26	CONSYST	Het 1D	Het 2D without correction	FARCOB	Diffusion

Differences between calculated power deviation and measured power deviation (C - M in %)
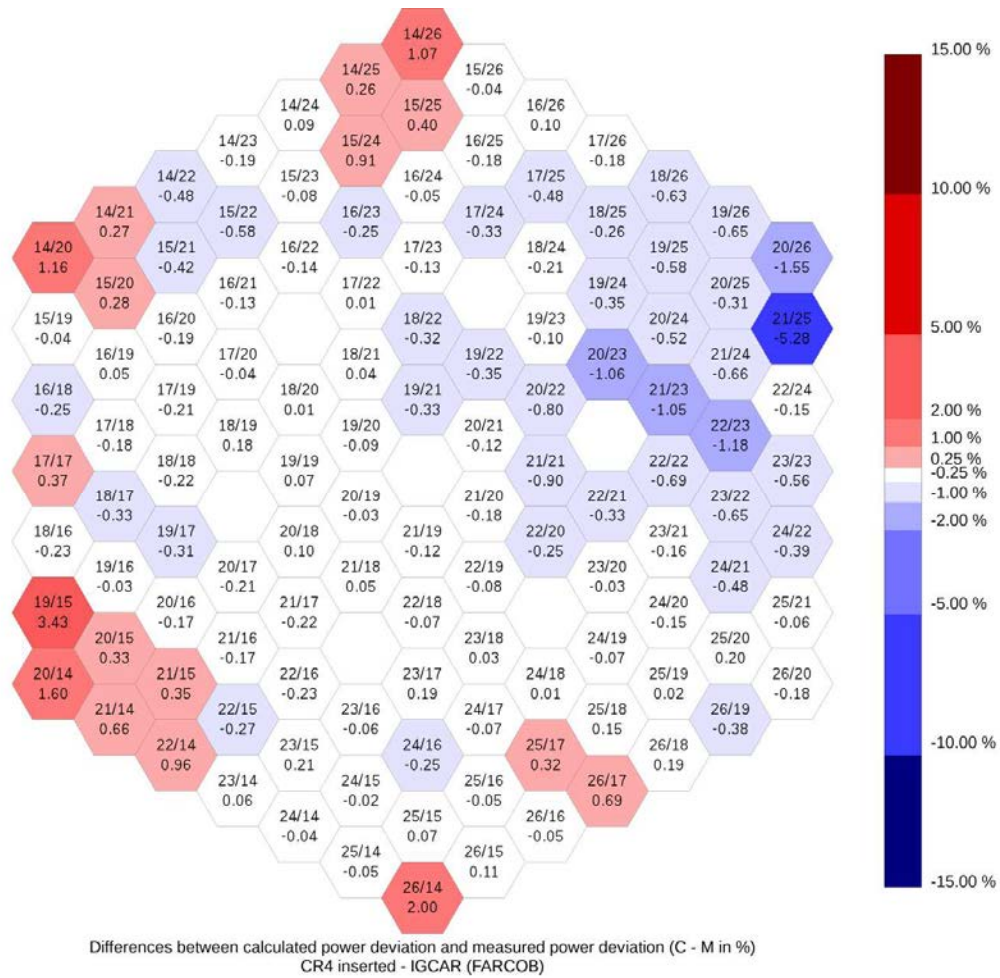CR4 inserted - IGCAR (FARCOB)

FIG. 254. Differences between calculated and measured power deviation (C-M in %) – CR#4 inserted – IGCAR (FARCOB).
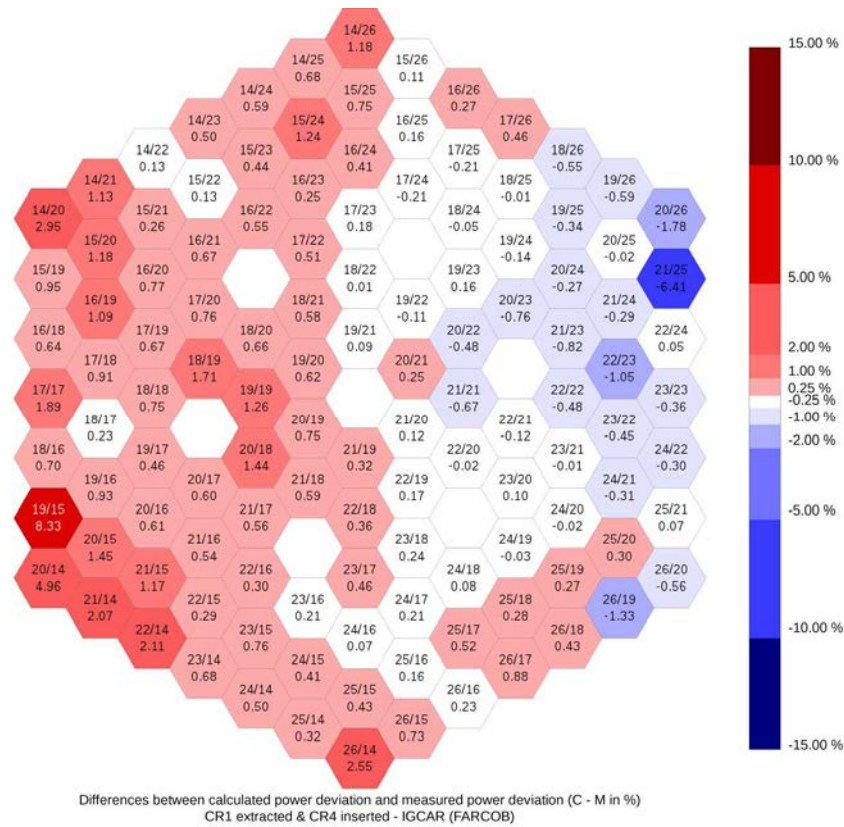
FIG. 255. Differences between calculated and measured power deviation (C-M in %) – CR#4 inserted & CR#1 extracted - IGCAR (FARCOB).
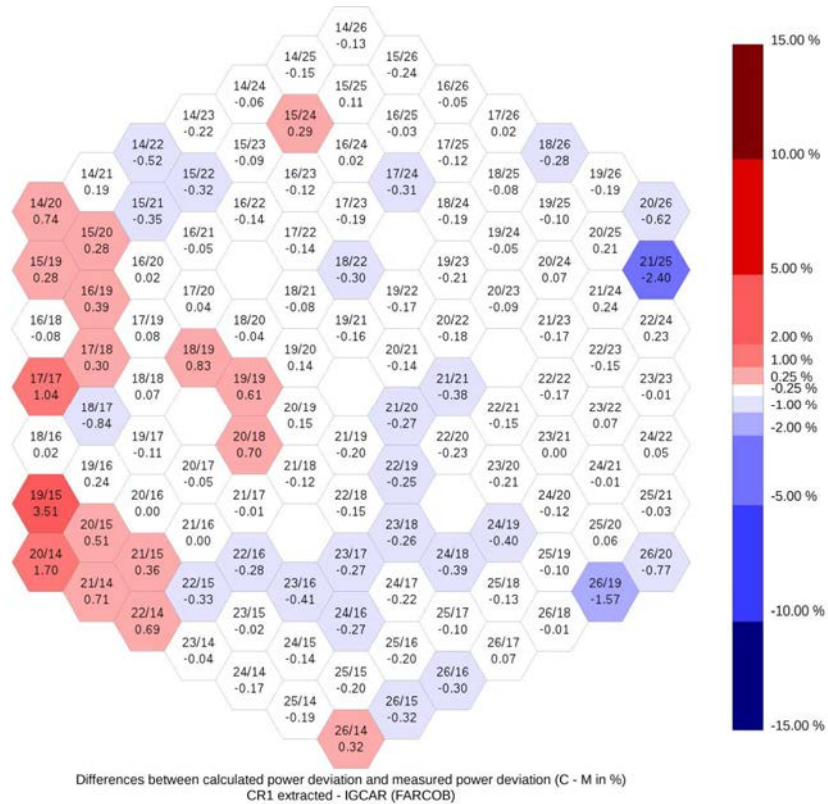

FIG. 256. Differences between calculated and measured power deviation (C-M in %) – CR#1 extracted – IGCAR (FARCOB).

8.4.2.4. IPPE (MMKKENO)

Table 62 summarizes the calculation options used by IPPE to compute power deviation maps with the code MMKKENO. Fig. 257–259 illustrate the difference between calculated and measured power deviation. Calculated deviations are quite coherent with test values with raw differences mainly lower than 1.5%. However, an overestimation of the impact of the control rod shifting is notable for all steps of the test. Raw differences increase slightly near the core boundary due to the thermal hydraulic influence of hot sodium plenum. Strongest differences are located on blanket (14/20; 14/26; 20/26; 26/20; 26/14; 20/14) and internal shielding (21/25; 26/19; 19/15; 15/24).

TABLE 62. IPPE(MMKKENO)'S CALCULATION OPTIONS

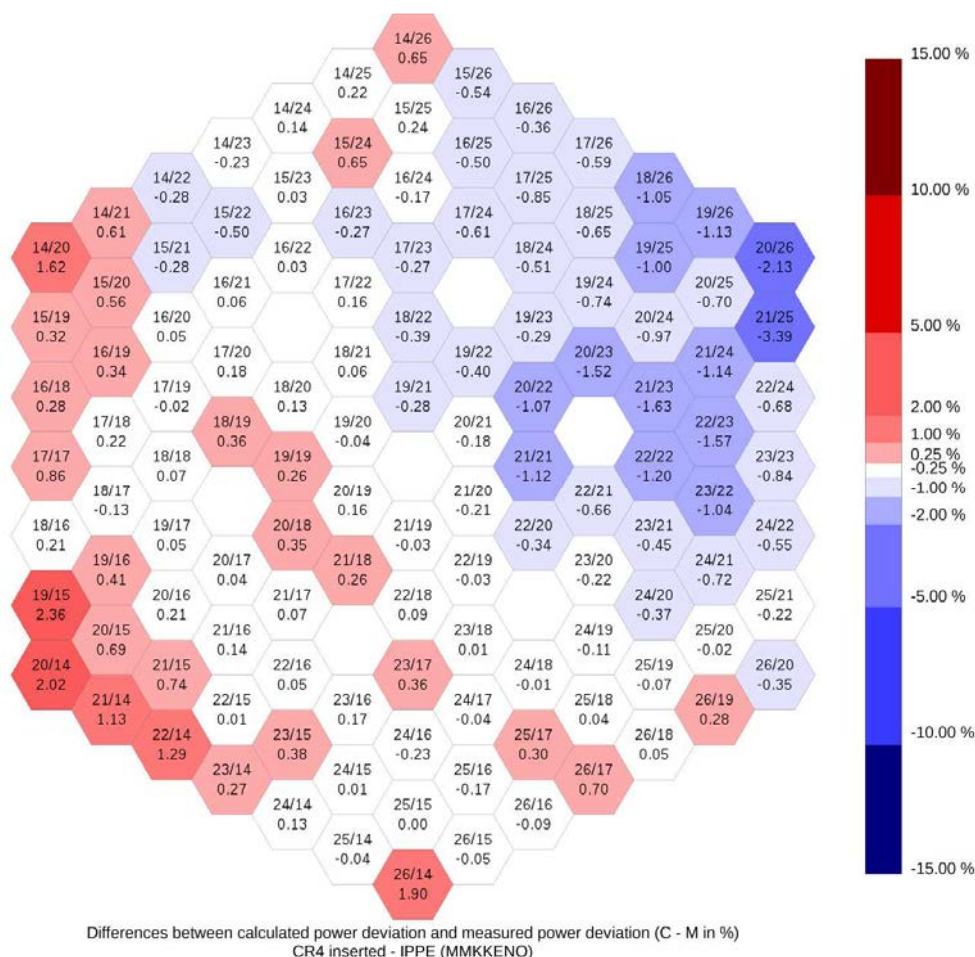|	Participant	Nuclear library	Energetic structure	Cell code	Cell Treatment	Control Rod Treatment	Code	Method
	IPPE	ABBN-93	299	CONSYST	Het 2D	Het 2D	MMKKENO	Monte-Carlo

FIG. 257. Differences between calculated and measured power deviation (C-M in %) – CR#4 inserted – IPPE (MMKKENO).
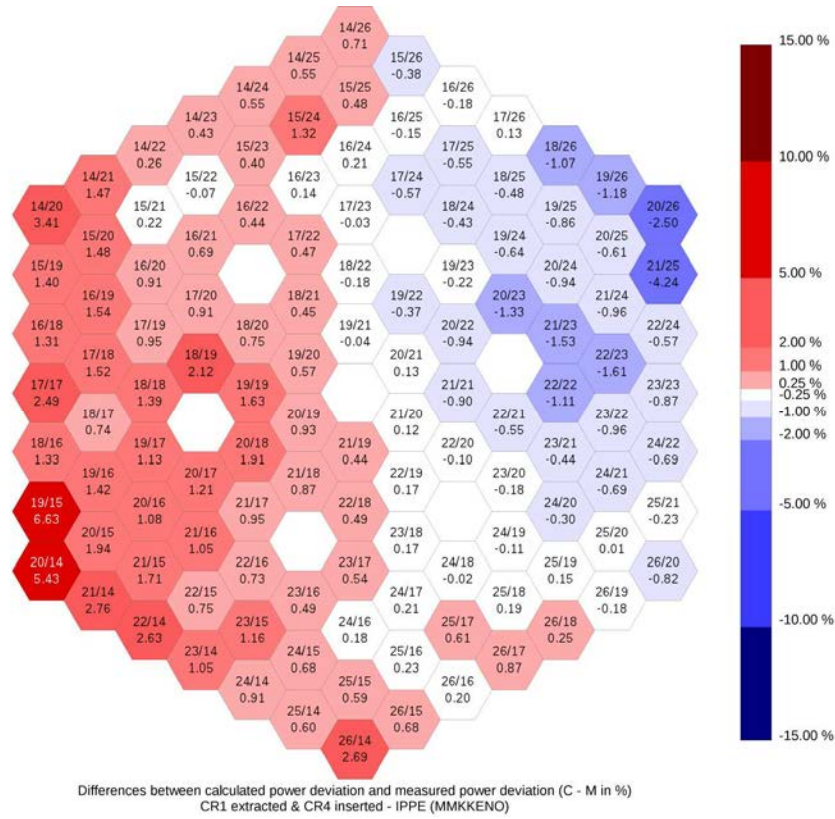
FIG. 258. Differences between calculated and measured power deviation (C-M in %) – CR#4 inserted & CR#1 extracted - IPPE (MMKKENO).
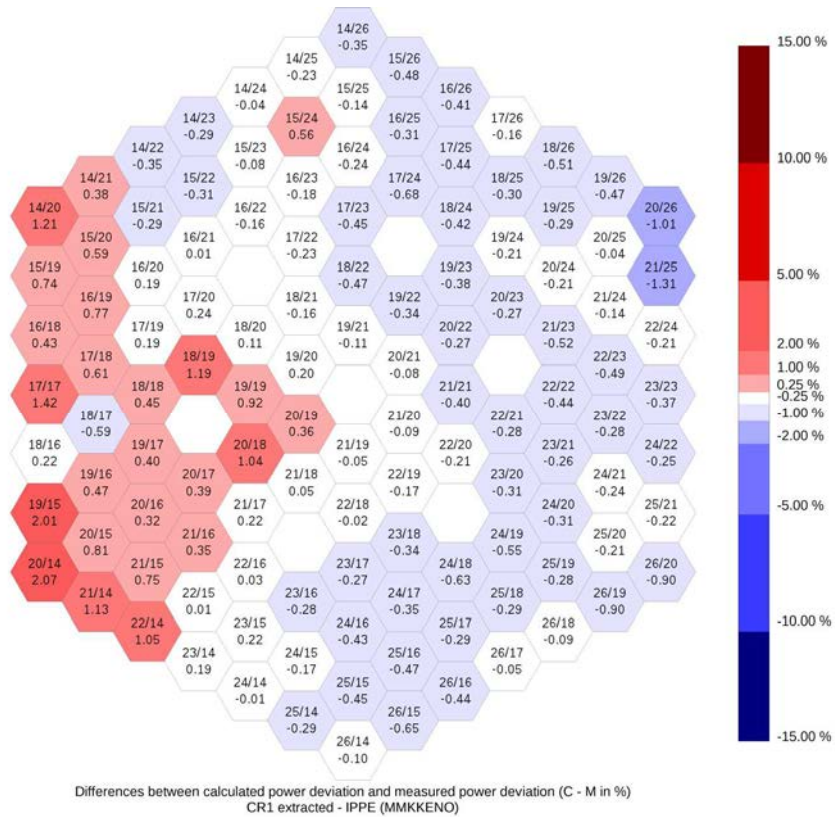

FIG. 259. Differences between calculated and measured power deviation (C-M in %) – CR#1 extracted – IPPE (MMKKENO).

8.4.2.5. IPPE (TRIGEX)

Table 63 summarizes the calculation options used by IPPE to compute power deviation maps with the code TRIGEX. Fig. 260–262 illustrate raw differences between calculated and measured power deviation. Raw differences between calculated and measured values are mainly lower than 4%, which is not negligible. An important overestimation of the impact of the control rod shifting is notable for all steps of the test, even near stationary rods. The use of a diffusion solver tends to smooth the impact of control rod insertion/withdrawal on the whole core. Raw differences increase near the core boundary due to the thermal hydraulic influence of hot sodium plenum. Strongest differences are located on blanket (14/20; 14/26; 20/26; 26/20; 26/14; 20/14) and internal shielding (21/25; 26/19; 19/15; 15/24).

TABLE 63. IPPE(TRIGEX) CALCULATION OPTIONS

	Participant	Nuclear library	Energetic structure	Cell code	Cell Treatment	Control Rod Treatment	Code	Method
	IPPE	ABBN-93	26	TRIGEX	Homogeneous	**Homogeneous** <u>**without**</u> **corrections**	TRIGEX	Diffusion

Differences between calculated power deviation and measured power deviation (C - M in %)
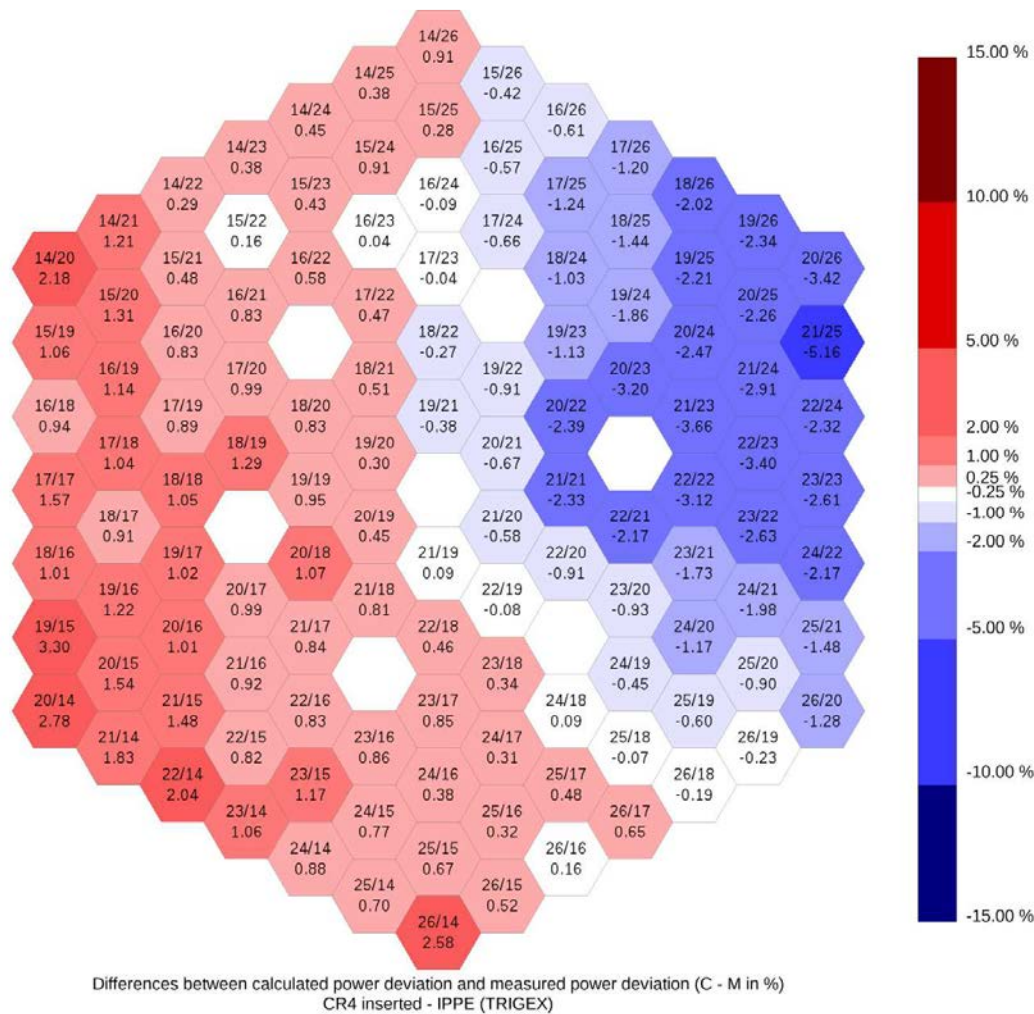CR4 inserted - IPPE (TRIGEX)

FIG. 260. Differences between calculated and measured power deviation (C-M in %) – CR#4 inserted – IPPE (TRIGEX).
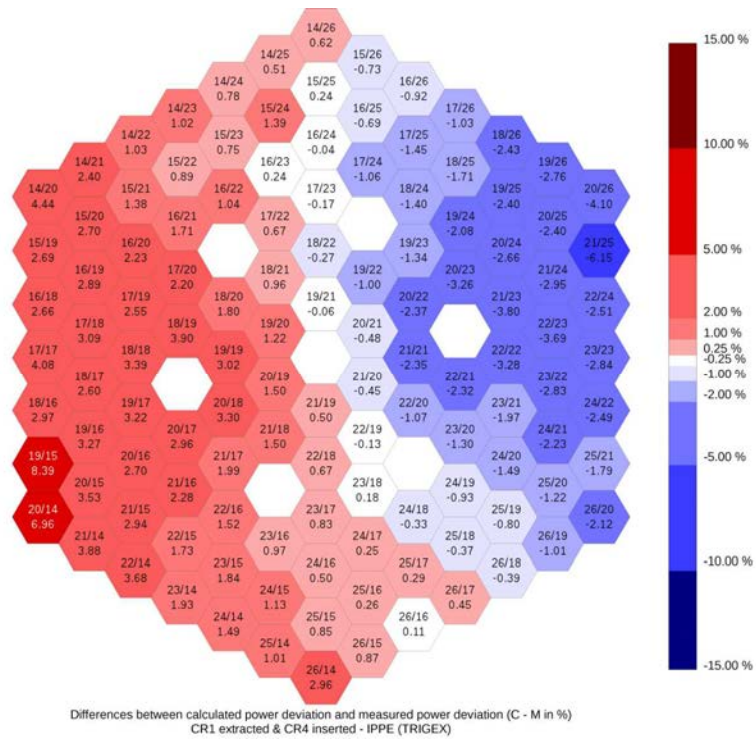
222

FIG. 261. Differences between calculated and measured power deviation (C-M in %) – CR#4 inserted & CR#1 extracted - IPPE (TRIGEX).
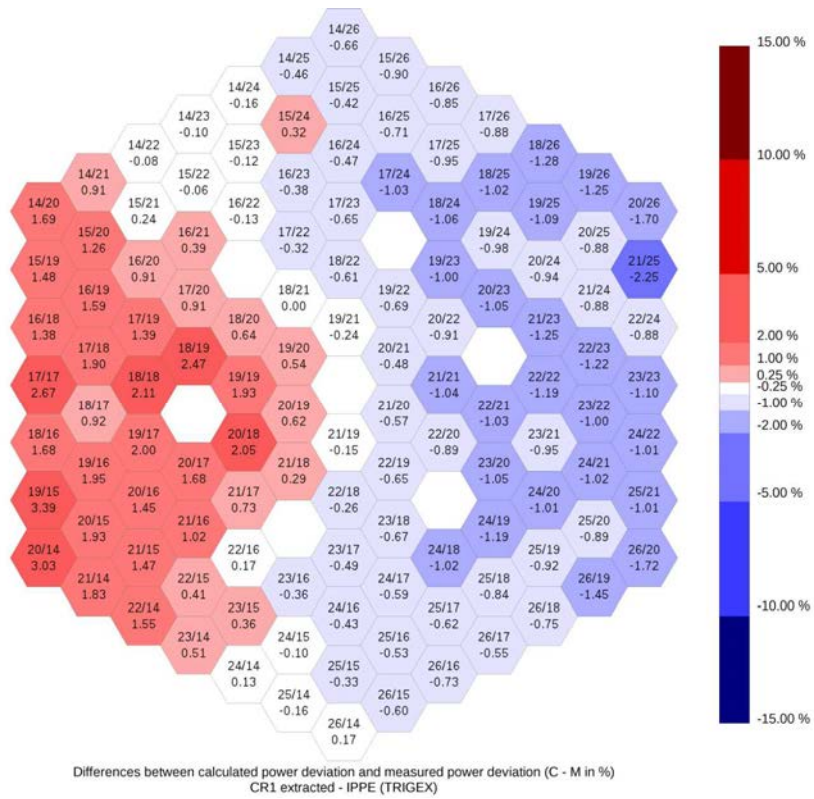

FIG. 262. Differences between calculated and measured power deviation (C-M in %) – CR#1 extracted – IPPE (TRIGEX).

8.4.2.6. IRSN (ERANOS)

Table 64 summarizes the calculation options used by IRSN to compute power deviation maps. Fig. 263–265 illustrate raw differences between calculated and measured power deviation. Calculated deviations are coherent with test values with raw differences mainly lower than 1%. However, an overestimation of the impact of the control rod shifting is notable for all steps of the test. Raw differences increase slightly near the core boundary due to the thermal hydraulic influence of hot sodium plenum. Strongest differences are located on blanket (14/20; 14/26; 20/26; 26/20; 26/14; 20/14) and internal shielding (21/25; 26/19; 19/15; 15/24).

TABLE 64. IRSN CALCULATION OPTIONS

	Participant	Nuclear library	Energetic structure	Cell code	Cell Treatment	Control Rod Treatment	Code	Method
	IRSN	ERALIB-1	33	ECCO	Het 2D	Het 2D + 2D SN transport calculation	ERANOS/VARIANT	Transport

Differences between calculated power deviation and measured power deviation (C - M in %)
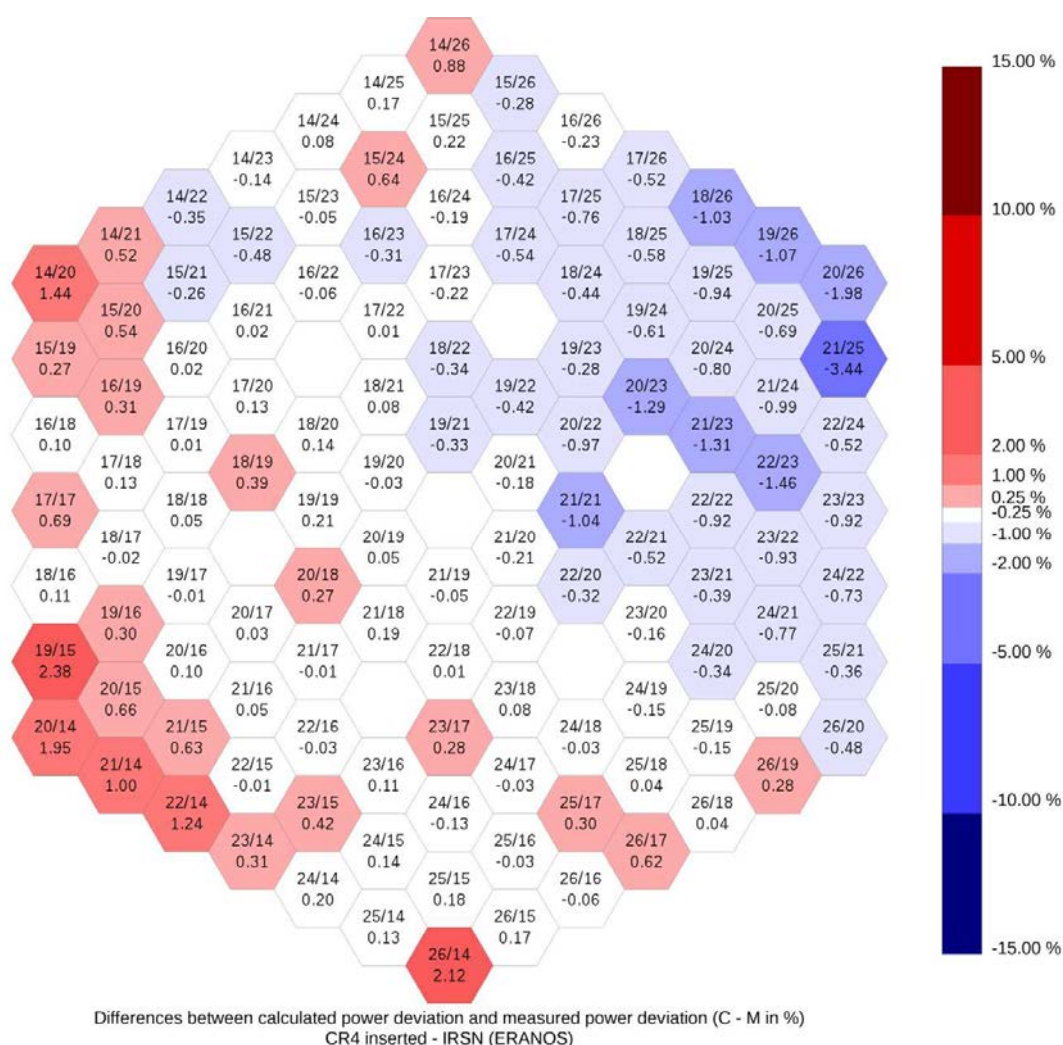CR4 inserted - IRSN (ERANOS)

FIG. 263. Differences between calculated and measured power deviation (C-M in %) – CR#4 inserted – IRSN (ERANOS).
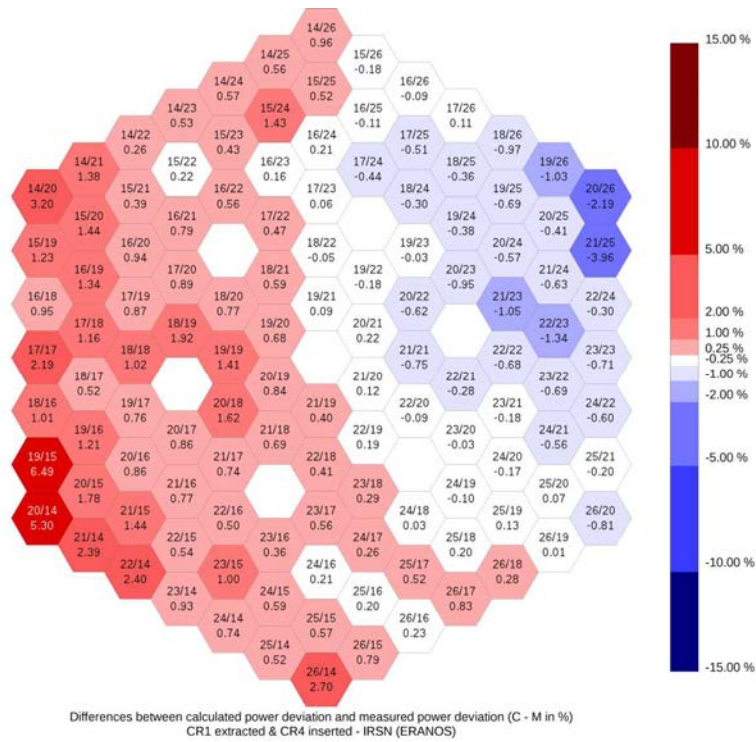
FIG. 264. Differences between calculated and measured power deviation (C-M in %) – CR#4 inserted & CR#1 extracted - IRSN (ERANOS).
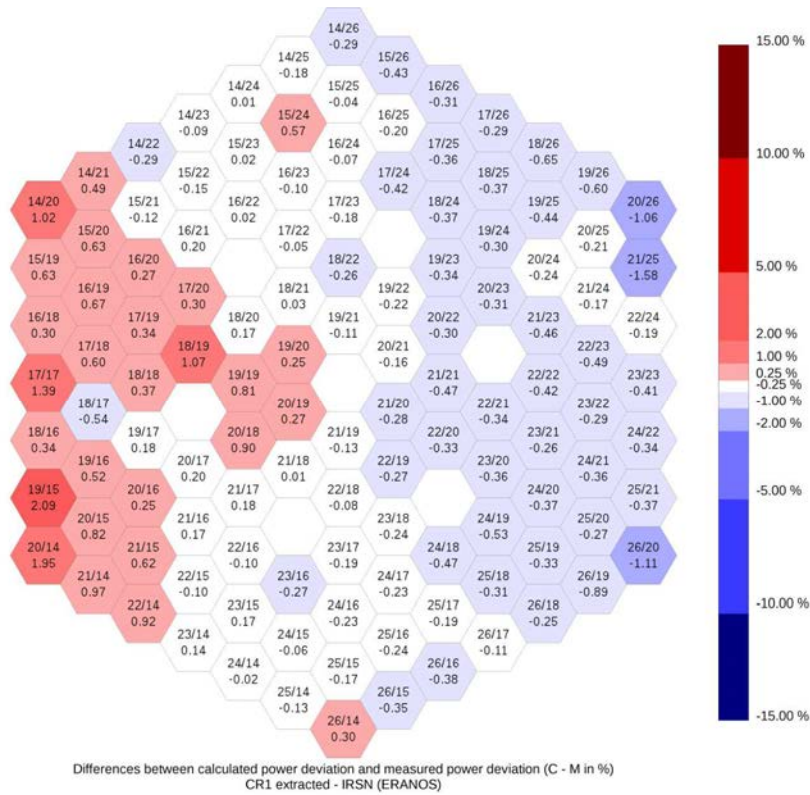

FIG. 265. Differences between calculated and measured power deviation (C-M in %) – CR#1 extracted – IRSN (ERANOS).

8.4.2.7. JAEA (DIF3D)

Table 65 summarizes the calculation options used by JAEA to compute power deviation maps. Fig 266–268 illustrate raw differences between calculated and measured power deviation. Calculated deviations are coherent with test values with raw differences mainly lower than 1%. However, an overestimation of the impact of the control rod shifting is notable for all steps of the test. Raw differences increase slightly near the core boundary due to the thermal hydraulic influence of hot sodium plenum. Strongest differences are located on blanket (14/20; 14/26; 20/26; 26/20; 26/14; 20/14) and internal shielding (21/25; 26/19; 19/15; 15/24).

TABLE 65. JAEA CALCULATION OPTIONS

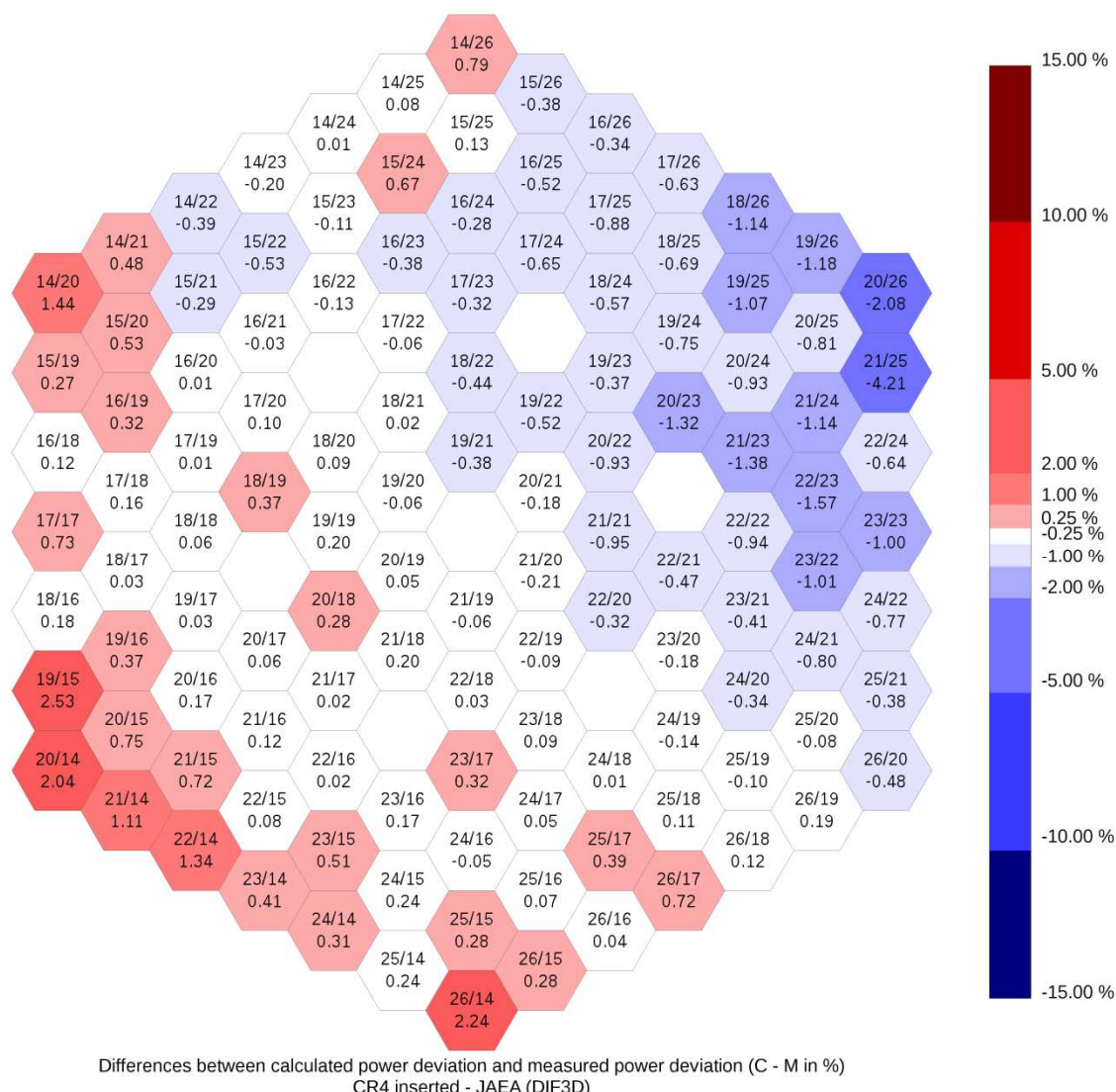|	Participant	Nuclear library	Energetic structure	Cell code	Cell Treatment	Control Rod Treatment	Code	Method
	JAEA	JENDL-3.3	70	SLAROM-UF	Het 1D	Het 1D + correction on cross-sections	DIF3D	Diffusion

FIG. 266. Differences between calculated and measured power deviation (C-M in %) – CR#4 inserted – JAEA (DIF3D).
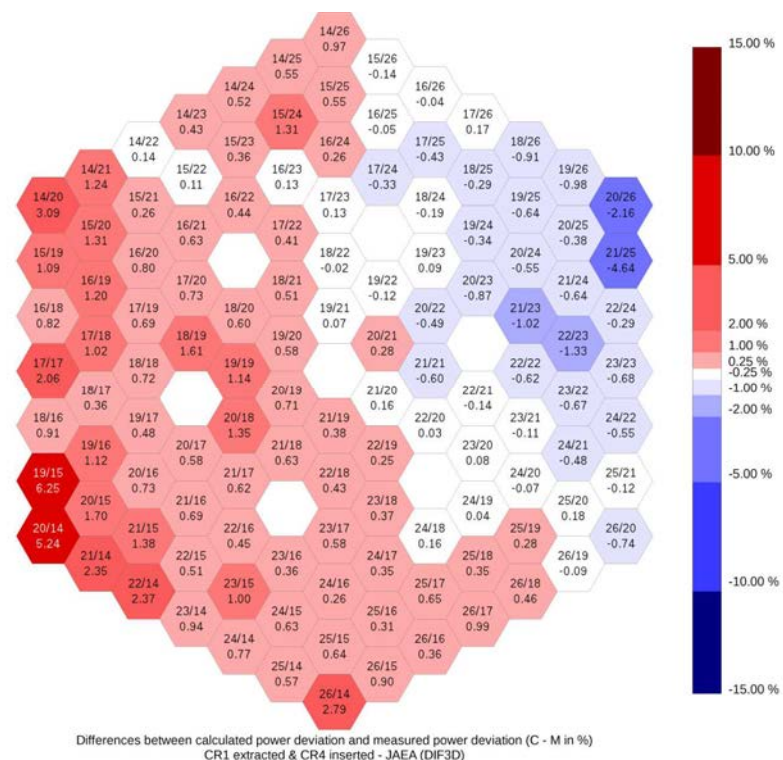
FIG. 267. Differences between calculated and measured power deviation (C-M in %) – CR#4 inserted & CR#1 extracted - JAEA (DIF3D).
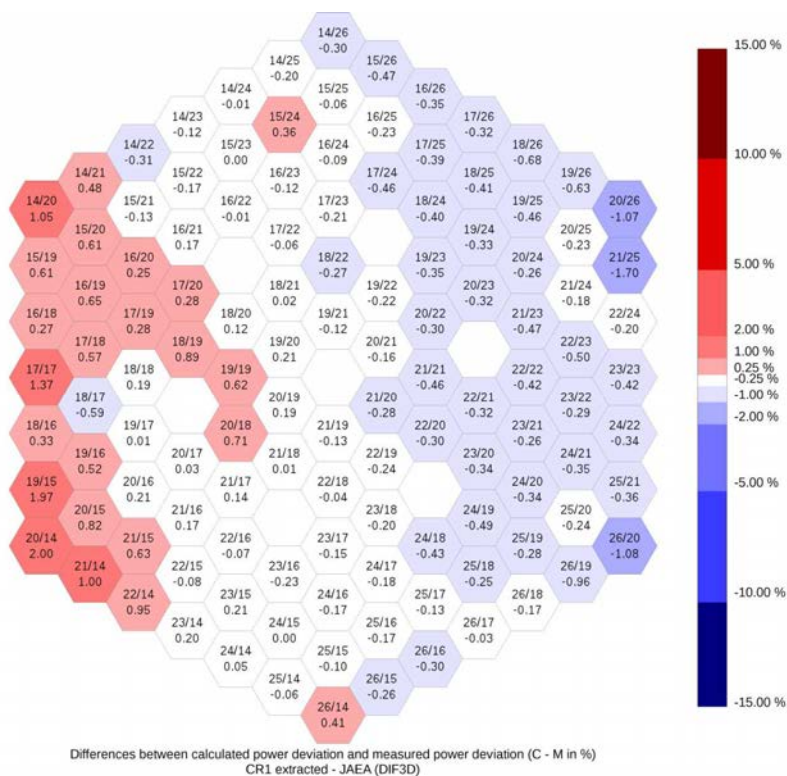

FIG. 268. Differences between calculated and measured power deviation (C-M in %) – CR#1 extracted – JAEA (DIF3D).

8.4.2.8. KIT (SIMMER IV)

Table 66 summarizes the calculation options used by KIT to compute power deviation maps with the code SIMMER-IV. Fig. 269–271 illustrate raw differences between calculated and measured power deviation. Raw differences between calculated and measured values are mainly lower than 4.5%, which is not negligible. A strong overestimation of the impact of the control rod shifting is notable for all steps of the test, even near stationary rods. However KIT has used the post-test isotopic compositions and the pre-test core loading plan. Raw differences increase near the core boundary due to the thermal hydraulic influence of hot sodium plenum. Strongest differences are located on blanket (14/20; 14/26; 20/26; 26/20; 26/14; 20/14) and internal shielding (21/25; 26/19; 19/15; 15/24).

TABLE 66. KIT CALCULATION OPTIONS

	Participant	Nuclear library	Energetic structure	Cell code	Cell Treatment	Control Rod Treatment	Code	Method
	KIT	KFKINR-26	11	SIMMER-IV	Homogeneous	Homogeneous without correction	SIMMER-IV/ THREDANT	Transport

Differences between calculated power deviation and measured power deviation (C - M in %)
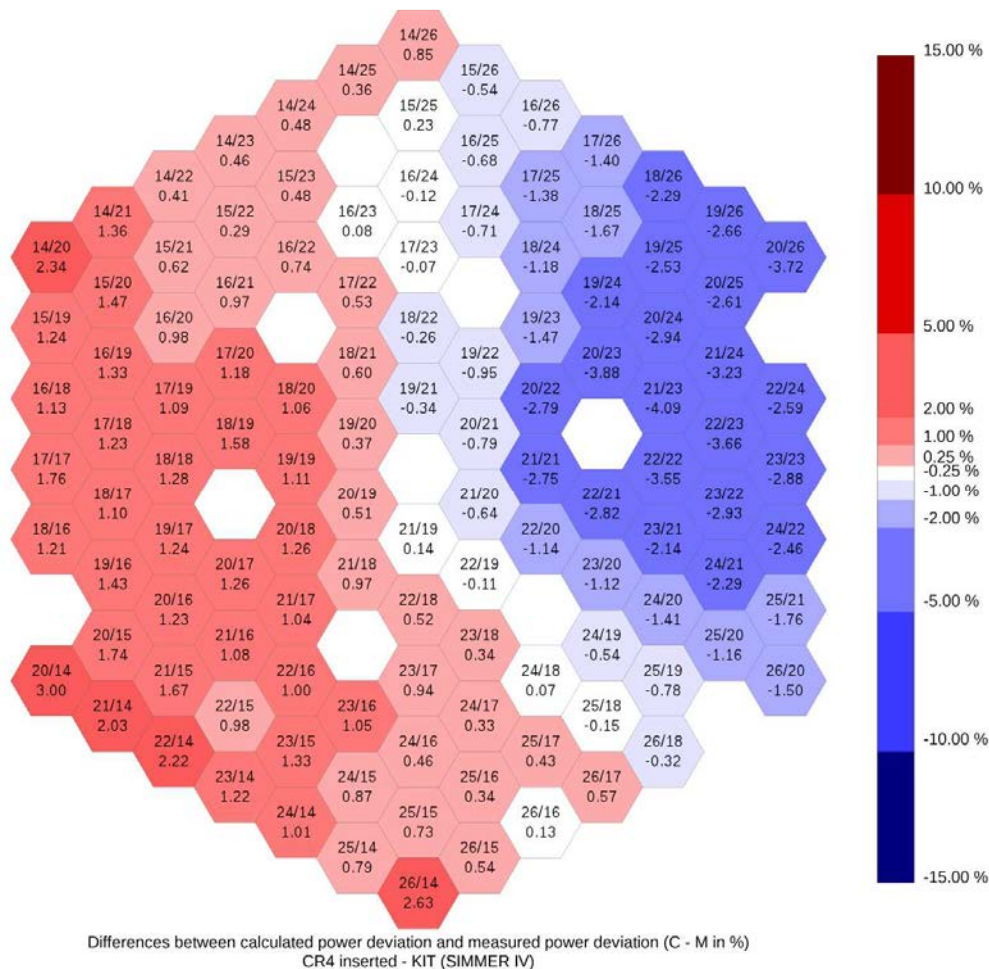CR4 inserted - KIT (SIMMER IV)

FIG. 269. Differences between calculated and measured power deviation (C-M in %) – CR#4 inserted – KIT (SIMMER IV).

Differences between calculated power deviation and measured power deviation (C - M in %)
CR1 extracted & CR4 inserted - KIT (SIMMER IV)

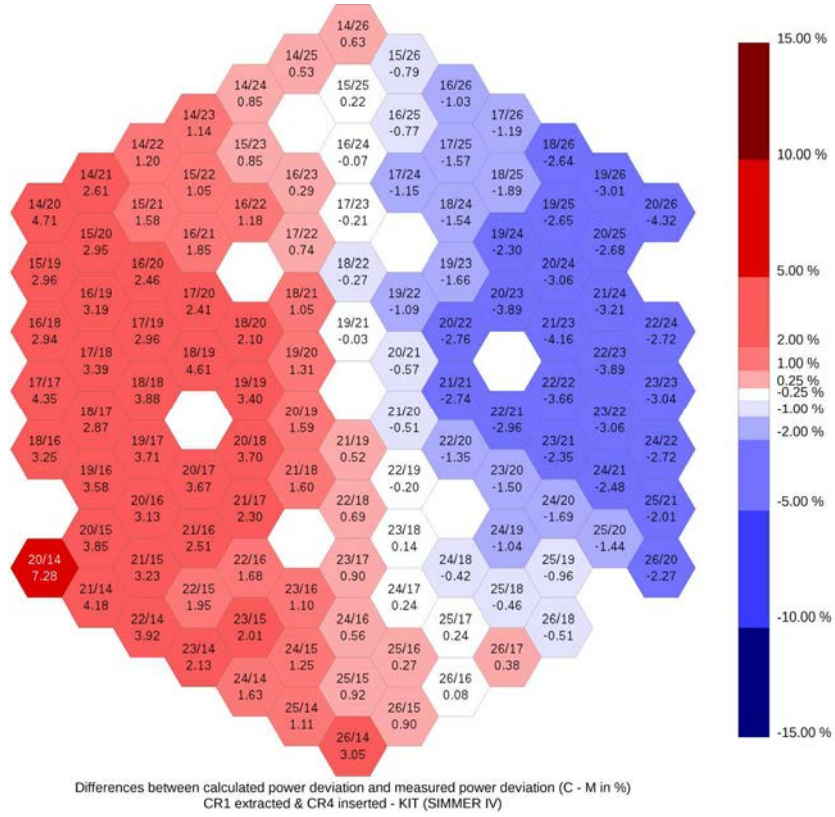*FIG. 270. Differences between calculated and measured power deviation (C-M in %) – CR#4 inserted & CR#1 extracted - KIT (SIMMER IV).*
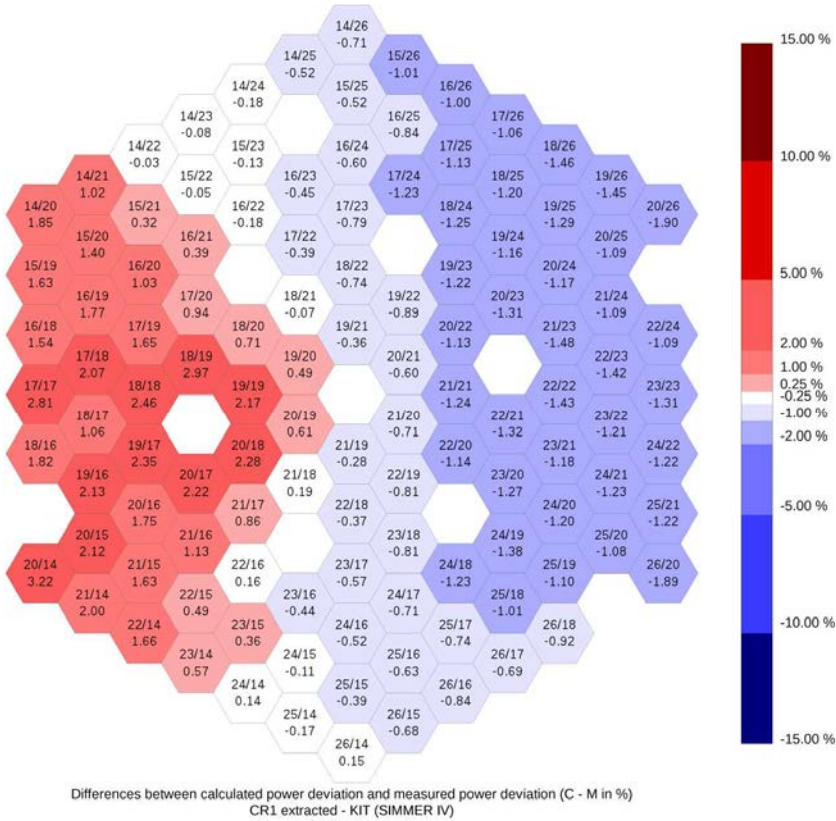

Differences between calculated power deviation and measured power deviation (C - M in %)
CR1 extracted - KIT (SIMMER IV)

FIG. 271. Differences between calculated and measured power deviation (C-M in %) – CR#1 extracted – KIT (SIMMER IV).

229

8.4.2.9. PSI (ERANOS)

Table 67 summarizes the calculation options used by PSI to compute power deviation maps. Fig. 272–274 illustrate raw differences between calculated and measured power deviation. Calculated deviations are quite coherent with test values with raw differences mainly lower than 2%. However, an overestimation of the impact of the control rod shifting is notable for all steps of the test, even near stationary rods. Raw differences increase slightly near the core boundary due to the thermal hydraulic influence of hot sodium plenum. Strongest differences are located on blanket (14/20; 14/26; 20/26; 26/20; 26/14; 20/14) and internal shielding (21/25; 26/19; 19/15; 15/24).

TABLE 67. PSI CALCULATION OPTIONS

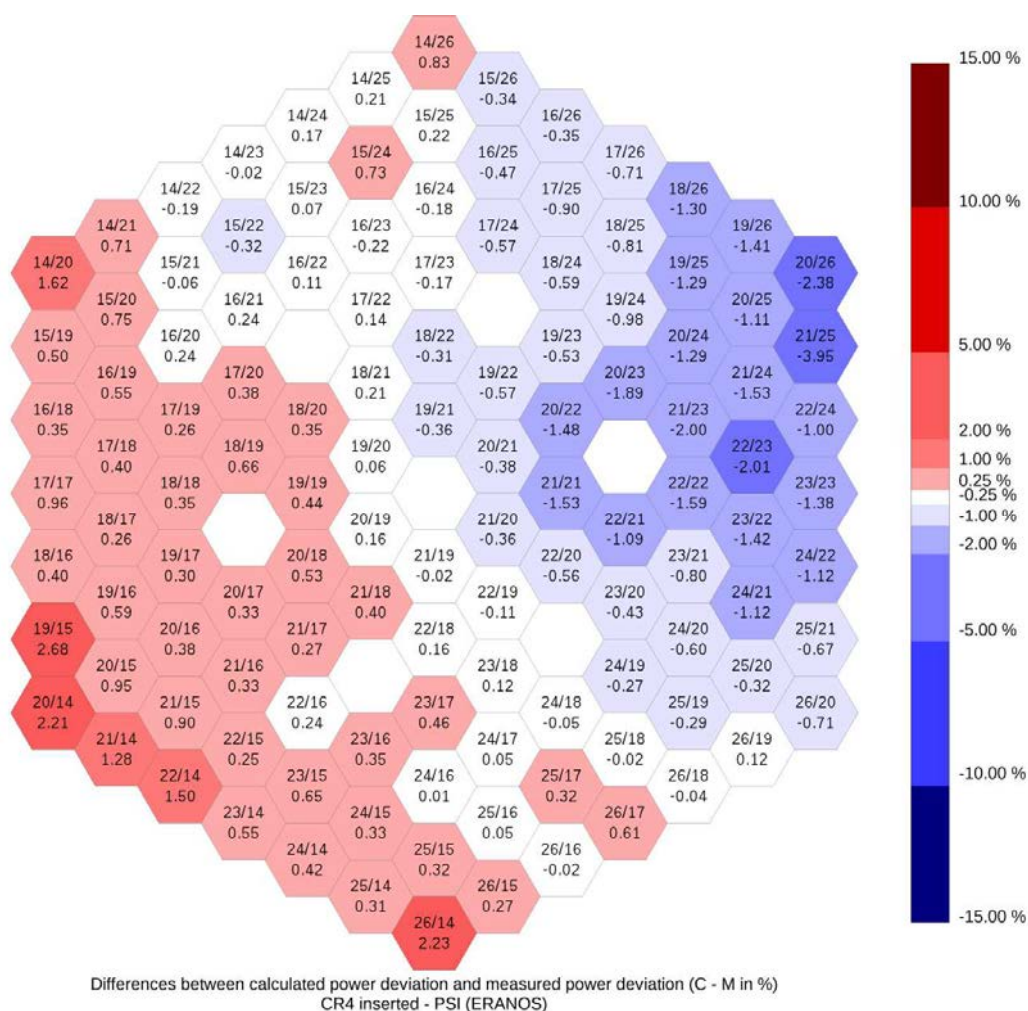|	Participant	Nuclear library	Energetic structure	Cell code	Cell Treatment	Control Rod Treatment	Code	Method
	PSI	ERALIB-1	33	ECCO	Het 2D	Het 2D without correction	ERANOS/VARIANT	Transport

FIG. 272. Differences between calculated and measured power deviation (C-M in %) – CR#4 inserted – PSI (ERANOS).

Differences between calculated power deviation and measured power deviation (C - M in %)
CR1 extracted & CR4 inserted - PSI (ERANOS)

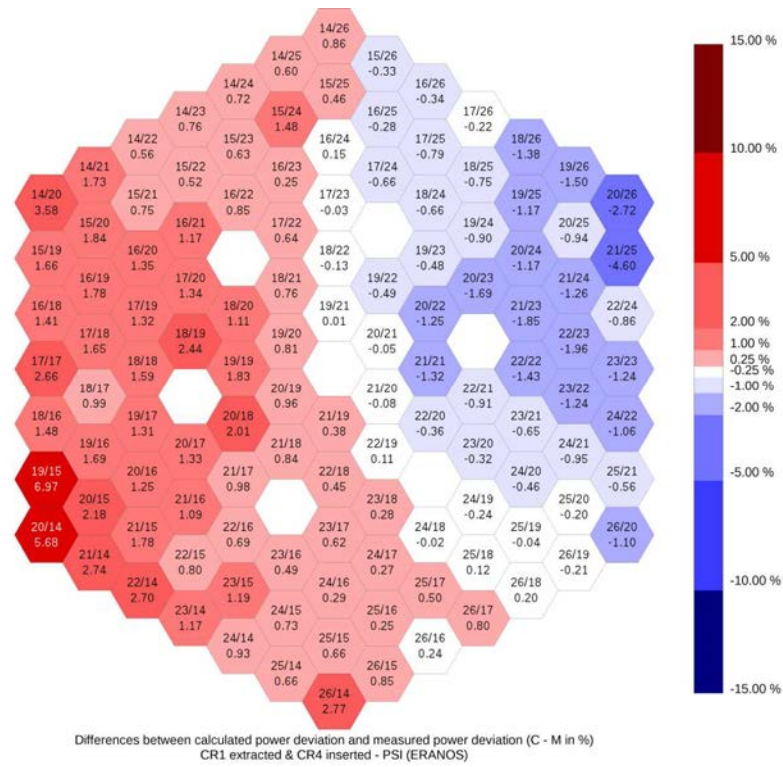*FIG. 273. Differences between calculated and measured power deviation (C-M in %) – CR#4 inserted & CR#1 extracted - PSI (ERANOS).*
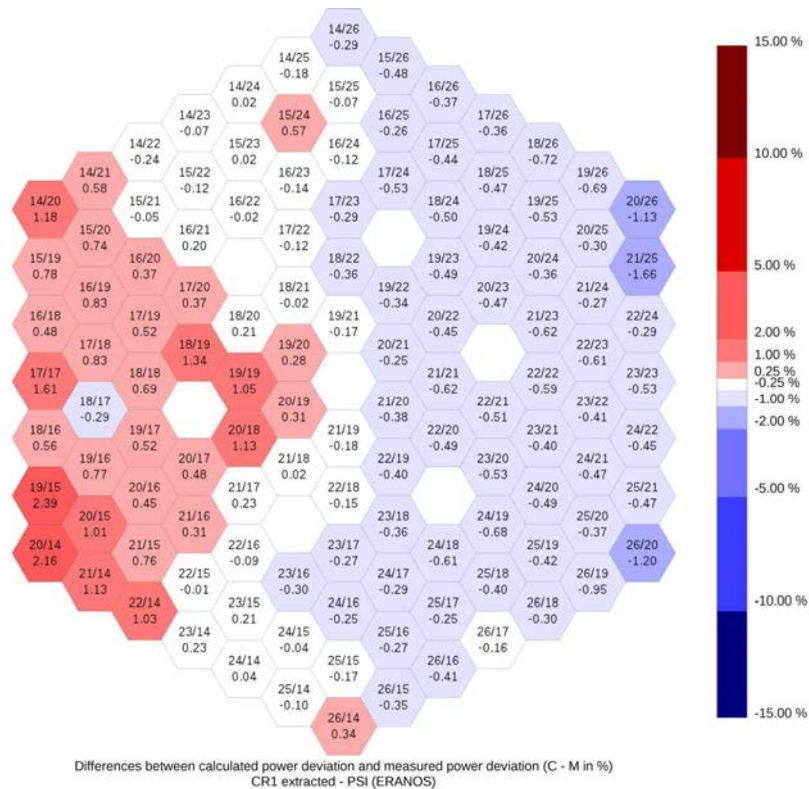

Differences between calculated power deviation and measured power deviation (C - M in %)
CR1 extracted - PSI (ERANOS)

FIG. 274. Differences between calculated and measured power deviation (C-M in %) – CR#1 extracted – PSI (ERANOS).

8.5. COMPARISONS OF FLUX ESTIMATIONS

Maximum fluxes in all the S/As for each step are shown in Table 68 and Fig. 275. The tendency of deviations among participants hardly depends on the steps. The standard deviation among the participants is around ±1% in all the steps. Maximum flux distribution in a S/A line from '(20, 8)' to '(20, 32)' for each step is shown from Fig. 276 to Fig. 280[14]. The deviations of the distributions also hardly depend on the steps. Deviation of the maximum flux for step 2 with respect to the Reference is shown in Fig. 281. The maximum increases are +8.4% ~ +10.1% and the maximum decreases are -9.7%~ -14.4% for the S/A line.

TABLE 68. MAXIMUM S/A FLUX FOR ALL CASES (×1015 N/CM2/S)

	Reference	Step-1	Step-2	Step-3	Step-4
CEA	3.94 (21-19)	4.02 (20- 19)	4.07 (20- 19)	3.99 (20- 19)	3.94 (21- 19)
IGCAR (ERANOS)	3.98 (21-19)	4.05 (20- 19)	4.10 (20- 19)	4.01 (20- 19)	3.98 (21- 19)
IGCAR (FARCOB)	4.02 (21-19)	4.10 (20- 19)	4.14 (20- 19)	4.06 (20-19)	4.02 (21-19)
IPPE	4.02 (21-19)	4.09 (20-18)	4.13 (19-19)	4.05 (19-19)	-
IRSN	3.98 (21-19)	4.05 (20-19)	4.10 (20-19)	4.02 (20-19)	4.00 (21-19)
JAEA	4.02 (21-19)	4.10 (20-19)	4.15 (20-19)	4.06 (20-19)	4.02 (21- 19)
KIT	3.90 (21-19)	4.00 (20-19)	4.06 (20-19)	3.96 (20-19)	3.90 (21-19)
PSI	3.95 (21-19)	4.07 (20-19)	4.11 (20-19)	3.99 (20-19)	-
Average	3.98	4.06	4.11	4.02	3.98
Standard Deviation: Absolute: Relative:	0.04 1.1%	0.04 0.9%	0.03 0.8%	0.04 0.9%	0.05 1.2%

Note: The numbers in the bracket indicates sub-assembly location

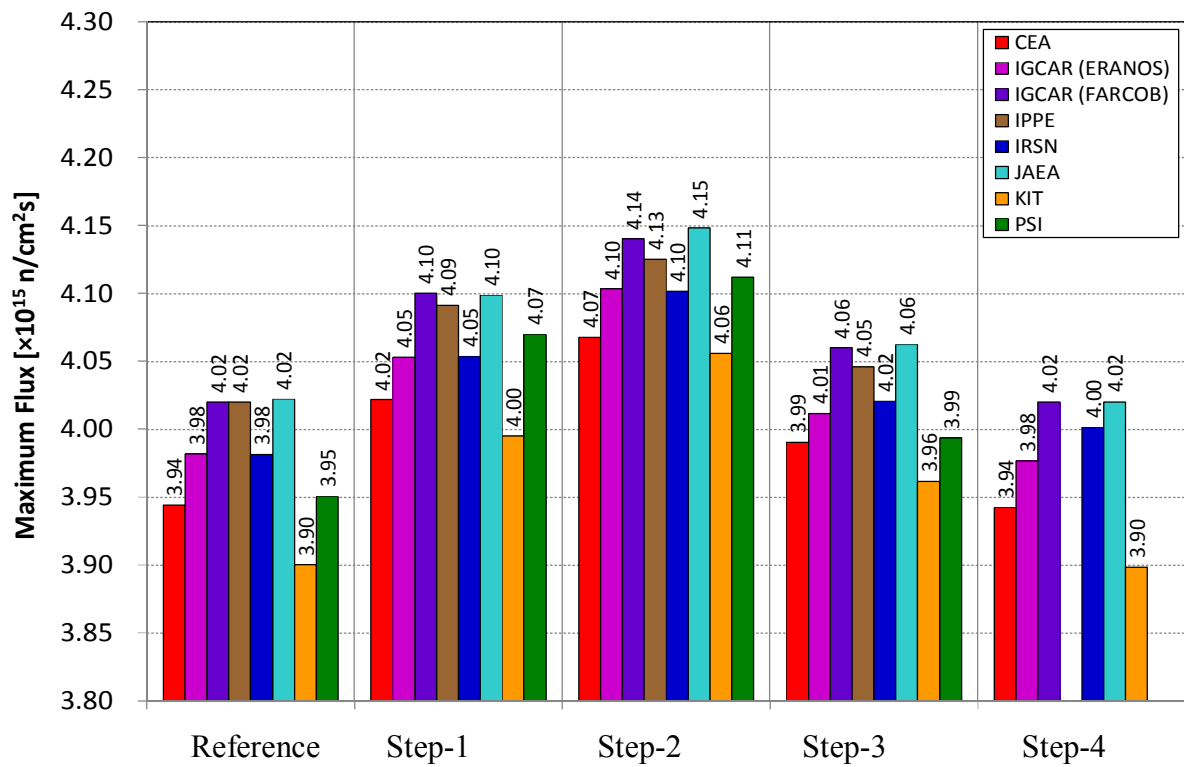---

[14] The graphs are drawn as a smoothed curve.

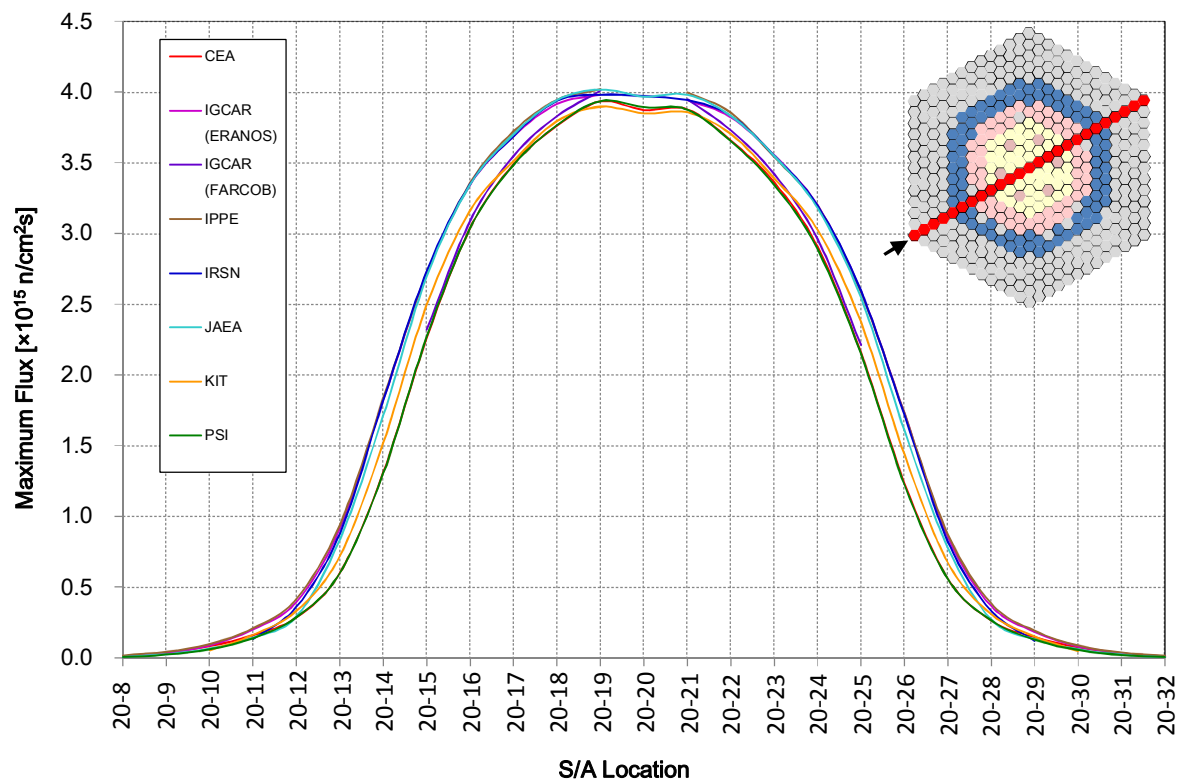*FIG. 275. Maximum flux value in all the S/As.*

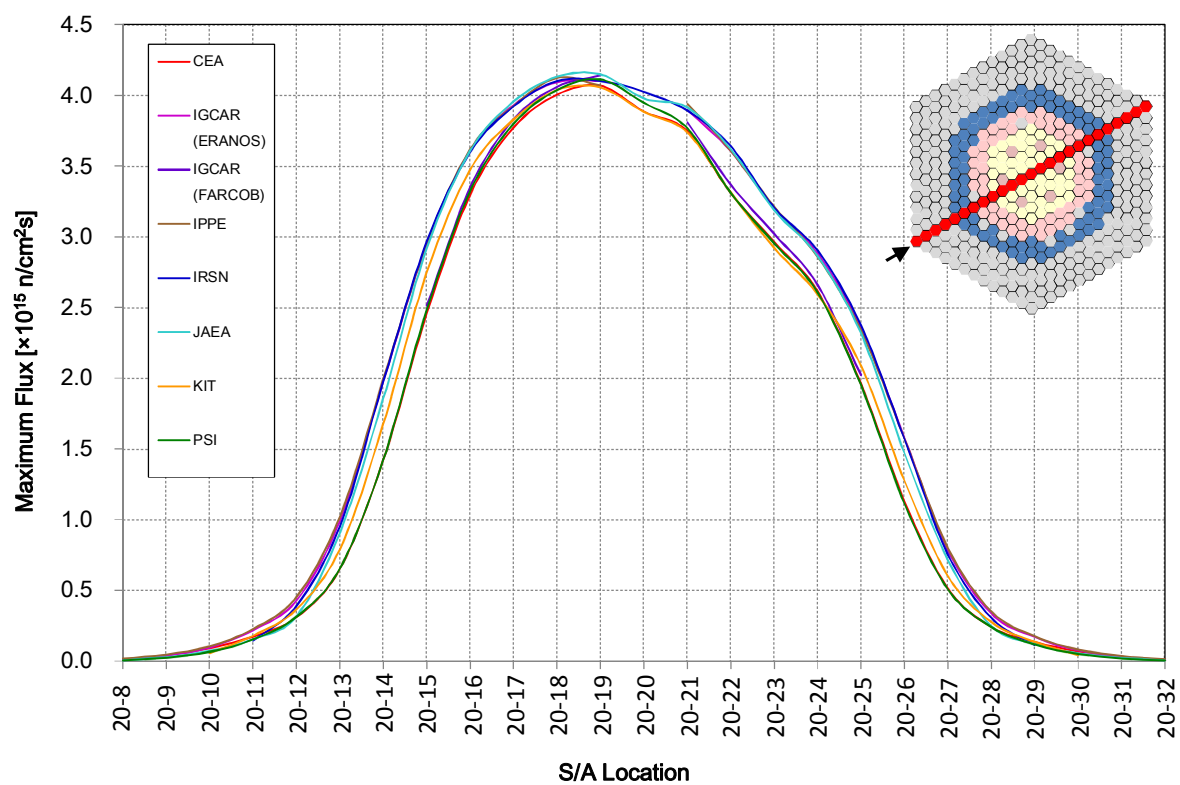*FIG. 276. Maximum flux distribution (reference).*

233

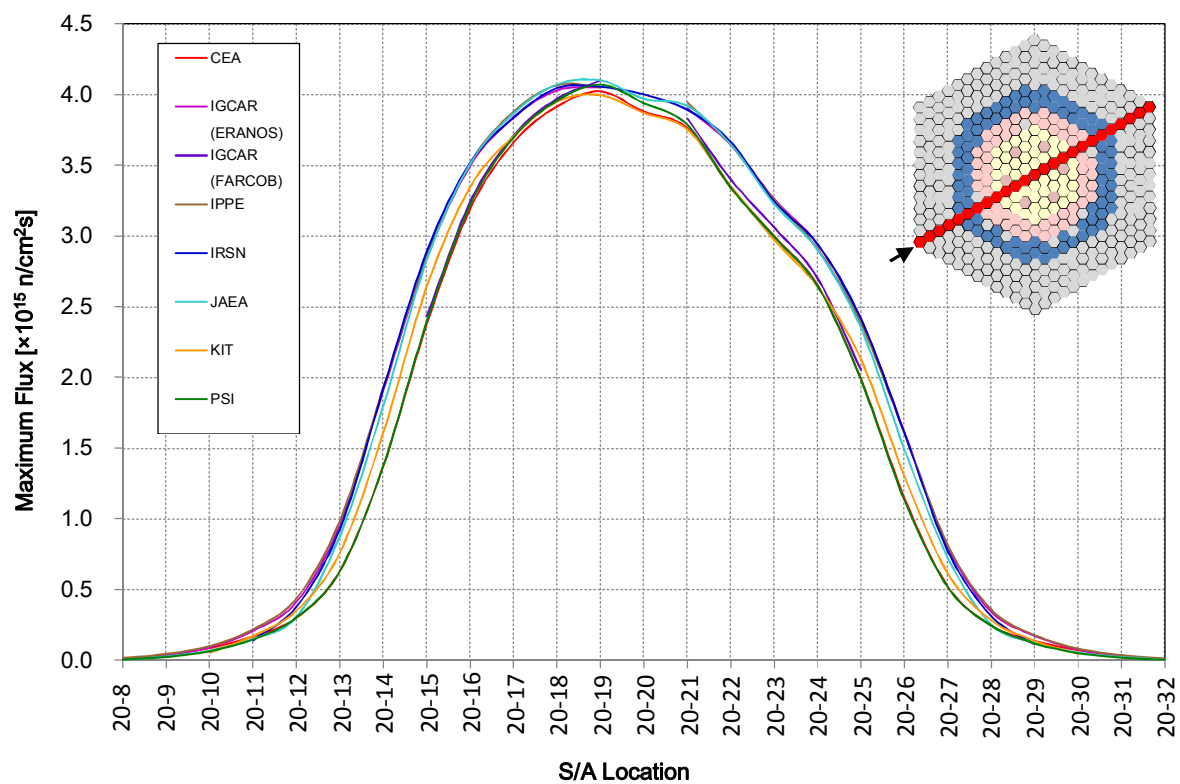*FIG. 277. Maximum flux distribution (step 1).*

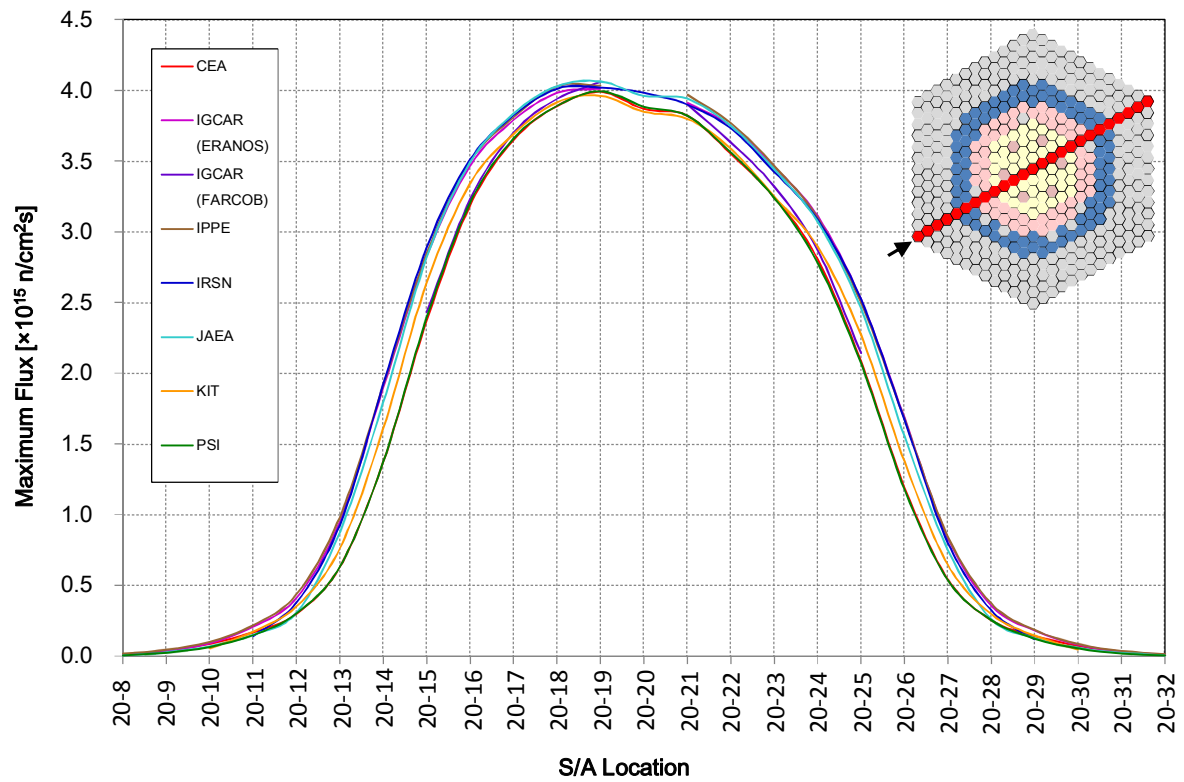*FIG. 278. Maximum flux distribution (step 2).*

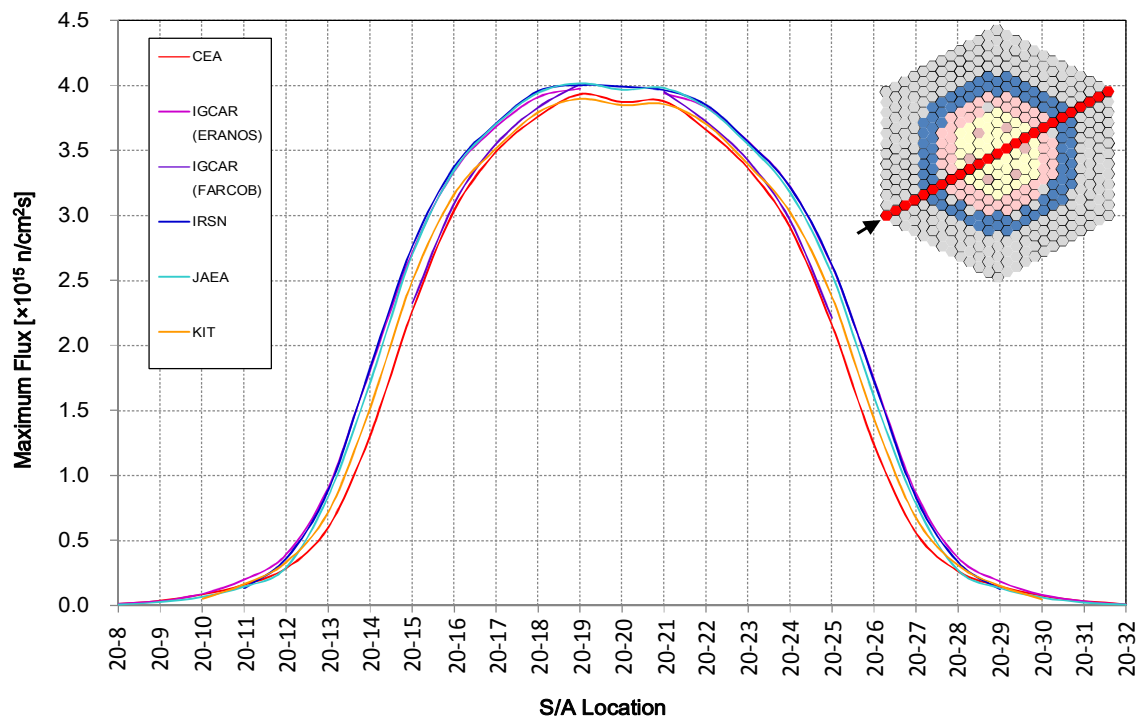*FIG. 279. Maximum flux distribution (step 3).*

FIG. 280. Maximum flux distribution (step 4).
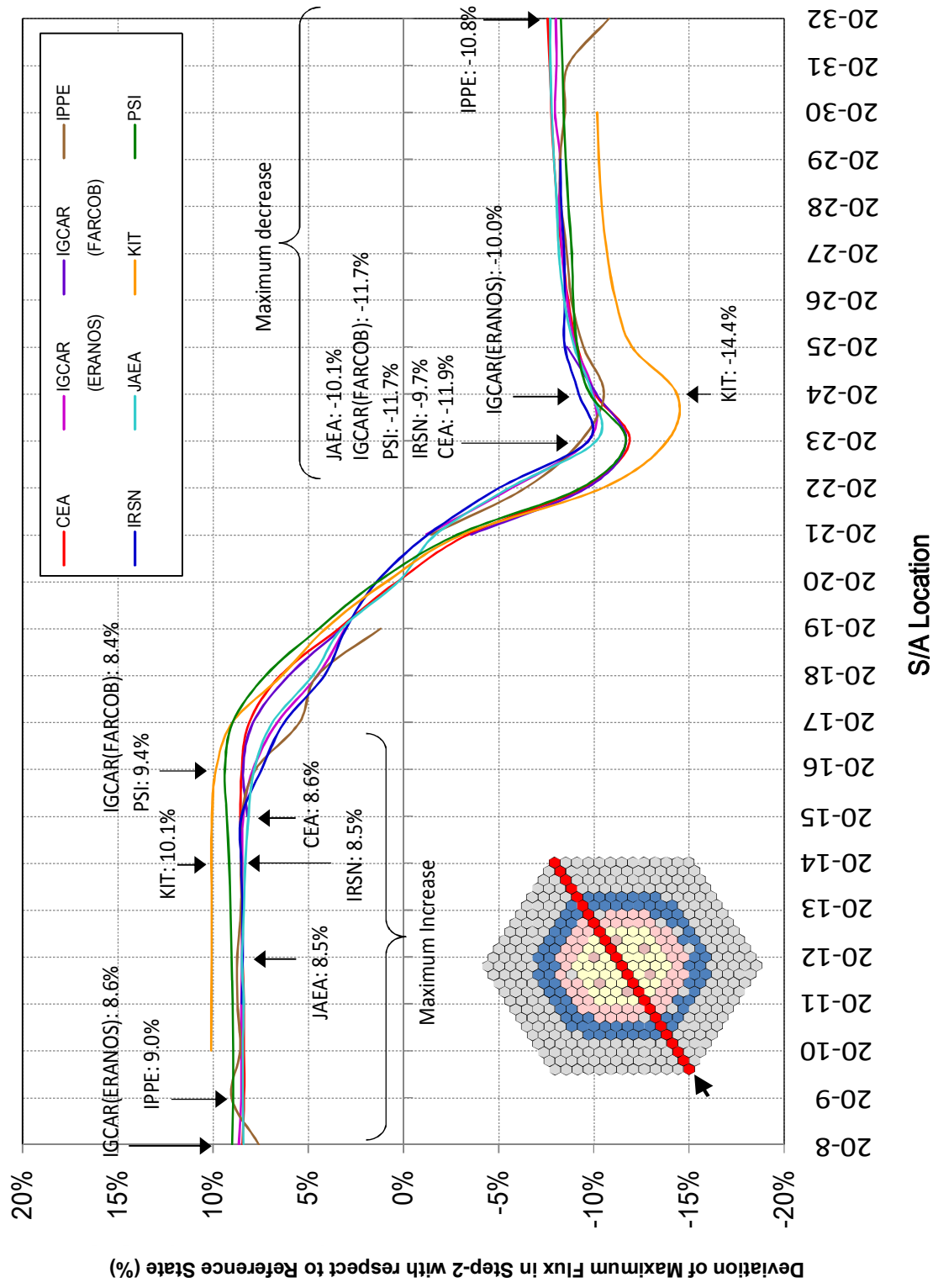
235

FIG. 281. Deviation of maximum flux in step 2 w.r.t reference state.

8.6. CONCLUSION

The analysis, within the framework of the benchmark, has shown a quite satisfactory agreement between calculated and measured relative parameters (reactivity swing, control rod efficiencies, power deviations) while discrepancies have been highlighted on raw parameters (reactivity and powers) due to imprecise benchmark assumptions (uncertainties on axial control rod positions due to core/control rod/vessel differential expansions, averaged core description in terms of nuclide compositions) and different calculation schemes (nuclear library, fission product treatment, core and cell solvers).

Comparisons of control rod efficiencies and power deviation maps have shown the necessity to use refined models to process control rod effective cross-sections in order to take into account self-shielding effects in absorber pins. Unsuited models can lead to notable overestimation up to 10% on Phénix control rod worth. Moreover, comparisons have revealed a low impact of nuclear library (ERALIB-1, JENDL-3.3, ABBN-93), core solvers (diffusion, transport, Monte-Carlo) and of the 'average compositions' assumption on relative core parameters.

The largest discrepancies between calculated and measured power deviations are linked to measurement problems. The systematic overestimation in power deviation calculations is due to the uncertainties associated with the core/vessel/control rod expansion empirical models used to determine axial control rod positions during the test. Finally, heat transfers and sodium mixing phenomena strengthened by sodium turbulent flows in the hot plenum disturb power balances on breeder, shielding and outer core sub-assemblies and degrade the comparisons. The assessment of such complex thermal-hydraulic phenomena requires time-consuming CFD simulation and was not included in this benchmark exercise.

9. CONCLUSION

Before the definitive shutdown of the prototype sodium cooled fast reactor Phénix, occurred in 2009, the French Commissariat à Energie Atomique et aux Energies Alternatives (CEA) performed several tests in order to gain additional knowledge on the operation of sodium cooled reactors. Within this experimental programme, the 'Control Rod Withdrawal' (CRW) test was carried out with the aim of measuring the impact of control rod insertion/withdrawal on local power distribution in the core. The overall goal of this test was to gather data on the possible scenario of an inadvertent withdrawal of a control rod, which could induce a general power increase and local deformations of the power shape, and, consequently, possible fuel melting and clad failure. A complementary objective of the test was the improvement of neutronics codes used for sodium cooled reactors design and analysis.

The CRW test was performed in two phases: an off-power test with control rods worth measurement by using balancing method, and an on-power test with the progressive shift of two of the six control rods while preserving stable the power and the sodium flow.

Thanks to the CEA availability to open the results of the tests to international cooperation, in 2007 the IAEA launched the CRP on 'Control rod withdrawal and sodium natural circulation tests performed during the Phénix end-of-life experiments', which focused on benchmark analyses of the experimental results obtained during the Phénix EOL tests. In particular, the benchmark on the control rod withdrawal test allowed CRP participants to investigate and

verify several neutronics calculation codes currently used in the analyses of liquid metal cooled fast reactors, as far as their capability to correctly evaluate the control rod efficiency, also called the reactivity S-curve, and the core power deformation due to insertion and withdrawal of control rods. The benchmark analyses were carried out by comparing the results of the calculations with the large amount of experimental data obtained in Phénix. The evaluation of a large set of plant parameters allowed performing accurate code-to-code comparisons, with the overall purpose to understand the critical open issues and recognize gaps which will require further investigations.

The first part of the CRP was dedicated to perform blind calculations, in order to compare results of each participant without any reference in terms of experimental data. Objectives of the calculations were the estimation of the control rods worth, integral worth value and S-curve, the value of K_{eff} for each step of the test, the average and maximum flux per sub-assembly and power distributions for each step of the test. Concerning the control rod worth, even though a good coherence on S-curves shape was observed, two groups of integral control rod worth values - about 9,000 pcm and about 7,600 pcm - were individuated. The reason of such difference can be ascribed to the utilization or not of a special treatment applied to the control rods cross-sections generation. A relevant dispersion was observed on absolute reactivity calculated for each step of the test, explained by the different calculation methods and nuclear data libraries used by the CRP participants. A very good consistency was noted on power calculations and power deviations. A quite good coherence between results was observed also for the flux calculations, and all the participants gave similar results for the evaluation of the maximum flux deviation profile.

The second phase of the CRP was devoted to the improvement of the neutronic models developed in the first phase on the basis of the experimental data provided by CEA. For this second step of the analysis, transport theory was used by most of the participants except IGCAR and JAEA, which performed diffusion theory estimations by applying transport theory correction on core reactivity. Monte Carlo estimations were made by the IPPE. Quite satisfying agreement was reached between calculated and measured parameters (reactivity swing, power deviations), while discrepancies were highlighted on raw parameters (reactivity, powers).

For the total worth, similarly to the blind calculations, two groups of results were observed. The difference between the two groups can be explained on the basis of the control rod model treatment; participants belonging to the first group used either a Monte-Carlo code (IPPE) or performed a correction for control rod cross-sections. On the contrary, participants belonging to the second group used deterministic codes (transport and diffusion) without a special treatment for control rods. These comparisons underlined the need of using precise calculation schemes to process self-shielded cross-sections of absorbing media with deterministic codes. The S-curves shape was found to be almost the same for all the participants; the only differences were found on the absolute values of the differential efficiency which are due to the differences on the total control rods worth.

As for reactivity calculations, discrepancies were found to be caused by several reasons, including the use of average core description, uncertainties on axial control rod position, discrepancies on control rod efficiencies, choice of core solvers and discrepancies coming from nuclear data and cell calculation methods. Special attention will have to be paid to the treatment of fission products reactivity worth.

The systematic overestimation in power deviation calculations was due to the uncertainties associated with the core/vessel/control rod expansion empirical models used to determine axial control rod positions during the test. Heat transfers and sodium mixing phenomena

strengthened by sodium turbulent flows in the hot plenum disturb power balances and degrade the comparisons. The assessment of such complex thermal-hydraulic phenomena requires time-consuming CFD simulation and was not included in this benchmark exercise

In conclusion, it is definitely possible to state that the CRP offered to participants an important occasion to further improve the understanding of several key aspects of sodium cooled fast reactors core physics. In particular, by comparing the achieved results between participants and with the experimental data, analyzing sources of uncertainties and individuating causes of discrepancies, the benchmark exercises allowed improving neutronic calculation methods and tools which will be used for the design and analysis of innovative fast reactor cores.

REFERENCES

[1] INTERNATIONAL ATOMIC ENERGY AGENCY, Benchmark Analyses on the Natural Circulation Test Performed during the PHENIX End-of-life Experiments, IAEA-TECDOC-1703, IAEA, Vienna (2013).

[2] SAUVAGE, J. F., Phénix: 35 years of history: the heart of a reactor, CEA-EDF, May 2004.

[3] VASILE, A., et al., "The Phénix final tests", Proc. of Int. Congress on Advances in Nuclear Power Plants - ICAPP 2011, Nice, France, May 2–5, 2011, pp. 11298

[4] PASCAL, V., PRULHIERE, G., VANIER, M., FONTAINE, B., "Main results of Phénix core physics tests", Proc. of Int. Congress on Advances in Nuclear power Plants - ICAPP 2012, Chicago, USA, June 24–28, 2012, pp. 12027.

[5] GAUTHÉ, P., "IAEA CRP on natural convection test in Phénix", Technical Report No. CEA/DEN/CAD/DER/SESI/LSMR/NT DO 4, CEA, France, 2010.

[6] PASCAL, V., PRULHIERE, G., VANIER, M., FONTAINE, B., Interpretation of the control rod withdrawal test in the sodium-cooled fast reactor Phénix, Nuclear Science and Engineering, **175** (2013), pp. 109–123.

[7] MC^2-2 (Fast Reactor Cross-section Processing Codes), http://www.ne.anl.gov/codes/mc2-2/.

[8] LEE, C. H., YANG, W. S., "MC^2-3: Multigroup cross-section generation code for fast reactor analysis", Technical Report No. ANL/NE-11-41 Rev.1, Argonne National Laboratory, Argonne, USA, 2012.

[9] ETOE-2 (Fast Reactor Cross-section Processing Codes), http://www.ne.anl.gov/codes/etoe-2/ .

[10] DIF3D (Diffusion and Transport Theory Codes) http://www.ne.anl.gov/codes/dif3d/.

[11] RIMPAULT, G., et. al., "The ERANOS code and data system for fast reactor neutronic analyses", Proc. of PHYSOR 2002, Seoul, Republic of Korea, October 7–10, 2002.

[12] DORIATH, J.Y., MCCALLIEN, C.W., KIEFHABER, E., WEHMANN, U., RIEUNIER, J. M., "ERANOS: The advanced European system of codes for reactor physics calculations", Proc. of the Int. Conf. on Mathematical Methods and Super Computing in Nuclear Computations, Karlsruhe, Germany, April 1993.

[13] RUGGIERI, J. M., et al., "ERANOS 2.1: International code system for GEN IV fast reactor analysis", Proc. of ICAPP06, Reno, NV, USA, June 4–8, 2006.

[14] FORT, E., et al., "Realisation and performance of the adjusted nuclear data library ERALIB1 for calculating fast reactor neutronics", Proc. of the Physics of Fuel Cycles and Advanced Nuclear Systems - PHYSOR 1996, Mito, Ibaraki, Japan, September 16–20, 1996.

[15] FORT, E., et al., Improved performances of the fast reactor calculational system ERANOS-ERALIB1 due to improved a priori nuclear data and consideration of additional specific integral data, Ann. Nucl. Energy, **30** (2003), pp. 1879–1898.

[16] RIMPAULT, G., "Algorithmic features of the ECCO cell code for treating heterogeneous fast reactor sub-assemblies", Proc. Int. Conf. on Mathematics and Computations, Reactor Physics, and Environmental Analyses, Portland, Oregon, USA, May 1–5, 1995.

[17] ROWLANDS, J. L., EATON, C. R., "The spatial averaging of cross-sections for use in transport theory calculations with an application to control rod fine homogenisation", Proc. of a Specialists' Meeting on Homogenisation Methods in Reactor Physics, Lugano, Switzerland, 13–15 November, 1978.

[18]   PALMIOTTI, G., et al., "BISTRO: Optimised two dimensional Sn transport code", Proc. of the International Topical Meeting on Advances in Reactor Physics, Mathematics and Computations, CEC & OECD/NEA, Paris, France, 27–30 April, 1987.

[19]   DEVAN, K., M. ALAGAN, BACHCHAN A., MOHANAKRISHNAN, P., CHELLAPANDI, P., CHETAL, S. C., A comparative study of FARCOB and ERANOS-2.1 neutronics codes in predicting the Phénix control rod withdrawal end-of-life experimental results, Nuclear Engineering and Design, **245** (2012), pp. 89–98.

[20]   MOHANAKRISHNAN, P., Development and validation of a fast reactor core burnup code-FARCOB, Ann. Nucl. Energy, **35** (2008), pp.158–166.

[21]   MANTUROV, G. N., "ABBN-93 Group Data Library Part-I: Nuclear data for the calculations of neutron and photon radiation functions", INDC (CCP)-409/L, IAEA, Vienna, 1997.

[22]   MOHANAKRISHNAN, P., "COHINT - A computer code to treat control rod heterogeneity and its application to fast reactor core analysis", Technical Report No. IGC-130, IGCAR, Kalpakkam, India, 1992.

[23]   HAZAMA, T., KITANO, A., KISHIMOTO, Y., Criticality evaluation for the Monju restart core, Nucl. Technol., **179** (2012), No. 2, pp. 250–265.

[24]   TAKANO, K., FUKUSHIMA, M., HAZAMA, T., SUZUKI, T., Control rod worth evaluation for the Monju restart core, Nucl. Technol., **179** (2012), No. 2, pp.266–285.

[25]   MOURI, T., MARUYAMA, S., HAZAMA, T., SUZUKI, T., Isothermal temperature coefficient evaluation for the Monju restart core, Nucl. Technol., **179** (2012), No. 2, pp. 286–307.

[26]   SHIBATA, K., et al., Japanese evaluated nuclear data library version 3 revision-3: JENDL-3.3, J. Nucl. Sci. Technol., **39** (2002), No. 11, pp.1125–1136.

[27]   HAZAMA, T., CHIBA, G., SATO, W., NUMATA, K., "SLAROM-UF; Ultra-fine group cell calculation code for fast reactor, Version 20090113", Technical report No. JAEA-Review 2009-003, JAEA, Japan, 2003.

[28]   OAK RIDGE NATIONAL LABORATORY, "DIF3D 7.0: Code system for solving finite difference diffusion theory problems", RSICC, CCC-649, March 1997.

[29]   ISHIKAWA, M., et al., "Development of a standard data base for FBR core nuclear design (VIII) - Compilation of JUPITER analytical results -", Technical Report No. PNC TN9400 97-009, Japan, 1997.

[30]   SUGINO, K., IWAI, T., "Advances in methods of commercial FBR core characteristics analyses - investigations of a treatment of the double-heterogeneity and a method to calculate homogenized control rod cross-sections -", Technical Report No. PNC TN9410 98-067, Japan, 1998.

[31]   KITADA, T., KOSAKA, S., TAKEDA, T., HOJUYAMA, T., YANO, M., New control rod homogenization method for fast reactors, J. Nucl. Sci. Technol., **31** (1994), No. 7, pp. 647.

[32]   OAK RIDGE NATIONAL LABORATORY, "DANTSYS3.0: One-, two-, and three-dimensional, multigroup, discrete ordinates transport code system", RSICC CCC-547, 1997.

[33]   TAKANO, K., MOURI, T., KISHIMOTO, Y., HAZAMA, T., "IAEA benchmark calculations on control rod withdrawal test performed during PHÉNIX end-of-life experiments – JAEA's calculation results", Proc. of PHYSOR 2014, Kyoto, Japan, September 28–October 3, 2014.

[34] BOHL, W. R., LUCK, L. B., "SIMMER-II: A computer program for LMFBR disrupted core analysis", Technical Report No. LA-11415-MS, Los Alamos National Laboratory, USA, 1990.

[35] TOBITA, Y., KONDO, SA., YAMANO, H., FUJITA, S., MORITA, K., MASCHEK, W., COSTE, P., PIGNY, S., LOUVET, J., CADIOU, T., "The development of SIMMER-III, an advanced computer program for LMFR safety analysis", Proc. of the IAEA/NEA Technical Meeting on Use of Computational Fluid Dynamics (CFD) Codes for Safety Analysis of Reactor Systems Including Containment, Pisa, Italy, November, 11–14, 2002.

[36] YAMANO, H., FUJITA, S., TOBITA, Y., KAMIYAMA, K., KONDO, SA., MORITA, K., FISCHER, E.A., BREAR, D.J., SHIRAKAWA, N., CAO, X., SUGAYA, M., MIZUNO, M., HOSONO, S., KONDO, T., MASCHEK, W., KIEFHABER, E., BUCKEL, G., RINEISKI, A., FLAD, M., SUZUKI, T., COSTE, P., PIGNY, S., LOUVET, J., CADIOU, T., "SIMMER-III: A computer program for LMFR core disruptive accident analysis, Version 3. A model summary and program description", Technical Report No. JNC TN9400 2003-071, JNC Report, Japan Atomic Energy Agency, Japan, 2003.

[37] YAMANO, H., FUJITA, S., TOBITA, Y., KONDO, SA., MORITA, K., SUGAYA, M., MIZUNO, M., HOSONO, S., KONDO, T., "SIMMER-IV: A three-dimensional computer program for LMFR core disruptive accident analysis, Version 2. A model summary and program description", Technical Report No. JNC TN9400 2003-070, JNC Report, Japan Atomic Energy Agency, 2003.

[38] YAMANO, H., FUJITA, S., TOBITA, Y., SATO, I., NIWA, H., Development of a three-dimensional CDA analysis code: SIMMER-IV, and its first application to reactor case. Nucl. Eng. Des. **238** (2008), pp. 66–73.

[39] YAMANO, H., TOBITA, Y., FUJITA, S., A three-dimensional neutronics-thermohydraulics simulation of core disruptive accident in sodium-cooled fast reactor. Nucl. Eng. Des. **239** (2009), pp. 1673–1681.

[40] BOHL, W.R., WILHELM, D., BERTHIER, J., PARKER, F.R., "The AFDM program: scope and significance", Proc. of the International Fast Reactor Safety Meeting, Snowbird, Utah, USA, vol. 2, August, 12–16, 1990, pp. 155–164.

[41] ALCOUFFE, R.E., BAKER, R.S., BRINKLEY, F.W., MARR, D.R., O'DELL, R.D., WALTERS, W.F., "DANTSYS: A Diffusion Accelerated Neutral Particle Transport Code System", Technical Report no. LA-12969-M, LANL Report, Los Alamos National Laboratory, USA, 1995.

[42] BUCKEL, G., HESSELSCHWERDT, E., KIEFHABER, E., KLEINHEINS, S., MASCHEK, W., "A new SIMMER-III version with improved neutronics solution algorithms", Technical Report No. FZKA 6290, FZK Report, Forschungszentrum Karlsruhe, Germany, 1999.

[43] VARAINE, F., et. al., "IAEA CRP on Phénix end of life tests control rod withdrawal" Technical Report No. CEA/DEN/CAD/DER/SPRC/LEDC, CEA – Cadarache Research Centre, France, 2009.

[44] COMMISSARIAT À L'ENERGIE ATOMIQUE ET AUX ENERGIES ALTERNATIVES, "IAEA CRP on Phénix end of life tests, control rod withdrawal test, data for post-calculations", CEA Cadarache Research Centre, France, 2010.

[45] PALMIOTTI, G., et al., "VARIANT: Variational anisotropic nodal transport for multidimensional cartesian and hexagonal geometry calculation" Technical Report No. ANL-95/40, Argonne National Laboratory, USA, 2005.

[46]   SPORE, J.W., et al., "TRAC-M/FORTRAN 90 (version 3.0) Theory Manual", Technical Report No. NM 87545 LA-UR-00-910, Los Alamos National Laboratory, Los Alamos, USA, 2000.

[47]   DOWNAR, T., XU, Y., KOZLOWSKI, T., "PARCS v2.7 U.S. NRC Core Neutronics Simulator" USER MANUAL. Purdue University, USA, 2006.

[48]   POUNDERS, J., BANDINI, B., XU, Y., DOWNAR, T., "Calculation of accurate hexagonal discontinuity factors for PARCS", International RELAP5 Users' seminar, Report No. B-T-3711, Idaho Falls, USA, November 7 – 9, 2007.

[49]   SMITH, K.S., Assembly homogenization techniques for light water reactor analysis, Progress in Nuclear Energy, **17** (1986), pp. 303 – 335.

[50]   JAAG, S., KIEFHABER, E., "Definition of a suitable project route for CAPRA neutronic calculations", Technical Report No. 32.23.01, FZK (Forschungszentrum Karlsruhe), Germany, 1997.

[51]   GABRIELLI, F., RINEISKI, A., et al., "Study of the effect of heterogeneity of the control rods in the Phénix reactor", Proc. Int. Conf. PHYSOR 2014, Kyoto, Japan, September 28 – October 3, 2014.

[52]   PALMIOTTI, G., RIEUNIER, J. M., GHO, C., SALVATORES, M., Optimized two dimensional Sn transport (BISTRO), Nucl. Sc. and Eng., **104** (1990), pp. 26-33.

[53]   KONING, A., et. al., "The JEFF-3.1 Nuclear Data Library", JEFF Technical Report No. 21, NEA/OECD, Paris, France, 2006.

[54]   MIKITYUK, K., PELLONI, S., CODDINGTON, P., BUBELIS, E., CHAWLA, R., FAST: an advanced code system for fast reactor transient analysis, Annals of Nuclear Energy **32** (2005), pp. 1613–1631.

[55]   MIKITYUK, K., KREPEL, J., PELLONI, S., CHENU, A., PETKEVICH, P., CHAWLA, R., FAST code system: review of recent developments and near-future plans, Journal of Engineering for Gas Turbines and Power, **132** (2010), 102915.

[56]   CHENU A., ADAMS, R., MIKITYUK, K., CHAWLA, R., Analysis of selected Phénix EOL tests with the FAST code system – Part I: Control-rod-shift experiments, Annals of Nuclear Energy, **49 (**2012), pp. 182–190.

[57]   CHENU, A., MIKITYUK, K., CHAWLA, R., Analysis of selected Phénix EOL tests with the FAST code system - Part II: Unprotected phase of the Natural Convection Test, Companion paper, Ann. Nucl. Energy **49** (2012), pp. 191–199.

LIST OF ABBREVIATIONS

ANL	Argonne National Laboratory
AURN	Arrêt d'Urgence par Réactivité Négative
CA	Control Assembly
CDA	Core Disruptive Accident
CEA	Commissariat à l'Energie Atomique et aux Energies Alternatives
CR	Control Rod
CRBR	Clinch River Breeder Reactor
CRP	Coordinated Research Project
CRS	Control Rod Shift
CRW	Control Rod Withdrawal
EBR	Experimental Breeder Reactor
EDF	Electricité de France
EFR	European Fast Reactor
EOL	End Of Life
FBR	Fast Breeder Reactor
FBTR	Fast Breeder Test Reactor
GEN IV	Generation IV
GIF	Generation IV International Forum
IGCAR	Indira Gandhi Centre for Atomic Research
IPPE	Institute of Physics and Power Engineering
IRSN	Institut de Radioprotection et de Sûreté Nucléaire
JAEA	Japan Atomic Energy Agency
KIT	Karlsruhe Institute of Technology
LAB	Lower Axial Blanket
MOX	Mixed Oxide
PFBR	Prototype Fast Breeder Reactor
PRISM	Power Reactor Innovative Small Module
PSI	Paul Scherrer Institute
RCM	Research Coordination Meeting
S/A	Sub-Assembly
SG	Steam Generator
TWG-FR	Technical Working Group on Fast Reactors
UAB	Upper Axial Blanket

ULOF   Unprotected LOss of Flow

CONTRIBUTORS TO DRAFTING AND REVIEW

Adams, R.	Paul Scherrer Institut, Switzerland
Chawla, R.	Paul Scherrer Institut, Switzerland
Chellapandi, P.	Indira Gandhi Centre for Atomic Research (IGCAR), India
Chenu, A.	Paul Scherrer Institut, Switzerland
Devan, K.	Indira Gandhi Centre for Atomic Research (IGCAR), India
Fontaine, B.	Commissariat à l'énergie atomique et aux énergies alternatives (CEA), France
Herrenschmidt, A.	Commissariat à l'énergie atomique et aux énergies alternatives (CEA), France
Kiefhaber, E.	Karlsruhe Institute of Technology, Germany
Kriventsev, V.	Karlsruhe Institute of Technology, Germany
Maschek, W.	Karlsruhe Institute of Technology, Germany
Mikityuk, K.	Paul Scherrer Institut, Switzerland
Monti, S.	International Atomic Energy Agency
Pascal, V.	Commissariat à l'énergie atomique et aux énergies alternatives (CEA), France
Prulhiere, G.	Commissariat à l'énergie atomique et aux énergies alternatives (CEA), France
Rineiski, A.	Karlsruhe Institute of Technology, Germany
Semenov, M.	Institute of Physics and Power Engineering, Russian Federation
Stanculescu, A.	International Atomic Energy Agency
Taiwo, T.	Argonne National Laboratory, U.S.A.
Takano, K.	Japan Atomic Energy Agency, Japan
Tiberi, V.	Institut de Radioprotection et de Sûreté Nucléaire (IRSN), France
Toti, A.	International Atomic Energy Agency
Vanier, M.	Commissariat à l'énergie atomique et aux énergies alternatives (CEA), France
Varaine, F.	Commissariat à l'énergie atomique et aux énergies alternatives (CEA), France
Vasile, A.	Commissariat à l'énergie atomique et aux énergies alternatives (CEA), France

ORDERING LOCALLY

In the following countries, IAEA priced publications may be purchased from the sources listed below or from major local booksellers.

Orders for unpriced publications should be made directly to the IAEA. The contact details are given at the end of this list.

AUSTRALIA
DA Information Services
648 Whitehorse Road, Mitcham, VIC 3132, AUSTRALIA
Telephone: +61 3 9210 7777 • Fax: +61 3 9210 7788
Email: books@dadirect.com.au • Web site: http://www.dadirect.com.au

BELGIUM
Jean de Lannoy
Avenue du Roi 202, 1190 Brussels, BELGIUM
Telephone: +32 2 5384 308 • Fax: +32 2 5380 841
Email: jean.de.lannoy@euronet.be • Web site: http://www.jean-de-lannoy.be

CANADA
Renouf Publishing Co. Ltd.
5369 Canotek Road, Ottawa, ON K1J 9J3, CANADA
Telephone: +1 613 745 2665 • Fax: +1 643 745 7660
Email: order@renoufbooks.com • Web site: http://www.renoufbooks.com

Bernan Associates
4501 Forbes Blvd., Suite 200, Lanham, MD 20706-4391, USA
Telephone: +1 800 865 3457 • Fax: +1 800 865 3450
Email: orders@bernan.com • Web site: http://www.bernan.com

CZECH REPUBLIC
Suweco CZ, spol. S.r.o.
Klecakova 347, 180 21 Prague 9, CZECH REPUBLIC
Telephone: +420 242 459 202 • Fax: +420 242 459 203
Email: nakup@suweco.cz • Web site: http://www.suweco.cz

FINLAND
Akateeminen Kirjakauppa
PO Box 128 (Keskuskatu 1), 00101 Helsinki, FINLAND
Telephone: +358 9 121 41 • Fax: +358 9 121 4450
Email: akatilaus@akateeminen.com • Web site: http://www.akateeminen.com

FRANCE
Form-Edit
5 rue Janssen, PO Box 25, 75921 Paris CEDEX, FRANCE
Telephone: +33 1 42 01 49 49 • Fax: +33 1 42 01 90 90
Email: fabien.boucard@formedit.fr • Web site: http://www.formedit.fr

Lavoisier SAS
14 rue de Provigny, 94236 Cachan CEDEX, FRANCE
Telephone: +33 1 47 40 67 00 • Fax: +33 1 47 40 67 02
Email: livres@lavoisier.fr • Web site: http://www.lavoisier.fr

L'Appel du livre
99 rue de Charonne, 75011 Paris, FRANCE
Telephone: +33 1 43 07 50 80 • Fax: +33 1 43 07 50 80
Email: livres@appeldulivre.fr • Web site: http://www.appeldulivre.fr

GERMANY
Goethe Buchhandlung Teubig GmbH
Schweitzer Fachinformationen
Willstätterstrasse 15, 40549 Düsseldorf, GERMANY
Telephone: +49 (0) 211 49 8740 • Fax: +49 (0) 211 49 87428
Email: s.dehaan@schweitzer-online.de • Web site: http://www.goethebuch.de

HUNGARY
Librotade Ltd., Book Import
PF 126, 1656 Budapest, HUNGARY
Telephone: +36 1 257 7777 • Fax: +36 1 257 7472
Email: books@librotade.hu • Web site: http://www.librotade.hu